Full-Scale Testing of a New Double-Beam Coupling Beam (DBCB) with a Simplistic Reinforcing Layout

Final Report

by:

Kyoungsub Park, Ph.D., Postdoctoral Research Fellow
Shih-Ho (Simon) Chao, Professor, Ph.D., P.E.

The University of Texas at Arlington
Department of Civil Engineering

July 2023

University of Texas Arlington | Department of Civil Engineering

EXECUTIVE SUMMARY

Tests were carried out on a series of double-beam coupling beams (DBCBs), including two full-scale DBCBs and one half-scale DBCB. The beams had aspect ratios (beam span/beam depth, l_n/h) of either 2.4 or 3.2 and were tested with or without a slab. These specimens were tested to study the seismic behaviors and performance of double-beam coupling beams (DBCBs) using the design procedure proposed by Choi and Chao (Choi et al., 2020). In recent half-scale tests using Gr. 60 rebars, double-beam coupling beams (DBCBs) have been demonstrated to be a promising alternative to diagonally reinforced concrete coupling beams (DCBs). These tests, conducted by Choi et al. (2018, 2020), showed that the seismic performance of DBCBs is equivalent to that of DCBs, even without the use of diagonal reinforcements. This has the potential to significantly reduce reinforcement congestion and construction difficulties. This study aimed to investigate various aspects of DBCBs under fully reversed cycling loading. The objectives were: (1) to verify a proposed DBCB design procedure, (2) to examine the size effect on the spacing of transverse reinforcement, (3) to evaluate the performance of DBCBs made with high-strength rebars (ASTM A706 Gr. 80) and determine their required development length, (4) to assess the size and location of utility duct openings, and (5) to examine the effect of the slab on the performance of the DBCBs.

According to the experimental results, all three specimens that were reinforced with high-strength rebars (ASTM A706 Gr. 80) showed excellent ductility and stable performance until their shear strength decreased significantly. Specifically, the half-scale DBCB specimen with a slab demonstrated a stable hysteresis loop up to a chord rotation of 8%, with only a slight loss of strength. The two full-scale DBCB specimens also exhibited stable hysteresis loops up to a chord rotation of 6% without any significant loss of strength. No noticeable size effect associated with hoop spacing was observed in full-scale specimens. However, the larger longitudinal rebars used in the full-scale specimens experienced inelastic buckling after a 6% chord rotation. This was not observed in the half-scale specimens. While the full-scale 2.4 aspect ratio DBCB specimen without middle layer longitudinal reinforcement performed satisfactorily, it is highly recommended to include middle layer of longitudinal reinforcement in each individual beam to improve the confinement of the concrete core and impede the crack propagation.

The longitudinal high-strength reinforcement (Gr. 80), which was anchored in the end concrete blocks representing wall piers, experienced higher strains compared to the previous half-scale specimens that used conventional reinforcement (Gr. 60) (Choi. et al, 2018). However, the strain distributions in the Gr. 80 reinforcement were very similar to those of the Gr. 60 reinforcement. This implies that the development length defined as 60% of that required by ACI 18.8.5.3 is valid for Gr. 60 conventional steel, as well as with Gr. 80 high-strength steel. The full-scale specimens were tested with horizontally inserted circular PVC pipes for utility ducts, and the results indicate that it is possible to place four 3-inch-diameter circular penetrations simultaneously at both ends of a DBCB, as well as at the midspan of the upper and lower beams, without compromising its shear strength, stiffness, or ductility. The addition of a slab changes the elastic neutral axis and the location of the maximum horizontal shear in the gross section, which is above the unreinforced concrete strip (UCS) located at the beam's mid-height (Naaman and Chao, 2022). This causes a slight delay in the concentration of diagonal shear cracks within mid-height UCS. However, this delay has no effect on the separation of the UCS at larger rotations. On the other hand, the slab provides additional confinement to the coupling beam, reducing the width of diagonal shear cracks. A comparison of half-scale specimens with and without a slab reveals that the slab improves the shear strength and energy dissipation capacity, resulting in a "fuller" hysteresis loop for DBCBs.

No evidence suggests that Gr. 80 rebars have any negative impact on shear strength and ductility compared to Gr. 60 rebars. The test results show that both full-scale DBCB specimens with aspect ratios of 2.4 and 3.2 reached an ultimate chord rotation of 6%, which is approximately equivalent to the rotational demand of an MCE level earthquake, before their strengths decreased below 80% of the peak shear force. Additionally, both specimens achieved a peak shear stress of around $10\sqrt{f_c'}$ psi ($0.83\sqrt{f_c'}$ MPa). The experimental results support the conclusions of the previous half-scale DBCB tests and suggest that a coupling beam with an aspect ratio between 2.4 and 3.2 can employ non-diagonal reinforcement layouts and up to four circular openings (two at the beam ends and two at the mid-span of the beam) without compromising its seismic performance.

Lastly, an updated design flowchart and a comprehensive design example based on research findings in this study are included.

ACKNOWLEDGEMENTS

The American Concrete Institute (ACI) Foundation and Concrete Reinforcing Steel Institute (CRSI) Foundation provided primary financial support for this experimental program. We express our heartfelt appreciation to Ann Masek, Executive Director at ACI Foundation, and Amy Trygestad, Vice President of Engineering at CRSI, for their tremendous assistance and support. Harris Rebar in Washington generously donated all the ASTM A706 Gr. 80 rebars, David Fields at MKA provided invaluable guidance throughout the research, and Dr. Sharon Wood, who previously chaired ACI 318-0H Committee on Seismic Provisions, provided significant support for this research. A number of dedicated students including Hussain Anas, Vineethreddy Bandi, Rushabh Vardhama Munot, Chandra Sekhar Cherukuri, Meetkumar Lakhani, and Shashidhar Bontha were involved in the construction of specimens and test programs. Special thanks are also due to Bhupendra Raj Acharya, Sujan Kumar Singh, Suman Rijal, and Vesal Shakibaie for their help and support.

TABLE OF CONTENTS

LIST OF FIGURES

LIST OF TABLES

CHAPTER 1: INTRODUCTION

1.1 Background and Motivation

In earthquake-prone areas, high-rise buildings commonly rely on coupled reinforced concrete (RC) shear walls as their primary seismic force-resisting system. This system is comprised of slender shear walls that are rigidly connected by coupling beams which are aligned over the height of the structure. As depicted in Figure 1.1, the coupling beams are positioned within the shear walls, between openings such as elevators, windows, and doors. Under seismic forces, the movement between the two adjacent vertical wall segments generates bending moments and shear forces at the ends of each coupling beam in a coupled shear wall system. The shear forces amass into a tensile force in one vertical wall segment and a compressive force in the other. The combined moment generated by these forces serves to counteract a portion of the overturning moment at the base of the wall system, while the remaining overturning moment is withstood by the vertical wall segments themselves.

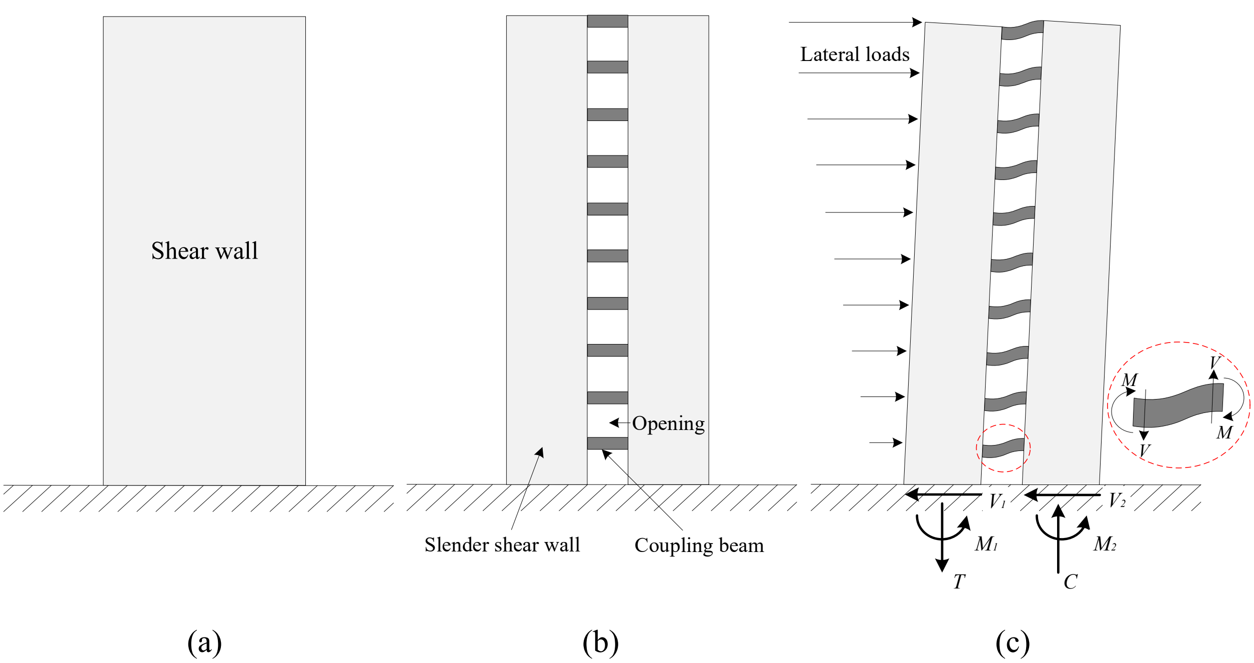

Fig. 1.1 (a) Isolated shear wall, (b) Coupled shear wall, and (c) Force resisting mechanism in a coupled shear wall system

In typical building designs, coupling beams typically have an aspect ratio (span-to-depth ratio) of less than 4. This results in a shear-dominated behavior for RC coupling beams, which means that they must possess high shear strength, ductility, and energy dissipation characteristics to effectively resist seismic induced lateral loads. Failure to ensure adequate performance of the RC coupling beams could compromise the overall performance of the coupled wall system. Due to the structural configuration of the coupled wall system, the coupling beams are subjected to significant deformation when subjected to lateral loads from earthquakes. Additionally, these coupling beams are designed to act as the primary structural "fuse," and are expected to yield before the adjacent wall piers. As a result, specific reinforcement detailing is necessary for the RC coupling beam to meet the aforementioned requirements. The ACI 318-19 code (ACI, 2019) provides provisions for two types of coupling beams based on their span-to-depth ratio (l_n/h) and shear demand. Coupling beams with a span length-to-depth ratio not less than 4 and a shear stress demand $V_u < 4\sqrt{f_c'}$ psi ($0.33\sqrt{f_c'}$ MPa) are designed as conventionally reinforced coupling beams (CCBs) and are similar to beams in special moment frames (SMFs). For coupling beams with a span-to-depth ratio less than 2 and a shear stress demand $V_u \geq 4\sqrt{f_c'}$ psi ($0.33\sqrt{f_c'}$ MPa), two intersecting groups of diagonal reinforcing bars are required, resulting in diagonally reinforced coupling beams (DCBs), with a nominal shear stress of V_n not exceeding $10\sqrt{f_c'}$ psi ($0.83\sqrt{f_c'}$ MPa) (ACI 18.10.7.4). For aspect ratios between 2 and 4, coupling beams can be designed as either CCB or DCB.

Modern high-rise buildings typically employ RC coupling beams with a slender span-to-depth ratio of 2.4 to 4, which are required to sustain a high shear stress approximately $10\sqrt{f_c'}$ psi ($0.83\sqrt{f_c'}$ MPa) up to large rotations. As a result, DCB is commonly utilized in RC coupled shear walls to provide high shear strength, ductility, and energy dissipation under seismic-induced lateral loads. The DCB's large span-to-depth ratio leads to a low angle of inclination for the diagonal reinforcement. This, in turn, diminishes the effectiveness of the diagonal reinforcement in resisting shear force. The heavy confining reinforcement required, along with the intersection between the diagonal rebars and the reinforcement in the adjacent wall piers, resulted in highly congested reinforcement and challenging construction (Harries et al, 2005), as illustrated in Figure 1.2 (a).

To address these issues, a novel type of coupling beam, known as the double-beam coupling beam (DBCB), was proposed by Choi et al. (2018) and Choi and Chao (2020). The DBCB features a simple reinforcement layout without diagonal reinforcement, where an upper and lower steel cage is separated by an unreinforced concrete strip (UCS), as depicted in Figure 1.2 (b). The reinforcement detailing of each cage is similar to those utilized in beams for RC special moment frames (SMFs), significantly reducing the aforementioned reinforcement congestion and construction challenges.

The cracking in DBCBs originates from the midspan and mid-height regions, where the unreinforced concrete strip (UCS) is located. From there, it progressively spreads towards both ends of the beam. As a result, the beam ends remain undamaged at lower beam rotations and retain their structural integrity even when subjected to significant rotations. This mechanism eliminates the typical sliding shear failure that occurs at the interface between the beam and wall in conventional coupling beams lacking diagonal reinforcement. Additionally, the UCS permits utility ducts to be located near the beam's ends without adversely affecting the DBCB's seismic performance. In half-scale DBCB experimental results reported by Choi et al. (2018) and Choi and Chao (2020), DBCBs with aspect ratios of 2.4 and 3.3 exhibited comparable or superior behavior concerning shear strength and ductility in comparison to half-scale DCBs (Naish et al., 2013).

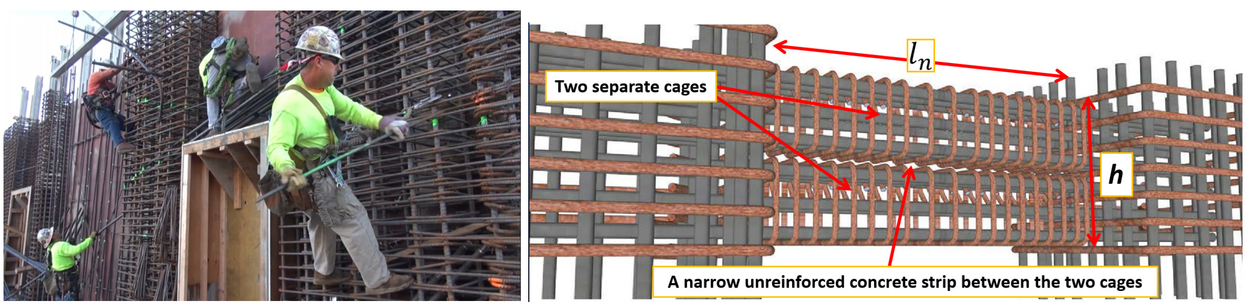

(a) (b)

Fig. 1.2 Reinforcement detail:(a) construction of DCB with large aspect ratio and (b) the DBCB reinforcing layout

1.2 Objectives

Half-scale experiments using Gr. 60 rebars have demonstrated that double-beam coupling beams (DBCBs) offer a promising alternative to diagonally reinforced concrete coupling beams (DCBs). As a result of these tests, Choi and Chao (2020) proposed a design procedure for DBCBs, which closely resembles the ACI procedure for beams in a special moment frame (SMF). Ensuring adequate ductility for DBCBs to undergo large rotations is reliant on meeting the confinement requirement for transverse reinforcement. The spacing requirements for confining transverse reinforcement in DBCBs are identical to those stipulated in ACI 318-19 (ACI, 2019) for beams in a special moment frame (SMF). This spacing is directly proportional to the depth of the beam and the diameter of the rebars, which may result in a potential size effect when specimens are at full-scale or near full-scale due to larger beams having wider transverse reinforcement spacing.

Incorporating utility ducts often requires horizontal openings to penetrate through a coupling beam. Previous half-scale experiments on DBCBs have demonstrated that placing these openings in the UCS and between transverse hoops at both ends of the coupling beam does not negatively impact its strength and ductility. However, the maximum allowable opening size is limited to the thickness of the UCS in the half-scale DBCB. To validate these findings for full-scale DBCBs with larger UCS and openings, additional experimental investigations are necessary. Additionally, earlier tests revealed that other areas, such as the middle of each upper and lower beam, are not under significant stress. Further experimental research could help determine if these locations can also be utilized for openings.

In typical building structures, a coupling beam is usually cast monolithically with a slab (as shown in Fig. 1.3), resulting in a flanged beam or T-beam. In this case, the elastic neutral axis of the T-beam is not situated at the mid-height of the beam, as opposed to the isolated DBCB without a slab that was previously tested.

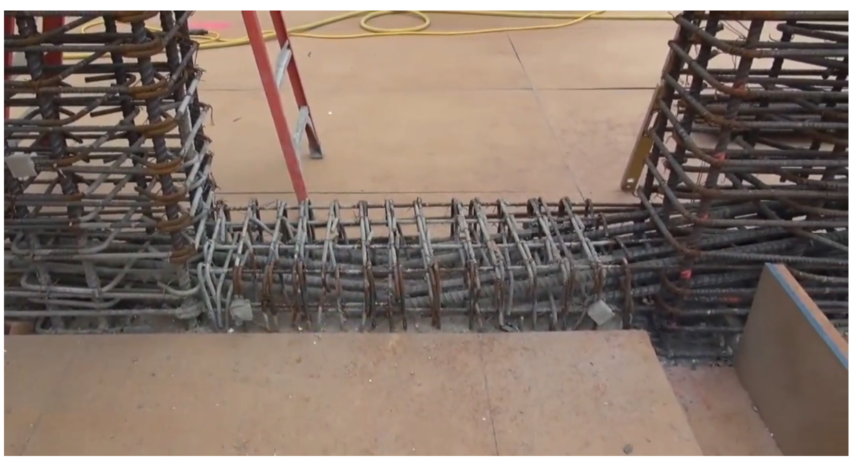

Fig. 1.3 Monolithic concrete cast of coupling beam and slab

Furthermore, ACI 318-19 (ACI, 2019) allows for the utilization of high-strength rebars with a nominal yield strength of up to 100 ksi (690 MPa) in coupling beams to alleviate reinforcement congestion in DCBs. The use of higher strength rebars is also advantageous for constructing DBCBs, which were previously tested using only Gr. 60 (420 MPa) rebars.

The present study aimed to examine various factors by conducting experiments on three specimens. The first specimen was a full-scale DBCB with an aspect ratio of 3.2, which represents the typical ratio for an office building. The second specimen was a full-scale DBCB with an aspect ratio of 2.4, representing the typical ratio for a residential building. Lastly, a half-scale DBCB with an aspect ratio of 2.4 was tested, also representing a typical ratio for a residential building. All specimens were reinforced with Gr. 80 (550 MPa) high-strength rebars and subjected to symmetrical fully reversed cyclic loading. The objectives of the study were as follows:

1. To validate the proposed DBCB design procedure.
2. To investigate the potential size effect on the spacing of transverse reinforcement.
3. To examine the performance of a DBCB reinforced with Gr. 80 high-strength rebars and the required development length.
4. To investigate the size and location of utility duct openings in DBCBs.
5. To investigate the effect of slabs connected to the DBCBs.

CHAPTER 2: LITERATURE REVIEW

Coupled shear walls are a common choice for high-rise buildings as they offer substantial strength and stiffness for lateral force-resistance. To ensure the desired performance of the structural system, it is crucial that the coupling beams maintain the necessary shear strength, stiffness, and ductility when subjected to large displacement reversals. However, the short span length of the coupling beam, combined with these demands, can make construction of the coupling beam complex and challenging.

Paulay (1969, 1971) conducted research on conventionally coupled beams (CCBs) by testing twelve 3/4-scale coupling beams with aspect ratios of 1.02, 1.29, and 2.0 under both monotonic and cyclic loading. The deep coupling beams failed in a brittle manner due to either diagonal shear crack or sliding shear failure near the beam-to-wall interface. The ultimate shear capacity of the tested specimens was lower than that predicted by conventional reinforced concrete flexural theory. Therefore, it was found that CCBs with aspect ratios between 1.0 and 2.0, consisting of longitudinal flexural reinforcement parallel to the beam and vertical hoops, were not sufficient to withstand the demands of coupled shear walls subjected to large earthquake-induced displacement. These results prompted further research into alternative reinforcement detailing.

The diagonally reinforced coupling beam (DCB) was first proposed by Binney and Paulay (Binney, 1972; Paulay and Binney, 1974) as an improvement to the conventional coupling beam (CCB), which failed in a brittle manner under large earthquake-induced displacements. The DCB features two intersecting diagonal steel cages at the beam midspan, providing equal diagonal tensile and compressive capacity as cross tension ties to resist shear forces. Three large-scale DCB specimens with aspect ratios of 1.29 and 1.02 were tested under fully reversed cyclic loading. The measured strains along the diagonal reinforcement showed nearly uniform steel bar stresses over the entire span of the coupling beam, indicating effective diagonal reinforcement load-carrying capacity. The DCBs exhibited less severe diagonal and flexural cracks and crushing than the CCB and sustained high ductility and shear demand without sliding shear failure up to large inelastic displacement reversals. The buckling of diagonal bars near the beam ends initiated the failure of the DCBs. Therefore, the test results demonstrated that the DCBs possess excellent deformation capacity and energy dissipation when adequately restrained from buckling.

Further research has confirmed the significant improvement in ductility, stiffness retention, and energy dissipation provided by DCBs. However, due to the reinforcement congestion and construction challenges at the intersection of diagonal bars and adjacent wall piers, researchers have explored alternative reinforcement arrangements to address the time-consuming and cumbersome construction process of DCBs (as illustrated in Fig. 1.2 (a)).

Binney et al. (1976, 1980) conducted tests on eight 1/3-scale coupling beams under fully reversed cyclic loading to investigate the performance of three different reinforcement layouts, including conventionally reinforced concrete coupling beams (CCBs), diagonally reinforced coupling beams (DCBs) with aspect ratios of 2.5 and 5.0, and beams with a rhombic reinforcement layout. The rhombic layout featured longitudinal reinforcement in the beam span and X-shaped diagonal bars near both beam-to-wall interfaces, with diagonal reinforcement in the end plastic hinge zone designed to resist the entire shear force. Short-span coupling beams were subjected to high shear stresses ranging from 7 to $11\sqrt{f_c'}$ psi (0.58 to $0.91\sqrt{f_c'}$ MPa), while long-span coupling beams ranged from 4 to $5\sqrt{f_c'}$ psi (0.33 to $0.42\sqrt{f_c'}$ MPa). The tests showed that CCBs failed due to sliding shear failure near the ends of the beams under large inelastic deformation. The rhombic reinforcement layout successfully eliminated sliding shear failure, but the concrete in the diagonal reinforcement region crumbled under large rotation, causing the bent points of the diagonal bars to loosen, and resulting in the loss of efficient truss action. In contrast, DCBs with full-length diagonal reinforcement demonstrated the most excellent performance among all tested specimens, effectively improving the strength, ductility, and energy dissipation of the coupling beams with a small aspect ratio. However, the improvement in the hysteretic response of the slender coupling beams with full-length diagonal reinforcement was relatively small.

Tegos and Penelis (1988) carried out experimental tests on twenty-four coupling beams under either monotonic or cyclic loading with aspect ratios of 2.0, 3.0, and 4.0. The main objective was to propose a simple technique to prevent premature splitting shear. Out of the total specimens, eighteen were tested with an inclined rhombic reinforcement layout, which was suggested as a simplified alternative to DCBs, while three specimens were tested with DCBs and three with CCBs. Unlike previous studies, axial load was applied to the specimens through an oil jack at one end. The results showed that coupling beams with a rhombic layout of reinforcement significantly improved deformation capacity, similar to DCBs, compared to CCBs.

Tassios et al. (1996) tested ten half-scale coupling beams with five different reinforcement layouts and two different aspect ratios of 1.0 and 1.66 under fully reversed cyclic loading. Three new reinforcement schemes were investigated and their behavior were compared with that of CCBs and DCBs. The first one with rhombic layout, which is similar to the one tested by prior researchers (Binney et al., 1980; Tegos and Penelis, 1988), had additional bent-up bars intersecting at the coupling beam ends to resist the sliding failure. The second and third one contained long and short dowels across the ends of the coupling beams to prevent the sliding shear failure close to both beam-to-wall boundaries. Test results showed that the coupling beam with the rhombic layout had larger shear strength and deformation capacity than the CCB specimens and required less complicated detailing than diagonally reinforced coupling beams. However, severe pinching of the hysteresis loops was still observed which led to the reduction of energy dissipation. For the coupling beam with dowel bars, it was found that dowel bars in the end regions of the beam may help prevent a sliding shear failure. However, stiffness degradation and severe pinching in the hysteresis loops were still present. A comparison of hysteresis loops indicated that the DCBs exhibited the best performance in term of shear resistance and energy dissipation. In summary, for coupling beams with span-to-depth ratio less than approximately 1.5, diagonal reinforcement was still found to be the best solution.

Galano and Vignoli (2000) reported results from experimental tests for fifteen short coupling beams with aspect ratio of 1.5 under three different fully reversed cyclic loadings and one monotonic loading. A series of tests were carried out on specimens with four different reinforcement layouts: (a) conventional layout (CCB); (b) diagonal layout without confining ties (DCB); (c) diagonal layout with confining ties (DCB); and (d) rhombic layout. Test results showed that the beams with diagonal or rhombic layout behaved better than beams with conventional layout. Moreover, the rhombic layout exhibited greater rotational capacity and strength retention compared to diagonal layouts, which contradicts the findings of Tassios et al. (1996).

The ACI 318 code (ACI, 1999) permitted the use of diagonally reinforced coupling beams (DCBs) in 1999, based on prior research. Since then, DCBs have become a popular choice for medium- to high-rise buildings. Contemporary architectural designs often call for DCBs with span-to-depth ratios ranging from 2.4 to 4, and shear stress demands exceeding the maximum allowable shear stress ($4.0\sqrt{f_c'}$ psi ($0.33\sqrt{f_c'}$ MPa)) for CCBs (ACI, 2005).

Naish et al. (2009, 2013) conducted experimental tests on coupling beams with aspect ratios of 2.4 and 3.3. Eight approximately half-scale coupling beams were tested under fully reversed cyclic loading. Five of them had a span-to-depth ratio of 2.4 for residential buildings and the rest had a ratio of 3.3 for commercial buildings. For the coupling beams with aspect ratio of 2.4, four specimens had full-section confinement and the separate confinement around each group of diagonal bars were eliminated to simplify the congestion and construction. One control specimen with aspect ratio of 2.4 contained hoops along diagonal bars according to the detailing requirements in ACI 318-05 (ACI, 2005). For more slender beams with aspect ratio of 3.3, three specimens featuring either diagonal bars with full-section confinement, or diagonal bars with diagonal confinement, or longitudinal bars without diagonal reinforcement were tested. Test results indicated that the use of full-section confinement provides comparable, if not improved, behavior compared to the confinement around diagonal bars previously required, and that the inclusion of a slab a slab had only a modest impact on strength, stiffness, ductility, and observed damage. This full-section confinement detailing option was subsequently incorporated into ACI 318-08 (ACI, 2008) for design of DCBs.

Lim et al. (2016) proposed a coupling beam with a hybrid layout that combines conventional layout (CCB) and diagonal reinforcing bars to overcome construction difficulties. The proposed reinforcement layout is similar to the HPFRC coupling beam layout proposed by Canbolat et al. (2005). To assess the seismic performance of the hybrid layout, the researchers tested six specimens with aspect ratios of 3.0 and 4.0, including two CCBs, two DCBs, and two coupling beams with the hybrid layout.. Under fully reversed cyclic loading, the coupling beam with the hybrid reinforcement maintained 80% of the maximum shear strength until 5.5% chord rotation, which is between 4.1% chord rotation of CCB and 7% chord rotation of DCB. The coupling beam with the hybrid layout showed the moderate deformation capacity between CCB and DCB.

The use of diagonal reinforcement layout is often preferred for RC coupling beams, as it can provide high shear strength, ductility, and energy dissipation even under large inelastic deformation. However, one of the notable challenges with DCBs is the difficulty of passing diagonal bars through hoops and crossties. Consequently, several researchers have explored alternative solutions such as using steel sections in order to reduce construction difficulties.

Harries et al. (1993) published test results from two full-scale steel coupling beams with aspect ratio of 3.4 under fully reversed cyclic loading. The steel coupling beam were designed using a wide-flange section with steel stiffeners, which followed the seismic design requirement for eccentrically brace frame (EBF) in the Canadian steel design standard. The steel section is embedded in the RC wall piers to resist the moment and shear force. The tests showed that when properly embedded into the adjacent RC wall piers, the steel coupling beams could exhibit larger strength than slender RC coupling beam and provide excellent deformation capacity and energy dissipation.

Gong et al. (1998) reported results from tests on four 1/3-scale composite coupling beams consisting of wide-flange steel section encased in reinforced concrete. The main goal was to investigate the effect of concrete encasement and the number of web stiffeners as well as the capacities of each specimen. The tests showed that the encasement around the steel coupling beam increased the beam stiffness by 25% and the shear strength by 18% and the stiffeners hardly affected the performance of the encased specimens. In addition, the composite coupling beams exhibited expected strength and deformation capacity while the concrete encasement prevented undesirable web and flange buckling of the steel section but failed due to less than desirable performance of the connection.

Park and Yun (2005) proposed an equation to compute the required embedment length of steel coupling beams considering the effect of vertical auxiliary bars and horizontal ties in a hybrid coupled shear wall system. Three specimens were tested under fully reversed cyclic loading. From the test results, it was found that it is more effective to design the steel coupling beam as shear-yielding members since a shear-critical coupling beam exhibited a more desirable energy dissipation than a flexure-critical one as well as conventionally and diagonally reinforced concrete coupling beams; however, the embedment with vertical bars and horizontal ties caused significant interference with reinforcement in the adjacent wall piers.

Lam et al. (Lam et al., 2005) proposed another alternative consisting of a steel plate encased in reinforced concrete. Three specimens with aspect ratios of 2.5 were tested under fully reversed cyclic loading. One of them was conventionally reinforced coupling beam (CCB) and the remainders were coupling beams with embedded steel plate along the entire span, either with or without studs. From the test results, it was shown that embedded steel plates improved the strength and stiffness of coupling beams.

Motter et al. (Motter et al., 2017) tested four large-scale steel-reinforced concrete (SRC) coupling beam with aspect ratios of 2.4 and 3.33 under fully revered cyclic loading to investigate the effect of structural steel section embedment length, span-to-depth ratio, quantities of wall boundary longitudinal and transverse reinforcement, and applied wall loading. The test results showed that the performance of SRC coupling beam was depended on both embedment length and boundary reinforcement in RC wall piers; the long embedment length and heavy wall boundary reinforcement enhanced the performance of SRC coupling beam; however, the short embedment length and light wall boundary reinforcement reduced the beam performance due to the significant damage in the embedment region.

As discussed above, steel and hybrid coupling beams are capable of providing outstanding strength, ductility, and energy dissipation. Nonetheless, these alternatives can create challenges when it comes to placing longitudinal and transverse reinforcement in the adjacent wall piers as special details are needed to accommodate the steel beam and ensure confinement to the wall boundary elements.

In the past few decades, high-performance fiber-reinforced concrete (HPFRC) has been proven through experiments to possess high tensile ductility. These materials undergo multiple cracking under uniaxial tension and compression similar to well-confined concrete, resulting in higher ductility compared to traditional concrete. The outstanding tensile behavior of HPFRC makes it a desirable material for members that are dominated by shear, such as coupling beams, beam-column connections, and squat walls that are subject to large inelastic deformations. Test results from Parra-Montesinos (2005) demonstrated that HPFRC is a feasible alternative to regular concrete for shear-critical members.

Canbolat et al. (Canbolat et al., 2005) carried out tests on four 3/4-scale HPFRC coupling beams under fully reversed cyclic loading. The first specimen, used as the control specimen, was diagonally reinforced coupling beam (DCB) which was designed and detailed according to the ACI 318-99 code (ACI, 1999). The second one was a precast HPFRC coupling beam with no diagonal bars like conventionally reinforced coupling beam (CCB). The other specimens were precast HPFRC coupling beams with diagonal reinforcement but the confinement around diagonal bars was eliminated to simplify the reinforcement detailing. A span-to-depth ratio of 1.0 was used for the coupling beam to ensure a shear-dominant behavior. Results demonstrated that HPFRC can provide effective confinement of diagonal reinforcement, thereby eliminating the need for transverse reinforcement around diagonal bars. HPFRC coupling beam also exhibited higher shear strength and stiffness retention than RC coupling beam, thereby potentially allowing for a reduction in the amount of diagonal reinforcement required to attain a target shear strength. In addition, the use of HPFRC material was shown to improve the damage tolerance by spreading damage over the whole beam with multiple cracking pattern.

Lequesne et al. (Lequesne et al., 2009, 2010; Lequesne, 2011) conducted a series of tests on large-scale HPFRC coupling beams with span-to-depth ratio of 1.75 subjected to fully reversed cyclic loading. All specimens were precast with a new design approach for HPFRC coupling beams of which diagonal bars were bent at the beam-to-wall interface like Canbolat et al. (2005) to easily insert them to adjacent wall piers without interfering with wall reinforcement. Three component HPFRC coupling beams and two reduced scaled four-story coupled-wall specimens were tested. Test results confirmed that HPFRC could provide adequate confinement to the diagonal reinforcement thereby successfully eliminating the problem of reinforcement congestion without compromising seismic performance and showed that HPFRC coupling beams with short aspect ratios had the superior damage tolerance and stiffness retention capacity under large inelastic deformation.

Subsequently, Setkit (Setkit, 2012) tested slender large-scale precast HPFRC coupling beams with aspect ratios of 2.75 and 3.3 subjected to fully reversed cyclic loading. The series of six specimens included one RC coupling beam as the control specimen, three HPFRC coupling beams with diagonal bar, and two HPFRC coupling beams without diagonal bars. The detailing approach for slender HPFRC coupling beam is very similar to that of Lequesne (Lequesne, 2011). Test results exhibited that the use of HPFRC for slender coupling beam improved the damage tolerance by dispersing damage over more numerous and finer cracks thereby, sustaining the adequate strength, ductility and energy dissipation despite the significant reduction or elimination of diagonal reinforcement.

These findings led to the use of HPFRC coupling beams in a few high-rise structures in the west coast of the United States. However, despite early adoption, their use has not become widespread due to the relatively higher cost of HPFRC and contractors' lack of experience in sourcing and handling it. (Ameen, 2019).

The incorporation of high-strength steel bars as reinforcement in RC members presents an attractive opportunity to reduce the size and number of reinforcing bars, thereby mitigating reinforcement congestion and construction challenges in RC coupling beams. Nevertheless, the use of high-strength steel bars as primary longitudinal reinforcement in special seismic systems is not permitted by ACI 318-14 building code (ACI, 2014) due to insufficient experimental evidence. As a result, recent studies have been carried out to examine the behavior of coupling beams reinforced with high-strength reinforcement in coupling beams with short and intermediate span-to-depth ratios.

Ameen. (Ameen, 2019, 2020) tested five large-scale DCB specimens with span-to-depth ratio of 1.9 under fully reversed cyclic loading. Gr. 120 (830 MPa) high-strength bars were used as diagonal reinforcement in DCBs except for one control specimen with Gr. 60 (420 MPa) for diagonal reinforcement. Gr. 60 (420 MPa) steel bars were also used for all non-diagonally oriented reinforcement. All specimens were designed as per ACI 318-14 (ACI, 2014). However, one specimen had higher design shear stress ($15\sqrt{f_c'}$ psi ($1.25\sqrt{f_c'}$ MPa)) than maximum allowable shear stress ($10\sqrt{f_c'}$ psi ($0.83\sqrt{f_c'}$ MPa)); in addition, three specimens extended the secondary longitudinal reinforcement into the wall pier. From the test results, the specimens with Gr. 120 (830 MPa) reinforcement exhibited chord rotation capacities between 5.1 and 5.6%, which is less than 7.1% of the control specimen with Gr. 60 (420 MPa) reinforcement. The most likely reason is because the diagonal reinforcements with wider transverse reinforcement spacing were buckled prematurely in a prior cyclic loading. The development of the secondary reinforcement distributed more the damage over the beam span but did not improve the chord rotation capacity. Besides, a 50% increase in design shear stress also did not affect the deformation capacity.

Weber-Kamin et al. (2020) conducted a series of tests on eleven 1/2-scale coupling beams with span-to-depth ratios of 1.5, 2.5, and 3.5 under fully reversed cyclic loading. Gr. 80, 100, and 120 (550, 690, and 830 MPa) high-strength bars were used as the primary longitudinal reinforcement for nine DCB specimens and two CCB specimens; Gr. 80 (550 MPa) for transverse reinforcement in all specimens but one with Gr. 120 (830 MPa). The DCB specimens and CCB specimens were designed for target shear stresses of $8\sqrt{f_c'}$ psi ($0.67\sqrt{f_c'}$ MPa) and $6\sqrt{f_c'}$ psi ($0.5\sqrt{f_c'}$ MPa), respectively. The nominal compressive strength of concrete used in all coupling beams was 8,000 psi (55 MPa). The test results exhibited that chord rotation capacities of DCBs with Gr. 100 or Gr. 120 were similar, which had deformation capacities of 5, 6, 7% for beams with aspect ratios of 1.5, 2.5, and 3.5, respectively; however, DCBs with Gr. 80 had 25% higher chord rotation capacities because of delayed buckling of Gr. 80 diagonal reinforcement. In addition, the secondary longitudinal reinforcement extended into the wall piers tended to increase the chord rotation capacity and the measured shear strength of DCBs. Chord rotation capacities of CCBs with Gr. 80 or Gr. 100 were similar, with a deformation capacity of 4% for beams with aspect ratio of 2.5.

Previous experimental studies typically allowed coupling beam specimens to elongate as inelastic bar strains and concrete damage accumulated. However, in an actual building, structural walls and floor diaphragms passively restraint a coupling beam's elongation, and provide non-negligible resistance to beam elongation upon cracking (Teshigawara et al. 1998; Lequesne 2011; Barbachyn et al. 2012). The actual stiffness of this restraint and the magnitude of the resulting axial forces are unknown.

Poudel et al. (2021) reported the effect of axial restraint force comparing axially unrestrained and restrained beams subjected to reversed cyclic displacement. Two pairs of large-scale coupling beams with 1.9 aspect ratio were tested and each pair was reinforced with Gr. 60 (420 MPa) and Gr. 120 (830 MPa) bar, respectively. The results of the test indicated that the maximum shear strength was enhanced by the axial restraint; however, the chord rotation capacity was decreased due to earlier buckling of diagonal reinforcing bars and more significant damage compared to the unrestrained specimen. As the magnitude of the induced axial force increased, these effects of axial force were intensified. However, the effect of passive axial restraint on the stiffness of coupling beam was very small. In addition, reinforcement ratio, detailing, grade of reinforcement may have impact on coupling beam elongate and therefore the magnitude of the axial force induced by axial restraint.

Four conventionally reinforced coupling beams with a span-to-depth ratio of 1.37 were tested by Mihaylov et al. (2021) to investigate the effect of axial restraint. Three levels of axial restraint (no restraint, intermediate, and full restraint) and two types of loading (monotonic versus cyclic) were considered. The study showed that axial restraint induced significant compression in the beams, leading to changes in crack patterns and shear strength. In general, the shear strength increased due to the axial constraint, but the drift capacity decreased with increasing restraint. However, the fully restrained beam exhibited very low shear strength due to major diagonal cracks opening at low shear levels. Additionally, the strength of coupling beams was minimally affected by large inelastic pulses, but their drift capacity was significantly impacted.

Modern architectural specifications typically require span-to-depth ratios between approximately 2.4 and 4, which decrease the efficiency of diagonal reinforcement due to a small angle of inclination (~10 degrees) when using the current detailing requirements for diagonally reinforced coupling beams (DCBs) specified in the ACI 318 code Section 18.10.7.4 (ACI, 2019). These details result in complicated detailing, leading to difficulties in construction and meeting architectural needs such as access to utility ducts within a DCB (as shown in Figure 1.2 (a))..

Choi et al. (2018) investigated an innovative and simple reinforcing layout for RC coupling beams that can considerably decrease the design and construction complexities of diagonally reinforced coupling beams. The new double-beam coupling beam (DBCB) is composed of two separate cages, resembling those employed in typical beams for reinforced concrete special moment frames (Fig. 1.2 (b)). The two cages are positioned apart by a small gap of one to two inches, requiring solely vertical and horizontal rebars.

Upon large displacements, cracks begin developing at the DBCB's mid-span and mid-height, then gradually propagate towards the beam's ends. The cracks eventually separate the coupling beam into two relatively slender beams where each has nearly twice the aspect ratio of the original coupling beam. This split essentially transforms the shear-dominated single deep beam behavior into a flexure-dominated slender beam behavior combined with an interface shear resistance mechanism. Because damage initiates from the center of the beam and then spreads towards the ends, the beam ends can maintain their integrity even under very large displacements, thereby eliminating the sliding shear failure at the beam-to-wall interface (Choi et al., 2018; Choi and Chao, 2020). In addition, because the beam-to-wall interface in DBCBs experiences much less damage when compared to that of DCBs, a smaller development length is needed for the longitudinal rebars (approximately 60% of that required by ACI 318-19, Sect. 18.8.5.3(b)).

The results of the experiments show that a DBCB has high shear strength and ductility (refer to Fig. 2.1). In particular, the rotational ductility and shear strength of a DBCB with a 3.3 aspect ratio are greater than that of an ACI-compliant DCB with the same aspect ratio. Fig. 2.2 demonstrates that the ductility of the tested DBCB specimen is significantly higher under MCE-level ground motion, which is featured by one-sided excitations, than when tested under symmetrical fully reversed loading conditions (Choi et al., 2018).

Fig. 2.3 shows the cracking patter and propagation process. Diagonal cracking begins at the mid-height of the beam and then gradually propagates towards the beam ends as large chord rotations occur. Eventually, the coupling beam separates into two slender beams. The displacement of the drawn vertical lines serves as a clear indication of the slip at the UCS. Notably, certain areas of the beam have experienced relatively minor damage compared to other parts. These regions are primarily located at the mid-span area and at the beam ends close to the UCS. These areas may potentially allow for the installation of utility openings or more relaxed reinforcing detailing. Furthermore, the severely damaged zones located at the beam ends have a length along the beam that is approximately equal to the overall height of the beam, *h*/2.

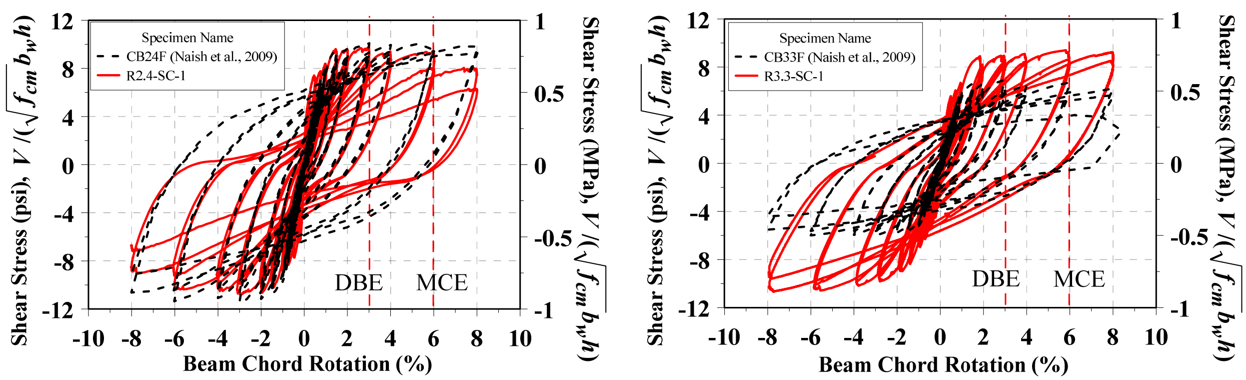

(a) (b)

Fig. 2.1 Comparison between hysteresis curves of DBCBs (Choi et al., 2018) and DCBs described by Naish et al. (2009): (a) aspect ratio of 2.4 and (b) aspect ratio of 3.3

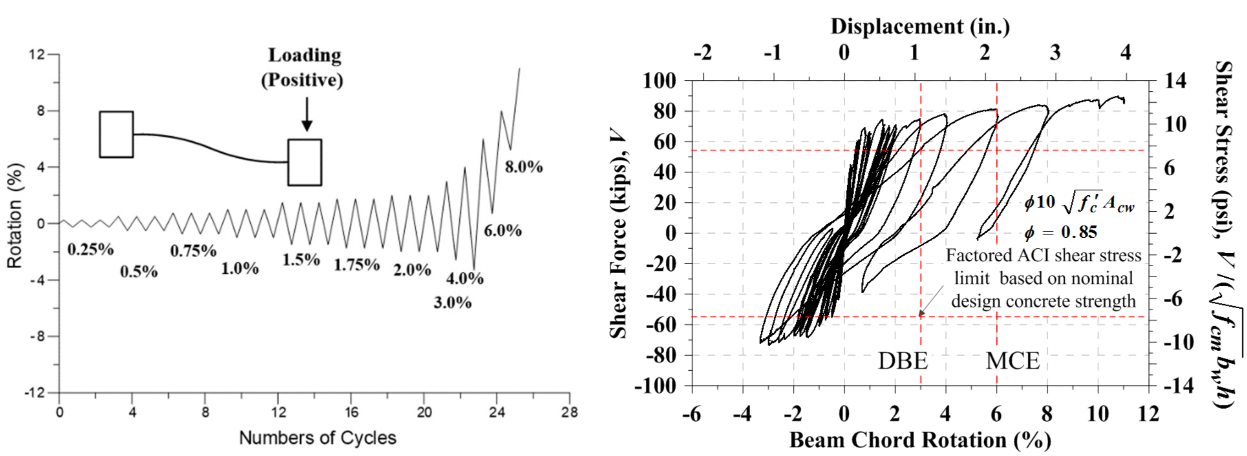

Fig. 2.2 Response of DBCB (l_n/h =2.4) subjected to MCE level excitation (Choi et al., 2018)

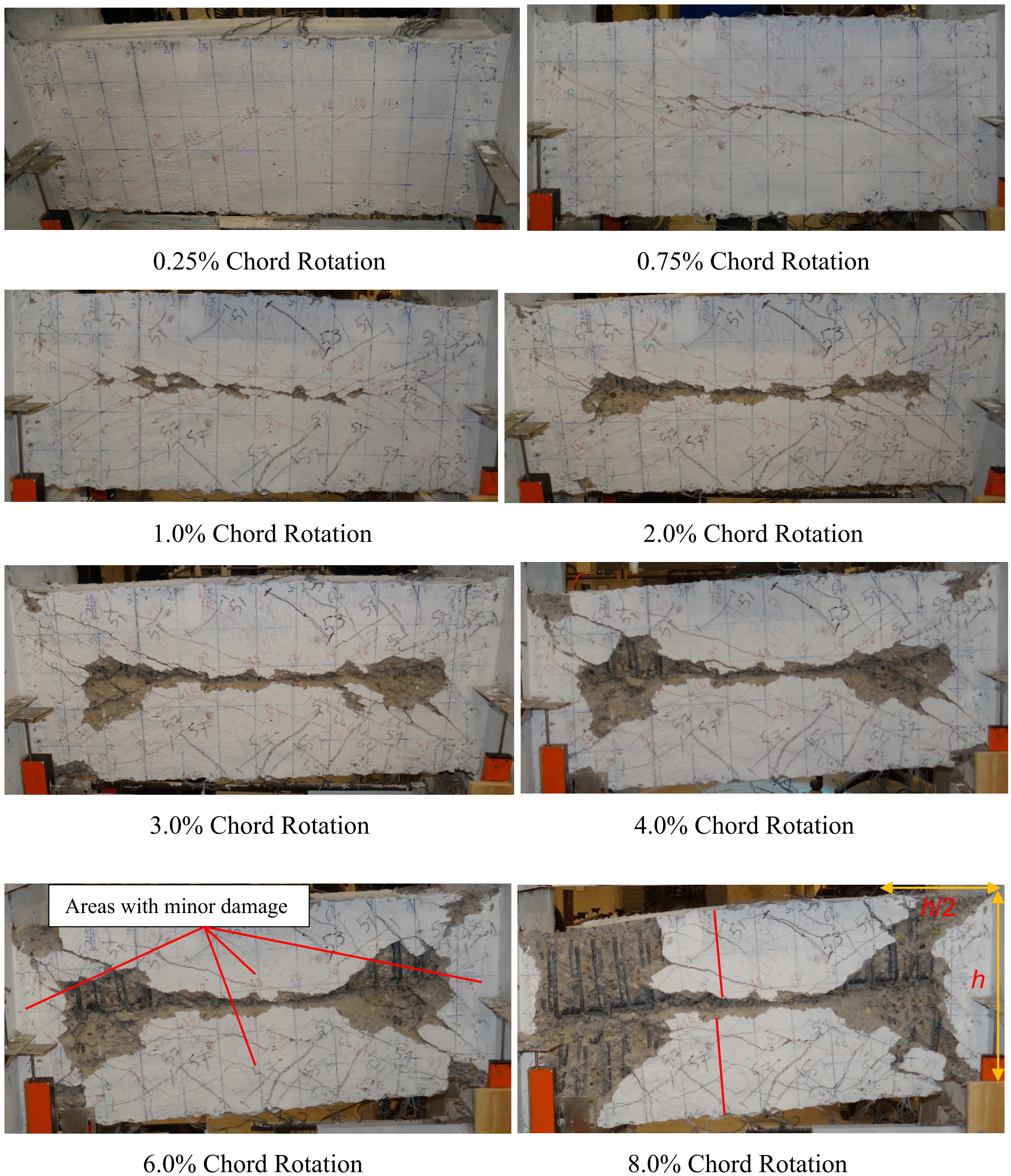

Fig. 2.3 Cracking and damage pattern of typical DBCBs (Specimen R2.4-SC-1) (Choi et al., 2018)

Choi and Chao (2020) proposed a design procedure for DBCBs, similar to the ACI requirement for beams in a special moment frame. The confinement requirement is crucial for providing ductility for DBCBs when deforming into large rotations. However, the ACI requirements for spacing of confining transverse reinforcement are dependent on the depth of the beam and the rebar diameter, which may lead to a potential size effect when the specimens are in full-scale or near full-scale. A design example of a DBC using A706 Gr. 60 reinforcement, resulting in a large No. 14 bar size, is shown in Fig. 2.4 (a). To compare the details, Fig. 2.4 (b) illustrates the designs of two options for diagonally reinforced concrete coupling beams (DCBs) according to ACI 318-19.

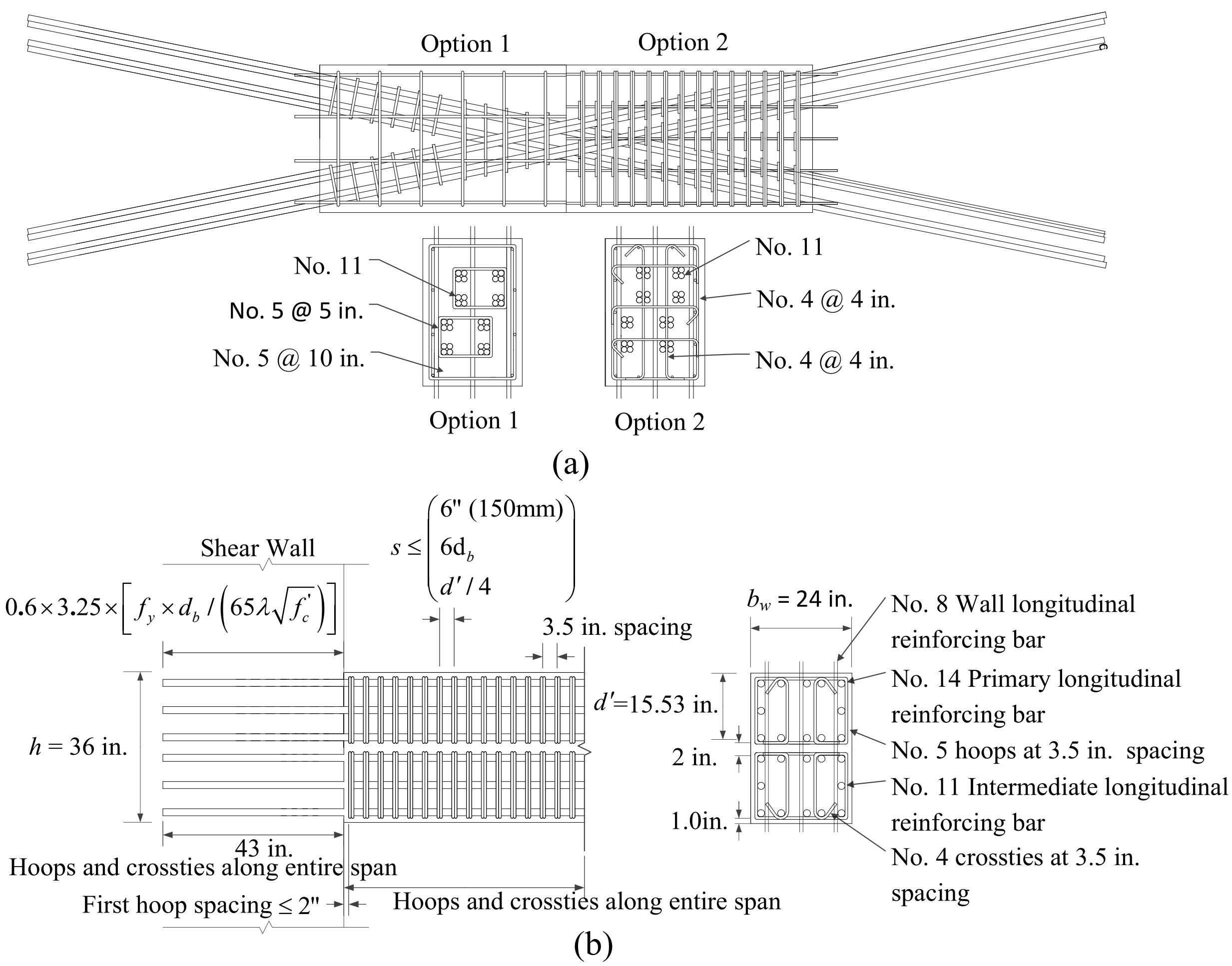

Fig. 2.4 Reinforcement details for coupling beams with a span-depth ratio ≥ 3.0: (a) DCB with both ACI options and (b) DBCB having the same shear capacity

DBCBs offer architectural flexibility and can address several construction issues that arise with DCBs. For instance, DBCBs do not require an increase in the width of adjacent walls because their width can be narrower than DCBs. Additionally, the placement of longitudinal rebars in DBCBs can be easily adjusted to accommodate the locations of vertical longitudinal rebars in the wall pier's boundary elements. Unlike DCBs, which require diagonal bars to be bent at the top floor to prevent protrusion, DBCBs do not have this issue. Utility ducts often need to be accommodated in the coupling beam to run through the core of a building. In this regard, DBCBs offer an advantage as they allow utility ducts to be placed inside the unreinforced concrete strip between the two steel cages, as shown in Figure 2.5.

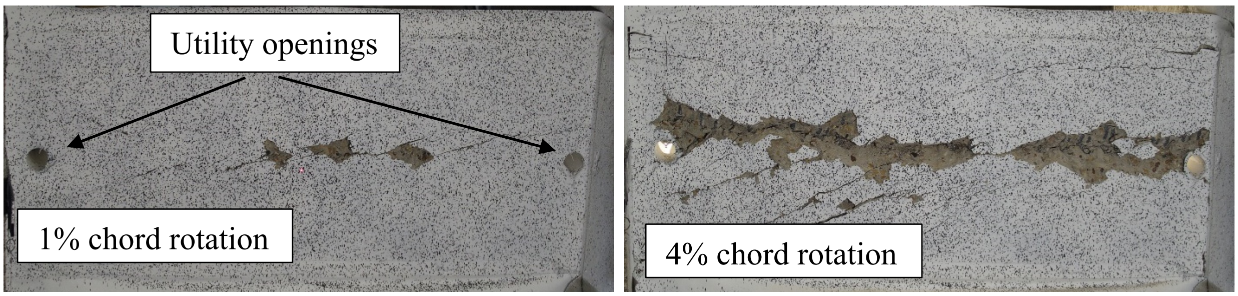

Fig. 2.5 DBCB (l_n/h =2.4) with utility openings close to beam ends (Choi and Chao, 2020)

However, if the opening region is not carefully detailed, these openings may cause performance degradation in DCBs. To address this concern, Abdullah et al. (2023) suggested a specific location and size for penetrations based on limited experimental tests (18 coupling beams with diagonal reinforcement and penetrations) conducted by Japanese researchers. The proposed guidelines include: (1) Circular penetrations may be located horizontally through the DCBs in the triangular window created by the diagonal bundles and the beam-to-wall interfaces or near the beam midspan in the triangular window created by the diagonal bundles and the top or bottom face of the beam. However, a maximum of two penetrations are allowed, which must not be on the same vertical line or in the same triangular window created by the diagonal bars. (2) The diameter of circular penetrations must not exceed one-fifth of the total depth (h) and 150 mm (6 in.). They also recommended special detailing for penetration regions located near beam-to-wall interfaces.

CHAPTER 3: EXPERIMENTAL PROGRAM

3.1 Specimens

3.1.1 Design and detailing of Double-Beam Coupling Beam (DBCB)

The cross section of a typical full-scale DBCB, designed according to Choi and Chao's (2020) proposed design flowchart (Fig. 3.2), is illustrated in Fig. 3.1. The anticipated shear strength of the DBCB is approximately 500 kips. However, the compression capacity of the hydraulic actuator at UTA's Civil Engineering Laboratory Building (CELB) is limited to 450 kips, with a smaller tension capacity of 300 kips. To ensure that the specimens do not exceed the allowable limits of the actuator and maintain a reasonable fixture and setup size, a beam width, b_w, of 10 in. (b_w is 24 in. in an actual coupling beam) was utilized, while maintaining the same height (h = 30 inches) and length (l_n = 72 or 96 inches) as the actual coupling beams (Fig. 3.1). In essence, the specimens' capacities are roughly half that of an actual coupling beam. Nonetheless, for the purposes of this study, the specimens are referred to as full-scale DBCBs, unless stated otherwise.

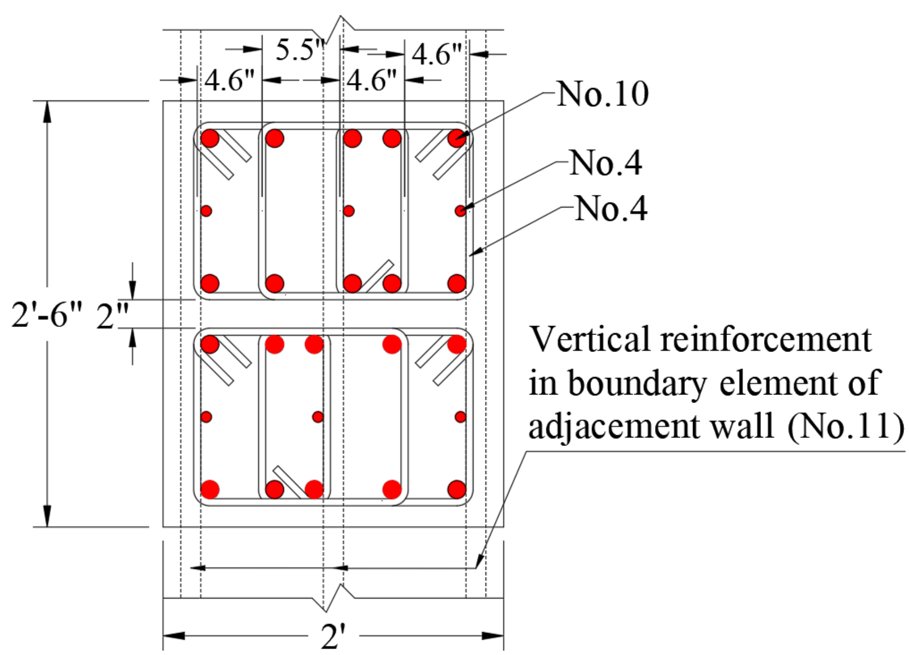

Fig. 3.1 Cross section of full-scale DBCB

Design of Double-Beam Coupling Beam (DBCB)

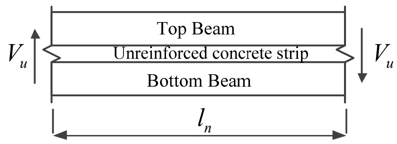

Determine the design shear force, V_u, for the entire coupling beam according to structural analysis

↓

Select Thickness of Unreinforced Concrete Strip

1.5 in. (38.1 mm) ≤ w ≤ 2.0 in. (50.8 mm)

↓

Determine Nominal Moment, M_n, for Each Beam

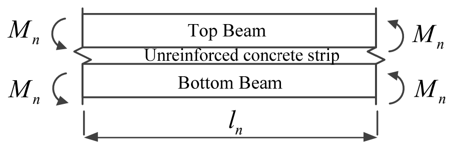

$$M_n = \frac{l_n}{4}\left(\frac{V_u}{\phi} - \frac{v_{UCS} b_w h}{2}\right); \ \phi = 0.85$$

$$v_{UCS} = 0.3 \text{ ksi (2.1 MPa)}$$

↓

Design of Longitudinal Reinforcement

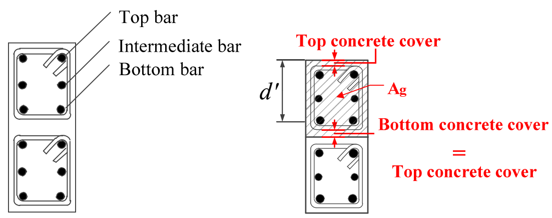

- Minimum three layers of vertically distributed longitudinal reinforcement
- Reinforcement ratio ρ_l shall not exceed 0.035 for Gr. 60 reinforcement for top and bottom reinforcement
- Maximum usable concrete strain $\varepsilon_{cu} = 0.004$
- Development length:
  $l_d = 0.6 \times 3.25 f_y d_b / (65\lambda\sqrt{f'_c})$

↓

Determine the Probable Design Shear Force, V_e, for Each Beam

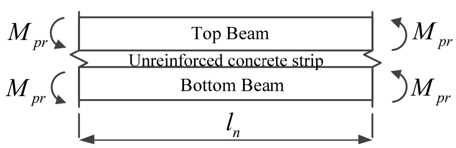

The probable flexural strength, M_{pr}, is calculated based on a steel tensile stress of 1.25 f_y where f_y is the specified yield strength of the longitudinal reinforcement

$$V_e = \frac{2M_{pr}}{l_n}$$

$$V_s \geq \frac{V_e}{\phi} \Rightarrow s = \frac{A_v f_{yt} d}{V_s}$$

$$\phi = 0.75$$

↓

Check Confinement Requirement (ACI code Section 18.6.4.4)

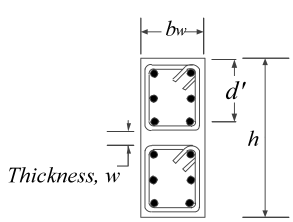

$$s \leq \begin{cases} d'/4 \\ 6d_b \text{(Gr. 60); } 5d_b \text{ (Gr. 80)} \\ 6 \text{ in. (150 mm)} \end{cases}$$

↓

Check Span-to-Effective Depth Ratio

$$\frac{l_n}{0.5(h-w)} \geq 5$$

Fig. 3.2 Flowchart for DBCB design

Fig. 3.1 shows that the leg spacing of shear reinforcements is not uniform across the specimen's width to prevent any conflict between the longitudinal rebars and the vertical reinforcement in the structural wall's boundary element, where the maximum leg spacing is 5.5 in. In order to simulate a more congested hoop layout, two full-scale DBCB specimens with a width of 10 in. were designed with a leg spacing of approximately 5.2 in. as a worst-case scenario. It should be noted that this design spacing complies with the maximum allowed spacing specified in ACI 9.7.6.2.2 (ACI, 2019).

This study involved testing three DBCB specimens using symmetric fully reversed cyclic loading. The first specimen was a full-scale DBCB with a 3.2 aspect ratio (l_n/h). The second specimen was a half-scale DBCB with a 2.4 aspect ratio (l_n/h). Finally, the third specimen was a full-scale DBCB with a 2.4 aspect ratio (l_n/h). Additionally, the last two specimens had overhanging flanges on each side of the coupling beam to assess the impact of the slab. All three specimens utilized ASTM A706 Gr. 80 rebars for the longitudinal reinforcement. However, while the first specimen used A706 Gr. 80 for the transverse reinforcement, the remaining two specimens used A615 Gr. 60 rebars instead. A concrete compressive strength of f_c' = 5,000 psi was assumed in the design. For this design, the maximum usable compressive strain of concrete, ε_{cu}, was set to 0.004. Although previous DBCB tests had identified ε_{cu} as 0.006 (Choi et al., 2018), a lower value was chosen in this design.

Design of full-scale DBCB with 3.2 aspect ratio (without slab)

Choi et al. (Choi et al. 2018; Choi and Chao, 2020) tested half-scale DBCB specimens that consisted of top and bottom beams divided by a UCS. The steel cage of each beam comprised upper and lower layers of longitudinal reinforcement, as well as an additional middle layer of longitudinal reinforcement. This middle layer served to restrain crack propagation and maintain aggregate interlocking, while also contributing to the flexural capacity of the beams. The use of this additional layer of reinforcement allowed for the use of smaller top and bottom bars or a reduced number of such bars, which facilitated the concrete casting process. Therefore, the first full-scale DBCB specimen used three longitudinal reinforcement layers for each steel cage of the coupling beam. In prior half-scale DBCB tests, the middle layer of longitudinal rebars used the same size or slightly smaller rebars. However, in this specimen, smaller No. 6 rebars were used for the middle layer while a combination of No. 10 and No. 8 rebars were used for the top and bottom layers.

The transverse reinforcement spacing was determined based on the confinement requirement outlined in Section 18.6.4.4 of the ACI 318 code (ACI, 2019) to ensure high ductility of DBCBs under large inelastic rotation. To maintain consistency with the half-scale specimens, the same ACI 18.6.4.4 (ACI, 2019) spacing requirement for confining reinforcement was implemented. This approach enables the investigation of potential size effect between the half-scale and full-scale specimens, since larger beams typically have wider transverse reinforcement spacing as per ACI code.

Design of half-scale DBCB with 2.4 aspect ratio (with slab)

A coupling beam is usually cast monolithically with the slab (Fig. 1.3), which can provide additional strength and confinement to the coupling beam. Previous research has demonstrated that, while there was no significant change in ductility and stiffness, the shear strength of diagonally reinforced concrete coupling beams (DCBs) increased by 15% to 20% due to the slab (Naish et al., 2013).

Research conducted previously (Choi et al., 2018; Choi and Chao, 2020) has shown that the main mechanism leading to the enhanced strength and ductility of a DBCB is the splitting of the UCS at the mid-height of the beam. This location often experiences the greatest elastic horizontal shear in a rectangular section. Due to the inclusion of a slab, the cross-section transforms into a T-section. The T-section's centroid undergoes the greatest elastic horizontal shear, which is higher than the mid-height (centroid) of the rectangular beam where the UCS is located. This difference in the location of the maximum horizontal shear and UCS could potentially result in a delayed or incomplete splitting of the UCS. To investigate this issue, an experimental test was carried out on a half-scale DBCB that included a slab to assess its impact. Furthermore, to simplify the reinforcement details in DBCBs, the longitudinal reinforcement in the middle layer was eliminated from each steel cage.

Design of full-scale DBCB with 2.4 aspect ratio (with slab)

The test results revealed that the aforementioned half-scale DBCB specimen, which included a slab, was able to achieve the first positive 8% chord rotation without experiencing any significant shear strength degradation. This was attributed to the confined concrete at the plastic hinging zone of the coupling beam sustaining only minor damage. In addition, the shift of cross-section centroid did not cause any incomplete or delayed split of the UCS, and removing the middle layer longitudinal reinforcement in each steel cage did not have any significant negative impact on the development of shear cracks. After analyzing the experimental findings and conducting nonlinear finite element simulations on beams with various hoop spacings, as outlined in Section 5.2.1 of this report, modifications were made to the full-scale 2.4 aspect ratio DBCB with a slab. These adjustments included:

(1) although the transverse reinforcement spacing for each steel cage follows the confinement requirement outlined in Section of ACI 18.6.4.4 (ACI, 2019), the close spacing required for confinement was only applied over a length equivalent to the depth of either the upper or lower beam (or half of the overall DBCB height). Note that for beams in a special moment frame, ACI 18.6.4.1 specifies that the hoop spacing should have been extended to twice the beam depth, measured from the face of the support towards midspan at both ends of the beam (ACI, 2019), and

(2) the thickness of UCS was increased up to 3 in. to accommodate larger PVC pipes at both ends of the coupling beam, and two PVC pipes were added at the midspan and mid-height of each individual beam where only minor damage was observed from prior DBCB tests.

3.1.1.1 Design of full-scale DBCB with 3.2 aspect ratio (without slab)

Dimensions of DBCB

The dimensions of the full-scale DBCB specimen with a 3.2 aspect ratio are shown in Fig. 3.3. The specimen has a height (h) of 30 in., a width (b_w) of 10 in., and a length (l_n) of 96 in., resulting in an aspect ratio (l_n/h) of 3.2, which is commonly used for office buildings.

Required shear strength (V_u)

Prior experiments (Choi and Chao, 2020) recommended using a design interface shear strength for the unreinforced concrete strip (UCS) of 0.3 ksi, which is a conservative estimated lower bound value. Considering potential overstrength, a shear demand of V_u = 155 kips was used to design the full-scale 3.2 aspect ratio DBCB. However, the actual shear strength obtained from experiment exceeded this value due to the overstrength of both the rebars and the UCS. It is important to note that, for experimental purposes, the design of the specimen involved a different approach. Instead of following the conventional design practice, the longitudinal reinforcement in the coupling beam was first selected. Subsequently, the shear demand (V_u) of 155 kips was back-calculated based on the actual nominal moment capacity of the coupling beam, taking into account the specific longitudinal reinforcement used. This experimental design process differs from the typical practice, where the shear demand (V_u) is usually first determined through structural analysis, and then the reinforcement is designed accordingly.

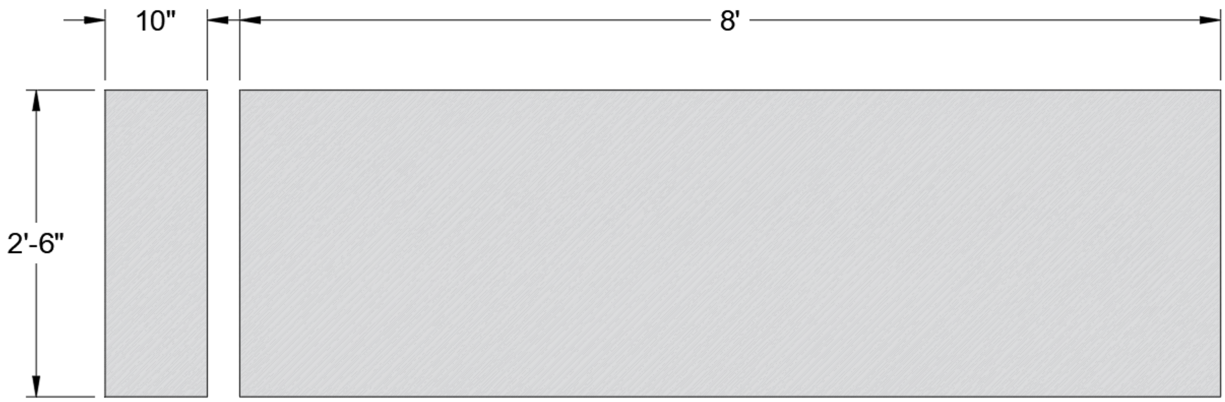

Fig. 3.3 Dimension of full-scale DBCB with 3.2 aspect ratio

Required nominal moment (M_n) for each of the upper or lower beam

A required nominal moment (M_n) for each individual beam in DBCB is calculated by using the equation defined in the design flowchart shown in Fig. 3.2, with v_{UCS} assumed to be 0.3 ksi. The strength reduction factor, ϕ, is 0.85, the same value assigned to DCBs (diagonally reinforced concrete coupling beams) by ACI 318-19.

$$M_n = \frac{l_n}{4}\left(\frac{V_u}{\phi} - \frac{v_{UCS} b_w h}{2}\right) = \frac{96}{4}\left(\frac{155}{0.85} - \frac{0.3 \times 10 \times 30}{2}\right) = 3{,}300 \text{ kip-in.} \qquad \text{Eq. 3.1}$$

Thickness of UCS, *w*

The thickness of the unreinforced concrete strip (UCS) in the DBCB is 2 in., as shown in Fig. 3.4. The UCS was placed between the upper and lower beams, and PVC pipes with a 2.5-inch nominal diameter were inserted between the hoops to accommodate utilities. As shown in Fig. 3.7, the center of each PVC pipe was located at a distance of 3.5 in. away from both ends of the beam, or alternatively, the outer edge of each PVC pipe was located 5.0 in. from both ends of the beam.

Flexure strength design

For the design of each individual DBCB beam, the spColumn software (StructurePoint, 2019) was used to ensure that its moment capacity, $(M_n)_{actual}$, was greater than or equal to the required nominal moment, M_n, as shown in Eq. 3.1, where a concrete crushing strain (ε_{cu}) of 0.004 was assumed. Figure 3.5 illustrates the location and size of the longitudinal reinforcement for the full-scale 3.2 aspect ratio DBCB, where Grade 80 rebar (f_y = 80 ksi) was used for all longitudinal reinforcement.

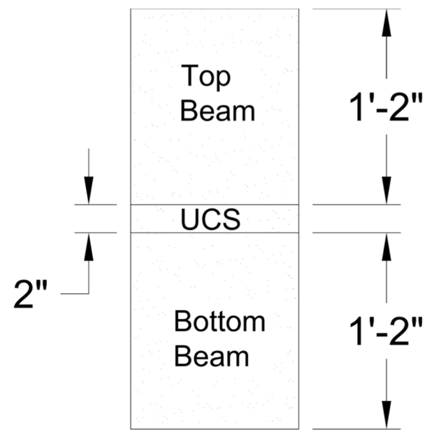

Fig. 3.4 Thickness of UCS

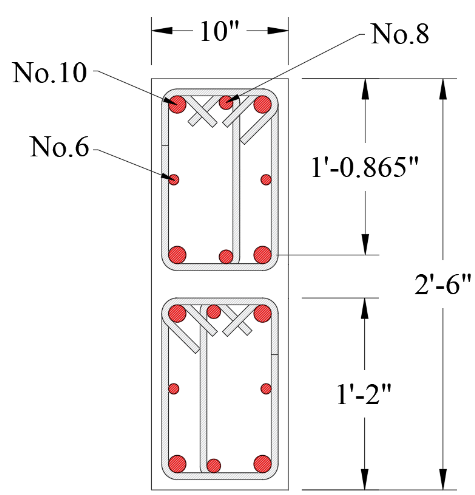

Fig. 3.5 Longitudinal reinforcement details of the first full-scale coupling beam specimen

Nominal design shear strength (V_n)

The nominal design shear strength of the specimen, V_n, is estimated based on the nominal moment strength $(M_n)_{actual}$ according to the specific longitudinal reinforcement used, and the interface shear strength of the UCS. It should be noted that the actual interface shear strength can further increase the expected shear strength.

For each individual beam, the shear strength can be calculated by:

$$V_n = \frac{v_{UCS} b_w h}{4} + \frac{2\left(M_n\right)_{actual}}{l_n} \quad \text{Eq. 3.2}$$

Therefore, for the entire DBCB (two beams):

$$V_{n\_total} = 2\left(\frac{v_{UCS} b_w h}{4} + \frac{2\left(M_n\right)_{actual}}{l_n}\right) \quad \text{Eq. 3.3}$$

As mentioned earlier, in the experimental design, the longitudinal reinforcement was selected first, followed by the back-calculation of the shear demand. Therefore, in this equation, the actual nominal moment strength $(M_n)_{actual}$ is the same as the nominal moment strength M_n:

$$V_{n\_total} = 2\left(\frac{0.3 \times 10 \times 30}{4} + \frac{2 \times 3,300}{96}\right) = 182.5 \text{ kips} = 8.6\sqrt{f_c'}A_{cw}$$

Notably, the maximum allowable shear strength by ACI 18.10.7.4 for a DCB is $10\sqrt{f_c'}A_{cw} = 212$ kips, where A_{cw} ($= b_w \times h$) represents the area of the DBCB. Note that when computing the nominal shear strength of the DBCB, the cross-sectional area considered is the gross area of the beam section, which is consistent with that of DCBs.

Development length, l_d

The development length of the longitudinal reinforcement was determined based on previous experimental results and was taken as 60% of the length required by ACI 18.8.5.3 (ACI, 2019):

$$l_d = \frac{0.6\left(3.25\right) f_y d_b}{65\lambda\sqrt{f_c'}} \quad \text{Eq. 3.4}$$

For No. 10 bars:

$$l_d = 0.6(3.25) f_y d_b / \left(65\lambda\sqrt{f_c'}\right) = 0.6(3.25)(80{,}000)(1.27) / \left[(65)\sqrt{5{,}000}\right] = 43 \text{ in.}$$

For No. 8 bars:

$$l_d = 0.6(3.25) f_y d_b / \left(65\lambda\sqrt{f_c'}\right) = 0.6(3.25)(80{,}000)(1.0) / \left[(65)\sqrt{5{,}000}\right] = 34 \text{ in.}$$

For No. 6 bars:

$$l_d = 0.6(3.25) f_y d_b / \left(65\lambda\sqrt{f_c'}\right) = 0.6(3.25)(80{,}000)(0.75) / \left[(65)\sqrt{5{,}000}\right] = 26 \text{ in.}$$

Design of transverse reinforcement within the flexural yielding region

(a) Shear strength requirement

In accordance with ACI 18.6.4.1 for moment frame beams, the flexural yielding zone for this specimen was defined as twice the overall height of each of the upper or lower beams, or the overall height of the entire DBCB (*h*). The probable design shear force (V_e) was used to calculate the shear force (V_s) that the shear reinforcement carries. This calculation was based on the probable moment strength (M_{pr}) and utilizes a rebar tensile strength of 1.25 f_y (which is equivalent to 100 ksi, i.e., 1.25 times 80 ksi):

$$V_e = \frac{2M_{pr}}{l_n} = \frac{2 \times 3{,}941}{96} = 82 \text{ kips} \qquad \text{Eq. 3.5}$$

where M_{pr} can be found by using spColumn software (StructurePoint, 2019). The shear force (V_s) for each individual beam carried by the shear reinforcement was determined using the following equation, where the strength reduction factor (ϕ) is equal to 0.75. In accordance with ACI 18.6.5.2, considering $V_e > (V_u/2)/2 = 155/4 = 38.75$ kips and neglecting the compressive force in the coupling beam,, the contribution of concrete to the shear strength was ignored, namely, $V_c = 0$.

$$V_s = \frac{V_e}{\phi} - V_c = \frac{82}{0.75} - 0 = 109 \text{ kips} \qquad \text{Eq. 3.6}$$

This shear force corresponds to a shear force of $12\sqrt{f_c'}b_wd$ (in psi unit) or $1.0\sqrt{f_c'}b_wd$ (in MPa unit). Note that ACI 22.5.1.2 imposes an upper bound limit of $8\sqrt{f_c'}b_wd$ (in psi unit) or $0.67\sqrt{f_c'}\,b_wd$ (in MPa unit) for the shear force that can be carried by shear reinforcement in a beam. However, this limit was not applied in the DBCB specimen under consideration. This is because no severe diagonal concrete crushing was observed in the half-scale DBCB specimens even when the calculated V_s is much greater than $8\sqrt{f_c'}b_wd$, as shown in Figure 2.3.

The maximum leg spacing (s_{max}) of the shear reinforcement across beam width is determined according to ACI 9.7.6.2.2. For $V_s > 4\sqrt{f_c'}b_wd$ (= 109 kips > 36 kips):

$$s \text{ is lesser of } d/2 \text{ and 12 in., or } s_{max\_w} = d/2 = 12.865/2 = 6.43 \text{ in.}$$

Considering the specimen width of 10 in. and a clear cover of 0.75 in., the spacing (across width of the beam) between two legs of transverse reinforcement is 8 in., which exceeds the limit of 6.43 in. Consequently, an additional crosstie is necessary across the width of the beam to meet the requirement of s_{max_w} = 6.43 in., as illustrated in Fig. 3.6. This additional crosstie also increases the shear strength. Note the detail shown in Fig. 3.6 is consistent with “Detail A” illustrated in Fig. R18.6.4 of ACI code.

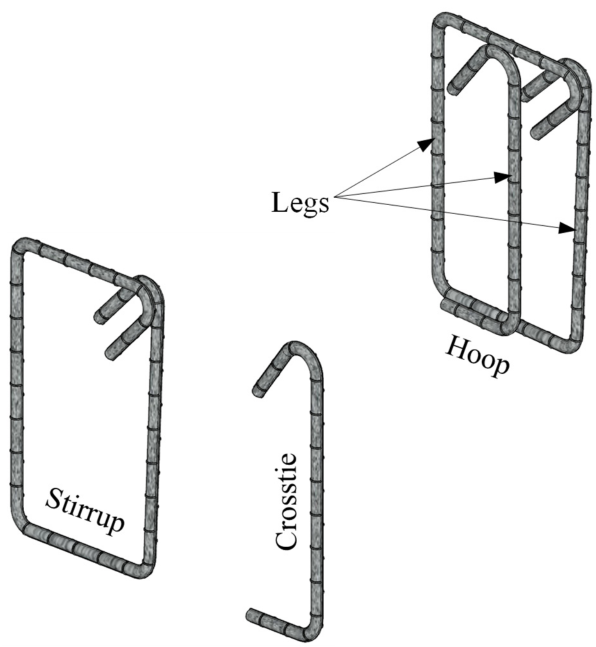

Fig. 3.6 Hoop details

Note that according to ACI 9.7.6.2.2, the maximum spacing between the legs of shear reinforcement along the beam should be the lesser of $d/4$ and 12 in. if $V_s > 4\sqrt{f_c'}b_w d$. However, this requirement does not govern in this case, as the confinement requirement imposed a stricter spacing requirement.

The spacing (s) of the shear reinforcement based on the shear strength was calculated according to ACI 22.5.8.5.3:

$$s = \frac{A_v f_{yt} d}{V_s} \qquad \text{Eq. 3.7}$$

Gr. 80 No. 4 rebars were used for the transverse reinforcement. Therefore,

$$s = \frac{A_v f_{yt} d}{V_s} = \frac{3 \times 0.2 \times 80 \times 12.865}{109} = 5.64 \text{ in.}$$

Where A_v represents the total area of shear reinforcement within the spacing (s), while f_{yt} denotes the specified yield stress of the transverse reinforcement. Additionally, the value of d = 12.865 in. corresponds to the distance from the extreme compression fiber to the centroid of the longitudinal tension reinforcement in each of the upper or lower beams.

(b) Confinement requirement

The spacing of transverse reinforcement along the beam length should also meet the confinement requirement according to ACI 18.6.4.4:

s is lesser of $d/4$, 6 in., and $5 \times d_b$ for Grade 80 rebars.

$s = d/4 = 12.865 / 4 = 3.22$ in. (governs)

where d_b is nominal diameter of bar.

In the case of the 3.2 aspect ratio DBCB, the spacing of the transverse reinforcement within the flexural yielding region is determined by the confinement requirement of 3.22 in. Consequently, a spacing of 3 in. was used over a length equal to twice the individual beam depth (or the overall depth of the DBCB, h) measured from the face of the beam-to-wall interface toward the midspan from both ends of the beam, in accordance with ACI 18.6.4.1.

Design of transverse reinforcement outside of the flexural yielding region

For the remaining middle length of the beam, which spans 32 in., the spacing of transverse reinforcement required to meet the shear strength requirement remains unchanged at 5.64 in. This is because the shear induced by gravity loads is typically small for a typical coupling beam. As a result, the shear strength requirement remains nearly constant along the length of the beam. As per ACI 9.7.6.2.2, the maximum spacing (s) of shear reinforcement along the beam should be the smaller value between $d/4$ (= 3.22 in.) and 12 in. if $V_s > 4\sqrt{f_c'}b_w d$. However, for DBCB, this provision was not applied due to previous experimental tests indicating that the region around the mid-span of a DBCB typically remains undamaged, as illustrated in Fig. 2.3. Therefore, a spacing of 5.3 in. ($\leq$ 5.64 in.) was used instead (Fig. 3.7).

Note that the minimum shear reinforcement requirement prescribed in ACI Table 9.6.3.4 ($s \leq A_v f_{yt}/0.75\sqrt{f_c'}b_w$ or $s \leq A_v f_{yt}/50b_w$) does not apply for typical coupling beams that sustain a very high shear.

The reinforcement details of a DBCB with a 3.2 ratio are illustrated in Fig. 3.7. As per ACI 18.6.4.4, the first transverse reinforcement is positioned 2 in. away from the interface of the beam and the wall.

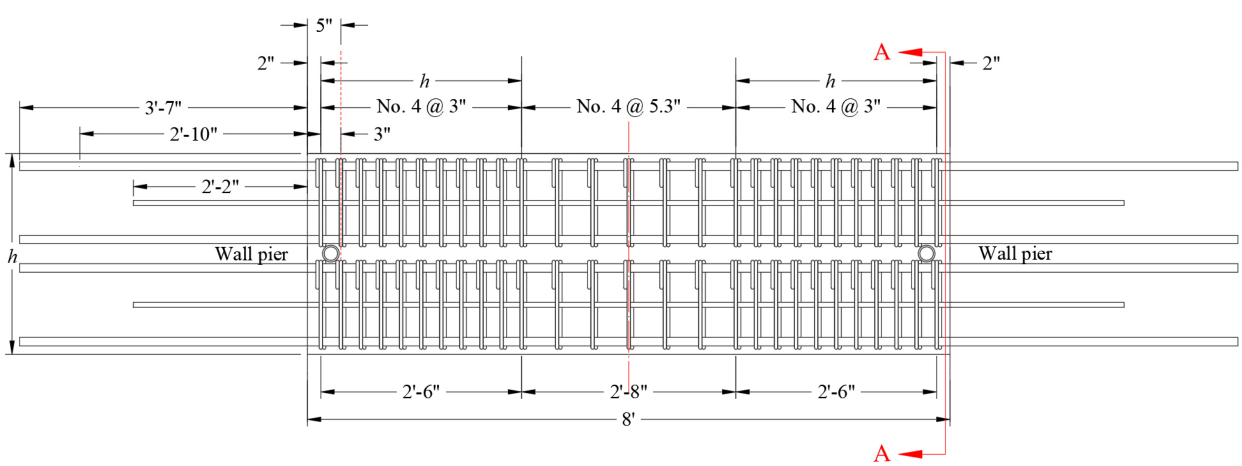

(a)

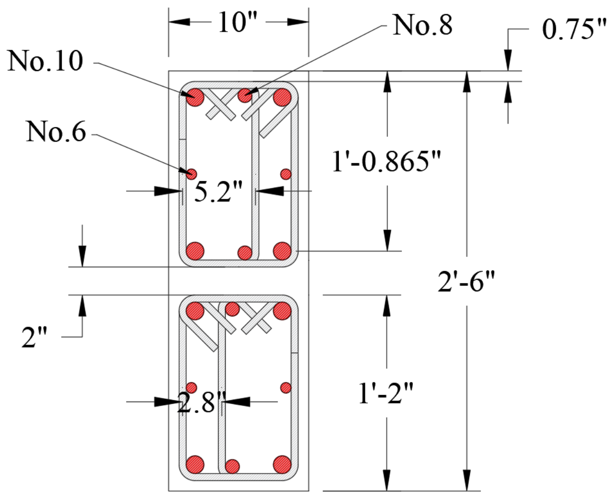

Section A-A

(b)

Fig. 3.7 Reinforcement details of full-scale DBCB with 3.2 aspect ratio: (a) Elevation View (b) Cross-section view

Minimum span-to-effective depth ratio of each individual beam

According to Fig. 3.2, a minimum span-to-effective depth ratio of each individual beam should be checked to ensure that the UCS is sufficiently large to permit separation of a DBCB (Choi and Chao, 2020):

$$\frac{l_n}{0.5(h-w)} \geq 5 \qquad \text{Eq. 3.8}$$

$$\frac{l_n}{0.5(h-w)} = \frac{96}{0.5(30-2)} = 6.86 \geq 5 \quad \text{O.K.}$$

3.1.1.2 Design of half-scale DBCB with 2.4 aspect ratio (with slab)

Dimensions of DBCB

The dimensions of the half-scale DBCB specimen with a 2.4 aspect ratio are shown in Fig. 3.8. The specimen has a height (h) of 15 in., a width (b_w) of 6 in., and length (l_n) of 36 in., resulting in aspect ratio (l_n/h) of 2.4, which is commonly used for residential buildings.

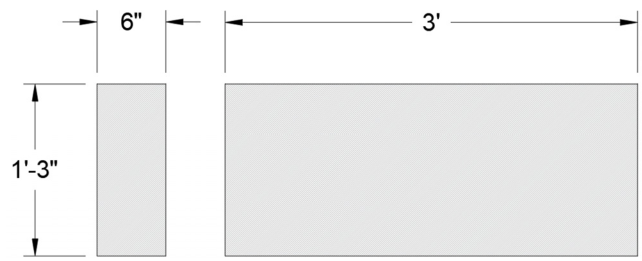

Fig. 3.8 Dimension of half-scale DBCB with 2.4 aspect ratio

Required shear strength (V_u)

A shear demand of V_u = 45 kips was used to design the half-scale 2.4 aspect ratio DBCB. Based on prior tests (Choi et al., 2020), the design interface shear strength of UCS was assumed to be a value of 0.3 ksi, which serves as a conservative lower bound estimate. Notably, for experimental purposes, the design of the specimen involved a different approach. Instead of following the conventional design practice, the longitudinal reinforcement in the coupling beam was first selected. Subsequently, the shear demand (V_u) of 45 kips was back-calculated based on the actual nominal moment capacity of the coupling beam, taking into account the specific longitudinal reinforcement used. This experimental design process differs from the typical practice, where the shear demand (V_u) is usually first determined through structural analysis, and then the reinforcement is designed accordingly.

Required nominal moment (M_n) for each of the upper or lower beam

The required nominal moments (M_n) for each individual beam in DBCB is calculated by using the equation defined in the design flowchart shown in Fig. 3.2, where v_{UCS} is 0.3 ksi. The strength reduction factor, ϕ, is 0.85 which is the same value assigned to DCBs (diagonally reinforced concrete coupling beams) by ACI 318-19.

$$M_n = \frac{l_n}{4}\left(\frac{V_u}{\phi} - \frac{v_{UCS} b_w h}{2}\right) = \frac{36}{4}\left(\frac{45}{0.85} - \frac{0.3 \times 6 \times 15}{2}\right) = 355 \text{ kip-in.}$$

Thickness of UCS, *w*

As shown in Figure 3.9, the thickness of the UCS positioned between the top and bottom beams is 1 inch. However, PVC pipes were not installed at both ends of the coupling beam due to the relatively small thickness of 1.0 inch for the UCS.

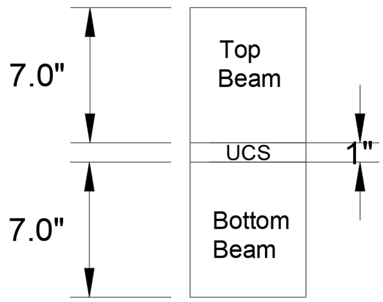

Fig. 3.9 Thickness of UCS

Flexure strength design

The design of each individual beam in the DBCB ensures that its moment capacity is equal to or greater than the required nominal moment (M_n) obtained from the equation provided above. This design process is carried out using the spColumn software (spColumn, 2019), with the assumption of a concrete crushing strain (ε_{cu}) of 0.004

Each individual beam of DBCB is designed to have the moment capacity greater than or equal to the required nominal moment (M_n) obtained by the above equation, using spColumn software (spColumn, 2019), where the crushing strain of concrete (ε_{cu}) is assumed as 0.004. Fig. 3.10 shows the location and the sizes of longitudinal reinforcement for the half-scale 2.4 aspect ratio DBCB, with Gr. 80 rebar ($f_y = 80$ ksi) used for all longitudinal reinforcement.

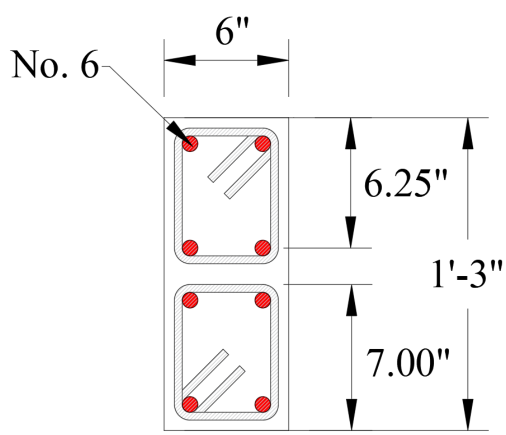

Fig. 3.10 Longitudinal reinforcement details of the second coupling beam specimen

Nominal design shear strength (V_n)

The nominal design shear strength, V_n. is estimated based on the actual nominal moment strength $(M_n)_{actual}$ and the interface shear strength of the UCS. This calculation is used to determine the rebar tensile strength. Notably, the actual interface shear strength could further increase the expected shear strength.

For the entire DBCB (two beams):

$$V_{n\_total} = 2\left(\frac{v_{UCS} b_w h}{4} + \frac{2(M_n)_{actual}}{l_n}\right) = 2\left(\frac{0.3\times 6\times 15}{4} + \frac{2\times 355}{36}\right) = 53 \text{ kips} = 8.4\sqrt{f_c'}A_{cw}$$

Note that the maximum allowable shear strength $10\sqrt{f_c'}A_{cw}$ = 63.6 kips, where A_{cw} (= $b_w \times h$) is the area of DBCB. For comparison, the design shear strength in the prior test (Specimen R2.4-SC-1) (Choi et al., 2018) is nearly identical to the design shear strength in the current test.

Development length, l_d

The development length of longitudinal reinforcement bars was taken as 60% of that required by ACI 318 18.8.5.3 (ACI, 2019):

For No. 6 rebar:

$$l_d = 0.6(3.25) f_y d_b / \left(65\lambda\sqrt{f_c'}\right) = 0.6(3.25)(80{,}000)(0.75)/\left[(65)\sqrt{5{,}000}\right] = 25 \text{ in.}$$

Transverse reinforcement design within the flexural yielding region

(a) Shear strength requirement

For this specimen, the flexural yielding zone was defined as twice the overall height of the beam, as per the requirement for beams provided in ACI 18.6.4.1. The probable design shear force (V_e) was used to determine the shear force (V_s) carried by the shear reinforcement of the top and bottom beams. This calculation was based on the probable moment strength (M_{pr}), where 1.25 f_y (which is equivalent to 100 ksi, i.e., 1.25 times 80 ksi) is used for the rebar tensile strength:

$$V_e = \frac{2M_{pr}}{l_n} = \frac{2\times 455}{36} = 25.3 \text{ kips}$$

where M_{pr} can be found by using spColumn software (StructurePoint, 2019). The shear force (V_s) for each individual beam carried by shear reinforcement was calculated by using the following equation, where strength reduction factor (ϕ) is 0.75. The contribution of concrete to the shear strength was ignored according to 18.6.5.2 of ACI 318 (ACI, 2019). Namely, $V_c = 0$.

$$V_s = \frac{V_e}{\phi} - V_c = \frac{25.3}{0.75} - 0 = 33.7 \text{ kips}$$

This shear force corresponds to a shear force of $12.7\sqrt{f_c'}b_wd$ (in psi unit) or $1.06\sqrt{f_c'}b_wd$ (in MPa unit). Note that ACI 22.5.1.2 imposes an upper bound limit of $8\sqrt{f_c'}b_wd$ (in psi unit) or $0.67\sqrt{f_c'}$ b_wd (in MPa unit) for the shear force that can be carried by shear reinforcement in a beam. However, this limit was not applied in the DBCB specimen under consideration as the same reason described above.

Note that as per 9.7.6.2.2 of ACI 318 (ACI, 2019), one additional crosstie is required across the width of the beam as shown in Fig. 3.6. However, this requirement is not considered for the half-scale DBCB. It was proven by the prior tests (Choi et al., 2018, 2020) that additional crosstie is not needed for half-scale DBCB. The requirement for the maximum spacing between the legs of shear reinforcement along the beam does not control, as the confinement requirement imposed a stricter spacing requirement.

The spacing (s) of transverse reinforcement is calculated using the equation defined below. For hoops, Gr. 60 No. 3 rebars were used. Therefore,

$$s = \frac{A_v f_{yt} d}{V_s} = \frac{2 \times 0.11 \times 60 \times 6.25}{33.7} = 2.45 \text{ in.}$$

(b) Confinement requirement

The spacing of transverse reinforcement should also meet the confinement requirement according to ACI 18.6.4.4 (ACI, 2019):

s is lesser of $d/4$, 6 in., and $6\times d_b$ for Grade 60 rebars.

$s = d/4 = 6.25 / 4 = 1.56$ in. (governs)

where d_b is nominal diameter of bar.

In the case of the half-scale 2.4 aspect ratio DBCB, the spacing of transverse reinforcement within the flexural yielding region is determined by the confinement requirement of 1.56 in.

Therefore, a leg spacing of 1.5 in. was used for the transverse reinforcement over a length equal to twice the individual beam depth (or overall height of the entire DBCB, h) measured from the face of the beam-to-wall interface toward midspan, at both ends of the beam.

Design of transverse reinforcement outside of the flexural yielding region

The transverse reinforcement spacing for the remaining middle length of the beam (4 in.) is also determined to be 2.45 in. in order to meet the shear strength requirement. For the remaining middle length of the beam (4 in.), the spacing of transverse reinforcement according to the shear strength requirement is also 2.45 in. This is because the shear induced by gravity loads is typically small for a typical coupling beam, and therefore the shear strength requirement remains nearly constant along the beam. As per ACI 9.7.6.2.2, the maximum spacing (s) of shear reinforcement along the beam should be the smaller value between $d/4$ (= 1.56 in.) and 12 in. if $V_s > 4\sqrt{f_c'}b_w d$. However, for DBCB, this provision was not applied due to previous experimental tests indicating that the region around the mid-span of a DBCB typically remains undamaged, as illustrated in Fig. 2.3. Therefore, a spacing of 2 in. ($\leq$ 2.45 in.) was selected instead (Fig. 3.11).

Note that the minimum shear reinforcement requirement prescribed in ACI Table 9.6.3.4 ($s \leq A_v f_{yt}/0.75\sqrt{f_c'}b_w$ or $s \leq A_v f_{yt}/50 b_w$) does not apply for typical coupling beams that sustain a very high shear.

Fig. 3.11 (a) shows the reinforcement details of DBCB with 2.4 aspect ratio and Fig. 3.11 (b) depicts the cross section of the coupling beam with slab. Slab design is discussed in next section. The first transverse reinforcement is located 1 in. away from the beam-to-wall interface according to ACI 18.6.4.4.

Minimum span-to-effective depth ratio of each individual beam

According to Fig. 3.2, a minimum span-to-effective depth ratio of each individual beam should be checked to ensure that the UCS is sufficiently large to allow the separation of DBCB (Choi and Chao, 2020):

$$\frac{l_n}{0.5(h-w)} \geq 5$$

$$\frac{l_n}{0.5(h-w)} = \frac{36}{0.5(15-1)} = 5.14 \geq 5 \quad \text{O.K.}$$

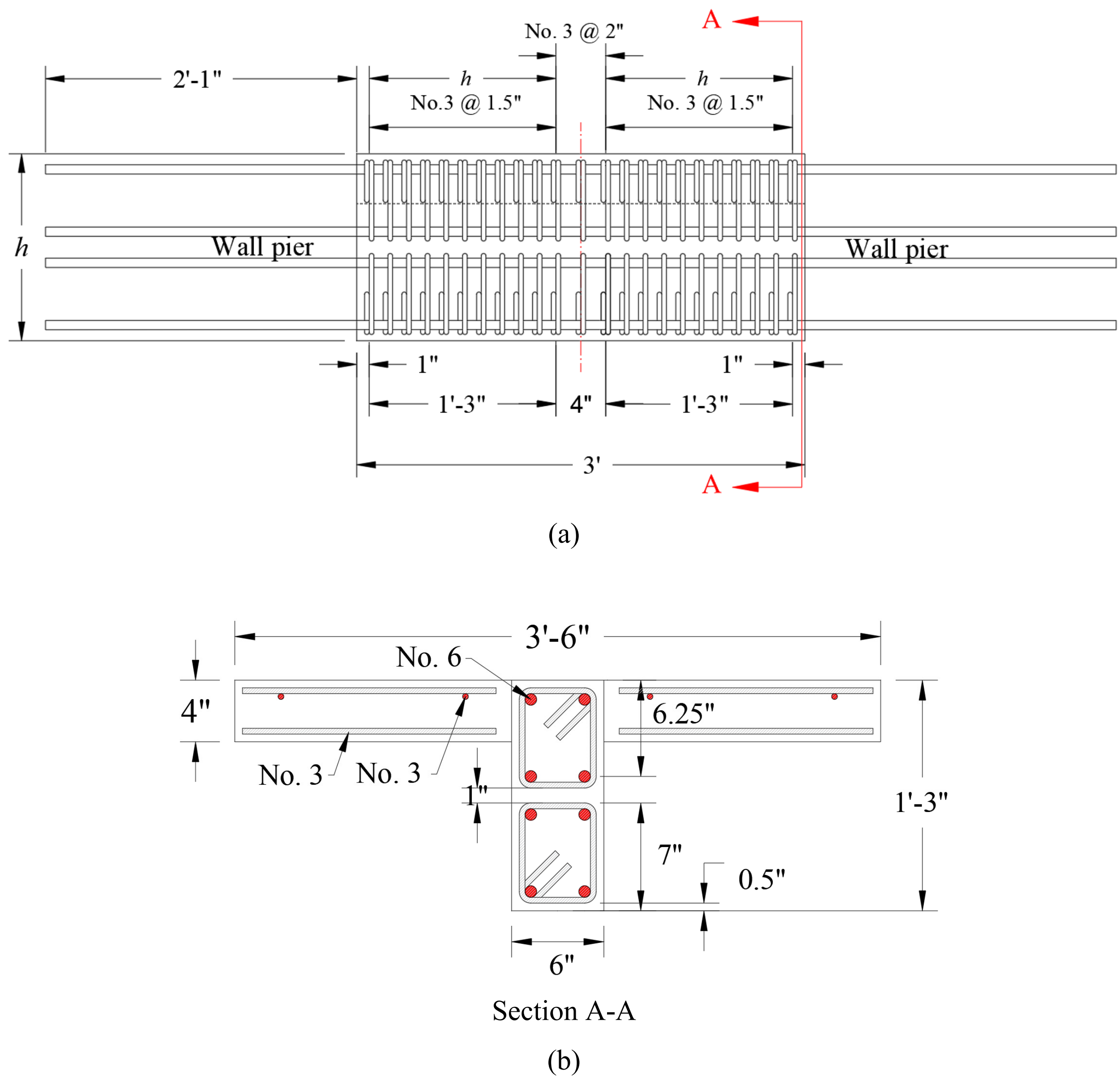

Fig. 3.11 Reinforcement details of half-scale DBCB with 2.4 aspect ratio: (a) Elevation View (b) Cross-section view

Slab design

The reinforcement details of the slab, as shown in Fig. 3.12, are based on the previous study conducted on DCBs with slabs (Naish et al. 2009). The 4-inch-thick slab is reinforced with Gr. 60 No. 3 bars. In the transverse direction, the bars are spaced 12 in. apart on both the top and bottom of the slab. In the longitudinal direction, the bars are only present on the top of the slab (Naish et al. 2009). To minimize the effect of the slab on the behavior of the DBCB, the transverse rebars of the slab, as illustrated in Figure 3.12, were terminated before the coupling beam.

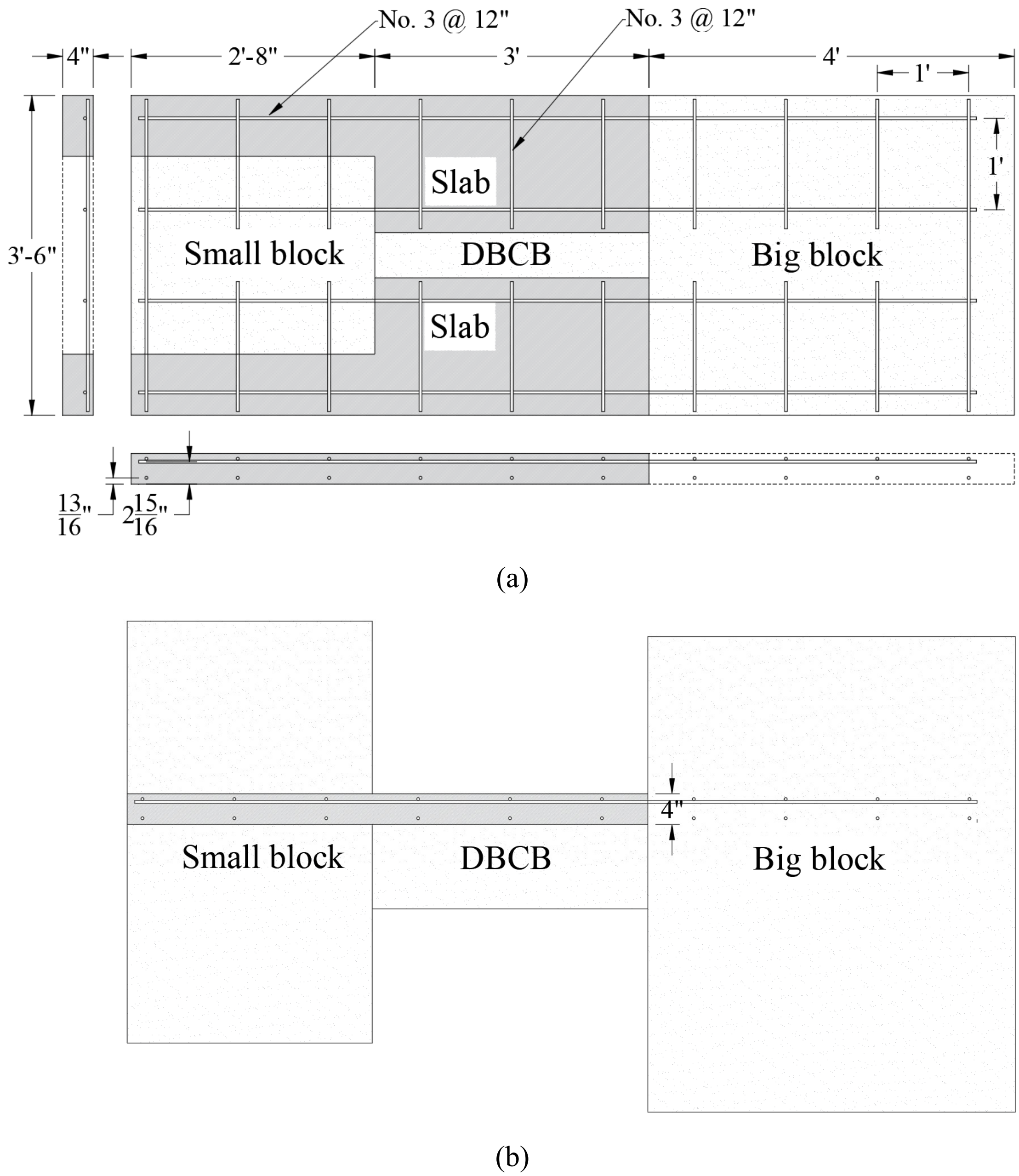

Fig. 3.12 Reinforcement details of half-scale 2.4 aspect ratio DBCB with slab (a) Plan view (b) Elevation view

3.1.1.3 Design of full-scale DBCB with 2.4 aspect ratio (with slab)

Dimensions of DBCB

Fig. 3.13 shows the dimensions of a full-scale 2.4 aspect ratio DBCB which has a height (h) of 30 in., a width (b_w) of 10 in., and length (l_n) of 72 in., resulting in aspect ratio (l_n/h) of 2.4, which is commonly used for residential buildings.

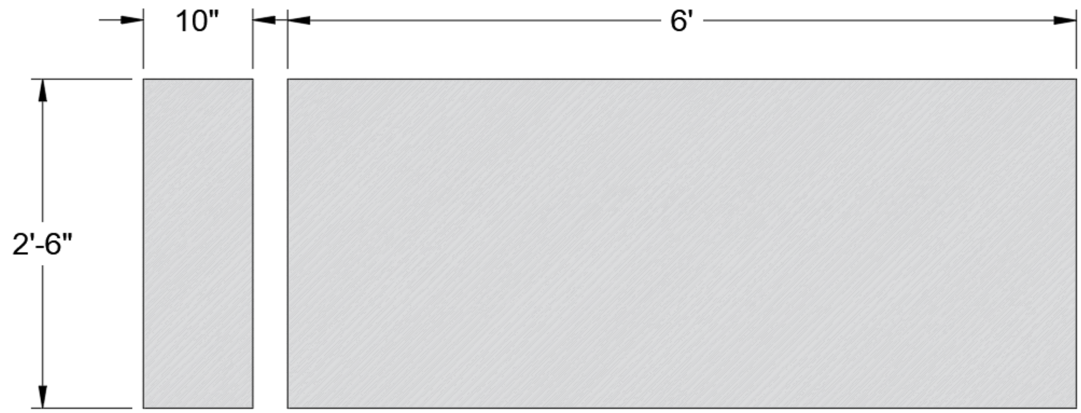

Fig. 3.13 Dimension of full-scale DBCB with 2.4 aspect ratio

Required shear strength (V_u)

A required shear strength of V_u = 123.5 kips was used to design the full-scale DBCB with a 2.4 aspect ratio. The assumed design interface shear strength of the UCS was 0.3 ksi, which is the same value used in the previous two specimens. It is important to note that, for experimental purposes, the design of the specimen involved a different approach. Instead of following the conventional design practice, the longitudinal reinforcement in the coupling beam was first selected. Subsequently, the shear demand (V_u) of 123.5 kips was back-calculated based on the actual nominal moment capacity of the coupling beam, taking into account the specific longitudinal reinforcement used. This experimental design process differs from the typical practice, where the shear demand (V_u) is usually first determined through structural analysis, and then the reinforcement is designed accordingly.

Required nominal moment (M_n) for each of the upper or lower beam

The required nominal moments (M_n) for each individual beam in the full-scale DBCB with a 2.4 aspect ratio is calculated as follows, where v_{UCS} is 0.3 ksi, strength reduction factor, ϕ is 0.85.

$$M_n = \frac{l_n}{4}\left(\frac{V_u}{\phi} - \frac{v_{UCS} b_w h}{2}\right) = \frac{72}{4}\left(\frac{123.5}{0.85} - \frac{0.3 \times 10 \times 30}{2}\right) = 1{,}806 \text{ kip-in.}$$

Thickness of UCS, *w*

As shown in Fig. 3.14, the thickness of UCS, *w*, located between the top and bottom beams is 3 in. PVC pipes with a 3.0-inch nominal diameter were inserted between the hoops to accommodate utilities. As shown in Fig. 3.16, the center of each PVC pipe was located at a distance of 3.5 in. away from both ends of the beam, or alternatively, the outer edge of each PVC pipe was located 5.0 in. from both ends of the beam.

Flexure strength design

Each individual beam of DBCB was designed to have the moment capacity greater than or equal to required nominal moment (M_n) as calculated above, where the crushing strain of concrete (ε_{cu}) was taken as 0.004. The design was carried out by using the spColumn software (spColumn, 2019). Fig. 3.15 shows the location and the sizes of longitudinal reinforcement for the full-scale DBCB with 2.4 aspect ratio. Gr. 80 rebar (f_y = 80 ksi) was used for all longitudinal reinforcement.

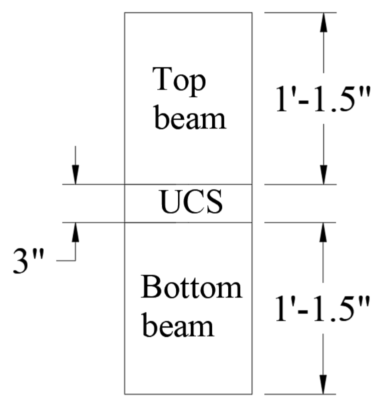

Fig. 3.14 Thickness of UCS

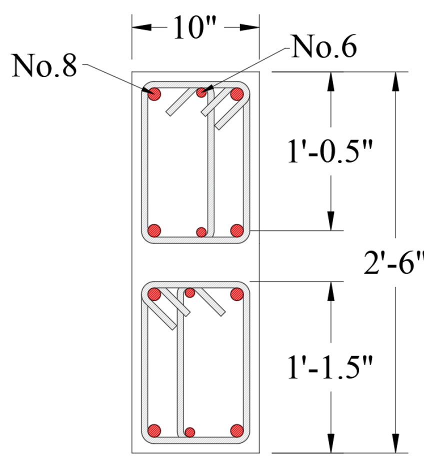

Fig. 3.15 Longitudinal reinforcement details of the third coupling beam specimen

Nominal design shear strength (V_n)

The nominal design shear strength, V_n, of the specimen is estimated based on the actual nominal moment strength $(M_n)_{actual}$ and the interface shear strength of the UCS.

For the entire DBCB (two beams):

$$V_{n\_total} = 2\left(\frac{v_{UCS} b_w h}{4} + \frac{2(M_n)_{actual}}{l_n}\right) = 2\left(\frac{0.3 \times 10 \times 30}{4} + \frac{2 \times 1{,}806}{72}\right) = 145 \text{ kips} = 6.9\sqrt{f_c'} A_{cw}$$

The maximum allowable shear strength is $10\sqrt{f_c'} A_{cw} = 212$ kips, where A_{cw} (= $b_w \times h$) is the area of DBCB. Note that when computing the nominal shear strength of DBCB, the cross-sectional area considered is the gross area of the beam section, which is consistent with that of DCBs.

Development length, l_d

The development length of longitudinal rebars was taken as 60% of length required by ACI 18.8.5.3 (ACI, 2019):

For No. 8 rebar:

$$l_d = 0.6(3.25) f_y d_b / \left(65\lambda\sqrt{f_c'}\right) = 0.6(3.25)(80{,}000)(1.0) / \left[(65)\sqrt{5{,}000}\right] = 34 \text{ in.}$$

For No. 6 rebar:

$$l_d = 0.6(3.25) f_y d_b / \left(65\lambda\sqrt{f_c'}\right) = 0.6(3.25)(80{,}000)(0.75) / \left[(65)\sqrt{5{,}000}\right] = 25 \text{ in.}$$

Design of transverse reinforcement within the flexural yielding region

(a) Shear reinforcement requirement

Based on the observations from the first two specimens, the flexural yielding zone for the current specimen was defined as a length equal to the depth of each upper or lower beam, which is equivalent to half the overall depth of the entire DBCB (h/2). This differs from the requirement in ACI 18.6.4.1, which states that the flexural yielding zone should be twice the moment frame beam depth. The probable design shear force (V_e) was used to calculate the shear force (V_s) that the shear reinforcement carries. This calculation was based on the probable moment strength (M_{pr})

and utilizes a rebar tensile strength of 1.25 f_y (which is equivalent to 100 ksi, i.e., 1.25 times 80 ksi):

$$V_e = \frac{2M_{pr}}{l_n} = \frac{2 \times 2,233}{72} = 62 \text{ kips}$$

where M_{pr} can be found by using spColumn software (StructurePoint, 2019). The shear force (V_s) for each individual beam carried by the shear reinforcement was determined using the following equation, where the strength reduction factor (ϕ) is equal to 0.75. In accordance with ACI 18.6.5.2, considering $V_e > (V_u/2)/2 = 123.5/4 = 30.9$ kips and neglecting the compressive force in the coupling beam, the contribution of concrete to the shear strength was ignored, namely, $V_c = 0$.

$$V_s = \frac{V_e}{\phi} - V_c = \frac{62}{0.75} - 0 = 82.7 \text{ kips}$$

This shear force corresponds to a shear force of $9.4\sqrt{f_c'}b_w d$ (in psi unit) or $0.78\sqrt{f_c'}b_w d$ (in MPa unit). Note that ACI 22.5.1.2 imposes an upper bound limit of $8\sqrt{f_c'}b_w d$ (in psi unit) or $0.67\sqrt{f_c'}b_w d$ (in MPa unit) for the shear force that can be carried by shear reinforcement in a beam. However, this limit was not applied in the DBCB specimen under consideration. This is because no severe diagonal concrete crushing was observed in the half-scale DBCB specimens even when the calculated V_s is much greater than $8\sqrt{f_c'}b_w d$, as shown in Figure 2.3.

The maximum leg spacing (s_{max}) of the shear reinforcement across beam width was determined according to ACI 9.7.6.2.2. For $V_s > 4\sqrt{f_c'}b_w d$ (= 82.7 kips > 36 kips):

s is lesser of $d/2$ and 12 in., or $s_{max\_w} = d/2 = 12.5/2 = 6.25$ in.

Considering the specimen width of 10 in. and a clear cover of 0.75 in., the spacing (across width of the beam) between two legs of transverse reinforcement is 8 in., which exceeds the limit of 6.25 in. Consequently, an additional crosstie is necessary across the width of the beam to meet the requirement of $s_{max\_w} = 6.25$ in., as illustrated in Fig. 3.6. This additional crosstie also increases the shear strength. Note the detail shown in Fig. 3.6 is consistent with "Detail A" illustrated in Fig. R18.6.4 of ACI code.

Note that according to ACI 9.7.6.2.2, the maximum spacing between the legs of shear reinforcement along the beam should be the lesser of $d/4$ and 12 in. if $V_s > 4\sqrt{f_c'}b_w d$. However, this requirement does not govern in this case, as the confinement requirement imposed a stricter spacing requirement.

The spacing (s) of the shear reinforcement based on the shear strength was calculated according to ACI 22.5.8.5.3:

$$s = \frac{A_v f_{yt} d}{V_s} = \frac{3 \times 0.2 \times 60 \times 12.5}{82.7} = 5.44 \text{ in.}$$

where A_v represents the total area of shear reinforcement within the spacing (s), while f_{yt} denotes the specified yield stress of the transverse reinforcement. Additionally, the value of d = 12.5 in. corresponds to the distance from the extreme compression fiber to the centroid of the longitudinal tension reinforcement in each of the upper or lower beams.

(b) Confinement requirement

The spacing of transverse reinforcement along the beam length should also meet the confinement requirement according to ACI 18.6.4.4 (ACI, 2019). Note that the requirement in ACI 18.6.4.4 was only applied over a length equal to half of overall DBCB depth ($h/2$). In this specimen, a slightly relaxed spacing requirement was used for the subsequent $h/2$ length.

For a length up to $h/2$ from the beam-to-wall interface:

s is lesser of $d/4$, 6 in., and $5\times d_b$ for Grade 80 rebars.

$s = d/4 = 12.5 / 4 = 3.13$ in. (governs)

For subsequent $h/2$ length:

s is lesser of $d/3$, 6 in., and $5\times d_b$ for Grade 80 rebars.

$s = d/3 = 12.5 / 3 = 4.17$ in. (governs)

where d_b is nominal diameter of the longitudinal rebars.

In the case of the 2.4 aspect ratio DBCB, the spacing of the transverse reinforcement within the flexural yielding region is determined by the confinement requirement of 3.13 in. Therefore, a spacing of 3 in. was used over a length of $h/2$ measured from the face of the beam-to-wall interface toward the midspan from both ends of the beam. Subsequently, a spacing of 4 in. was used over the subsequent length of $h/2$.

Design transverse reinforcement beyond *h*-distance

For the remaining middle length of the beam, which spans 8 in., the spacing of transverse reinforcement required to meet the shear strength requirement remains unchanged at 5.44 in. This is because the shear induced by gravity loads is typically small for a typical coupling beam. As a result, the shear strength requirement remains nearly constant along the length of the beam. As per ACI 9.7.6.2.2, the maximum spacing (s) of shear reinforcement along the beam should be the smaller value between $d/4$ (= 3.13 in.) and 12 in. if $V_s > 4\sqrt{f_c'}b_w d$. However, for DBCB, this provision was not applied due to previous experimental tests indicating that the region around the mid-span of a DBCB typically remains undamaged, as illustrated in Fig. 2.3. Therefore, a spacing of 4 in. (≤ 5.44 in.) was used for the remaining midspan (Fig. 3.16)

Note that the minimum shear reinforcement requirement prescribed in ACI Table 9.6.3.4 ($s \leq A_v f_{yt}/0.75\sqrt{f_c'}b_w$ or $s \leq A_v f_{yt}/50b_w$) does not apply for typical coupling beams that sustain a very high shear.

Fig. 3.16 (a) illustrates the reinforcement details of the DBCB with a 2.4 ratio, while Fig. 3.16 (b) shows the cross-section of the coupling beam with the slab. The design of the slab will be discussed in the subsequent section. According to ACI 18.6.4.4, the first transverse reinforcement is positioned at a distance of 2 inches from the beam-to-wall interface.

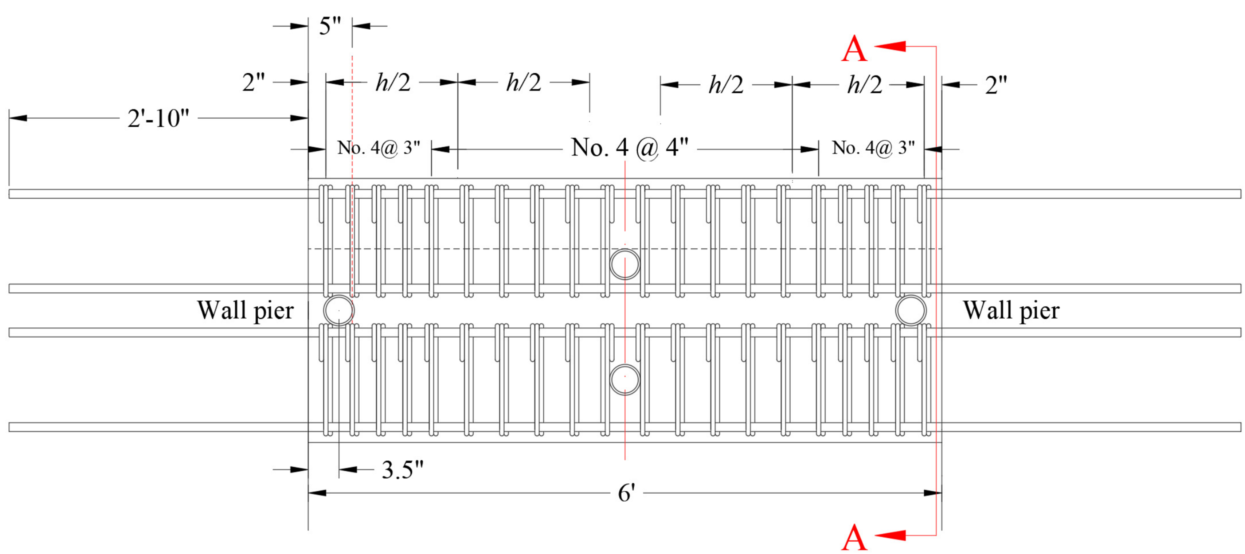

(a)

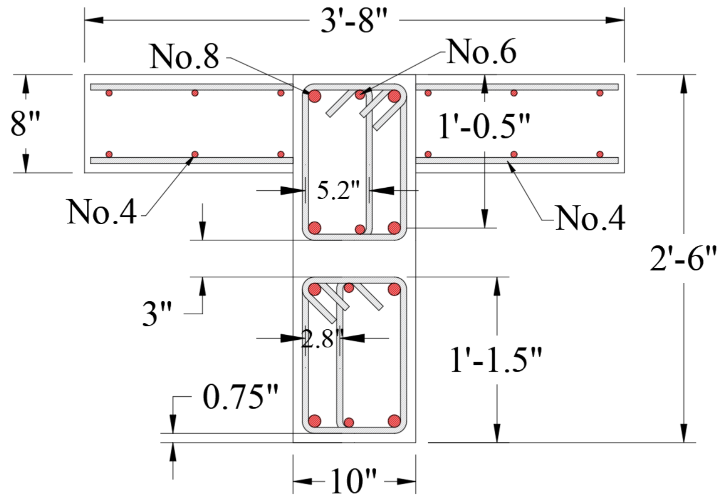

(b)

Fig. 3.16 Reinforcement details of full-scale DBCB with 2.4 aspect ratio: (a) Longitudinal section (b) Cross section

Minimum span-to-effective depth ratio of each individual beam

According to Fig. 3.2, a minimum span-to-effective depth ratio of each individual beam should be checked to ensure that the UCS is sufficiently large to permit separation of a DBCB (Choi and Chao, 2020):

$$\frac{l_n}{0.5(h-w)} \geq 5$$

$$\frac{l_n}{0.5(h-w)} = \frac{72}{0.5(30-3)} = 5.33 \geq 5 \quad \text{O.K.}$$

Slab design

Fig. 3.16 (b) shows the cross-section of a T-beam which consists of DBCB and a slab span on both sides. The effective flange width (b_f) includes the width of the beam web (b_w) plus a slab span on both sides. As per ACI 6.3.2.1 (ACI, 2019):

b_f is least of b_w+2×8h_f, b_w+2×(S_w/2), and b_w+2×(l_n/8),

Therefore, $b_f = b_w+2\times(l_n/8) = 24+2\times(72/8) = 42$ in. (governs)

where h_f is the slab thickness, S_w is the clear distance to the adjacent web, and l_n is the length of beam clear span. Note that b_w = 24 in. was used to calculate the b_f instead of b_w = 10 in. This adjustment was made to accurately represent the effective flange width of the actual full-scale DBCB with a slab. In Fig. 3.17 (a), it can be observed that the effective flange width (b_f) was slightly increased to 44 in. due to construction convenience. Figs. 3.17 (a) and (b) provide the reinforcement details of the slab. The slab, which has a thickness of 8 in., is reinforced with Gr. 60 No. 4 bars. The transverse direction features bars spaced 12 in. apart on both the top and bottom, while the longitudinal direction has bars spaced 6 in. apart on both the top and bottom. To align with common construction practices, the reinforcement of the slab in the transverse direction extends over the top of the coupling beam. This allows for a more accurate representation of the typical construction methods employed.

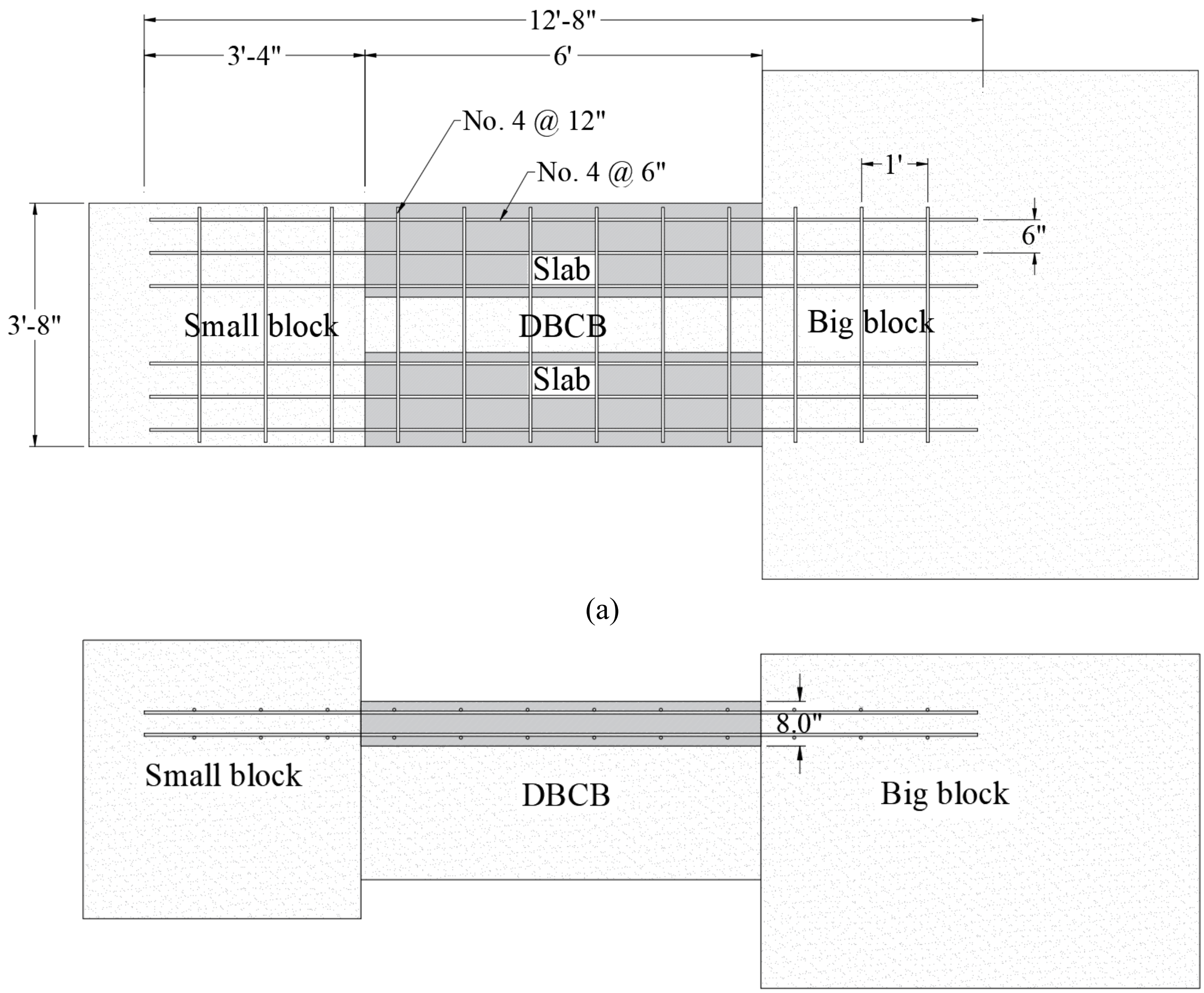

Fig. 3.17 Reinforcement details of full-scale 2.4 aspect ratio DBCB with slab: (a) Plan view (b) Elevation view

3.1.1.4 Design of adjacent concrete blocks (wall piers)

In Figs. 3.12 and 3.17, each side of the designed DBCB specimen is connected to a reinforced concrete block. These blocks represent the adjacent walls or wall piers in the actual structure. The longitudinal bars in the coupling beam are embedded within these blocks, ensuring the required development lengths are achieved. In the setup, one block, referred to as the "big block," is connected to the strong floor or reaction floor. On the other hand, the second block, known as the "loading block," is connected to an actuator through the loading beam. Fig. 3.18 provides an illustration of the reinforcement details for both the big block and loading block in the full-scale DBCB. In this configuration, Gr. 60 rebar was used for the reinforcement of both blocks. As shown in Fig. 3.18, the big block is considerably larger in size compared to the loading block. The size of the big block is determined based on the number of post-tensioned anchor rods required to secure the specimen to the strong floor and effectively resist the shear force and moment generated in the coupling beam during the test, while preventing any damage. Conversely, for the half-scale DBCB, smaller versions of both the big block and loading block were employed.

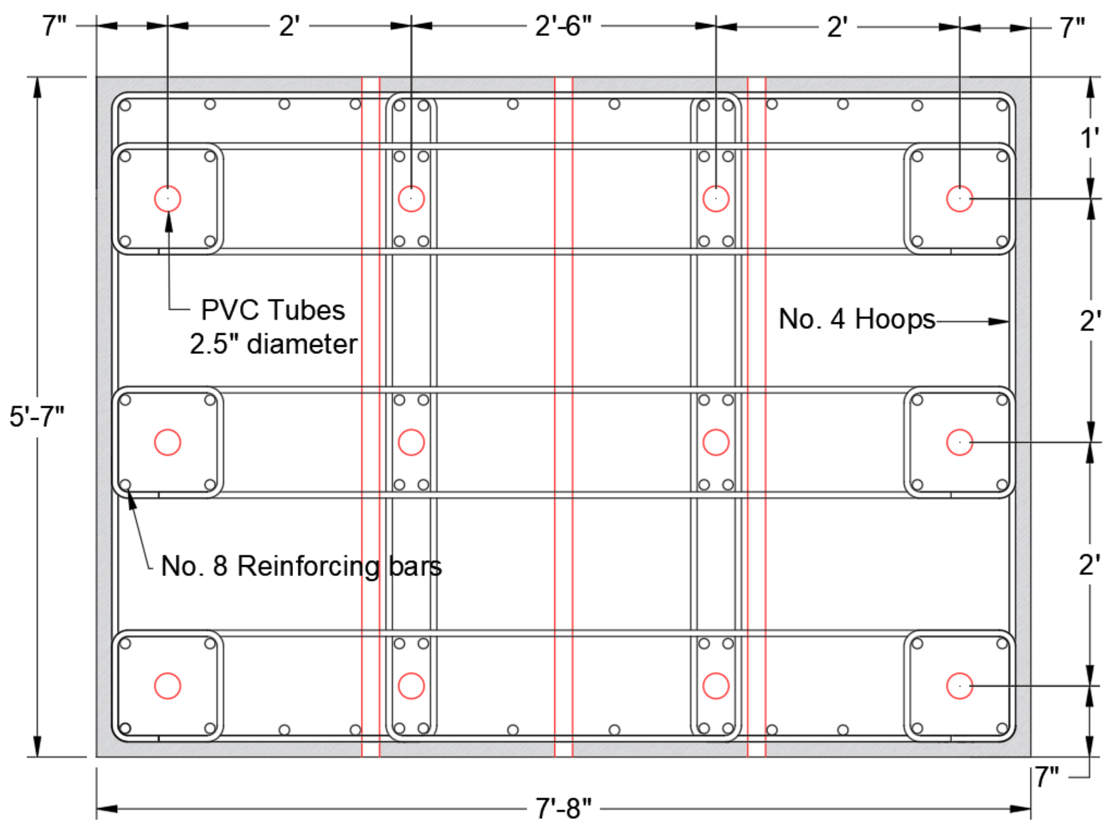

(a)

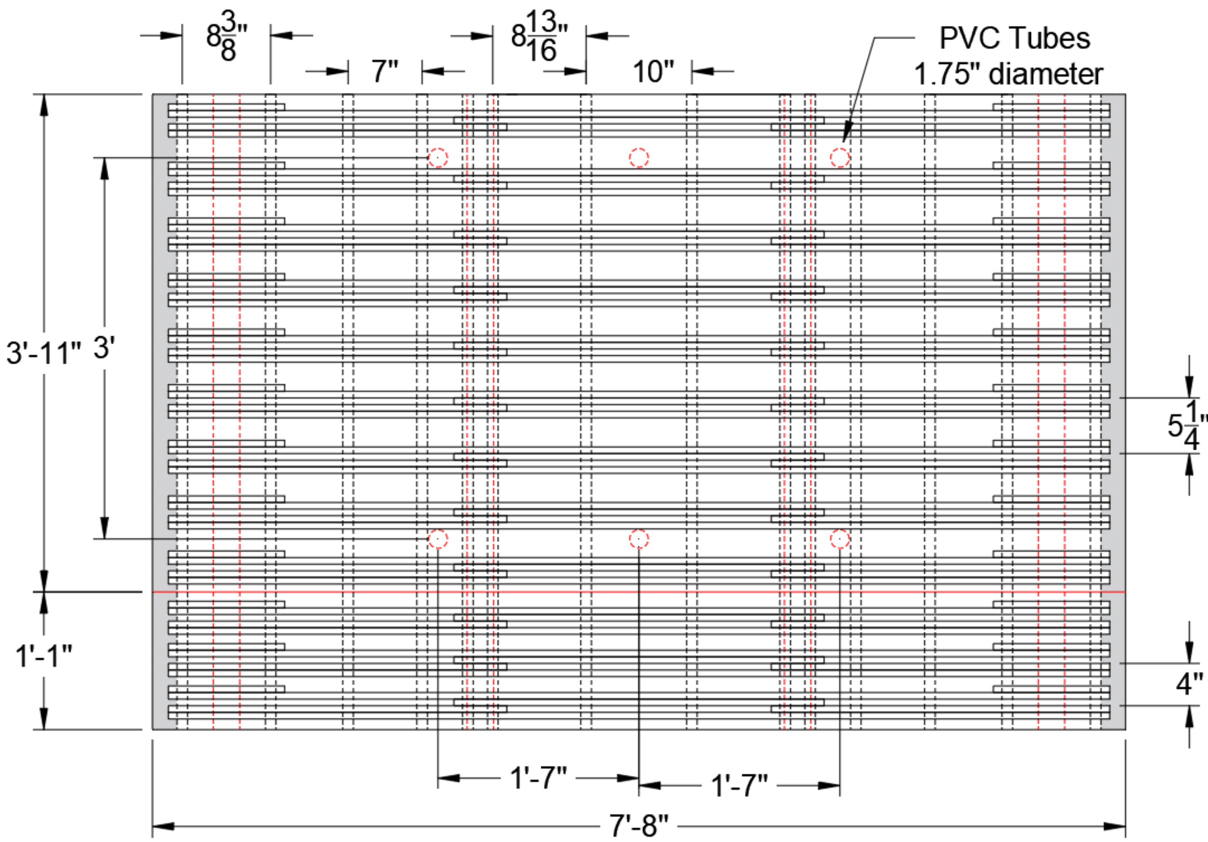
8 3/8"
7"
8 13/16"
10"
PVC Tubes
1.75" diameter
3'-11"
3'
5 1/4"
1'-1"
4"
1'-7"
1'-7"
7'-8"

(b)

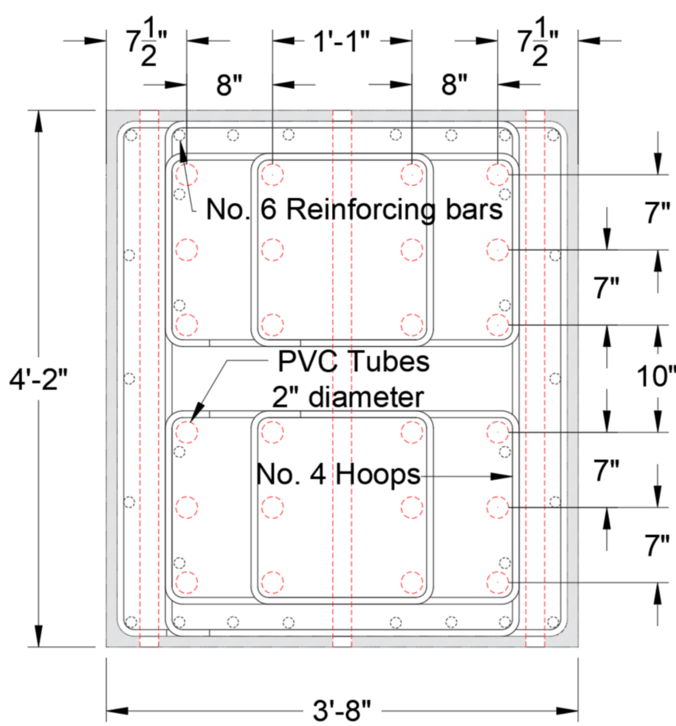
7 1/2"
1'-1"
7 1/2"
8"
8"
No. 6 Reinforcing bars
7"
7"
4'-2"
PVC Tubes
2" diameter
10"
No. 4 Hoops
7"
7"
3'-8"

(c)

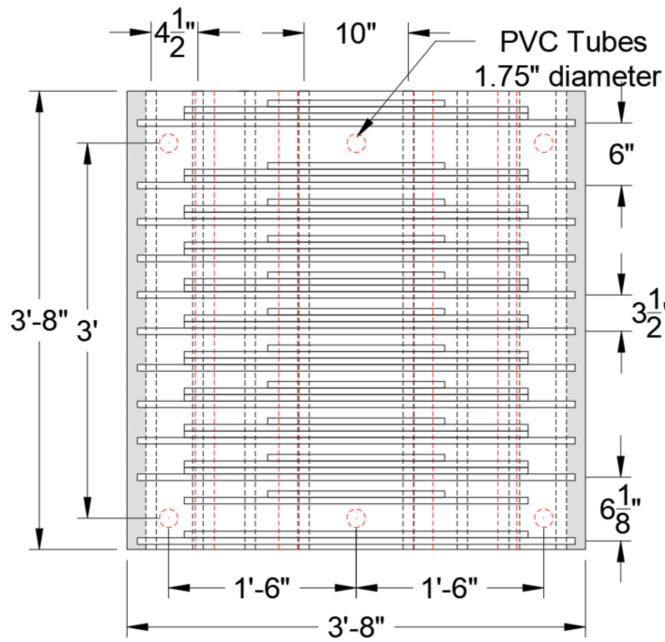

(d)

Fig. 3.18 Big block and small block reinforcement details for full-scale DBCB: (a) Plan of big block, (b) Elevation of big block, (c) Plan of loading block, and (d) Elevation of loading block

3.1.1.5 Design summary

In Sections 3.1.1.1 to 3.1.1.3, the detailed design of three DBCB specimens was described. Table 3.1 provided a summary of the information for each specimen. The name assigned to each specimen was based on the test variables, including the scale of the specimen (half scale: HS; full scale: FS), the span-to-depth ratio (3.2 or 2.4), the presence or absence of a slab (S: with a slab; N: without a slab), and the size (inches) of the unreinforced concrete strip (UCS). For example, the specimen named FS-R3.2-N-2 represents a full-scale (FS) DBCB with a span-to-depth ratio of 3.2 (R3.2), without a slab (N), and a UCS size of 2 inches (2). Table 3.2 shows reinforcement ratio (ρ) of the coupling beam for each specimen. Table 3.2 shows that FS-R2.4-S-3 had a comparatively lower reinforcement ratio (ρ) compared to the other specimens. The reinforcement ratio (ρ) for the slab of each specimen is summarized in Table 3.3. In the longitudinal direction, HS-R2.4-S-1 had a significantly smaller reinforcement ratio (ρ_{s1}) than FS-R2.4-S-3. This difference stems from HS-R2.4-S-1 being reinforced with No. 3 bars spaced 12 in. apart exclusively on the top of the slab, whereas FS-R2.4-S-3 was reinforced with No. 4 bars spaced 6 in. apart on both the top and bottom of the slab.

Reinforcement ratio (ρ_{st}) in the transverse direction satisfies the reinforcement requirement for shrinkage and temperature as specified in ACI 24.4.3.2 (ACI, 2019).

Table 3.1 Specimen information

Specimen	l_n/h	l_n/d	Unreinforced concrete strip (UCS) (in.)	Nominal design shear strength, V_n (kips)	$V_{normalized}$*
FS-R3.2-N-2	3.2	7.46	2	182.5	8.6
HS-R2.4-S-1	2.4	5.76	1	53	8.4
FS-R2.4-S-3	2.4	5.76	3	145	6.9

*Normalized shear stress: $V_{normalized}=V_n/(\sqrt{f_c'}b_w h)$, where f_c' = 5 ksi (design compressive strength)

Table 3.2 Reinforcement ratio (ρ) of coupling beam

Specimen	Longitudinal reinforcement ρ_{bl}, % (main bar [intermediate bar])*	Transverse reinforcement $\rho_{plastic\ hinge}$, % (bar size[spacing])	Transverse reinforcement $\rho_{nonplastic\ hinge}$, % (bar size[spacing])
FS-R3.2-N-2	2.59 (No.10, No.8 [No.6])	2.00 (No.4[3.0 in.])	1.13 (No.4[5.3 in.])
HS-R2.4-S-1	2.35 (No.6 [-])	2.44 (No.3[1.5 in.])	1.83 (No.3[2.0 in.])
FS-R2.4-S-3	1.62 (No.8, No.6 [-])	2.00 (No.4[3.0 in.])	1.50 (No.4[4.0 in.])

*: ρ_{bl} is reinforcement ratio of either the top or bottom longitudinal bars of each individual beam, $\rho_{bl} = A_s/(b_w/d)$. Intermediate bars are not included in ratio.

Table 3.3 Reinforcement ratio (ρ) of slab

Specimen	Longitudinal direction ρ_{sl}, % (bar size[spacing])	Transverse direction ρ_{st}, % (bar size[spacing])
FS-R3.2-N-2	-	-
HS-R2.4-S-1	0.26 (No.3[12 in.])	0.46 (No.3[12 in.])
FS-R2.4-S-3	0.74 (No.4[6 in.])	0.42 (No.4[12 in.])

3.1.1.6 Nonlinear finite element analysis

Throughout the testing process, it is important to ensure that all testing setups and fixtures remain in the elastic range, except for the coupling beam. Among the three specimens designed, the full-scale DBCB with a 3.2 aspect ratio (FS-R3.2-N-2) has the highest nominal shear strength

(V_n) and moment (M_n). Consequently, a nonlinear finite element analysis (NLFEA) was conducted on the FS-R3.2-N-2 specimen using the commercial FEA software ABAQUS 6.14 to examine the stresses in the setups and fixtures (Dassault Systèmes Simulia 2019). The FE model incorporated material properties with geometrical and contact nonlinearities.

Fig. 3.19 (a) shows the overview of the test setup and fixtures while Fig. 3.19 (b) demonstrates the complete representation of the DBCB specimen, including the strong floor where post-tensioning was applied to the big block to simulate the actual specimen boundary conditions. In Fig. 3.19 (c), the FE model includes the embedded reinforcement cage of the DBCB. However, to simplify the model, the reinforcement cages of the big block and loading block were omitted. Fig. 3.19 (d) illustrates the fixed boundary conditions imposed on the strong floor. Fig. 3.19 (e) shows the FE model of post-tensioning rods used for the big and loading blocks.

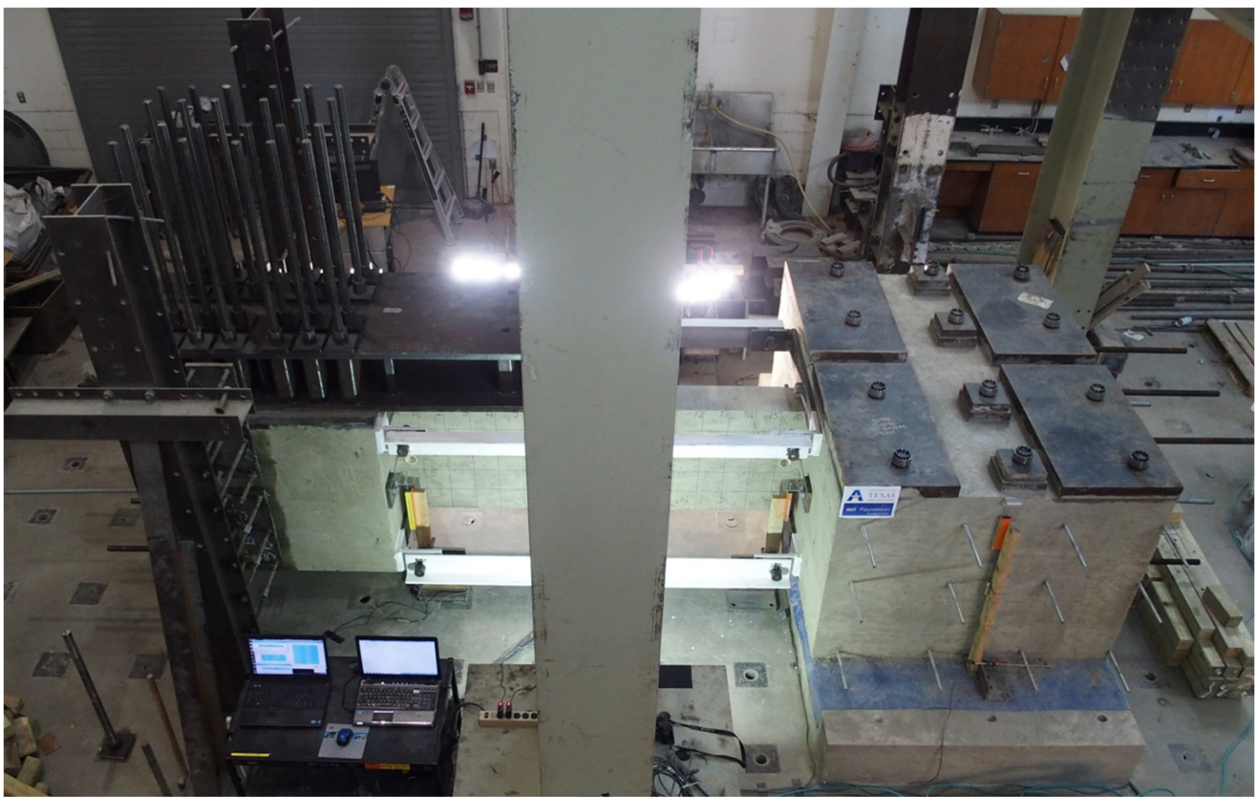

(a) Overview of the test setup

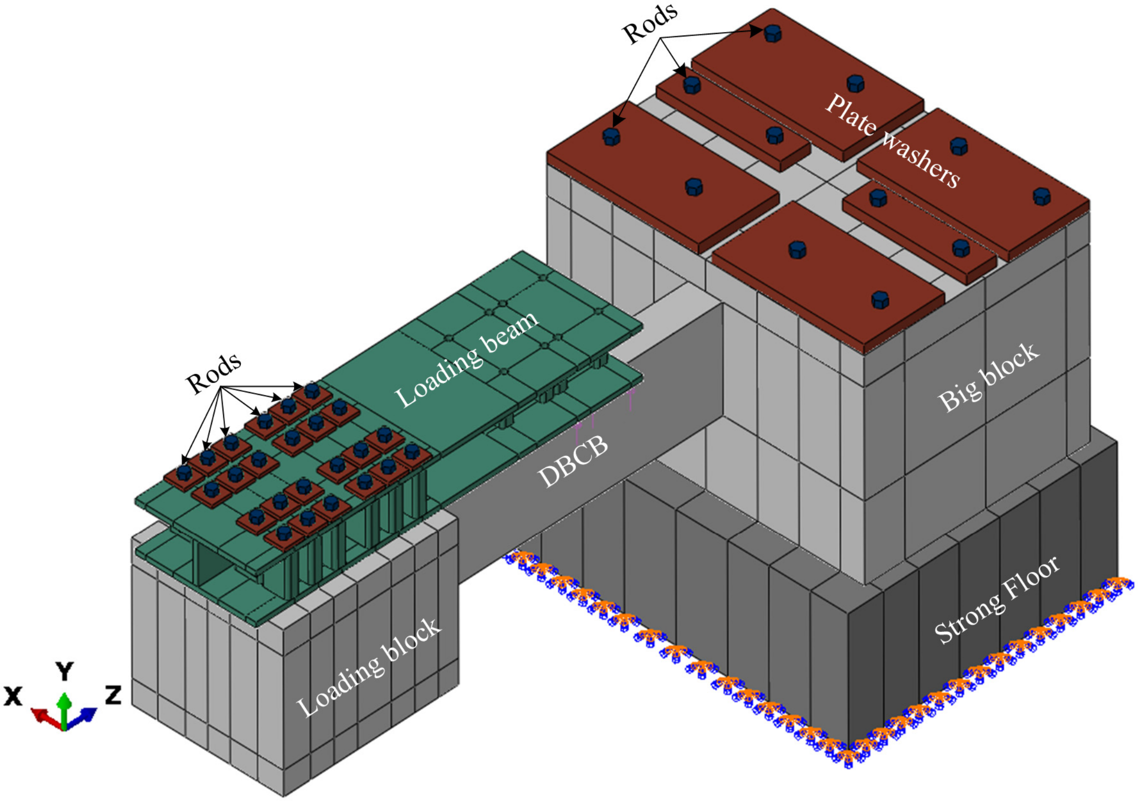
Rods
Plate washers
Loading beam
Rods
Big block
DBCB
Strong Floor
Loading block
X
Y
Z

(b)

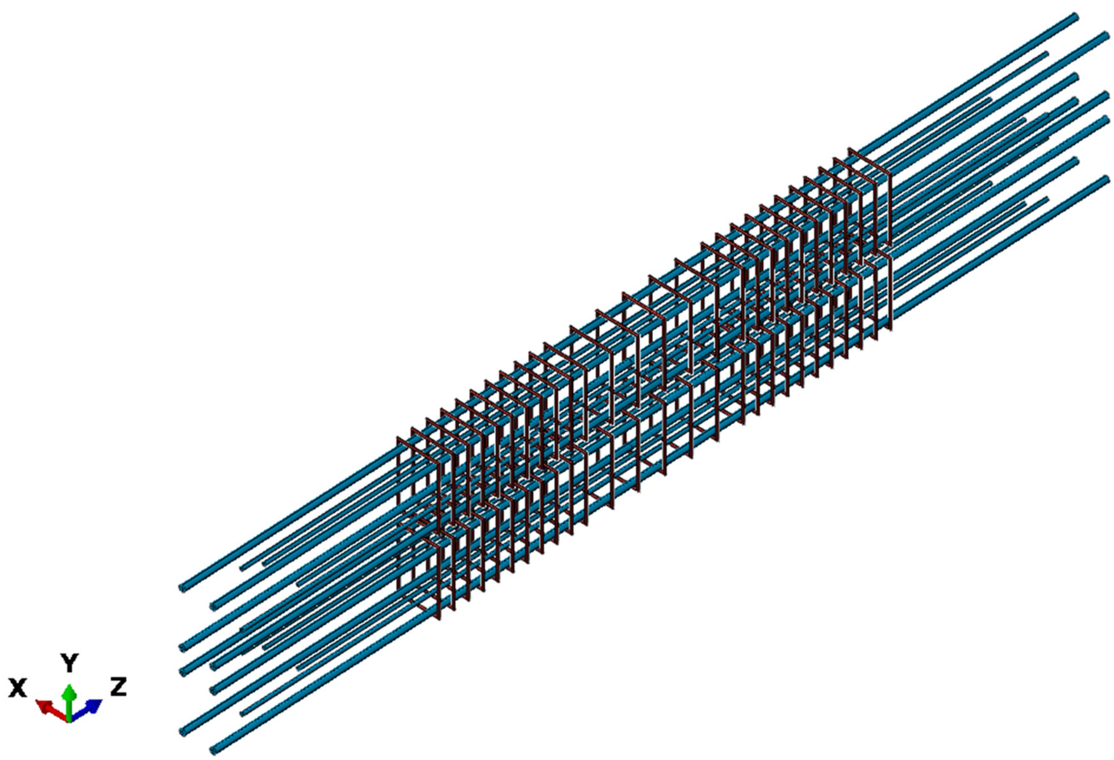
X
Y
Z

(c)

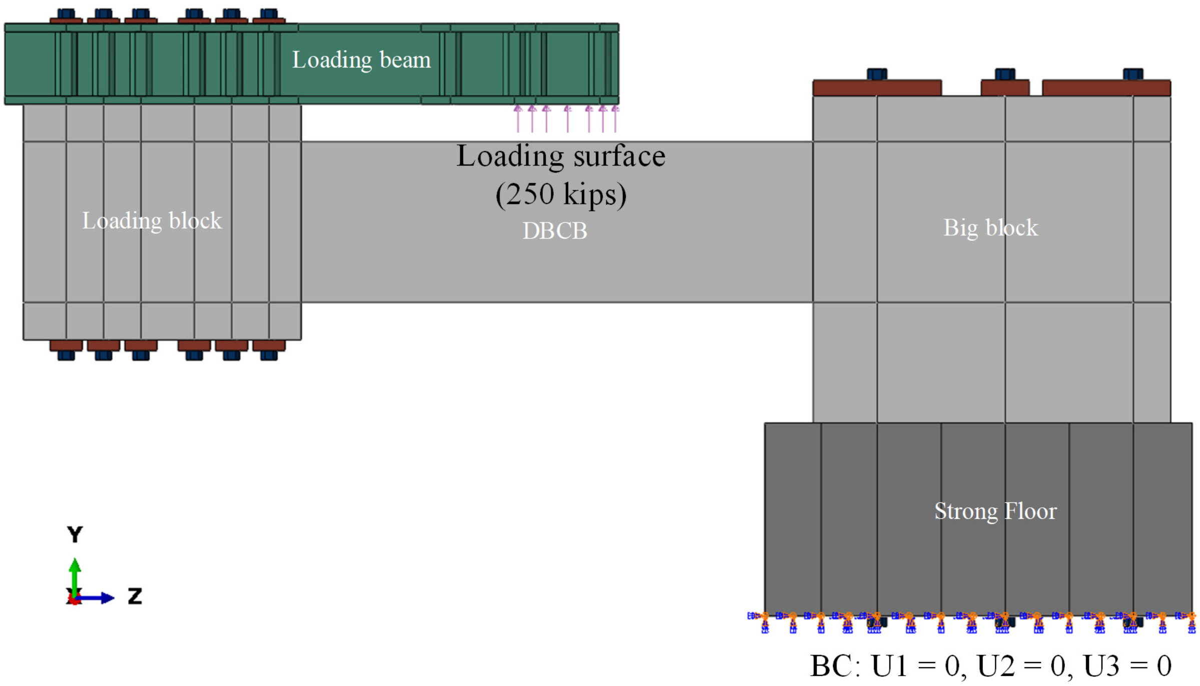

(d)

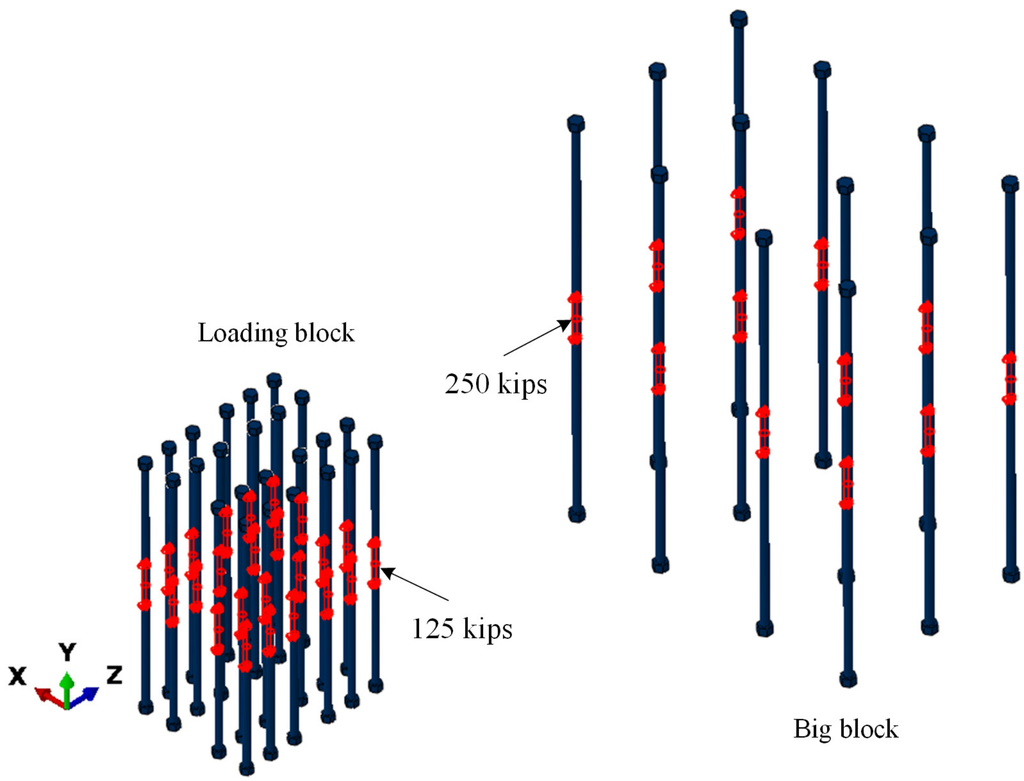

(e)

Fig. 3.19 (a) Overview of the test setup, (b) FE model: DBCB specimen, (c) FE model: DBCB reinforcement cage, (d) FE model: boundary conditions, and (e) FE model: post-tensioning rods used for the big and loading blocks

Fig. 3.20 illustrates the contact surface of the DBCB specimen, where the interactions between the two surfaces were simulated using a deformable surface-to-surface contact approach with a finite-sliding contact formulation. In the tangential direction, a friction coefficient value of μ = 0.3 was assumed, while in the normal direction, a "hard" contact pressure-overclosure relationship was utilized. However, separation was permitted after contact. The FE model, as shown in Fig. 3.21, was discretized using an 8-node linear solid element. This element employed reduced integration and the hourglass control technique. To ensure accurate numerical results without mesh sensitivity concerns, approximately 250,000 elements were utilized in the model. To capture the nonlinear behavior of concrete, the concrete damaged plasticity model was implemented. The specific properties used for concrete damage were provided in Table 3.4. The material properties of concrete were assumed to follow an elastic-perfectly plastic strain-stress curve, as illustrated in Figure 3.22 (a).

Table 3.4 Concrete damaged properties

Dilation angle (ψ)[1]	Eccentricity (ε)[2]	f_{b0}/f_{c0}[3]	K_c[4]	Viscosity Parameter (μ)[5]
31	0.1	1.16	0.667	0

1. ψ is the dilation angle measured in the p-q plane at high confining pressure, where p is the hydrostatic pressure stress (I_1), and q is the von Mises equivalent effective stress ($\sqrt{3J_2}$).
2. ε is the eccentricity, which defines the rate at which the plastic potential function approaches the asymptote.
3. f_{b0}/f_{c0} is the ratio of the biaxial compressive yield stress to the uniaxial compressive yield stress.
4. K_c is the ratio of the second stress invariant (I_2) on the tensile meridian to that on the compressive meridian.
5. μ is the viscosity parameter, which is used for the visco-plastic regularization of the concrete constitutive equation.

To represent the nonlinear material behavior of steel, various material nonlinearities were considered. These include the classical metal plasticity theory, which is based on the von Mises yield criterion, associated flow rule, and isotropic hardening assumption. Figs. 3.22 (b) and (c) illustrate the tensile stress-strain curves for the longitudinal bar (ASTM A706, Gr.80) and threaded rod (ASTM A193, Gr. B7), respectively. Fig. 3.22 (d) displays the tensile stress-strain curve for the steel (ASTM A572, Gr.50) used in the built-up loading beam, which is determined based on the nominal yield and ultimate strengths provided in the AISC Steel Construction Manual, 15th edition (AISC 2017). In the FE analysis, geometric nonlinearities were considered using a large strain formulation with a consideration for large deformations. Initial imperfections were not assigned in this analysis. The loading process was divided into two steps. In the first step, the post-tensioning was simulated by applying an initial force to the cross-section in the middle of the threaded rods, as shown in Fig. 3.19 (e). Specifically, 250 kips of force was applied to each rod of the big block, while 125 kips of force was imposed on each rod of the loading block. In the second step, as shown in Fig. 3.19 (d), a vertical force of 250 kips, equivalent to the expected shear strength of the DBCB specimen, was applied to the surface of the loading beam. This surface is connected to the actuator. Fig. 3.23 shows the stress distribution after applying the vertical load. As shown in Fig. 3.23, the loading beam, threaded rods, and big block remained elastic. Nevertheless, it was observed that the minimum principal stresses (compression stress) in the loading block exceeded the nominal strength (5 ksi) of plain concrete. This was particularly evident in the vicinity of the top and bottom holes through which the post-tensioned threaded rods passed. To mitigate any potential concrete failure, a 1.5-inch-thick layer of ultra-high-performance fiber-reinforced Concrete (UHP-FRC) (Aghdasi et al., 2016) was cast at the top and bottom of the loading block. This additional layer of UHP-FRC helped to prevent any potential concrete failure.

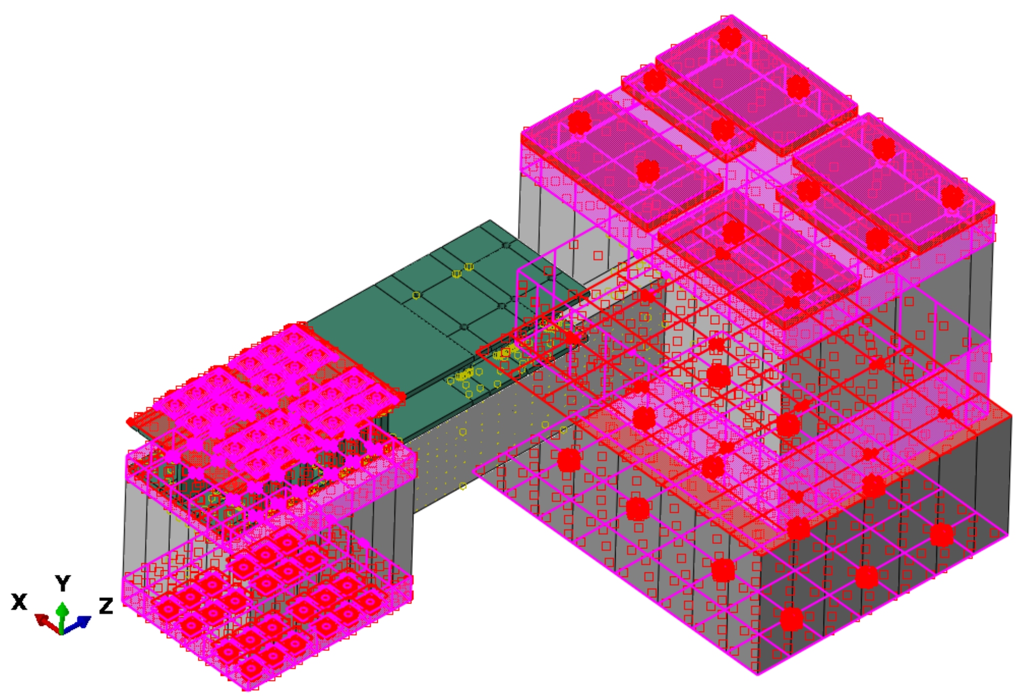

Fig. 3.20 Contact surfaces of DBCB specimens

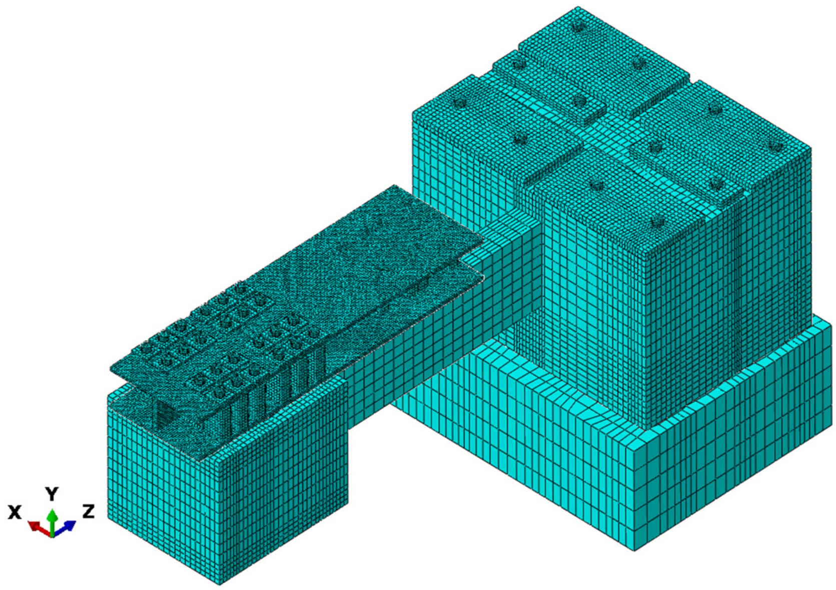

Fig. 3.21 FE mesh of DBCB specimen

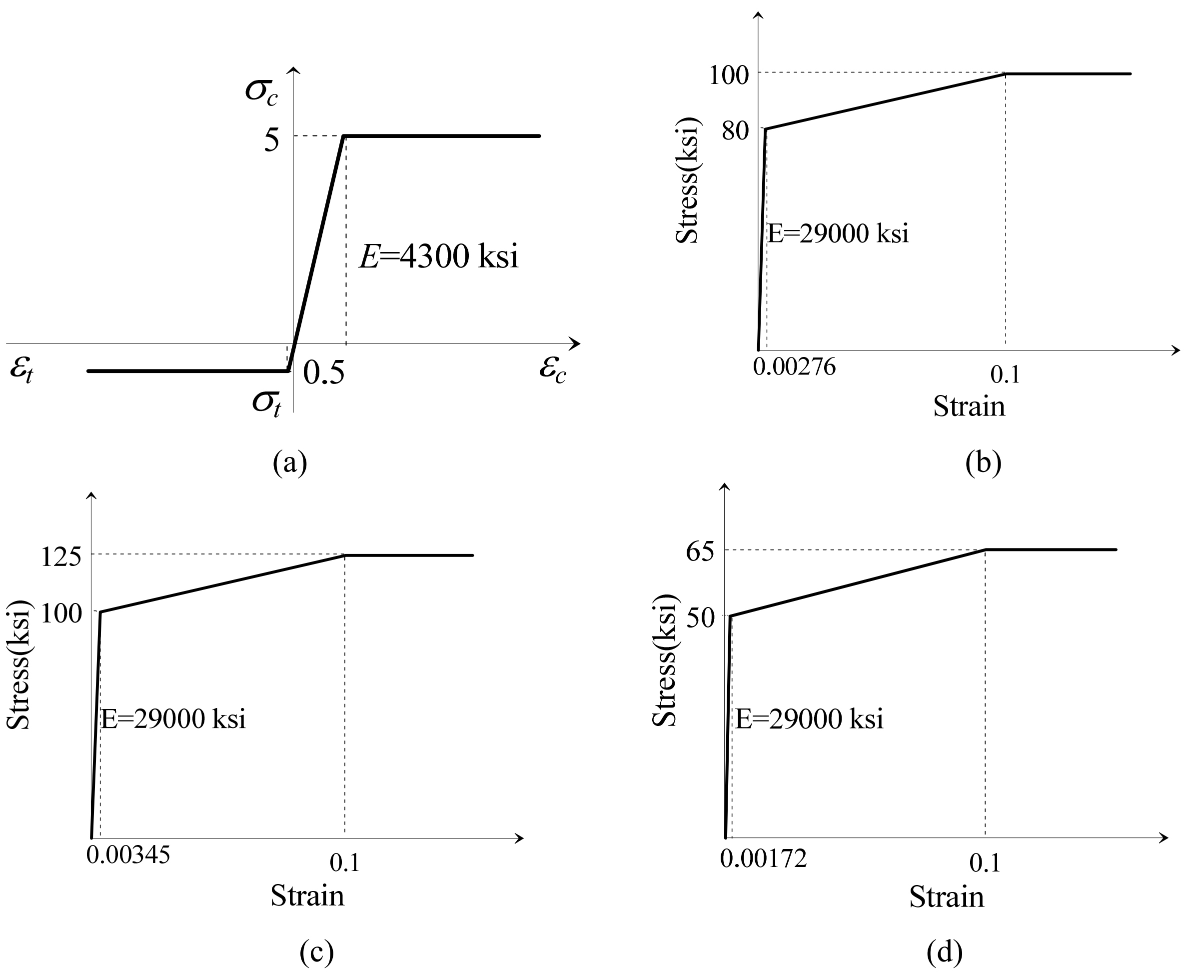

Fig. 3.22 Material properties: (a) Concrete, (b) Longitudinal bar and hoop, (c) Threaded rod, and (d) Loading beam

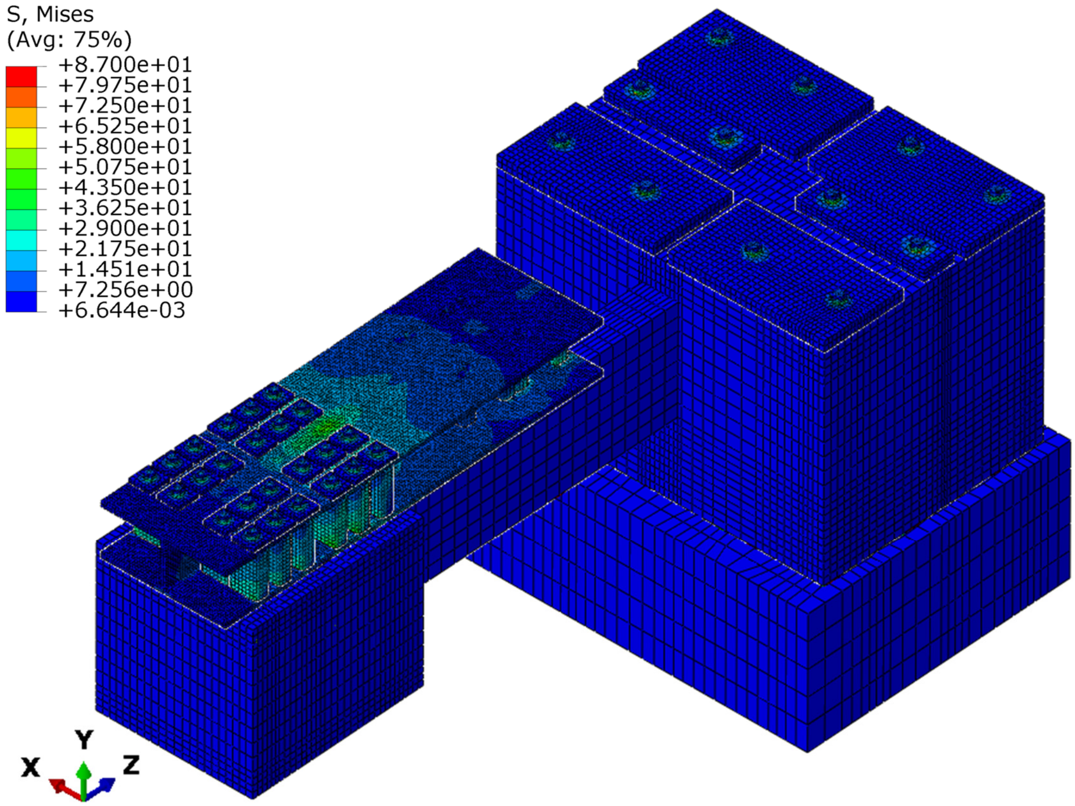
S, Mises
(Avg: 75%)
+8.700e+01
+7.975e+01
+7.250e+01
+6.525e+01
+5.800e+01
+5.075e+01
+4.350e+01
+3.625e+01
+2.900e+01
+2.175e+01
+1.451e+01
+7.256e+00
+6.644e-03
Y
X
Z

(a)

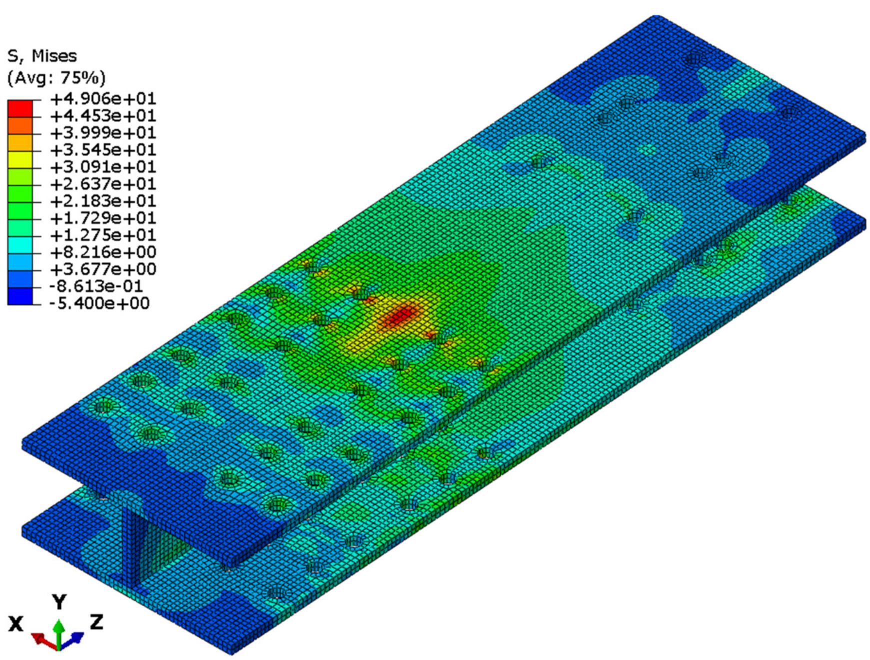
S, Mises
(Avg: 75%)
+4.906e+01
+4.453e+01
+3.999e+01
+3.545e+01
+3.091e+01
+2.637e+01
+2.183e+01
+1.729e+01
+1.275e+01
+8.216e+00
+3.677e+00
-8.613e-01
-5.400e+00
Y
X
Z

(b)

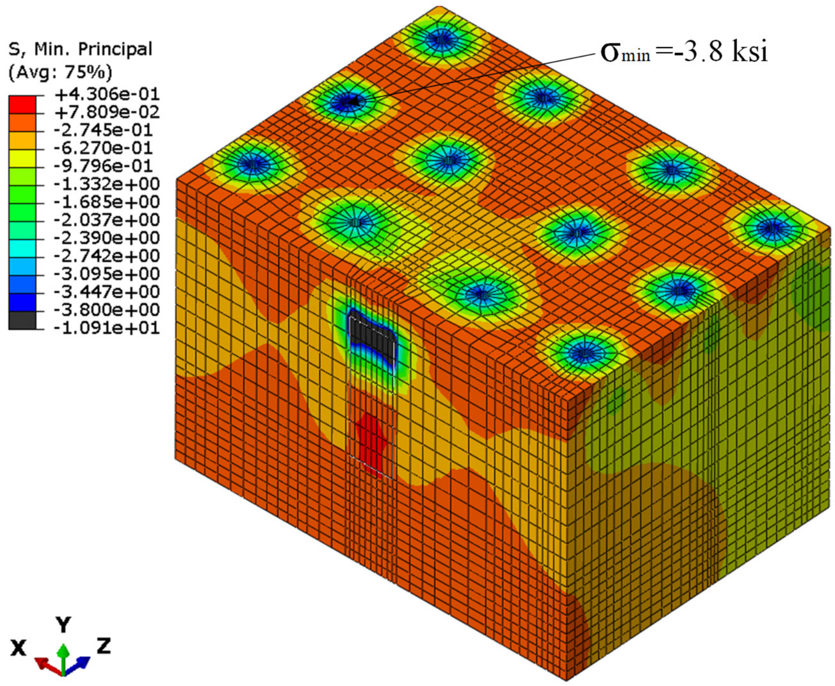
S, Min. Principal
(Avg: 75%)
+4.306e-01
+7.809e-02
-2.745e-01
-6.270e-01
-9.796e-01
-1.332e+00
-1.685e+00
-2.037e+00
-2.390e+00
-2.742e+00
-3.095e+00
-3.447e+00
-3.800e+00
-1.091e+01
σmin =-3.8 ksi
X
Y
Z

(c)

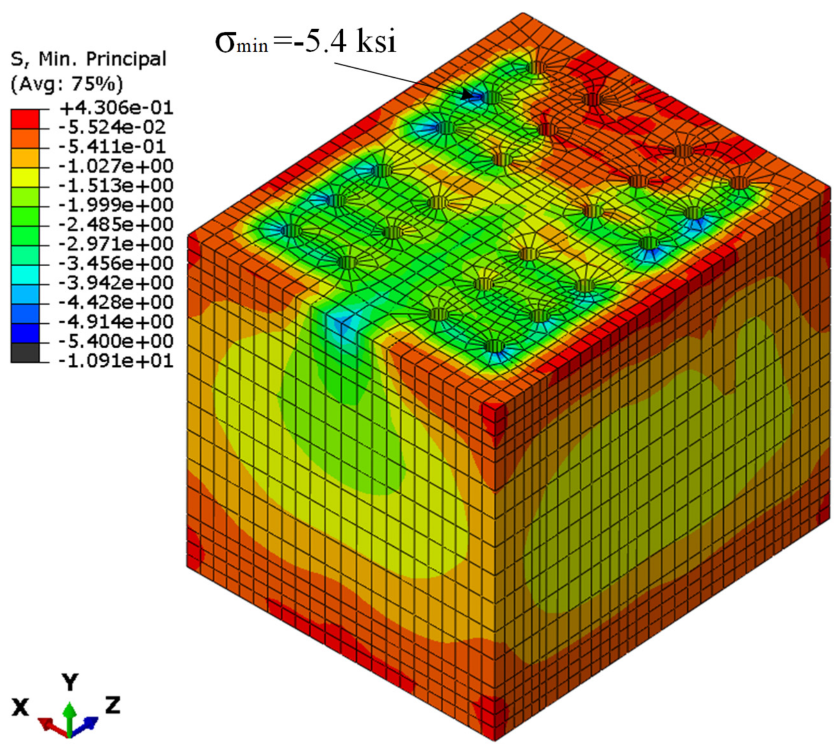
S, Min. Principal
(Avg: 75%)
+4.306e-01
-5.524e-02
-5.411e-01
-1.027e+00
-1.513e+00
-1.999e+00
-2.485e+00
-2.971e+00
-3.456e+00
-3.942e+00
-4.428e+00
-4.914e+00
-5.400e+00
-1.091e+01
σmin =-5.4 ksi
X
Y
Z

(d)

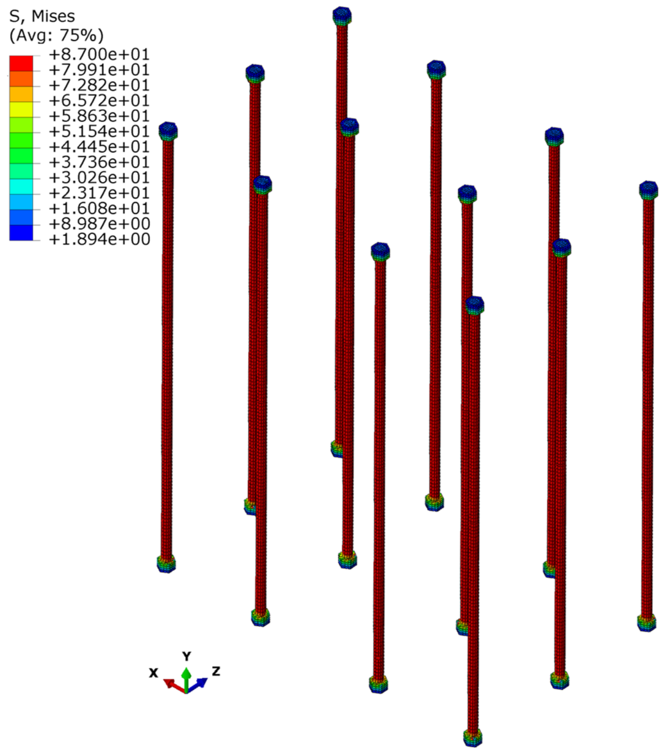

(e)

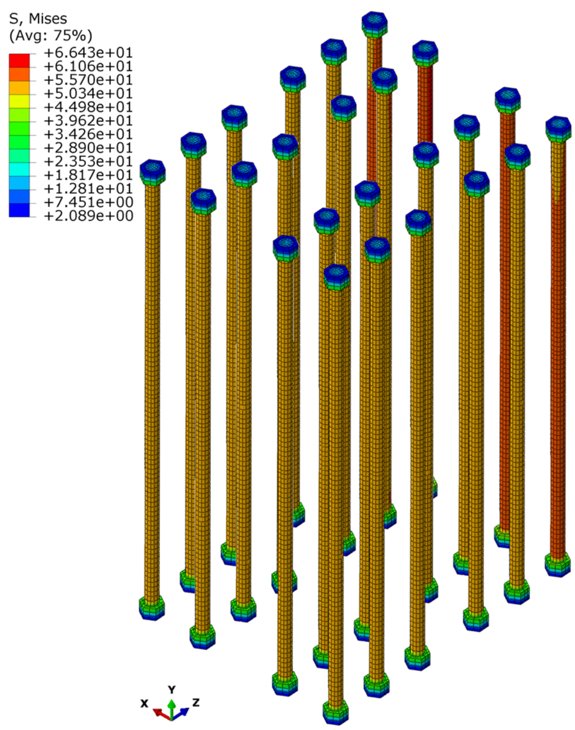

(f)

Fig. 3.23 Stress distributions: (a) DBCB specimen, (b) Loading beam, (c) Big block, (d) Loading block, (e) Threaded rods of the big block, and (f) Threaded rods in the loading block

3.1.2 Construction

Three DBCB specimens were constructed at the Civil Engineering Laboratory Building (CELB) in the University of Texas at Arlington. The construction process for each specimen involved four steps:

1. Formwork construction: The formworks for the coupling beam and two blocks were individually constructed using materials such as plywood, lumbers, threaded rods, and screw nails.
2. Reinforcement cage fabrication: The reinforcement cages for the coupling beam and two blocks were separately fabricated according to the design layout described in detail in Sections 3.1.1.1 to 3.1.1.4.
3. Assembly: The assembly process began by first assembling the formwork elements for the big block. Following that, the formwork elements for the coupling beam and loading block were subsequently attached. Fig. 3.24 (a), 3.25 (a), and 3.26 (a) illustrate the completed formwork assembly of each specimen, respectively.
4. Concrete casting: Finally, the specimens were cast using ready-mix concrete supplied by a local supplier. The concrete had a design strength of 5 ksi and an average aggregate size of 3/8 in. (10mm).

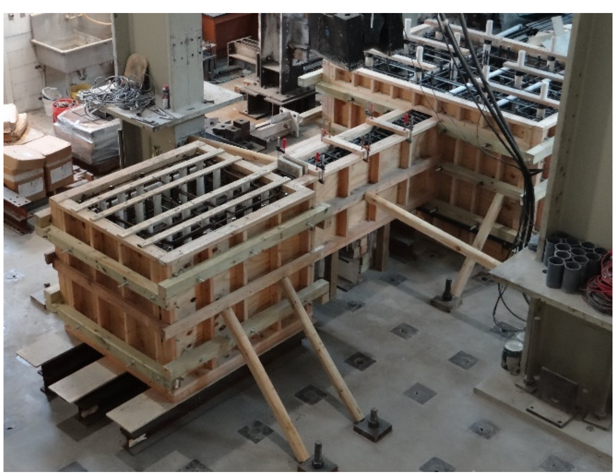

(a)

(b)

(c) (d)

Fig. 3.24 FS-R3.2-N-2: (a) Completed formwork (b) Cured specimen (c) Close-up view of beam (right) (d) Close-up view of beam (left)

(a) (b)

(c) (d)

Fig. 3.25 HS-R2.4-S-1: (a) Completed formwork (b) Cured specimen (c) Close-up view of beam (right) (d) Close-up view of beam (left)

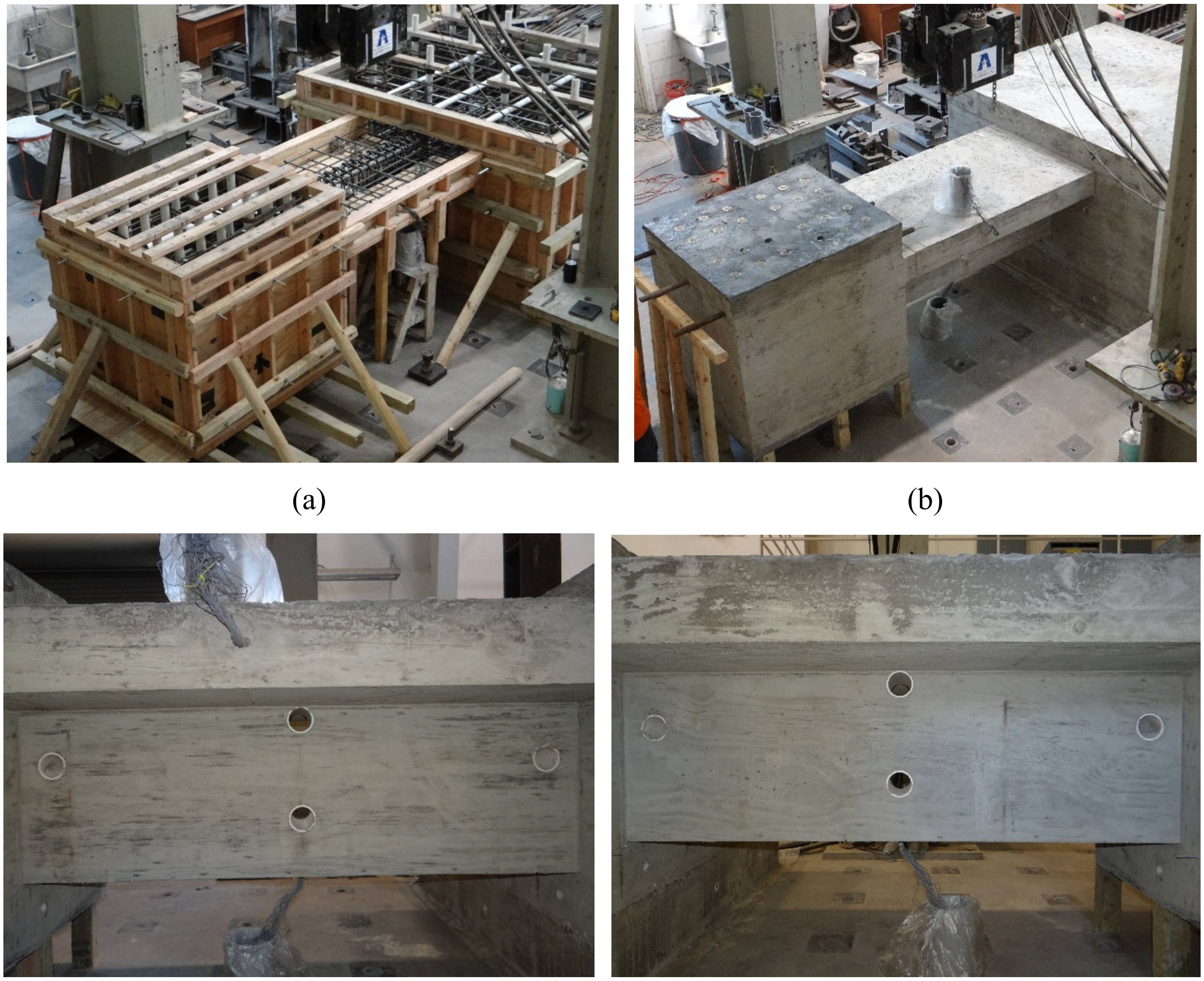

(a) (b)

(c) (d)

Fig. 3.26 FS-R2.4-S-3: (a) Completed formwork (b) Cured specimen (c) Close-up view of beam (right) (d) Close-up view of beam (left)

3.1.3 Material properties

Fig. 3.27 (a) illustrates the preparation of twelve 4 in. × 8 in. (100 mm × 200 mm) concrete cylinders for each specimen, following ASTM C39 (ASTM C39, 2018). These cylinders were created from the delivered batch of ready-mix concrete and served the purpose of evaluating the actual strength of the cast concrete for each specimen. Once the concrete cylinder samples were placed in the curing room for the designated period (typically up to the same day of the coupling test), the compressive strength tests of the concrete cylinders were conducted, as shown in Fig. 3.27 (b). Prior to the tests, the concrete cylinders were slightly trimmed by approximately 2-3mm to ensure flat and smooth top and bottom surfaces. Table 3.5 presents a summary of the average actual compressive strength for each specimen on the test day. As shown in Table 3.5, the measured compressive strength of the first specimen was considerably lower than the design compressive strength of 5 ksi. However, for the remaining two specimens, their strengths were closer to the design strength of 5 ksi

Table 3.5 Compressive strength tests of concrete cylinders (1 ksi = 6.89 MPa)

Specimen	Design compressive strength f'_c ksi (MPa)	Measured compressive strength at test day f_{cm} ksi (MPa)
FS-R3.2-N-2		3 (20.7)
HS-R2.4-S-1	5 (34.5)	4.6 (31.7)
FS-R2.4-S-3		4.8 (33.1)

(a)

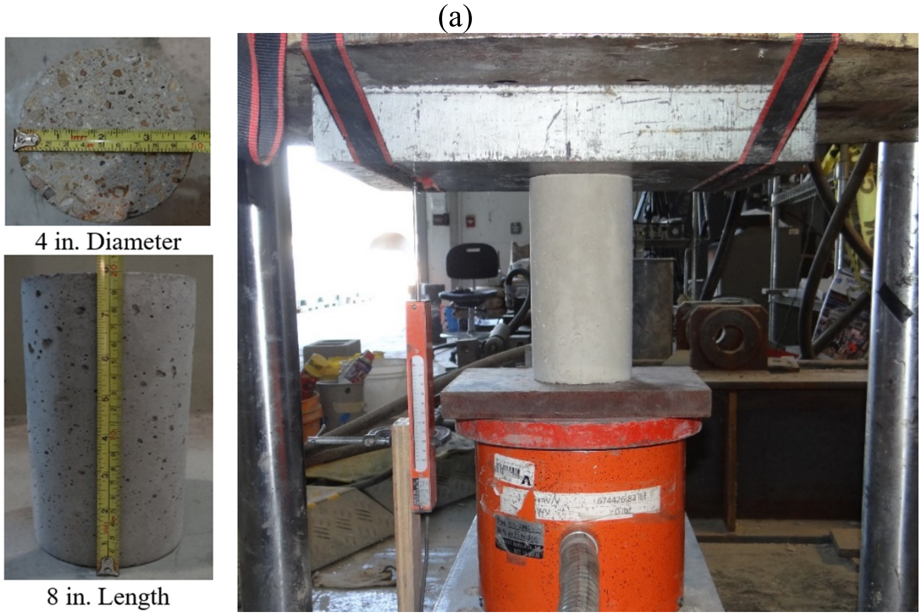

(b)

Fig. 3.27 Compressive tests of concrete cylinders: (a) Concrete cylinder samples (b) Test setup

3.2 Instrumentation

In order to accurately assess the deformation behavior of the coupling beam specimen during cyclic loading, several measurement instruments were used. These included strain gauges, linear variable differential transformers (LVDTs), and string pots. Additionally, a non-contact deformation measurement system called digital image correlation (DIC) was utilized. This DIC system offered a measuring strain accuracy of 0.01% (in./in.) and enabled the observation of the complete field of strains and displacements as they evolved on the surface of the specimen.

3.2.1 Strain gauge

During the tests, 120-ohm electrical resistance post-yield strain gauges were utilized to monitor strains at critical locations of the longitudinal reinforcing bars and the hoops. To ensure accurate measurements, the strain gauges were carefully mounted on selected reinforcing bars individually prior to the fabrication of the steel cages for the coupling beam. However, for the steel links (used to provide axial restraints), the strain gauges were attached after the completion of the test setup and instrumentation. Appendix B provides a detailed description of the installation process for strain gauges on the reinforcing bars.

Fig. 3.28 shows the location of strain gauges in Specimen FS-R3.2-N-2. The locations of strain gauges were mainly determined based on the results of the prior half-scale DBCB tests (Choi et al., 2018). To monitor the behavior of the longitudinal reinforcement (No. 10) in the top and bottom layers of each steel cage, six strain gauges were installed along the anticipated plastic hinge region of the beam. Additionally, eight strain gauges were added to the two longitudinal rebars embedded in the blocks, with four strain gauges on each bar. One bar was positioned at the top right, while the other was located at the bottom left of the coupling beam. These strain gauges were specifically utilized to study the development length of the high-strength reinforcing bars in the wall piers. To monitor the behavior of the longitudinal bar (No. 6) in the middle layer of each steel cage, three strain gauges were positioned in the anticipated plastic hinge region of the beam. For the transverse reinforcing bars (No. 4), eight strain gauges were attached to the top cage, while five strain gauges were mounted on the bottom cage. Additionally, two strain gauges were installed at the midspan of the steel links to measure the axial strains resulting from the axial restraints of the coupling beam.

Figs. 3.29 and 3.30 show the detailed locations of strain gauges on the longitudinal and transverse reinforcements of the coupling beam. All strain gauges were installed carefully according to procedures described at Appendix B. Fig. 3.31 shows the completed installation of strain gauges on hoops and longitudinal reinforcement.

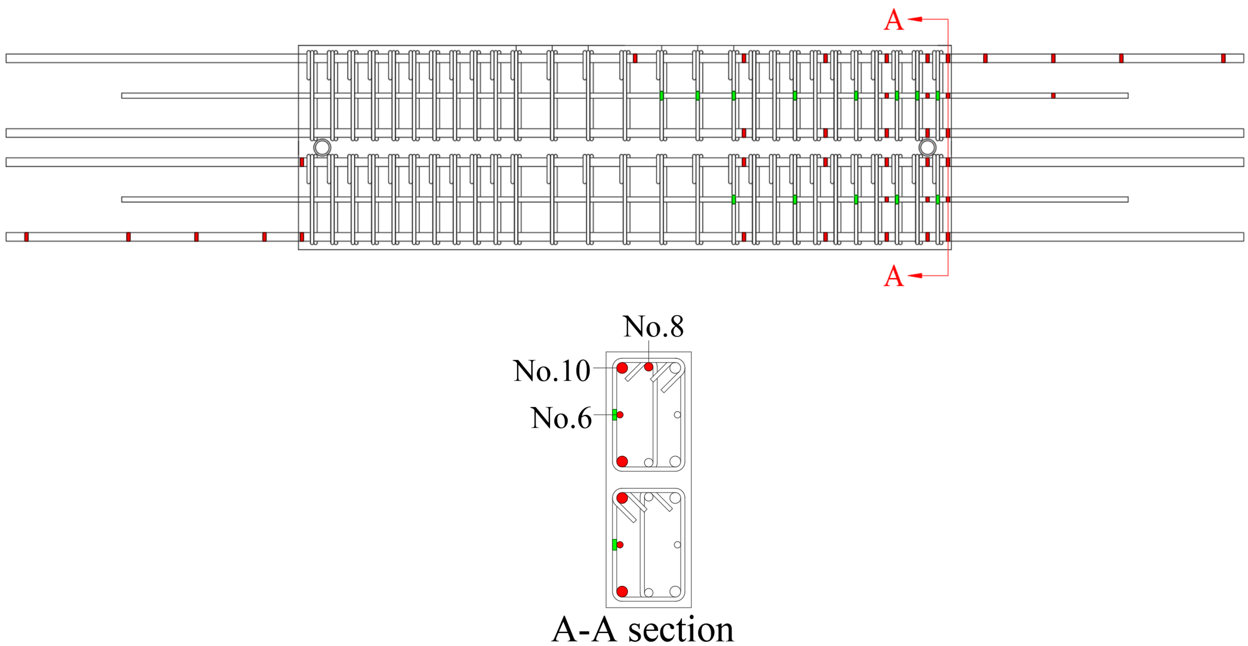

(a)

(b)

Fig. 3.28 Strain gauge locations in Specimen FS-R3.2-N-2: (a) Coupling beam, and (b) Steel angle link

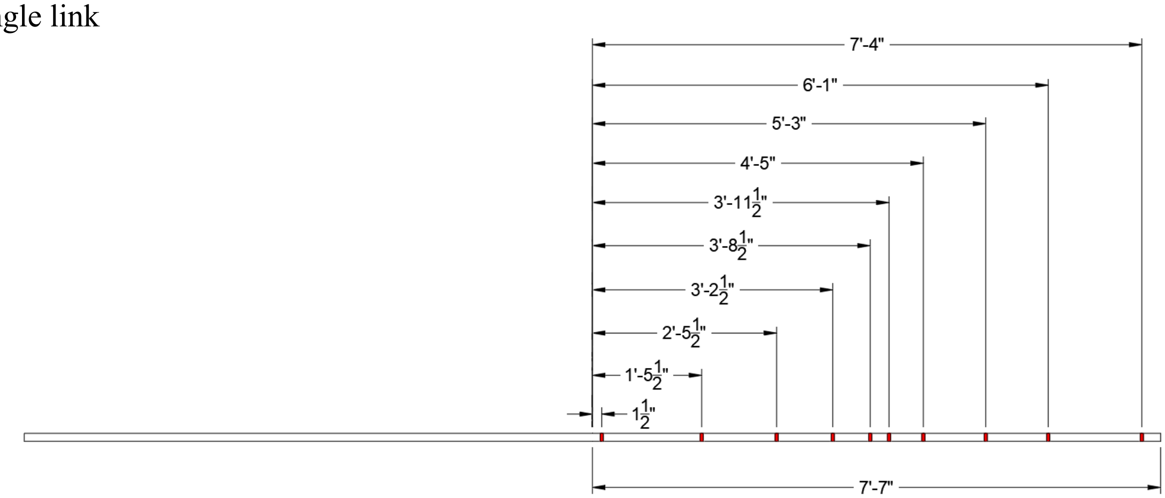

(a)

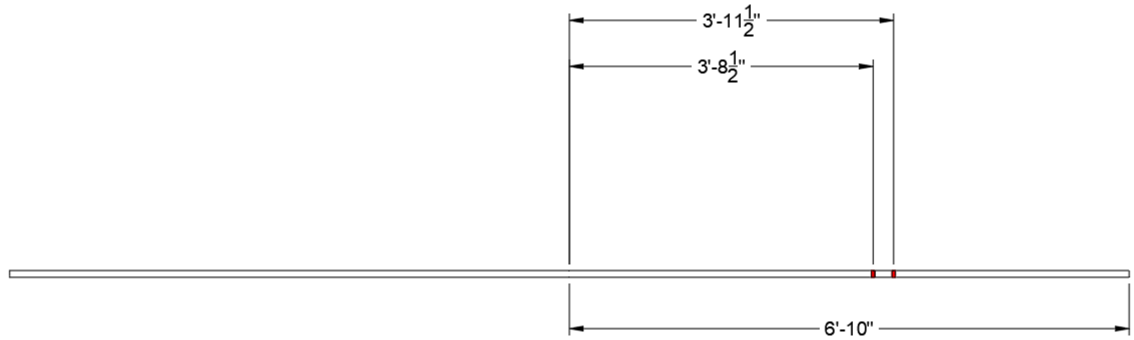

(b)

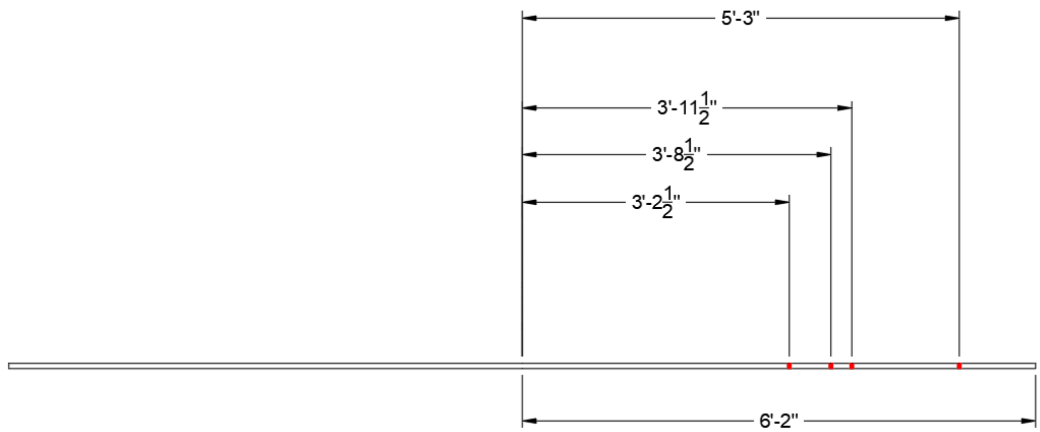

(c)

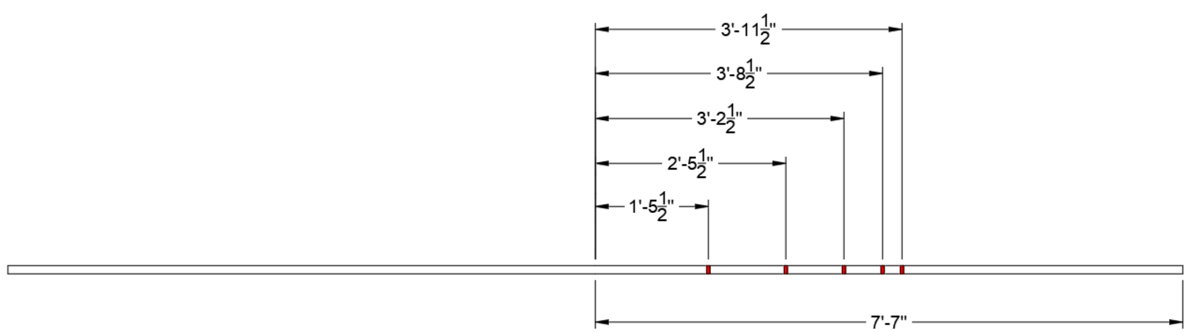

(d)

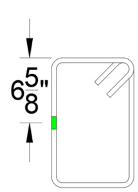

(e)

Fig. 3.29 Detailed locations of strain gauges in the upper steel cage of Specimen FS-R3.2-N-2: (a) Top longitudinal bar (No.10), (b) Top longitudinal bar (No. 8), (c) Middle longitudinal bar (No. 6), (d) Bottom longitudinal bar, and (e) Hoop (No. 4)

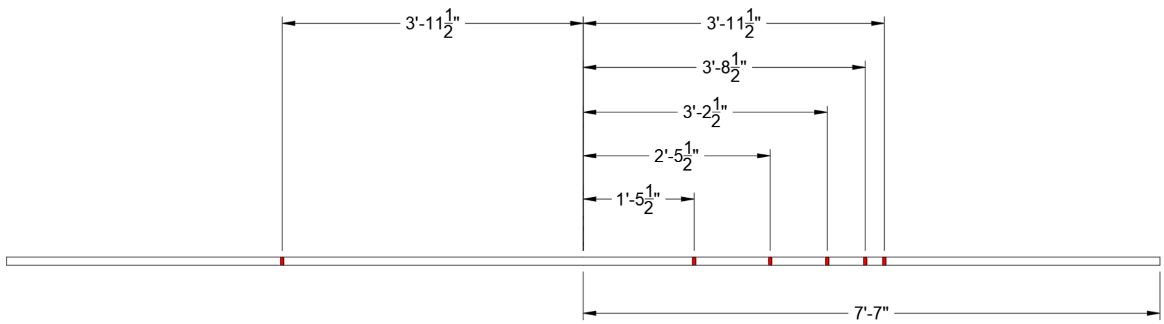

(a)

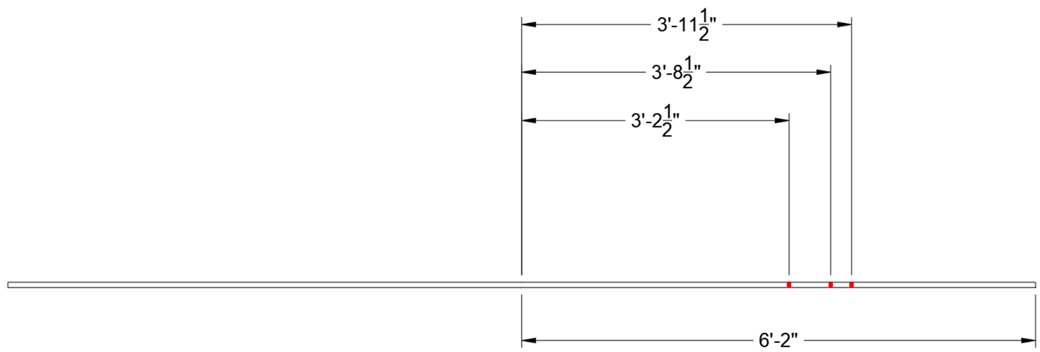

(b)

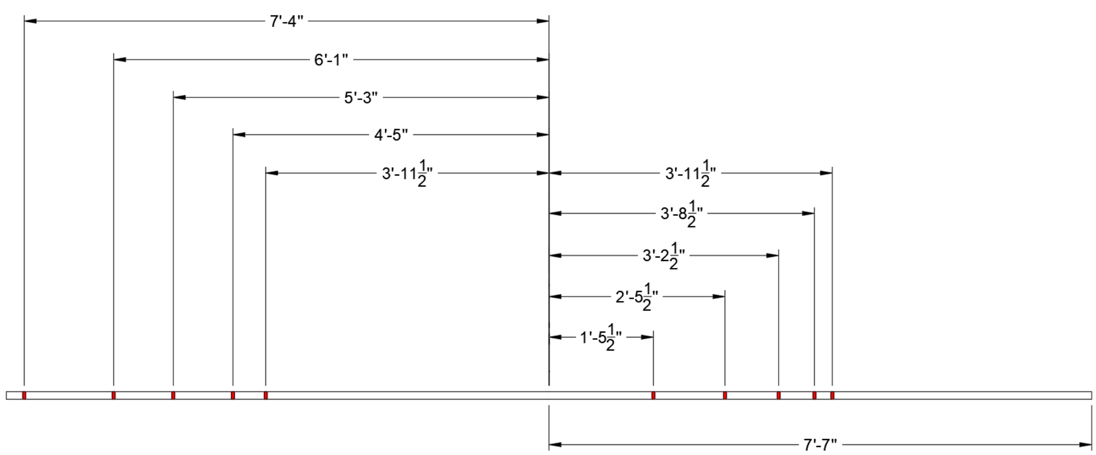

(c)

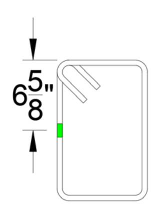

(d)

Fig. 3.30 Detailed locations of strain gauges in the lower steel cage of Specimen FS-R3.2-N-2: (a) Top longitudinal bar (No. 10), (b) Middle longitudinal bar (No. 6), (c) Bottom longitudinal bar, and (d) Hoop (No. 4)

(a) (b)

Fig. 3.31 Completed installation of strain gauges of Specimen FS-R3.2-N-2: (a) Hoops, (b) Longitudinal reinforcement

Fig. 3.32 shows the locations of strain gauges in Specimen HS-R2.4-S-1. For the coupling beam, the strain gauges were mounted on the similar locations as Specimen FS-R3.2-N-2. In addition, four strain gauges were attached to the locations close to slab-to-wall interface to evaluate the yielding of slab longitudinal reinforcing bars and four strain gauges were mounted at the midspan of steel links to measure the axial strains induced due to axial restraints. Fig. 3.33 shows the detailed locations of strain gauges on the longitudinal and transverse reinforcements of the coupling beam. All strain gauges were installed carefully according to procedures described at Appendix B. Fig. 3.34 shows the completed installation of strain gauges on stirrup hoops and longitudinal reinforcement bars.

Fig. 3.35 shows the locations of strain gauges in Specimen FS-R2.4-S-3. Based on the results of the previous two coupling beam tests, it was observed that large strain levels were predominantly concentrated in the plastic hinge zone near the beam-to-wall interface. As a result, the majority of strain gauges were positioned in the areas adjacent to both ends of the coupling beam. Furthermore, to assess the yielding of slab longitudinal reinforcing bars, six strain gauges were affixed to the top slab bars near the interface between the slab and the wall. Additionally, four strain gauges were installed at the midspan of the steel links to measure the axial force arising from the axial restraints imposed on the coupling beam. Fig. 3.36 shows the detailed locations of strain gauges on the longitudinal and transverse reinforcements of coupling beam. All strain gauges were installed carefully according to procedures described at Appendix B. Fig. 3.37 shows the completed installation of strain gauges on stirrup hoops and longitudinal reinforcement bars.

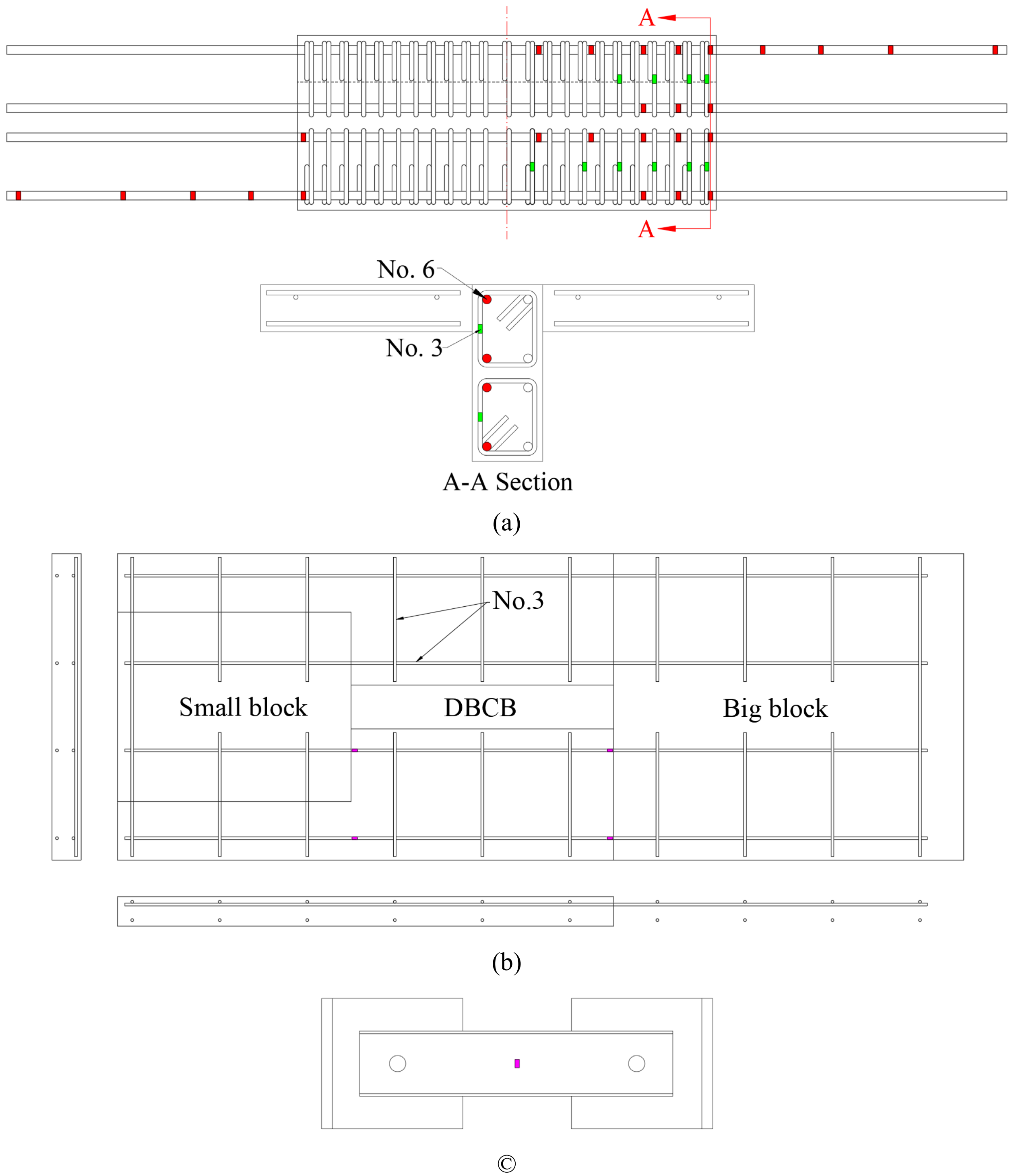

Fig. 3.32 Strain gauge locations in Specimen HS-R2.4-S-1: (a) coupling beam, (b) Slab, and (c) Steel channel

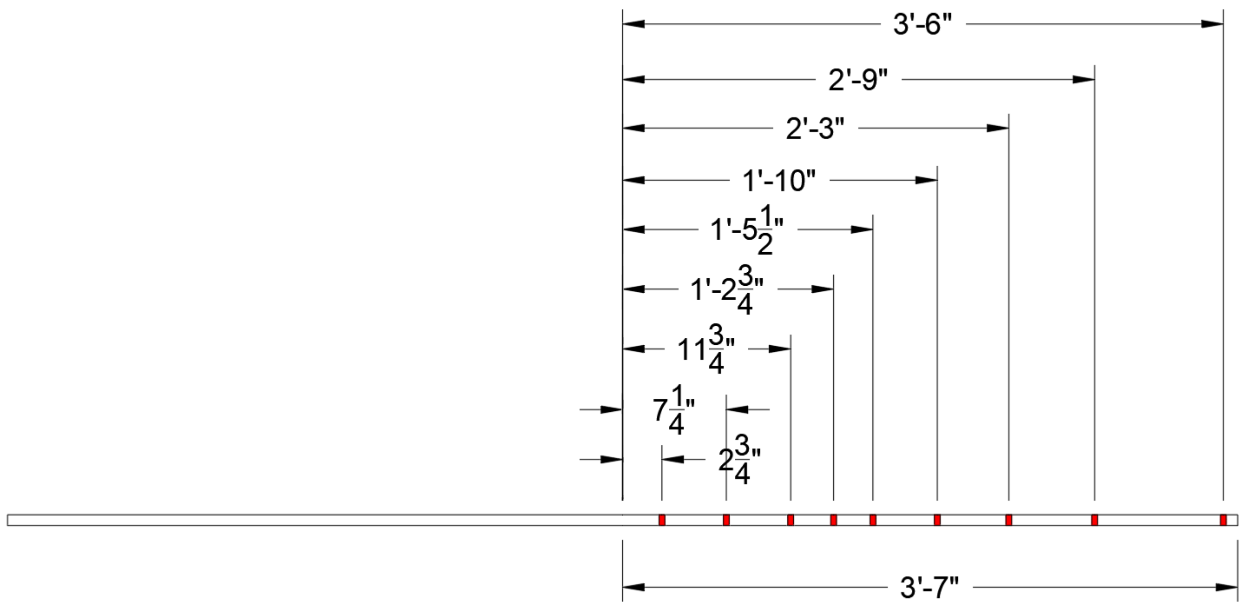

3'-6"
2'-9"
2'-3"
1'-10"
1'-5 1/2"
1'-2 3/4"
11 3/4"
7 1/4"
2 3/4"
3'-7"

(a)

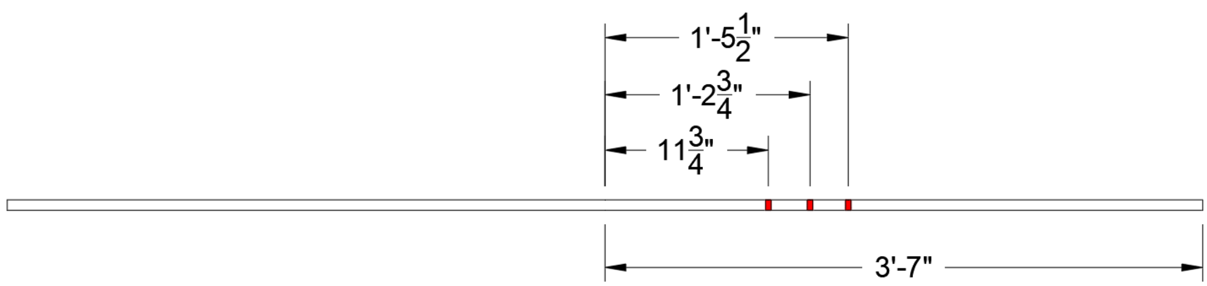

1'-5 1/2"
1'-2 3/4"
11 3/4"
3'-7"

(b)

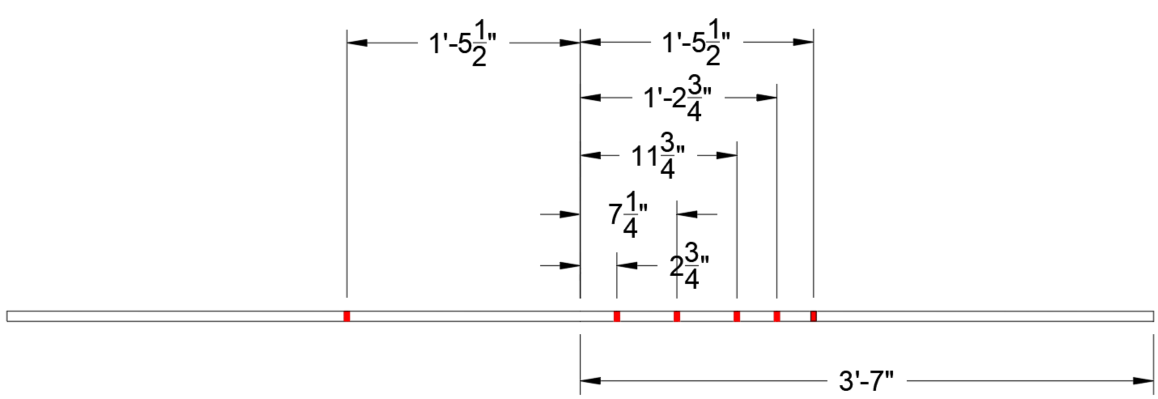

1'-5 1/2"
1'-5 1/2"
1'-2 3/4"
11 3/4"
7 1/4"
2 3/4"
3'-7"

(c)

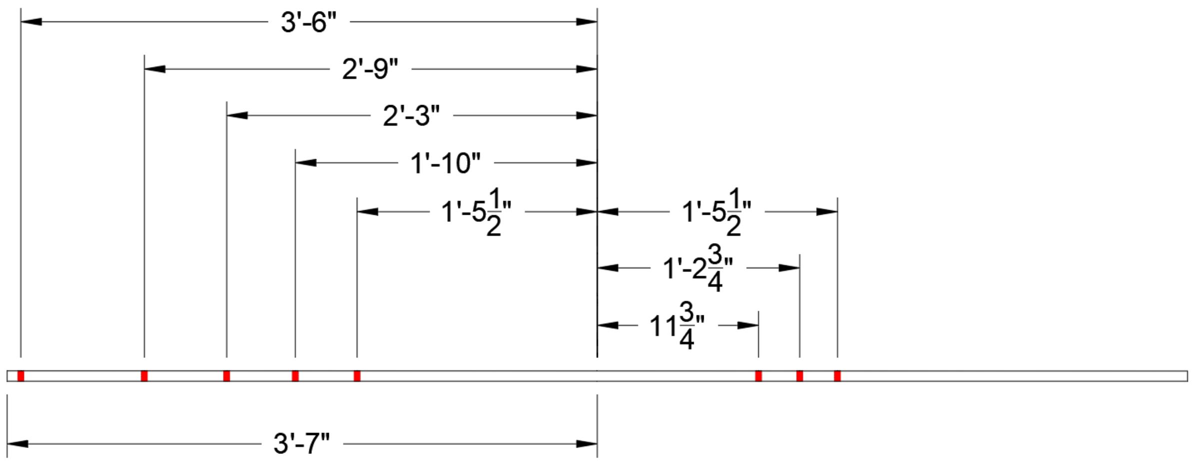

(d)

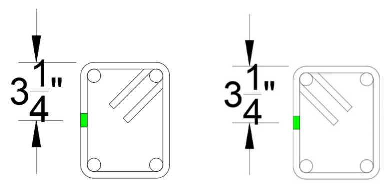

(e)

Fig. 3.33 Detailed locations of strain gauges in Specimen HS-R2.4-S-1: (a) Top longitudinal bar in the upper steel cage (No. 6), (b) Bottom longitudinal bar in the upper steel cage (No. 6), (c) Top longitudinal bar in the lower steel cage (No. 6), (d) Bottom longitudinal bar in the lower steel cage (e) Hoops (No. 3)

(a) (b)

Fig. 3.34 Completed installation of strain gauges of Specimen HS-R2.4-S-1: (a) Hoops, and (b) Longitudinal reinforcement

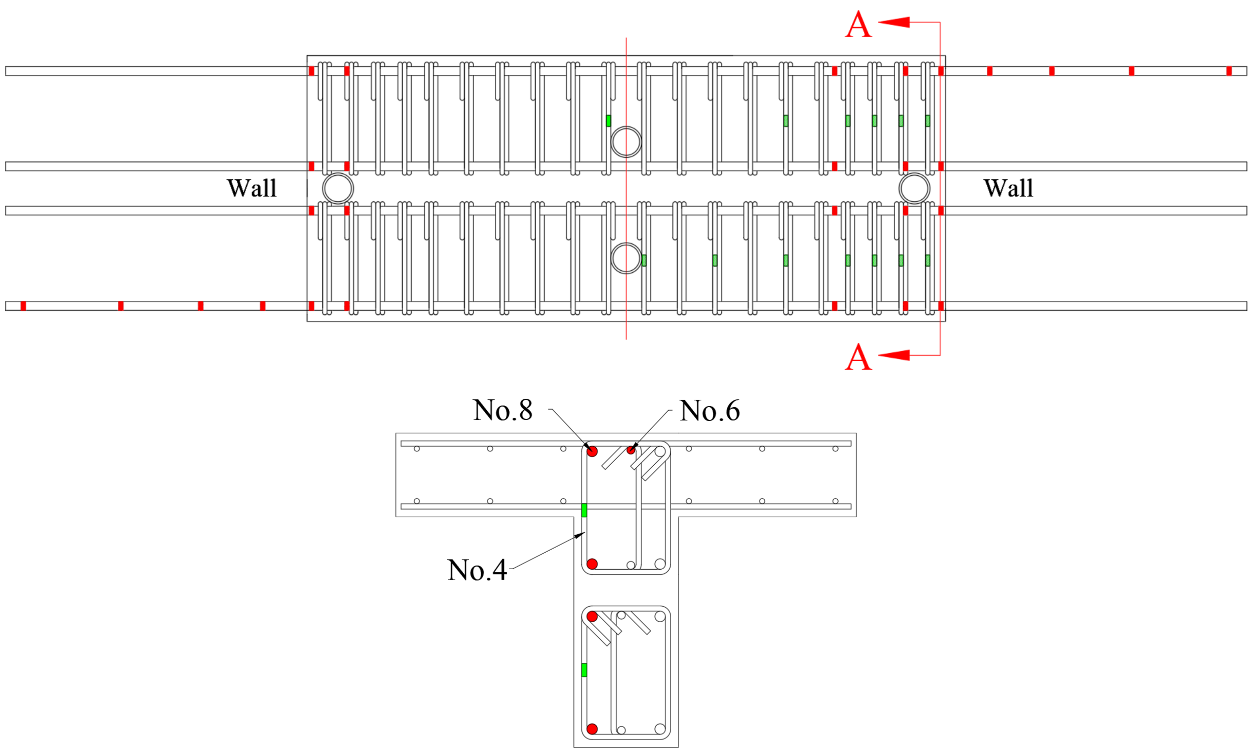

Section A-A

(a)

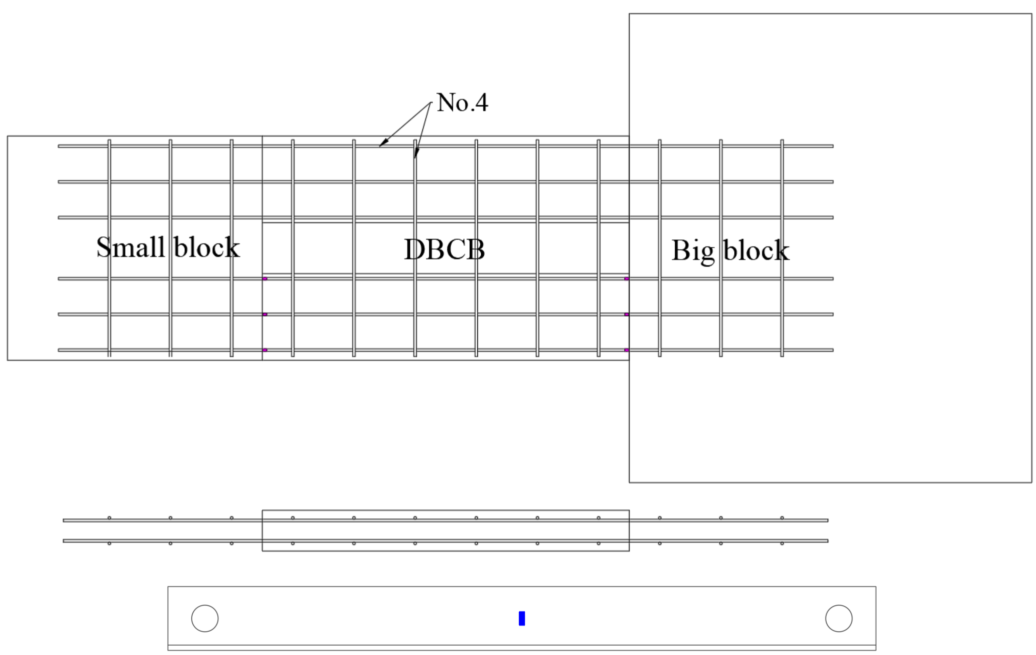

(c)

Fig. 3.35 Strain gauge locations in Specimen FS-R2.4-S-3: (a) coupling beam, (b) Slab, (c) Steel angle

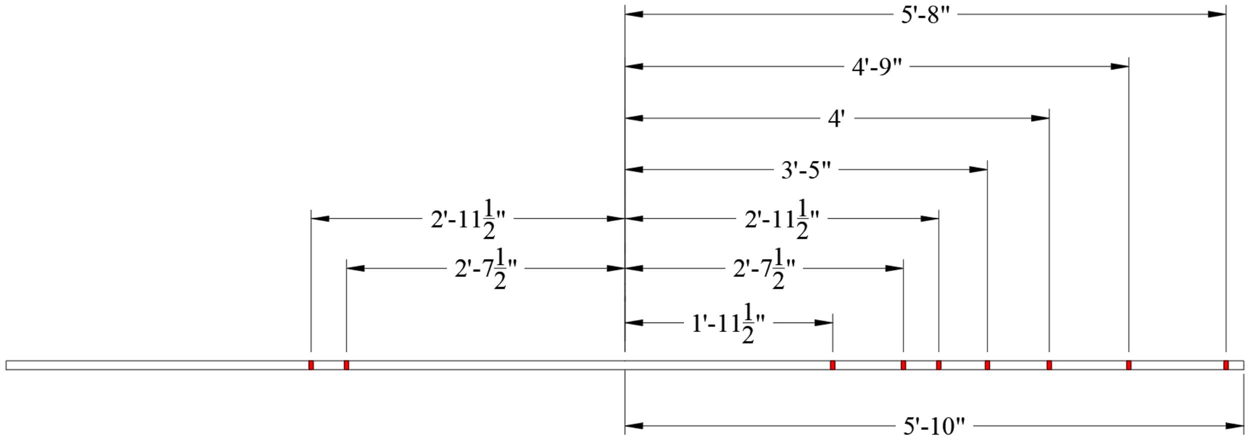
5'-8"
4'-9"
4'
3'-5"
2'-11½"
2'-11½"
2'-7½"
2'-7½"
1'-11½"
5'-10"

(a)

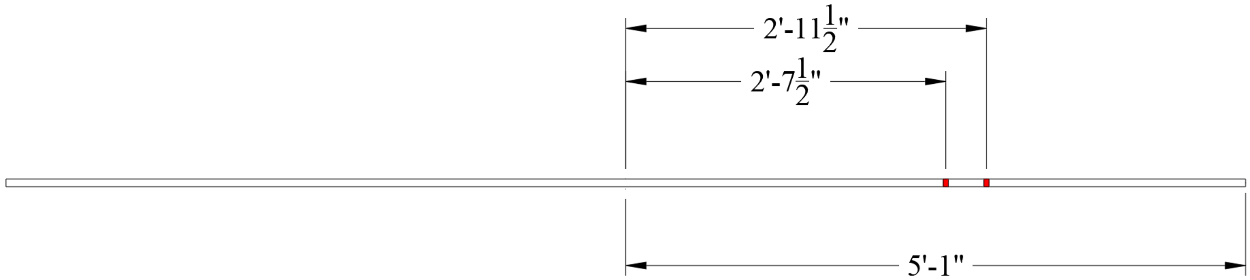
2'-11½"
2'-7½"
5'-1"

(b)

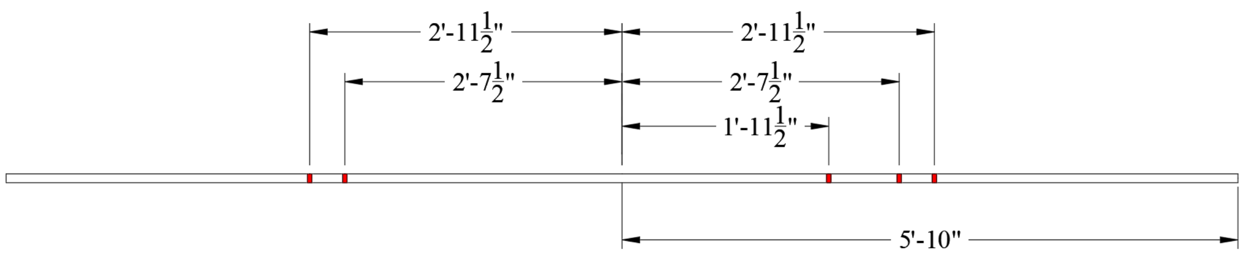
2'-11½"
2'-11½"
2'-7½"
2'-7½"
1'-11½"
5'-10"

(c)

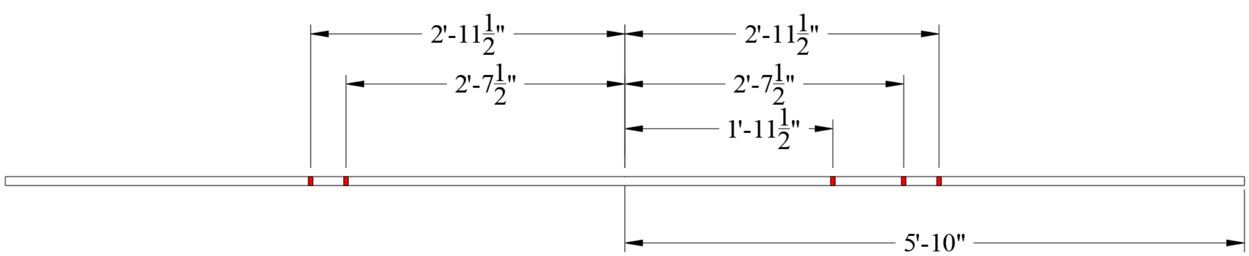
2'-11½"
2'-11½"
2'-7½"
2'-7½"
1'-11½"
5'-10"

(d)

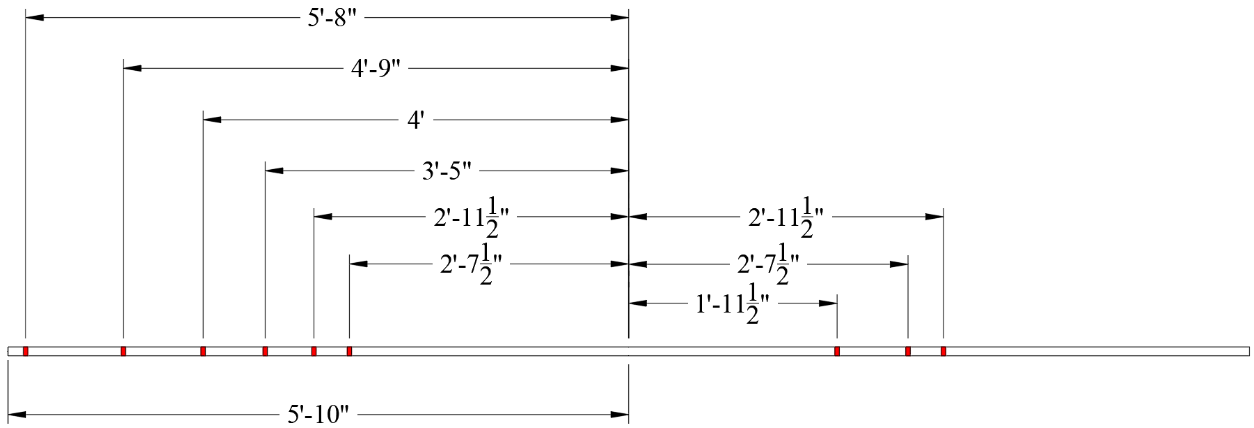

(e)

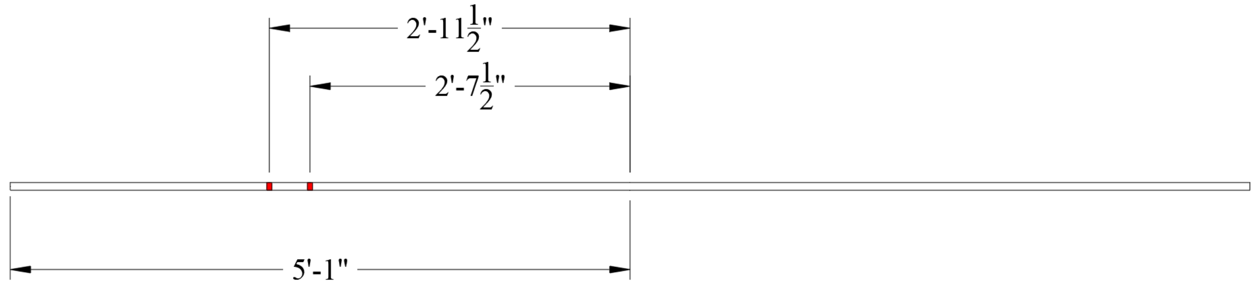

(f)

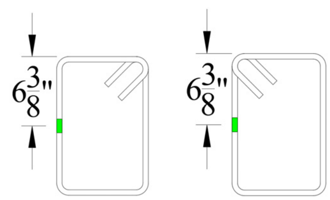

(g)

Fig. 3.36 Detailed locations of strain gauges: (a) Top longitudinal bar in the upper steel cage (No. 8), (b) Top longitudinal bar in the upper steel cage (No. 6), (c) Bottom longitudinal bar in the upper steel cage (No. 8), (d) Top longitudinal bar in the lower steel cage, (e) Bottom longitudinal bar of the lower steel cage (No. 8), (f) Bottom longitudinal bar in the lower steel cage (No. 6), (g) Hoops (No. 4)

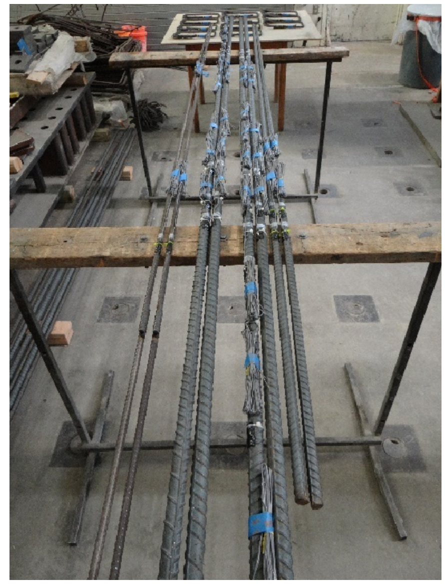

(a) (b)

Fig. 3.37 Completed installation of strain gauges: (a) Hoops and (b) Longitudinal reinforcement

3.2.2 Linear Variable Differential Transformers and string pots

Shear force applied to the coupling beam was measured by the load cell built-in the hydraulic actuator throughout the tests. The chord rotation of the coupling beam is determined by dividing the relative displacement between both ends of the beam by the clear span of the beam and subtracting the rotation of the big block. The measurements or calculations of these displacements or rotations were obtained using linear variable differential transformers (LVDTs) and string pots mounted on the specimen, as shown in Fig. 3.38. At the end of the beam closest to the loading block, where the largest vertical displacement occurs, one LVDT and one string pot were installed. Another LVDT was attached to the opposite end of the beam near the big block. Additionally, one LVDT was positioned at the back of the big block. These LVDTs (LVDT1, LVDT2, and LVDT4) were aligned at the mid-height of the DBCB. Furthermore, an LVDT (LVDT3) was placed at the middle of the big block to measure its vertical displacement, which is generally negligible. Fig. 3.39 illustrates the deformed shape of the specimen, highlighting the displacement components. In Eq. 3.9, the calculation for beam chord rotation is shown, considering that the vertical displacement of the big block is negligible.

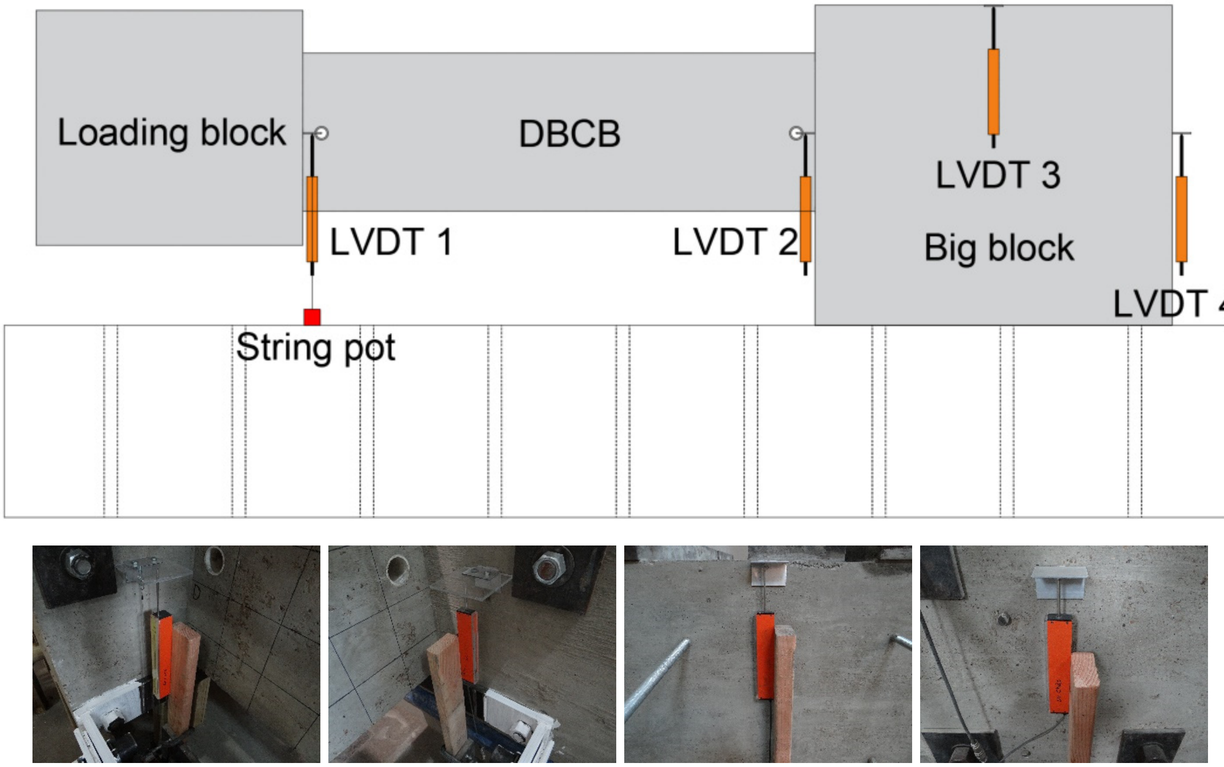

LVDT 1, String pot LVDT 2 LVDT 3 LVDT 4

Fig. 3.38 Location of the LVDTs and string pot

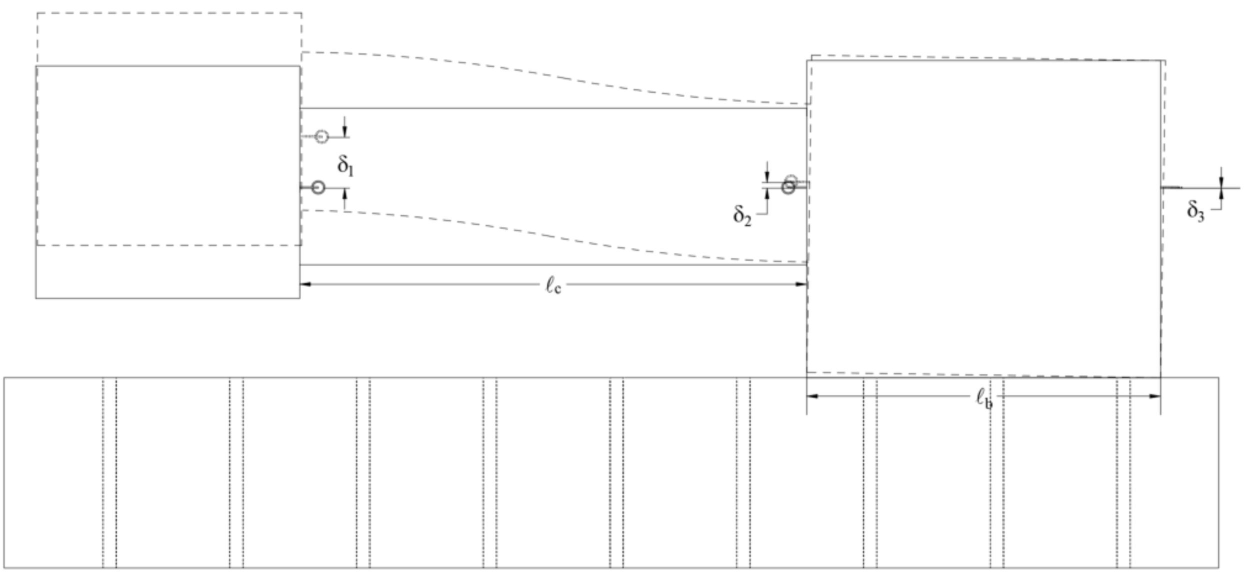

Fig. 3.39 Deformed shape of specimen

$$\theta = \left[\frac{(LVDT\ 1 - LVDT\ 2}{Beam\ clear\ span} - \frac{(LVDT\ 2 - LVDT\ 4)}{Big\ block\ span} \right] \times 100 = \left[\frac{\delta_1 - \delta_2}{l_c} - \frac{\delta_2 - \delta_3}{l_b} \right] \times 100 \qquad \text{Eq. 3.9}$$

3.2.3 Digital image correlation (DIC) system

ARAMIS digital image correlation (DIC) system was utilized to observe and visualize the full-field deformation and strain of DBCB specimens. This system allowed for the visualization of strain distribution, crack initiation, propagation, and the failure process. DIC is a non-contact and material-independent optical 3D measurement system that can measure the deformations and dynamic behaviors of specimens and objects of any shape, which is based on point tracking technology and the digital image correlation approach. The basic principle of this technique is to use a series of digital images taken from the different loading steps as input data to determine the changes between image areas. As shown in Fig. 3.40, the system computes 3D coordinates utilizing stochastic patterns (speckle patterns) and compares its initial and final positions to estimate the deformation of specimens. The change in position of the reference points allows the software to calculate displacements and strains. The determination of the 3D coordinates is possible by means of the angled two stereo camera sensors and the application of different types of patterns in the surface of specimens, as shown in Fig 3.41. Prior to commencing the measurement, a system calibration must be conducted to establish the 3D space in which the experiment is being performed.

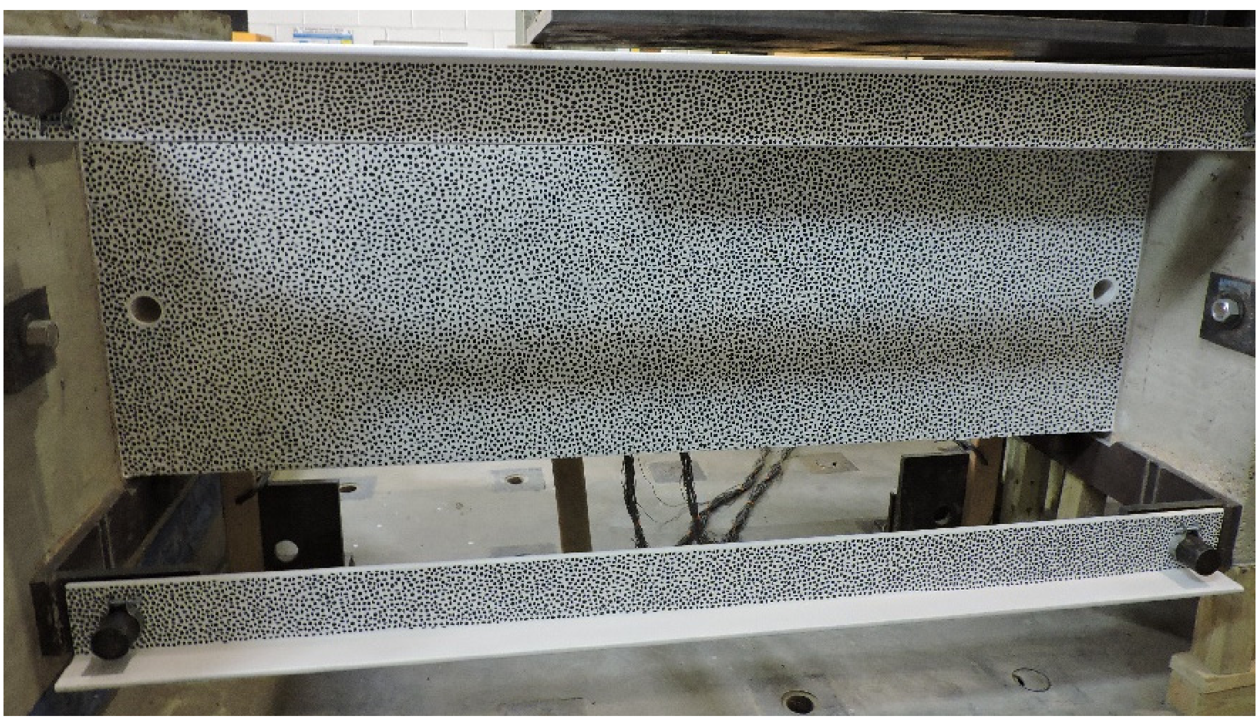

(a)

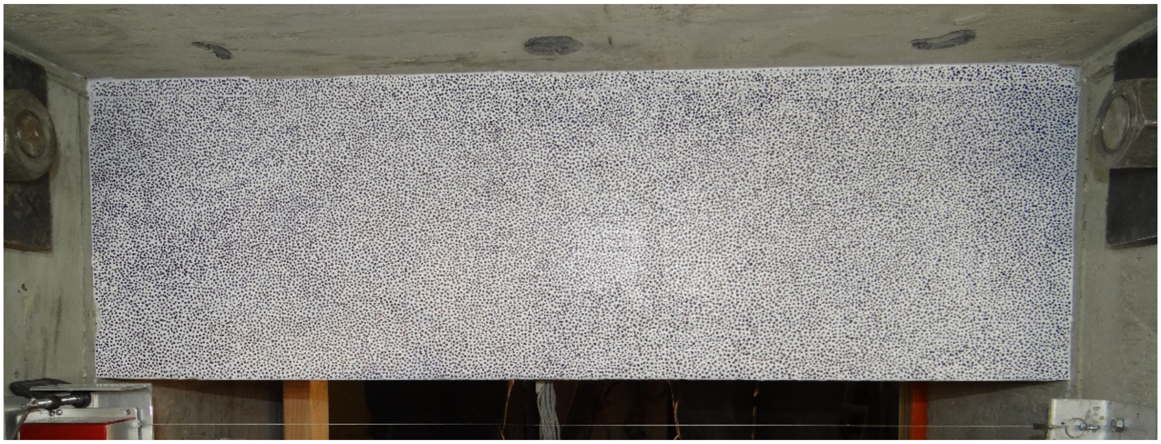

(b)

(c)

Fig. 3.40 Speckle patterns: (a) FS-R3.2-N-2, (b) HS-R2.4-S-1, and (c) FS-R2.4-S-3

Fig. 3.41 ARAMIS DIC system

3.3 Test setup

Fig. 3.42 depicts the test setup for the full-scale DBCB with a 3.2 aspect ratio (Specimen FS-R3.2-N-2). As illustrated in Fig. 3.42 (a), the specimen was positioned horizontally, with two end blocks representing the adjacent walls (wall piers). The big block was post-tensioned to the strong floor to ensure a fixed end condition and minimize its rotation. To apply simulated seismic loads from the actuator to the coupling beam, the loading block was post-tensioned to the horizontal steel loading beam connected to the vertical actuator. The post-tensioning of the blocks was accomplished using high-strength threaded rods, employing a hydraulic jack and super nuts for the process. Furthermore, the two concrete blocks were fitted with horizontally installed threaded rods to secure four steel links above and below the coupling beam. These links connect the big block with the loading block, effectively limiting the rotation of the loading block. Additionally, these threaded rods provide axial restraint to the coupling beam, mimicking the axial restraint provided by wall piers and the surrounding slab. This axial restraint is essential in preventing substantial elongation of the beam upon cracking (Teshigawara et al. 1998; Lequesne 2011; Barbachyn et al. 2012). As illustrated in Fig. 3.42 (b), the hydraulic actuator was positioned in the middle of the steel reaction frame and aligned with the center line of the coupling beam. This configuration ensures that the actuator force acts through the midspan of the coupling beam, resulting in an antisymmetrical moment pattern within the beam. Consequently, the midspan of the beam experiences a relatively low magnitude of moment. Furthermore, a lateral bracing system was installed on both sides of the loading block to prevent out-of-plane rotation or twisting. The other two specimens, which included a slab, were arranged in the same manner as the full-scale DBCB with a 3.2 aspect ratio. Fig. 3.43 shows the completed test setup for each specimen.

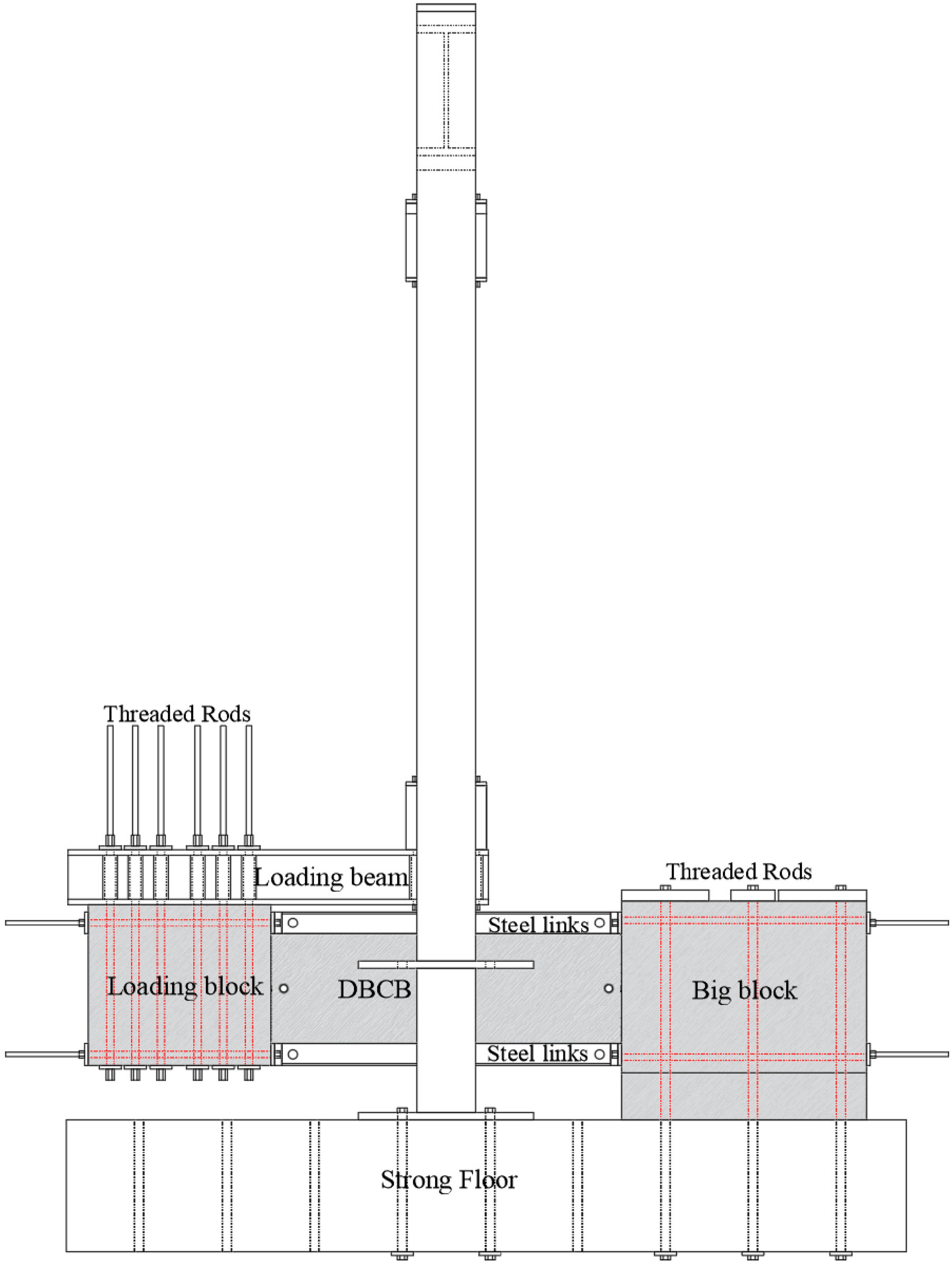

Threaded Rods
Loading beam
Threaded Rods
Steel links
Loading block
DBCB
Big block
Steel links
Strong Floor

(a)

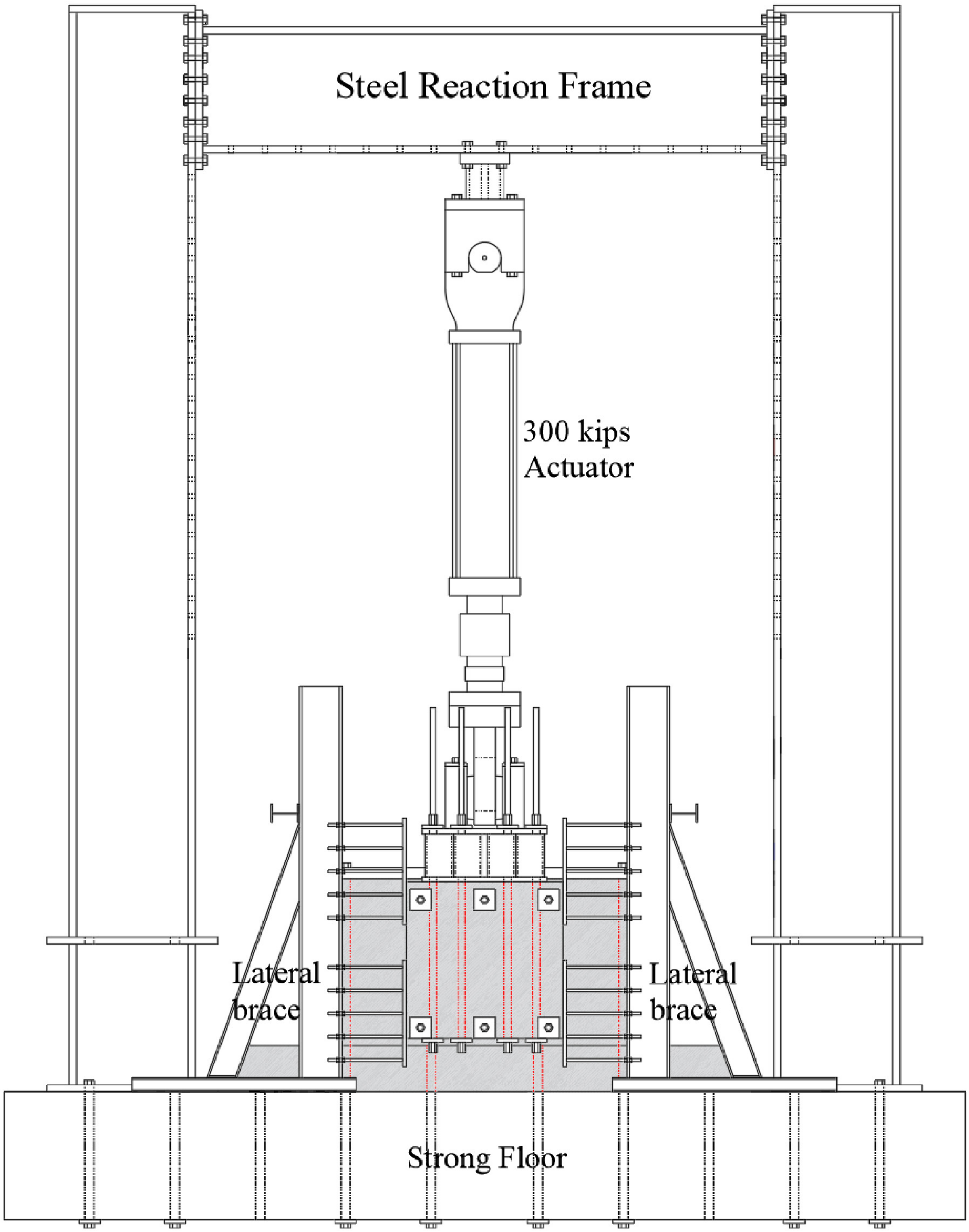

(b)

Fig. 3.42 Test setup: (a) Side view, and (b) Front view

(a)

(b)

(c)

Fig. 3.43 Completed test setups for each specimen: (a) FS-R3.2-N-2, (b) HS-R2.4-S-1, and (c) FS-R2.4-S-3

3.4 Loading protocol

All the specimens underwent the same fully reversed cyclic loading, which was identical to the method employed for the half-scale coupling beam (Choi et al., 2018). The displacement-control method was implemented using a servo-controlled hydraulic actuator. As shown in Table 3.6, three cycles were applied at each increment of chord rotation up to 3% and then two cycles were applied at each increment of chord rotation in excess of 3%. As shown in Fig. 3.44, the two chord rotations 3% and 6% represent approximately the upper bound rotational demands of coupling beams for design basis earthquakes (DBEs) and maximum considered earthquakes (MCEs) level ground motions, respectively (Harries and McNeice, 2006), which is equivalent to the acceptance limit (total chord rotation of 6%) for diagonally reinforced coupling beams (DCBs) recommended by LATBSDC (LATBSDC, 2020). These rotational capacities help maintain the integrity of a coupled wall system. Note that DBE has a 10% probability of exceedance in 50 years and MCE has a 2% probability of exceedance in 50 years.

Table 3.6 Loading protocol for each specimen

Symmetric cyclic loading				
Number of cycles	Chord rotation (%)	Vertical displacement		
		FS-R3.2-N-2 (in.)	HS-R2.4-S-1 (in.)	FS-R2.4-S-3 (in.)
3	0.25	0.24	0.09	0.18
3	0.50	0.48	0.18	0.36
3	0.75	0.72	0.27	0.54
3	1.0	0.96	0.36	0.72
3	1.5	1.44	0.54	1.08
3	2.0	1.92	0.72	1.44
3	3.0	2.88	1.08	2.16
2	4.0	3.84	1.44	2.88
2	6.0	5.76	2.16	4.32
2	8.0	7.68	2.88	5.76
2	10.0	9.6	3.6	7.2

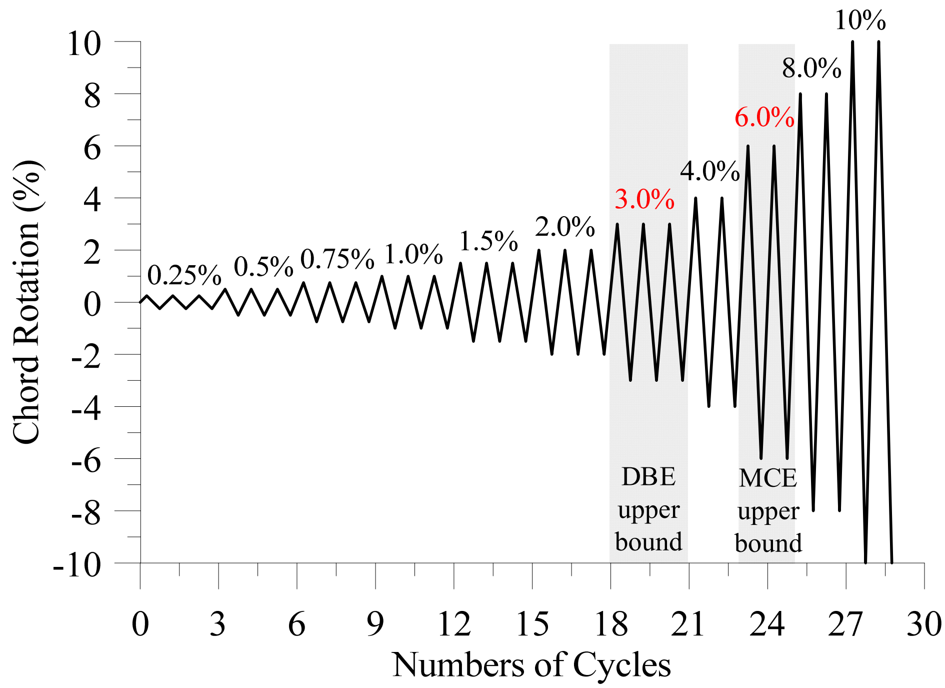

Fig. 3.44 Loading protocol

CHAPTER 4: EXPERIMENTAL RESULTS

To investigate various factors, three DBCB specimens described in detail in Section 3.1 were subjected to fully reversed cyclic loading. The loading involved increasing displacement levels as presented in Table 3.6 and depicted in Fig. 3.44. The purpose was to examine the following aspects:

1. The impact of size effect on the spacing of transverse reinforcement.
2. The performance of high-strength rebars (ASTM A706 Gr. 80) in DBCBs.
3. The required development length of rebars.
4. The size and location of openings for utility ducts.
5. The influence of slab impact on DBCBs,
6. The effect of removing the middle longitudinal bars of steel cages, and
7. The impact of the adjusted spacing of hoops in the plastic hinge zone.

4.1 Cracking and damage patterns

4.1.1 FS-R3.2-N-2 (full-scale without slab)

Fig. 4.1 illustrates the progression of the cracking and damage pattern in the specimen as the beam chord rotations increase under cyclic loading. Before implementing the loading protocol presented in Fig. 3.44, a displacement cycle with a 0.1% chord rotation was performed to verify the functionality of the data acquisition system (DAQ), which records data from strain gauges, LVDTs, and the actuator. During this specific loading, the shear force applied was approximately 58 kips. Only very fine cracks were observed at the top surface of th' coupling beam's end near the big block, with no significant damage present. During the initial positive cycle loading with a rotation of 0.25%, diagonal tension cracks were observed to initiate at the midspan and mid-height of the coupling beam. These cracks specifically developed in the area where an unreinforced concrete strip (UCS) with a thickness of 2 inches was located. Throughout the three constant amplitude displacement reversals, a consistent crack pattern emerged within the UCS layer, resulting in intersecting diagonal grids of cracks. This crack pattern can be observed in Fig. 4.1 (a). Furthermore, a few flexural cracks were noticed on both ends of the beam. As the cyclic loading intensified, the diagonal shear cracks became concentrated in the UCS layer, which lacks transverse reinforcement but experiences the highest shear stress. The concrete along the UCS layer underwent progressive crushing as a result of the relative horizontal sliding between the upper and lower beams. As the chord rotation increased, the crushing spread from the midspan towards both ends of the beam. Choi et al. (2018) explained that the presence of two concrete blocks (wall piers) acting as restrained boundaries causes the separation of the coupling beam to initiate from the mid-span of the beam.

At a chord rotation of 1.5%, the separation of the UCS extended to the end of the utility pipes positioned 3.5 in. away from the beam ends. Additionally, numerous diagonal cracks emerged across the surface of the coupling beam, as shown in Fig. 4.1 (e). Nevertheless, the width of the diagonal cracks did not expand beyond 0.8 mm (0.03 in.) after reaching this width at the midspan of the beam during the initial positive 1% chord rotation. Notably, this maximum width of the diagonal crack is significantly smaller than the 4 mm (0.16 in.) observed in half-scale DBCB tests. (Choi et al., 2018). At this rotation, the strains measured in the longitudinal reinforcement had reached the yield strain.

At 2% chord rotation, the upper and lower beams were totally separated so that they behaved like two independent slender beams bent in double curvature. As a consequence, the two PVC pipes positioned near the beam ends experienced slight deformation due to the relative slip between the upper and lower beams. As shown in Figs. 4.1 (f) to (k), the relative displacement of the top and bottom beams with double-curvature bending was clearly noticeable. This displacement was observed through the grid marked on the specimen, and it became more pronounced as the chord rotation increased. Furthermore, noticeable concrete crushing and vertical flexural cracks were observed at the top and bottom corners of the coupling beam. As the chord rotations increased to 3% to 4%, the concrete crushing extended to all corners, resulting in the spalling of the concrete covers. The damage to the concrete also spread into both blocks, leading to minor cracks occurring at the interface between the beam and the wall. During the initial 3% positive cyclic loading, the strains measured on the middle layer longitudinal reinforcement reached the yield strain.

At a chord rotation of 6%, the spalling of the concrete cover became severe, and the confined concrete core started to crumble in the plastic region adjacent to the beam ends. This deterioration resulted in a significant degradation of the shear strength of the coupling beam.

Additionally, flaking with a fan-shaped pattern due to diagonal cracks became evident in the vicinity of the beam ends, as illustrated in Fig. 4.1 (i). (Choi et al., 2018). At the first 7% positive chord rotation, the longitudinal rebars in the separated top slender beam buckled as shown in Fig. 4.1 (j). As a result, the experimental test was stopped after performing the subsequent 7% negative chord rotation. It should be noted that longitudinal bar buckling was not observed in the previous half-scale DBCB specimens. This difference can be attributed to the use of larger bars in the full-scale beam, which experiences significant bending moment and consequently higher axial forces in the bars. In comparison to smaller beams, the cover concrete in full-scale beams is less effective in restraining larger bars from buckling. This is due to the earlier cracking of the cover concrete caused by the larger outward forces exerted by the longitudinal bars during loading. Consequently, beams with larger cross-sectional dimensions are more susceptible to bar buckling. Additionally, the concrete surrounding the longitudinal bars in full-scale beams is more prone to cracking and crushing, as it must restrain larger bars that require significantly higher restraint stresses to prevent buckling. This phenomenon becomes particularly significant in the later stages of lateral loading, where the core concrete nearest to the hoops has already been damaged or softened due to cyclic shears. The higher tendency for bar buckling in large bars in full-scale specimens has also been observed and reported in other research studies (Visnjic et al., 2016; Nojavan et al., 2017; Choi and Chao, 2019). Moreover, as reported by Poudel et al. (2021), the presence of significant axial restraint in the DCB specimens led to earlier buckling of the diagonal bars. This indicates that the higher compression forces resulting from axial restraint in the full-scale DBCB could exacerbate the longitudinal rebar buckling.

As described in Section 3.3, four steel angle links were installed to restrain the rotation of the loading block and provide axial restraints to the coupling beam. However, following the last negative 3% cyclic loading, the top steel plate connected to the loading beam via post-tensioning (see Fig. 3.43 (a)), which linked the two blocks through the steel angle links, experienced bending due to axial forces. Consequently, an approximate 0.08-in. gap emerged between the steel plate and the beam-to-wall interface. With increasing chord rotation, the gap gradually widened, resulting in a reduction of axial restraint imposed by the top steel links and subsequent elongation of the specimen. Finally, the longitudinal reinforcement in the top slender beam buckled under the compressive force caused by bending, as shown in Fig. 4.1 (j). The gap size reached 0.3 in. prior to the buckling of the rebars.

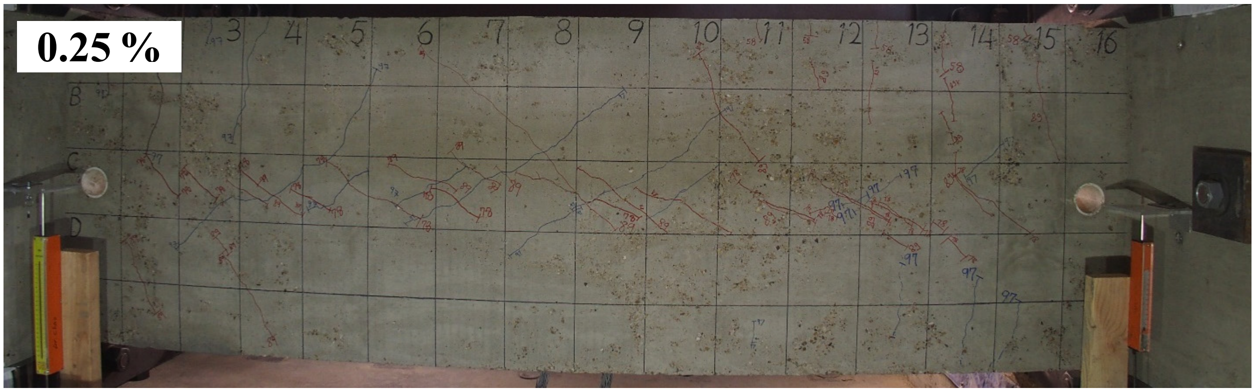

(a)

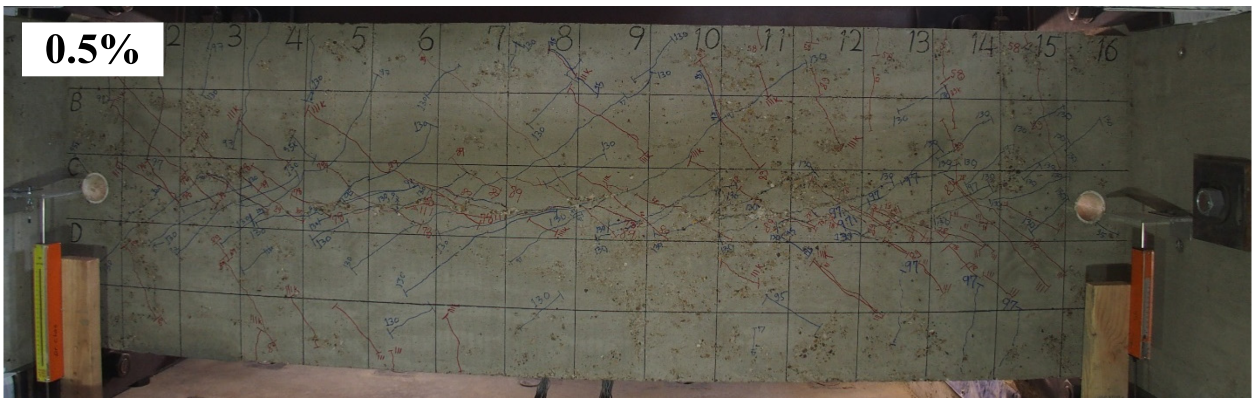

(b)

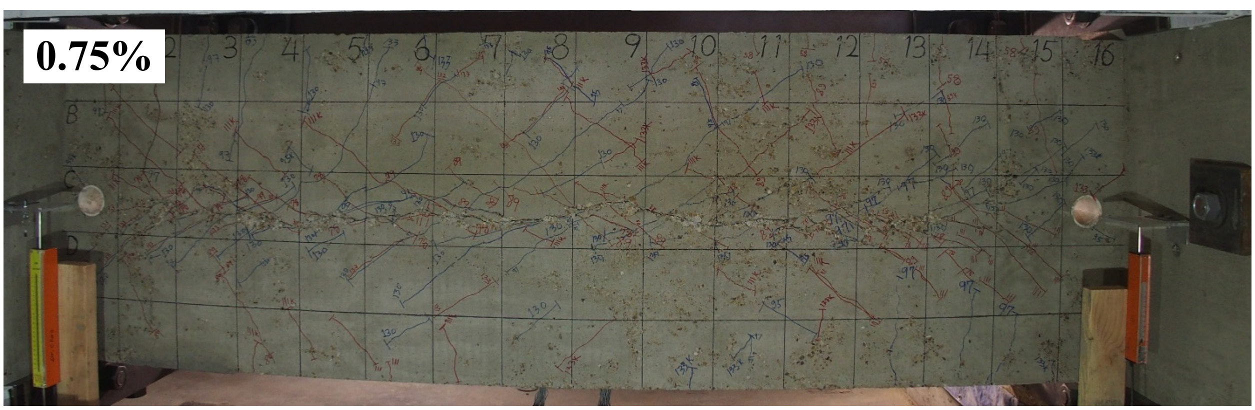

(c)

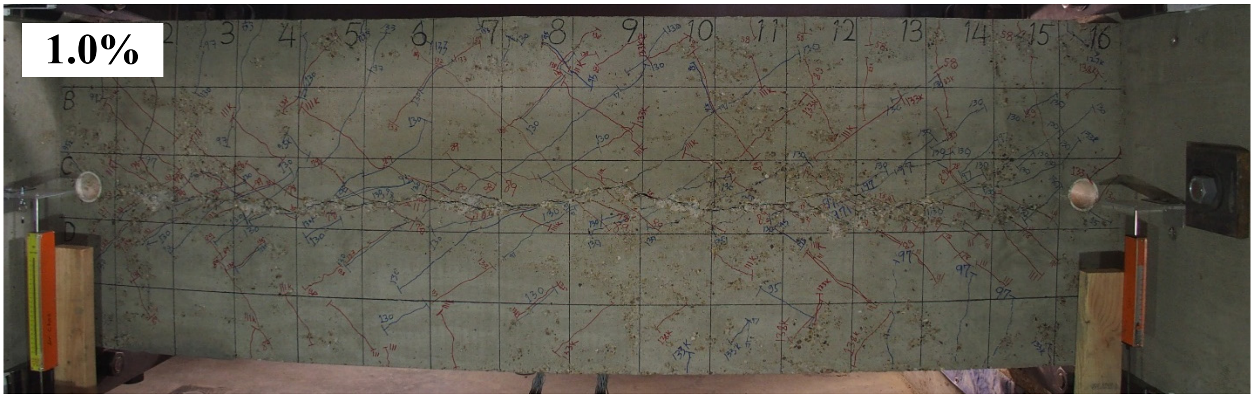

(d)

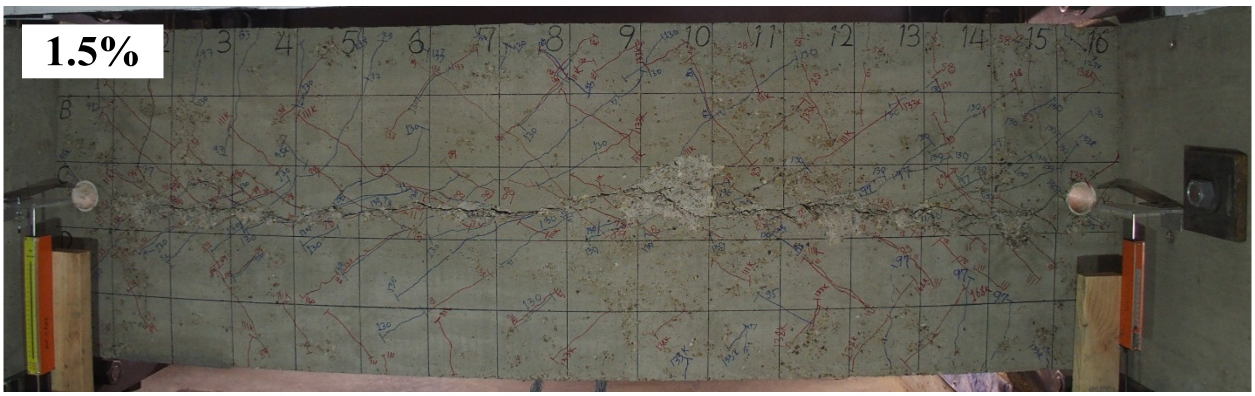

(e)

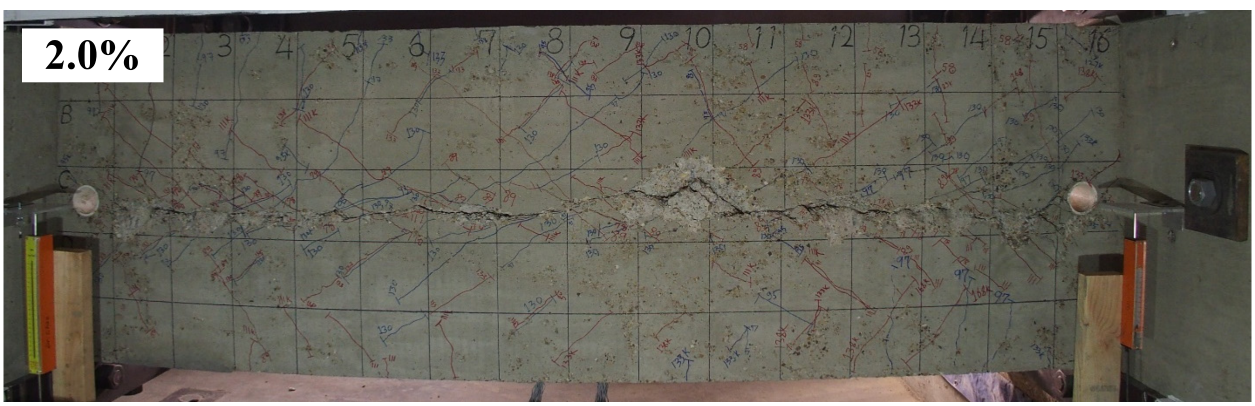

(f)

(g)

(h)

(i)

(j)

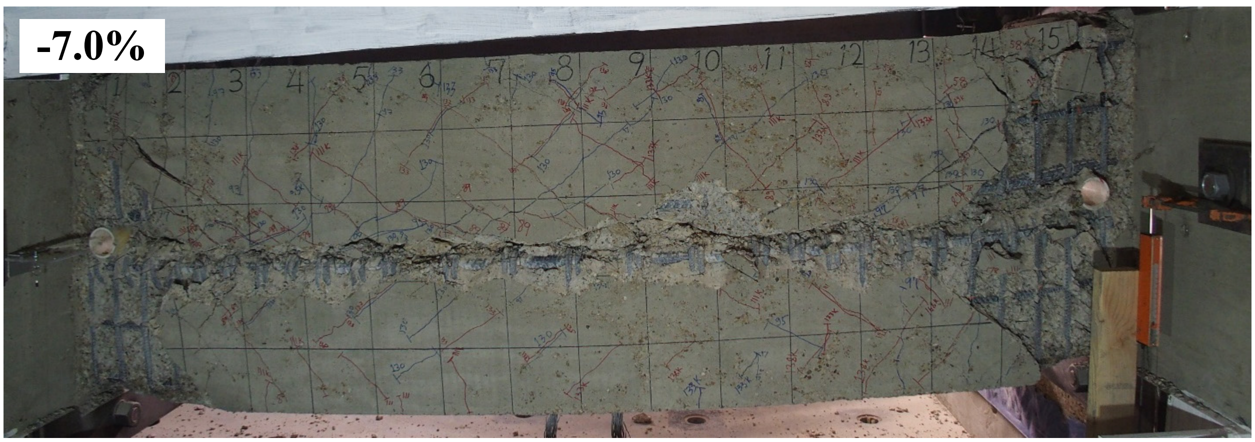

(k)

Fig. 4.1 Crack and damage pattern of FS-R3.2-N-2 according to the beam chord rotation: (a) 0.25% (b) 0.5% (c) 0.75% (d) 1.0% (e) 1.5% (f) 2.0% (g) 3.0% (h) 4.0% (i) 6.0% (j) +7.0%, (k)-7.0%

4.1.2 HS-R2.4-S-1 (half-scale with slab)

Fig. 4.2 shows the cracking and damage pattern of the specimen according to the beam chord rotation under large displacement reversals (Fig. 3.44). At the first positive cycle loading for 0.25% rotation, the diagonal tension cracks did not concentrate along the UCS layer, resulting in a different crack pattern compared to the DBCBs without the slab, as shown in Fig. 4.2 (a). However, as beam chord rotation increased, the diagonal shear cracks became more concentrated at the UCS layer and extended towards both ends of the coupling beam, as illustrated in Figs. 4.2 (b), (c), and (d). This behavior is similar to the previous tests conducted without a slab (Choi et al., 2018). Flexural cracks in the slab emerged at both ends right from the initiation of cyclic loading, and additional flexural cracks formed within the span of the slab as the cyclic loading progressed. When the rotation reached 0.5%, the longitudinal reinforcing bars within the slab started yielding.

Upon reaching a chord rotation of 1.5%, the cracking of the UCS extended up to 3 inches away from the ends of the beam. Additionally, numerous diagonal cracks emerged across the entire surface of the coupling beam, as depicted in Fig. 4.2 (e). However, the width of the diagonal crack remained constant after reaching a crack width of 0.6 mm (0.024 in.) at the midspan of the beam during the initial positive 0.75% chord rotation. This width is significantly smaller than the 4 mm (0.16 in.) observed in half-scale DBCBs without a slab (Choi et al., 2018). Vertical flexural cracks were observed at the bottom corner of the beam. Concurrently, some of the longitudinal reinforcements in the two steel cages began to yield, as indicated by the measured strains.

Upon reaching a chord rotation of 2%, clear relative slip between the upper and lower beams was evident, as indicated by the visible displacement of the grid markings on the specimen. This observation suggests that the top and bottom beams behaved as two separate slender beams, resulting in concrete crushing and the development of vertical flexural cracks at both bottom corners of the coupling beam, as depicted in Fig. 4.2 (f). Furthermore, additional diagonal shear cracks emerged at both ends of the coupling beam. Subsequently, during larger displacement reversals, these cracks led to flaking with a fan-shaped pattern near the beam-to-wall interface (Fig. 4.3 (i)). Concurrently, the remaining longitudinal reinforcements in the steel cages reached their yield point. As the chord rotations reached 3% to 4%, concrete crushing at the bottom corners of the beam extended and resulted in the spalling of all concrete covers, as shown in Figs. 4.2 (g) and (h). The concrete damage extended into both blocks, resulting in minor cracks occurring at the beam-to-wall interface. Additionally, substantial widening of the crack width was observed at the slab-to-wall interface, accompanied by concrete crushing in the slab.

At 6% chord rotation, the spalling of concrete cover expanded further, and the confined concrete core began to crumble in the plastic hinge region near the beam ends, as shown in Fig. 4.2 (i). However, the shear strength did not decrease until the first positive 8% chord rotation, likely due to the strain-hardening of the reinforcing bars and the limited damage observed in the confined concrete at the plastic zone of the coupling beam, as shown in Fig. 4.2 (j). Subsequently, the shear strength experienced a sudden drop as the confined concrete damage deteriorated rapidly, as illustrated in Fig. 4.2 (k). Following the extensive damage to the core concrete, the steel cage began to experience buckling. Additionally, the slab suffered complete fragmentation. However, the coupling beam maintained its structural integrity, enabling the experimental test to proceed up to 10% chord rotations, as shown in Fig. 4.2 (l).

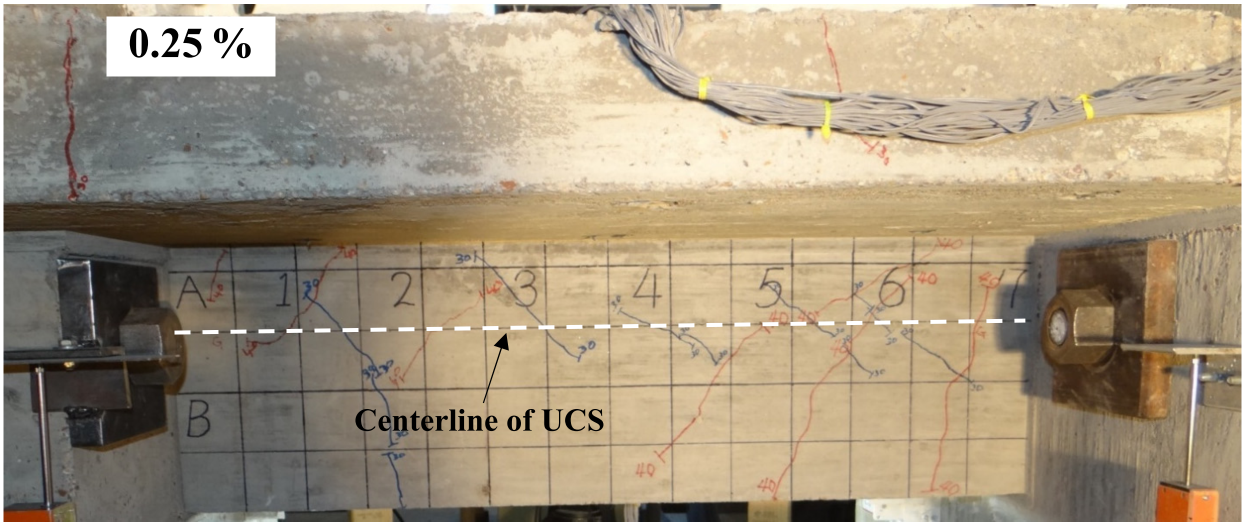

(a)

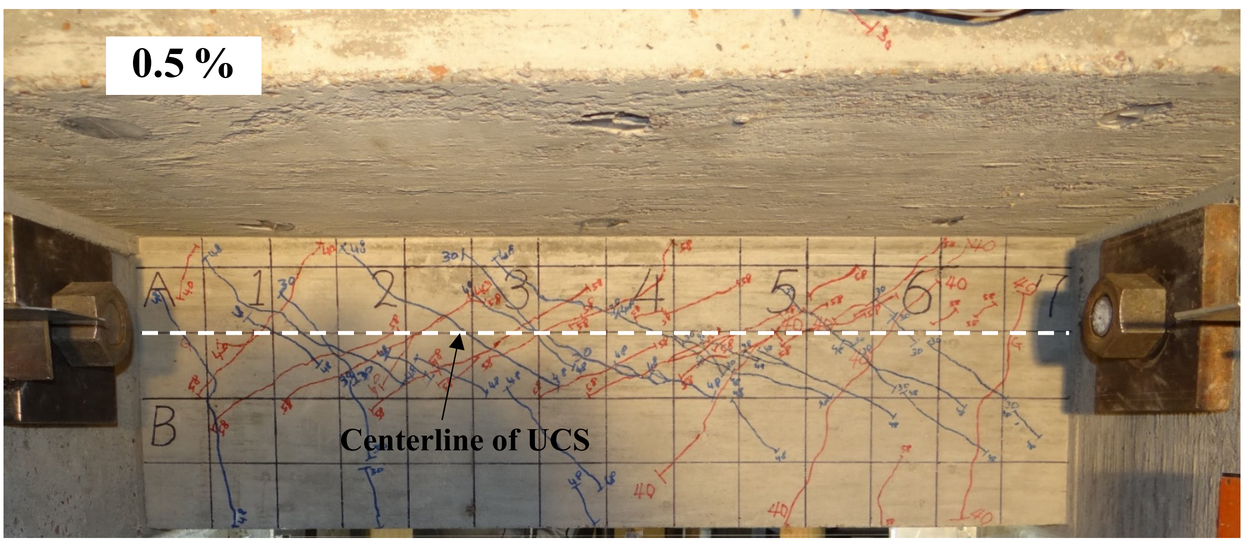

(b)

(c)

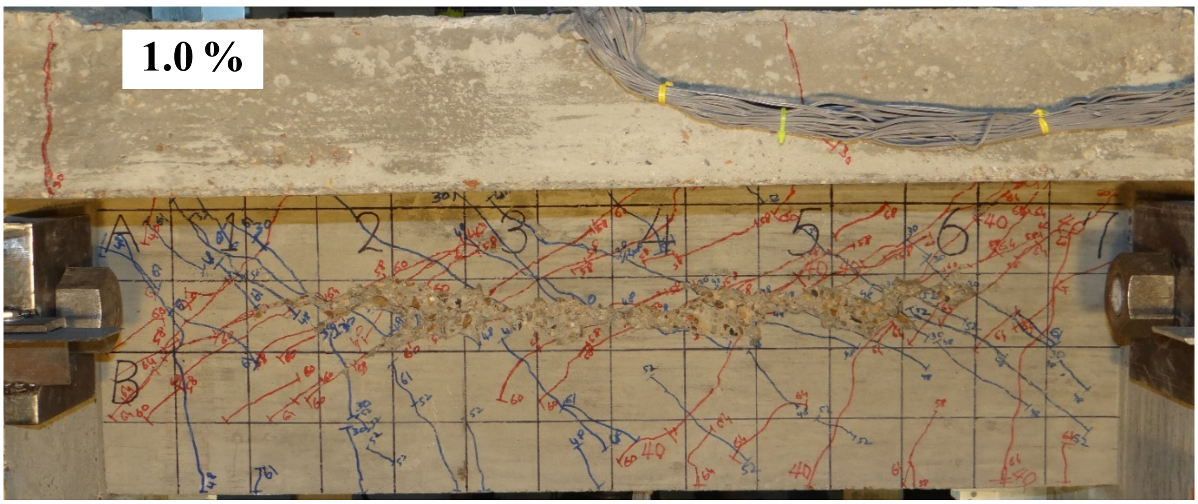

(d)

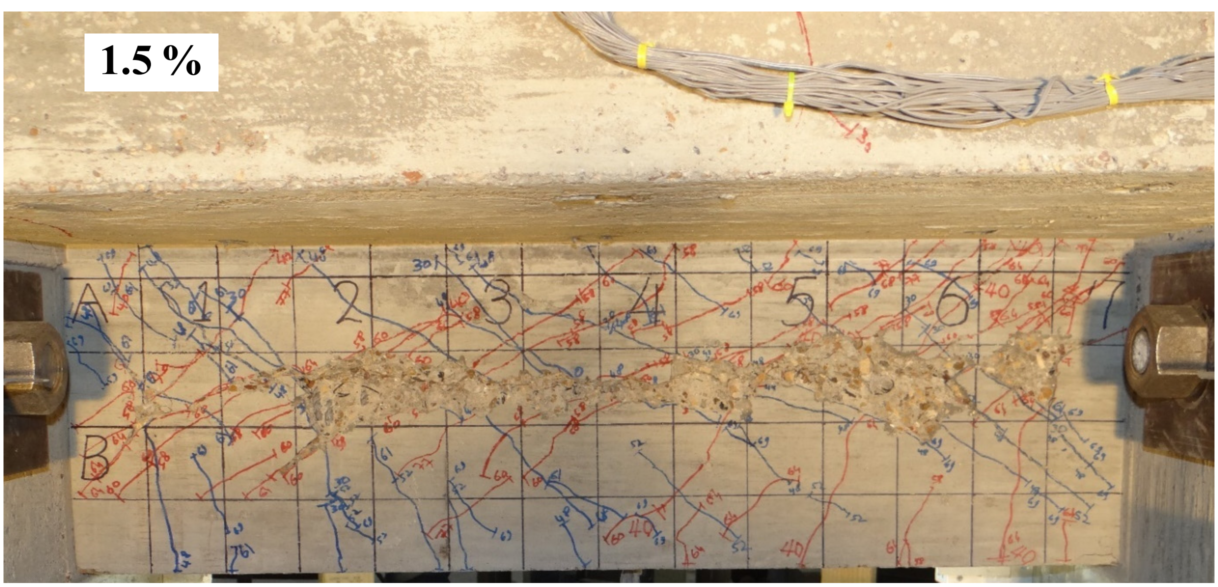

(e)

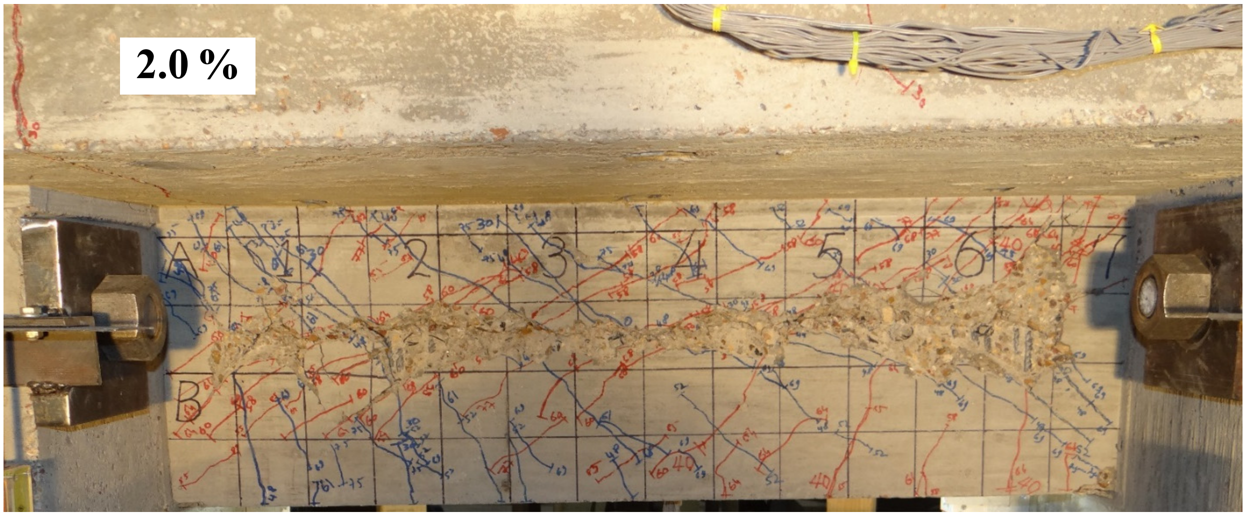

(f)

(g)

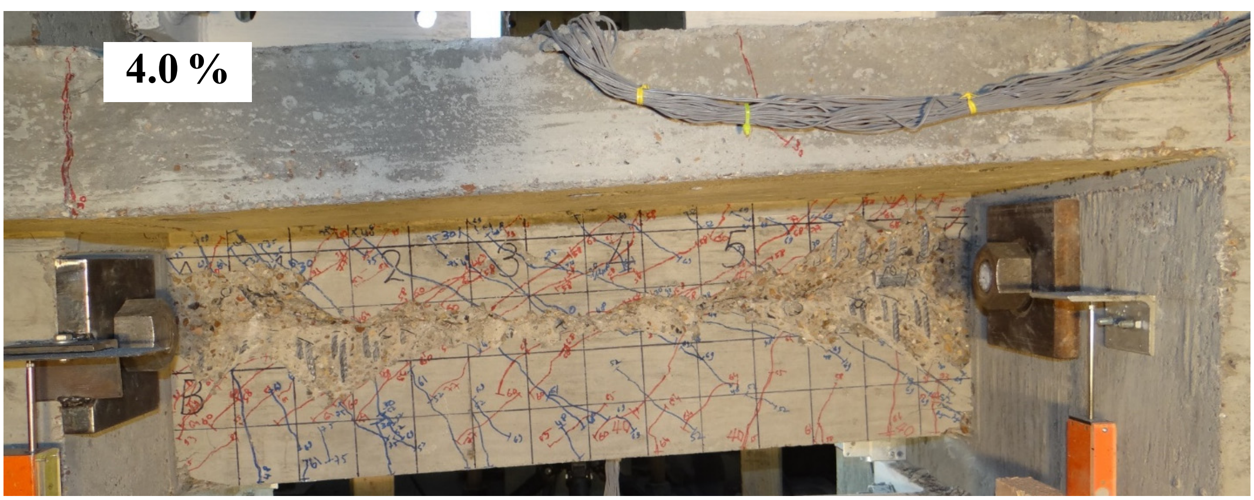

(h)

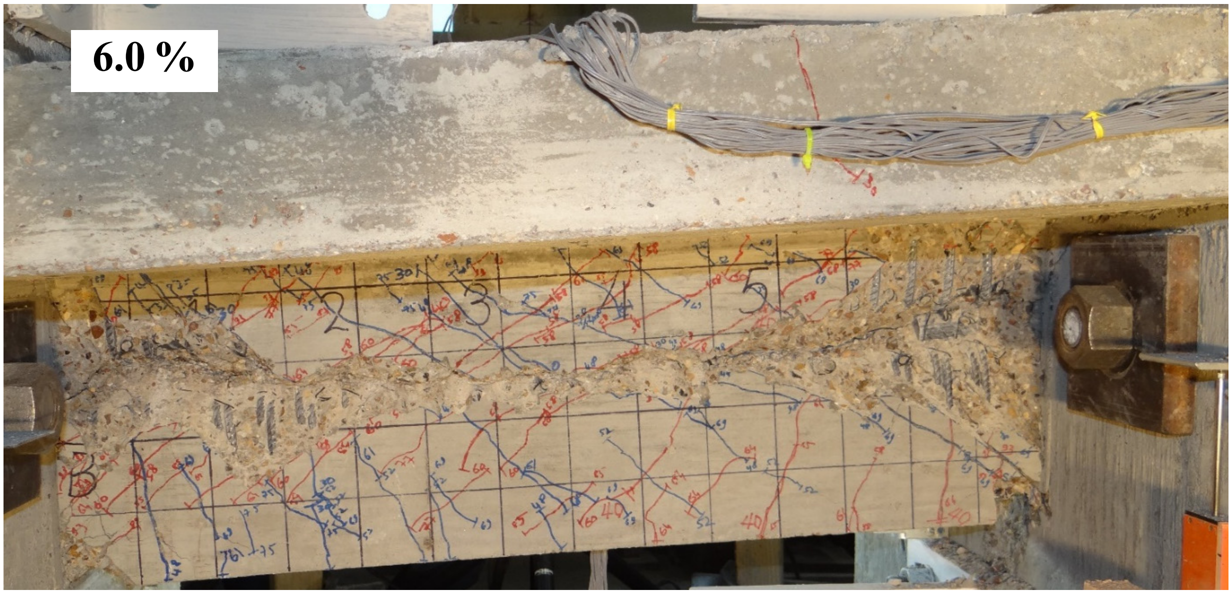

(i)

(j)

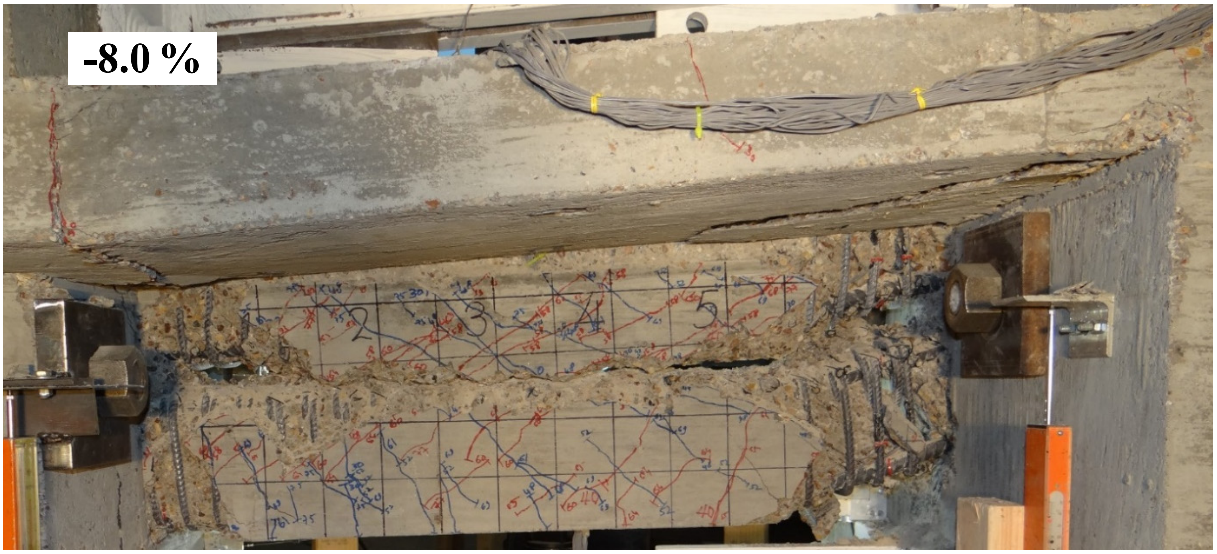

(k)

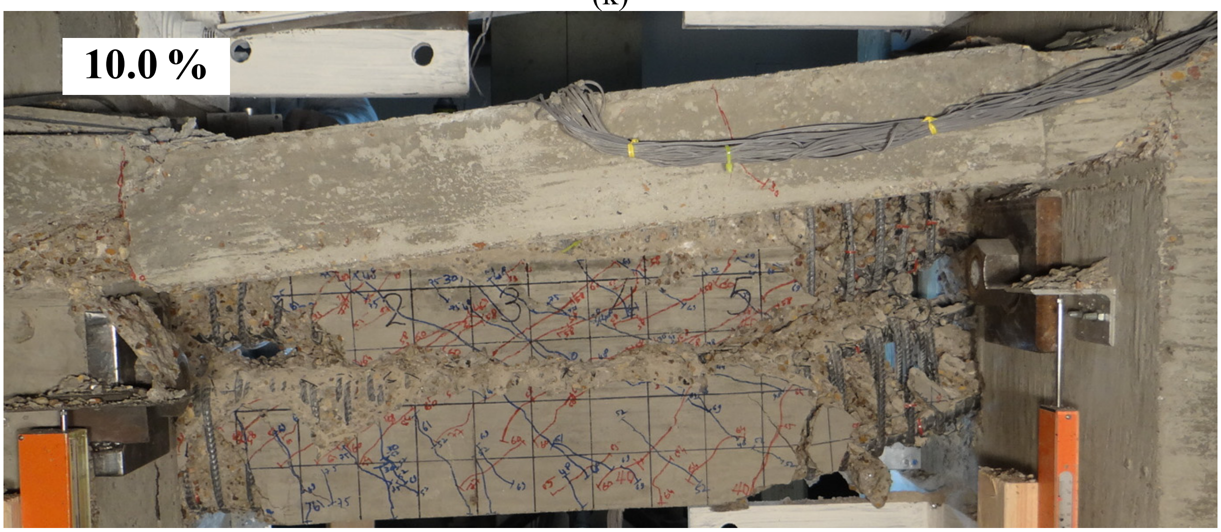

(l)

Fig. 4.2 Crack and damage pattern of HS-R2.4-S-1 according to beam chord rotation: (a) 0.25% (b) 0.5% (c) 0.75% (d) 1.0% (e) 1.5% (f) 2.0% (g) 3.0% (h) 4.0% (i) 6.0% (j) first positive +8% (k) 8% (l) 10.0%

4.1.3 FS-R2.4-S-3 (full-scale with slab)

Fig. 4.3 depicts the cracking and damage pattern of the specimen based on the magnitude of the beam chord rotation subjected to displacement reversals (Fig. 3.44). At the first positive cycle loading for 0.25% rotation, the diagonal tension cracks did not concentrate along the UCS layer, resulting in a different crack pattern compared to the DBCBs without the slab, as shown in Fig. 4.3 (a). However, as beam chord rotation increased, the diagonal shear cracks became more concentrated at the UCS layer and extended towards both ends of the coupling beam, as illustrated in Figs. 4.3 (b) to (f). The crack patterns observed in this test are similar to those observed in the previous half-scale DBCB test with a slab (HS-R2.4-S-1). At 0.5% chord rotation, vertical flexural cracks became noticeable at the bottom of the coupling beam. Simultaneously, the flexural cracks in the slab originated at both ends of the slab right from the start of the cyclic loading and spread inward from the outer surface as the loading progressed. By the time the chord rotation reached 0.75%, the outer longitudinal reinforcing bars within the slab exhibited the first signs of yielding. As the beam chord rotation increased, there was a greater concentration of diagonal shear cracks at the UCS layer. Subsequently, relative horizontal slip between the top and bottom beams initiated at the midspan of the UCS layer and spread towards both ends of the coupling beam, as shown in Figs. 4.3 (b), (c), and (d). This crack propagation behavior is consistent with that observed in the HS-R2.4-S-1 test. However, it should be noted that the slip between the two beams tended to propagate more rapidly towards both ends of the coupling beam compared to the half-scale DBCBs. At 1.0% chord rotation, the separation of the UCS had already reached the end of the utility PVC pipes, with their centers located 3.5 in. away from the beam ends, as shown in Fig. 4.3 (d). At this stage, the measured strains in certain longitudinal reinforcements of the coupling beam began to yield near the beam-to-wall interface.

As the chord rotation increased to 1.5%, 2%, and 3%, the coupling beam displayed stable behavior without significant propagation of shear cracks. This was due to the fact that the coupling beam had separated into two independent slender beams after a chord rotation of 1.0%. Consequently, the width of diagonal cracks did not continue to expand beyond the initial crack width of 2.5 mm (0.098 in.) at the midspan of the beam, which was reached during the first positive 0.75% chord rotation. Illustrated in Figs. 4.3 (e), (f), and (h), the cyclic relative displacement between the upper and lower beams resulted in noticeable horizontal slip cracks. In Fig. 4.3 (g), it can be observed that although the two PVC pipes located near the beam ends experienced significant deformation caused by the relative slip of the two beams, they remained intact and acted as obstacles, hindering or delaying the propagation of horizontal cracks towards the beam-to-wall interface. Consequently, the diagonal crack near the beam-to-wall interface became more severe. This can be attributed to the enhanced slip resistance offered by the larger dimensions of PVC pipes, specifically the 3.0-inch nominal diameter as opposed to the 2.5-inch nominal diameter used in FS-R3.2-N-2. On the other hand, the two PVC pipes positioned in the midspan of each beam remained undistorted until the conclusion of the test.

When the chord rotation reached 1.5%, the coupling beam experienced slight concrete crushing at its bottom corners, accompanied by noticeable vertical flexural cracks at both the corners of the slab and the bottom corners of the beam. Simultaneously, all measured strains in the longitudinal reinforcement of the coupling beam surpassed the yielding strain near the beam-to-wall interface. Beyond this rotation, the concrete crushing intensified, and the vertical cracks progressively propagated and widened, leading to the spalling of all concrete covers. Additionally, at chord rotations of 2% to 3%, the diagonal crack extended into both blocks, resulting in the occurrence of minor cracks at the beam-to-wall interface.

At 4.0% chord rotation of, the spalling of concrete cover became more extensive, and the confined concrete core started to crumble at the plastic hinge region adjacent to beam ends. This can be seen in Fig. 4.3 (i). Notably, diagonal cracks developed throughout the entire coupling beam, including the slab, which differs from the crack pattern observed in the half-scale DBCB with a slab. These shear cracks led to a decrease in shear strength in the subsequent drift cycle. By the time the chord rotation reached 6.0%, the shear strength experienced a 20% degradation as the damage to the confined concrete core at the plastic hinge region worsened due to the combined presence of flexural and shear cracks. This is illustrated in Fig. 4.3 (j). Furthermore, at a positive chord rotation of 6.0%, the longitudinal reinforcement exhibited inelastic buckling as a result of the severe damage to the confined concrete core near the beam ends and the compression caused by flexural bending. Consequently, the test was concluded at a positive chord rotation of 7%.

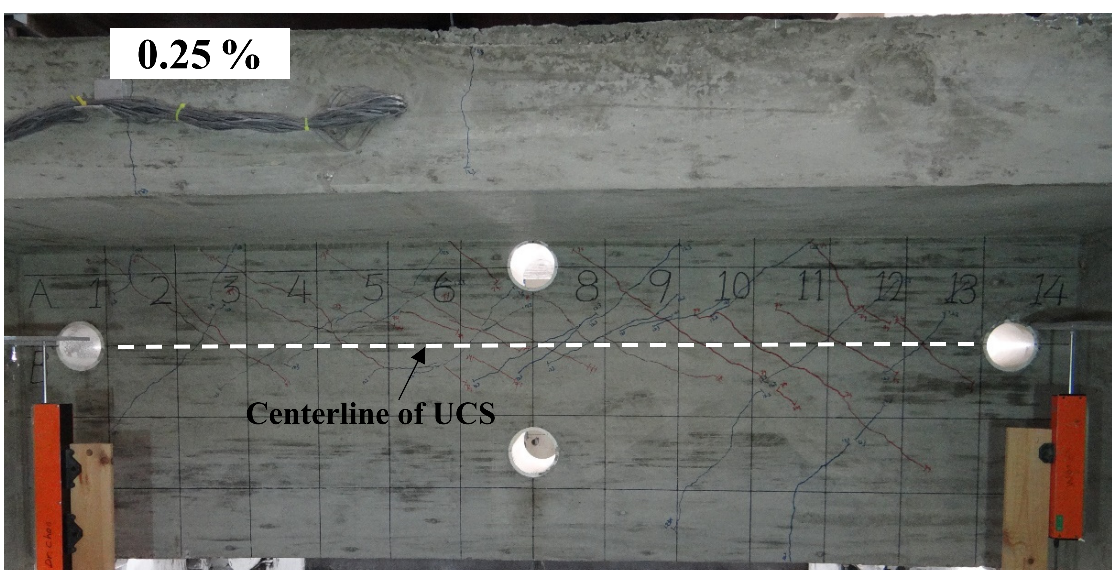

(a)

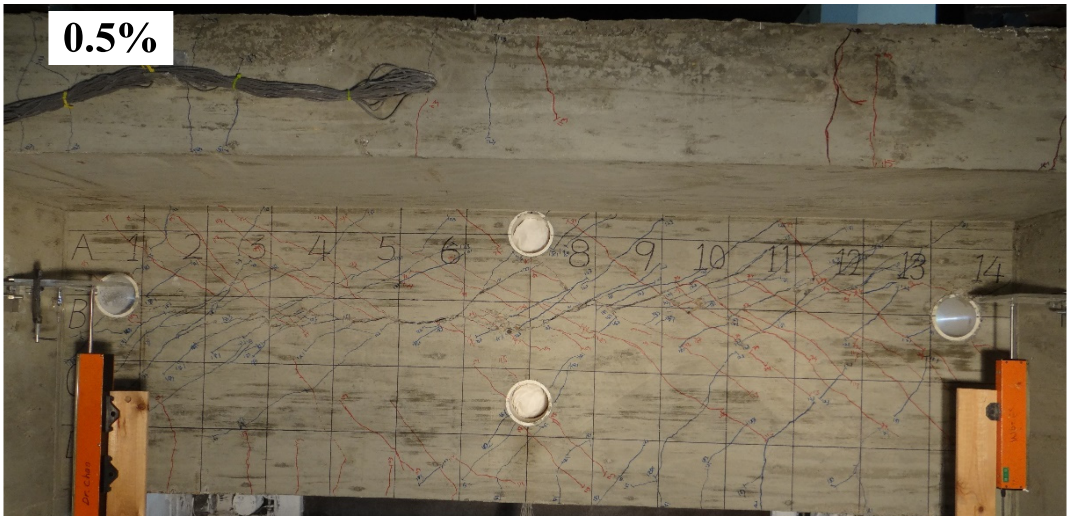
0.5%
A
1
2
3
4
5
6
8
9
10
11
12
13
14
B

(b)

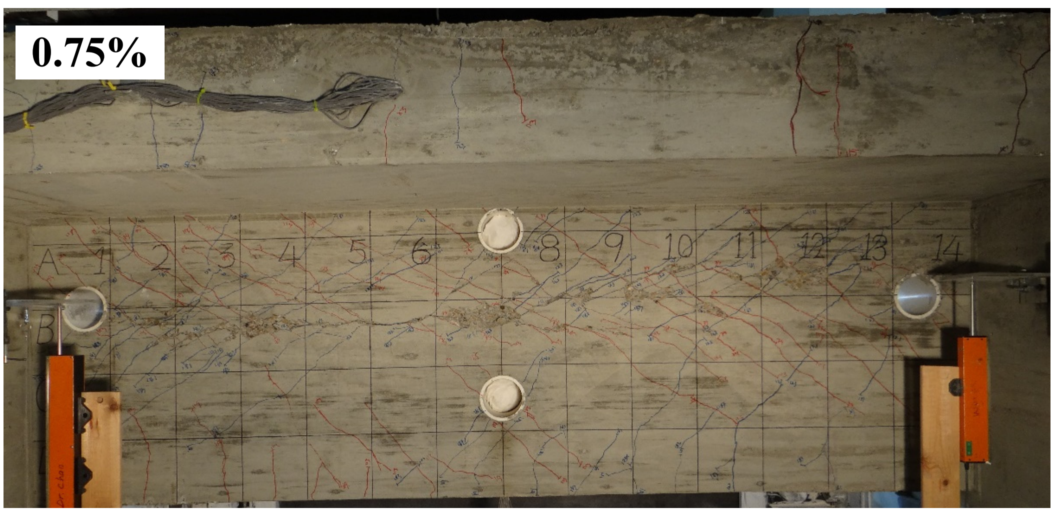
0.75%
A
1
2
3
4
5
6
8
9
10
11
12
13
14
B

(c)

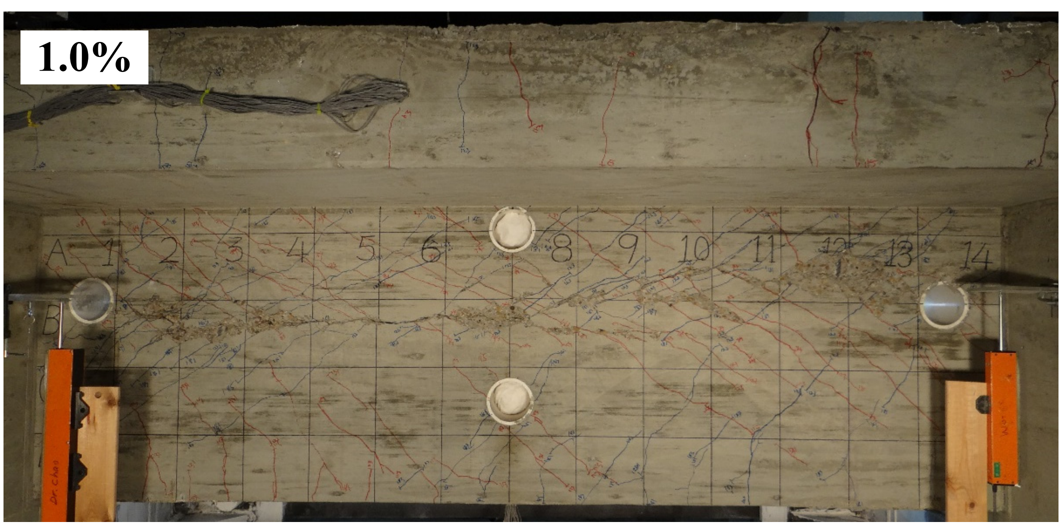
1.0%
A
1
2
3
4
5
6
8
9
10
11
12
13
14
B

(d)

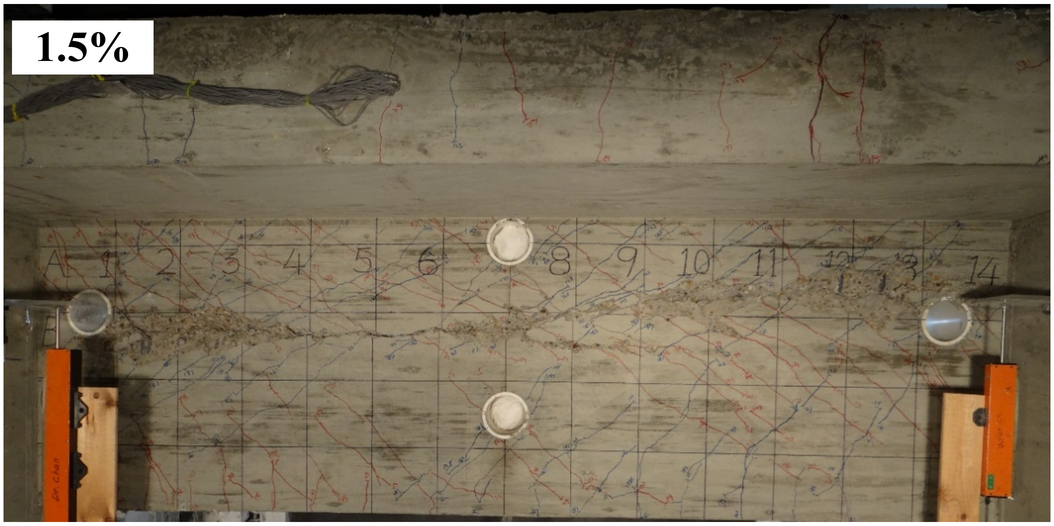

(e)

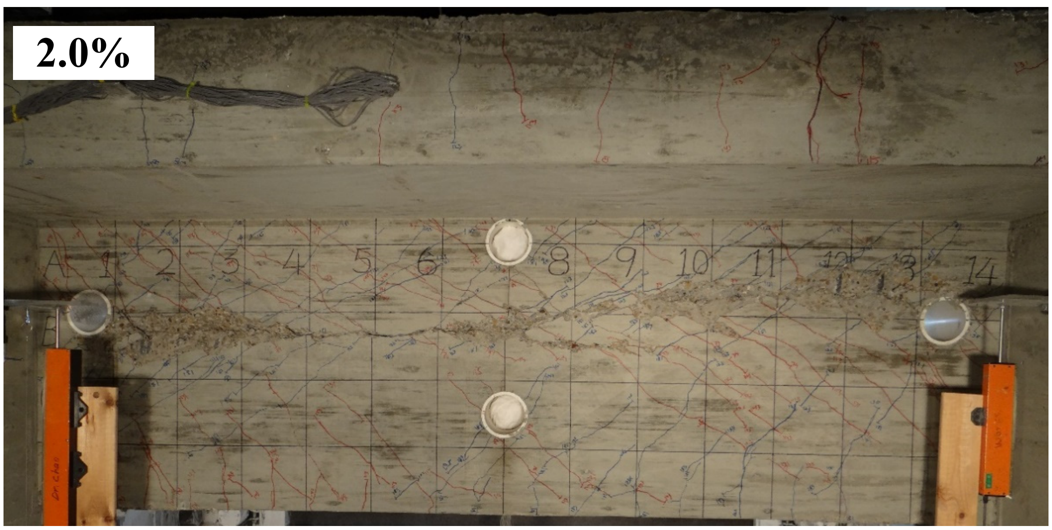

(f)

(g)

(h)

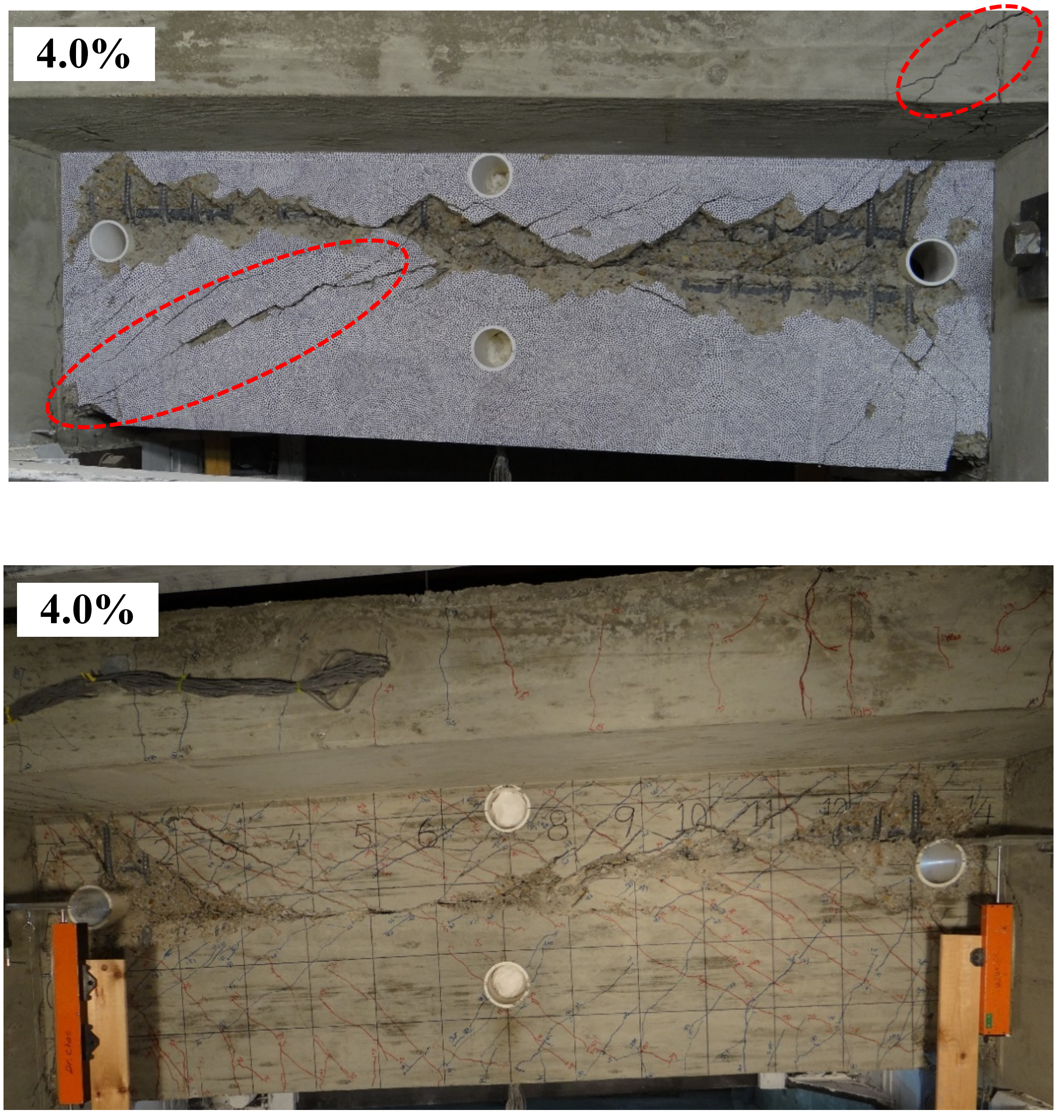

(i)

(j)

(k)

Fig. 4.3 Crack and damage pattern of FS-R2.4-S-3 according to the beam chord rotation: (a) 0.25% (b) 0.5% (c) 0.75% (d) 1.0% (e) 1.5% (f) 2.0% (g) +3.0% (h) 3.0% (i) 4.0% (j) 6.0% (k) +7%

4.1.4 Summary of the experimental results

The test results for three specimens, which were subjected to the fully reversed cyclic loading protocol illustrated in Figure 3.44, are summarized in Table 4.1.

Table 4.1 Experimental test results

Specimen	θ_{yield} [*] (%)	V_{max} (kips)	V_{max}/V_{design}	θ_{max} (%)	$V_{normalized}$ [**]
FS-R3.2-N-2	1.5~2.0	198	1.08	6	12.1
HS-R2.4-S-1	1.5~2.0	94.6	1.74	8	15.4
FS-R2.4-S-3	1.0~1.5	215	1.48	4	10.4

[*] θ_{yield} is the beam chord rotation when the longitudinal reinforcing bar yields
[**] Normalized shear stress $V_{normalized} = V_{max}/(\sqrt{f_{cm}}\, b_w h)$, where f_{cm} is the measured compressive strength

The cracking and damage patterns observed in all specimens were very similar to prior half-scale DBCB tests (Choi et al., 2018, 2020). Namely, during the first positive cycle loading, diagonal tension cracks were observed in close proximity to location where the UCS is positioned. During load reversal, the same crack pattern reappeared at the same location, resulting in diagonal grids of intersecting cracks. As the cyclic load increased, these cracks extended towards both ends of the specimens due to relative slip between the upper and lower beams. In the case of specimens with the slab (HS-R2.4-S-1, FS-R2.4-S-3), the initial diagonal tension cracks were observed slightly away from the UCS location. This occurred because the concentration of diagonal shear cracks at the UCS layer was slightly delayed due to the difference between the UCS level and the elastic neutral axis level of the DBCB with the slab. However, this discrepancy did not result in incomplete splitting of the UCS.

The first full-scale specimen (FS-R3.2-N-2) was constructed following the design procedure outlined in Fig. 3.2, which included three longitudinal reinforcement layers for each steel cage. This design configuration was consistent with the previous half-scale specimens (Choi et al. 2018, 2020). During the test, the maximum width of the diagonal crack was minimal, measuring only 0.8 mm. Additionally, there was no significant size effect observed due to the doubled spacing of the transverse reinforcement. at the beam-to-wall interfaces throughout the test, without experiencing sliding shear failure. The test was concluded when local buckling of the longitudinal rebars occurred in the plastic hinge zone adjacent to the beam-to-wall interface. The second half-scale specimen (HS-R2.4-S-1) had two longitudinal reinforcement layers in each cage, omitting the middle longitudinal reinforcing bar. This simplifies the reinforcement layout in DBCB. During the test, HS-R2.4-S-1 exhibited a maximum width of 0.6mm for the diagonal crack, which is significantly smaller than the 4mm observed in half-scale DBCBs without a slab (Choi et al., 2018). It displayed stable behavior and retained its shear strength up to the first positive 8% chord rotation without any reduction. Subsequently, there was a rapid drop in shear strength as the core concrete damage intensified in the plastic hinging zones at the beam ends, resulting in significant sliding at the beam-to-wall interface. This behavior differed from that observed in prior half-scale DBCBs (Choi et al., 2018). Essentially, removing the middle longitudinal reinforcement in steel cages could have weakened the concrete confinement and the dowel strength in the plastic hinge zone, leading to a quick reduction in the performance of the coupling beam once an 8% chord rotation was reached.

Furthermore, as indicated in the second column of Table 4.1, there are differences in the initiation of yielding among the longitudinal reinforcement in each specimen closest to the beam-to-wall interface. In FS-R3.2-N-2, the longitudinal reinforcing bars began to yield at a chord rotation of either 1.5% or 2.0%. Similarly, in HS-R2.4-S-1, yielding was observed at a chord rotation of either 1.5% or 2.0%. However, for FS-R2.4-S-3, many longitudinal reinforcements yielded at a chord rotation of 1.5%, while the remaining reinforcements initiated yielding at a chord rotation of 1.0%. The removal of the middle longitudinal bars from each steel cage in the DBCB appears to accelerate the onset of yielding, which becomes more apparent when compared to the prior half-scale specimens that began yielding at a 2.0% chord rotation (Choi et al., 2018). Ameen et al. (2020) and Weber-Kamin et al. (2020) found that the inclusion of secondary longitudinal reinforcement in DCB led to a reduction in the concentration of chord rotation at the beam-to-wall interface and a more distributed damage pattern across the beam span, ultimately enhancing the deformation capacity. This supports the notion that the removal of the middle longitudinal bars accelerates the onset of yielding in the longitudinal reinforcement due to the concentration of chord rotation near the beam-to-wall interface. Furthermore, the yielding of longitudinal bars tends to occur earlier in full-scale specimens compared to half-scale specimens.

The longitudinal reinforcing bars in FS-R2.4-S-3 exhibited yielding at a chord rotation of 1%, which is earlier compared to the other specimens. This suggests a higher concentration of chord rotation near the beam-to-wall interface for FS-R2.4-S-3. Additionally, the relatively smaller reinforcement ratio (ρ) of the primary reinforcement in FS-R2.4-S-3 may have contributed to the concentration of chord rotation. This concentrated rotation could have resulted in a faster separation between the upper and lower beams and led to the accumulation of damage near the beam ends. FS-R2.4-S-3 was designed with a slight relaxation of the confinement requirement specified in ACI 18.6.4.4 (ACI, 2019), and it also omitted the middle longitudinal reinforcement in each beam. As a consequence, the concrete core in FS-R2.4-S-3 experienced quicker deterioration due to the combined flexural and shear stresses near the beam ends. This resulted in the formation of longer diagonal shear cracks extending across the depth of the beam, even after it was completely separated into two independent slender beams, which differed from the behavior observed in previous specimen tests. In addition, compression axial force induced by axial restraint might have an additional adverse effect on the ductility of concrete (Mihaylov et al., 2021, Poudel et al., 2021). This effect can potentially lead to earlier deterioration of the diagonal compression struts. At the first positive chord rotation of 7%, a notable difference is observed in the extent of damage to the concrete core near the beam ends between FS-R3.2-ES-2 and FS-R2.4-S-3.

Figs. 4.1(j) and 4.3(k) illustrate that the full-scale specimens (FS-R3.2-N-2 and FS-R2.4-S-3) exhibited significant longitudinal rebar buckling under high chord rotation, a phenomenon that was not observed in the previous half-scale specimens (Choi et al., 2018). As discussed previously, bar buckling in full-scale DBCBs can be attributed to the use of larger bars in the full-scale beam, which experiences significant bending moment and consequently higher axial forces in the bars. In comparison to smaller beams, the cover concrete in full-scale beams is less effective in restraining larger bars from buckling. This is due to the earlier cracking of the cover concrete caused by the larger outward forces exerted by the longitudinal bars during loading. Consequently, beams with larger cross-sectional dimensions are more susceptible to bar buckling. Additionally, the concrete surrounding the longitudinal bars in full-scale beams is more prone to cracking and crushing, as it must restrain larger bars that require significantly higher restraint stresses to prevent buckling. Moreover, as reported by Poudel et al. (2021), the presence of significant axial restraint in the DCB specimens led to earlier buckling of the diagonal bars. This indicates that the higher compression forces resulting from axial restraint in the full-scale DBCB could exacerbate the longitudinal rebar buckling. This phenomenon becomes particularly significant in the later stages of lateral loading, where the core concrete nearest to the hoops has already been damaged or softened due to cyclic shears. In FS-R2.4-S-3, the concentrated concrete damage near the beam ends, following the separation of the beam into two slender beams, exacerbated the inelastic buckling of the longitudinal reinforcement. This can explain why the longitudinal rebars in FS-R2.4-S-3 buckled earlier compared to FS-R3.2-N-2.

As mentioned earlier, HS-R2.4-S-1, despite eliminating the middle layer of longitudinal reinforcement for each beam, exhibited minimal diagonal cracking with a maximum width of only 0.6 mm. This is significantly smaller than the 4 mm observed in half-scale DBCBs without a slab (Choi et al., 2018). Additionally, HS-R2.4-S-1 demonstrated stable behavior up to the first positive 8% chord rotation without any noticeable loss in shear strength. The full-scale specimen, FS-R2.4-S-3, was also designed with a slab and did not include the middle layer of longitudinal reinforcement for each beam. Additionally, the hoop spacing in FS-R2.4-S-3 was slightly relaxed compared to the confinement requirement specified in ACI 18.6.4.4. Nevertheless, the maximum width of the shear crack in FS-R2.4-S-3 was 2.5 mm, which is still smaller than the 4 mm observed in previous half-scale DBCB studies. This suggests that the presence of the slab offers additional confinement to the coupling beam, leading to a reduced width of diagonal shear cracks and improved performance of DBCBs.

4.2 Shear versus rotation response

4.2.1 FS-R3.2-N-2

Fig. 4.4 illustrates the hysteresis response showing the relationship between shear force and beam chord rotation for Specimen FS-R3.2-N-2. For the purpose of comparison, the upper bound shear stress equation from ACI 318, $V_u = \phi 10\sqrt{f'_c}\, A_{cw}$, was also included in Fig. 4.4 as blue dashed lines, where ϕ is equal to 0.85. Notably, the figure demonstrates that the specimen maintains a high shear stress level of $12.1\sqrt{f_{cm}}$ or $9.3\sqrt{f'_c}$, without any noticeable strength degradation, up to a chord rotation of 6%. This rotation level corresponds approximately to the demand of MCE (Maximum Considered Earthquake) level ground motions (Harries and McNeice, 2006). Here, f_{cm} represents the measured concrete compressive strength, equal to 3.0 ksi, and f'_c represents the design concrete compressive strength, equal to 5.0 ksi.

The shear force in the coupling beam exhibited a linear increase up to 0.5% chord rotation. However, once the chord rotation reached 1.0%, the rate of shear force increase began to decrease. This decrease can be attributed to the separation of the coupling beam into upper and lower beams during the test. Additionally, beyond a chord rotation of 1.5%, there was a rapid decrease in both the unloading and reloading stiffness. This behavior closely corresponds to the yielding of the longitudinal reinforcing bars, as observed through strain gauges. Similar behavior was also observed in prior tests conducted on half-scale DBCBs (Choi et al., 2018, 2020).

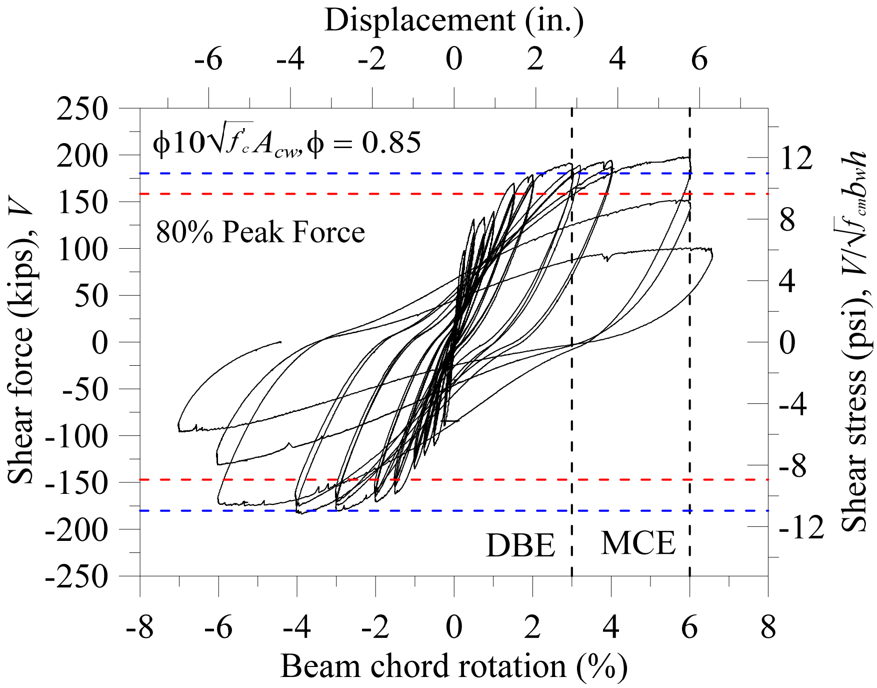

Fig. 4.4 Shear force versus beam chord rotation response of FS-R3.2-N-2

4.2.2 HS-R2.4-S-1

Fig. 4.5 illustrates the hysteresis response showing the relationship between shear force and beam chord rotation for Specimen HS-R2.4-S-1. For the purpose of comparison, the upper bound shear stress equation from ACI 318, $V_u = \phi 10\sqrt{f'_c} A_{cw}$, was also included in Fig. 4.5 as blue dashed lines, where ϕ is equal to 0.85. As shown in Fig. 4.5, the specimen maintains the high shear stress level of $15.4\sqrt{f_{cm}}$ or $14.9\sqrt{f'_c}$, without any noticeable strength degradation, up to a chord rotation of 8%. Here, f_{cm} represents the measured concrete compressive strength, equal to 4.6 ksi, and f'_c represents the design concrete compressive strength, equal to 5.0 ksi.

The inclusion of the slab enhances the shear strength of the coupling beam, and the increase in strength can be attributed to the increase in nominal moment strength (M_n) resulting from the presence of the slab (Naish et al. 2009). DBCB is composed of upper and lower beams separated vertically by the UCS layer. As the DBCB undergoes significant rotation, it eventually separates into two individual beams. Therefore, the total nominal moment strength of the coupling beam can be obtained by summing up the nominal strength of each beam. To provide an example, the nominal moment strength of HS-R2.4-S-1 was calculated by considering two components: the upper beam with a slab and the lower beam. Using spColumn software, the upper beam with a slab exhibited a nominal moment capacity (M_n) of 45.35 kip-ft, while the lower beam had an M_n of 30.76 kip-ft. Therefore, the DBCB with a slab (HS-R2.4-S-1) has an overall M_n of 76.11 kip-ft (calculated as 45.35 + 30.76). If this particular DBCB specimen does not have a slab, its M_n would be 61.52 kip-ft (calculated as 2×30.76). Consequently, the presence of the slab increased the shear strength by approximately 24% (76.11 kip-ft / 61.52 kip-ft). The measured maximum shear strength of HS-R2.4-S-1 was approximately 94.6 kips, indicating that the shear strength of HS-R2.4-S-1 without a slab can be expected to be around 76.3 kips (calculated as 94.6 kips / 1.24). Therefore, HS-R2.4-S-1 without a slab can withstand a shear stress of $12.4\sqrt{f_{cm}}$ or $12\sqrt{f'_c}$.

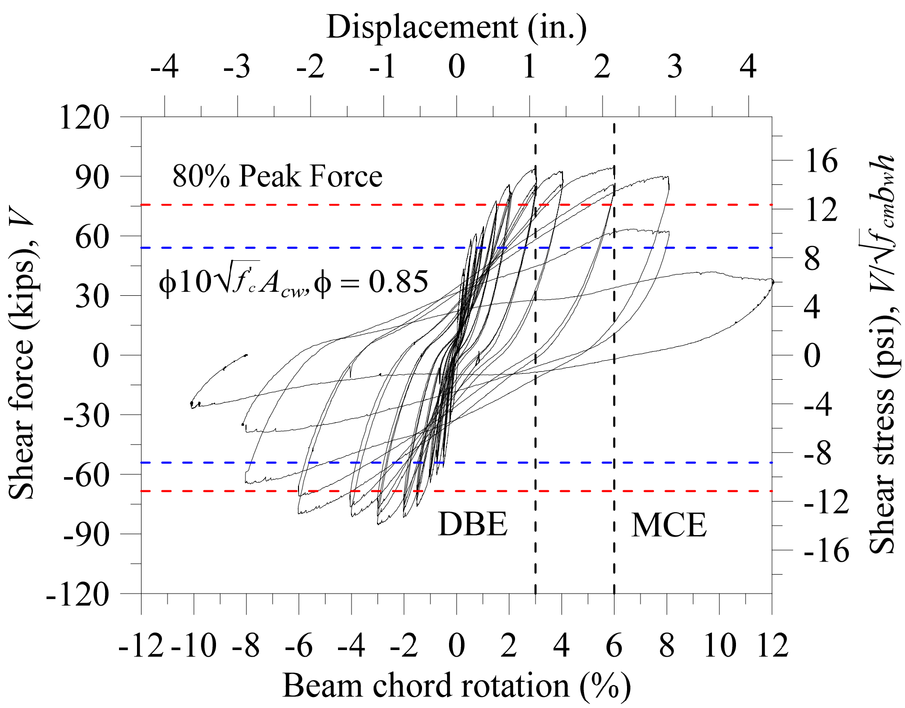

Fig. 4.5 Shear force versus beam chord rotation response of HS-R2.4-S-1

The shear force exhibited a linear increase up to approximately 0.5% chord rotation. At around this point, the yielding of the slab, as observed in strain gauges, and the separation of the two beams began. Following this, the rate of shear force increase slightly decreased and then rapidly increased again until reaching 2.0% chord rotation, where all longitudinal reinforcing bars on the beam yielded. Subsequently, the rate of shear force increase quickly reduced until reaching the maximum shear strength.

4.2.3 FS-R2.4-S-3

Fig. 4.6 illustrates the hysteresis response showing the relationship between shear force and beam chord rotation for Specimen FS-R2.4-S-3. For the purpose of comparison, the upper bound shear stress equation from ACI 318, $V_u = \phi 10\sqrt{f'_c} A_{cw}$, was also included in Fig. 4.6 as blue dashed lines, where ϕ is equal to 0.85. FS-R2.4-S-3 maintains a high shear stress level of $10.4\sqrt{f_{cm}}$ or $10.1\sqrt{f'_c}$, without any noticeable strength degradation, up to a chord rotation of 4%. Here, f_{cm} represents the measured concrete compressive strength, equal to 4.79 ksi, and f'_c represents the design concrete compressive strength, equal to 5.0 ksi. FS-R2.4-S-3 was designed taking into account the additional strength provided by the presence of the slab, aiming to achieve a shear stress close to $10\sqrt{f'_c}$. Subsequently, the strength of the coupling beam decreased as diagonal cracks propagated throughout the entire coupling beam. However, 80% of the maximum shear strength was maintained until the first positive 6% chord rotation, which can be considered as the ultimate chord rotation of FS-R2.4-S-3. Notably, the ductility of an RC member is commonly assessed by the ultimate drift ratio (or chord rotation), which refers to the post-peak drift ratio corresponding to a 20% decrease in the lateral load-carrying capacity from the peak strength (Park, 1988).

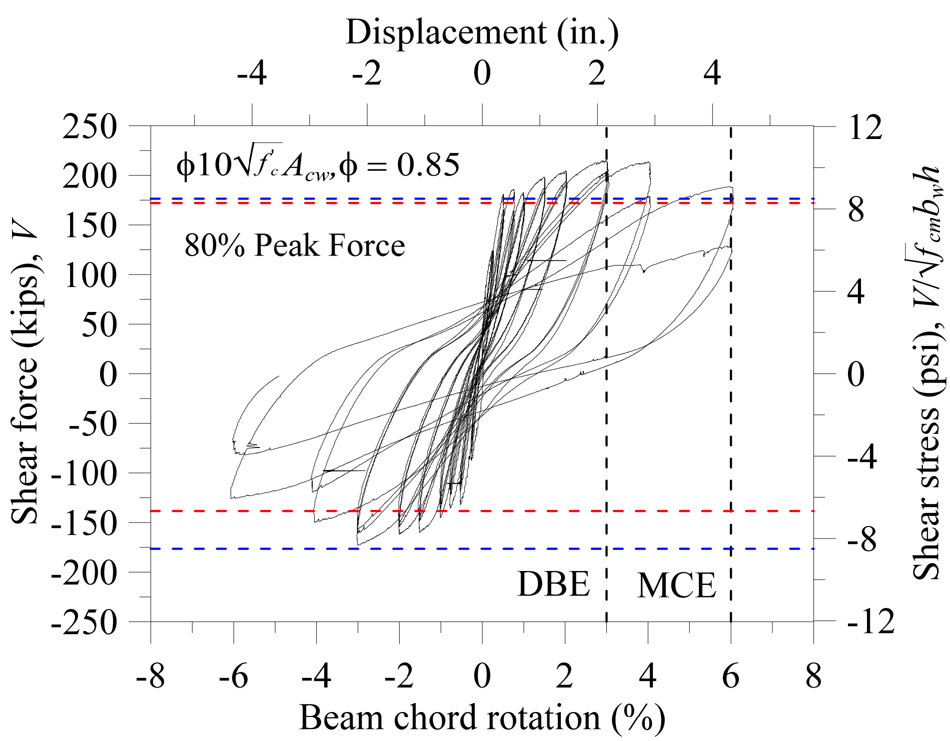

Fig. 4.6 Shear force versus beam chord rotation response of FS-R2.4-S-3

After the shear force increased linearly up to approximately 0.5% chord rotation, the rate of shear force increase in the coupling beam decreased due to the presence of cracks in the UCS and the yielding of the longitudinal reinforcing bars in the beam and the slab. According to the information provided in Table 4.1, the longitudinal reinforcing bar of the beam began yielding at a chord ratio of 1.0%, while the slab exhibited yielding at a chord ratio of 0.75%.

4.3 Strains in reinforcing bars

Based on the strain gauge layout described in Section 3.2.1, post-yield strain gauges were installed on the longitudinal and transverse reinforcing bars, as well as steel links, to measure the strains in each specimen. Appendix C presents the measured strains versus chord rotations for each specimen. The appendix includes a sketch depicting the reinforcement layout of the specimen, with the location of the strain gauge indicated by a circle. The yield strains of the high-strength rebar (ASTM A706 Gr. 80) and conventional rebar (ASTM A706 Gr. 60) are defined as 3,300 (= 0.0033×10^{6}) and 2,300 (= 0.0023×10^{6}), respectively, where 0.0033 and 0.0023 are the mean strain values (Overby et al., 2015).

In the case of FS-R3.2-N-2 (refer to Section C1.2 in Appendix C), the measured strains on the longitudinal reinforcing bars, both at the top and bottom layers, surpassed the yield strains of the bars at approximately 1.5% to 2.0% chord rotation. The yielding of the longitudinal bars extended up to approximately 18.5 in. away from the beam-to-wall interface. Furthermore, the strain measured on the longitudinal rebar at the middle layer exceeded the yield strain at a chord rotation of 3.0%, and the yielding of the bar propagated up to around 9.5 in. away from the beam end as the chord rotation increased. For HS-R2.4-S-1 (refer to Section C2.1 and C2.2 in Appendix C), the strains measured on the longitudinal reinforcements of the two steel cages surpassed the yield strains of the bars at approximately 1.5% to 2.0% chord rotation. The yielding of the reinforcing bars occurred up to a distance of 6.25 in. away from the beam-to-wall interface. Regarding FS-R2.4-S-3 (see Section C3.1 and C3.2 in Appendix C), the yielding of the longitudinal reinforcing bars within the two steel cages initiated at a chord rotation of 1.0% to 1.5%. The yielding of the reinforcing bars extended up to a distance of 12.5 in. away from the beam-to-wall interface.

As shown in Figs. 4.7, 4.8, and 4.9, at a distance of 0.5 in. measured from the beam ends, it was observed that for chord rotations less than 6%, FS-R2.4-S-3 exhibited higher strain values compared to the other specimens (FS-R3.2-N-2, HS-R2.4-S-1). This indicates a concentration of deformation at the beam ends specifically in FS-R2.4-S-3. However, at a chord rotation of 6%, the strain in FS-R2.4-S-3 became lower than that in HS-R2.4-S-1. This can be attributed to the strength loss experienced by FS-R2.4-S-3, which was a result of the buckling of the primary longitudinal bars and severe damage to the concrete core. These factors led to a decrease in the demand for flexural tension strain.

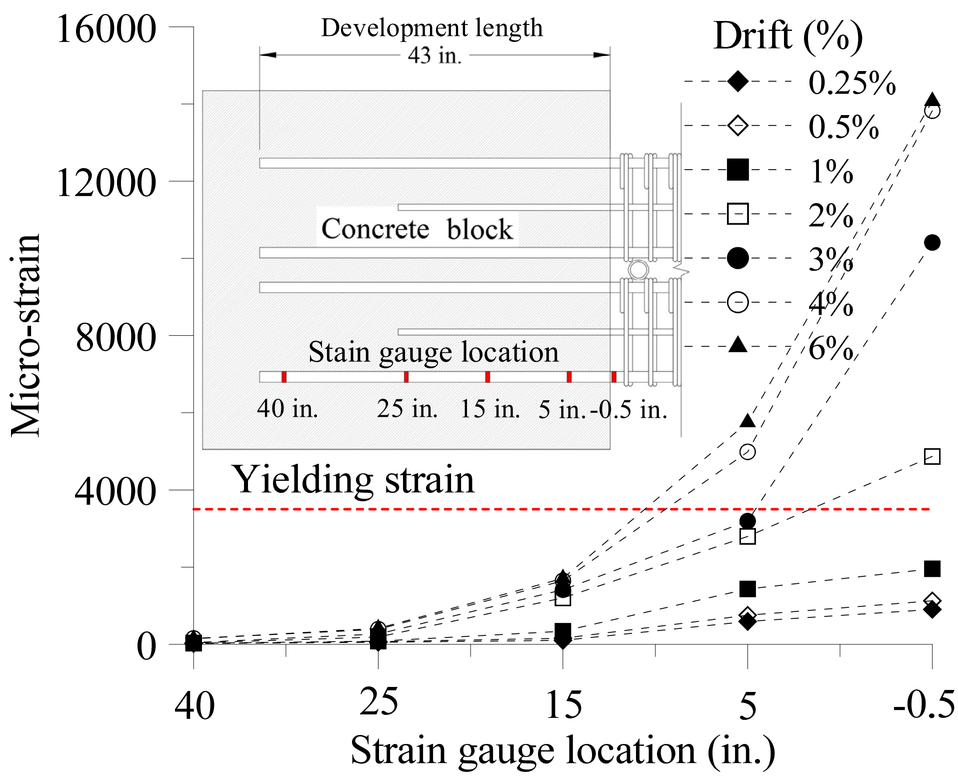

Fig. 4.7 Maximum strains of the longitudinal reinforcement within the loading block of FS-R3.2-N-2.

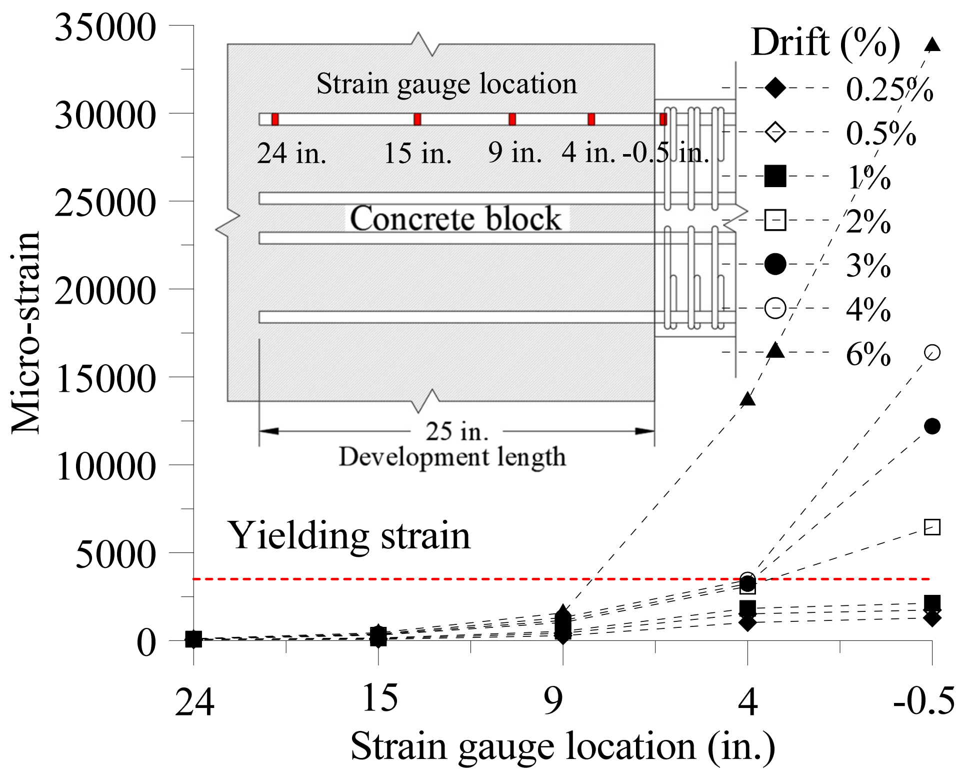

Fig. 4.8 Maximum strains of the longitudinal reinforcement within the big block of HS-R2.4-S-1

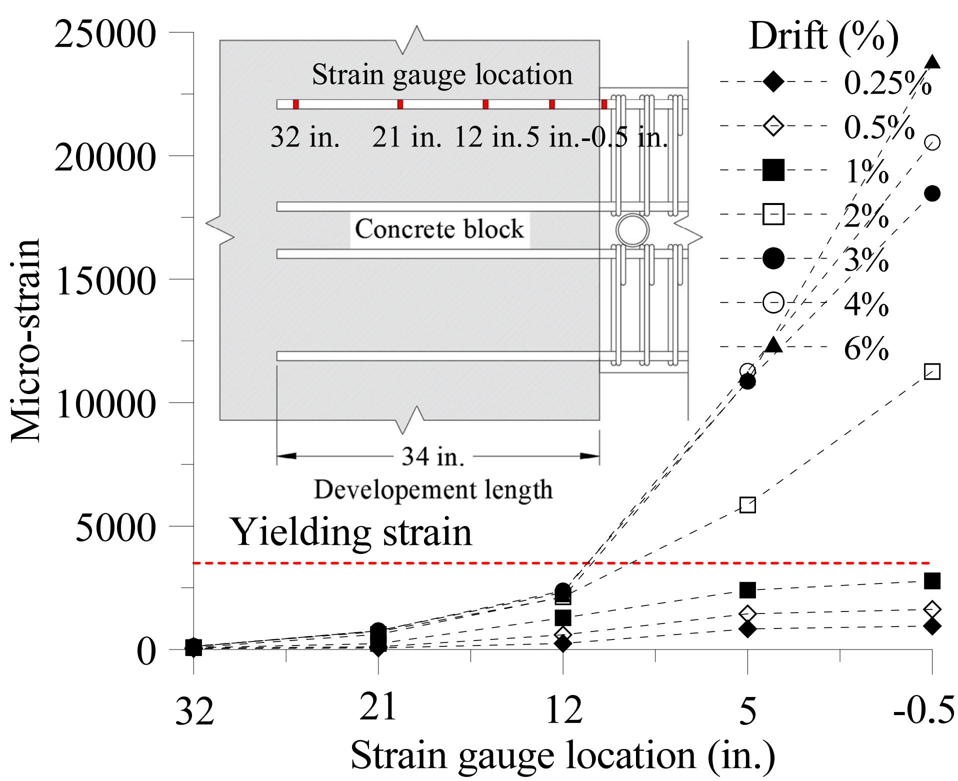

Fig. 4.9 Maximum strains of the longitudinal reinforcement within the big block of FS-R2.4-S-3

For all three DBCB specimens, the strains of the longitudinal bars on the upper beam had the same sign as those of the lower beam. However, the strains of the top and bottom longitudinal bars of each beam showed clear opposite signs as the loading cycle increased. Furthermore, the middle longitudinal bar of the lower beam in FS-R3.2-N-2 exhibited symmetric patterns for the flexural tension strain under fully reversed cyclic loading. These findings indicate that as the cyclic loading increased, the DBCB gradually separated into two independent slender beams. Subsequently, the behavior shifted from shear-dominated to flexure-dominated, which is consistent with previous findings for half-scale DBCB (Choi et al., 2018).

The measured strain in transverse reinforcement is shown in Appendix C.1.2.2, C.2.1.2, C2.2.2, C.3.1.2, and C.3.2.2. It is observed that the strains in the transverse reinforcements of FS-R3.2-N-2 and FS-R2.4-S-3 were not significantly high until a chord rotation of 6.0%. Yielding in the transverse reinforcement was rarely observed in the two full-scale DBCB specimens. However, for HS-R2.4-S-1, the strains in the transverse reinforcements started yielding at approximately 3% chord rotation and increased up to 6% chord rotation. The yielding in transverse reinforcement occurred up to 5.5 in. away from the beam end. This behavior can be attributed to the differences in maximum shear force and concrete cross-section area between the full-scale specimens and the half-scale specimen HS-R2.4-S-1. While the full-scale specimens carried approximately twice the maximum shear force, the concrete cross-section area used to resist shear in the full-scale DBCBs was about 3.33 times that of the half-scale specimen. Consequently, the contribution of transverse reinforcement in resisting shear was smaller in the full-scale specimens. Furthermore, the test results indicate that the design assumption of $V_c = 0$, which assumes no shear resistance from the concrete core, is conservative. In reality, the core of the concrete remained intact, providing a significant amount of shear resistance even at large chord rotations.

Sections C2.3 and C3.3 in Appendix C show the strain data measured at the longitudinal bars of the slab on HS-R2.4-S-1 and FS-R2.4-S-3, respectively. For the HS-R2.4-1, the yielding of the slab initiated from the outside longitudinal rebar approximately at 0.5% chord rotation and then appeared at the inside ones at 1.0% chord rotation. On the other hand, for the FS-R2.4-3, the onset of yielding was observed at the outside longitudinal rebar at 0.75% chord rotation, followed by appearing at the inside ones at 1.5% chord rotation, which is equivalent to slab's crack propagation at the slab-to-wall interface. After that, the strains of longitudinal steel bars increased rapidly until the end of tests, which corresponds with the decrease in the stiffness of the coupling beam at about 0.5% chord rotation. FS-R2.4-S-3 exhibited a large decrease in stiffness than HS-R2.4-S-1 because FS-R2.4-S-3 is much higher in the reinforcement ratio for slab than HS-R2.4-S-1.

Sections C2.4 and C3.4 in Appendix C present the strain data obtained at the center of the top and bottom steel links for HS-R2.4-S-1 and FS-R2.4-S-3, respectively. These strains gradually increased up to the first positive 8% and 6% chord rotation, respectively. However, their magnitudes were relatively small, indicating that the steel links remained in the elastic range during the tests. It is worth noting that the axial force for FS-R3.2-N-2 could not be computed due to a malfunction of the strain gauges attached to the steel links. The axial force was estimated using the strain data recorded by the strain gauges mounted on each steel link. Table 4.2 provides a summary of the axial force information for the two specimens. According to the fourth column of Table 4.2, the maximum axial restraining force for each specimen was estimated to be approximately 242.5 kips and 259.7 kips, respectively, corresponding to axial force-to-axial strength ratios ($P_u/A_g f_{cm}$) of 0.59 and 0.18 when excluding the slab. However, when considering the slab's area, these ratios ($P_u/A_{gs} f_{cm}$) become 0.23 and 0.1. In the case of FS-R2.4-S-3, its $P_u/A_{gs} f_{cm}$ ratio is smaller than that of HS-R2.4-S-1. This could be attributed to the elongation of the threaded rods used to fasten the steel links, which started at 4% chord rotation and resulted in a reduction of the axial restraint force. Consequently, it is expected that FS-R2.4-S-3 would have a larger axial restraint force than 259.7 kips. Notably, Poudel et al. (2021) indicate that an axial force-to-axial strength ratio more than 0.1 is large enough to increase a coupling beam's strength and decrease its deformation capacity.

Table 4.2 Axial force induced by the axial restraint in specimens

Specimen	Average maximum tensile strain $\mu\varepsilon$, ($\varepsilon \times 10^{-6}$)	Steel link area A, (in.^{2})	Axial force $P_u = AE\varepsilon$, (kips)	Axial force to axial strength ratio $P_u/A_g f_{cm}$	Axial force to axial strength ratio $P_u/A_{gs} f_{cm}$
HS-R2.4-S-1	425	15.28*	242.5	0.59	0.23
FS-R2.4-S-3	382	23.44§	259.7	0.18	0.1

*: (Nominal area of C6×13) ×4, §: (Nominal area of L6×4×5/8) ×4, E=29,000 ksi
A_g: Gross cross-sectional area of coupling beam, A_{gs}: A_g +slab area

4.4 Development length of longitudinal rebars

In Section 3.1.1, it is explained that the development length (l_d) of the longitudinal rebar for each specimen was set at 60% of the requirement specified by ACI 18.8.5.3, following the approach adopted in previous half-scale DBCB tests (Choi et al., 2020). Eq. 4.1 illustrates the relationship between the development length and the yield strength (f_y) of the rebar, the diameter (d_b) of the rebar, and the compressive strength (f'_c) of the concrete. When aiming for the same tension strength requirement, it is expected that Gr. 80 high-strength steel bars would necessitate a longer development length compared to Gr. 60 rebars if the same compressive strength of concrete is used. However, it should be noted that using high-strength rebars typically involves a smaller diameter, which results in a reduction in the required development length.

$$l_d = \frac{0.6(3.25) f_y d_b}{65\lambda\sqrt{f_c'}} \quad \text{Eq. 4.1}$$

For each specimen, four strain gauges were mounted on selected longitudinal rebars within the concrete blocks. The strain measurements versus chord rotations for FS-R2.4-S-3, HS-R2.4-S-1, and FS-R2.4-S-3 can be found in Sections C.1.2.3, C.2.1.3, and C.3.1.3 of Appendix C, respectively. By analyzing the measured strains and corresponding chord rotations for each specimen, Figs. 4.7, 4.8, and 4.9 provide a summary of the maximum strains recorded at the respective strain gauge locations in relation to the chord rotation. Based on the information provided in Figs. 4.7, 4.8, and 4.9, it can be observed that among the strain gauges inside the blocks, only one strain gauge located at 5 in., 4 in., and 5 in. for FS-R2.4-S-3, HS-R2.4-S-1, and FS-R2.4-S-3, respectively, showed strain values exceeding the yield strain. On the other hand, the strain gauge at the beam-to-wall interface (at 0.5 in. measured from the beam end) exhibited significantly higher strains. Furthermore, Figs. 4.7, 4.8, and 4.9 provide insight into the depth of yielding from the beam-to-wall interface. The yield penetration of the longitudinal reinforcing bar was observed to be limited to approximately 10 in., 8 in., and 11 in. inward into the block for FS-R2.4-S-3, HS-R2.4-S-1, and FS-R2.4-S-3, respectively. Linear interpolation was employed to estimate the strain values between the recorded data from adjacent strain gauges. The limited yielding observed indicates a restricted bond slip between the concrete and reinforcing steel within the concrete block (wall piers). Despite the different sizes of rebar and corresponding development lengths, the strain patterns derived from their respective development lengths exhibit similar trends across the three specimens. The three specimens tested in this study, which were reinforced with high-strength Gr. 80 steel, exhibited higher strains compared to the previous specimens using Gr. 60 rebars (Choi et al., 2018). However, despite the use of high-strength reinforcement, the strain patterns observed were remarkably similar to those of the conventional reinforcement. This suggests that the development length of longitudinal reinforcement provided by Eq. 4.1 (60% of the requirement specified by ACI 18.8.5.3) is applicable not only to conventional Gr. 60 steel, but also to high-strength Gr. 80 steel.

4.5 Locations for coupling beam penetrations

In the full-scale specimens (FS-R3.2-NS-2, FS-R2.4-S-3), two PVC pipes were positioned near the end of each DBCB. These PVC pipes were placed at the UCS layer and located between the transverse hoops in the upper and lower cages. Their purpose was to mimic the presence of utility ducts. As the cyclic loading increased, the interface shear crack at the UCS layer extended towards the ends of the beam. However, the presence of PVC pipes obstructed the propagation of the horizontal crack. These PVC pipes offered significant slip resistance between the upper and lower beams, as evident from their distorted appearance. Consequently, diagonal cracks emerged in the plastic hinge region of the beam, as illustrated in Figure 4.3 (g). Similar observations were reported by Choi et al. (2020). Specifically, it was observed that the severity of the diagonal crack near the ends of the beam increased as the size of the PVC became larger. Hence, it is not advisable to utilize PVC pipes with a nominal diameter exceeding 3 in. near the ends of the beam. Moreover, it is highly recommended to position the PVC pipes near the beam-to-wall interface, ideally within a distance of 5 in. measured from the end of the beam. This placement helps to minimize any impediment to the propagation of the interface crack at the UCS layer.

Fig. 3.16 shows that Specimen FS-R2.4-S-3 incorporated additional PVC pipes at the midspan and mid-height of both the upper and lower beams. Notably, the PVC pipes positioned beneath the upper beam were situated directly beneath an 8-inch-thick slab. Unlike the PVC pipes located at the UCS layer, these PVC pipes maintained their original shape throughout the entire test, exhibiting no distortion. This can be attributed to the minimal damage observed at the midspan of each beam in the DBCB. Consequently, the installation of PVC pipes at the midspan of both the upper and lower beams has a negligible impact on the performance of DBCBs. Furthermore, it is expected that the midspan of each slender beam can accommodate PVC pipes with a nominal diameter exceeding 3 in. (depending on the spacing of the transverse reinforcement) since no severe damage was observed. An important finding reported by Abdullah et al. (2023) is that in diagonally reinforced coupling beams (DCBs), circular penetrations or openings horizontally passing through the coupling beam can be positioned within the triangular area formed by the diagonal bundles and the beam-to-wall interfaces. Alternatively, they can be placed near the beam midspan within the triangular region created by the diagonal bundles and the top and bottom surfaces of the beam. Interestingly, these locations closely resemble the positions of the four PVC pipes used in the FS-R2.4-S-3 shown in Fig. 3.16. Based on their suggestion, a maximum of two circular penetrations with a diameter of 6 in. or less is allowed, and it is important to ensure that they are not positioned along the same vertical line. However, if there is a slab present, it may not be feasible to place the circular penetration near the beam midspan within the triangular region formed by the diagonal bundles and the top surface of the beam due to the slab's presence.

As previously mentioned, DBCBs permit the incorporation of four circular penetrations, situated simultaneously at both ends of the coupling beam and at the midspan of the upper and lower beams. Importantly, this configuration maintains the shear strength, stiffness, and ductility of the structure.

4.6 Effective stiffness

Fig. 4.10 shows envelopes of the measured shear force-chord rotation responses for the three coupling beam specimens. These envelopes were constructed by identifying the chord rotation corresponding to the maximum shear force recorded during the first cycle of each loading stage. Fig. 4.11 illustrates the definition of the secant stiffness associated with approximately 67% of the maximum shear force ($2/3V_{max}$) and the corresponding chord rotation (θ_{67}). This secant stiffness, defined at $2/3V_{max}$, was adopted by Abdullah et al. (2023) for evaluating the effective stiffness of diagonally reinforced coupling beams. Consequently, an effective initial stiffness (K_{eff}) was determined using Equation 4.1.

$$K_{eff} = \frac{2/3V_{max}}{\theta_{67} l_n} \quad \text{Eq. 4.1}$$

Using the shear force-chord rotation envelopes presented in Figure 4.10, the effective initial stiffness (K_{eff}) was determined for both loading directions by identifying the intersection points of the envelope and a horizontal line corresponding to 67% of the maximum shear force. Table 4.3 provides a summary of the shear force values associated with 67% of the maximum shear force, along with the corresponding secant stiffness and chord rotation, for all the half and full-scale DBCB specimens that were tested. Table 4.3 shows that Specimen FS-R3.2-NS-2 exhibited a similar secant stiffness in both loading directions. On the other hand, Speicmesn HS-R2.4-ES-1 and FS-R2.4-ES-3 showed significant differences in secant stiffness between the two loading directions. However, for effective flexural stiffness (E_cI_{eff}) evaluation purposes, an average value from the two directions was adopted.

The findings from the limited experimental tests indicate that the full-scale coupling beam exhibited a higher stiffness compared to the half-scale coupling beam. Additionally, the coupling beam with a higher aspect ratio displayed a lower effective initial stiffness (K_{eff}) value compared to the one with a lower aspect ratio. These results are consistent with the coupling beam tests (CCB and DCB) reported by Naish et al., Weber-Kamin et al., and Abdullah et al (Naish et al., 2009, Weber-Kamin et al., 2020, and Abdullah et al., 2023).

Table 4.3 Shear force, secant stiffness, and chord rotation associated with 67% of the maximum shear force for all DBCB specimens

Specimen	Shear force at 2/3 V_{max} (kips)		Effective initial stiffness (K_{eff}) at 2/3 V_{max} (kips/in.)		Chord rotation (θ_{67}) at 2/3 V_{max} (%)	
	+*	-*	+	-	+	-
FS-R3.2-NS-2	132.11	122.58	206	191	0.671	0.669
HS-R2.4-ES-1	63.12	57.04	198	297	0.887	0.534
FS-R2.4-ES-3	143.30	115.45	595	395	0.335	0.405
R3.3-SC-1	42.61	48.35	103	93	0.834	1.049
R2.4-SC-1	44.01	49.03	337	340	0.363	0.400
R2.4-NC-1	59.80	48.96	343	371	0.484	0.367
R2.4-SC-0.25	43.08	48.95	418	372	0.286	0.366
R2.2-SC-1.5-PM	108.39	101.92	453	459	0.399	0.370
R2.4-SC-2-P	45.97	39.80	239	135	0.534	0.818
R2.4-SC-2-W	73.92	68.54	495	437	0.415	0.436

*: + positive direction, - negative direction

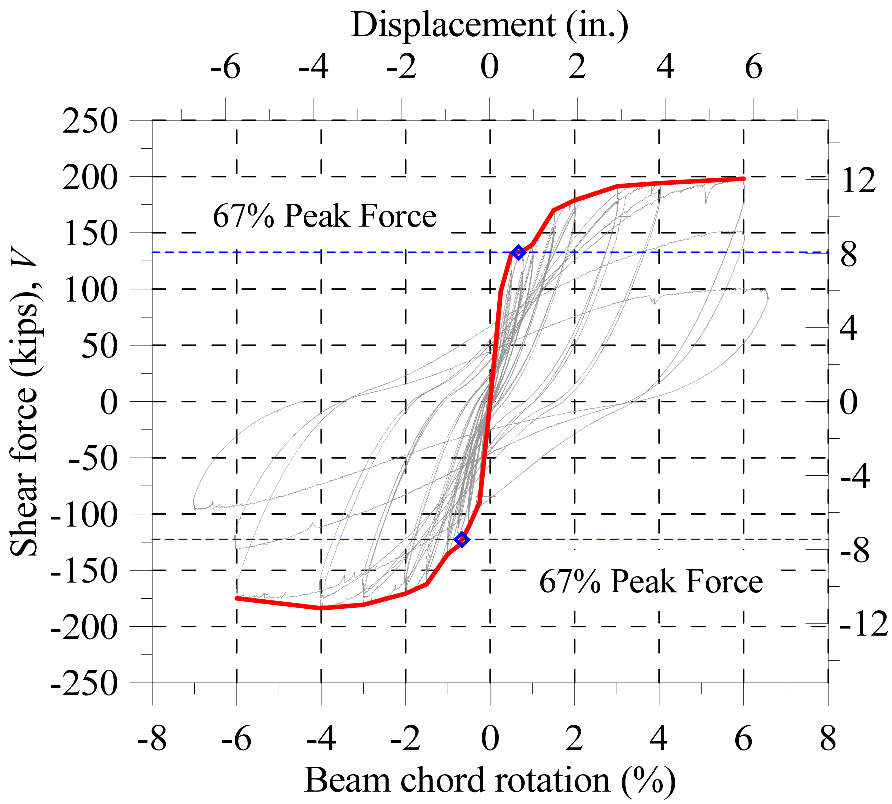
Displacement (in.)
-6
-4
-2
0
2
4
6
250
200
150
100
50
0
-50
-100
-150
-200
-250
Shear force (kips), V
67% Peak Force
67% Peak Force
12
8
4
0
-4
-8
-12
Shear stress (psi), $V/\sqrt{f_{cm}}b_wh$
-8
-6
-4
-2
0
2
4
6
8
Beam chord rotation (%)

(a)

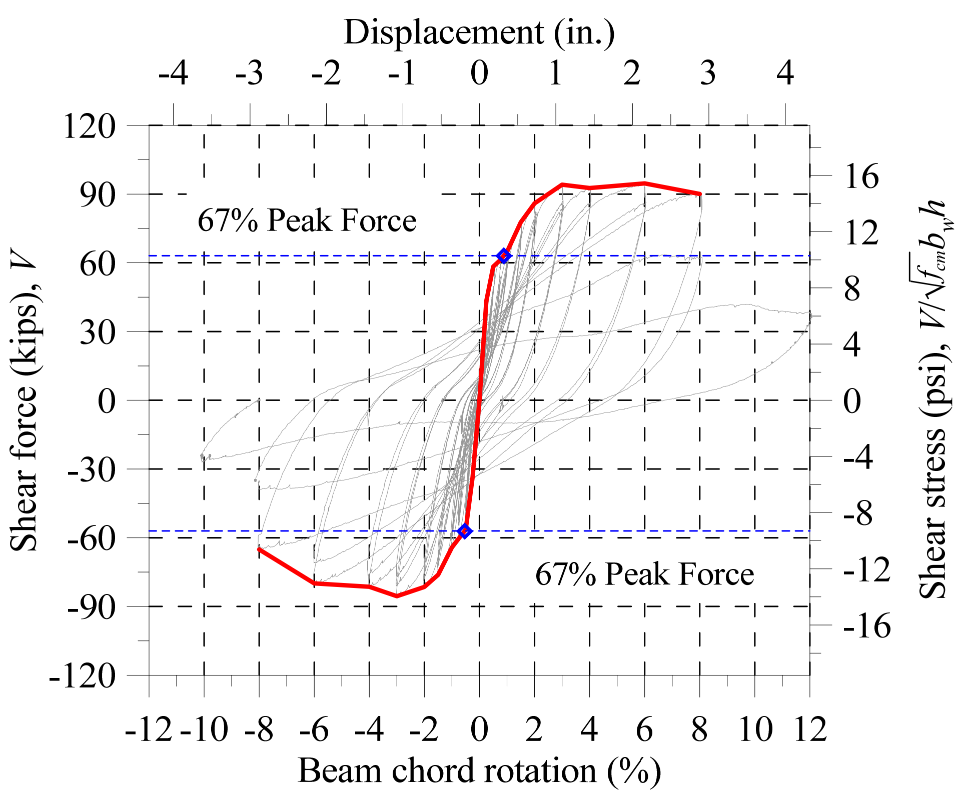
Displacement (in.)
-4
-3
-2
-1
0
1
2
3
4
120
90
60
30
0
-30
-60
-90
-120
Shear force (kips), V
67% Peak Force
67% Peak Force
16
12
8
4
0
-4
-8
-12
-16
Shear stress (psi), $V/\sqrt{f_{cm}}b_wh$
-12
-10
-8
-6
-4
-2
0
2
4
6
8
10
12
Beam chord rotation (%)

(b)

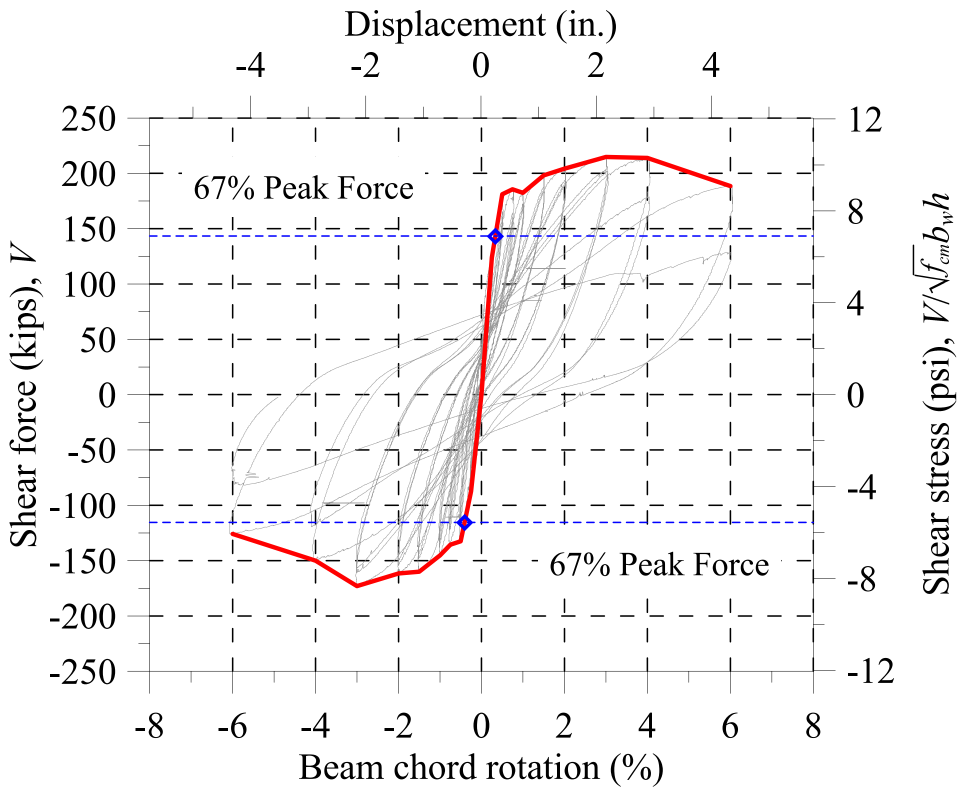

(c)

Fig. 4.10 Shear versus chord rotation envelopes for each specimen identifying $2/3V_{max}$: (a) FS-R3.2-NS-2 (b) HS-R2.4-ES-1 (c) FS-R2.4-ES-3

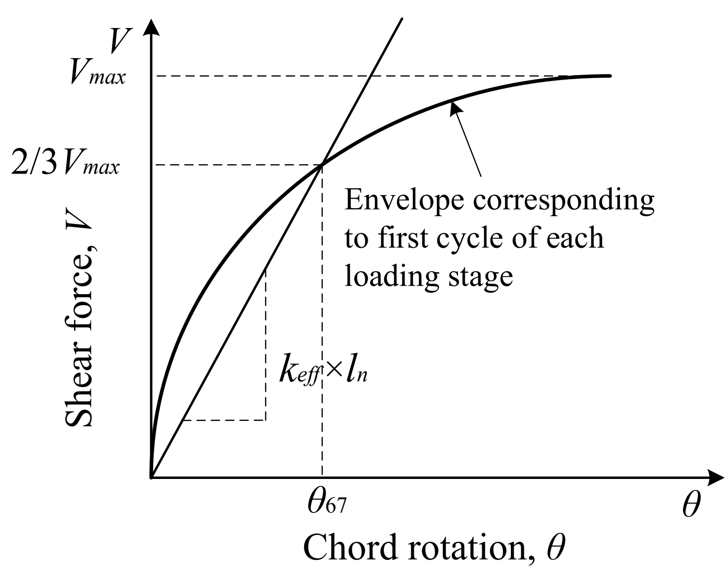

Fig. 4.11 Determination of effective initial stiffness

An effective flexural stiffness (E_cI_{eff}) was calculated for both loading directions using Eq. 4.2. This equation is based on the fixed end moment resulting from support translation in a fixed-end beam. It assumes that there is no rotation occurring at both concrete blocks of the coupling beam:

$$E_c I_{eff} = \frac{2/3 V_{max} l_n^2}{12\theta_{67}} \qquad \text{Eq. 4.2}$$

where I_{eff} is the effective moment of inertia, E_c is the elastic modulus of concrete, which was calculated in accordance with $E_c = 57{,}000\sqrt{f'_c}$ (unit: psi = lb/in.^{2}) given in ACI 19.2.2.1, and the measured compressive strength of concrete (f_{cm}) was used for the compressive concrete strength (f'_c). The effective flexural stiffness was normalized by E_cI_g to compare with the flexural effective stiffness relationship given by LATBSDC and TBI (LATBSDC, 2020 and TBI, 2017) for performance-based seismic design ($E_cI_{eff}/E_cI_g = 0.07\ l_n/h \leq 0.3$). Table 4.4 shows the normalized effective stiffnesses for both loading directions, including the data drawn from the prior half-scale test results (Choi et al. 2018, 2020). The values of the normalized effective stiffness (E_cI_{eff}/E_cI_g) for each specimen are positively correlated with the values of the effective initial stiffness (K_{eff}).

Fig. 4.12 shows data distributions for the average normalized effective stiffness (E_cI_{eff}/E_cI_g) as function of coupling beam aspect ratio (l_n/h). Out of the ten data points presented in Fig. 4.12, the majority correspond to a 2.4 aspect ratio (l_n/h), with the exception of three data points (l_n/h = 2.2, 3.2, and 3.3). To establish a clearer trend, it may be necessary to include additional data points representing various aspect ratios. However, despite the limited data, the observed trend in the normalized effective stiffness of DBCBs, as depicted in Fig 4.12, is similar to that reported for DCBs by Abdullah et al. (2023). among all the half-scale DBCB specimens, R2.4-SC-0.25 exhibited the highest normalized effective stiffness of 0.206, which was relatively larger than the other half-scale coupling beams. This can be attributed to the incomplete separation between the upper and lower beams caused by the narrow thickness of the UCS layer. This incomplete separation resulted in a shear-dominated behavior and an increase in the effective initial stiffness (K_{eff}). The higher effective initial stiffness, in turn, leads to the larger normalized effective stiffness.

Notably, the normalized effective stiffness (= 0.173) of the full-scale specimen FS-R2.4-ES-3 was nearly equal to the predicted value of 0.168, which was calculated using the equation $0.07\ l_n/h \leq 0.3$. For Specimen FS-R3.2-NS-2, the effective stiffness value (= 0.208) was slightly smaller than the predicted value of 0.224 (= 0.07×3.2) based on the same equation. Thus, it appears that the full-scale DBCBs exhibit a flexural effective stiffness that aligns well with the equation ($E_cI_{eff}/E_cI_g = 0.07\ l_n/h \leq 0.3$) proposed by LATBSDC and TBI (LATBSDC, 2020; TBI, 2017) for performance-based seismic design.

Table 4.4 Normalized effective stiffness (E_cI_{eff}/E_cI_g)

Specimen	l_n/h	E_cI_{eff}/E_cI_g		
		+*	-*	Average
FS-R3.2-NS-2	3.2	0.216	0.200	0.208
HS-R2.4-ES-1	2.4	0.118	0.177	0.147
FS-R2.4-ES-3	2.4	0.208	0.139	0.173
R3.3-SC-1	3.3	0.144	0.130	0.137
R2.4-SC-1	2.4	0.180	0.182	0.181
R2.4-NC-1	2.4	0.175	0.189	0.182
R2.4-SC-0.25	2.4	0.218	0.194	0.206
R2.2-SC-1.5-PM	2.2	0.099	0.101	0.100
R2.4-SC-2-P	2.4	0.153	0.086	0.120
R2.4-SC-2-W	2.4	0.139	0.123	0.131

*: + positive direction, - negative direction

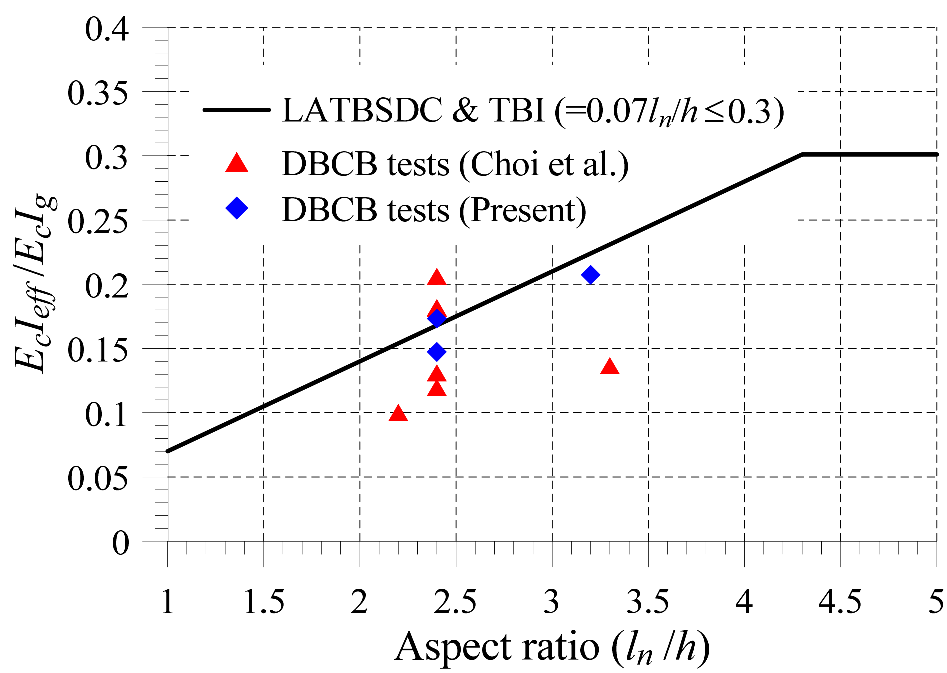

Fig. 4.12 Average normalized effective stiffness (E_cI_{eff}/E_cI_g) as function of aspect ratio (l_n/h)

4.7 Slab effect on initial cracking patterns

Double-beam coupling beams (DBCBs) are comprised of an upper and lower beam, with an unreinforced concrete strip (UCS) positioned along the mid-height of the coupling beam. When considering rectangular DBCBs without a slab and subjected to small shear forces, the shear stress distribution along the height of the beam exhibits symmetry about the elastic neutral axis. The elastic neutral axis coincides with the location of the UCS layer, where the maximum shear stress occurs. Consequently, diagonal shear cracks initiate and concentrate at the UCS layer from the onset of shear cracking under small displacements.

Figs. 4.13(a) and 4.14(a) display the crack patterns observed at 0.25% chord rotation for the previous half-scale DBCBs without a slab and the current full-scale DBCB without a slab, respectively. As shown in Figs. 4.13(a) and 4.14(b), the initial cracks in the DBCBs without a slab are predominantly located at the midspan and mid-height of the coupling beam, indicating significant cracking in these regions. For DBCB with a slab (T-beam), however, elastic shear stress distribution is not symmetrical about its elastic neutral axis and its elastic neutral axis shifts toward the top of the beam (Naaman and Chao, 2022). This leads to the difference in elevation between the UCS layer and the elastic neutral axis, where the maximum horizontal shear stress occurs. As shown in Figs. 4.13 (b) and 4.14 (b), it is evident that initial diagonal shear cracks did not form near the central axis of UCS. Despite the mismatch between the UCS layer and the elastic neutral axis of DBCB, which caused a delayed splitting of UCS, slip along the UCS eventually took place after a few cycles of loading.

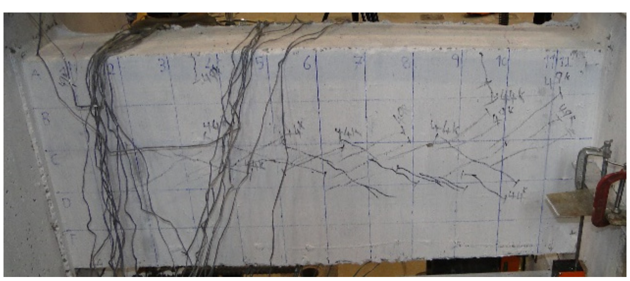

R2.4-SC-1

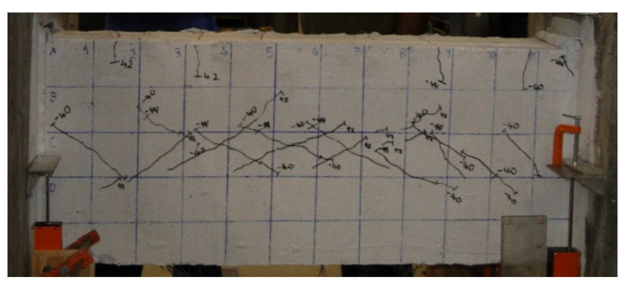

R2.4-NC-1

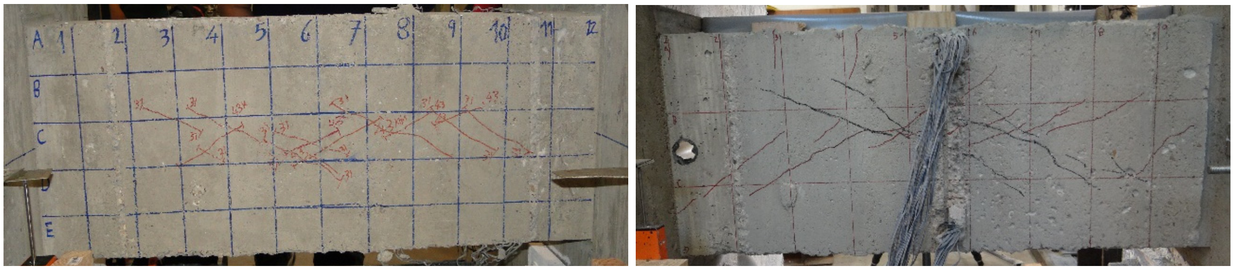

R2.4-SC-0.25 R2.4-SC-2-P

(a)

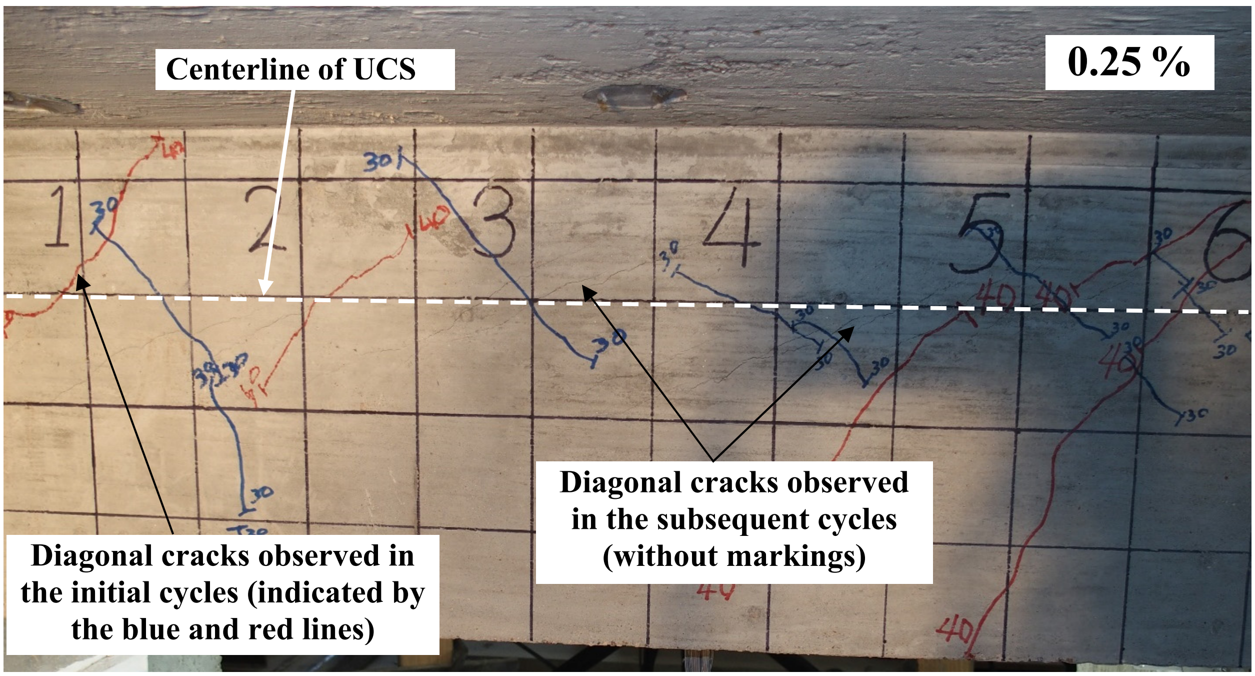

HS-R2.4-S-1

(b)

Fig. 4.13 Initial crack patterns of half-scale DBCB at 0.25% chord rotation: (a) DBCB without slab (b) DBCB with slab

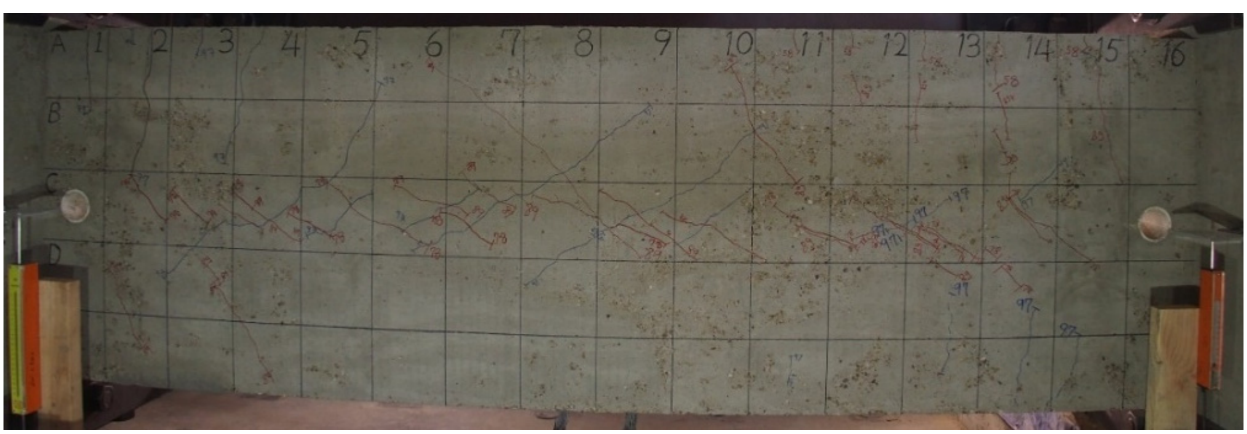

FS-R3.2-N-2

(a)

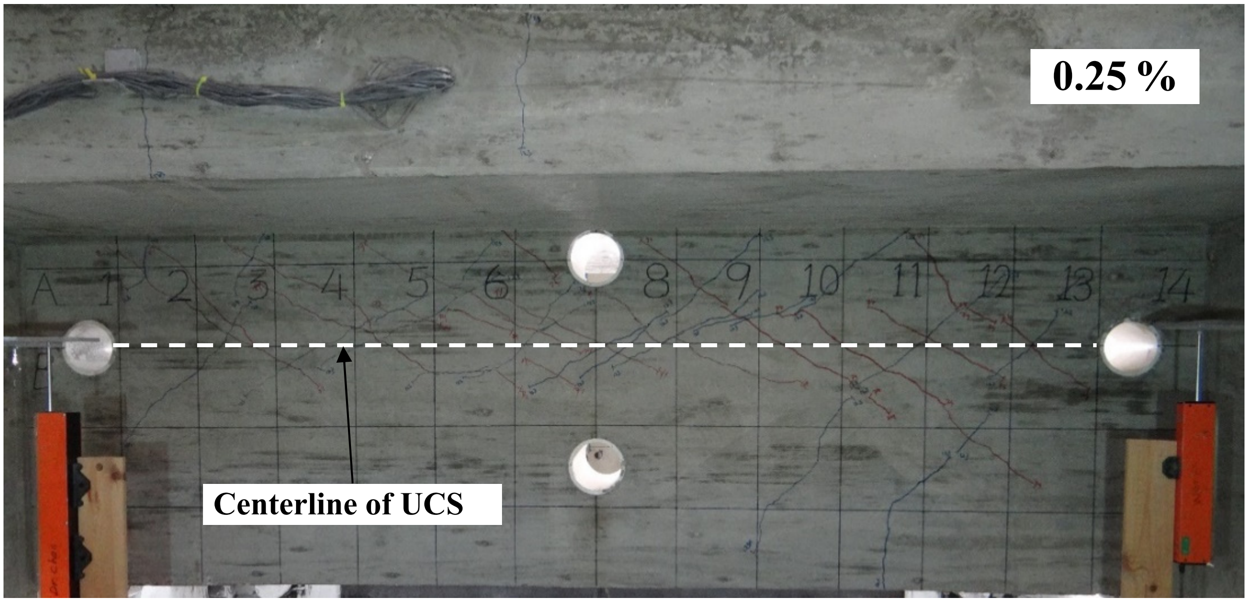

FS-R2.4-S-3

(b)

Fig. 4.14 Initial crack patterns of full-scale DBCB at 0.25% chord rotation: (a) DBCB without slab (b) DBCB with slab

4.8 Plastic hinge length

As per Section 18.6.4.4 of the ACI code, the transverse reinforcement for a special moment frame beam is placed at intervals equal to twice the depth of the beam. This is done to effectively confine the concrete within the flexural yielding region of the beam and maintain its ductility and strength. Based on Figs. 4.1 to 4.3, it can be observed that under large displacements, the significant concrete damages caused by flexure in each specimen were predominantly concentrated within a length approximately equal to the half of the full depth of the DBCB beam ($h/2$).

Figures 4.15 to 4.17 illustrate the measured values of strain gauges mounted on the longitudinal reinforcement of each specimen. For the first two specimens (FS-R3.2-N-2 and HS-R2.4-S-1), the strain gauges placed on the longitudinal reinforcements exhibited high strains along a length approximately equal to the half of the beam depth ($h/2$) from the beam-to-wall interfaces. However, they showed low strains in the region between $h/2$ and h from both ends of the beam. After analyzing the longitudinal reinforcement strains of the two specimens, it was decided to position the strain gauges on the last specimen (FS-R2.4-S-3) within the region of approximately half of the beam depth ($h/2$) where high strains were anticipated. As shown in Fig. 4.17, the strain values rapidly decreased at the strain gauge located within 12.5 in. from the beam ends, displaying a similar pattern to the earlier two specimens. In addition, as shown in Appendix C.1.2.2, C.2.1.2, C2.2.2, C.3.1.2, and C.3.2.2, the strains of transverse reinforcements typically remained elastic at the region between *h*/2 and *h* from both ends of the beam. Consequently, the concrete confinement requirements specified in Section 18.6.4.4 of the ACI code can be relaxed for the region between *h*/2 and *h* from both ends of a DBCB (as elaborated in the updated flowchart for DBCB in Chapter 6).

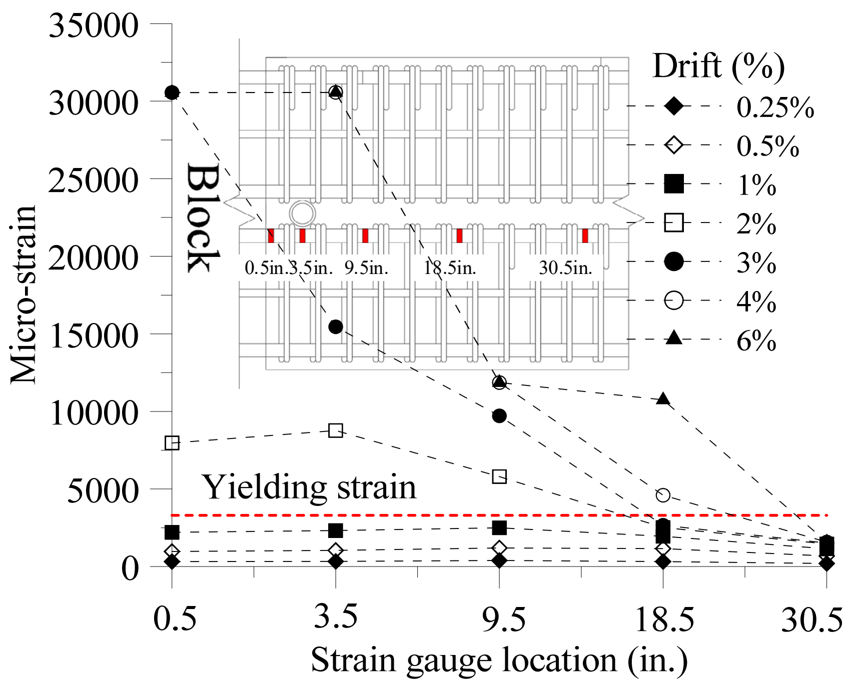

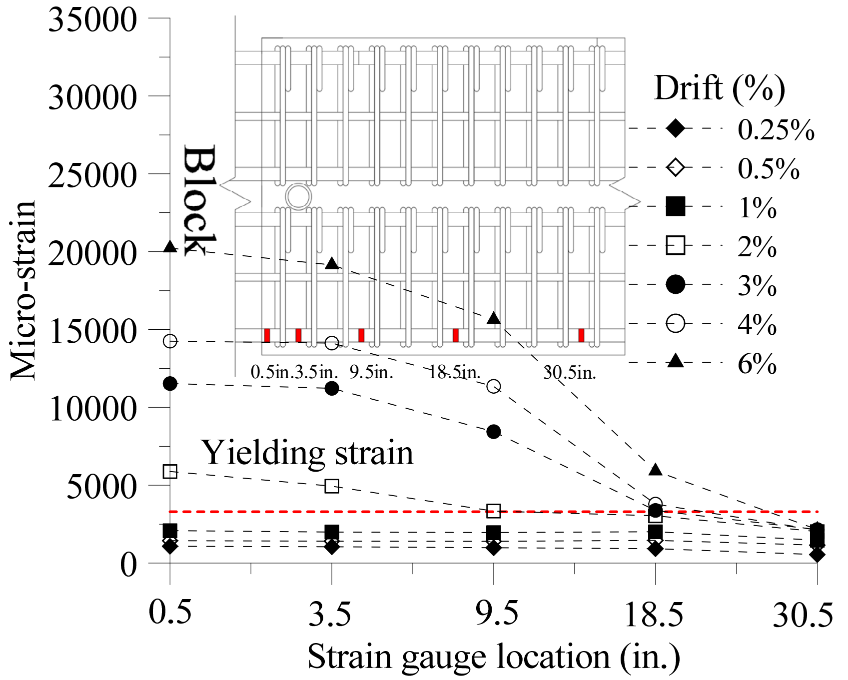

Fig. 4.15 Maximum strains of the longitudinal reinforcement within the beam (FS-R3.2-N-2, h = 30 in.)

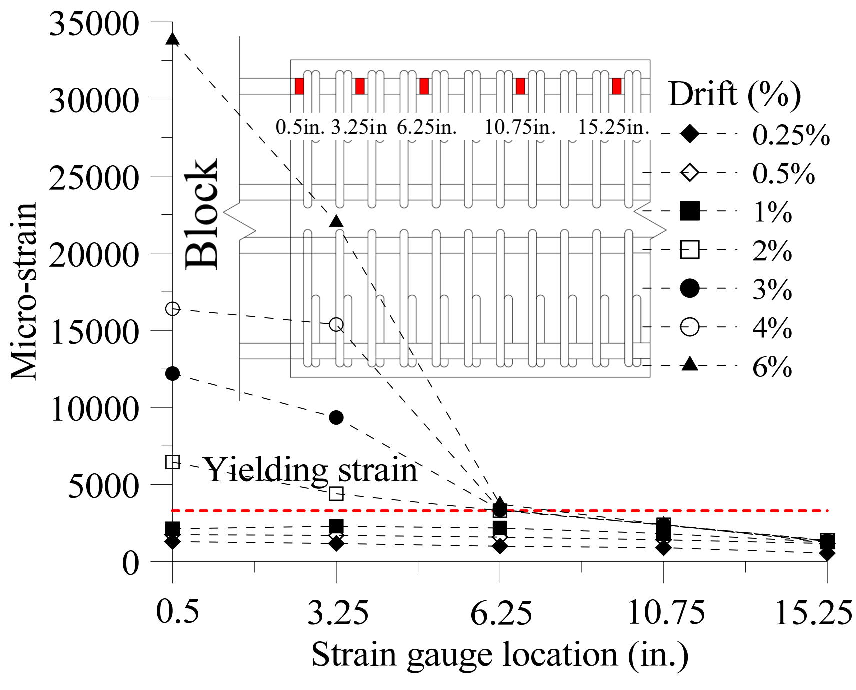

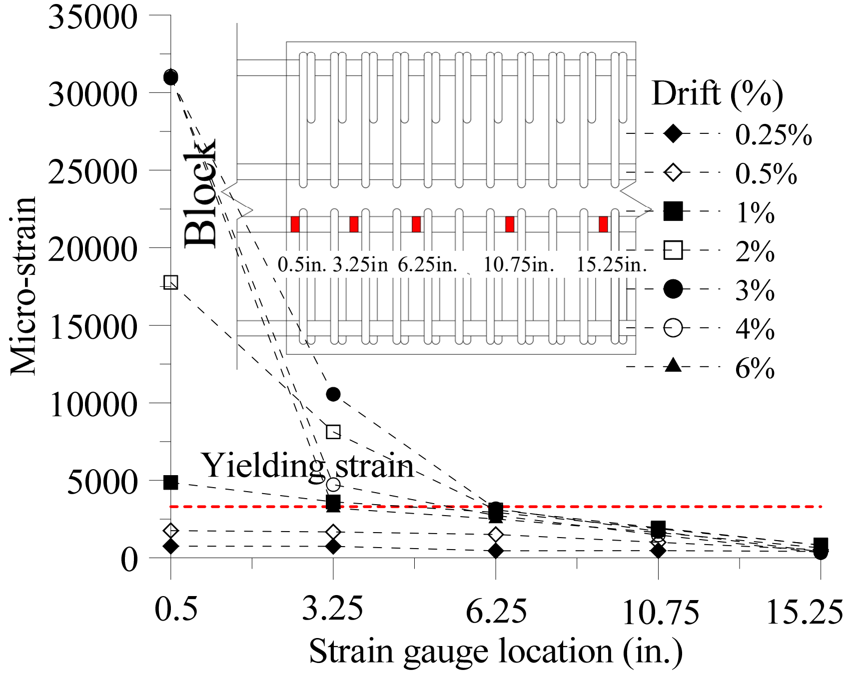

Fig. 4.16 Maximum strains of the longitudinal reinforcement within the beam (HS-R2.4-S-1 *h* = 15 in.)

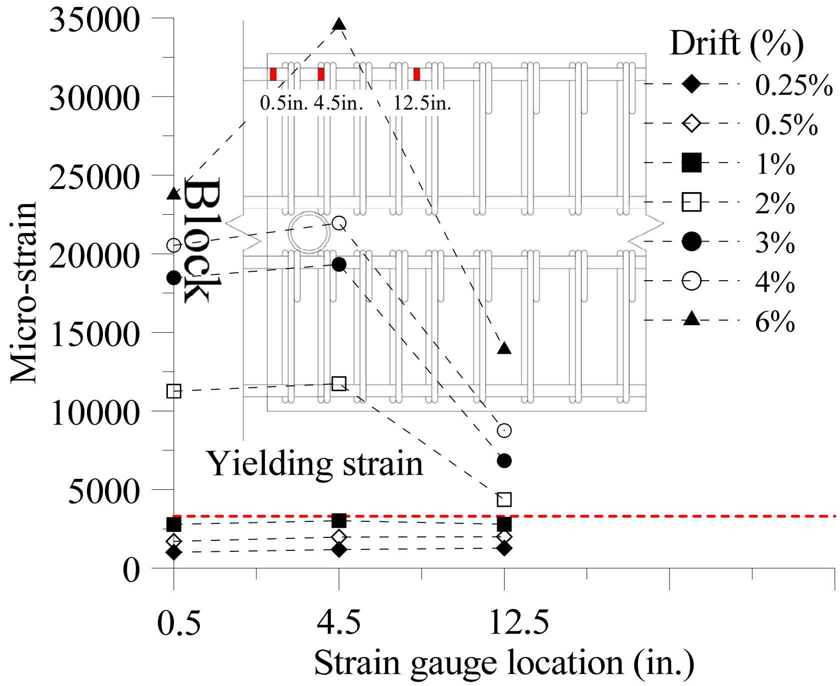

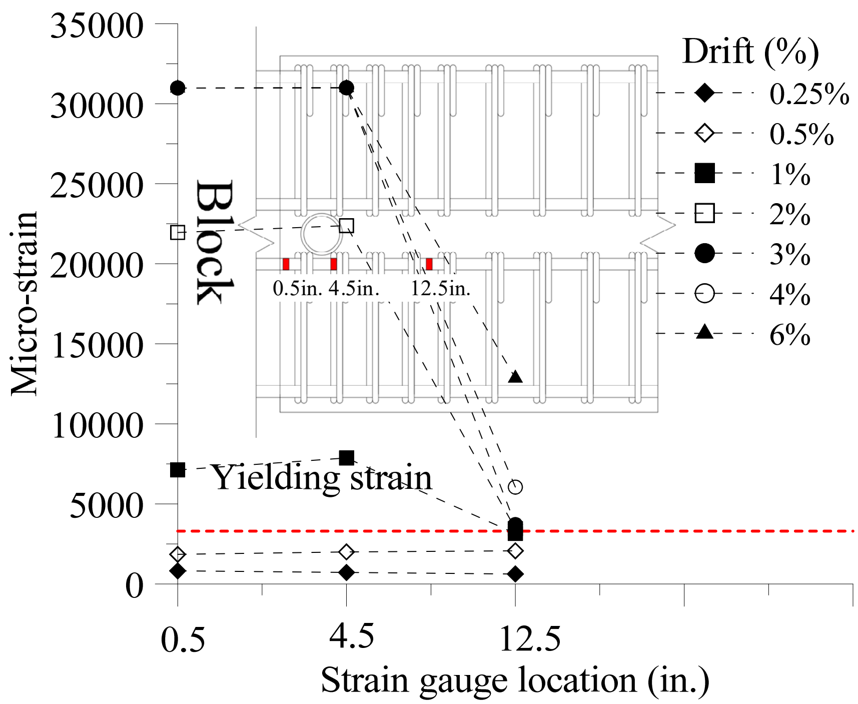

Fig. 4.17 Maximum strains of the longitudinal reinforcement within the beam (FS-R2.4-S-3 h = 30 in.)

4.9 Beam elongation

Figs. 4.18 and 4.19 display the measured elongations of Specimens HS-R2.4-S-1 and FS-R2.4-S-3, respectively. The beam elongation ratio (%) is determined by dividing the beam elongation by the original beam length, which is taken as the clear span of the specimens measured prior to testing. The elongation of each specimen was calculated using data obtained from string potentiometers (pots) equipped with linear position sensors. These sensors were horizontally installed at a distance of 3 in. away from the top and bottom surfaces of the coupling beam.

As shown in Fig. 4.18, during the first loading cycle of 8%, the measured maximum elongations at the top and bottom string pots in HS-R2.4-S-1 were approximately 0.8% (0.27 in.) and 0.45% (0.16 in.), respectively. Following this cycle, the beam elongation decreased. This reduction in elongation coincided with the buckling of the longitudinal steel cage after severe crushing and spalling took place in the concrete core within the plastic hinge region (as shown in Fig. 4.2 (k)). As shown in Fig. 4.19, the maximum beam elongation for FS-R2.4-S-3 reached approximately 0.83% (0.6 in.), as measured by the top string pot during the 6% chord rotation cycles. However, when measured by the bottom string pot, the maximum beam elongation was approximately 0.42% (0.3 in.) during the 4% chord rotation cycles. Subsequently, the beam elongation shortened because the buckling of longitudinal reinforcement started to appear near the end of the beam.

The average elongations of the two specimens with axial restraint are approximately 0.6% and 0.63%, respectively, which is similar to the measured elongations (ranging from 0.6% to 1%) of axially restrained DCBs with high-strength rebars as studied by Poudel et al. (2021).

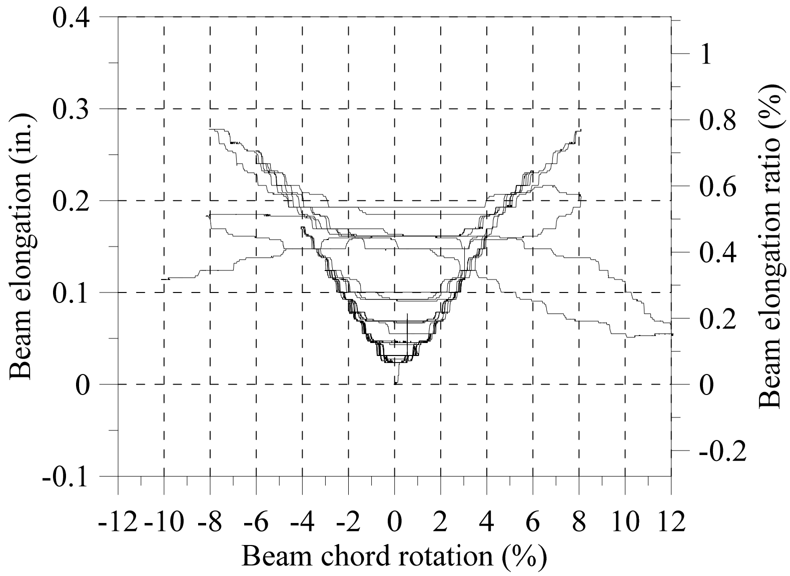

(a)

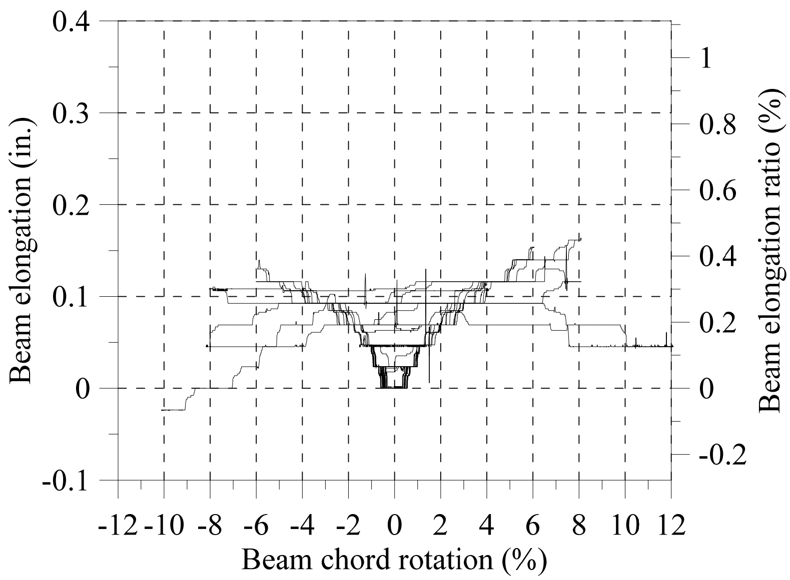

(b)

Fig. 4.18 Beam elongations of HS-R2.4-S-1: (a) top elongation (b) bottom elongation

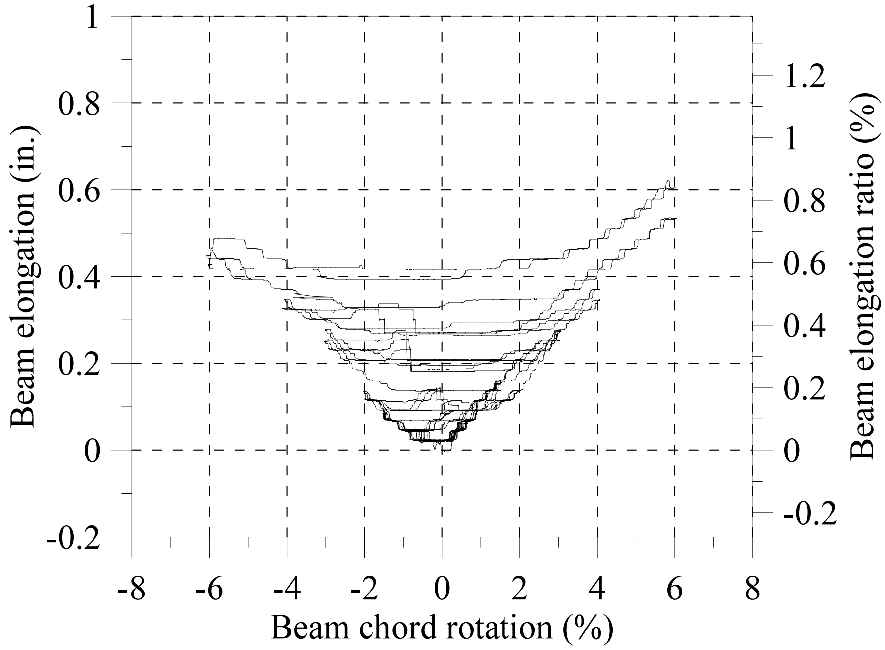

(a)

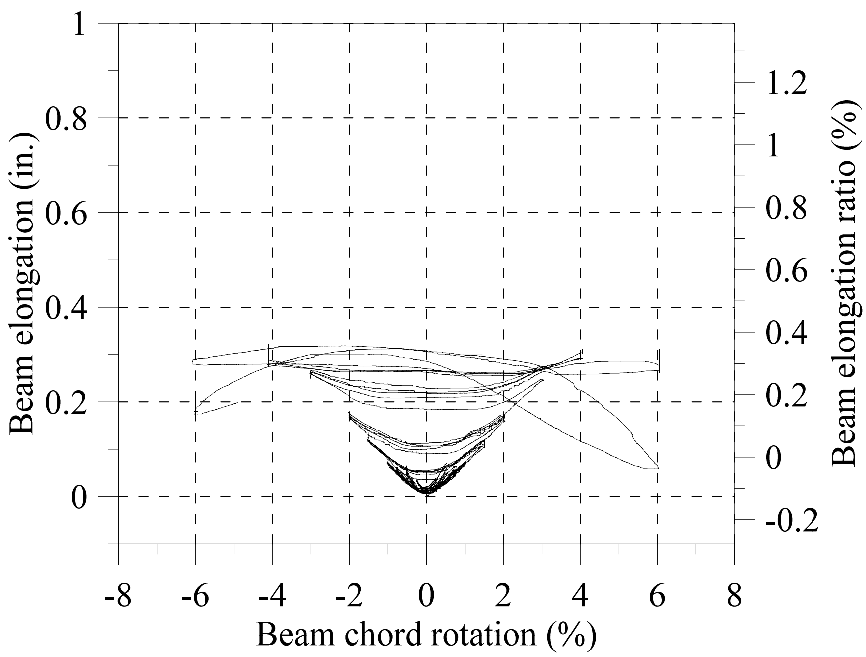

(b)

Fig. 4.19 Beam elongations of FS-R2.4-S-3: (a) top elongation (b) bottom elongation

CHAPTER 5: NONLINEAR FINITE ELEMENT ANALYSIS

To simulate the behavior of double-beam coupling beams (DBCBs), nonlinear finite element (FE) analyses were performed using VecTor3. VecTor3 is a FE computer program specifically designed for the nonlinear analysis of three-dimensional reinforced concrete structures (El Mohandes and Vecchio, 2013). These analyses aimed to determine the appropriate material models and analysis parameters necessary for accurately representing the DBCB behavior. Subsequently, the identified material models and analysis parameters were used in parametric analyses to determine the optimal spacing of transverse reinforcement in the coupling beam. The results obtained from the finite element analysis (FEA) were then compared with the experimental test results to assess the capability of the models in reasonably replicating the behavior of the coupling beam.

5.1 Finite element modeling

5.1.1 Geometric modeling and Element types

Figs. 5.1, 5.2, and 5.3 show the geometric modeling for the three specimens, respectively. In Figs. 5.1 and 5.2, the geometry of the first two specimens was simplified by excluding the concrete blocks in the FE model, while ensuring appropriate boundary conditions were applied. On the other hand, Fig. 5.3 shows the modeling of the last specimen, including the two concrete blocks. In all cases, the steel links were not considered in the model, but axial restraint was incorporated through the specified boundary conditions. For concrete modeling in VecTor3, a 3D hexahedral solid element with 8 nodes and three degrees of freedom per node was utilized. Table 5.1 provides an overview of the sizes of steel bars employed for the coupling beam and slab. In VecTor3, two types of models are available to represent the embedded reinforcing steel bars in concrete: the smear model and the discrete model. In accordance with Table 5.1, the smear model, which is smeared into the solid element, was adopted for the longitudinal reinforcement of the coupling beam. Conversely, the discrete model, represented as truss elements, was employed for the transverse reinforcement of the coupling beam and the reinforcing bar of the slab. It is important to note that the bond between concrete and steel was assumed to be perfect in these models.

Table 5.1 Size of reinforcements

Specimen	Coupling beam				Slab
	Top bar	Middle bar	Bottom bar	Hoop	
FS-R3.2-N-2	#10 (#8)*	#6	#10 (#8)*	#4	-
HS-R2.4-S-1	#6	-	#6	#3	#3
FS-R2.4-S-3	#8 (#6)*	-	#8 (#6)*	#4	#4

* Middle bar in coupling beam steel cage (Fig. 3.7 and Fig. 3.15)

The circular PVC pipes with certain thickness could not be accurately modeled using the available tool in VecTor3. Therefore, to represent the PVC pipes in the FE models, their shapes were approximated as solid rectangles, as shown in Figs. 5.1(a) and 5.3(a). It is worth noting that this approximation may have some influence on the numerical results.

For the first two FE models, the boundary conditions were specified as follows: one side of the beam ends had fixed conditions (U1 = 0, U2 = 0, and U3 = 0), while the other side had fixed conditions for U1 = 0 and U3 = 0, except for U2, which was free for vertical movement (U2 = 1). In the last FE model, boundary conditions were applied to the two concrete blocks. One block was fixed in all three directions (U1 = 0, U2 = 0, and U3 = 0), while the other block was free to move in the vertical direction (U1 = 0, U2 = 1, and U3 = 0). Note in Fig. 5.1, X = U1, Y = U2, and Z = U3.

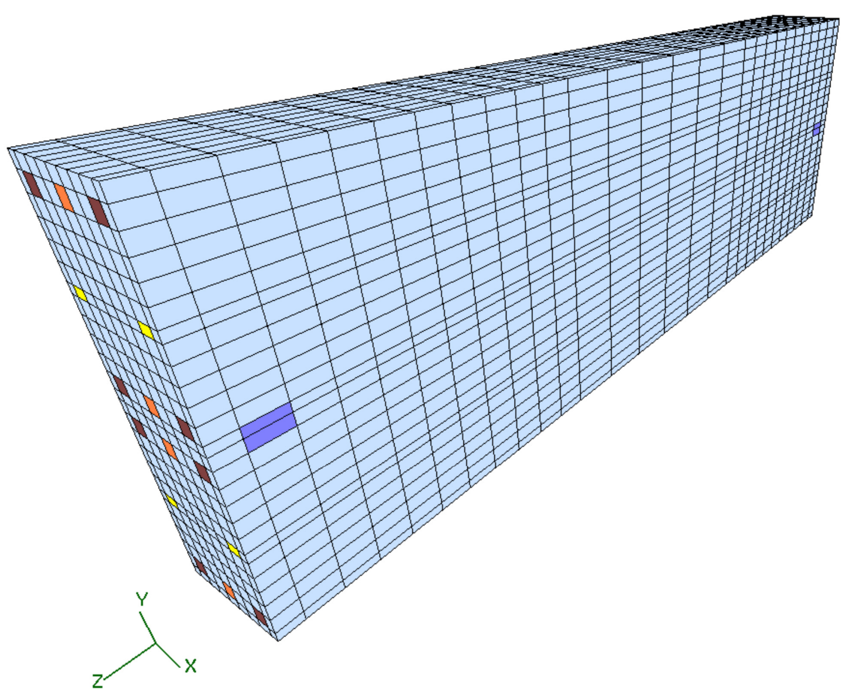

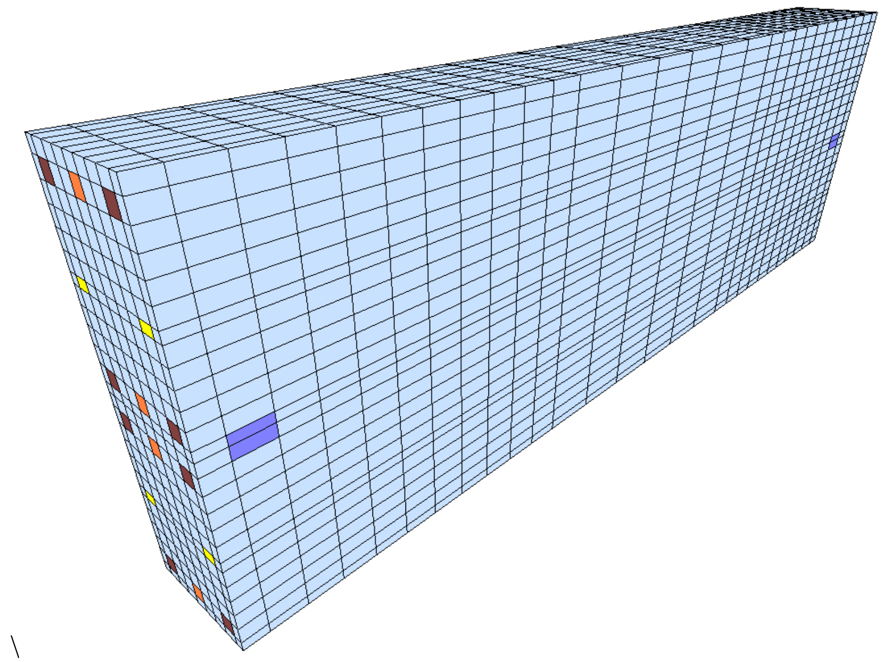

(a)

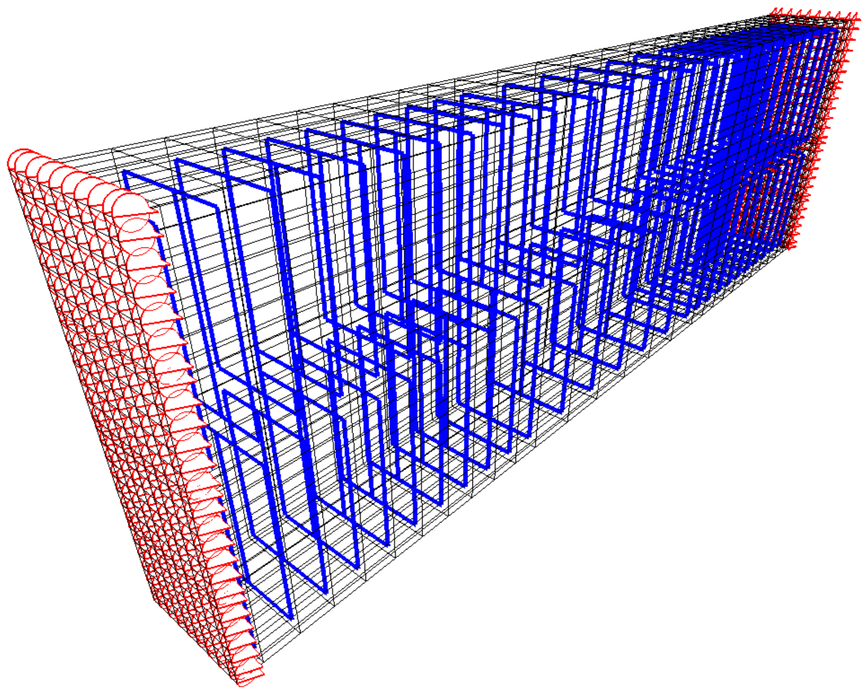

(b)

Fig. 5.1 FE model for FS-R3.2-N-2: (a) FE mesh for concrete and smeared longitudinal reinforcing bars (b) FE mesh for hoops and boundary conditions

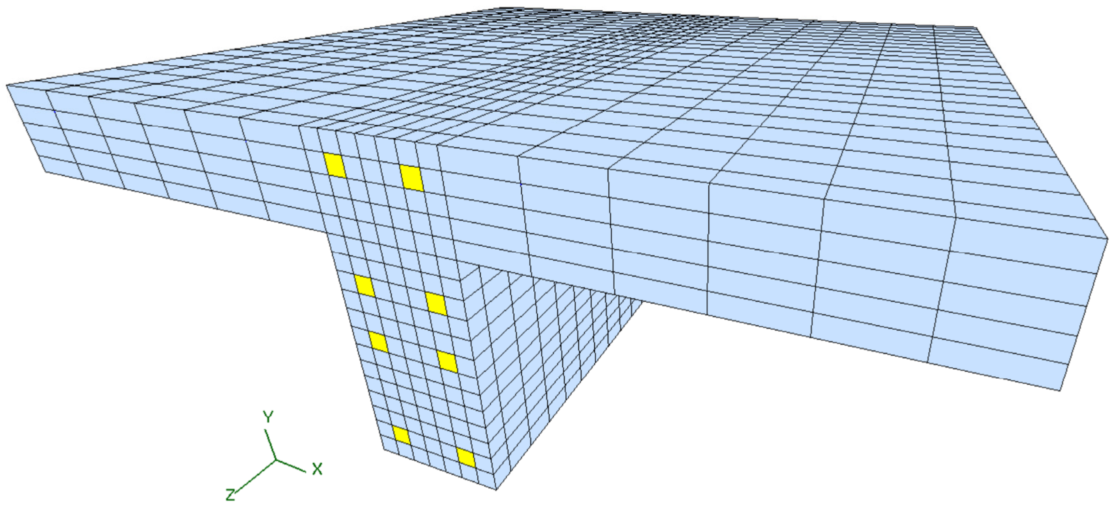

(a)

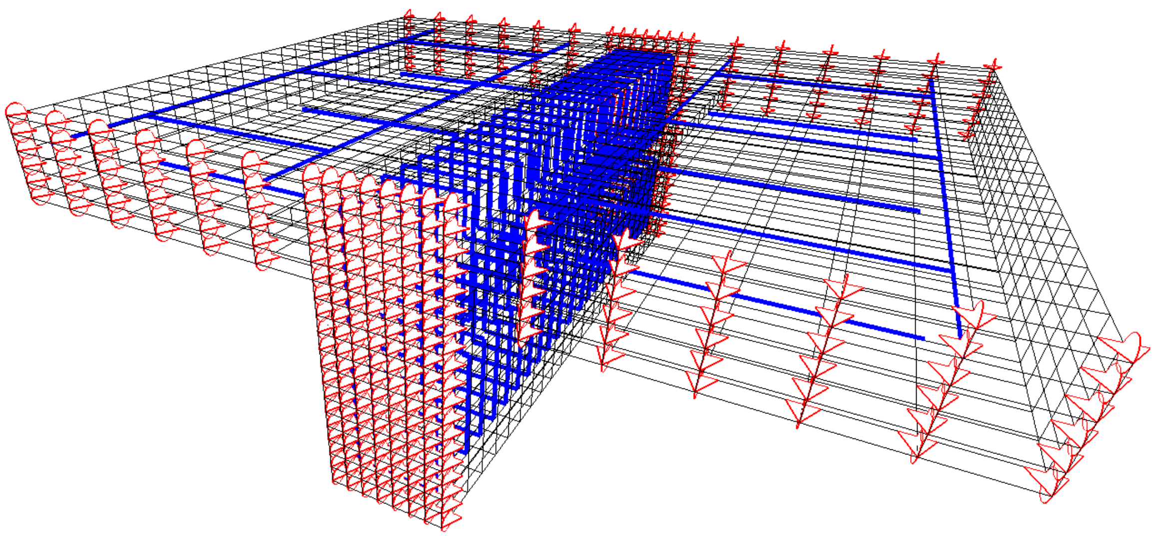

(b)

Fig. 5.2 FE model for HS-R2.4-S-1: (a) FE mesh for concrete and smeared longitudinal reinforcing bars (b) FE mesh for hoops and reinforcements of slab and boundary conditions

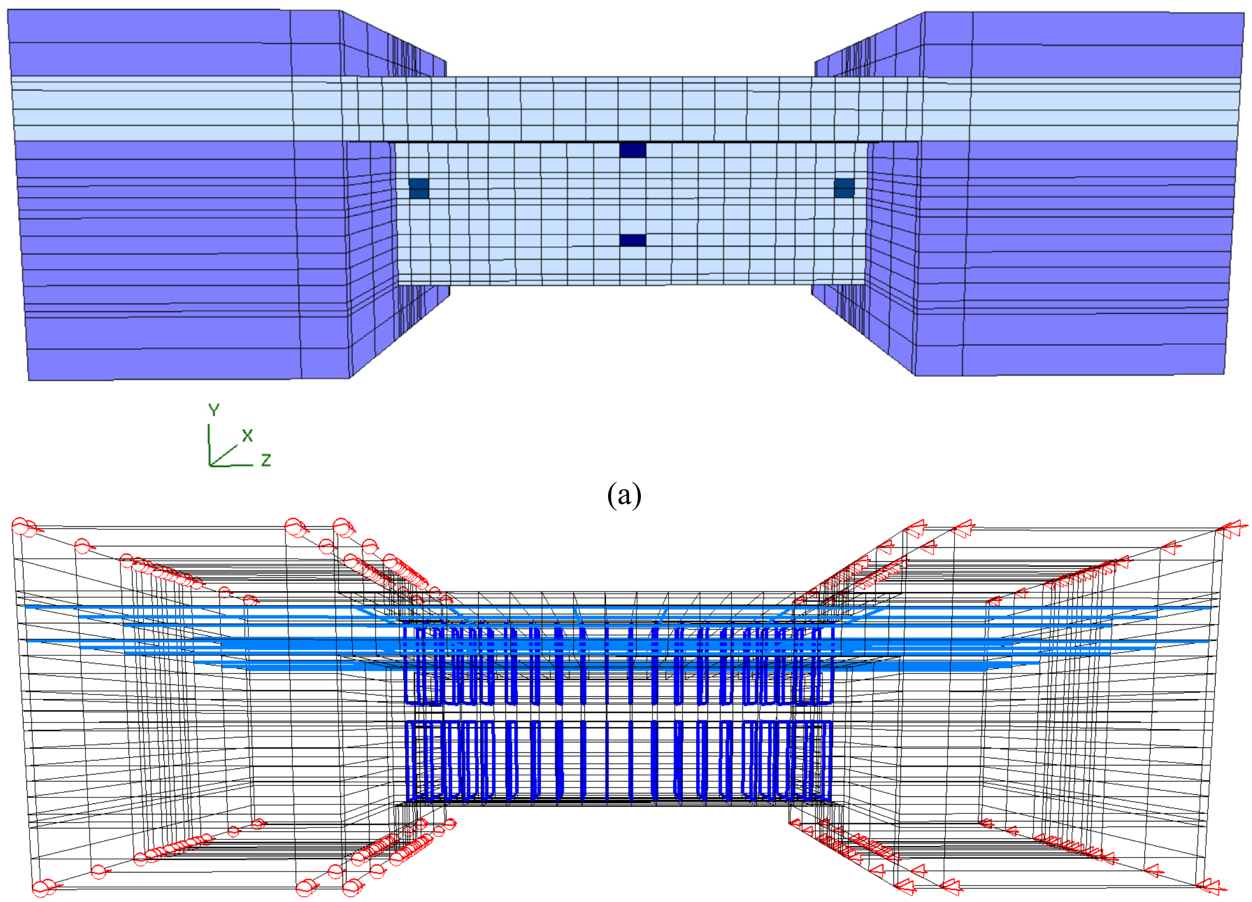

(a)

(b)

Fig. 5.3 FE model for FS-R2.4-S-3: (a) FE mesh for concrete and smeared longitudinal reinforcing bars (b) FE mesh for hoops and reinforcements of slab and boundary conditions

5.1.2 Material properties and material models

Table 5.2 presents the material properties for concrete, reinforcing bars, and PVC pipes used in the analysis. The design compressive strength of concrete was assumed to be 34.5 MPa (f'_c = 5 ksi). It is worth noting that the actual concrete compressive strength obtained from the concrete cylinder test for each specimen differ from the assumed design concrete strength. The tensile strength and elastic modulus of concrete were determined using default equations provided in VecTor3 User's Manual (El Mohandes and Vecchio, 2013). For the reinforcing bars, the nominal strengths were taken as the yield strengths (f_y), and the ultimate strengths (f_u) were assumed to be 1.25×f_y.

Regarding the PVC pipes, they were considered to be rigid, following a similar approach as done by Choi et al. (2020). As a result, the PVC pipes were assumed to have a significantly higher strength (f_a) than concrete, as shown in the fifth column of Table 5.2. Additionally, the elastic modulus for PVC pipes was assumed to be E = 200,000 MPa (29,000 ksi). These assumed material properties for the PVC pipes can be considered conservative as the simulated pipes can provide substantial resistance against slip and prevent the separation of the upper and lower beams (Choi et al., 2020).

VecTor3 offers a range of material models to accurately represent the behavior of concrete and reinforcement in nonlinear finite element analysis of RC coupling beams. Table 5.3 provides a summary of the material models used for concrete and reinforcement in this study. For a more comprehensive understanding of the properties and functions of these models, detailed explanations can be found in the work of Wong and Vecchio (2002).

Table 5.2 Material properties (Unit: MPa), (1 ksi = 6.895 MPa)

Specimen	Concrete	Longitudinal bar	Hoop	PVC*	Elastic modulus E	
	f'_c	f_y, f_u	f_y, f_u	f_y, f_u	Steel	PVC*
FS-R3.2-N-2	34.5	552, 689	552, 689	44, 52	200,000	3,300
HS-R2.4-S-1	34.5	552, 689	414, 517	-	200,000	-
FS-R2.4-S-3	34.5	552, 689	414,517	44, 52	200,000	3,300

f'_c : Compressive strength, f_y : Yield strength, f_u : Ultimate strength
* Mechanical properties data provided by Vinidex company

Table 5.3 Material models

Concrete models		Reinforcement models	
Compression prepeak:	Hognestad (Parabola)	Hysteretic response:	Bauschinger Effect (Seckin)
Compression post-peak:	Modified Park-Kent	Dowel action:	Tassios (crack slip)
Compression softenin:	Vecchio 1992-A	Buckling:	Refined Dhakal-Maekawa
Tension stiffening:	Modified Bentz 2003		
Tension stiffening:	Linear	**Bond models**	
FRC tension:	Not considered	Concrete bond:	Eligehausen
Confined strength:	Kupfer / Richart		
Dilation:	Variable – Kupfer	**Analysis models**	
Cracking criteria:	Mohr – Coulomb (stress)	Strain history:	Previous loading considered
Crack stress: calculation:	Basic (DSFM/MCFT)	Strain rate effects:	Not considered
Crack width check:	Agg/2.5 max. crack width	Structural damping:	Not considered

Crack slip calculation:	Walraven (monotonic)	Geometric nonlinearity:	Considered
Creep and relaxation:	Not available	Cracking spacing:	Uniform
Hysteretic response:	Nonlinear with plastic offsets		

5.1.3 Analysis parameters

VecTor3 performs nonlinear analysis of reinforced concrete structures based on the Modified Compression Field Theory (MCFT) in a total-load secant-stiffness approach, which was proposed by Vecchio and Collins in 1986 (Wong and Vecchio, 2002). This means that at each load stage, the total load is applied and the secant stiffnesses of the elements are used to calculate the displacements of the nodes comprising the structural model, which are, in turn, used to calculate the strains in the elements. The stresses are then calculated for the elements based on the calculated strains and the constitutive stress-strain models of the elements' materials. Finally, those strains and stresses are used to recalculate the value of the secant stiffnesses of the elements which are to be reused for the solution. This procedure is referred to as an "iteration" in the current load stage. The results of each iteration are compared to those of the previous iteration until certain criteria are met, after which the analysis proceeds to the next load stage.

In the analysis procedure, VecTor3 necessitates the user to define "Analysis Parameters" in the "Define Job" tab. The red square line in Figure 5.4 indicates the specific analysis parameters utilized for the coupling beam. Of particular importance is the 'Averaging factor,' which denotes a factor between 0 and 1. This factor represents the percentage of the secant stiffness value calculated from the previous iteration to be incorporated in the solution of the current iteration. The importance of this factor lies in the difficulty of reaching convergence for the highly nonlinear procedure involved in the analyses carried out using VecTor3. A smaller averaging factor results in a more stable analysis and smoother convergence from one iteration to the next. A larger averaging factor, on the other hand, results in faster convergence. Therefore, the user has to make a judgement on the value to be used for the averaging factor. In the highly nonlinear FE analysis using VecTor3, decreasing the averaging factor is crucial to improve convergence and analysis stability, thereby achieving accurate numerical analysis for RC structures. The specific averaging factors utilized for the DBCB corresponding to chord rotation are presented in Table 5.4. It is important to note that in VecTor3, the fully reversed cyclic loading employed in this study cannot be directly defined in the "Loading Data" all at once. Hence, the loading data was inputted in four stages for chord rotation, as demonstrated in Table 5.4.

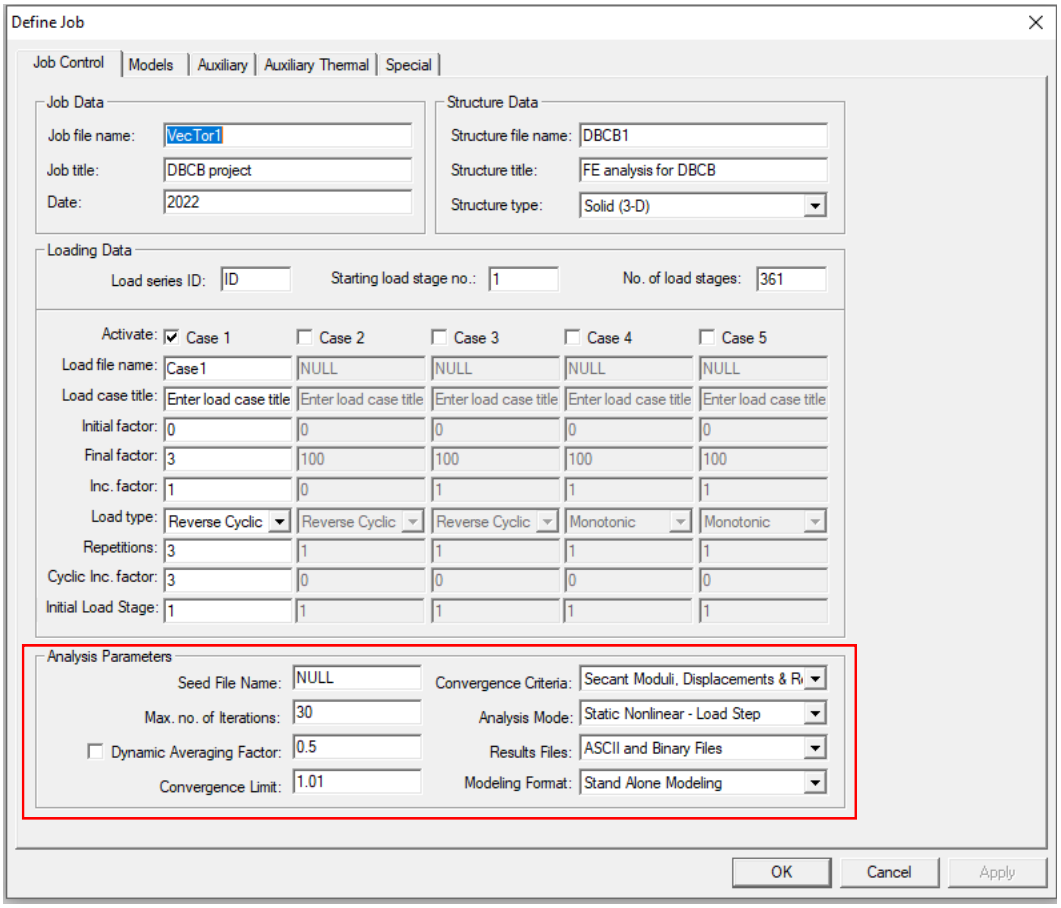

Fig. 5.4 Analysis parameter values

Table 5.4 Averaging factors

Parameter	Beam chord rotation (%)			
	0.25~1	1.5~2	3~4	6~8
Averaging factor	0.5	0.5	0.02	0.02

5.2 Analysis results

5.2.1 Parameter studies for the spacing of transverse reinforcement

Based on the test results of Specimens FS-R3.2-N-2 and HS-R2.4-S-1, the maximum widths of diagonal shear cracks were measured as 0.8 mm and 0.6 mm, respectively. These values are significantly smaller than the 4 mm observed in prior half-scale DBCB tests without the slab (Choi et al., 2018). However, as shown in Fig. 4.5, the performance of HS-R2.4-S-1 in terms of strength and ductility is slightly better than that of the equivalent prior half-scale DBCB without the slab (Choi et al., 2018). This indicates that the presence of the slab can enhance the confinement of the DBCB to some extent. To further investigate this effect, nonlinear finite element (FE) analyses were conducted using the VecTor3 software to explore the feasibility of relaxing the hoop spacing in a DBCB with a slab.

The analysis process began with nonlinear finite element analyses of Specimens FS-R3.2-N-2 and HS-R2.4-S-1 to compare the results with the experimental tests. As illustrated later in Figures 5.8 (a) and (b), although the FEA results displayed higher shear strengths compared to the test results, nonlinear FEA effectively simulates the rotational capacities for FS-R3.2-N-2 and HS-R2.4-S-1. In other words, according to FEA predictions, their shear strengths did not decrease beyond 6% and 8% chord rotation, respectively, which aligns with the experimental findings. Considering that the spacing of transverse reinforcement affects the ductility of concrete and, consequently, the rotational capacity of the coupling beam, it is considered appropriate to employ the FE models for conducting parametric studies to explore the impact of transverse reinforcement spacing.

Fig. 5.5 illustrates the hoop spacings used in the FE model of FS-R3.2-N-2. In Fig. 5.5 (a), the hoop spacing is set to 3 in. within the assumed plastic hinge region, which extends approximately to the depth of the DBCB beam (*h*) from the beam end towards the midspan (Fig. 3.7 (a)). Figs. 5.5 (b) and (c) show alternative hoop spacings of 4 in. and 6 in. within the plastic hinge region, respectively. Similar parametric studies for hoop spacing were conducted for the FE model of HS-R2.4-S-1 (with hoop spacings of 1.5 in., 2 in., and 3 in.).

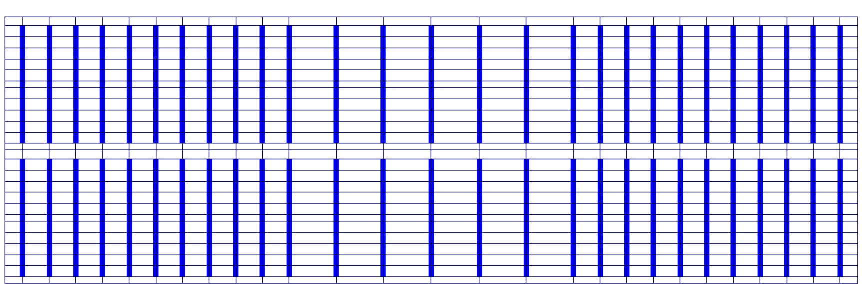

(a)

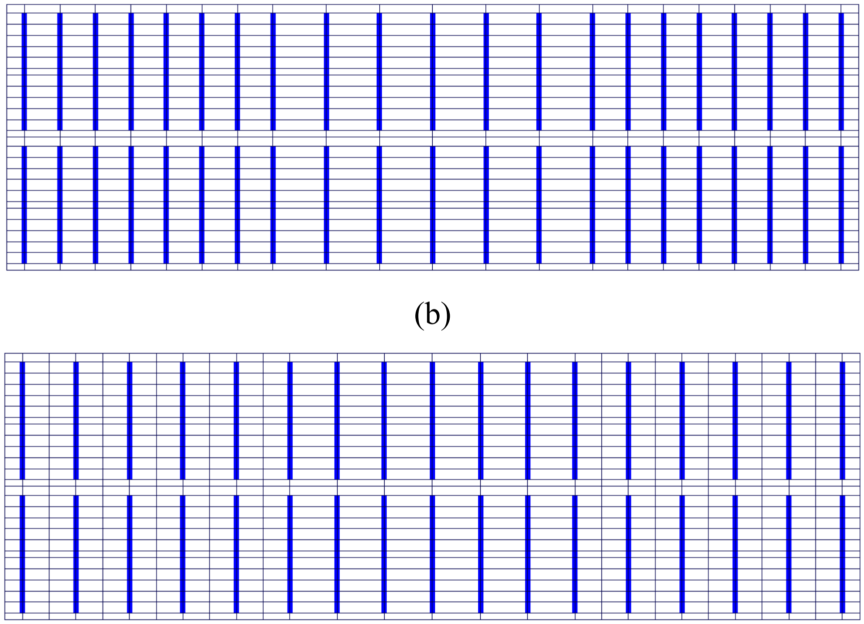

(b)

(c)

Fig. 5.5 Hoop spacings for FE model for FS-R3.2-N-2: (a) 3 in. (b) 4 in. (c) 6 in.

Fig. 5.6 (a) illustrates the FEA results for FS-R3.2-N-2 considering three different hoop spacings: 3 in., 4 in., and 6 in. As shown in Figure 5.6 (a), the FE model with a 4 in. hoop spacing displayed a performance similar to that of the 3 in. hoop spacing. However, for a hoop spacing of 6 in., the shear strength rapidly dropped at a small chord rotation of 1.5%. Fig. 5.6 (b) presents the FEA results for the half-scale specimen HS-R2.4-S-1, considering three different hoop spacings: 1.5 in., 2 in., and 3 in., which are half of those used in FS-R3.2-N-2. The half-scale FE model with a 2 in. hoop spacing exhibits nearly the same performance as the 1.5 in. hoop spacing used in HS-R2.4-S-1. However, for a 3 in. hoop spacing, the shear strength gradually decreases starting from a chord rotation of 2.0%. The results obtained from the parameter studies indicate that the hoop spacing could be increased up to 4 in. for the full-scale DBCB and 2 in. for the half-scale DBCB.

The FE analyses for Specimens FS-R3.2-N-2 and HS-R2.4-S-1 were conducted after the testing, while the investigation of hoop spacing for Specimen FS-R2.4-S-3 was carried out prior to the design to determine its appropriate hoop spacing. Fig. 5.6 (c) presents the FE results considering three hoop spacings: 3 in., 4 in., and 6 in. As anticipated, the FE model of the coupling beam with hoop spacings of 3 in. and 4 in. exhibited stable hysteresis curves, maintaining shear strength with minimal loss, even during the first cycle of 8% chord rotation. Even with a hoop spacing of 6 in., the coupling beam demonstrated high ductility, as its strength did not decline until a 6% chord rotation.

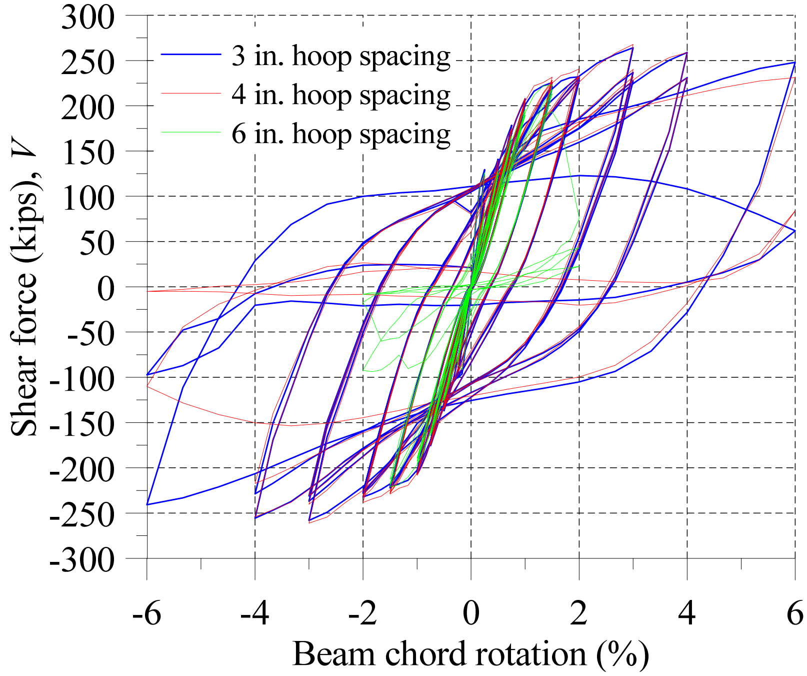

(a)

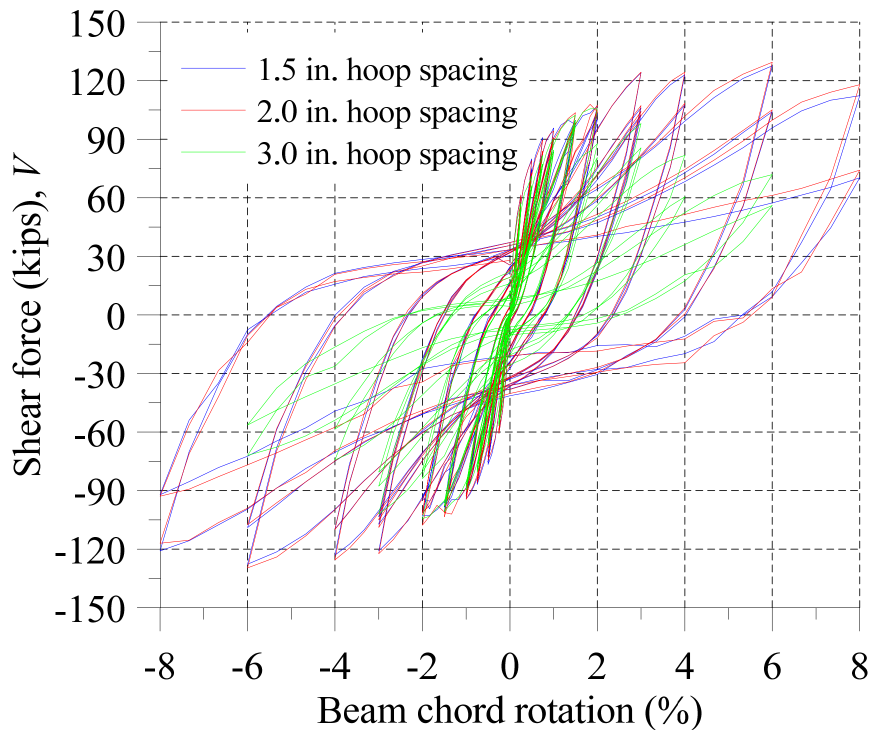

(b)

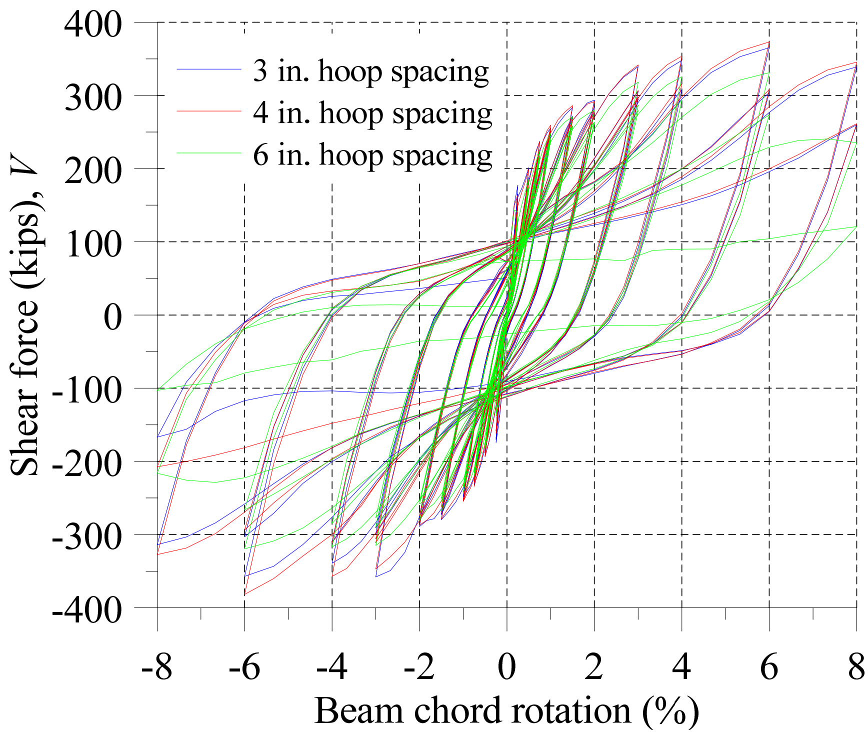

(c)

Fig. 5.6 Relationship between shear force and chord rotation according to three different hoops spacing: (a) FS-R3.2-N-2 (b) HS-R2.4-S-1 (c) FS-R2.4-S-3

The hoop spacing for the FS-R2.4-S-3 specimen was determined based on the FE simulation results, as illustrated in Fig. 3.16 (a). A hoop spacing of 3 in. was used over a length equal to half of the overall coupling beam depth (*h*/2), measured from the face of the beam-to-wall interface towards the midspan. Subsequently, a hoop spacing of 4 in. was used for the remaining length of the beam. Fig. 5.7 depicts the final hoop spacing for the FE model of FS-R2.4-S-3, along with the corresponding FEA results. In Fig. 5.7 (b), the coupling beam demonstrates stable hysteresis curves, maintaining shear strength with minimal loss, up to 8% chord rotation. Fig. 5.7 (c) illustrates the presence of severe cracks at the plastic hinge region and UCS layer, with prominent flexural vertical cracks observed at the beam ends, leading to flexural failure. Furthermore, Fig. 5.7 (d) shows the deformation of rectangular solid PVC pipes near the beam ends, indicating the occurrence of an interface crack resulting from relative horizontal sliding between the upper and lower beams, gradually propagating towards the ends of the coupling beam. However, the rectangular PVC pipes at the midspan remain undistorted.

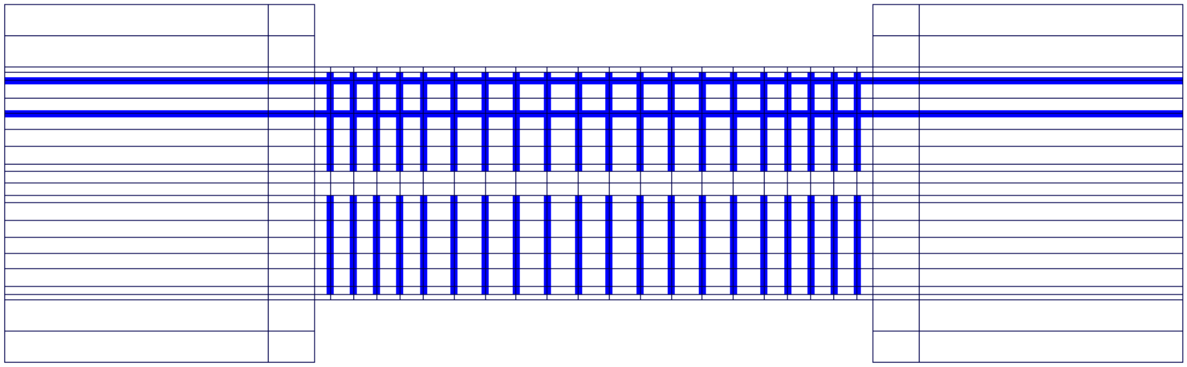

(a)

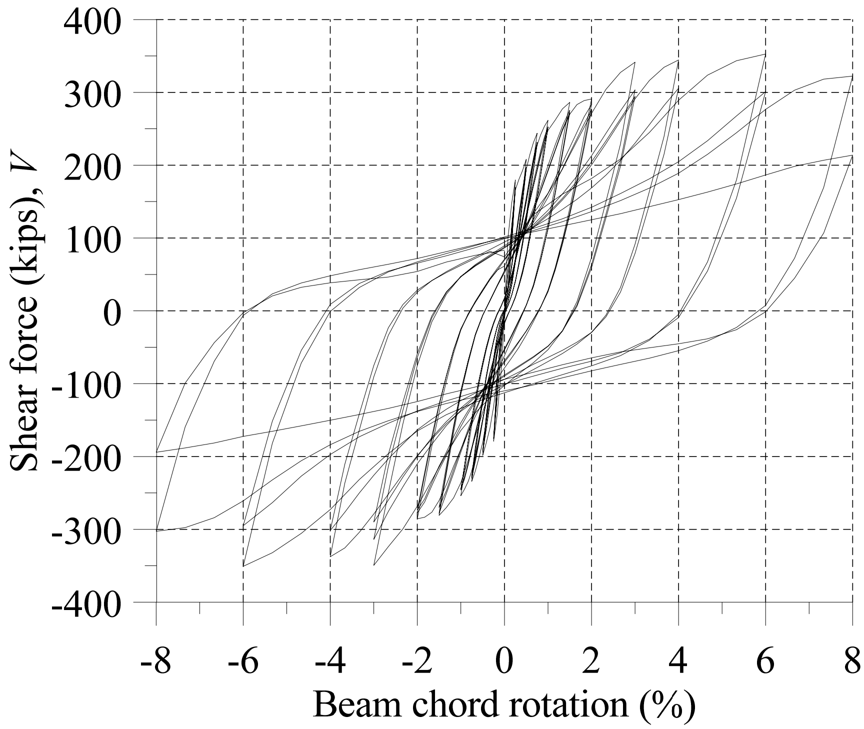
Shear force (kips), V
400
300
200
100
0
-100
-200
-300
-400
-8
-6
-4
-2
0
2
4
6
8
Beam chord rotation (%)

(b)

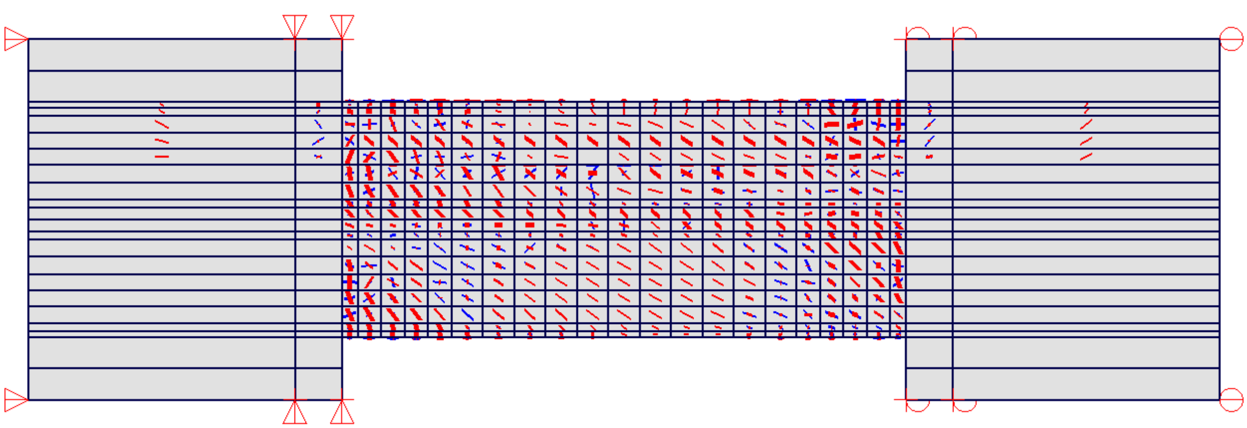

(c)

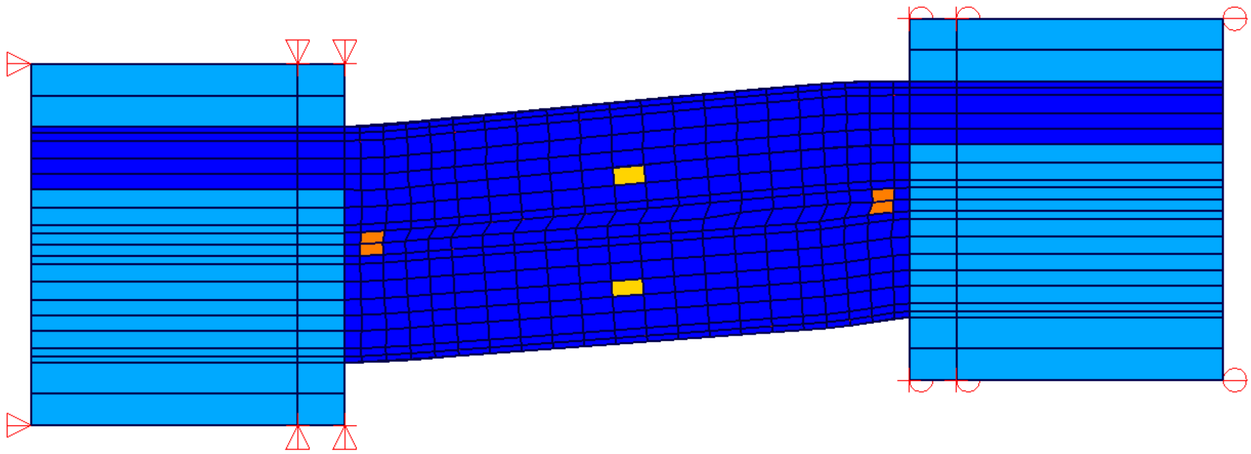

(d)

Fig. 5.7 Final FE model for FS-R2.4-S-3: (a) Hoop spacing (b) Shear force versus chord rotation (c) Crack patterns (d) Failure mode and PVC pipe distortion

5.2.2 Comparison in shear force versus chord rotation between test and FEA

Figs. 5.8 present a comparison of shear force versus chord rotation between the test and FEA results for FS-R3.2-N-2, HS-R2.4-S-1, and FS-R2.4-S-3. As discussed earlier in Section 5.2.1, the FEA results for the first two specimens exhibit behavior similar to the experimental results. In Figs. 5.8 (a) and (b), it can be observed that their shear strengths increase up to 6% and 8% chord rotation, respectively, before decreasing, which aligns with the experimental findings. However, it should be noted that the maximum strength obtained from the FEA results was approximately 30% higher than that of the test results. Figs. 5.9 and 5.10 show the crack patterns and failure modes of two specimens after experiencing significant degradation in shear strength, respectively. In Figs. 5.9 (a) and 5.10 (a), clear horizontal interface cracks at the UCS layer and flexural-shear cracks near the beam ends can be observed, which closely resemble the test results. Additionally, Figs. 5.9 (b) and 5.10 (b) demonstrate that the failure modes observed in the FE simulations closely resemble those observed in the corresponding specimens.

From nonlinear FE analysis, it was expected that FS-R2.4-S-3 specimen would have a stable hysteresis curves up to 8% chord rotation with little loss of shear strength as shown in Fig. 5.7 (b). However, FS-R2.4-S-3's strength started to decrease earlier at the first positive chord rotation of 6% as shown in Fig. 4.6. As shown in Section 4.1.3, using larger dimensions of PVC pipes leads to increased slip resistance, which hinders or delays the propagation of horizontal cracks towards the beam-to-wall interface (as illustrated in Fig. 4.3 (g)). Consequently, this facilitates the development of diagonal cracks near the beam-to-wall interface. Due to VecTor3's inability to directly simulate this effect, the greater slip resistance was simulated in the FS-R3.2-N-2 model by assuming an elastic modulus of 200,000 MPa, which is higher than the manufacturer's value of 3,300 MPa (Table 5.2). Subsequently, the FE simulation of the nonlinear FS-R2.4-S-3 model was conducted again.

The comparison between the test and modified FEA results regarding shear force versus chord rotation is presented in Fig. 5.8 (c). Despite the significant overestimation of shear strength by the FE simulation, the degradation of their strengths was observed to initiate at the same chord rotation (specifically, the first positive chord rotation of 6%). Moreover, the nonlinear behavior of the FE model closely resembled the test result. Figs. 5.11 (a) and (b) illustrate the presence of horizontal interface cracks at the UCS layer and flexural-shear cracks near the beam ends. Additionally, the FE results identified shear failure occurring at the plastic hinge region near the beam end.

Upon comparing Fig. 5.7 (c) with Fig. 5.11 (a), it can be observed that the FE model, utilizing PVC pipes with an elastic modulus of 3,300 MPa, failed due to flexural cracks at the beam ends. In contrast, the FE model incorporating PVC pipes with an elastic modulus of 200,000 MPa exhibited shear cracks near the beam ends. This occurred because the higher stiffness from the PVC pipes hinders the relative slip and propagation of interface cracks at the UCS layer, as shown in Fig. 5.11 (b). As mentioned earlier, VecTor3 software has inherent limitations when it comes to accurately modeling circular PVC pipes and considering the bond between concrete and PVC pipes. However, based on the numerical results, it is evident that the resistance provided by PVC pipes, particularly those positioned near the beam-to-wall interface at the UCS layer, can significantly impact the performance of DBCB. Therefore, it is recommended to limit the dimensions of PVC pipes at the UCS layer and position them as close as possible to the beam-to-wall interface.

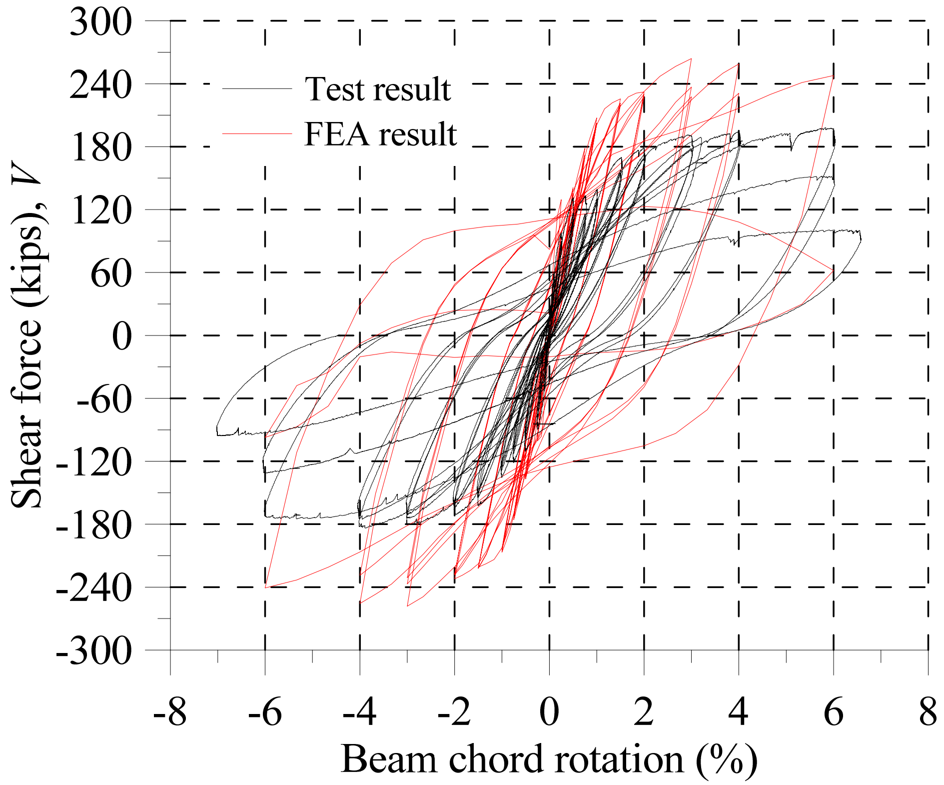
Test result
FEA result
Shear force (kips), V
Beam chord rotation (%)
300
240
180
120
60
0
-60
-120
-180
-240
-300
-8
-6
-4
-2
0
2
4
6
8

(a)

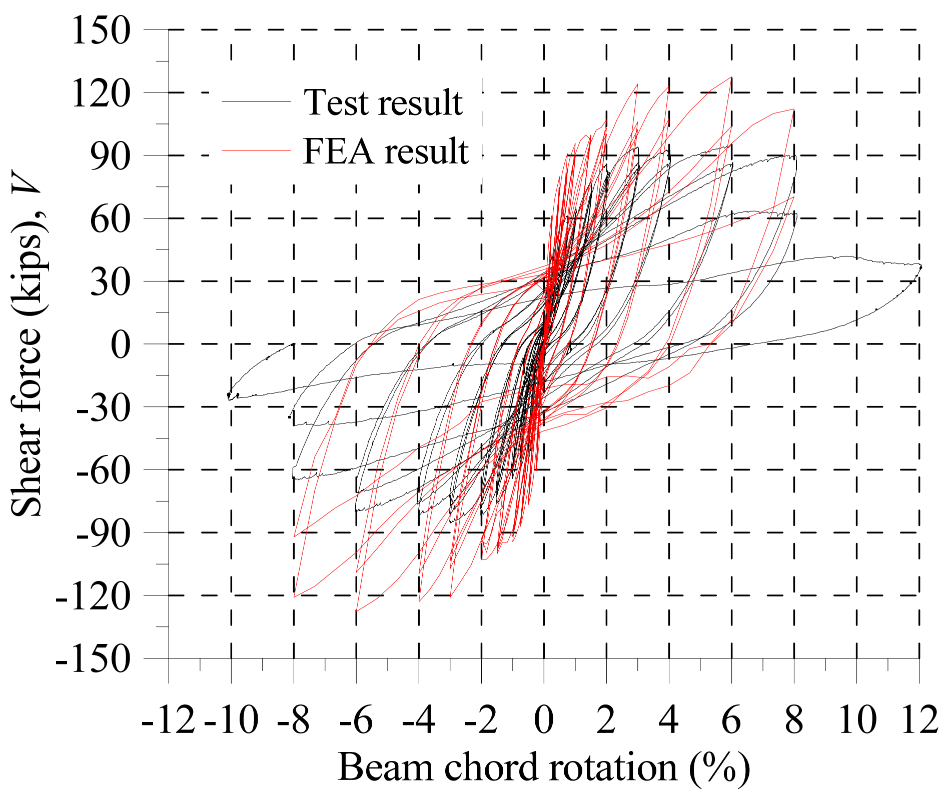
Test result
FEA result
Shear force (kips), V
Beam chord rotation (%)
150
120
90
60
30
0
-30
-60
-90
-120
-150
-12
-10
-8
-6
-4
-2
0
2
4
6
8
10
12

(b)

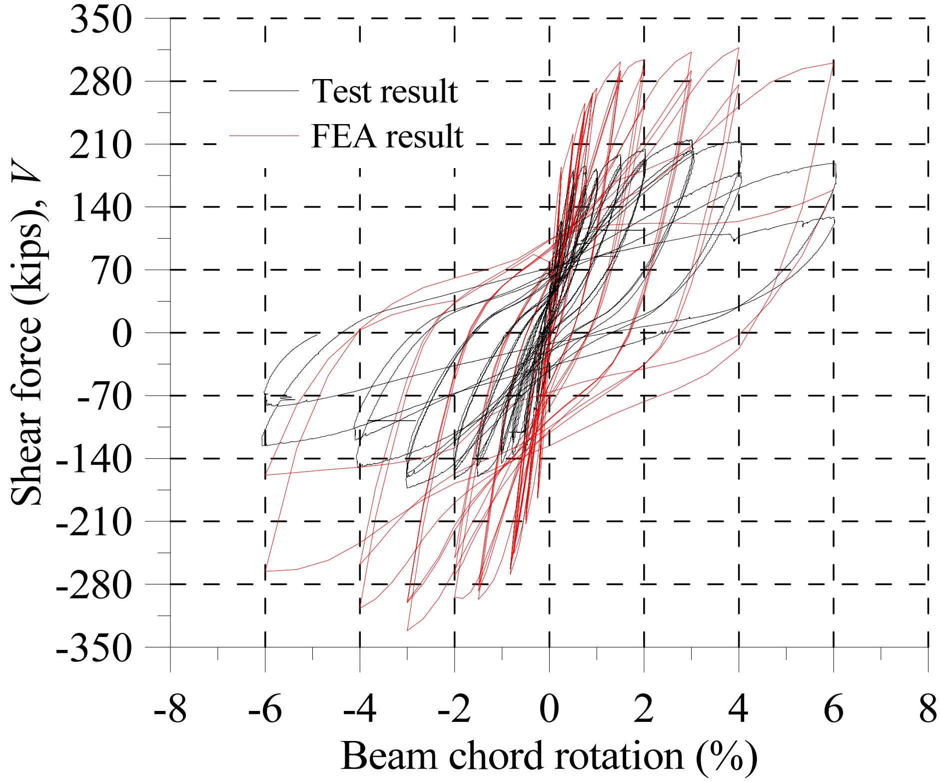

(c)

Fig. 5.8 Comparison in shear force versus chord rotation between test and FEA: (a) FS-R3.2-N-2 (b) HS-R2.4-S-1 (c) FS-R2.4-S-3

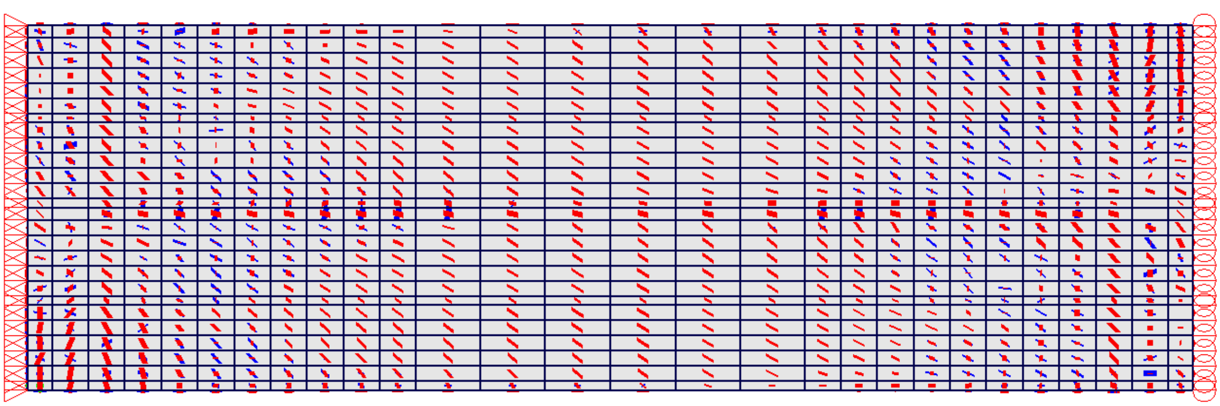

(a)

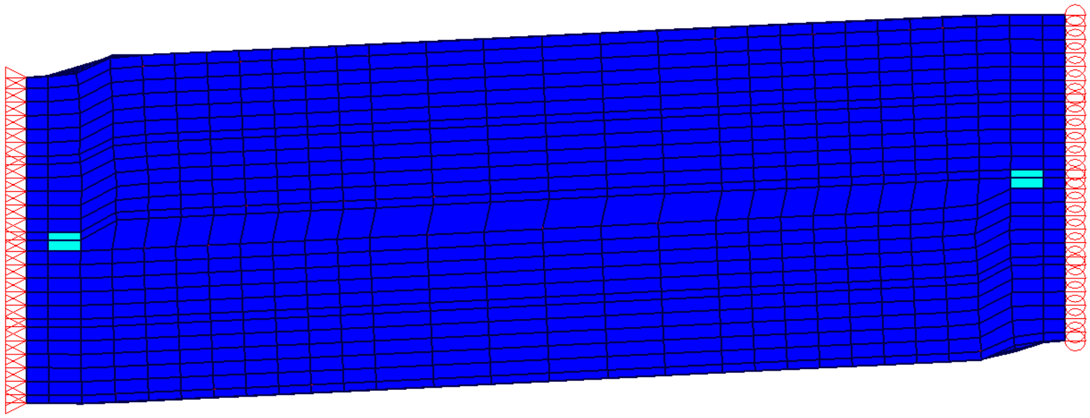

(b)

Fig. 5.9 FS-R3.2-N-2: (a) Crack patterns (b) Failure mode

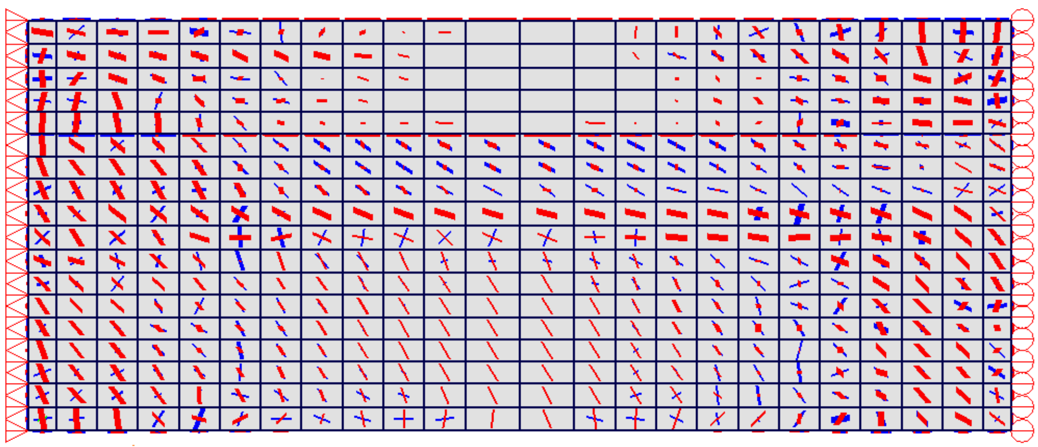

(a)

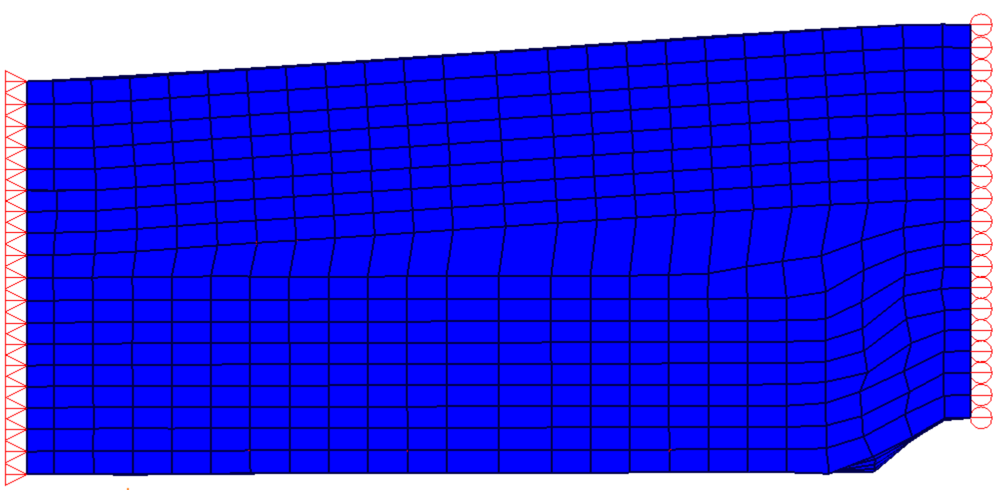

(b)

Fig. 5.10 HS-R2.4-S-1: (a) Crack patterns (b) Failure mode

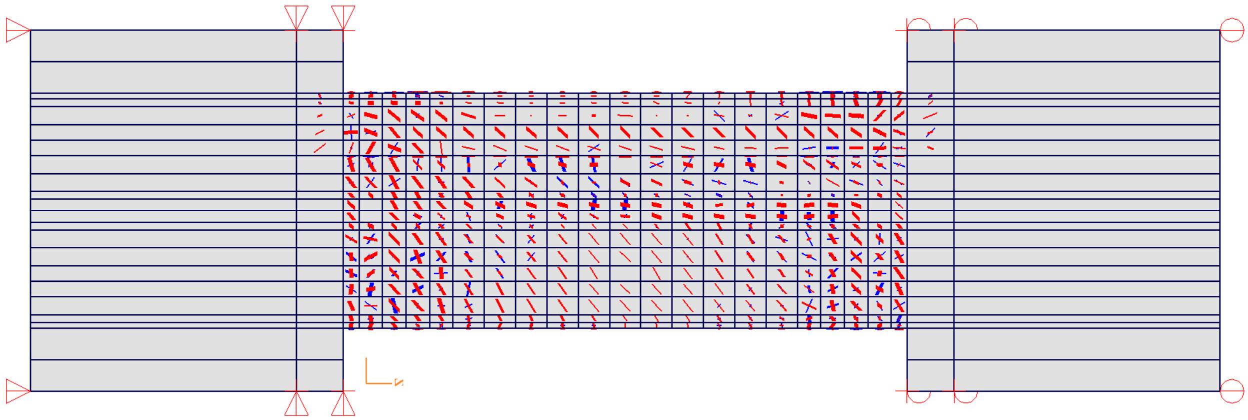

(a)

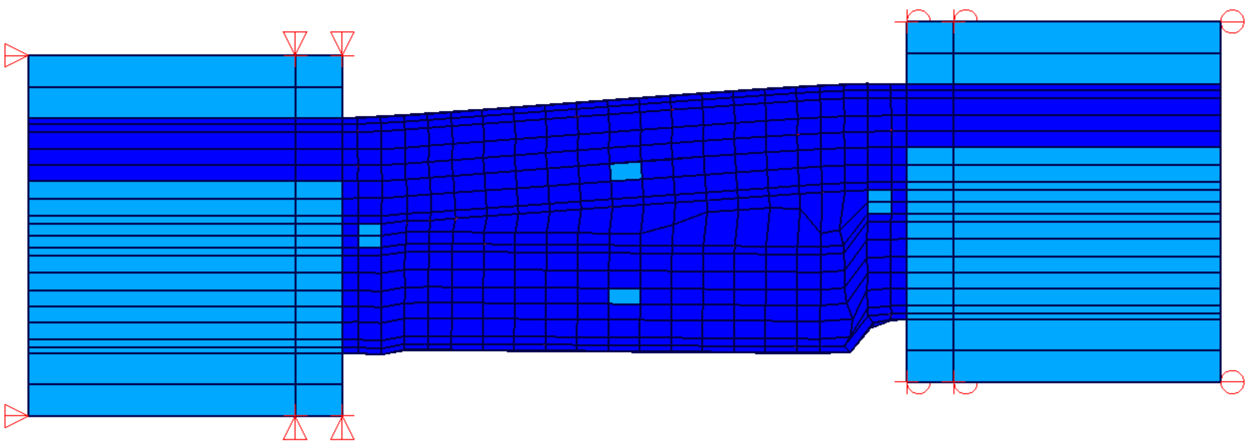

(b)

Fig. 5.11 FS-R2.4-S-3: (a) Crack patterns (b) Failure mode

5.2.3 Additional FE analysis for DBCB with full width

Based on the previous parametric studies conducted on hoop spacing within the plastic hinging region, approximately *h*/2 from both ends of the beam, it was determined that the FE results obtained from VecTor3 exhibited a strong agreement with the experimental tests. Furthermore, it was observed that full-scale specimens with 3 in. hoop spacing, which follows the confinement requirement specified in ACI 18.6.4.4, demonstrated a similar behavior to specimens with a slightly wider hoop spacing of 4 in. under cyclic loading.

As highlighted in Section 3.1.1, the full-scale specimens tested in this study had a beam width of 10 in., which is smaller than the actual width of 24 in. corresponding to the width of the wall piers. This deviation was due to the limitation of the actuator's maximum load capacity. To evaluate the potential impact of this reduced width on the behavior of DBCB, additional FE analysis was conducted on DBCB models with a full beam width of 24 in. This analysis aimed to determine if the reduced width had any significant effects on the behavior of DBCB. Fig. 3.1 shows in detail the cross section for the actual full-scale DBCB with 24 in. width, which was designed according to the same procedure used in the test specimens with narrow width (b_w = 10 in.). As illustrated in Fig. 3.1, No. 4 hoops and crossties were used for shear reinforcement with 4.6 in. and 5.5 in. leg spacing in the width direction. In this analytical study, the flexural yielding region in the longitudinal direction extended over a length of h from both ends of the beam, following the ACI 18.6.4.1. To satisfy the confinement requirement specified by ACI 18.6.4.4, a hoop spacing of 3 in. was implemented within the *h* region, while a hoop spacing of 4 inches was used for the remaining middle length ($l_n - 2h$) in accordance with the shear strength requirement.

Fig. 5.12 (a) shows the FE model of the full-scale 2.4 ratio DBCB with a width of 24 in., where the shear wall and the coupling beam have the same width. In Fig. 5.12 (b), the FE mesh for the concrete, smeared reinforcement, and the boundary conditions are illustrated. The boundary conditions were assigned to two blocks: one block was fixed (U1 = 0, U2 = 0, and U3 = 0), while the other block was free in the vertical direction (U1 = 0, U2 = 1, and U3 = 0).

Fig. 5.13 shows the FE results for the full-scale 2.4 ratio DBCB with a width of 24 in. As observed in Fig. 5.13, the DBCB with the full width exhibits stable hysteresis curves and maintains its shear strength up to a chord rotation of 6%, similar to the behavior observed in specimens with reduced widths. Moreover, the FE analysis indicates that the coupling beam with 3-in. hoop spacing over the plastic hinge region (*h* length) demonstrates nearly identical behavior to that with 4-in. hoop spacing, which is equivalent to the results obtained from an FE model with a width of 10 in. Fig. 5.14 illustrates the crack patterns and failure mode observed in FE results. In Fig. 5.14 (a), distinct horizontal interface cracks at the UCS layer and flexural-shear cracks near the beam ends are clearly visible, which aligns with the previous FE results obtained for a 10-in. width. Furthermore, Fig. 5.14 (b) shows that the failure mode is consistent with the specimens having a 10-in. width. Therefore, it is evident that the DBCB with a 24-in. width exhibits very similar behavior to the one with a 10-in. width, indicating that the reduced width used in the experimental tests does not impact the behavior or capacity of the DBCB.

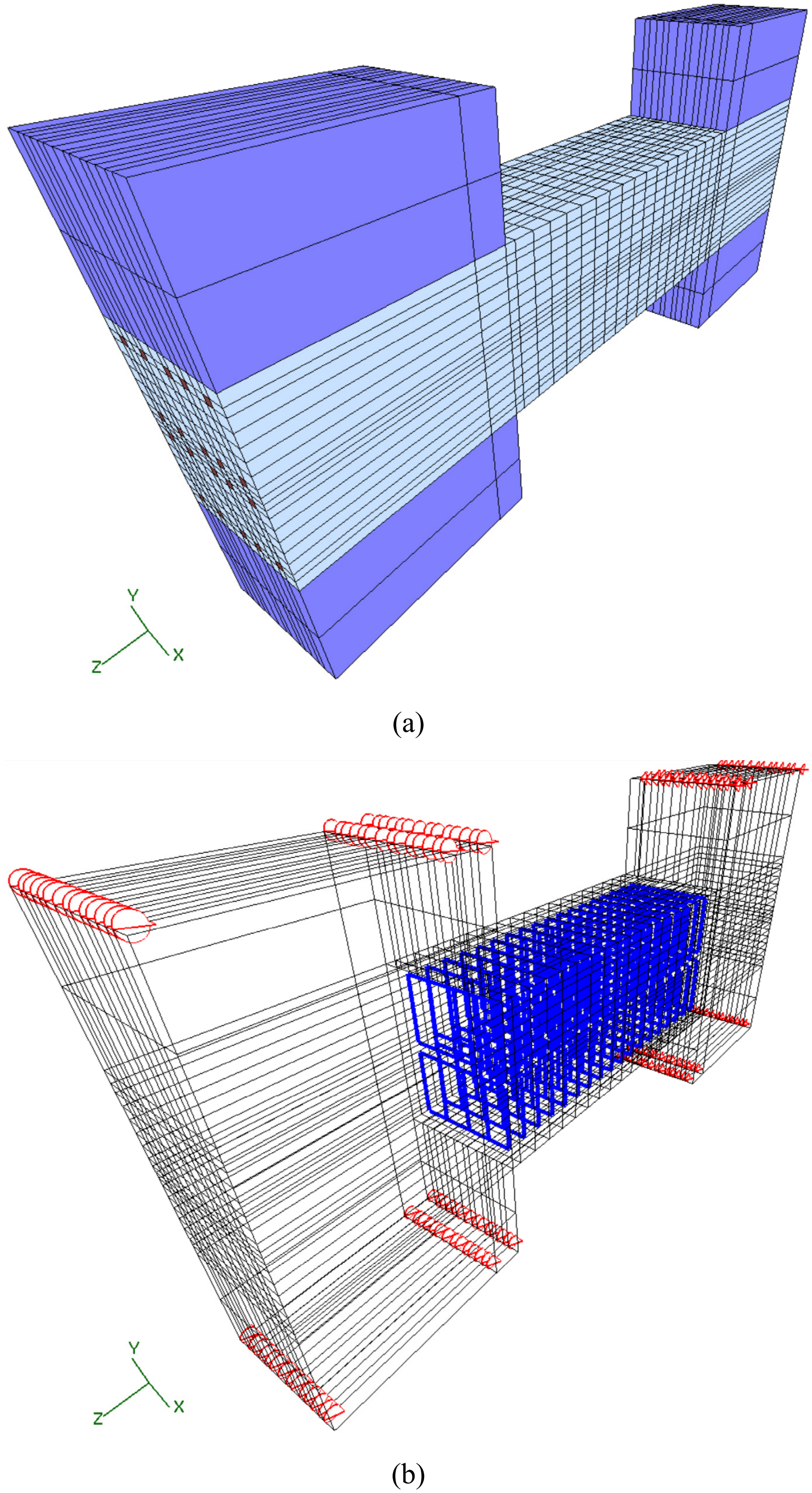

Fig. 5.12 FE model for full-scale DBCB: (a) FE mesh for concrete and smeared longitudinal reinforcing bars (b) FE mesh for hoops and boundary condition

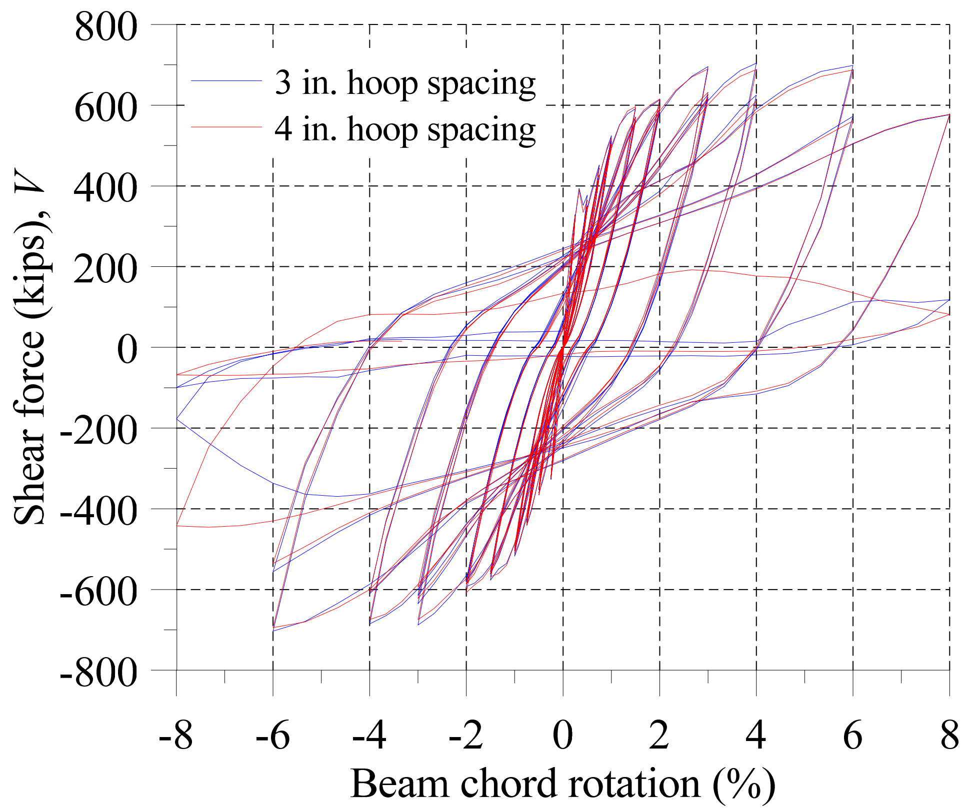

Fig. 5.13 Relationships between shear force and beam chord rotation for full-scale 2.4 ratio DBCB with 24 in. width

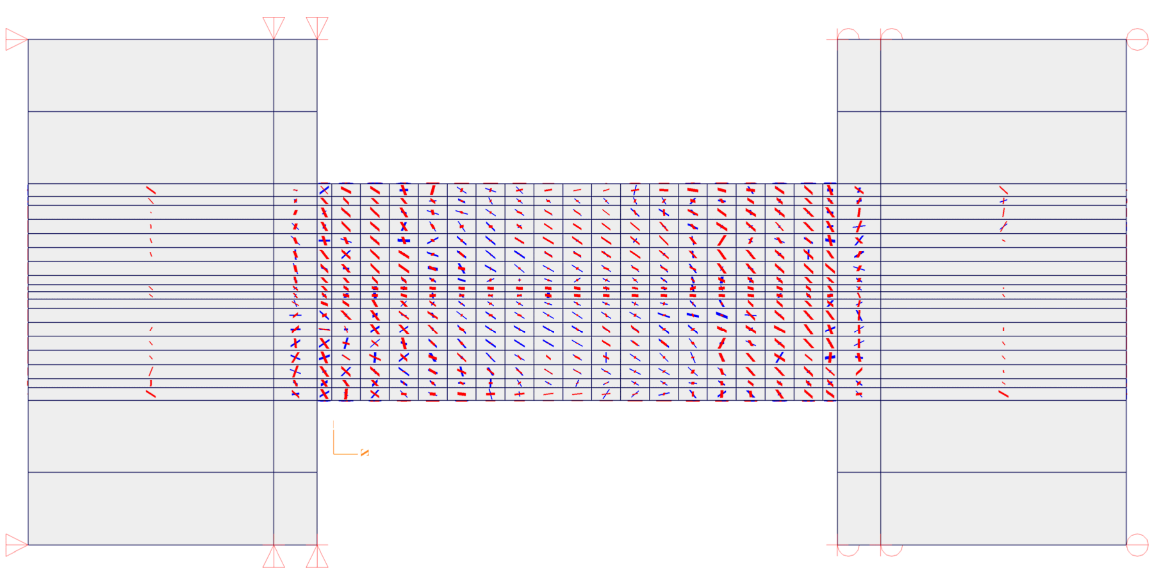

(a)

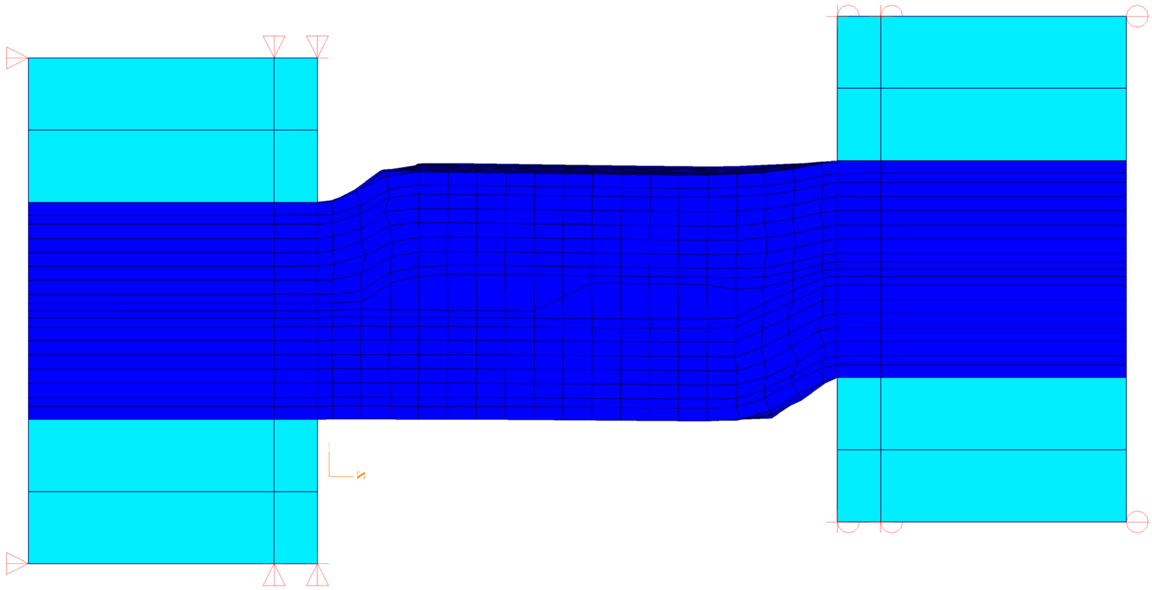

(b)

Fig. 5.14 FE result for full-scale 2.4 ratio DBCB with 24 in. width (a) Crack patterns (b) Failure mode

CHAPTER 6: SUMMARY AND CONCLUSIONS

Double-beam coupling beams (DBCBs) have proven to be a promising alternative to diagonally reinforced concrete coupling beams (DCBs) through half-scale DBCB experimental tests using Gr. 60 rebars (Choi and Chao, 2018; Choi et al., 2020). Their seismic performance has been experimentally shown as equivalent to or better than DCBs even though without the use of diagonal reinforcements, thereby considerably minimizing reinforcement congestion and construction difficulties. To verify or investigate the performance of DBCBs further, three double-beam coupling beams (FS-R3.2-N-2, HS-R2.4-S-1, and FS-R2.4-S-3), which were reinforced with ASTM A706 Gr. 80 high-strength rebars, were conducted under fully reversed cyclic loading to (1) verify a proposed DBCB design procedure, (2) examine the size effect on the spacing of transverse reinforcement, (3) evaluate the performance of DBCBs made with high-strength rebars (ASTM A706 Gr. 80) and determine their required development length, (4) assess the size and location of utility duct openings, and (5) examine the effect of the slab on the performance of the DBCBs. The information if these three specimens are summarized as follows:

- ✓ Specimen FS-R3.2-N-2: full-scale 3.2 aspect DBCB (representing the aspect ratio typically used for office building)
    - Height: 30 inches; length: 96 inches; thickness: 10 inches.
    - No slabs.
    - Longitudinal rebars – A706 Gr. 80; hoops – A706 Gr. 80.
    - One 2.5 in.-dia. opening at each end of the beam
- ✓ Specimen HS-R2.4-S-1: half-scale 2.4 aspect DBCB (representing the aspect ratio typically used for residential building)
    - Height: 15 inches; length: 36 inches; thickness: 6 inches.
    - 4-in.-thick slab.
    - Longitudinal rebars – A706 Gr. 80; hoops – A615 Gr. 60.
    - No openings in the beam
- ✓ Specimen FS-R2.4-S-3: full-scale 2.4 aspect DBCB (representing the aspect ratio typically used for residential building)
    - Height: 30 inches; length: 72 inches; thickness: 10 inches
    - 8- in.-thick slab.

- Longitudinal rebars – A706 Gr. 80; hoops – A615 Gr. 80.
- One 3.0 in.-dia. opening at each end of the beam; two 3.0 in.-dia. opening at middle of the beam

The main findings and observations from this study are summarized as follows:

1. According to the test results, it was shown that both the full-scale DBCB specimens with aspect ratios of 2.4 and 3.2 achieved a maximum chord rotation of 6%. This level of rotation is approximately equal to the expected rotational demand caused by a maximum considered earthquake (MCE) as described by Harries and McNeice (2006). Moreover, this rotational capacity meets the acceptance limit prescribed by LATBSDC (2020) for diagonally reinforced coupling beams. This rotation was attained before their strengths decreased below 80% of the peak shear force. Additionally, both specimens reached a peak shear stress of approximately $10\sqrt{f_{cm}}$, where f_{cm} represents the measured concrete compressive strength.

2. The performance of the full-scale DBCB is comparable to that of smaller-scale DBCBs tested in previous studies.

3. The full-scale specimens, FS-R3.2-N-2 and FS-R2.4-S-3, were designed with a hoop spacing of 3 inches within the plastic hinge region, following the confinement requirements specified in ACI 318 for special moment frame beams. This spacing is twice as wide as the 1.5 inches used in the half-scale specimen. Despite this difference, the maximum width of shear cracks observed in Specimens FS-R3.2-N-2 and FS-R2.4-S-3 was 0.8 mm and 2.5 mm, respectively. These values are smaller than the 4 mm observed in the previous half-scale DBCBs (Choi et al., 2018). FS-R3.2-N-2 exhibited stable hysteresis curves up to the first cyclic 6% chord rotation without any loss of strength. On the other hand, FS-R2.4-S-3 exhibited stable hysteresis curves up to the first positive 6% chord rotation, retaining over 80% of its maximum strength. However, unlike the half-scale DBCBs, the longitudinal reinforcement in FS-R3.2-N-2 experienced buckling at the first positive 7% chord rotation, while in FS-R2.4-S-3, it experienced buckling at the second positive 6% chord rotation. This buckling phenomenon led

to a rapid decrease in shear strength. In other words, noticeable size effects were not observed until buckling occurred.

4. The occurrence of longitudinal bar buckling in the full-scale DBCB specimens can be attributed to several factors. Firstly, the use of larger bars in the full-scale beams, which experience significant bending moments and consequently higher axial forces, contributes to bar buckling. Unlike smaller beams, the cover concrete in full-scale beams is less effective in restraining larger bars from buckling. This is primarily due to the earlier cracking of the cover concrete caused by the larger outward forces exerted by the longitudinal bars during loading. Moreover, beams with larger cross-sectional dimensions are inherently more susceptible to bar buckling. The concrete surrounding the longitudinal bars in full-scale beams is more prone to cracking and crushing, as it must endure the higher restraint stresses required to prevent buckling of large longitudinal bars. This phenomenon becomes particularly pronounced in the later stages of lateral loading, where the core concrete closest to the hoops has already been damaged or softened due to cyclic shearing forces. The higher tendency for bar buckling in large bars in full-scale specimens has also been observed and reported in other research studies (Visnjic et al., 2016; Nojavan et al., 2017; Choi and Chao, 2019). Moreover, as reported by Poudel et al. (2021), the presence of significant axial restraint in the diagonally reinforced concrete coupling beams led to earlier buckling of the diagonal bars. This indicates that the higher compression forces resulting from axial restraint in the full-scale DBCB could exacerbate the longitudinal rebar buckling.

5. In previous half-scale DBCB tests conducted by Choi et al. (2018), the middle layer of each steel cage utilized longitudinal reinforcement to effectively control crack propagation, maintain aggregate interlocking, and enhance the flexural capacity. However, in this study, certain modifications were made. In some cases, such as HS-R2.4-S-1 and FS-R2.4-S-3, the middle longitudinal reinforcing bars were eliminated to simplify the construction process. In other cases, like FS-R3.2-N-2, relatively smaller rebars were used instead of the same size of large bars used in the top and bottom rebars. Elimination of the middle layer of longitudinal reinforcement tend to increase the concentration of chord rotation at the beam ends, thereby causing the concentration of damage near the beam ends, which in turn led to early spalling

and crumbling within the confined concrete core of coupling beam like FS-R2.4-S-3. In addition, the relatively smaller reinforcement ratio (ρ) of the primary reinforcement in FS-R2.4-S-3 might have an additional effect on the earlier inset of yielding and the concentration of chord rotation. Notably, Ameen et al. (2020) and Weber-Kamin et al. (2020) found that the inclusion of secondary longitudinal reinforcement in DCB led to a reduction in the concentration of chord rotation at the beam-to-wall interface and a more distributed damage pattern across the beam span, ultimately enhancing the deformation capacity. This supports the notion that the removal of the middle longitudinal bars accelerates the onset of yielding in the longitudinal reinforcement due to the concentration of chord rotation near the beam-to-wall interface.

6. In full-scale DBCBs (HS-R2.4-S-1 and FS-R2.4-S-3), there is a tendency for rapid interface crack propagation from the midspan towards the beam ends between the upper and lower beams, in comparison to the half-scale DBCB (HS-R2.4-S-1). This leads to an earlier occurrence of flexural cracks near the beam ends. The removal of the middle layer of longitudinal reinforcement in steel cages could have weakened the concrete confinement and the dowel strength between the beam and the adjacent wall. Consequently, it becomes crucial to ensure proper confinement of the concrete core near the beam ends in order to delay crack propagation caused by shear and/or flexural stress. To achieve this, it is recommended to retain the longitudinal reinforcement in the middle layer of each steel cage in DBCBs. This will help enhance the confinement effect and effectively mitigate crack propagation in critical areas of the beam.

7. The yield penetration of the longitudinal reinforcing bar was observed to be limited to approximately 10 in., 8 in., and 11 in. inward into the concrete blocks for FS-R2.4-S-3, HS-R2.4-S-1, and FS-R2.4-S-3, respectively. The limited yielding observed indicates a limited bond slip between the concrete and reinforcing steel within the concrete block (wall piers). Despite the different sizes of rebar and corresponding development lengths, the strain patterns derived from their respective development lengths exhibit similar trends across the three specimens. The three specimens tested in this study, which were reinforced with high-strength Gr. 80 steel rebars, exhibited higher strains compared to the previous specimens using Gr. 60

rebars (Choi et al., 2018). However, despite the use of high-strength reinforcement, the strain patterns observed were very similar to those of the conventional reinforcement. This suggests that the development length of longitudinal reinforcement provided by Eq. 4.1 (60% of the requirement specified by ACI 18.8.5.3) is applicable not only to conventional Gr. 60 steel rebars, but also to high-strength Gr. 80 steel rebars.

8. The half-scale DBCB specimen with a slab, HS-R2.4-S-1, despite eliminating the middle layer of longitudinal reinforcement for each beam, exhibited minimal diagonal cracking with a maximum width of only 0.6 mm. This is significantly smaller than the 4 mm observed in half-scale DBCBs without a slab (Choi et al., 2018). Additionally, HS-R2.4-S-1 demonstrated stable behavior up to the first positive 8% chord rotation without any noticeable loss in shear strength. The full-scale specimen, FS-R2.4-S-3, was also designed with a slab and did not include the middle layer of longitudinal reinforcement for each beam. Additionally, the hoop spacing in FS-R2.4-S-3 was slightly relaxed compared to the confinement requirement specified in ACI 18.6.4.4. Nevertheless, the maximum width of the shear crack in FS-R2.4-S-3 was 2.5 mm, which is still smaller than the 4 mm observed in previous half-scale DBCB studies. This suggests that the presence of the slab offers additional confinement to the coupling beam, leading to a reduced width of diagonal shear cracks and improved performance of DBCBs.

9. It is observed that the strains in the transverse reinforcements of FS-R3.2-N-2 and FS-R2.4-S-3 were not significantly high until a chord rotation of 6%. Yielding in the transverse reinforcement was rarely observed in the two full-scale DBCB specimens. However, for HS-R2.4-S-1, the strains in the transverse reinforcements started yielding at approximately 3% chord rotation and increased up to 6% chord rotation. The yielding in transverse reinforcement occurred up to 5.5 in. away from the beam end. This behavior can be attributed to the differences in maximum shear force and concrete cross-section area between the full-scale specimens and the half-scale specimen HS-R2.4-S-1. While the full-scale specimens carried approximately twice the maximum shear force, the concrete cross-section area used to resist shear in the full-scale DBCBs was about 3.33 times that of the half-scale specimen. Consequently, the contribution of transverse reinforcement in resisting shear was smaller in

the full-scale specimens. Furthermore, the test results indicate that the design assumption of $V_c = 0$, which assumes no shear resistance from the concrete core, is conservative. In reality, the core of the concrete remained intact, providing a significant amount of shear resistance even at large chord rotations.

10. Based on the testing of two full-scale specimens (FS-R3.2-N-2, FS-R2.4-S-3), which used PVC pipes with nominal diameters of 2.5 inches and 3 inches, respectively, it was determined that DBCBs can accommodate four circular penetrations for utility ducts. These penetrations can be placed at the ends of the coupling beam at the UCS layer and the midspan of the upper and lower beams simultaneously, without compromising the shear strength, stiffness, and ductility of the DBCB. When PVC pipes are located at the UCS layer, it is recommended to use PVC pipes with a nominal diameter of no more than 3 inches. Using larger dimensions of PVC pipes leads to increased slip resistance, which hinders or delays the propagation of horizontal cracks towards the beam-to-wall interface (as illustrated in Fig. 4.3 (g)). Consequently, this facilitates the development of diagonal cracks near the beam-to-wall interface. Additionally, it is recommended to position the PVC pipes near the beam-to-wall interface, ideally within a distance of 5 inches from the end of the beam (Figs. 3.7 (a) and 3.16 (a)). This arrangement helps minimize any hindrance to the propagation of the interface crack at the UCS layer. For PVC pipes located at the midspan of the upper and lower beams, it is recommended to position the PVC pipe at the mid-height of each beam. The diameter of the PVC pipes can be determined by the maximum allowed spacing of the transverse reinforcement.

11. The testing of specimens with a slab (HS-R2.4-S-1, FS-R2.4-S-3) revealed that the presence of the slab caused a minor delay in the concentration of diagonal shear cracks within the UCS layer during the initial cyclic loading. This delay was attributed to the difference in level between the UCS layer and the elastic neutral axis of the DBCB with the slab. However, this delay did not result in an incomplete split of the UCS.

12. VecTor3 software was used to develop FE simulation model to predict the performance of DBCBs and facilitate the specimen design. After determining the material models and analysis parameters, nonlinear FE analyses were carried out to determine the spacing of transverse

reinforcement of the coupling beam and to compare with test results of three specimens. FE analysis results showed very similar DBCB rotational capacities even though FE model exhibited the higher shear strengths than test results. The FE models also appropriately simulated the crack patterns and failure mode of each DBCB. The FE results indicate that the behavior of DBCB with a width equivalent to that of the adjacent walls (24-in.) is very similar to the behavior of the DBCB with a reduced width of 10 in., which was used in the full-scale specimens. This indicates that the reduced width used in the experimental tests does not affect the behavior the DBCB. In addition, from FE simulation results, it was found that the behavior of PVC pipes has a major effect on the performance of DBCBs. Thus, it is recommended that PVC pipes at the UCS layer should be placed as close as possible to the beam-to-wall interface to minimize the inverse impact of PVC pipes on the behavior of DBCBs.

13. The effective flexural stiffness (E_cI_{eff}) for the DBCBs tested in this study was determined by calculating the secant stiffness associated with 67% ($2/3V_{\max}$) of the maximum shear force. Analysis of the limited experimental tests conducted in this study, as well as prior tests on DBCBs (Choi et al., 2018, 2020), revealed that full-scale DBCBs exhibited higher stiffness values compared to half-scale DBCBs. Additionally, DBCBs with higher aspect ratios demonstrated lower effective initial stiffness (K_{eff}) values than those with lower aspect ratios. These findings are consistent with the results obtained from coupling beam tests (CCB and DCB) (Naish et al., 2009, Weber-Kamin et al., 2020, and Abdullah et al., 2023). Furthermore, the average normalized effective stiffness (E_cI_{eff}/E_cI_g) trends observed in DBCBs, based on the aspect ratio (l_n/h), exhibit similarities to those reported for DCBs by Abdullah et al. (2023). In particular, the normalized effective stiffnesses of the full-scale DBCBs (FS-R3.2-NS-2 and FS-R2.4-ES-3) were found to be very close to the values obtained from the relation $E_cI_{eff}/E_cI_g = 0.07\ l_n/h \leq 0.3$ proposed by LATBSDC and TBI (LATBSDC, 2020; TBI, 2017) for performance-based seismic design. However, it is necessary to conduct further studies involving full-scale DBCBs with various aspect ratios to validate this observation.

14. No evidence indicates higher strength rebars (Gr. 80) have any adverse impact on shear strength and ductility when compared to Grade 60 rebars.

15. After analyzing the test results, modifications have been made to the design procedure originally proposed by Choi and Chao (2020). Fig. 6.1 presents the updated flowchart for DBCB design, while Fig. 6.2 provides the reinforcement details for DBCB. An example of full-scale DBCB design, following the procedure outlined in Figs. 6.1 and 6.2, can be found in Appendix D.

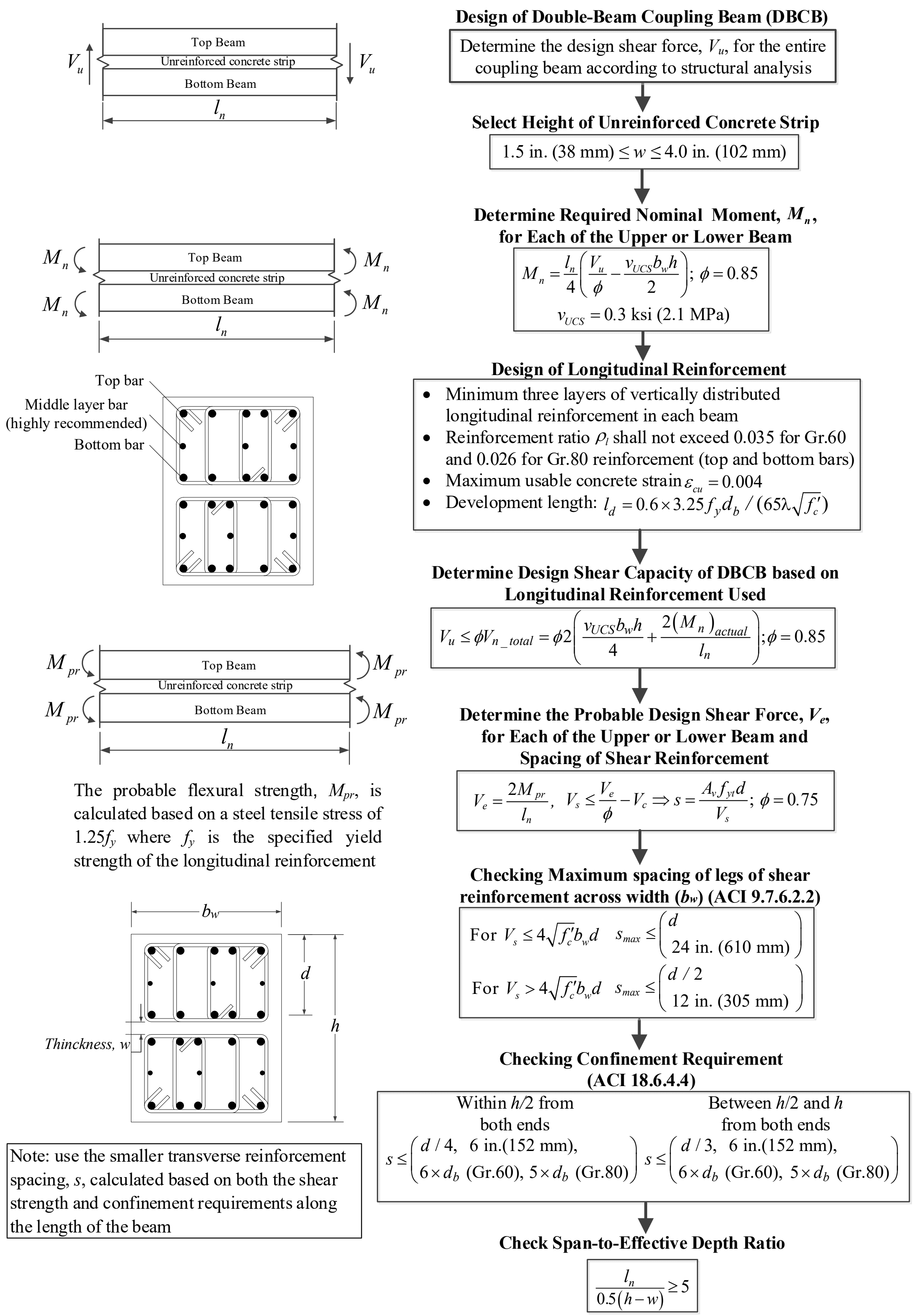

Fig. 6.1 Updated flowchart for DBCB design

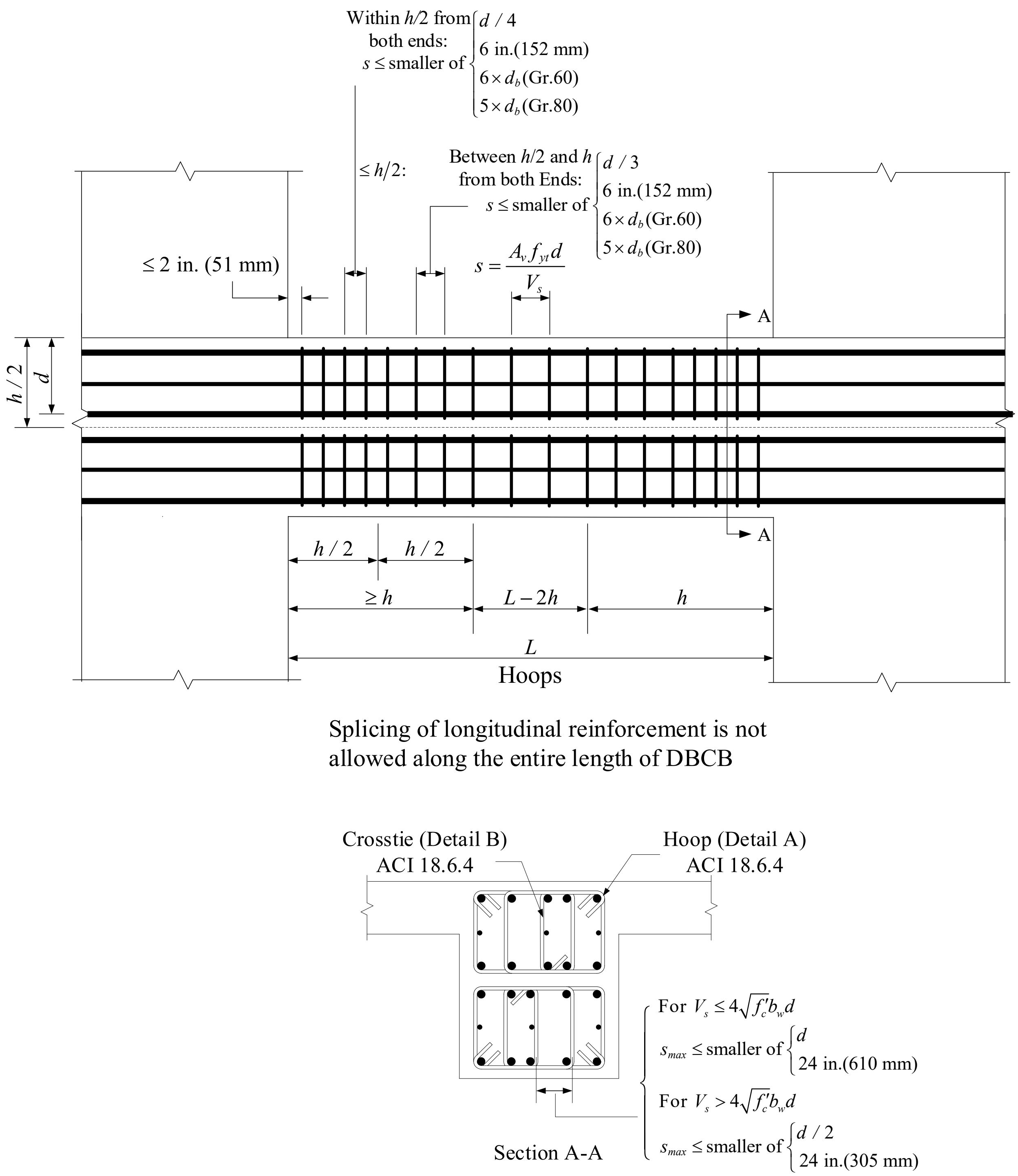

Fig. 6.2 Reinforcement details for DBCB

REFERENCES

1. ACI 318. (1999), "Building Code Requirements for Structural Concrete (ACI 318-99) and Commentary (ACI 318R-99)," American Concrete Institute, Farmington Hills, Michigan.
2. ACI Committee 318. (2005), "Building Code Requirements for Structural Concrete (ACI 318-05) and Commentary (ACI 318R-05)," American Concrete Institute, Farmington Hills, Michigan.
3. ACI Committee 318. (2008), "Building Code Requirements for Structural Concrete (ACI 318-08) and Commentary (ACI 318R-08)," American Concrete Institute, Farmington Hills, Michigan.
4. ACI Committee 318. (2014), "Building Code Requirements for Structural Concrete (ACI 318-14) and Commentary (ACI 318R-14)," American Concrete Institute, Farmington Hills, Michigan.
5. ACI Committee 318. (2019), "Building Code Requirements for Structural Concrete (ACI 318-19) and Commentary (ACI 318R-19)," American Concrete Institute, Farmington Hills, Michigan.
6. AISC. (2017), "Steel Construction Manual," 15th Edition, American Institute of Steel Construction, Chicago.
7. ASTM C39. (2018), "Standard Test Methods for Compressive Strength of Cylindrical Concrete Specimens," ASTM International, West Conshocken, PA.
8. Abdullah, S.A., Rafiq, S.K., Fields, D., and Wallace, J.W. (2023), "Seismic Performance of Diagonally Reinforced Concrete Coupling Beams with Penetrations," ACI Structural Journal, V. 120, No. 1, January 2023.
9. Aghdasi, P., Heid A. E., and Chao, S.-H. (2016), "Developing Ultra-High-Performance Fiber-Reinforced Concrete for Large-Scale Structural Applications," *ACI Materials Journal*, V. 113, No. 5, September-October 2016, pp. 559-570.
10. Ameen, S. (2019), "Diagonally Reinforced Concrete Coupling Beams with High-Strength Steel Bars," Doctoral dissertation, University of Kansas, Lawrence, KS, 343 pp.
11. Ameen, S., Lequesne, R.D., and Lepage, A. (2020), "Diagonally Reinforced Concrete Coupling Beams with Grade 120 (830) High-Strength Steel Bars," ACI Structural Journal, V. 117, No. 6, November 2020.

12. Barbachyn, S. M., Kurama, Y. C., and Novak, L. C. (2012), "Analytical Evaluation of Diagonally Reinforced Concrete Coupling Beams under Lateral Loads," ACI Structural Journal, V. 109, No. 4, July-Aug., pp. 497-507.
13. Barney, G. B., Shiu, K. N., Rabbat, B. G., and Fiorato, A. E. (1976), "Earthquake Resistant Structural Walls – Tests of Coupling Beams (Progress Report)," Portland Cement Association, Skokie, Illinois.
14. Barney, G.B., Shiu, K. N. Rabbat, B. G., Fiorato, A. E., Russell, H. G., and Corley, W. G. (1980), "Behavior of Coupling Beams Under Load Reversals," Portland Cement Association Bulletin RD068.01B, Skokie, Illinois.
15. Binney, J. R. (1972), "Diagonally Reinforced Coupling Beams," MS Thesis, University of Canterbury, Christchurch, New Zealand.
16. Canbolat, B. A., Parra-Montesinos, G. J., and Wight, J. K. (2005), "Experimental Study on Seismic Behavior of High-Performance Fiber-Reinforced Cement Composite Coupling Beams," ACI Structural Journal, 102(1), 159–166.
17. Choi, Y.-J., Hajyalikhani, P., and Chao, S.-H. (2018), "Seismic Performance of an Innovative RC Coupling Beam – The Double-Beam Coupling Beam," ACI Structural Journal, V. 115, No. 1, January 2018, pp. 113-125.
18. Choi, Y.-J. and Chao, S.-H. (2019), "Balanced Damage Concept for Beam-to-Column Connections of SMFs Using HPFRC," ACI Structural Journal, V. 116, No. 1, January 2019, pp. 237-249.
19. Choi, Y.-J. and Chao. S.-H. (2020), "Analysis and Design of Double-Beam Coupling Beams (DBCBs)," ACI Structural Journal, V. 117, No. 5, September 2020, pp. 79-95.
20. CRSI Design Guide. (2020), "Design Guide on the ACI 318 Building Code Requirements for Structural Concrete," Concrete Reinforcing Steel Institute.
21. Dassault Systèmes Simulia. (2019), "ABAQUS user's manual." V. 6.14. Pawtucket, RI: Dassault Systèmes Simulia.
22. El Mohandes, F. and Vecchio, F. J. (2013), "VecTor3: A. User's Manual; B. Sample Coupled Thermal and Structural Analysis," Dept. of Civil Engineering, University of Toronto. Toronto, Canada.
23. Galano, L., and Vignoli, A. (2000), "Seismic Behavior of Short Coupling Beams with Different Reinforcement Layouts," ACI Structural Journal, V. 97, No. 6, Nov.-Dec., pp. 876-885.

24. Gong, B., Shahrooz, B. M., and Gillum, A. J. (1998), "Cyclic Response of Composite Coupling Beams," ACI Special Publication, 174, 89-112.
25. Harries, K. A., Mitchell, D., Cook, W. D., and Redwood, R. G. (1993), "Seismic Response of Steel Beams Coupling Concrete Walls," Journal of Structural Engineering, 119(12), 3611-3629, 1993.
26. Harries, K. A., Fortney, P. J., Shahrooz, B. M.; and Brienen, P. J. (2005), "Practical Design of Diagonally Reinforced Concrete Coupling Beams—Critical Review of ACI 318 Requirements," ACI Structural Journal, V. 102, No. 6, Nov.-Dec., pp. 876-882.
27. Harries, K. A., and McNeice, D. S. (2006), "Performance-Based Design of High-Rise Coupling Wall Systems," Structural Design of Tall and Special Buildings, V. 15, No. 3, pp. 289-306.
28. Lam, W.-Y., Su, R. K.-L., and Pam, H.-J. (2005), "Experimental Study on Embedded Steel Plate Composite Coupling Beams," Journal of Structural Engineering, ASCE, 131(8), 1294-1302.
29. LATBSDC. (2020), "An Alternative Procedure for Seismic Analysis and Design of Tall Buildings Located in the Los Angeles Region," Los Angeles Tall Buildings Structural Design Council, Los Angeles, CA.
30. Lequesne, R., Parra-Montesinos, G. J., and Wight, J. K. (2009), "Test of a Coupled Wall with High-Performance Fiber-Reinforced Concrete Coupling Beams," ACI Special Publication (SP265-01), 1-18.
31. Lequesne, R., Setkit, M., Parra-Montesinos, G., and Wight, J. K. (2010), "Seismic Detailing and Behavior of Coupling Beams with High-Performance Fiber Reinforced Concrete," ACI Special Publication (SP 272-11), 189-204.
32. Lequesne, R. (2011), "Behavior and Design of High-Performance Fiber Reinforced-Concrete Coupling Beams and Coupled-Wall Systems," PhD dissertation, The University of Michigan, Ann Arbor, MI, 277 pp.
33. Lim, E., Hwang, S.-J., Cheng, C.-H., and Lin, P.-Y. (2016), "Cyclic Tests of Reinforced Concrete Coupling Beam with Intermediate Span-Depth Ratio," ACI Structural Journal, 113(3), 515-524.

34. Mihaylov, B., Trandafir, A., Palios, X., Strepelias, E., and Bousias, S. (2021), “Effect of Axial Restraint and Loading History on the Behavior of Short Reinforced Concrete Coupling Beams,” ACI Structural Journal, V. 118, No. 4, July 2021.
35. Motter, C. J., Fields, D. C., Hooper, J. D., Klemencic, R., and Wallace, J. W. (2017), “Steel-Reinforced Concrete Coupling Beams. I: Testing,” ASCE Journal of Structural Engineering, 143(3).
36. Naaman, A. E. and Chao, S.-H. (2022), *Prestressed Concrete Analysis and Design: Fundamentals*, 4th Edition, Technopress 3000, 2022, 1433 pages.
37. Naish, D. Wallace, J., Fry, J. A. and Klemencic, R. (2009), “Reinforced Concrete Link Beams: Alternative Details for Improved Constructability,” Report to Charles Pankow Foundation, UCLA-SGEL, 103 pp.
38. Naish, D., Fry, J. A.; Klemencic, R., and Wallace, J. (2013), “Reinforced Concrete Coupling Beams—Part I: Testing,” ACI Structural Journal, V. 110, No. 6, Nov.-Dec., pp. 1057-1066.
39. Nojavan, A., Schultz, A. E., Chao, S.-H., and Haselton, C. (2017), “Influence of Cross Sectional Size on Seismic Performance of Columns,” ACI Structural Journal, V. 114, No. 2, March-April, 2017, pp. 311-321.
40. Overby, D., Kowalsky, M., and Seracino, R. (2015), “A706 Grade 80 Reinforcement for Seismic Applications,” Technical Report No. CA16-2563, California Department of Transportation.
41. Park, W.-S. and Yun, H.-D. (2005), “Seismic Behaviour of Steel Coupling Beams Linking Reinforced Concrete Shear Walls,” Engineering Structures, 27, 1024-1039.
42. Park, R. (1988), “Ductility Evaluation from Laboratory and Analytical Testing,” Proceedings of Ninth World Conference on Earthquake Engineering (9WCEE), August 1988, Vol VIII, pp. 605-616.
43. Parra-Montesinos, G. J. (2005), “High-Performance Fiber-Reinforced Cement Composites: An Alternative for Seismic Design of Structures,” ACI Structural Journal, 102(5), 668-675.
44. Paulay, T. (1969), “The Coupling of Shear Walls,” PhD Dissertation, University of Canterbury, Christchurch, New Zealand.
45. Paulay, T. (1971), “Coupling beams of reinforced concrete shear walls,” Journal of the Structural Division, ASCE; 97(ST3): 843-862.

46. Paulay, T., and Binney, J. R. (1974) “Diagonally Reinforced Concrete Beams for Shear Walls,” Shear in Reinforced Concrete, SP-42, V. 2, American Concrete Institute, Farmington Hills, Mich, pp. 579-598.
47. PEER TBI. (2017), “Guidelines for Performance-Based Seismic Design of Tall Buildings,” Report No. 2017/06, Tall Buildings Initiative, Pacific Earthquake Engineering Research Center, University of California, Berkeley, Berkeley, CA, 147 pp.
48. Poudel, A., Ameen, S., Lequesne, R.D., and Lepage, A. (2021), “Diagonally Reinforced Concrete Coupling Beams: Effects of Axial Restraint,” ACI Structural Journal, V. 118, No. 6, November 2021.
49. Setkit, M. (2012), “Seismic Behavior of Slender Coupling Beams Constructed with High-Performance Fiber-Reinforced Concrete,” PhD Dissertation. The University of Michigan.
50. StructurePoint. (2019), *spColumn Engineering Software Program Manual*, v7.00.
51. Tegos, I. A. and Penelis, G. G. (1988) “Seismic Resistance of Short Columns and Coupling Beams Reinforced with Inclined Bars,” ACI Structural Journal, 85(1), 82-88.
52. Teshigawara, M.; Kato, M.; Sugaya, K.; and Matsushima, Y., (1998), “Energy Absorption Mechanism and the Fluctuation of Shear Force in the Coupled Shear Walls,” Structural Engineering World Wide 1998—Proceedings, Paper Number T-186-5, Elsevier Science Ltd., 8 pp.
53. Tassios, T. P., Moretti, M., and Bezas, A. (1996), “On the Behavior and Ductility of Reinforced Concrete Coupling Beams of Shear Walls,” ACI Structural Journal, V. 93, No. 6, Nov.-Dec., pp. 711-720.
54. Visnjic, T., Antonellis, G., Panagiotou, M., and Moehle J. P. (2016), “Large Reinforced Concrete Special Moment Frame Beams under Simulated Seismic Loading,” ACI Structural Journal, V. 113, No. 3, May-Jun 2011, pp. 469-480.
55. Weber-Kamin, A.S., Lequesne, R.D., Lepage, A. (2020), “Reinforced Concrete Coupling Beams with High-Strength Steel Bars,” University of Kansas Center for Research, Inc., SM Report No.143, 602 pp.
56. Wong, P. S. and Vecchio, F. J. (2002), *VecTor2 & Formworks User’s Manual*, Dept. of Civil Engineering, University of Toronto. Toronto, Canada.

APPENDIX A: CONSTRUCTION PROCESS

The construction, casting, and testing of all the specimens took place at the Civil Engineering Laboratory Building (CELB) located at the University of Texas at Arlington.

A.1 Full-scale DBCB with 3.2 aspect ratio (FS-R3.2-N-2)

A.1.1 Formwork

Fig. A.1 provides an overview of the formwork used for the full-scale double-beam coupling beam (DBCB) with a 3.2 aspect ratio. The formwork consists of four main parts: the loading block, DBCB, top big block, and bottom big block. To accommodate the limited crane capacity of 15 tons for disposing of the tested DBCB specimen, the big block was divided into a top big block and a bottom big block. Each part of the formwork was constructed separately and then assembled along with the reinforcement cages and PVC pipes required for the post-tensioning rods. Once all the pieces were assembled, 4 in. × 4 in. lumbers were added around the loading block and top big block to withstand the pressure exerted by the concrete during casting. The formwork pieces were made using plywood and 2 in. × 4 in. lumbers, connected using 3/8 in. threaded rods. In Fig. A.2, the formwork pieces for the DBCB specimen are illustrated. Wooden disks, matching the nominal circle of the PVC pipes, were attached to the bottom parts of the loading block formwork and big block formwork to securely hold the PVC pipes in place during concrete placement.

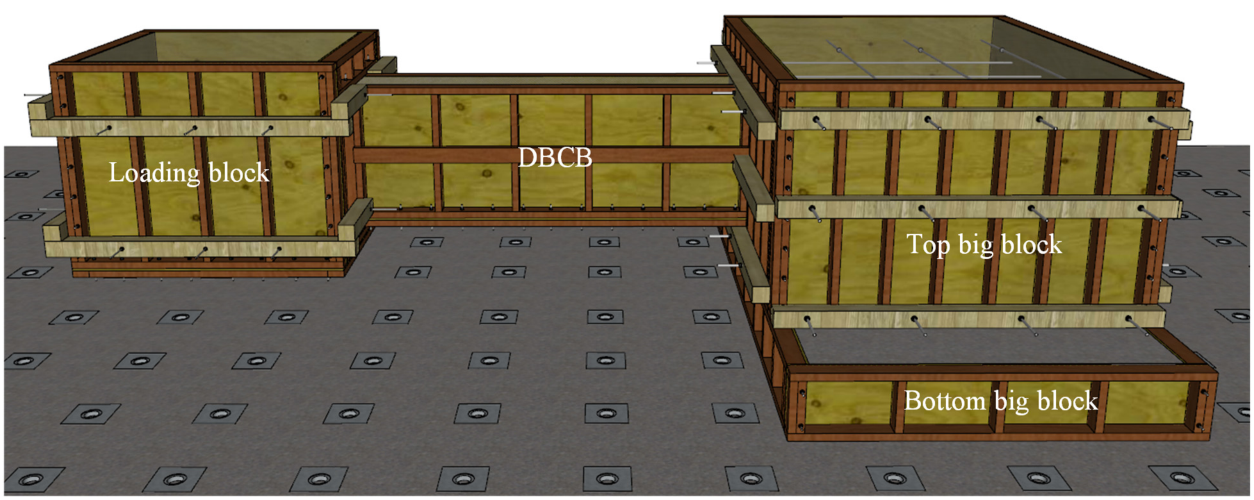

Fig. A.1 Formwork illustration of full-scale DBCB with 3.2 aspect ratio

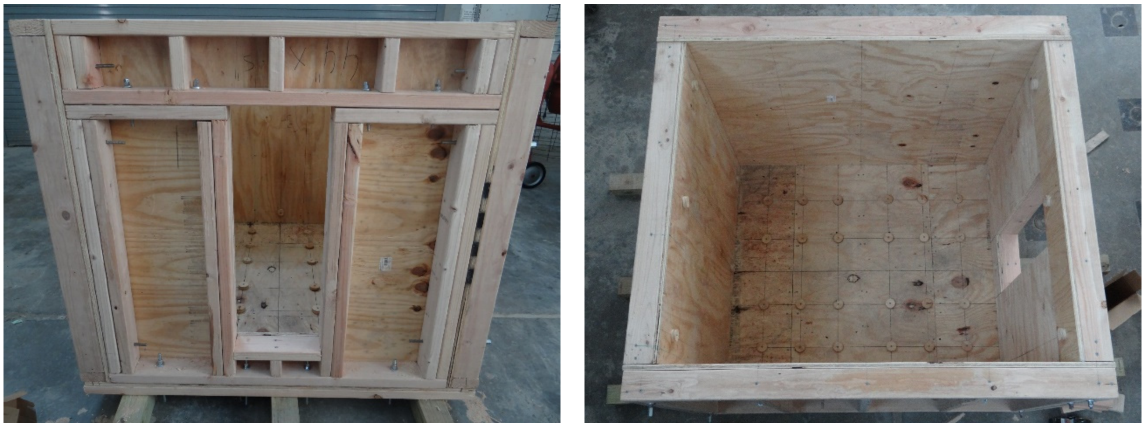

(a)

(b)

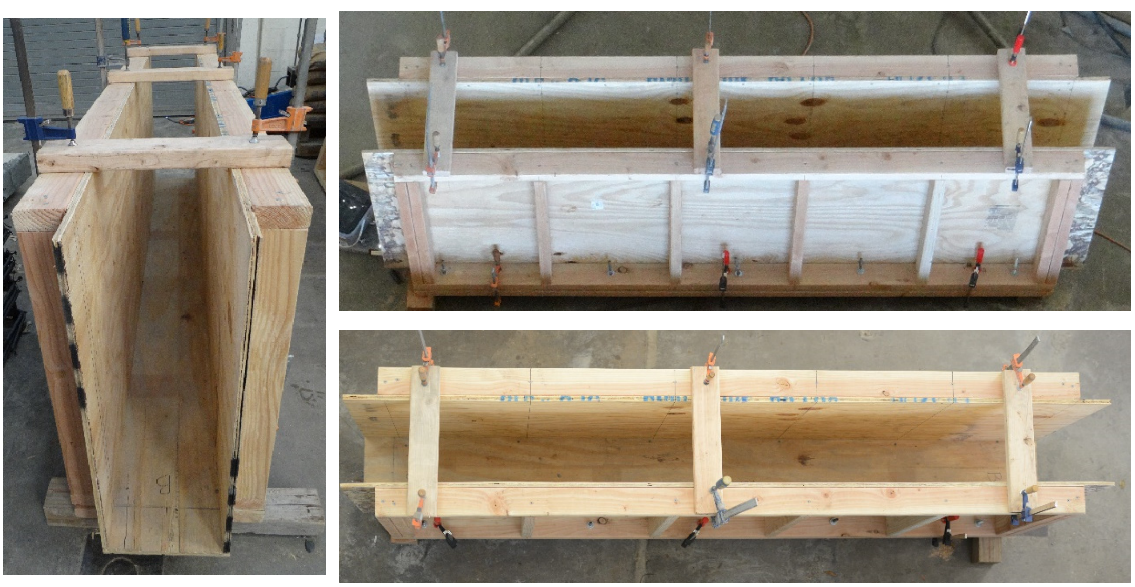

(c)

Fig. A.2 Formwork pieces : (a) Loading block, (b) Big block, and (c) Coupling beam

A.1.2 Reinforcement Cage Fabrication

According to reinforcement details described in Figs. 3.7 and 3.18, reinforcement cages for each formwork of the specimen were fabricated using hoops and reinforcing bars at CELB. Fig. A.3 shows the reinforcement cage fabrication of the loading block. As shown in Fig. A.3, the outside reinforcement cage was first fabricated and placed in the formwork using the 15-ton crane housed in CELB. Afterwards, the inside hoops and vertical reinforcing bars were installed, which were used to confine the concrete around the post-tensioning rods. Next, PVC pipes were put on the wooden disks that were attached at the bottom of the formwork. Fig. A.3 (c) shows the completed formwork for loading block. As previously mentioned, the big block was divided into two parts due to the limited crane capacity in CELB. Fig. A.4 illustrates the process of fabricating the reinforcement cage for the bottom part of the big block. In Figs. A.4 (a) and (b), the reinforcement cage was constructed and positioned within the formwork using a crane. Subsequently, as shown in Figs. A.4 (c) and (d), the bottom part of the big block was widened. This adjustment was made to facilitate the separation of the top part from the bottom part once the experimental test was completed.

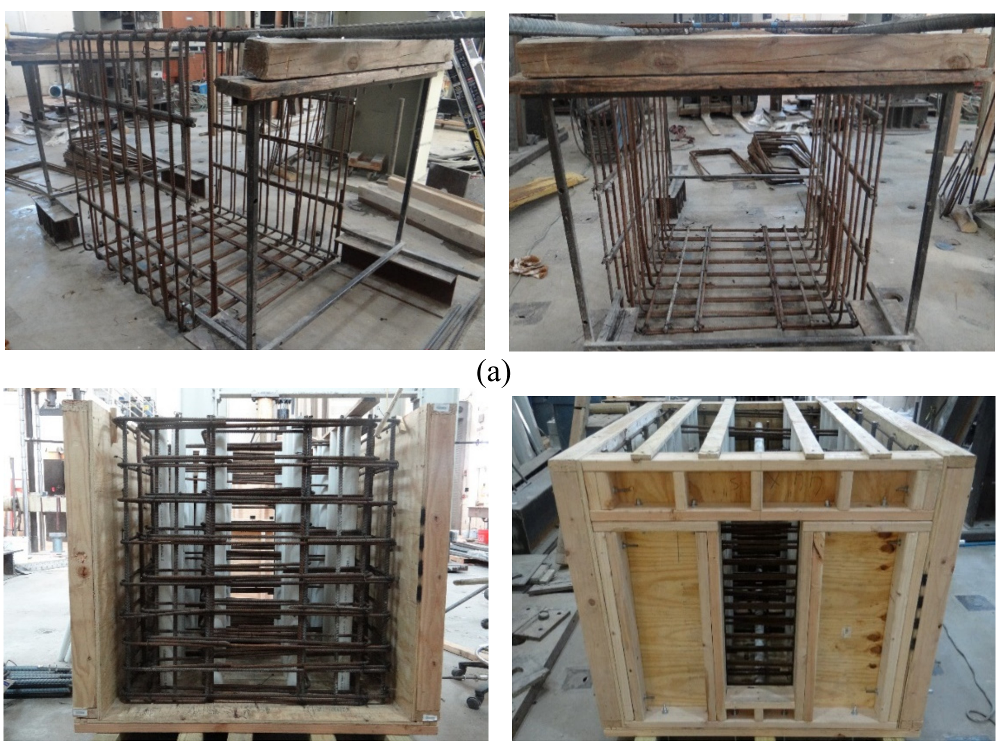

(a)

(b) (c)

Fig. A.3 Reinforcement cage fabrication of the loading block: (a) Outside reinforcement cage, (b) Reinforcement cage placed in the formwork, and (c) Completed loading block

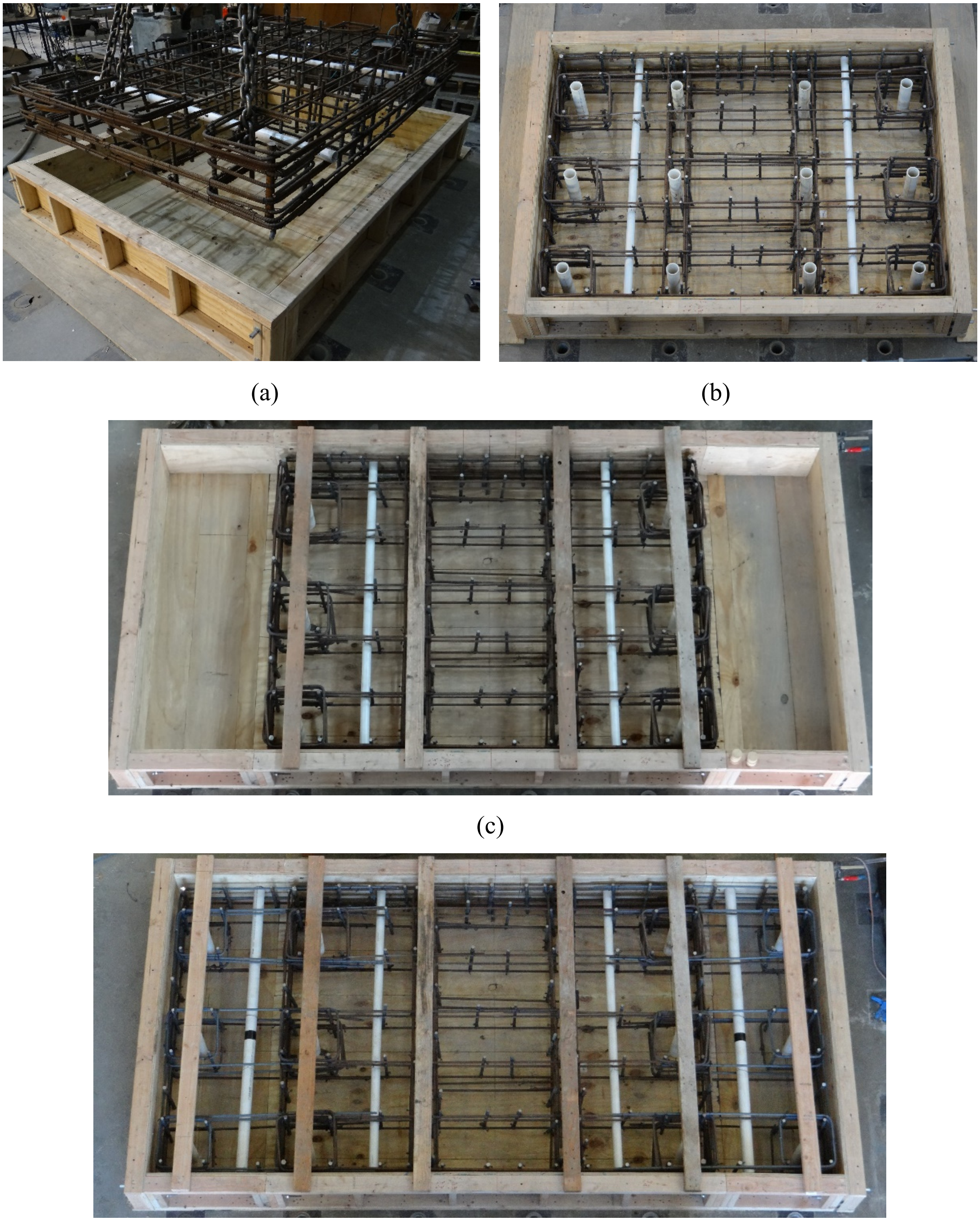

(a) (b)

(c)

(d)

Fig. A.4 Reinforced cage fabrication of the large bottom block: (a) Reinforcement cage, (b) Placement of reinforcement cage, (c) Extension of the formwork, and (d) Completed large bottom big block

The reinforcement cage for the top big block was constructed by layering closed hoops using a crane, as shown in Fig. A.5 (a). Subsequently, the cage reinforcement was finalized by securing the hoops to the vertical reinforcing bars using steel tie wires, as shown in Fig. A.5 (b). Fig. A.5 (c) presents the fully completed reinforcement cage for the top big block.

(a)

(b)

(c)

Fig. A.5 Reinforcement cage fabrication of the top big block: (a) Placement of hoop frames, (b) Tying hoop frames with vertical reinforcing bars, and (c) Completed reinforcement cage

DBCB comprises two reinforcement cages, as illustrated in Fig. 3.6. The construction of the top and bottom cages was carried out separately, as depicted in Fig. A.6. In Fig. A.6 (a), transverse hoops were inserted into the top longitudinal bars of each cage, following the specified spacing according to the DBCB design. Subsequently, the bottom and middle longitudinal bars were positioned, and steel tie wires were used to secure the longitudinal bars to the hoops, as shown in Fig. A.6 (b). Fig. A.6 (c) shows the two fully assembled DBCB reinforcement cages. It should be noted that the cages were built after mounting strain gauges on the longitudinal bars and hoops. Careful attention was given during the fabrication process to prevent any damage to the strain gauges and their wires.

(a)

(b)

(c)

Fig. A.6 Reinforcement cage fabrication of DBCB: (a) Placement of stirrup hoops (b) Tying stirrup hoops with longitudinal bars (c) Completion of two reinforcement cages

A.1.3 Assembly

The formwork and reinforcement cages for the DBCB specimen were assembled step by step, starting with the big block. Fig. A.7 (a) illustrates the process, where the bottom big block was cast first and allowed to cure before the other formworks and steel cages were added. This sequencing was necessary because the top big block needed to be constructed above the bottom big block. The completed bottom big block was positioned accurately, aligning the PVC pipes with the holes on the strong floor. Once the bottom big formwork was reassembled, a heavy-duty plastic tarpaulin sheet was placed on the surface of the bottom big block. This sheet facilitated the detachment of the top big block from the bottom big block after testing, as shown in Fig. A.7 (b). Following this, the PVC pipes for the top big block were set up vertically. The threaded rods for post-tensioning were inserted into the PVC pipes prior to concrete casting, and they were slightly tightened to maintain their vertical position, as depicted in Fig. A.7 (c). Using a crane, the reinforcement cage for the top big block was then installed, as shown in Fig. A.7 (d). Subsequently, the formwork for the top big block was erected above the formwork of the bottom big block. Horizontal PVC pipes were inserted, as shown in Figure A.7 (e), and a rectangular opening was created to connect the DBCB formwork.

(a)

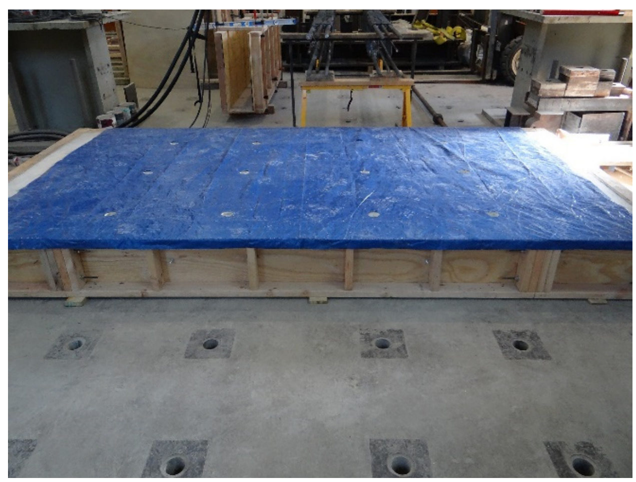

(b)

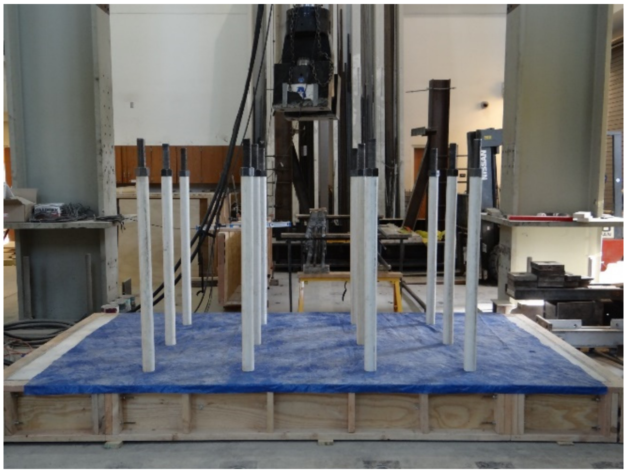

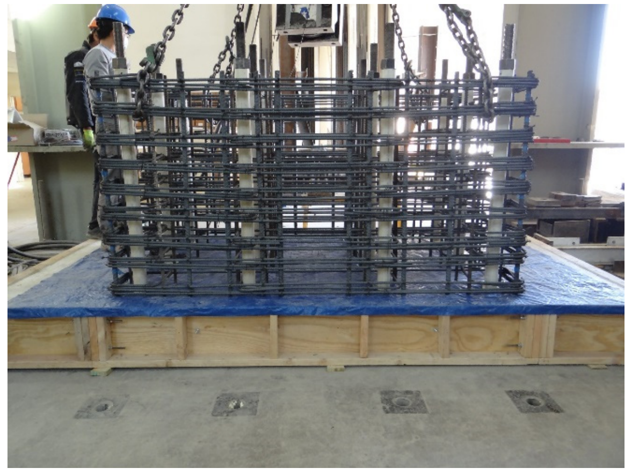

(c) (d)

(e)

Fig. A.7 Big block assembly: (a) Bottom big block placement, (b) Plastic sheet covering, (c) vertical PVC pipes setting up, (d) Reinforcement cage installation, and (e) Formwork erection for the top big block

The formwork and DBCB reinforcement cage were assembled and connected to the completed big block assembly. The process is illustrated in Fig. A.8 (a). Firstly, the bottom piece of formwork was inserted into the big block formwork, and supports were placed beneath the formwork's bottom plate to ensure accurate leveling. Next, the bottom cage was carefully slid into the big block cage using a crane and positioned on the bottom plate with a 0.75 in. gap left for the concrete cover. Following this, one side piece of the formwork was installed, and two PVC pipes, representing utility ducts, were placed on top of the bottom cage, each 3.5 in. away from both ends, as shown in Fig. A.8 (b). Subsequently, the top cage was slid into the big block cage, as shown in Fig. A.8 (c). All the strain gauge cables were then organized and positioned on the floor, ensuring they would pass through the bottom piece of the formwork. Finally, the assembly was completed by installing another side piece of the formwork, as demonstrated in Fig. A.8 (d). Fig. A.8 (e) and Fig. A.8 (f) illustrate a 2 in. gap left for the unreinforced concrete strip (UCS) in the DBCB. This gap represents the distance between the top and bottom transverse reinforcement.

(a)

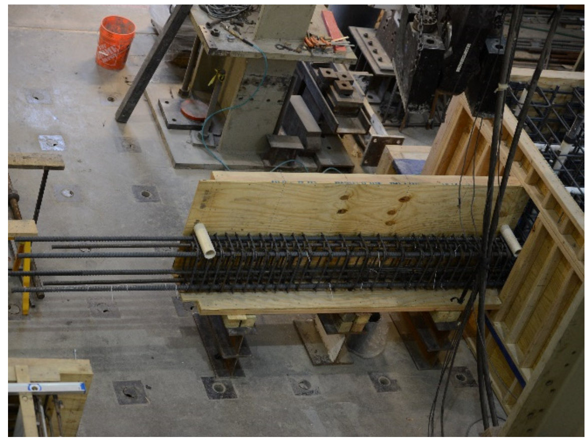

(b)

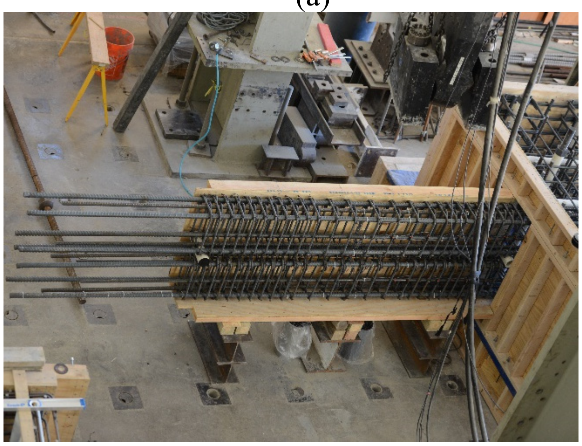

(c)

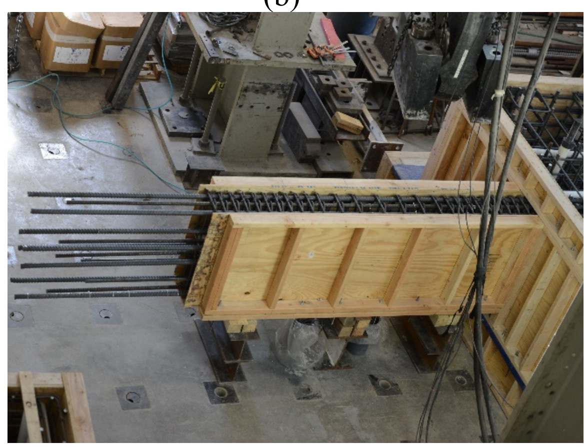

(d)

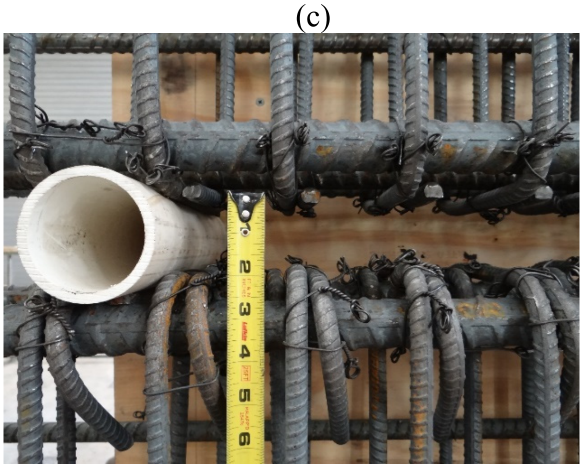

(e)

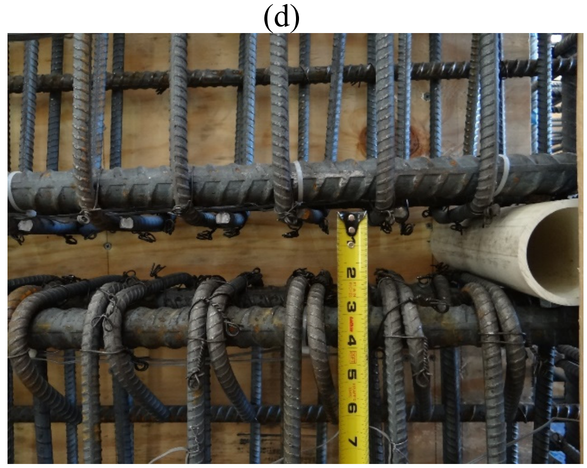

(f)

Fig. A.8 DBCB block assembly: (a) Bottom plate of the formwork, (b) Bottom cage installation, (c) Top cage installation, (d) Completed DBCB, (e) 2 in. gap for UCS (left), and (d) 2 in. gap for UCS (right)

The loading block was combined with the assembled DBCB block using a similar method. Fig. A.9 (a) illustrates the placement of steel supports on the floor to horizontally connect the loading block to the DBCB block. Next, the bottom, side, and front pieces of the formwork were assembled, as shown in Fig. A.9 (b). With the assistance of a crane, the reinforcement cage of the loading block was carefully positioned to prevent any damage to the strain gauges mounted on the longitudinal bars, as depicted in Fig. A.9 (c). Finally, the loading block was completed by installing the remaining formwork plates and PVC pipes, as shown in Fig. A.9 (d). To ensure the formwork could withstand the lateral pressure during concrete pouring without deformation, additional 4 in. × 4 in. lumbers were used around the loading block and top big block. Threaded rods with diameters of 3/4 in. or 3/8 in. were inserted from one side of the formwork to the opposite side to reinforce the formwork and additional lumbers.

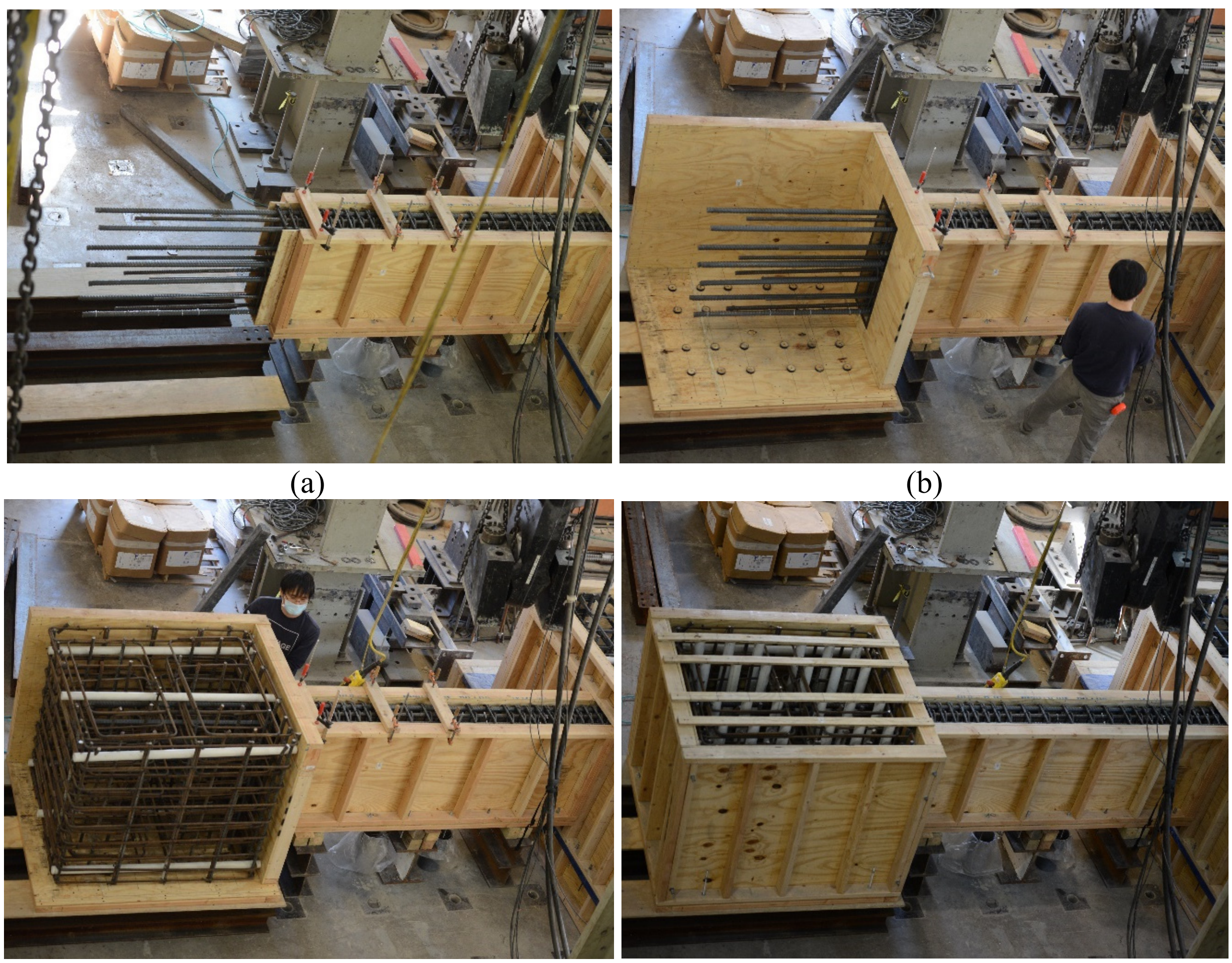

(a) (b)

(c) (d)

Fig. A.9 Loading block assembly: (a) Supports placement, (b) Formwork installation, (c) Reinforcement cage installation, and (d) Completed loading block

Fig. A.10 presents the completed DBCB formwork with a 3.2 aspect ratio.

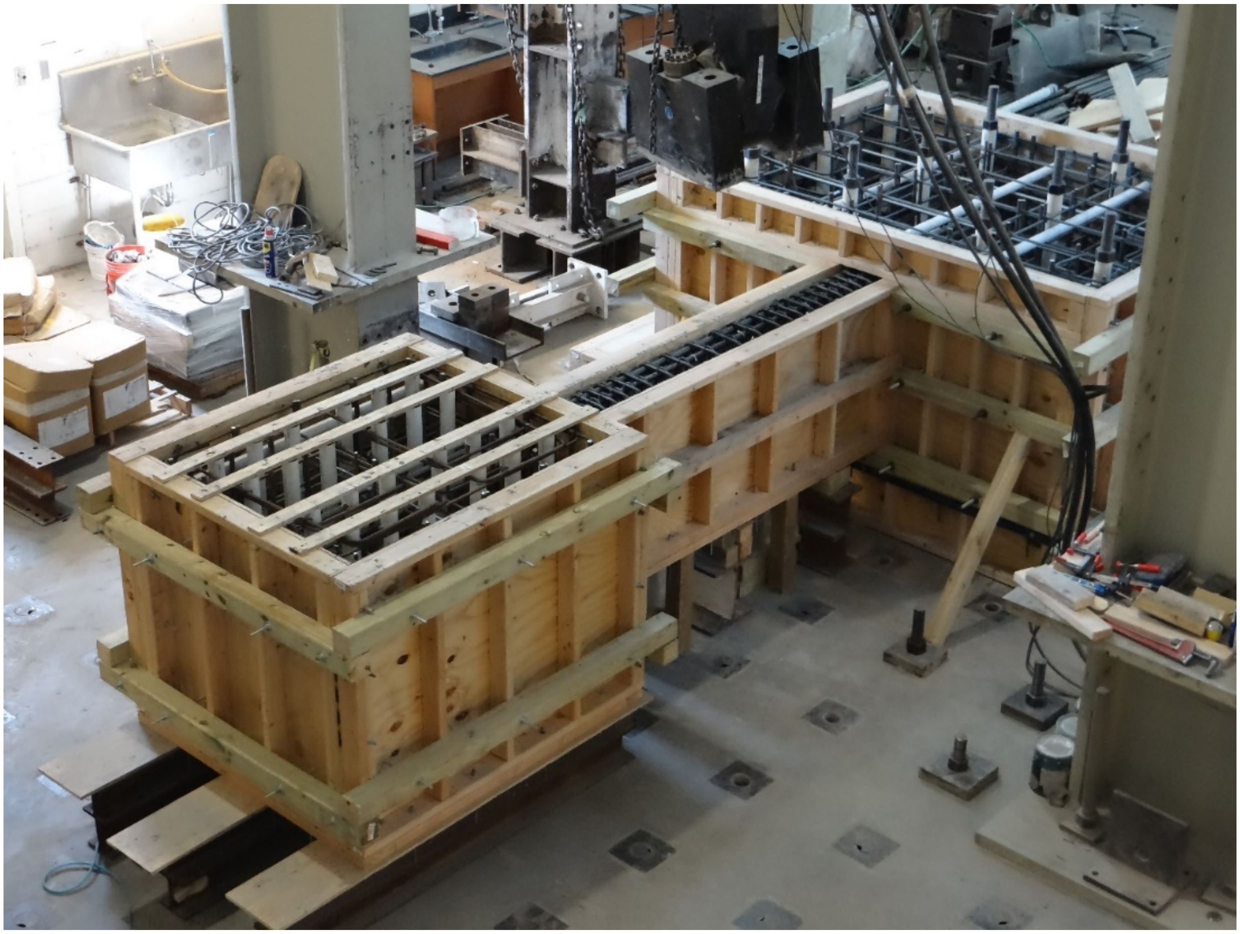

Fig. A.10 Completed DBCB formwork assembly

A.1.4 Concrete casting

As previously mentioned, the bottom big block was cast before the other blocks. Concrete with a design compressive strength of 5 ksi was used for casting the bottom big block. The concrete casting process of the bottom big block is illustrated in Fig. A.11. In the concrete casting process shown in Fig. A.11, concrete was directly poured from a volumetric concrete mixer truck provided by a local supplier. An internal concrete vibrator was employed during the casting to consolidate the concrete and remove any trapped air, ensuring proper settling of the concrete within the formwork. Once the concrete casting was complete, the exposed surfaces of the concrete were covered with a waterproof plastic sheet to retain moisture during the curing process.

Subsequently, the main DBCB specimen, as depicted in Fig. A.10, was cast using concrete with a design compressive strength of 5 ksi. The concrete was supplied by a volumetric concrete mixer truck. Concrete casting photos can be seen in Fig. A.12. The concrete was poured into a large concrete bucket, which was lifted by a crane and poured into the formwork. Similar to the casting of the bottom big block, a concrete vibrator was utilized to consolidate the freshly placed concrete, facilitate the release of entrapped air, enhance the concrete density, and promote bonding with the reinforcing bars. To assess the actual compressive strength of the concrete on the testing day of the coupling beam, twelve 4 in. × 8 in. concrete cylinders were prepared.

To secure the loading block to the built-up wide flange loading beam, significant post-tensioning forces will be applied to the threaded rods passing through them. The nonlinear FE analysis conducted for the DBCB specimen in Section 3.1.1.6 revealed that the top and bottom surfaces of the loading block would experience extremely high stresses around the post-tensioning rods. In response to this, ultra-high-performance fiber-reinforced concrete (UHP-FRC) was used with an anticipated strength of 15 to 20 ksi. To reinforce the area expected to experience high stresses, a layer of UHP-FRC with a thickness of 1.5 in. was cast at both the top and bottom of the loading block. The UHP-FRC used in the study shares a similar composition as reported by Aghdasi et al. (2016) but with a fiber volume fraction of 2%. It includes Type I cement, fly ash, coarse silica sand, fine silica sand, silica fume, ground granulated blast furnace slag, a high-range superplasticizer, high-strength micro steel fibers, and water. These components were carefully mixed using a high-shear pan mixer to ensure a homogeneous mixture. Before pouring the plain concrete, the bottom layer of UHP-FRC was cast. Then, four days after casting the plain concrete, the top layer of UHP-FRC was added. The UHPC casting process is illustrated in Fig. A.13. After a curing period of two weeks, the formwork for the DBCB specimen was removed, and the completed DBCB specimen is shown in Fig. A.14.

Fig. A.11 Concrete casting of the bottom big block

Fig. A.12 Concrete casting of the top big block, the DBCB, and the loading block






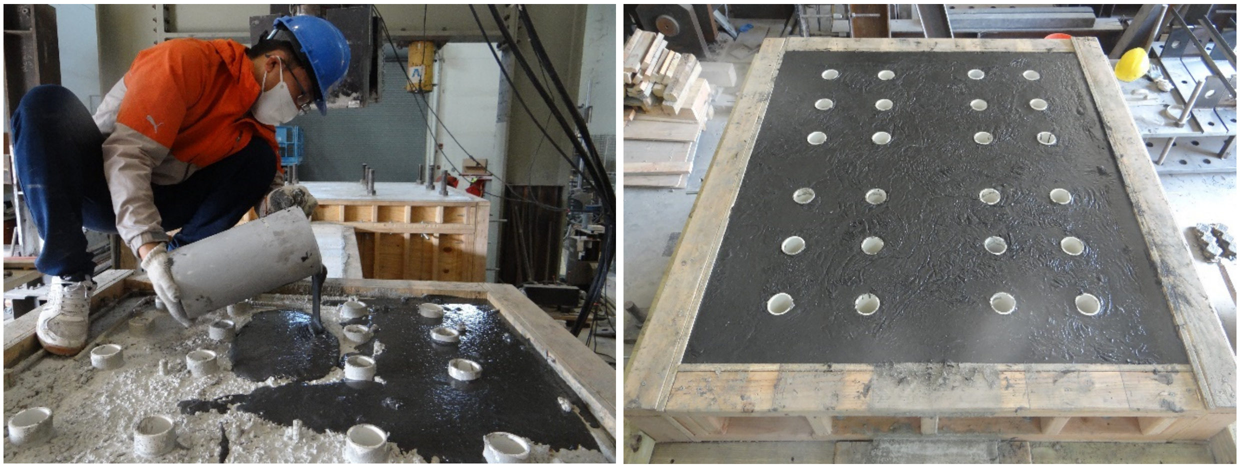

Fig. A.13 UHPC concrete casting of loading block

(a)

(b)

Fig. A.14 Completed DBCB specimen: (a) Isometric views and (b) Close-up view of coupling beam

A.2 Half-scale 2.4 aspect ratio DBCB with the slab (HS-R2.4-S-1)

A.2.1 Formwork

Fig. A.15 demonstrates the construction of formworks for the DBCB specimen, including the loading block, big block, and coupling beam with a slab. These formworks were created using lumbers, plywood, and threaded rods, following the same procedure as the previous specimen. The completed formwork pieces are illustrated in Fig. A.16. It is worth noting that the formwork for the slab was added after assembling both the formworks and reinforcement cages.

Fig. A.15 Formwork illustration of half-scale 2.4 aspect ratio DBCB with a slab

(a) (b)

(c)

Fig. A.16 Formwork pieces: (a) Loading block, (b) Big block (c) Coupling beam

A.2.2 Reinforcement Cage Fabrication

The reinforcement cages for the loading block and big block were constructed horizontally and lifted into place using a crane, as depicted in Fig. A.17. The fabrication process of the DBCB with two steel cages is illustrated in Fig. A.18. As shown in Figs. A.18 (a) and (b), each cage was individually constructed by arranging the longitudinal and transverse reinforcements according to the DBCB design. Fig. A.18 (c) shows the completed two steel cages of the DBCB, with strain gauges installed on the reinforcement prior to the fabrication of the reinforcement cages.

(a)

(b)

(c)

Fig. A.17 Reinforcement cage fabrication of two blocks: (a) Reinforcement cages (b) Completed big block (c) Completed loading block

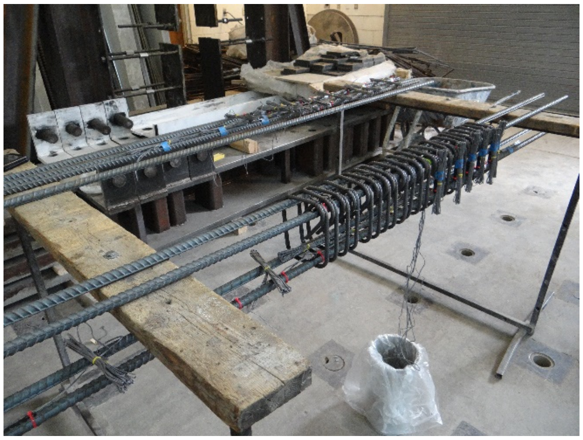

(a)

(b)

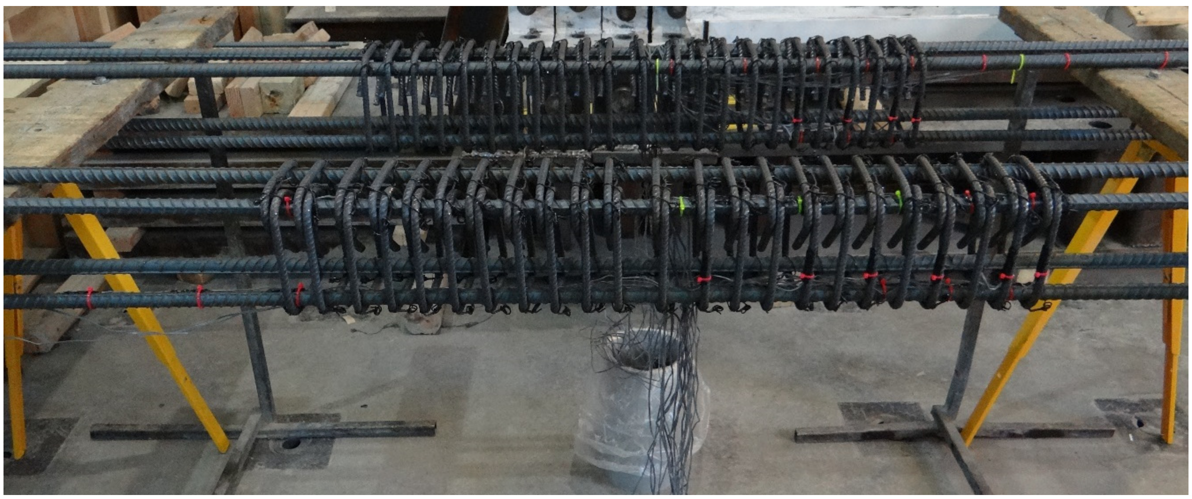

(c)

Fig. A.18 Reinforcement cage fabrication of DBCB: (a) Placement of stirrup hoops (b) Tying stirrup hoops to longitudinal bars (c) Completion of two reinforcement cages

A.2.3 Assembly

Fig. A.19 illustrates the step-by-step assembly process of the formworks and reinforcement cages for the DBCB specimen, including the slab. Firstly, the fabrication of the big block is shown in Fig. A.19 (a). Subsequently, in Fig. A.19 (b), the formwork and two steel cages for the coupling beam are connected to the big block, ensuring that the development length of the beam longitudinal reinforcement is embedded into the big block. In Fig. A.19 (c), it is evident that a 1-inch gap is maintained between the top and bottom cages for the UCS layer. Moving forward, the loading block is attached to the remaining side of the coupling beam in Fig. A.19 (d), and the slab portion is finally positioned parallel to both sides of the coupling beam in Fig. A.19 (e). Fig. A.19 (f) displays the completed assembly of the DBCB specimen with the slab.

(a)

(b)

(c)

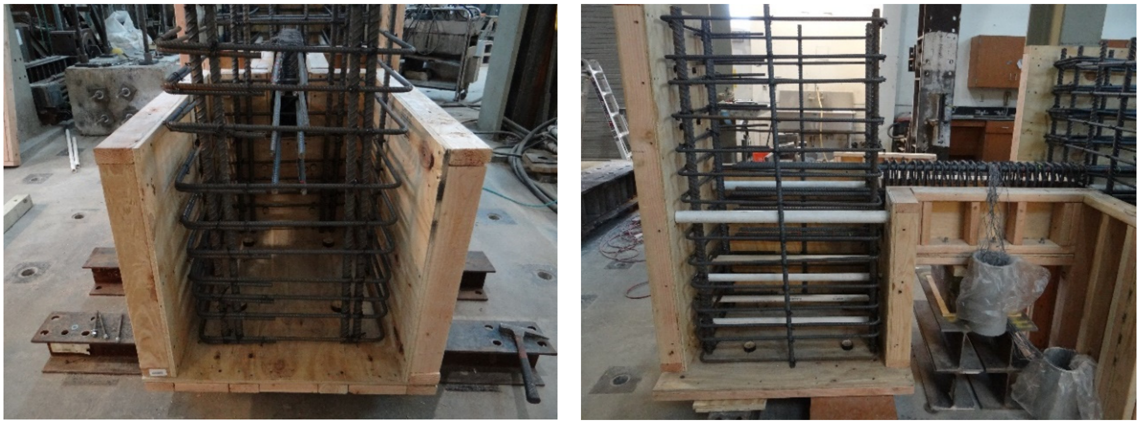

(d)

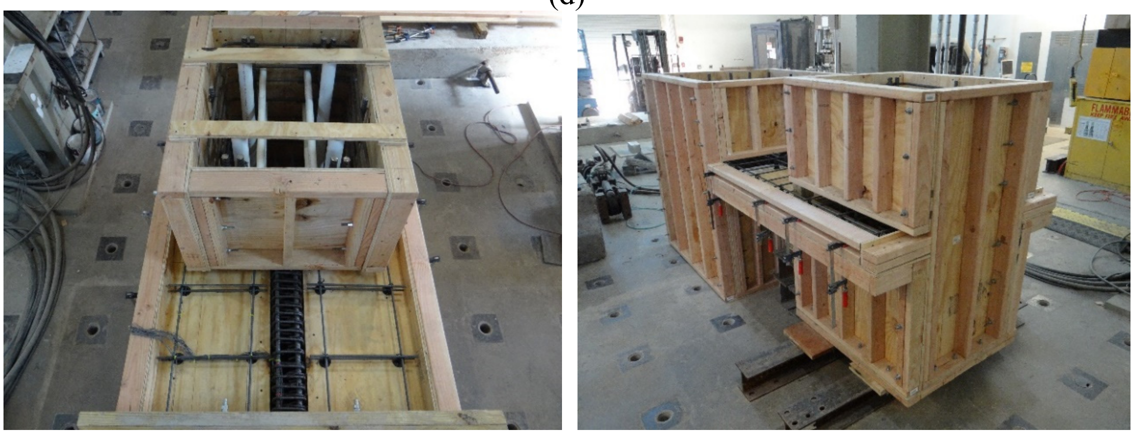

(e)

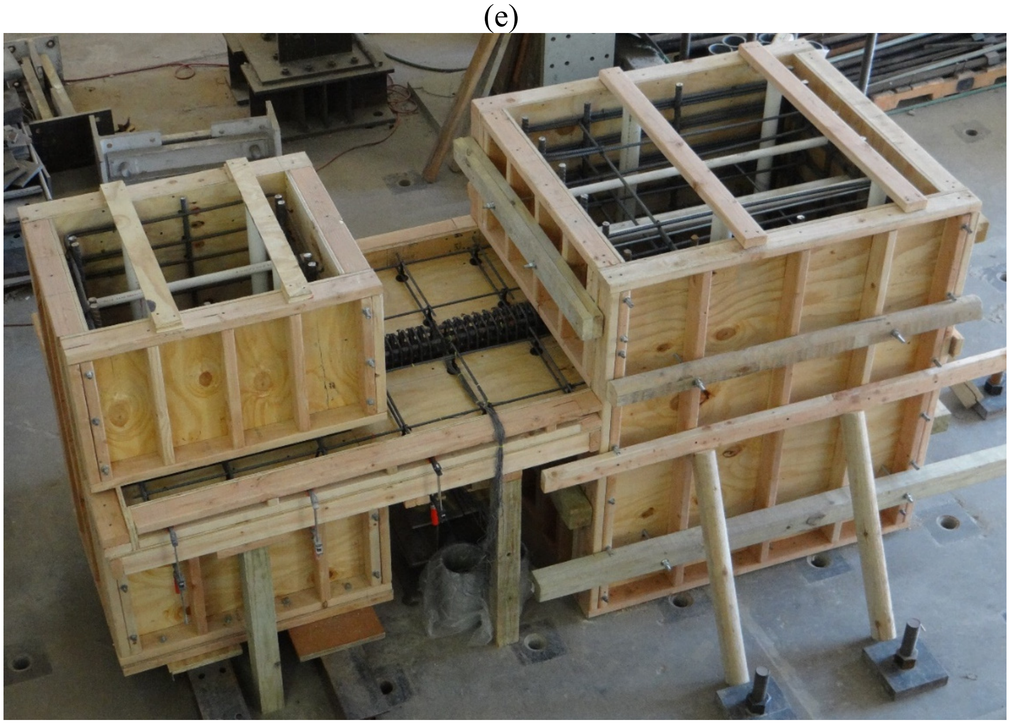

(f)

Fig. A.19 Assembly of DBCB with the slab (a) Big block assembly (b) DBCB assembly (c) Small block assembly (d) 1 in. gap for UCS (e) Slab assembly (f) Completed DBCB formwork assembly

A.2.4 Concrete casting

A local supplier provided ready-mix concrete with a design compressive strength of 5 ksi for casting the specimen. The concrete casting process and the completed specimen are shown in Fig. A.20. As shown in Fig. A.20, the concrete was poured into the formwork using a large concrete bucket. During the casting process, an internal concrete vibrator was used to consolidate the concrete and eliminate any trapped air, ensuring proper settlement within the formwork. Following the concrete casting, the exposed surfaces of the concrete were covered with a waterproof plastic sheet to maintain moisture during the curing period. Additionally, twelve 4 in. × 8 in. concrete cylinders were created to determine the actual compressive strengths of the concrete on the testing day of the coupling beam.

Fig. A.20 Concrete casting and completed DBCB specimen

A.3 Full-scale 2.4 aspect ratio DBCB with the slab (FS-R2.4-S-3)

A.3.1 Formwork

Fig. A.21 showcases the formworks employed for the full-scale 2.4 aspect ratio DBCB specimen with a slab. These formworks, constructed using timbers, plywood, and threaded rods, were also utilized for the fabrication of the loading block, big block, and coupling beam with slab in the DBCB specimen. Notably, as shown in Fig. A.21, the formworks of the two concrete blocks from the first full-scale DBCB specimen were reused with minor adjustments. Fig. A.22 shows the formwork specifically designed for the coupling beam with a slab.

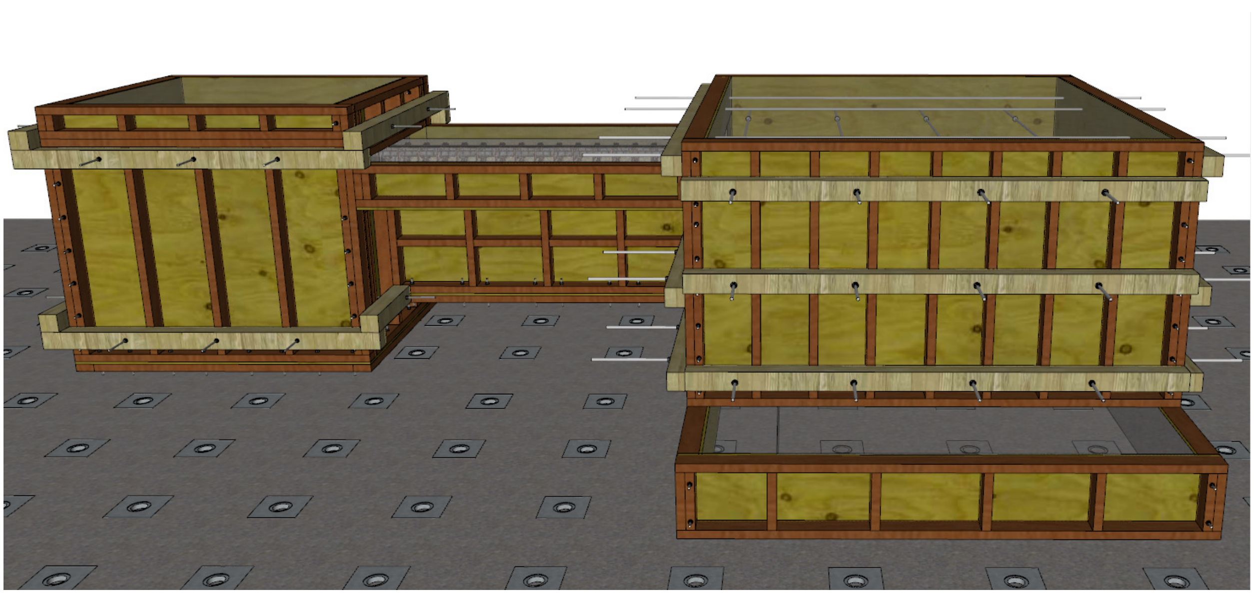

Fig. A.21 Formwork illustration of full-scale 2.4 aspect ratioDBCB with the slab

Fig. A.22 Formwork of coupling beam with slab

A.3.2 Reinforcement cage fabrication

The loading block and big block used in this full-scale DBCB specimen with a slab closely resemble those used in the first full-scale DBCB specimen. Therefore, following the reinforcement detailing shown in Fig. 3.18, reinforcing cages were fabricated at CELB using hoops and reinforcing bars. The fabrication process was the same with the former blocks as described in Section A.1.2. Figs. A.23 and A.24 display the steel cages for the loading block and top big block, respectively. Additionally, the previous bottom big block was reused with minor modifications, as illustrated in Fig. A.25.

(a)

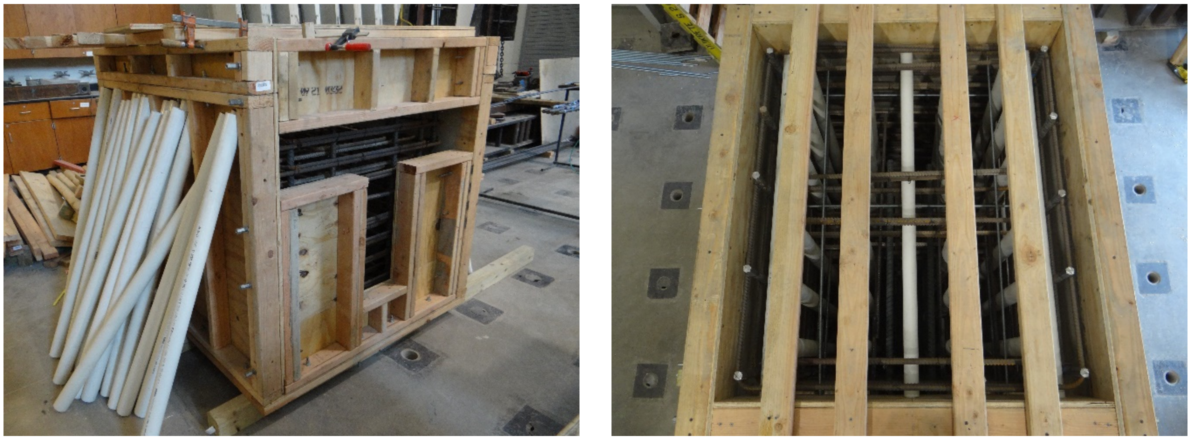

(b)

Fig. A.23 Reinforcement cage fabrication of the loading block: (a) Outside reinforcement cage, (b) Completed reinforcement cage placed in the formwork

(a) (b)

(c)

Fig. A.24 Reinforcement cage fabrication of the top big block: (a) Placement of hoop frames, (b) Tying hoop frames to vertical reinforcing bars, and (c) Completed reinforcement cage

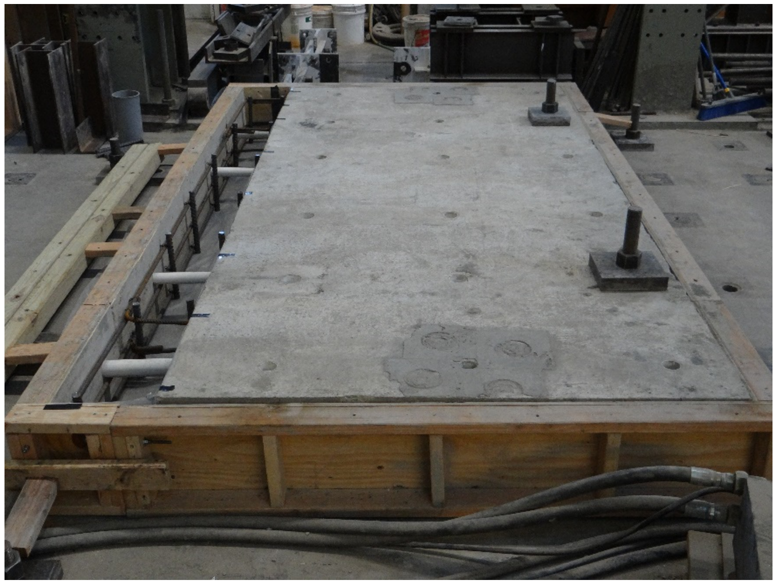

Fig. A.25 Extended bottom big block

Fig. A.26 (a) illustrates the process of placing transverse hoops along the top longitudinal bars of each cage, ensuring they are spaced according to the DBCB design. Subsequently, the bottom longitudinal bars of each cage are placed, as depicted in Fig. A.26 (a). In Fig. A.26 (b), the longitudinal bars are then secured to the hoops using steel tie wires. Fig. A.26 (c) displays two fully completed DBCB reinforcement cages. It should be noted that the construction of the DBCB cages took place after mounting the strain gauges onto both the longitudinal bars and the hoops.

(a)

(b)

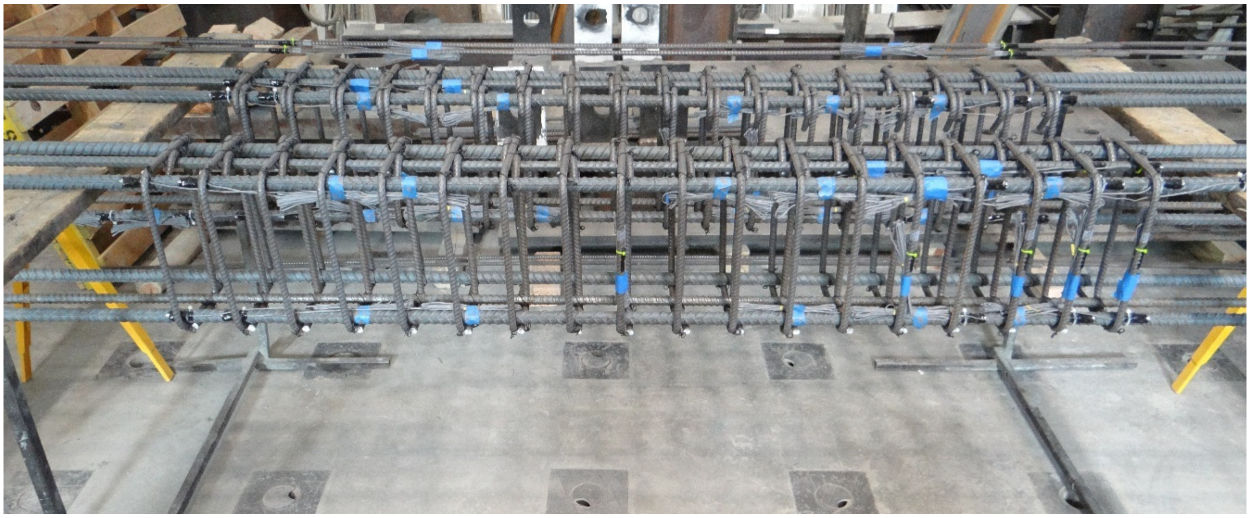

(c)

Fig. A.26 Reinforcement cage fabrication of DBCB: (a) Placement of stirrup hoops (b) Tying stirrup hoops to longitudinal bars (c) Completion of two reinforcement cages

A.3.3 Assembly

The assembly of formworks and reinforcement cages for the DBCB specimen followed a step-by-step process, similar to the first full-scale DBCB specimen described in Section 2.4. The construction sequence is depicted in Figs. A.7 (a), (b), (c), and (d), where the steel reinforcement cage for the big block was gradually built up. In Fig. A.27, the formwork for the big block was assembled after inserting horizontal PVC pipes. The formwork for the DBCB specimen with a slab was connected to the T-shaped opening in the completed formwork for the big block.

Fig. A.27 Completed formwork assembly for the big block

The formwork and reinforcement cage for the coupling beam were connected to the completed formwork of the big block. In Fig. A.28 (a), the bottom part of the formwork was inserted into the formwork of the big block and leveled horizontally with the support of additional structures. Following that, in Fig. A.28 (b), the bottom cage was smoothly slid into the cage of the big block using a crane and placed on the bottom plate, leaving a 0.75-in. gap for the concrete cover. As shown in Fig. A.28 (c), one side piece of the formwork was installed, and two PVC pipes were positioned 3.5 in. (measured from centroid of the PVC pipe) away from each end at the top of the bottom cage to simulate utility ducts.

The subsequent placement of the top cage involved sliding it into the cage of the big block and positioning it on the two PVC pipes. Additionally, two more PVC pipes were inserted at the midspan and mid-height of each steel cage. To complete the formwork assembly for the coupling beam, the opposite side piece of the formwork was installed, as shown in Fig. A.28 (d). Figs. A.28 (e) and (f) illustrate the 3-in. gap of the UCS layer in the coupling beam. Furthermore, it is important to note that the strain gauge cables were organized into two parts: the cables in the top beam were positioned above the top beam, while the cables in the bottom beam were placed below the bottom beam.

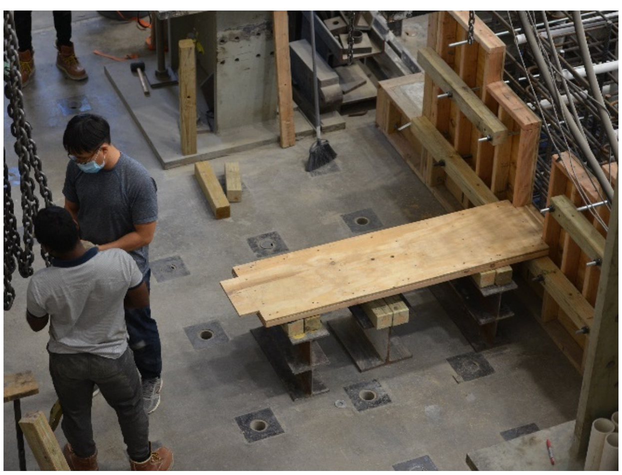

(a)

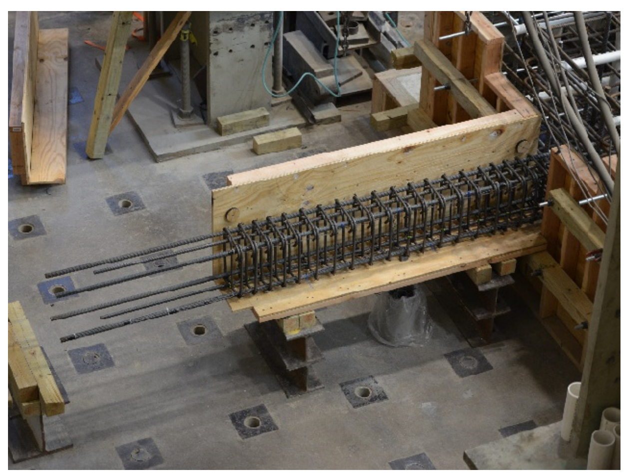

(b)

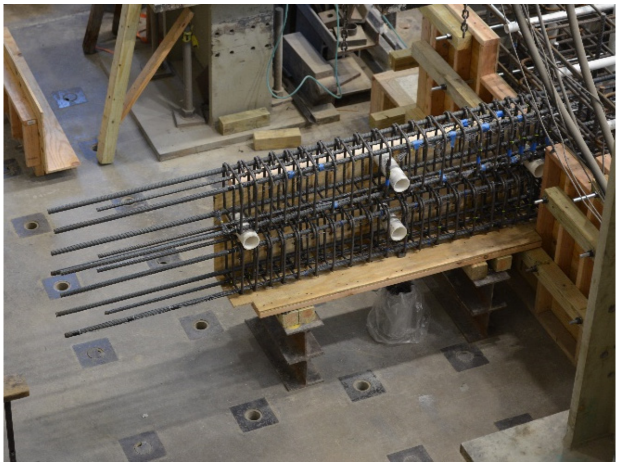

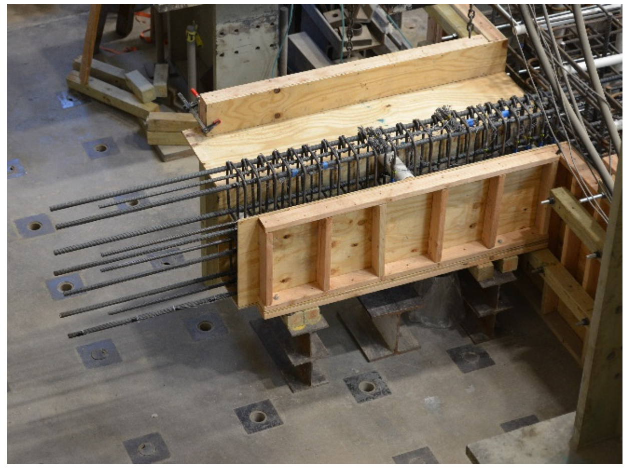

(c) (d)

(e) (f)

Fig. A.28 Formwork assembly for DBCB: (a) Bottom plate of the formwork, (b) Bottom cage installation, (c) Top cage installation, (d) Completed DBCB, (e) 3 in. gap for UCS (left), and (d) 3 in. gap for UCS (right)

The formwork for the loading block was subsequently integrated with the assembled DBCB formwork. In Fig. A.29 (a), steel-shape supports were placed on the floor to ensure the horizontal alignment of the loading block with the DBCB formwork. Following this, the bottom and front pieces of the formwork were assembled, as shown in Fig. A.29 (b), and the reinforcement cage for the loading block was carefully inserted using a crane, taking precautions not to damage the strain gauges mounted on the extended longitudinal bars, as shown in Fig. A.29 (c). In Fig. A.29 (d), the formwork for the slab was positioned between the formworks of both blocks, and the longitudinal bars of the slab were inserted through the cage of the loading block. The formwork for the loading block was completed, including the inclusion of PVC pipes, as seen in Fig. A.29

(e). Finally, in Fig. A.29 (f), the steel reinforcing bars for the slab were assembled into the formwork. Fig. A.30 illustrates the completed formwork assembly for the full-scale DBCB specimen with a 2.4 aspect ratio.

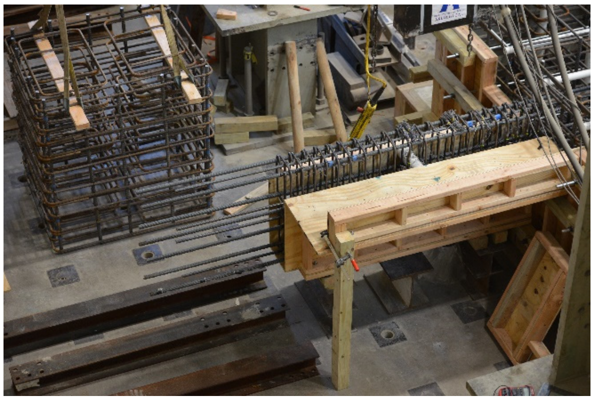

(a)

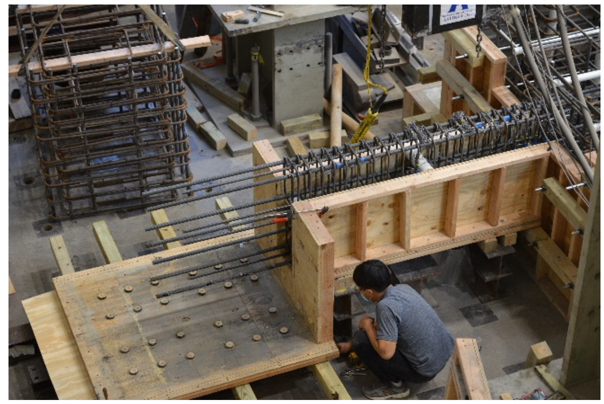

(b)

(c)

(d)

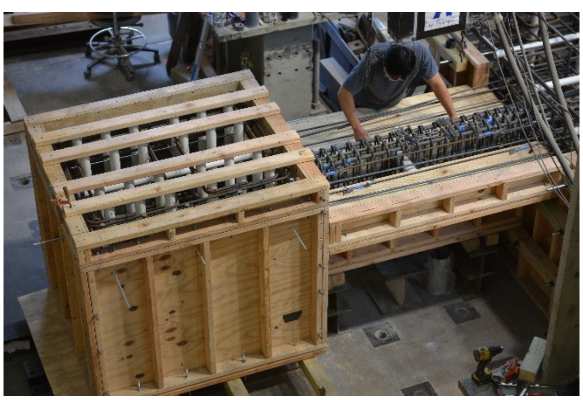

(e)

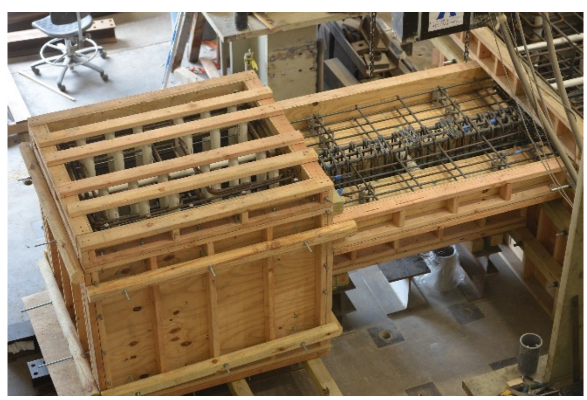

(f)

Fig. A.29 Loading block assembly: (a) Supports placement, (b) Formwork installation, (c) Reinforcement cage installation, (d) PVC pipes insertion, (e) Completed loading block, and (f) Completed slab

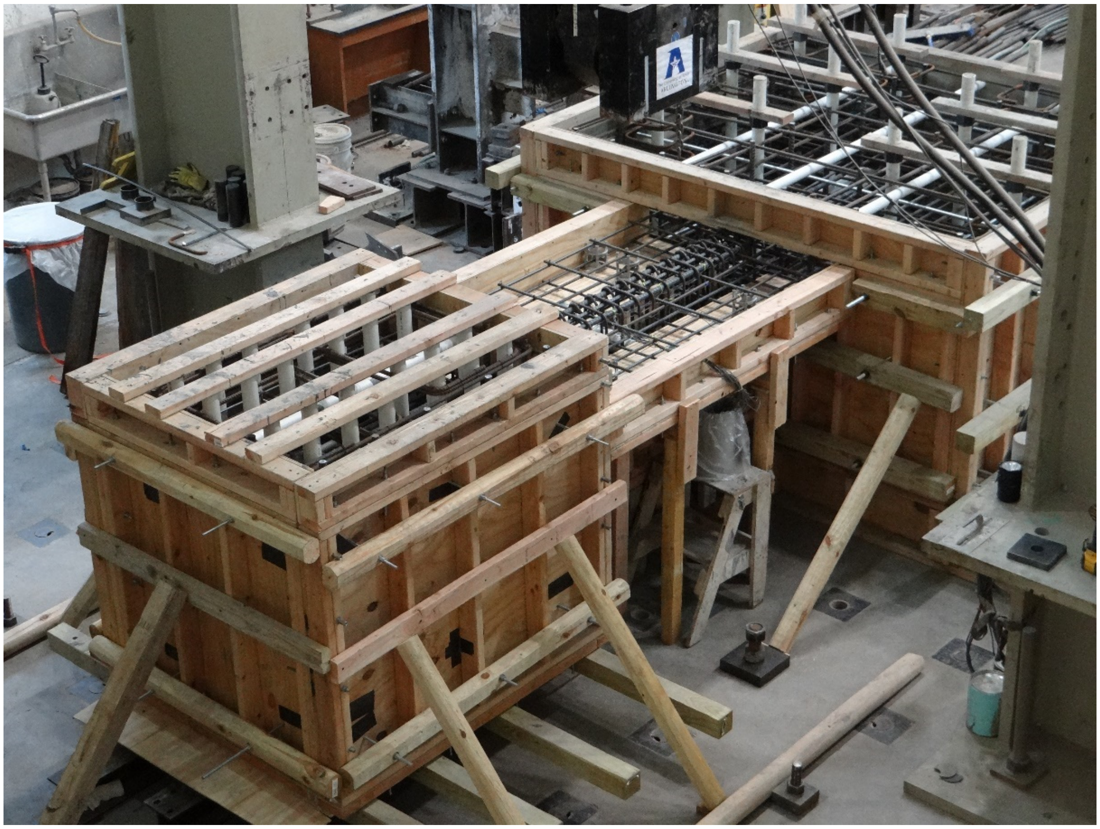

Fig. A.30 Completed formwork assembly for the full-scale DBCB specimen with 2.4 aspect ratio

A.3.4 Concrete casting

Fig. A.31 shows the formation of the bottom big block by extending the old bottom big block, which was previously cast using concrete mixed by a drum mixer at CELB. Following this, ready-mix concrete with a design compressive strength of 5 ksi, provided by a local supplier, was used for casting the full-scale DBCB specimen. Fig. A.32 provides visual documentation of the concrete casting process. As shown in Fig. A.32, the concrete for the top big block was directly poured into the formwork through the discharge hopper of the truck. For the formworks of the loading block and the coupling beam, the concrete was initially poured into a large concrete bucket and then lifted using a crane to be cast into the formworks. During the concrete casting process, a concrete vibrator was employed to consolidate the freshly placed concrete, allowing entrapped air to escape. This process improved the density of the concrete and enhanced its bond with the reinforcing bars. Additionally, twelve 4 in. × 8 in. concrete cylinders were prepared to determine the actual concrete strength on the testing day of the coupling beam. As mentioned in Section A.1.4, ultra-high-performance fiber-reinforced concrete (UHP-FRC) with an expected strength of

15 to 20 ksi was used. A 1.5-inch-thick layer of UHP-FRC was poured at the top and bottom of the loading block. The bottom layer of UHP-FRC was cast before the plain concrete, while the top layer of UHP-FRC was added four days after the casting of the plain concrete. The UHP-FRC casting process is illustrated in Fig. A.33. After a period of two weeks, the formworks were removed from the specimen, as shown in Fig. A.34, revealing the cured full-scale DBCB specimen.

Fig. A.31 Concrete casting of the bottom big block

Fig. A.32 Concrete casting of the top big block, the DBCB, and the loading block

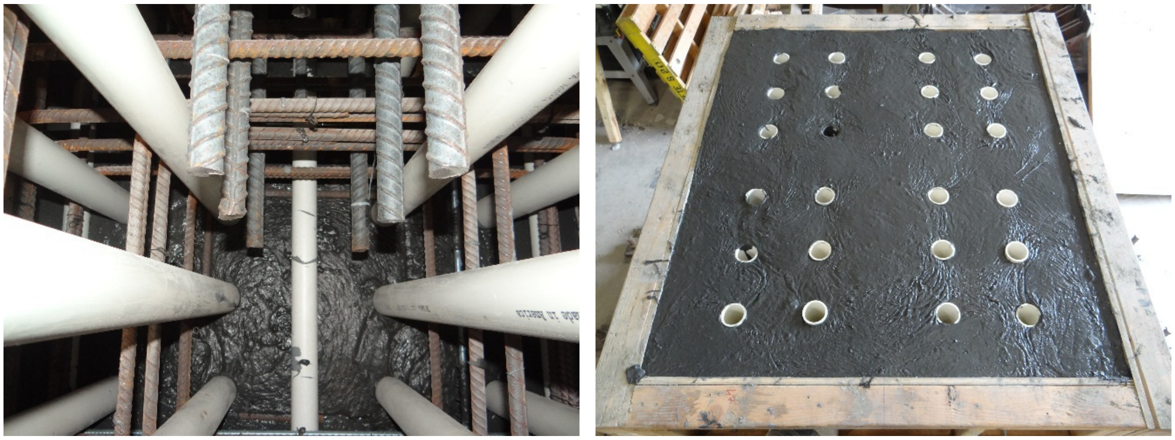

Fig. A.33 UHPC concrete casting of the loading block

(a)

(b)

Fig. A.34 Cured DBCB specimen: (a) isometric views and (b) close-up view of coupling beam

APPENDIX B: STRAIN GAUGE INSTALLATION

The strain gauges have to be mounted on the surface of reinforcement bars prior to constructing the cages and concrete pouring. Hence, the strain gauge should be protected from damage. Fig. B.1 shows the procedure used to protect the strain gauges. Fig. B.1(a) shows the materials and tools needed for strain gauge installation. The location of each strain gauge was first marked accurately on the reinforcement bars as shown in Fig. B.1(b). Next, the surface of the reinforcement bar was ground flat using a hand grinder machine and then sanded with 400 grit sandpaper to smoothen the surface as shown in Figs. B.1(c) and B.1(d), respectively. The smooth surface was then cleaned using an acid conditioner (an M-preconditioner A) and neutralized using a base conditioner (M-preneutralizer 5A), as shown in Fig. B.1(e). Then, the strain gauge was mounted on the rebar surface with a suitable adhesive (CN-Y adhesive) after lining up the center cross hairs on the strain gauge to the locations marked on the reinforcement bar as shown in Fig. B.1(f). Then, the strain gauge attached on the rebar surface was coated with a polyurethane coating (M-coat A). Once the M-Coat A dried, nitrile rubber coating (M-coat B) was put on the gauge, as shown in Fig. B.1(g). After the M-coat B dried, a piece of moisture sealing electrical tape was used to cover the entire strain gauge and liquid electrical tape was applied on it to seal the edges of the electrical tape as shown in Figs. B.1(h) and B.1(i), respectively. Once the liquid electrical tape dried, zip-ties were put on the top of the bottom edge of the electrical tap to fix the coated wires of the strain gauge to reinforcement bar, which helps protect the strain gauges from being pulled during the construction process as shown in Fig. B.1(j). Finally, all strain gauges were labeled as shown in Fig. B.1(l) after checking each strain gauge having the proper resistance (120 Ω), as shown in Fig. B.1(k). Note that the resistance had already been checked before mounting the strain gauges on the steel surface. Following this procedure, all strain gauges of the hoops and longitudinal bars were installed as shown in Fig. B.1.

(a) (b)

(c) (d)

(e)

(f)

(g)

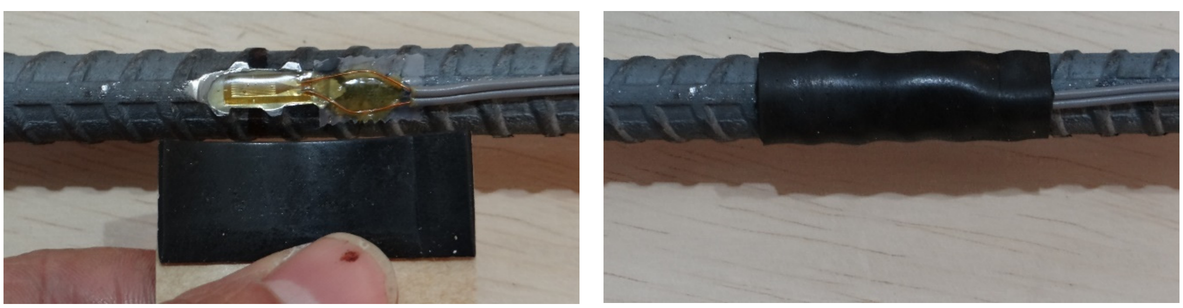

(h)

(i)

(j)

(k) (l)

Fig. B.1 Procedure of strain gauge installation: (a) materials and tools, (b) location, (c) grinding, (d) smoothing, (e) cleaning, (f) mounting, (g) coating, (h) rubber electrical tape, (i) liquid electrical tape, (j) Zip-tie, (k) resistance testing, and (l) labeling

APPENDIX C: STRAIN MEASUREMENTS

C.1 Full-scale DBCB with 3.2 aspect ratio (FS-R3.2-N-2)

Measured strain versus chord rotation for each strain gauge attached to the reinforcing bars is plotted. The location of each strain gauge was indicated with a black dashed line circle on the plot.

C.1.1 Upper steel cage

After 0.5% chord rotation, all the strain gauges in the upper steel cage ceased to function. Fig. C.1 illustrates the arrangement of the strain gauge wires in the two steel cages. As shown in Fig. C.1, the wires in the upper cage were horizontally oriented towards the beam's center and passed through the UCS, exiting at the bottom of the beam. As detailed in Section 4.1.1, the relative horizontal slip occurring at the UCS between the upper and lower cages could potentially cause significant damage to the strain gauge wires during the testing process.

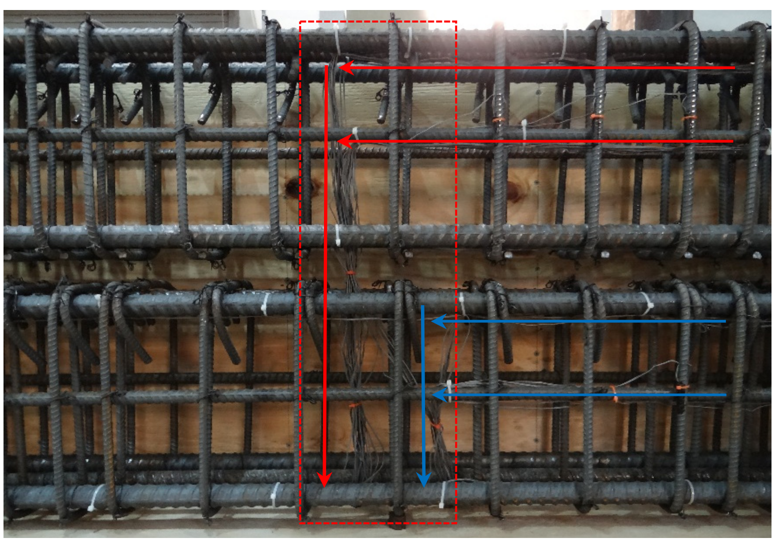

Fig. C.1 Orientation of the strain gauges wires in the two steel cages

C.1.2 Lower steel cage

C.1.2.1 Longitudinal reinforcement

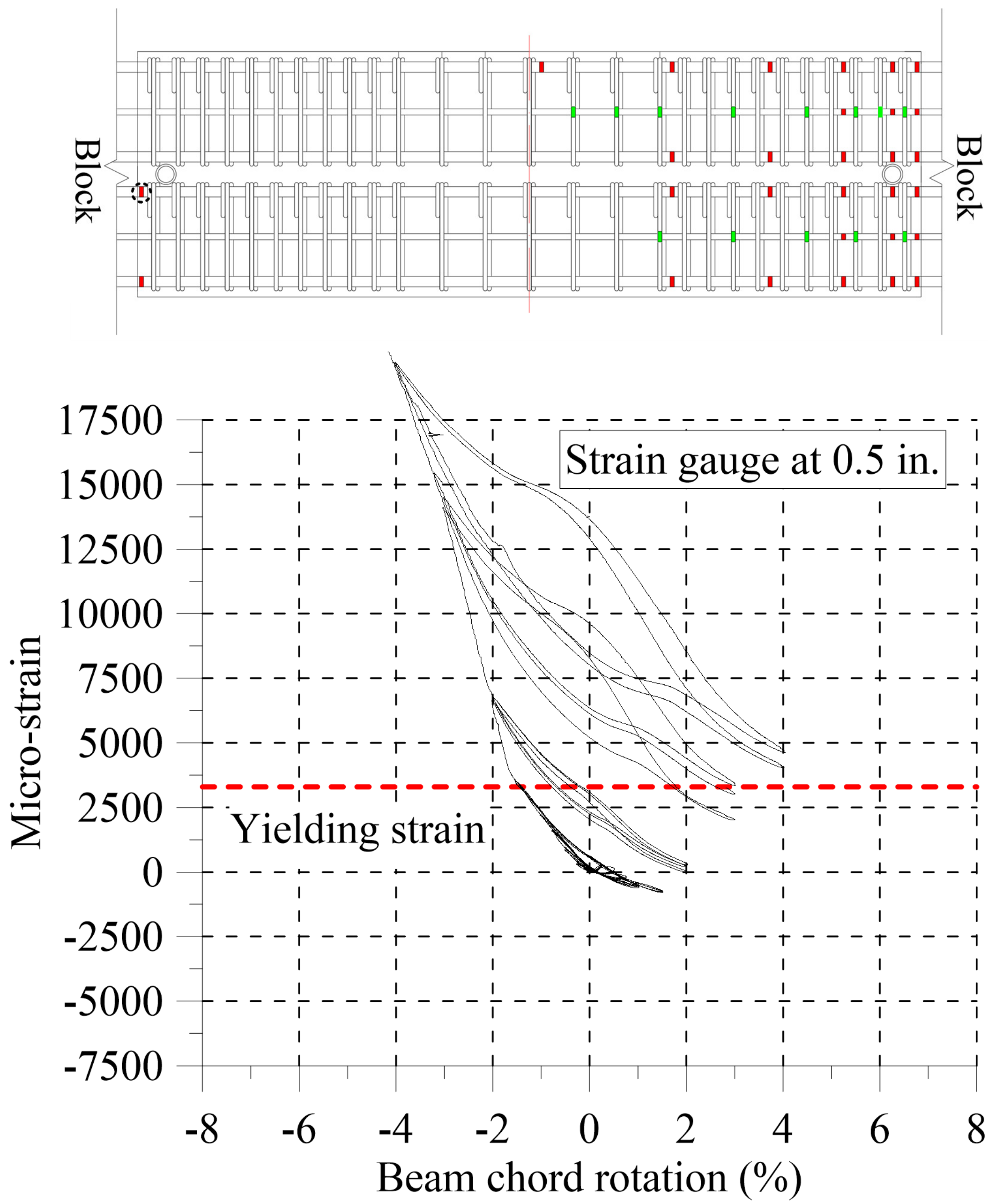

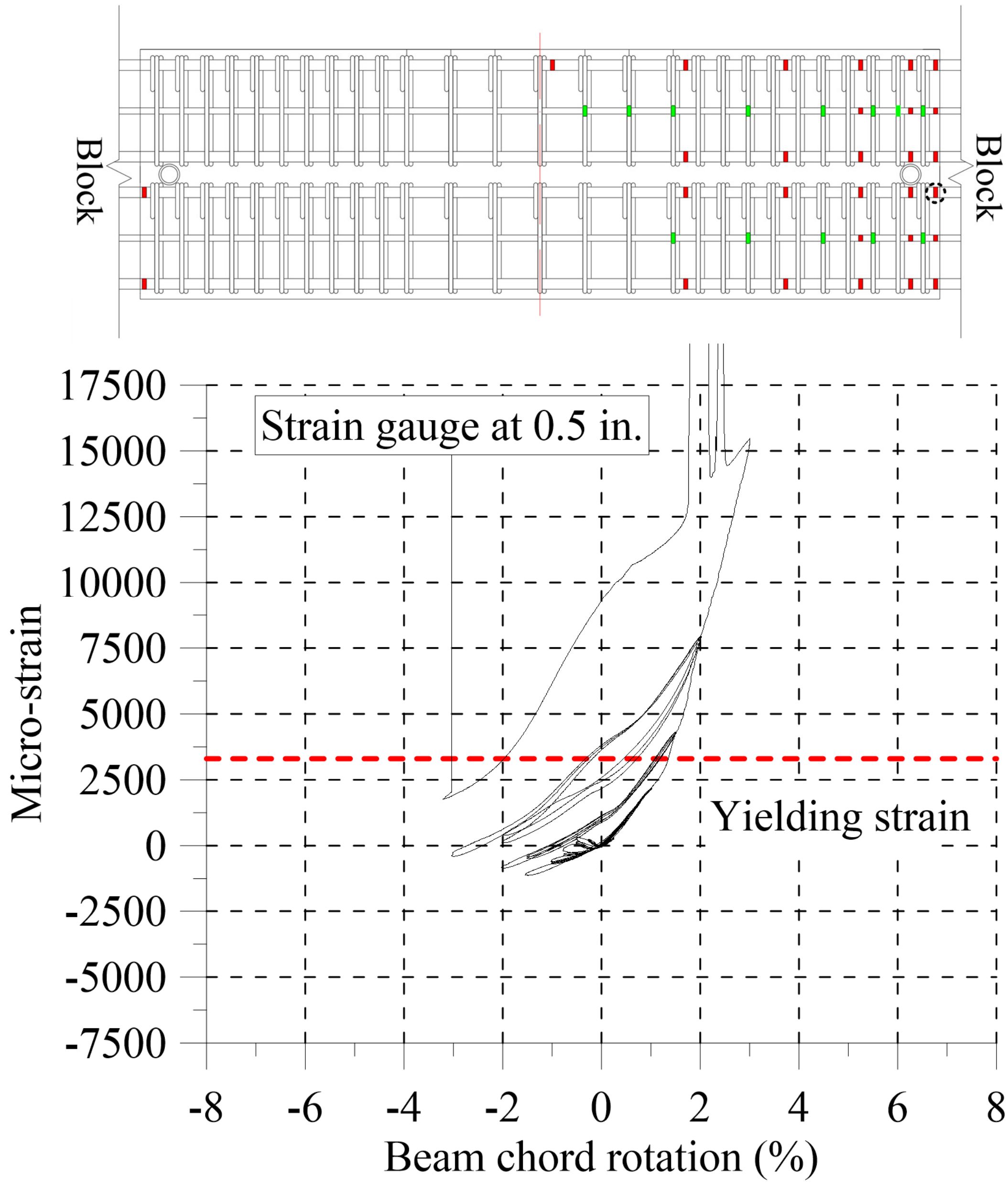
Block
Block
Strain gauge at 0.5 in.
Yielding strain
Micro-strain
Beam chord rotation (%)
17500
15000
12500
10000
7500
5000
2500
0
-2500
-5000
-7500
-8
-6
-4
-2
0
2
4
6
8

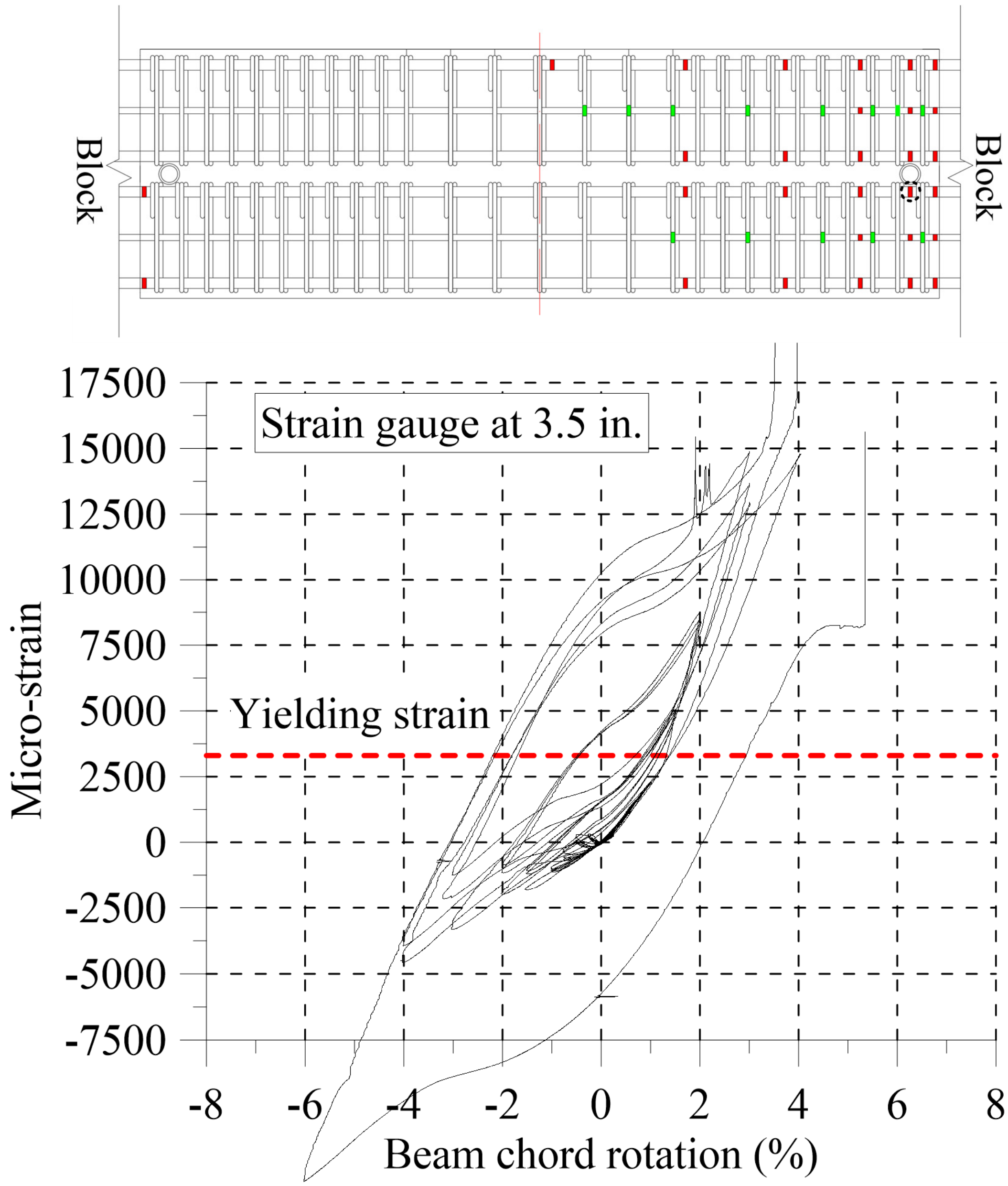
Block
Block
17500
15000
12500
10000
7500
5000
2500
0
-2500
-5000
-7500
Strain gauge at 3.5 in.
Yielding strain
Micro-strain
-8
-6
-4
-2
0
2
4
6
8
Beam chord rotation (%)

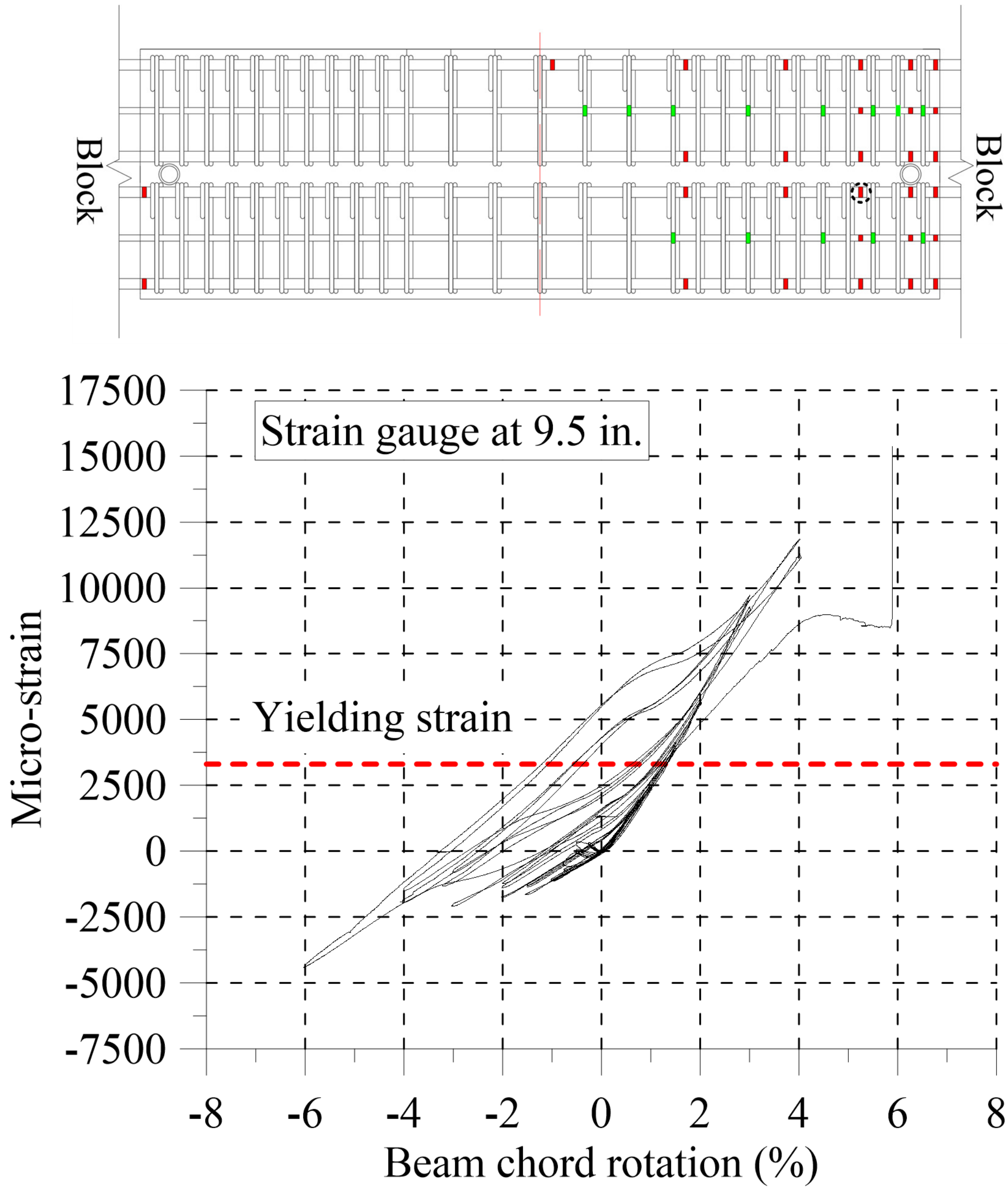

Block
Block
Strain gauge at 9.5 in.
Yielding strain
17500
15000
12500
10000
7500
5000
2500
0
-2500
-5000
-7500
Micro-strain
-8
-6
-4
-2
0
2
4
6
8
Beam chord rotation (%)

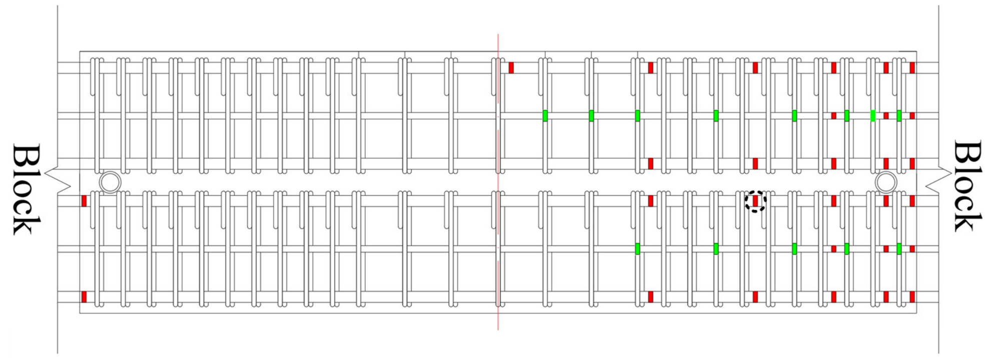
Block
Block

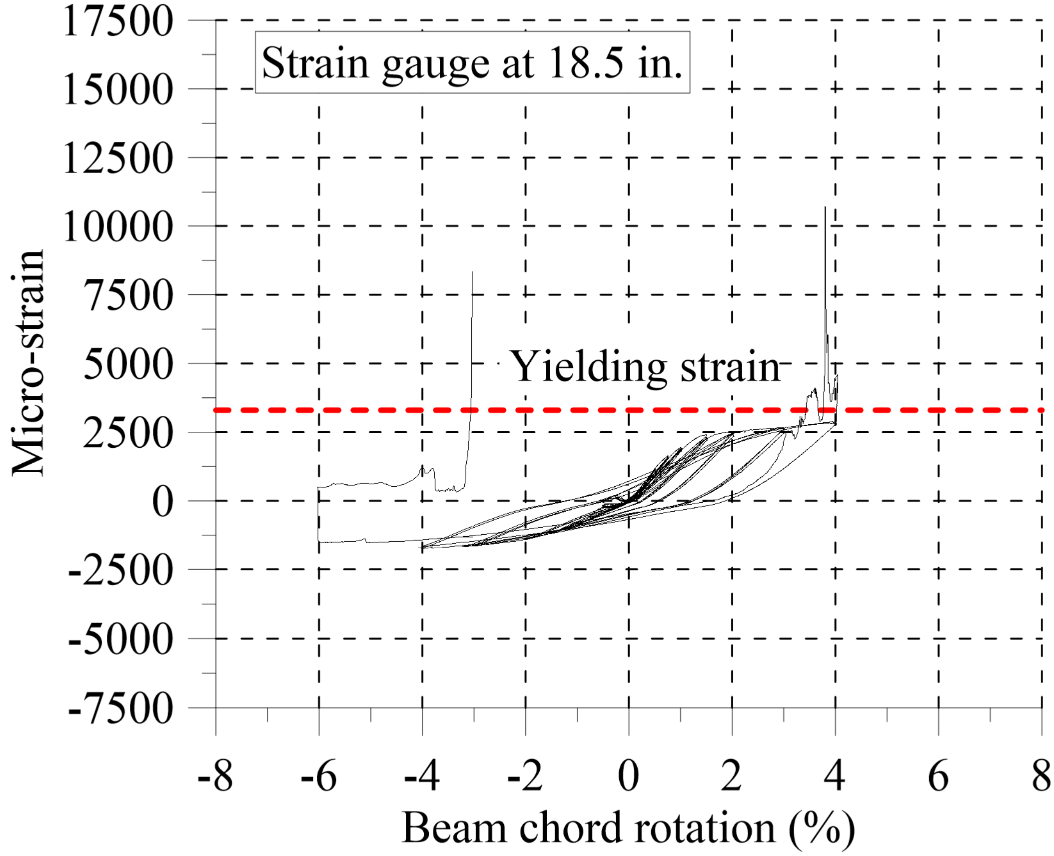
Strain gauge at 18.5 in.
Yielding strain
Micro-strain
Beam chord rotation (%)
17500
15000
12500
10000
7500
5000
2500
0
-2500
-5000
-7500
-8
-6
-4
-2
0
2
4
6
8

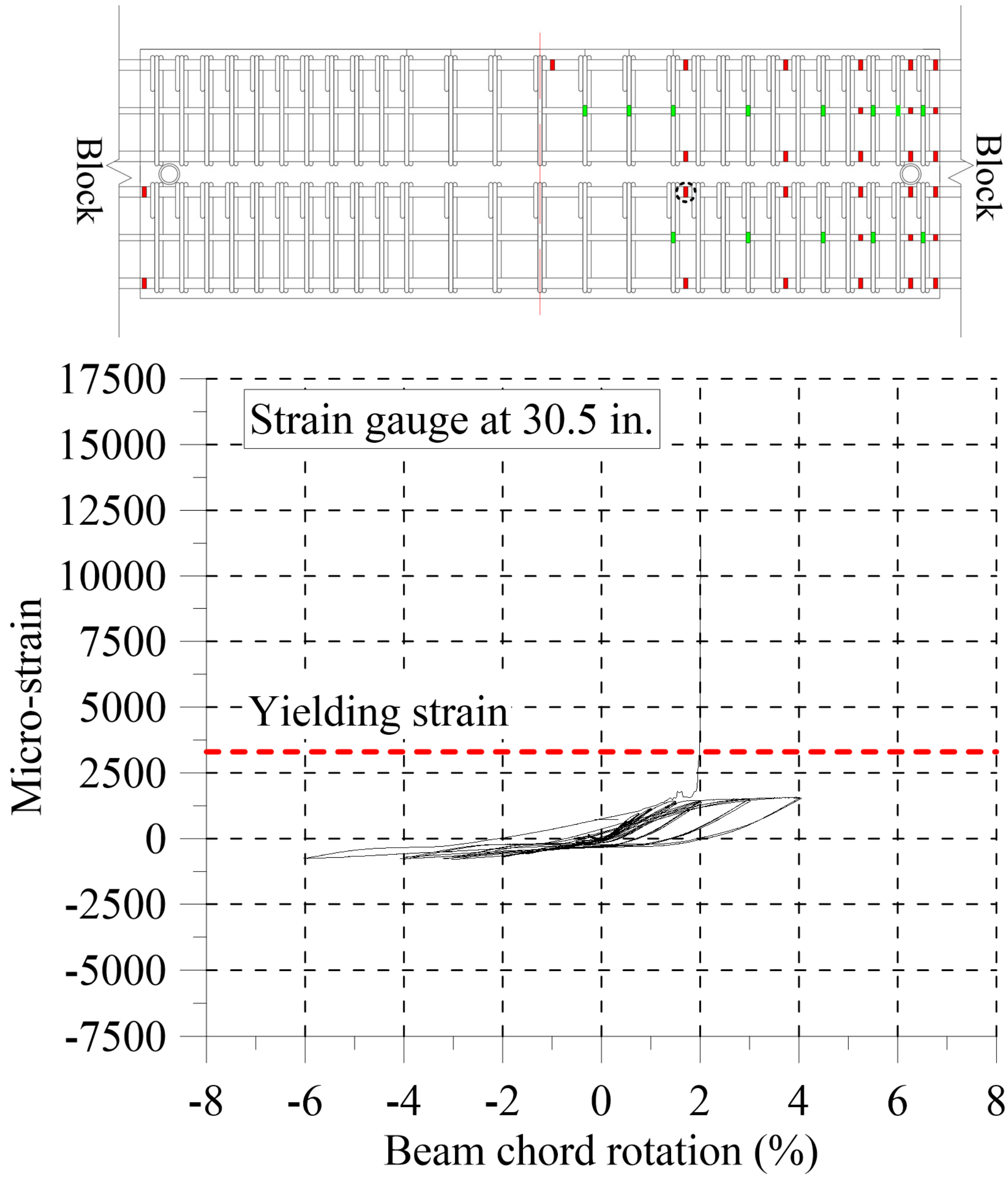
Block
Block
Strain gauge at 30.5 in.
Yielding strain
Micro-strain
Beam chord rotation (%)
17500
15000
12500
10000
7500
5000
2500
0
-2500
-5000
-7500
-8
-6
-4
-2
0
2
4
6
8

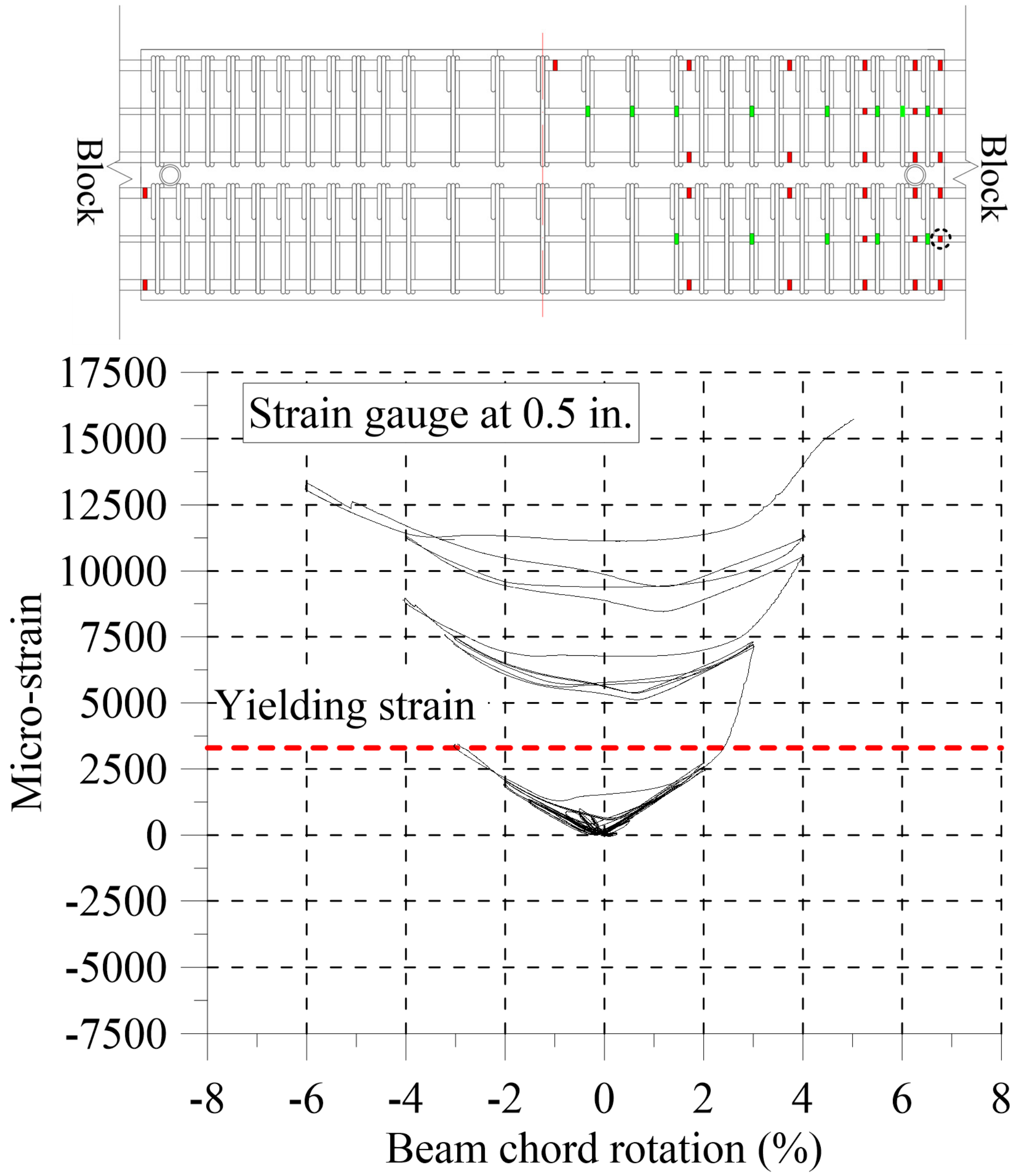
Block
Block
Strain gauge at 0.5 in.
Yielding strain
Micro-strain
Beam chord rotation (%)
17500
15000
12500
10000
7500
5000
2500
0
-2500
-5000
-7500
-8
-6
-4
-2
0
2
4
6
8

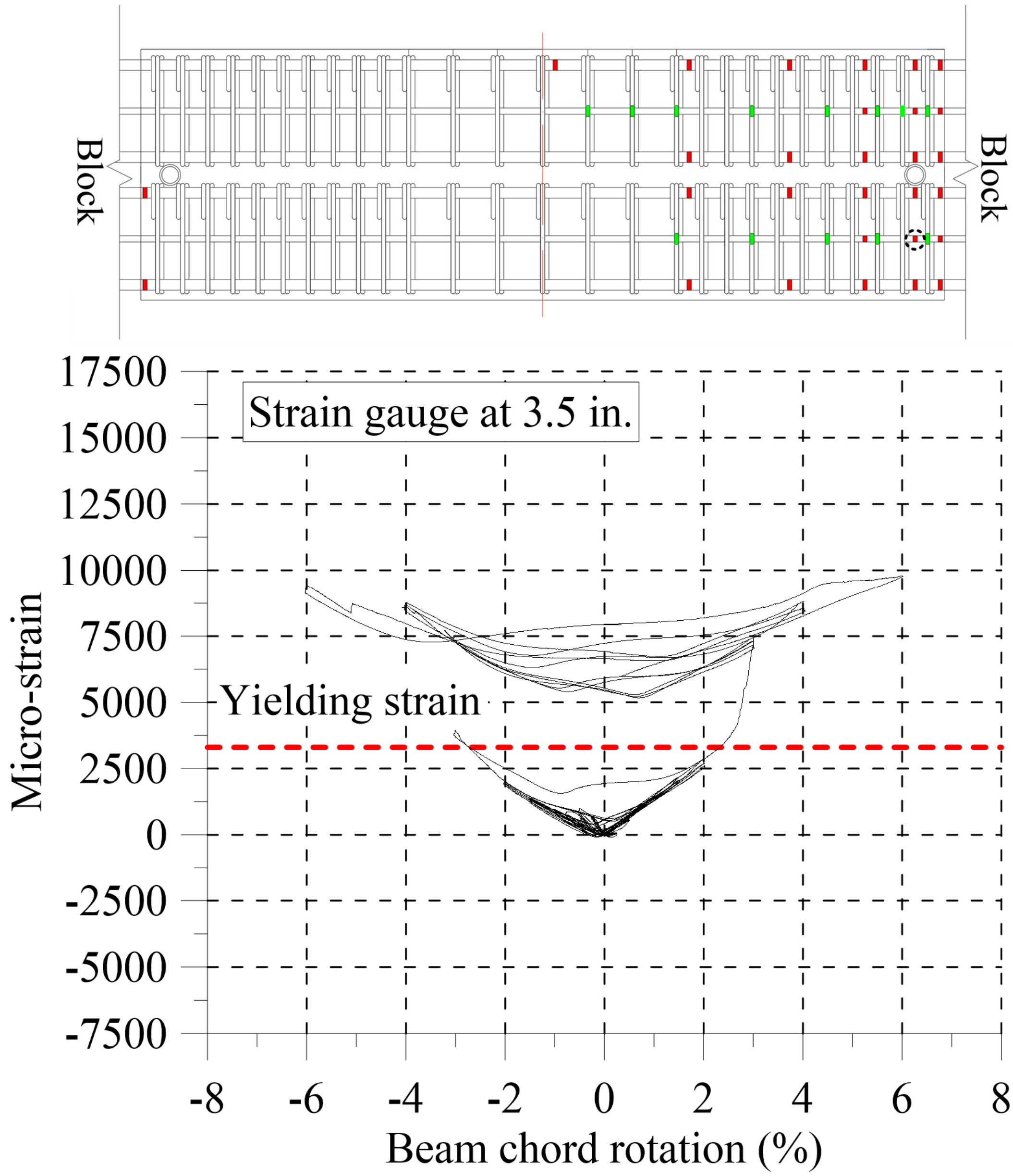

Block
Block
Strain gauge at 3.5 in.
Yielding strain
17500
15000
12500
10000
7500
5000
2500
0
-2500
-5000
-7500
Micro-strain
-8
-6
-4
-2
0
2
4
6
8
Beam chord rotation (%)

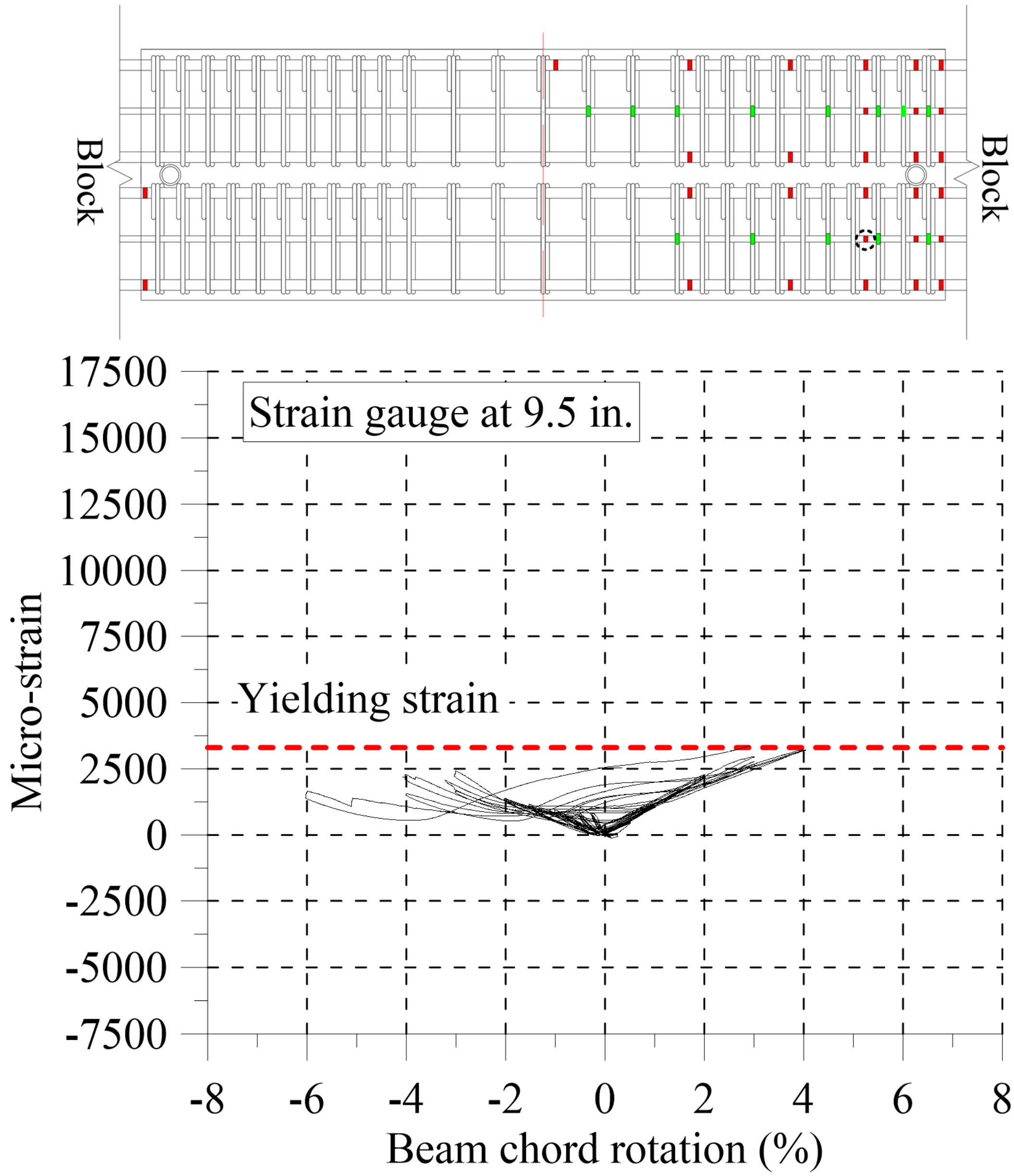
Block
Block
Strain gauge at 9.5 in.
Yielding strain
Micro-strain
17500
15000
12500
10000
7500
5000
2500
0
-2500
-5000
-7500
-8
-6
-4
-2
0
2
4
6
8
Beam chord rotation (%)

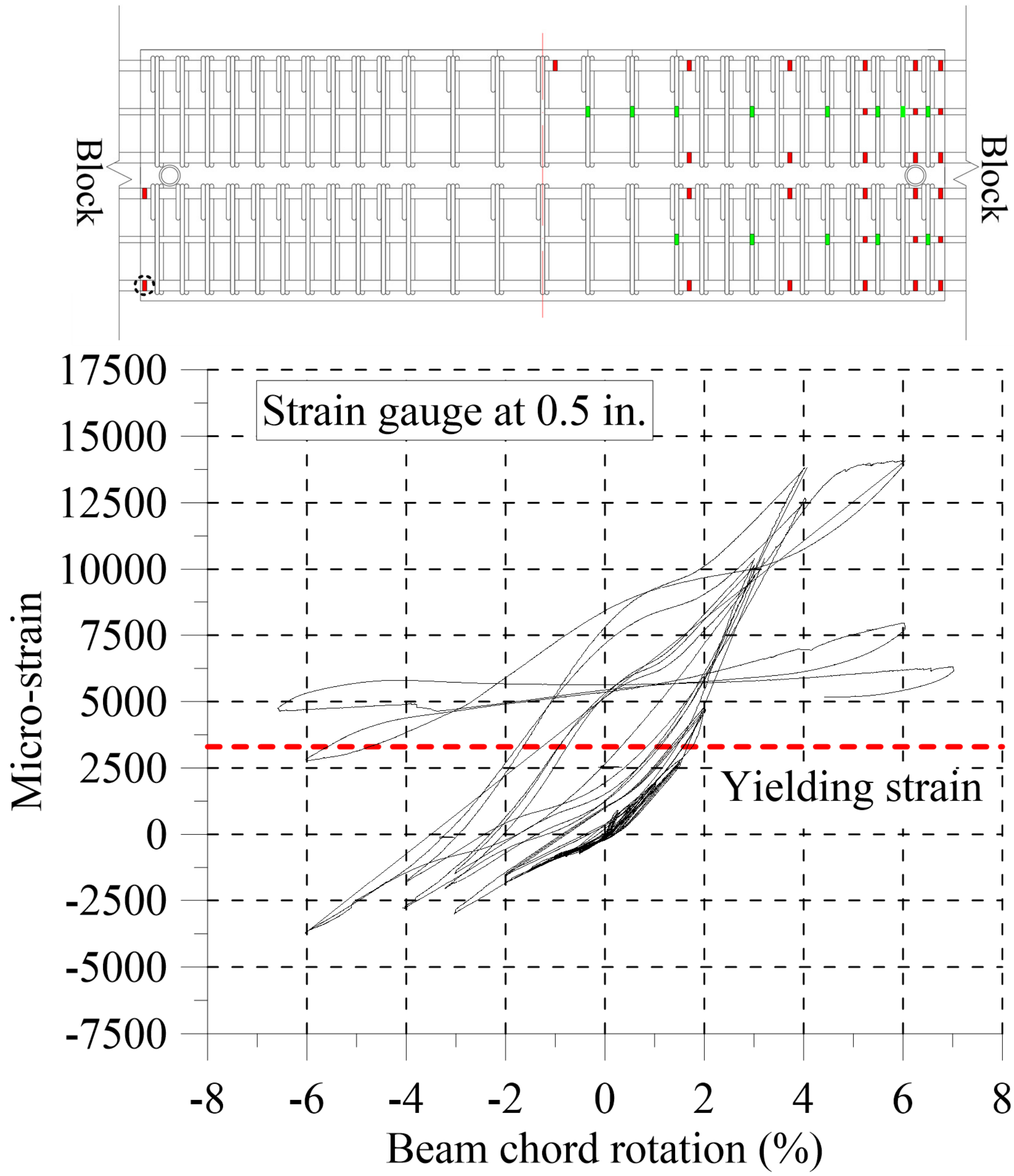
Block
Block
Strain gauge at 0.5 in.
Yielding strain
17500
15000
12500
10000
7500
5000
2500
0
-2500
-5000
-7500
Micro-strain
-8
-6
-4
-2
0
2
4
6
8
Beam chord rotation (%)

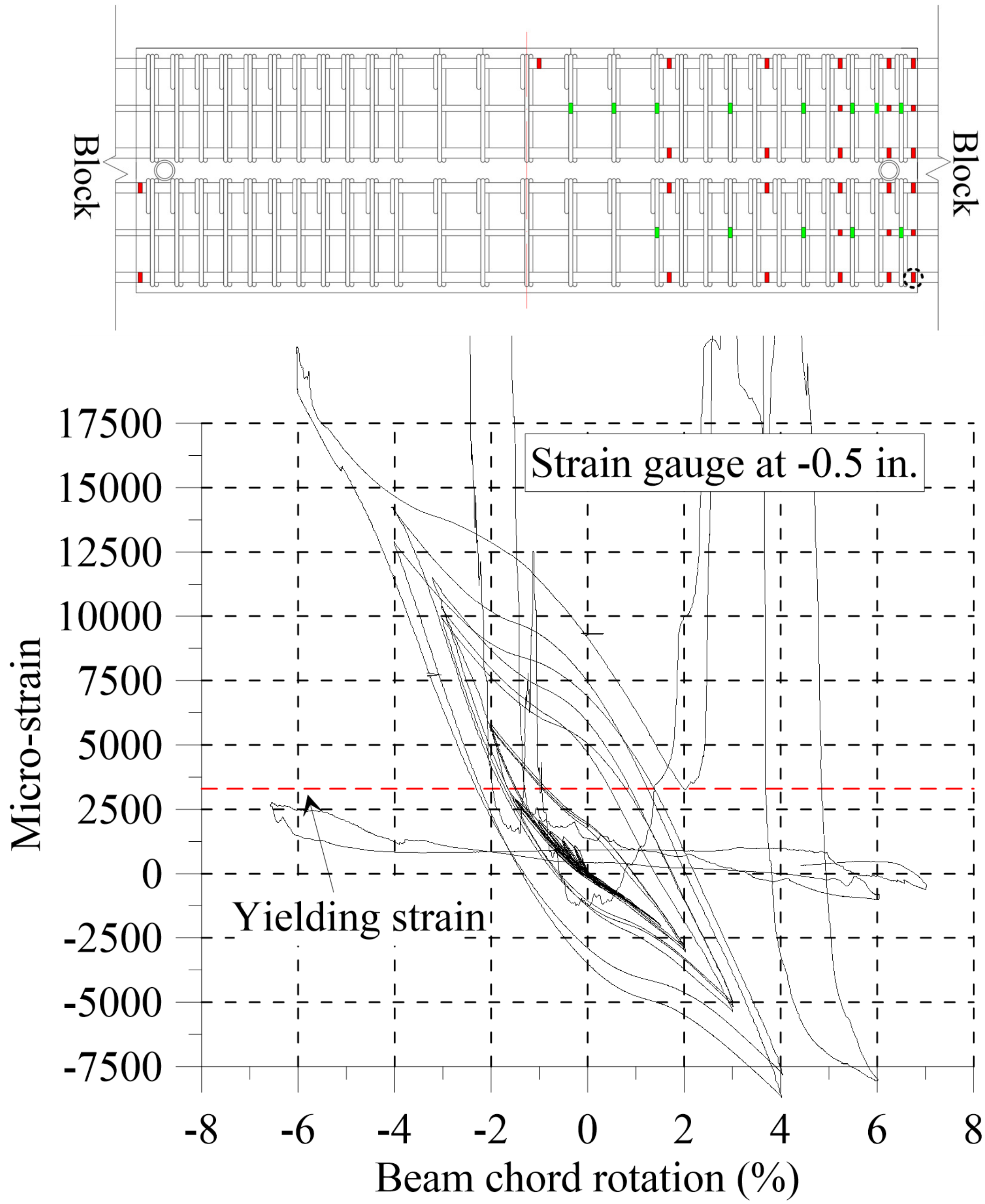
Block
Block
17500
15000
12500
10000
7500
5000
2500
0
-2500
-5000
-7500
Micro-strain
Strain gauge at -0.5 in.
Yielding strain
-8
-6
-4
-2
0
2
4
6
8
Beam chord rotation (%)

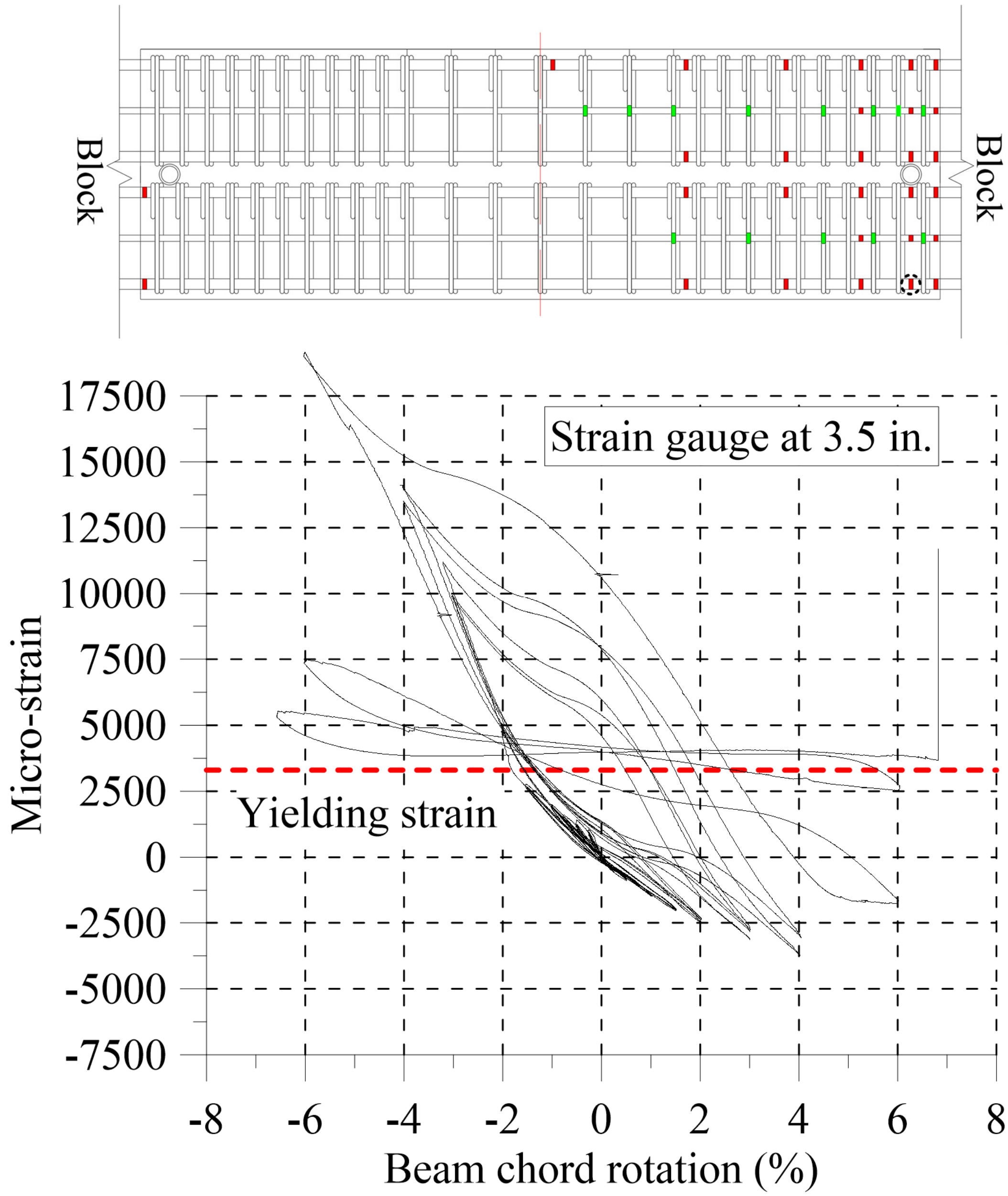

Block
Block
Strain gauge at 3.5 in.
Yielding strain
Micro-strain
Beam chord rotation (%)
17500
15000
12500
10000
7500
5000
2500
0
-2500
-5000
-7500
-8
-6
-4
-2
0
2
4
6
8

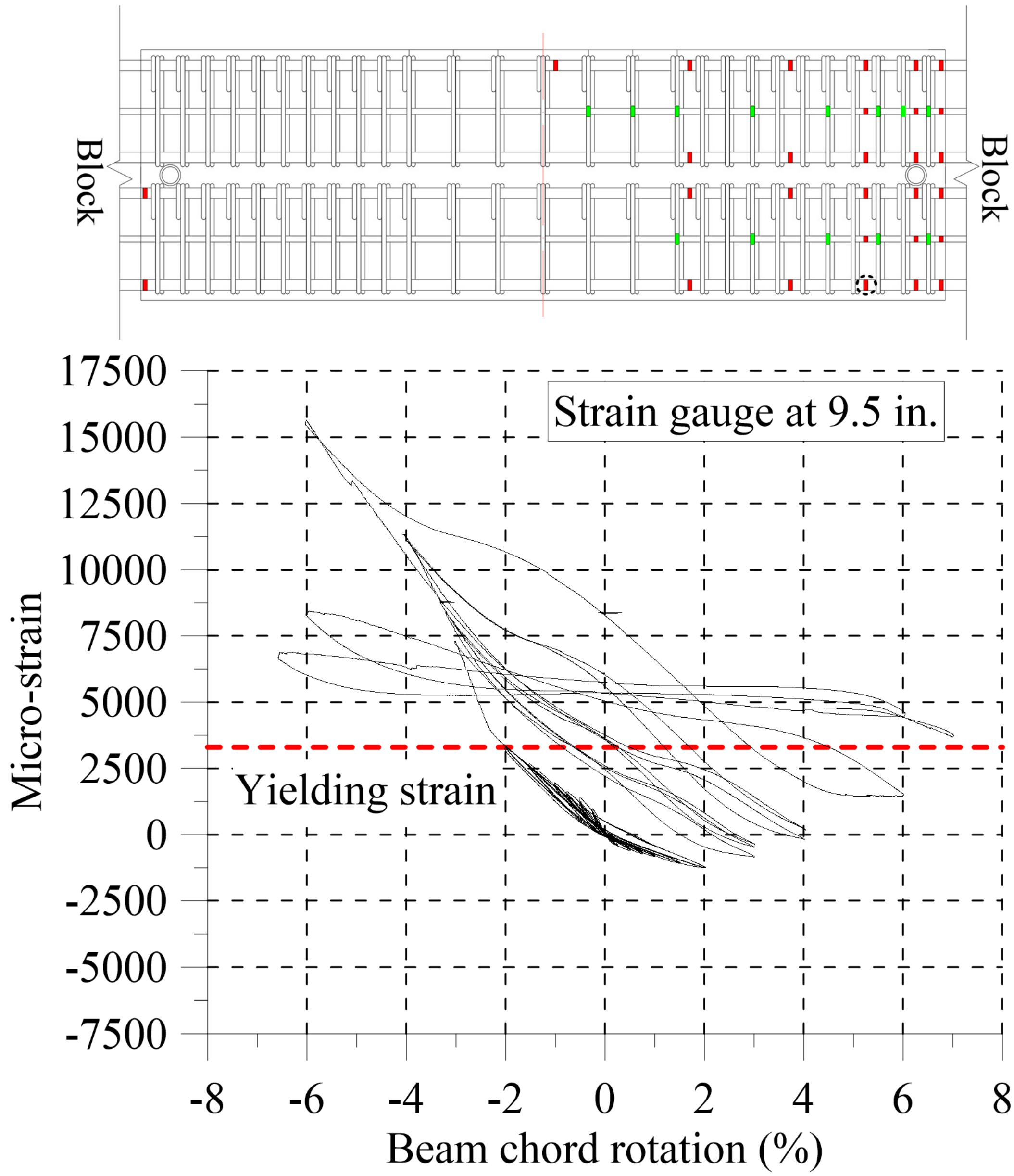
Block
Block
Strain gauge at 9.5 in.
Yielding strain
17500
15000
12500
10000
7500
5000
2500
0
-2500
-5000
-7500
Micro-strain
-8
-6
-4
-2
0
2
4
6
8
Beam chord rotation (%)

(d)

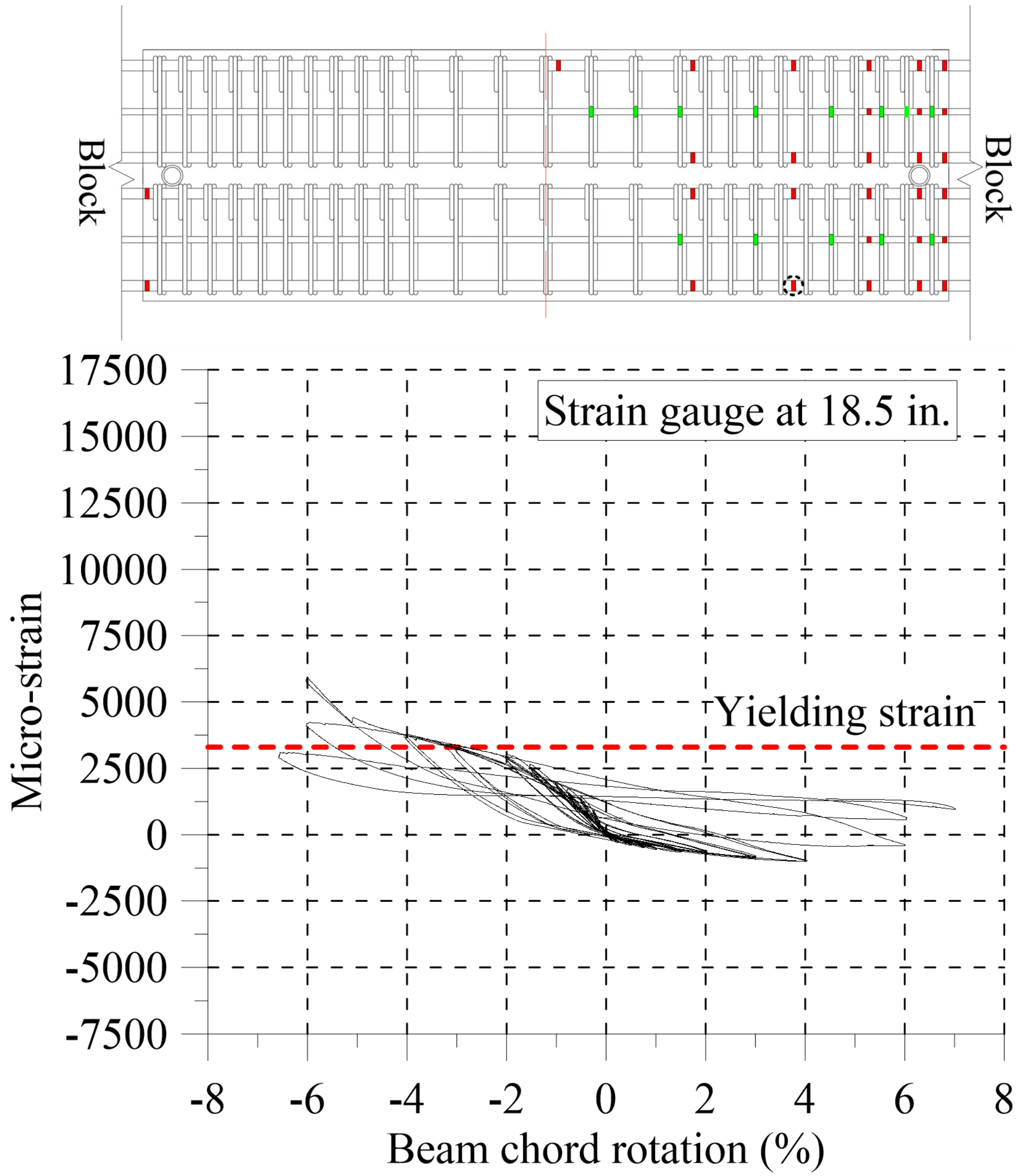

Block
Block
Strain gauge at 18.5 in.
Yielding strain
Micro-strain
17500
15000
12500
10000
7500
5000
2500
0
-2500
-5000
-7500
-8
-6
-4
-2
0
2
4
6
8
Beam chord rotation (%)

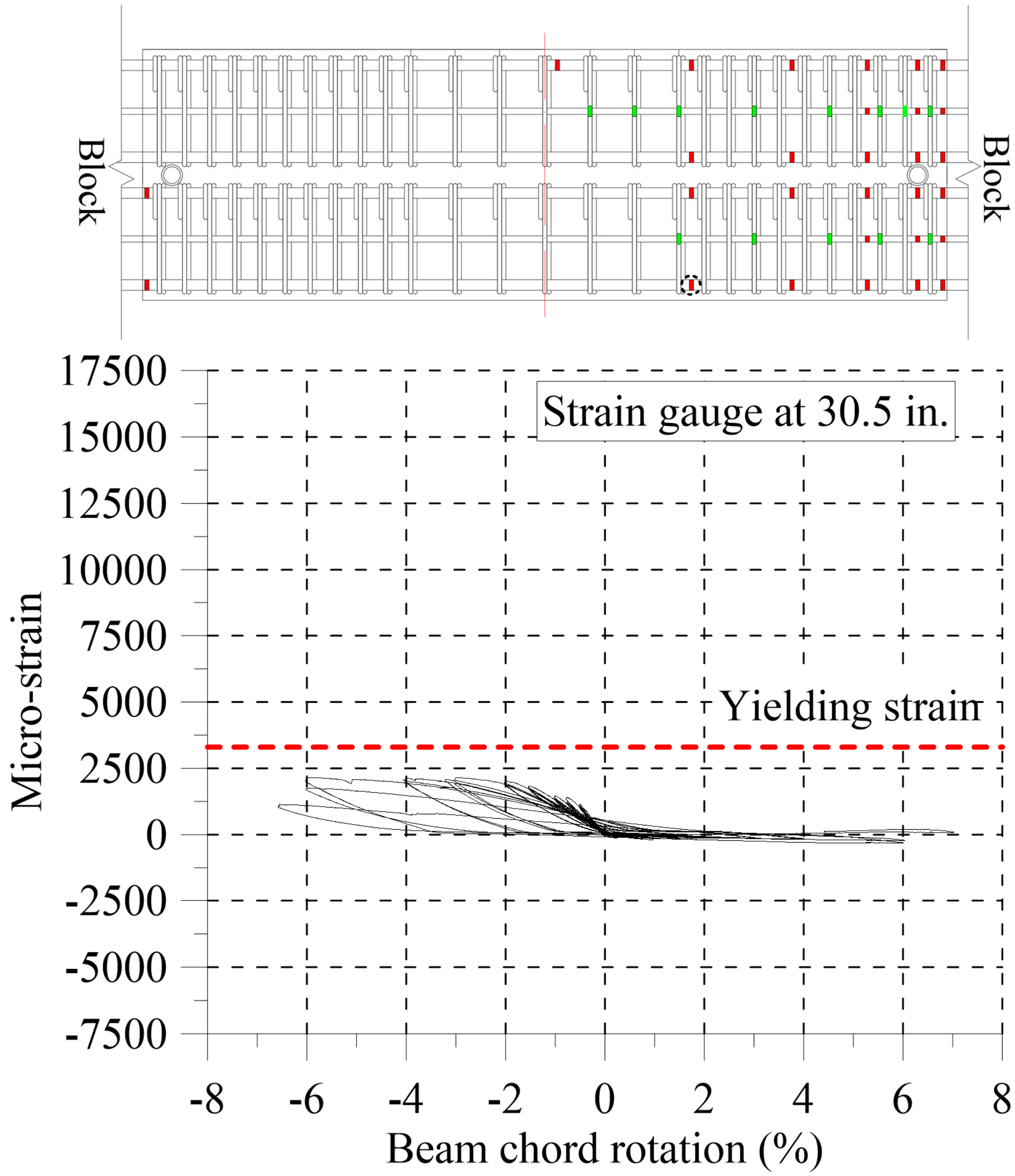
Block
Block
Strain gauge at 30.5 in.
Yielding strain
Micro-strain
Beam chord rotation (%)
17500
15000
12500
10000
7500
5000
2500
0
-2500
-5000
-7500
-8
-6
-4
-2
0
2
4
6
8

C.1.2.2 Transverse reinforcement

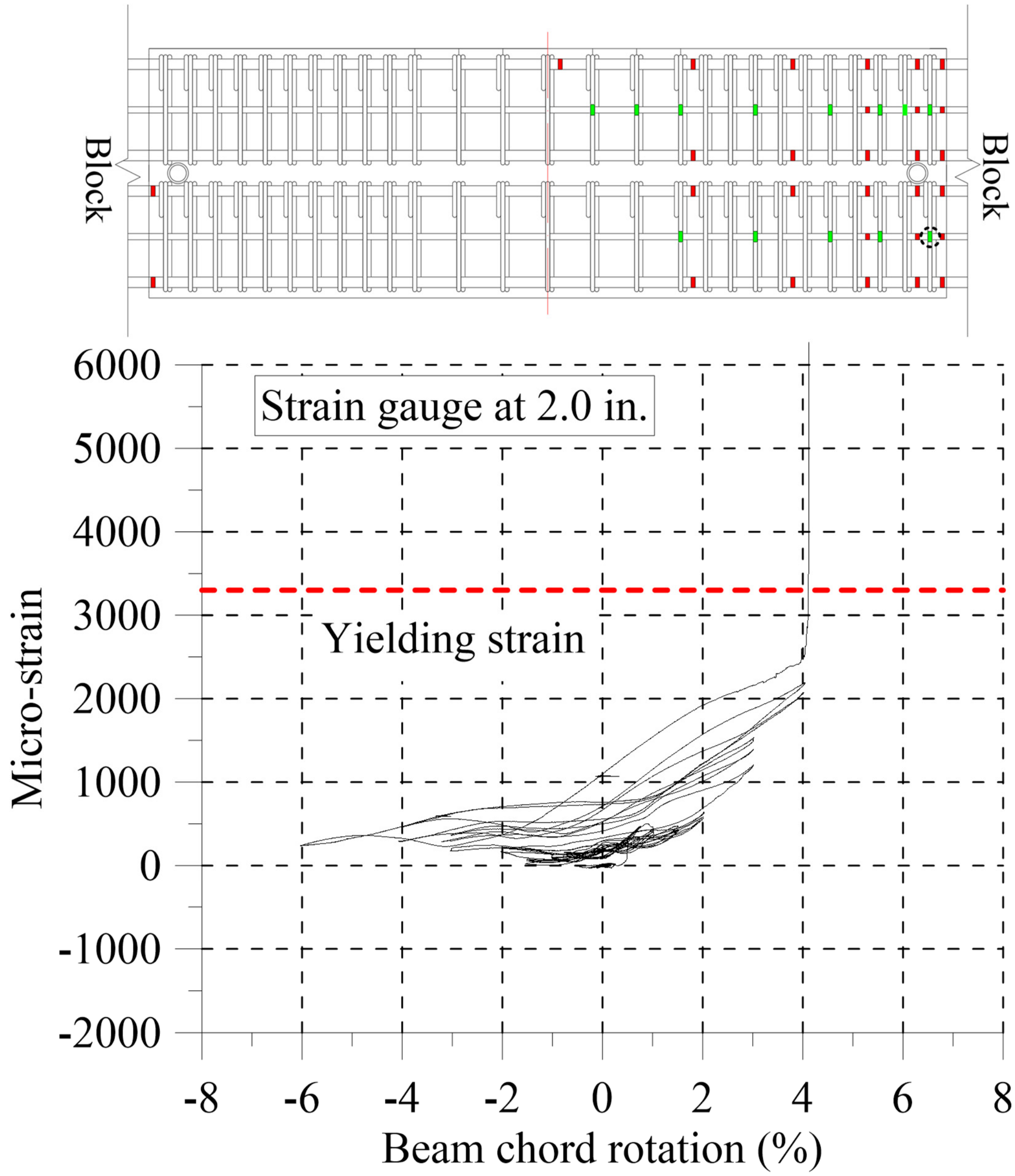

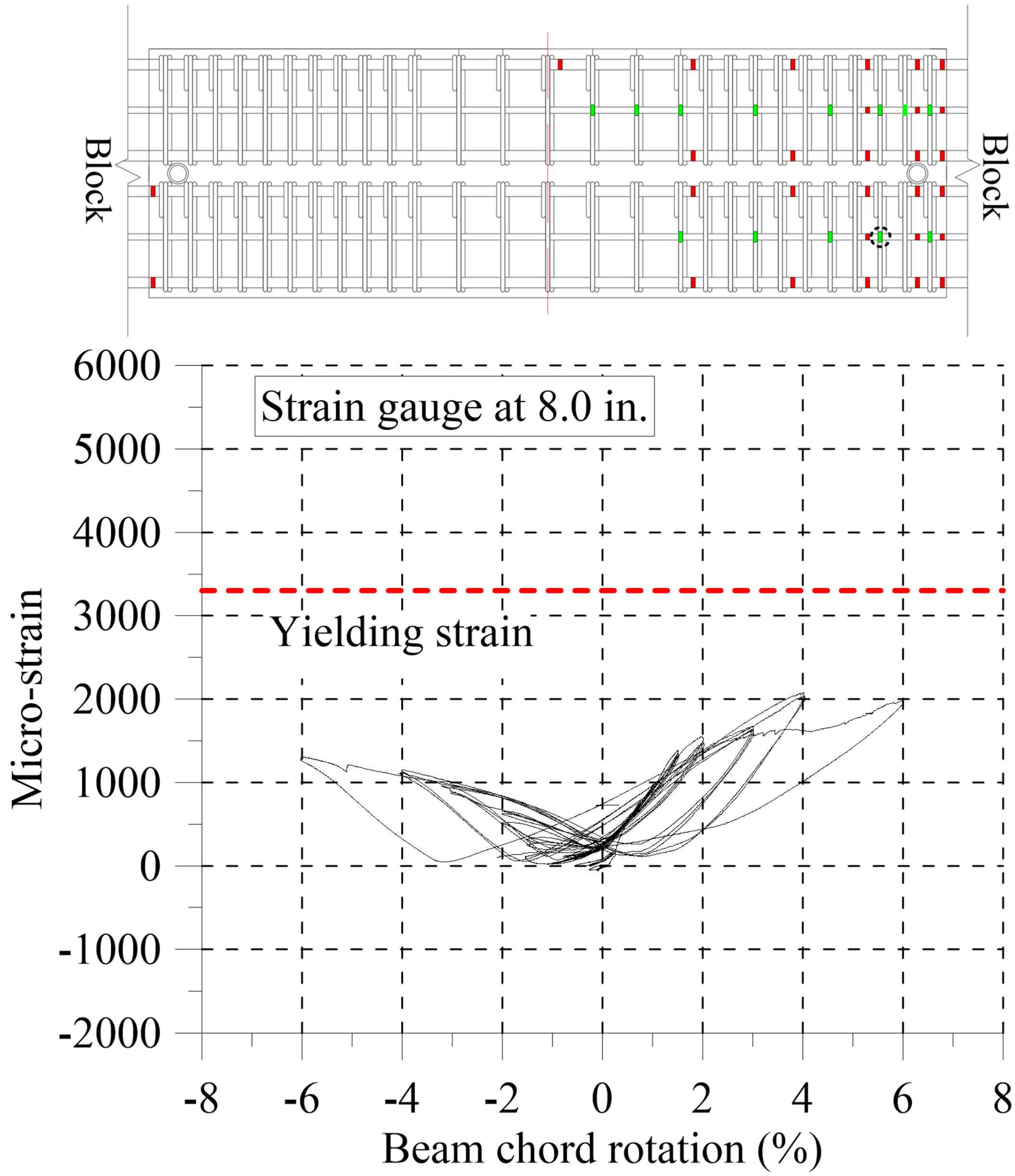
Block
Block
Strain gauge at 8.0 in.
Yielding strain
Micro-strain
6000
5000
4000
3000
2000
1000
0
-1000
-2000
-8
-6
-4
-2
0
2
4
6
8
Beam chord rotation (%)

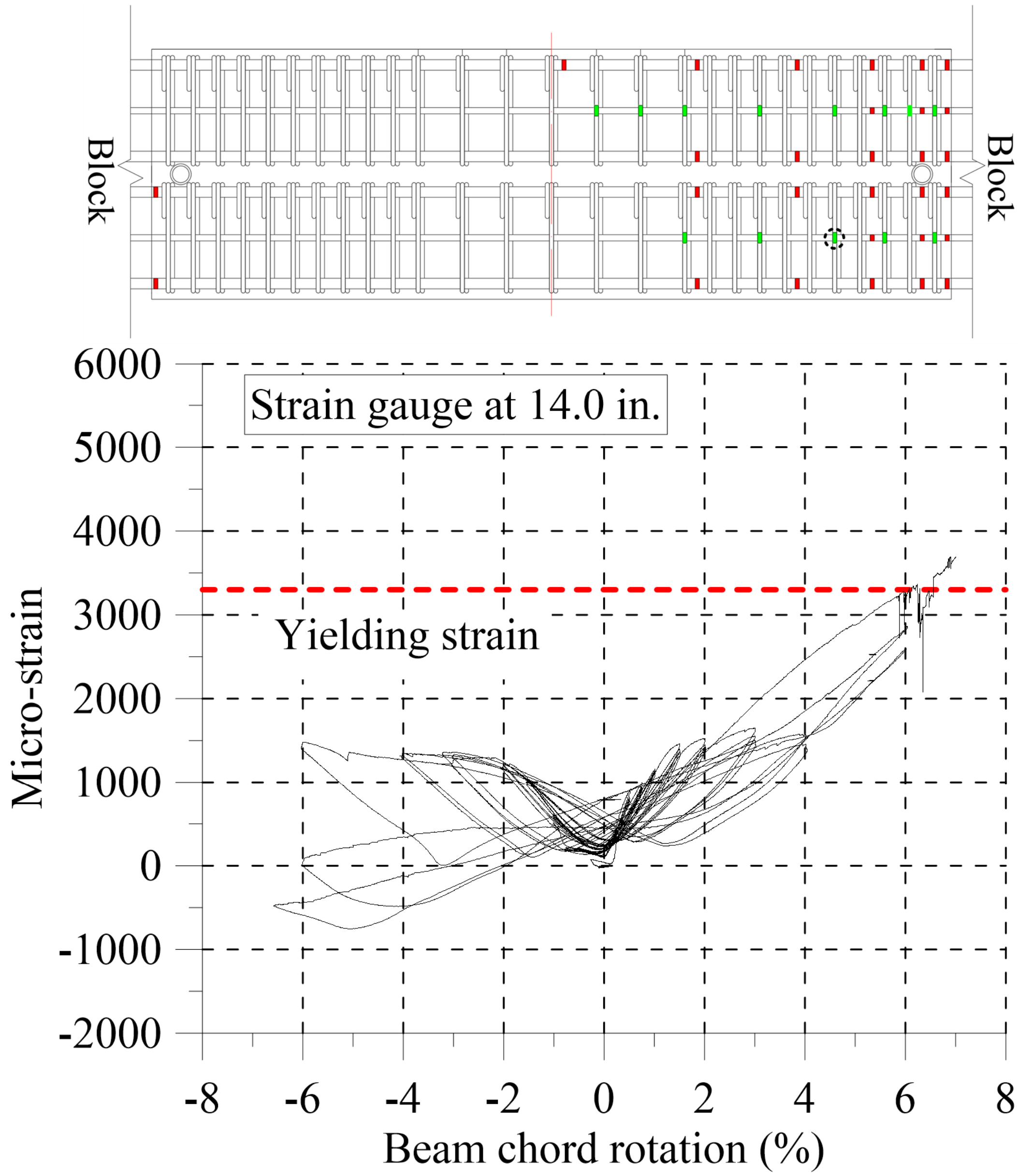
Block
Block
Strain gauge at 14.0 in.
Yielding strain
Micro-strain
6000
5000
4000
3000
2000
1000
0
-1000
-2000
-8
-6
-4
-2
0
2
4
6
8
Beam chord rotation (%)

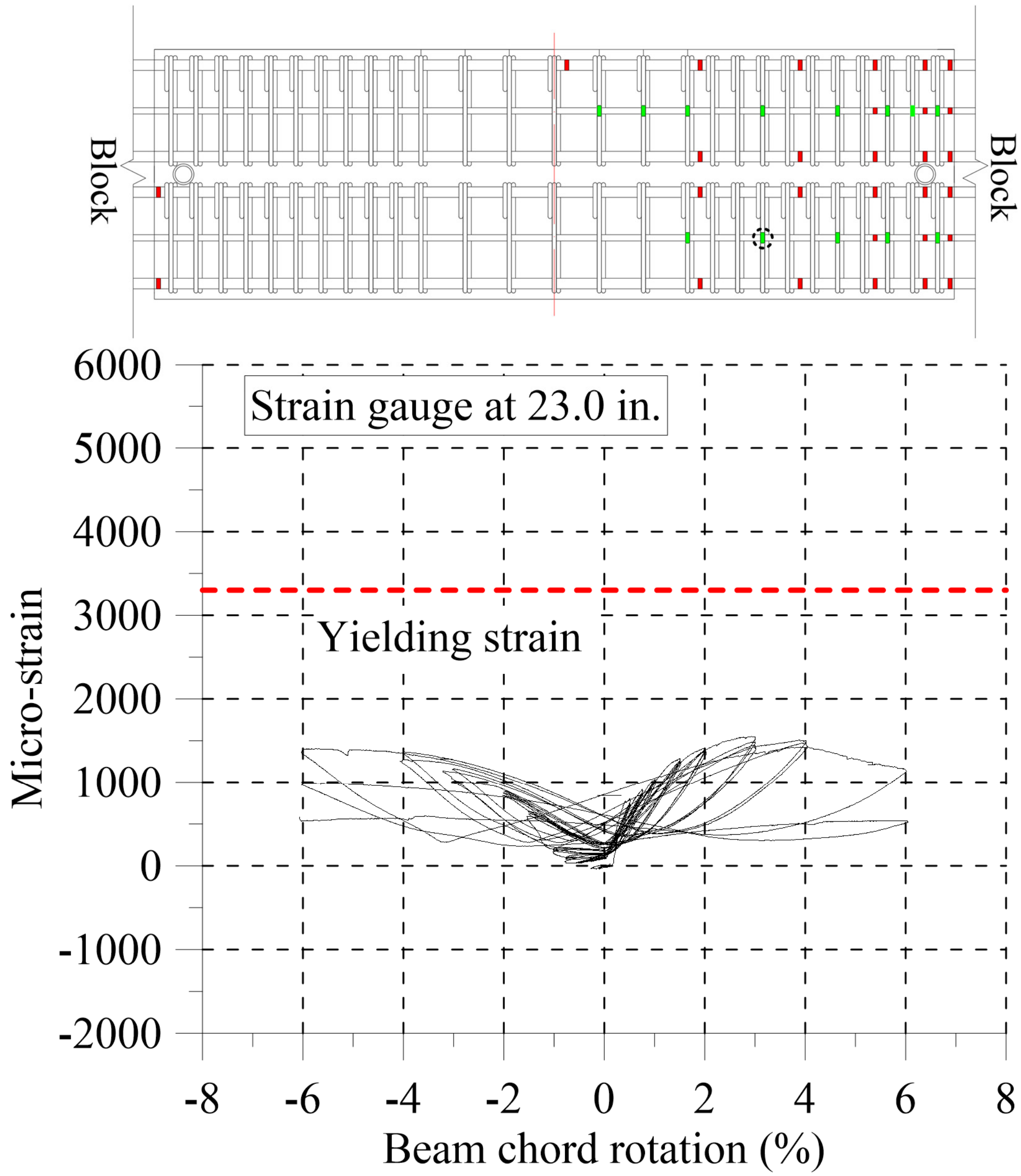
Block
Block
Strain gauge at 23.0 in.
Yielding strain
Micro-strain
Beam chord rotation (%)
6000
5000
4000
3000
2000
1000
0
-1000
-2000
-8
-6
-4
-2
0
2
4
6
8

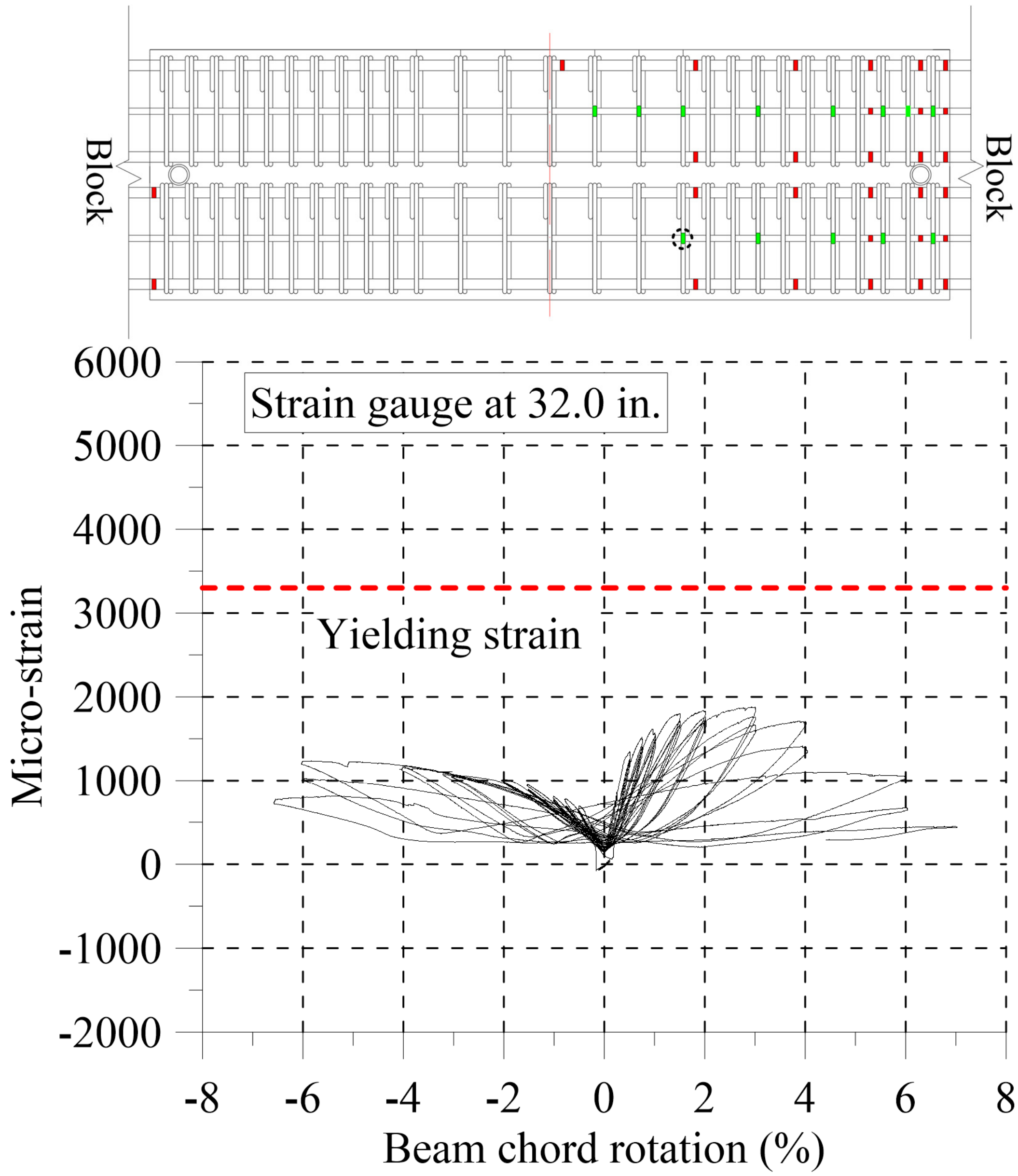

Block
Block
Strain gauge at 32.0 in.
Yielding strain
Micro-strain
Beam chord rotation (%)
6000
5000
4000
3000
2000
1000
0
-1000
-2000
-8
-6
-4
-2
0
2
4
6
8

C.1.2.3 Developed longitudinal reinforcement

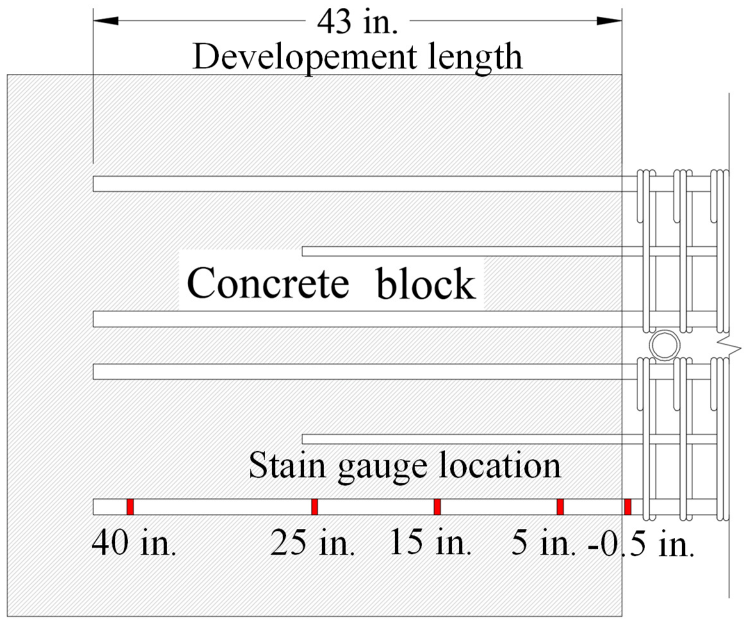

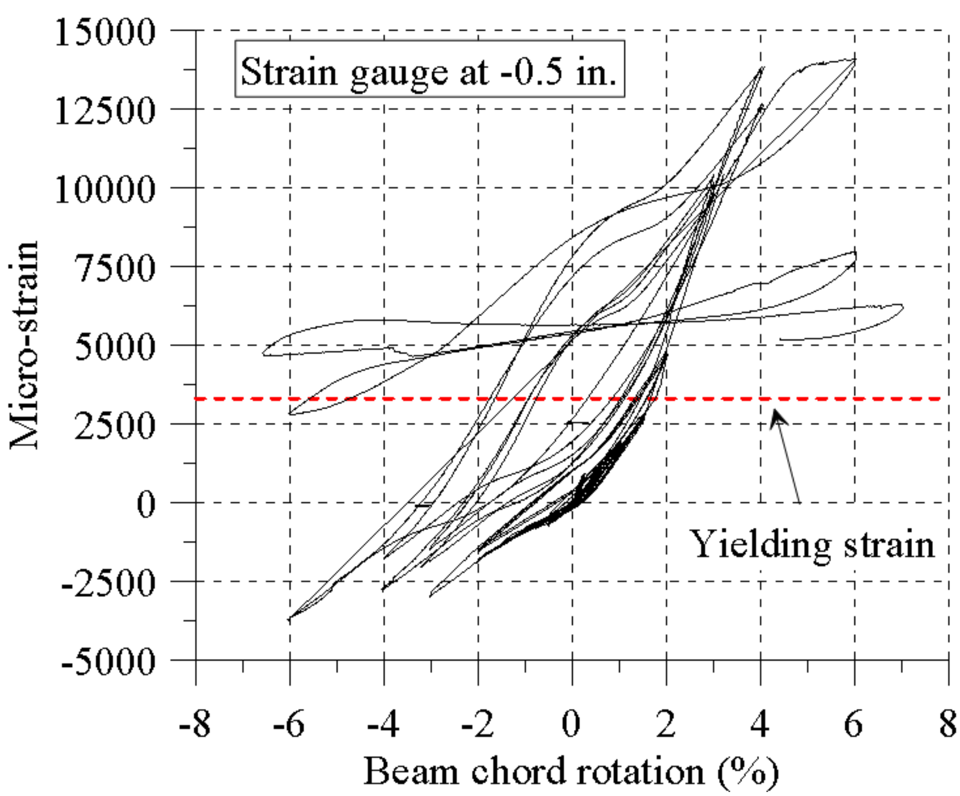

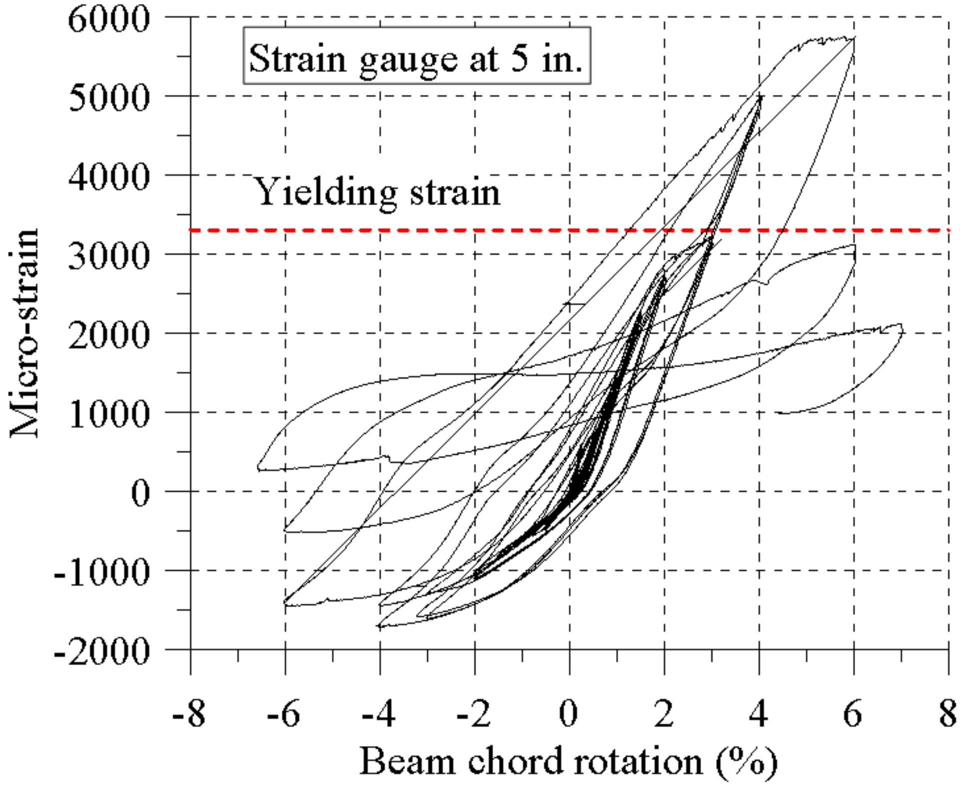
Strain gauge at 5 in.
Yielding strain
Micro-strain
Beam chord rotation (%)
6000
5000
4000
3000
2000
1000
0
-1000
-2000
-8
-6
-4
-2
0
2
4
6
8

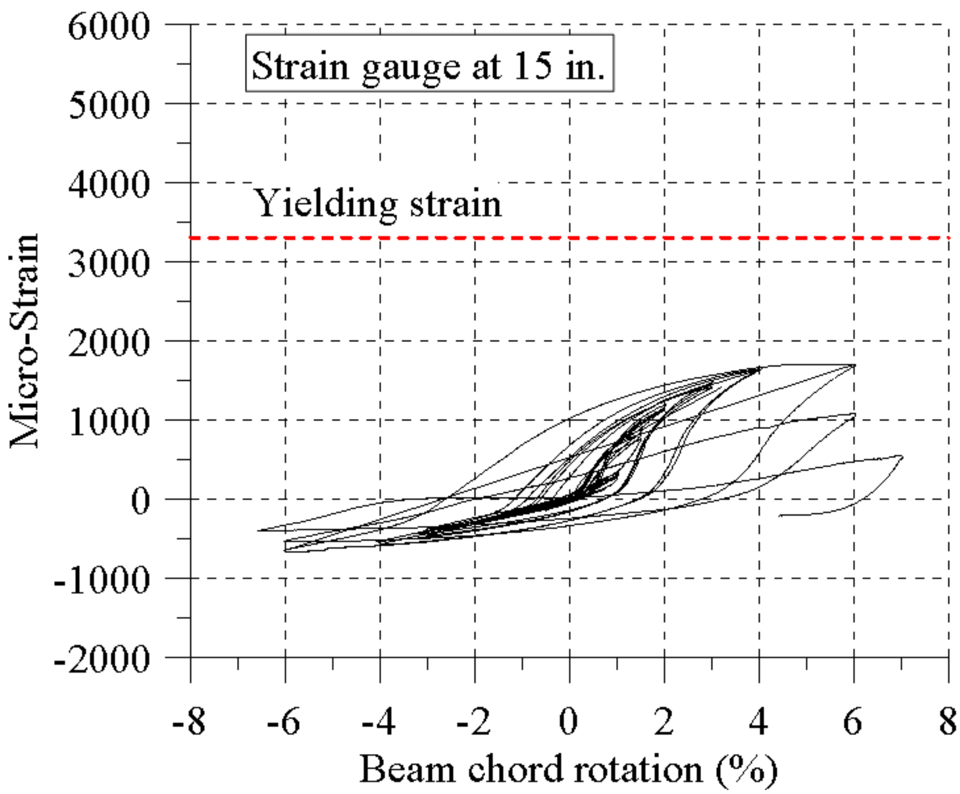
Strain gauge at 15 in.
Yielding strain
Micro-Strain
Beam chord rotation (%)
6000
5000
4000
3000
2000
1000
0
-1000
-2000
-8
-6
-4
-2
0
2
4
6
8

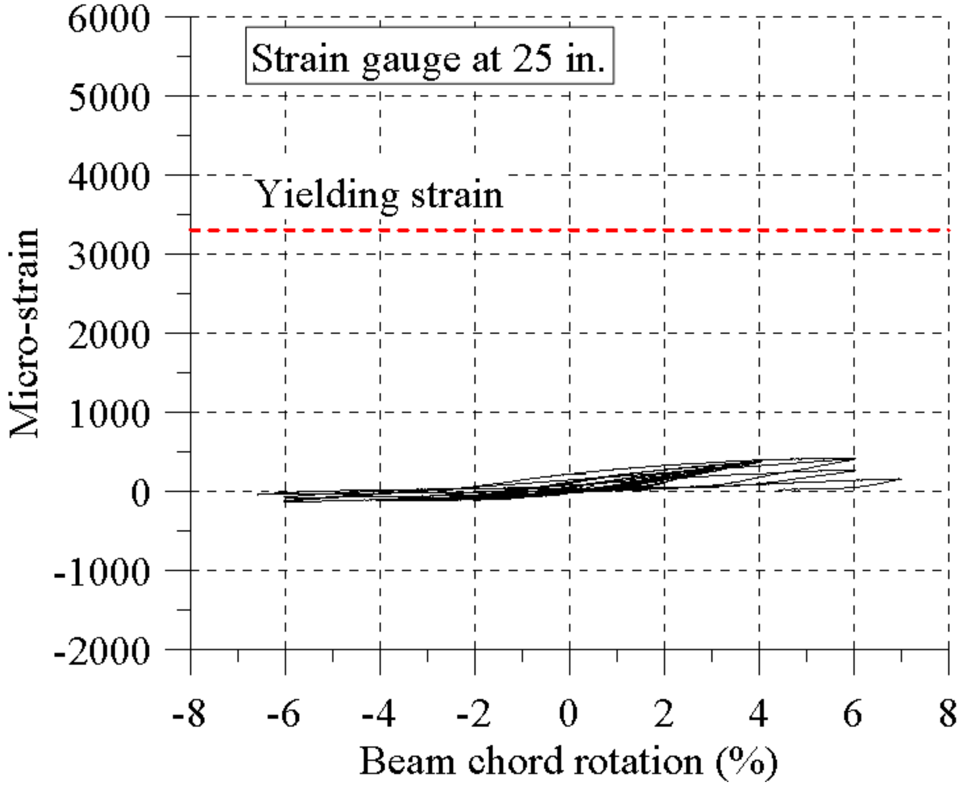
Strain gauge at 25 in.
Yielding strain
Micro-strain
6000
5000
4000
3000
2000
1000
0
-1000
-2000
-8
-6
-4
-2
0
2
4
6
8
Beam chord rotation (%)

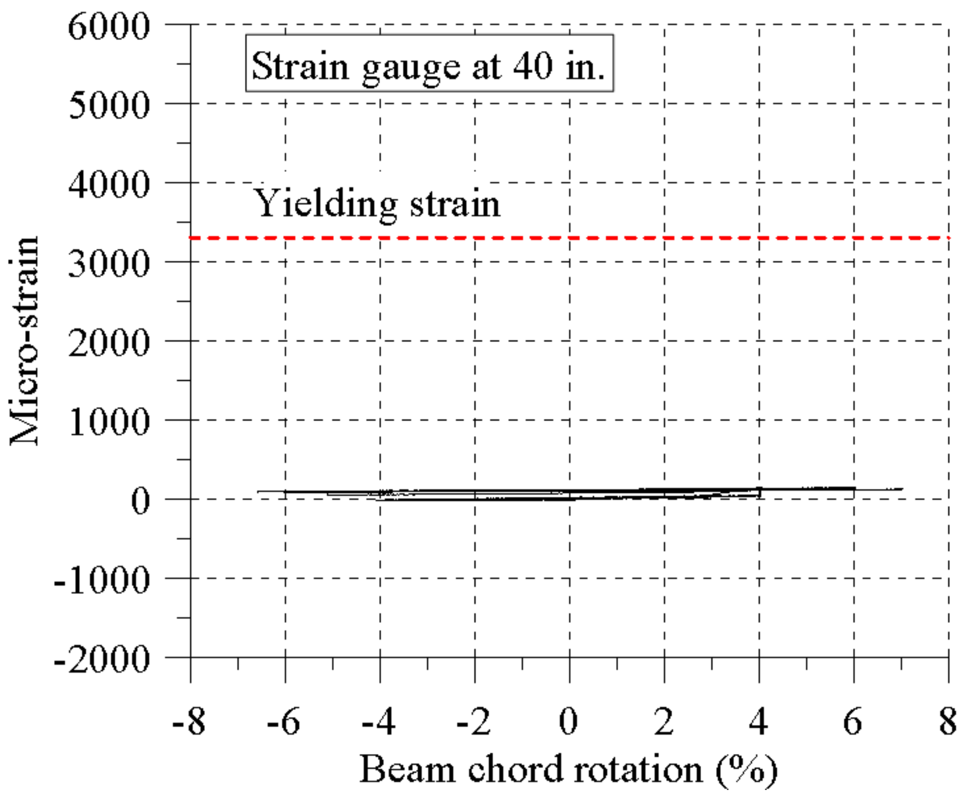
Strain gauge at 40 in.
Yielding strain
Micro-strain
6000
5000
4000
3000
2000
1000
0
-1000
-2000
-8
-6
-4
-2
0
2
4
6
8
Beam chord rotation (%)

C.2 Half-scale 2.4 aspect ratio DBCB with the slab (HS-R2.4-S-1)

Measured strain versus chord rotation for each strain gauge attached to the reinforcing bars is plotted. The location of each strain gauge was indicated with a black dashed line circle on the plot.

C.2.1 Upper steel cage

C.2.1.1 Longitudinal reinforcement

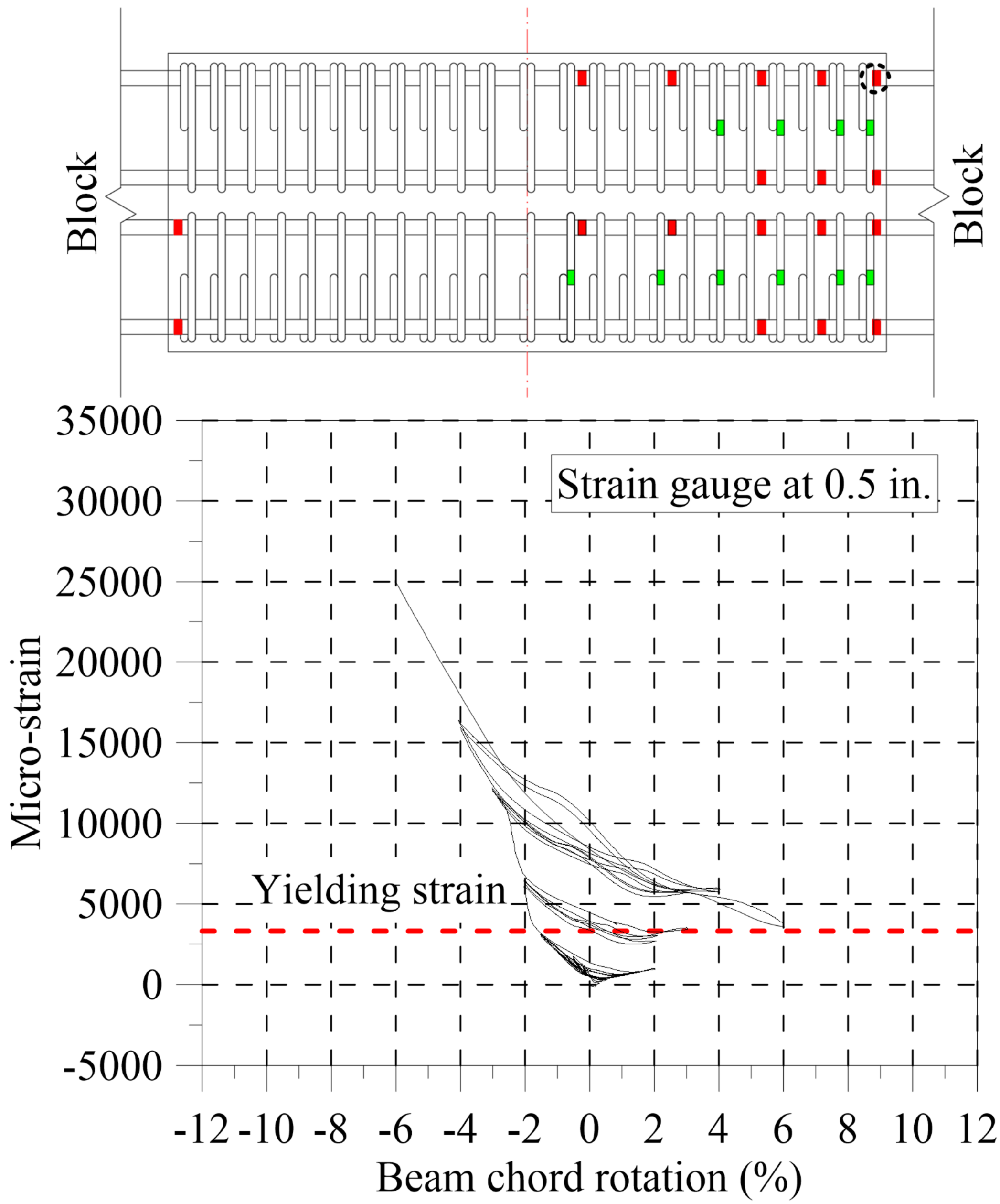

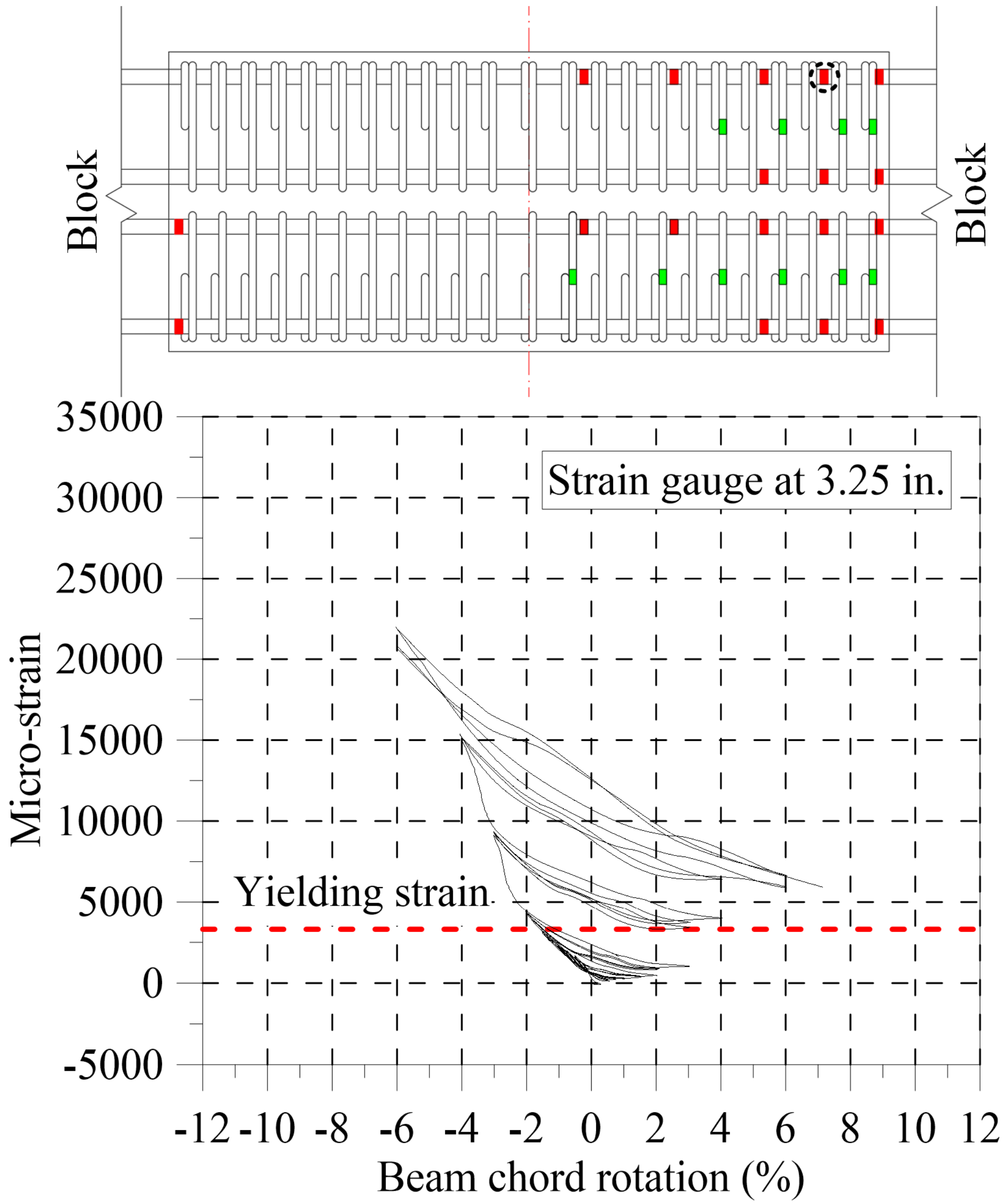
Block
Block
Strain gauge at 3.25 in.
Yielding strain
Micro-strain
Beam chord rotation (%)
35000
30000
25000
20000
15000
10000
5000
0
-5000
-12
-10
-8
-6
-4
-2
0
2
4
6
8
10
12

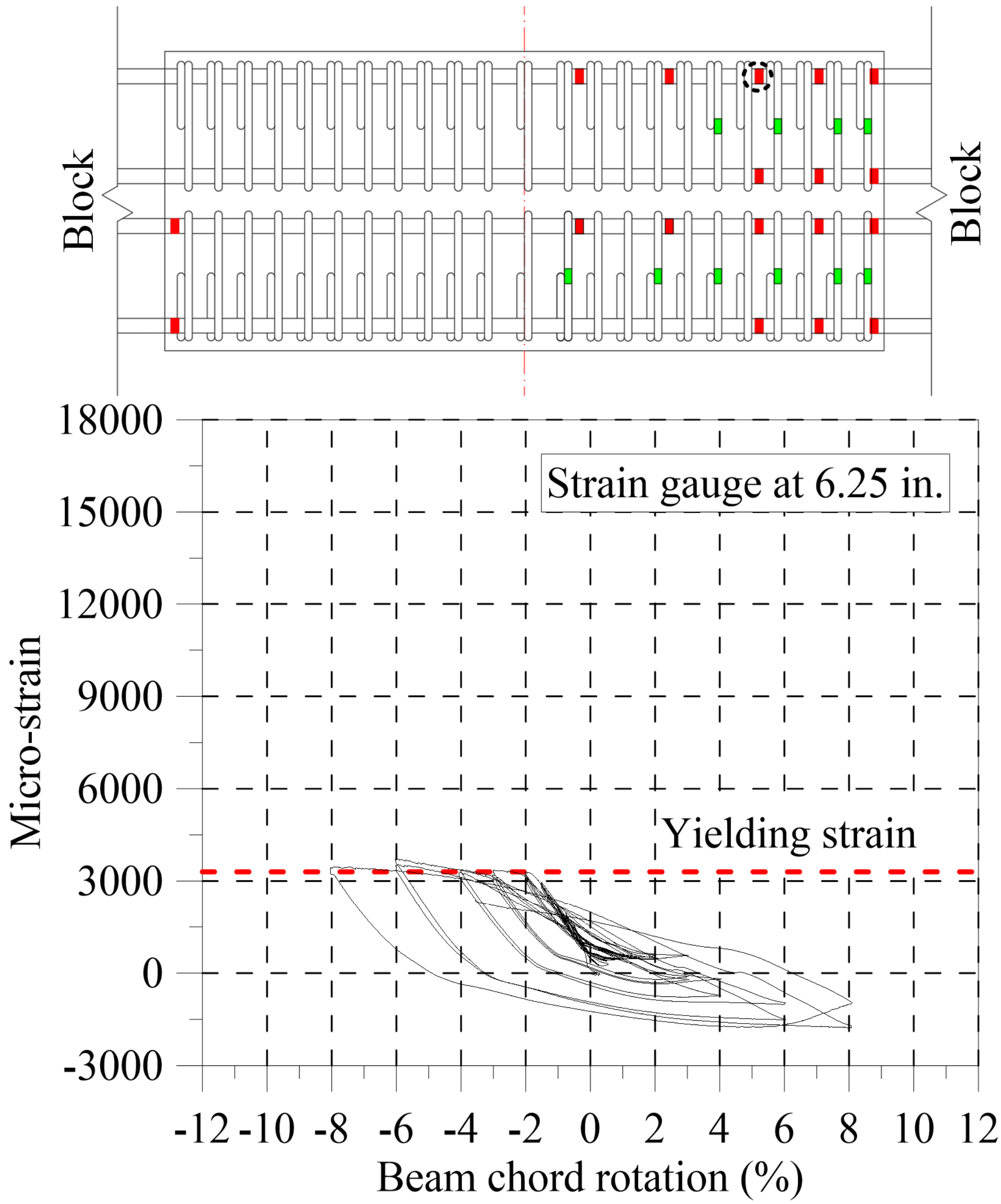
Block
Block
Strain gauge at 6.25 in.
Yielding strain
Micro-strain
Beam chord rotation (%)
18000
15000
12000
9000
6000
3000
0
-3000
-12
-10
-8
-6
-4
-2
0
2
4
6
8
10
12

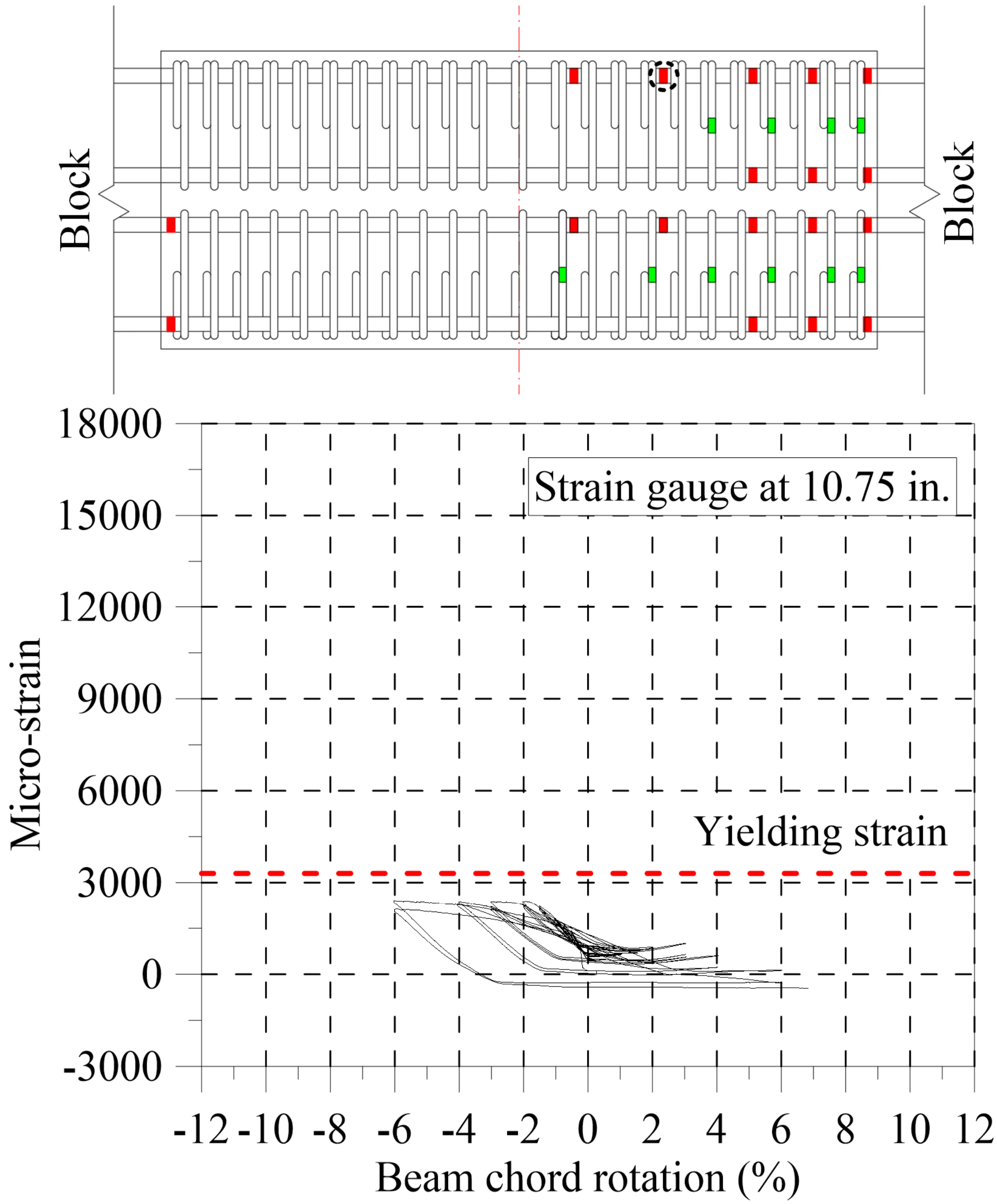

Block
Block
18000
15000
12000
9000
6000
3000
0
-3000
Micro-strain
Strain gauge at 10.75 in.
Yielding strain
-12
-10
-8
-6
-4
-2
0
2
4
6
8
10
12
Beam chord rotation (%)

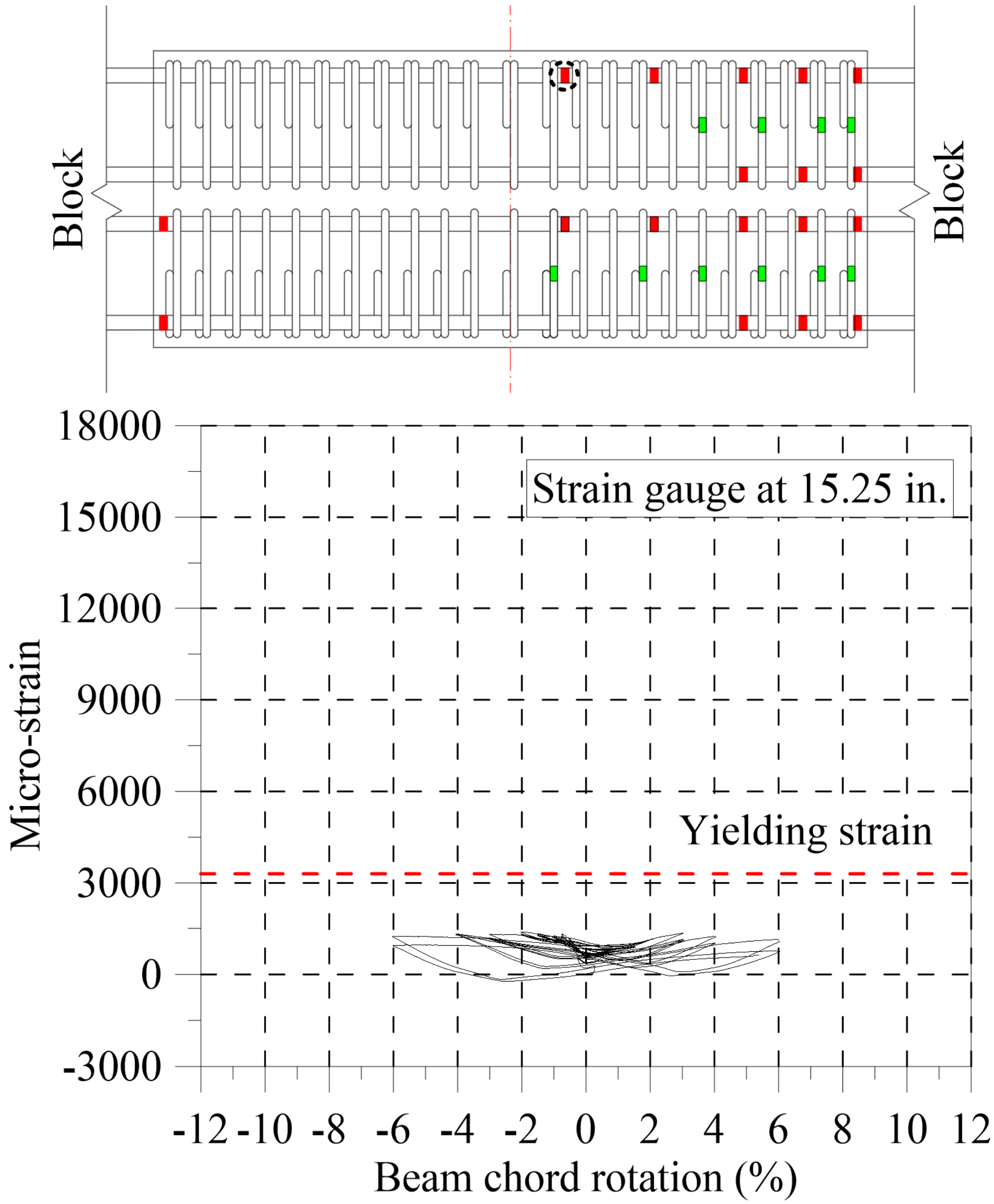
Block
Block
Strain gauge at 15.25 in.
Yielding strain
Micro-strain
Beam chord rotation (%)
18000
15000
12000
9000
6000
3000
0
-3000
-12
-10
-8
-6
-4
-2
0
2
4
6
8
10
12

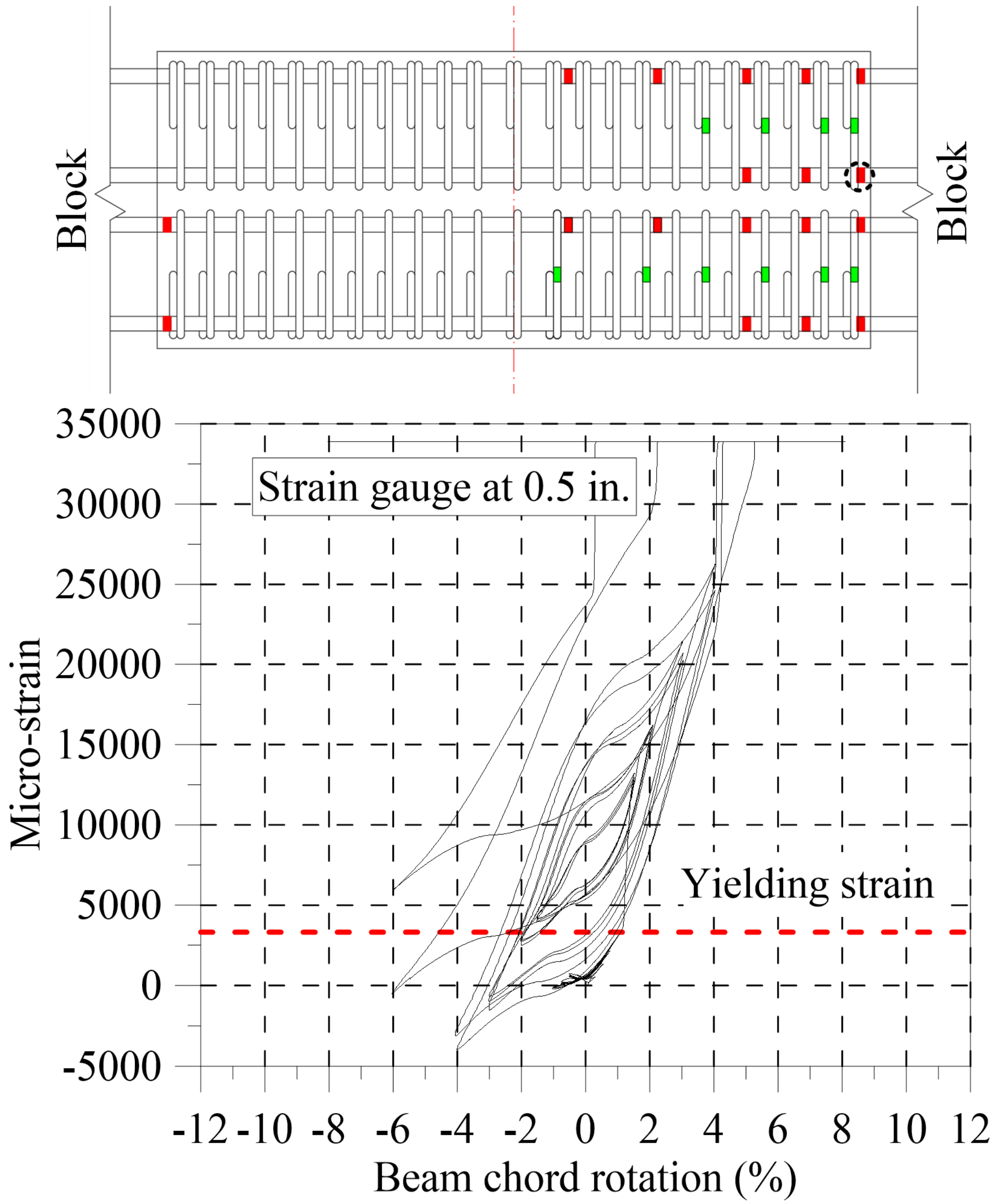
Block
Block
Strain gauge at 0.5 in.
Yielding strain
Micro-strain
35000
30000
25000
20000
15000
10000
5000
0
-5000
-12 -10 -8 -6 -4 -2 0 2 4 6 8 10 12
Beam chord rotation (%)

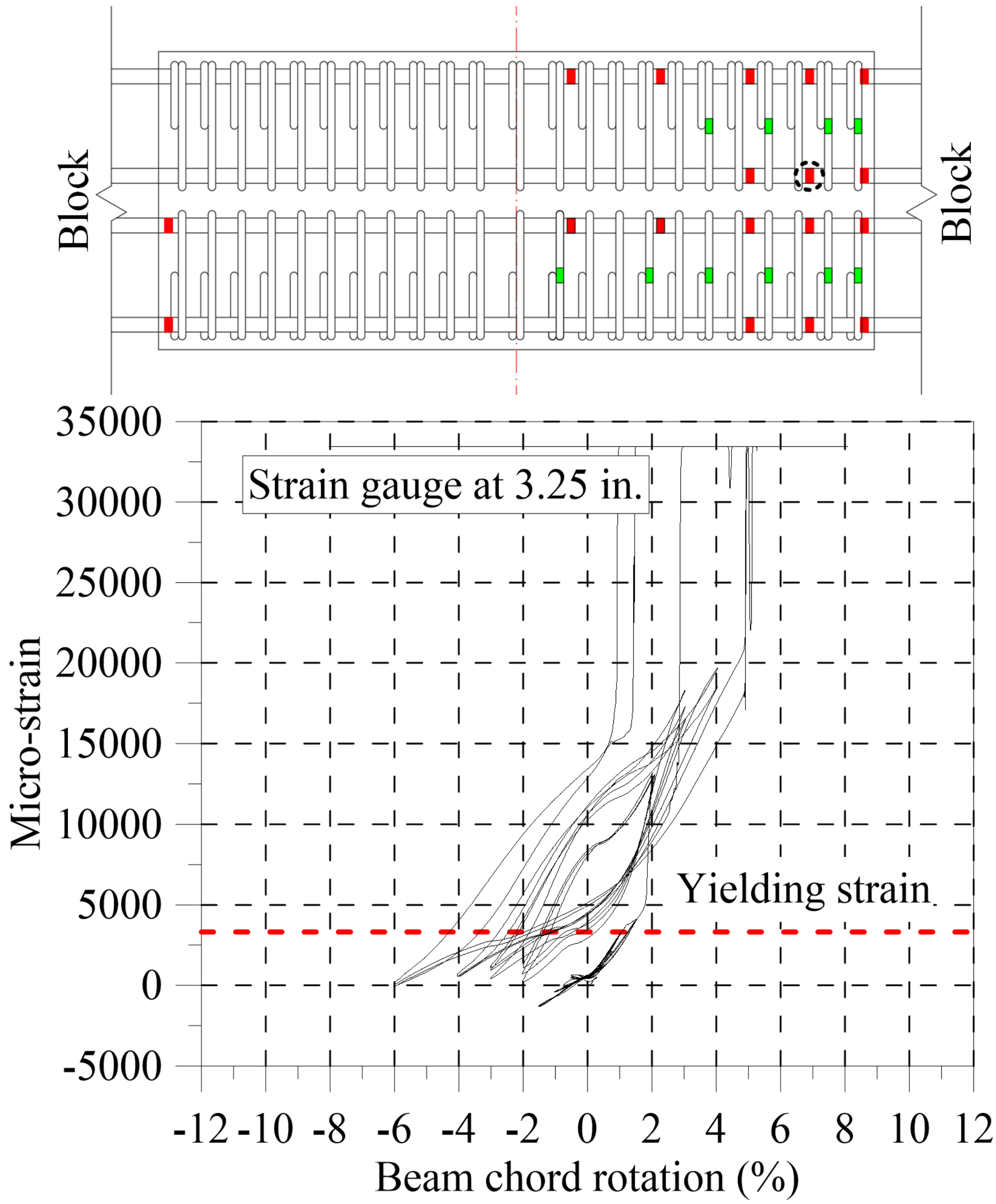
Block
Block
Strain gauge at 3.25 in.
Yielding strain
Micro-strain
Beam chord rotation (%)
35000
30000
25000
20000
15000
10000
5000
0
-5000
-12 -10 -8 -6 -4 -2 0 2 4 6 8 10 12

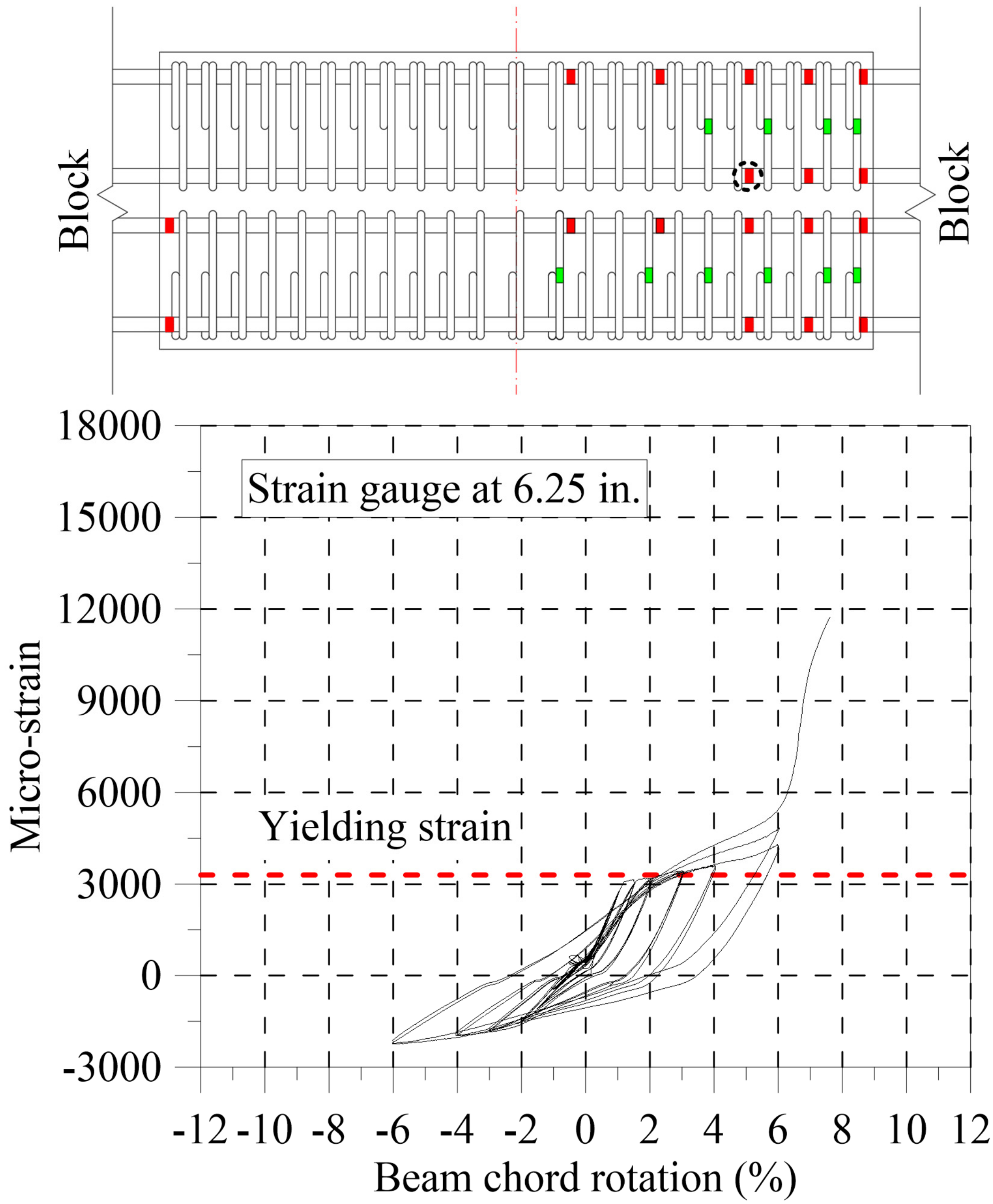

Block
Block
Strain gauge at 6.25 in.
Yielding strain
Micro-strain
18000
15000
12000
9000
6000
3000
0
-3000
-12 -10 -8 -6 -4 -2 0 2 4 6 8 10 12
Beam chord rotation (%)

C.2.1.2 Transverse reinforcement

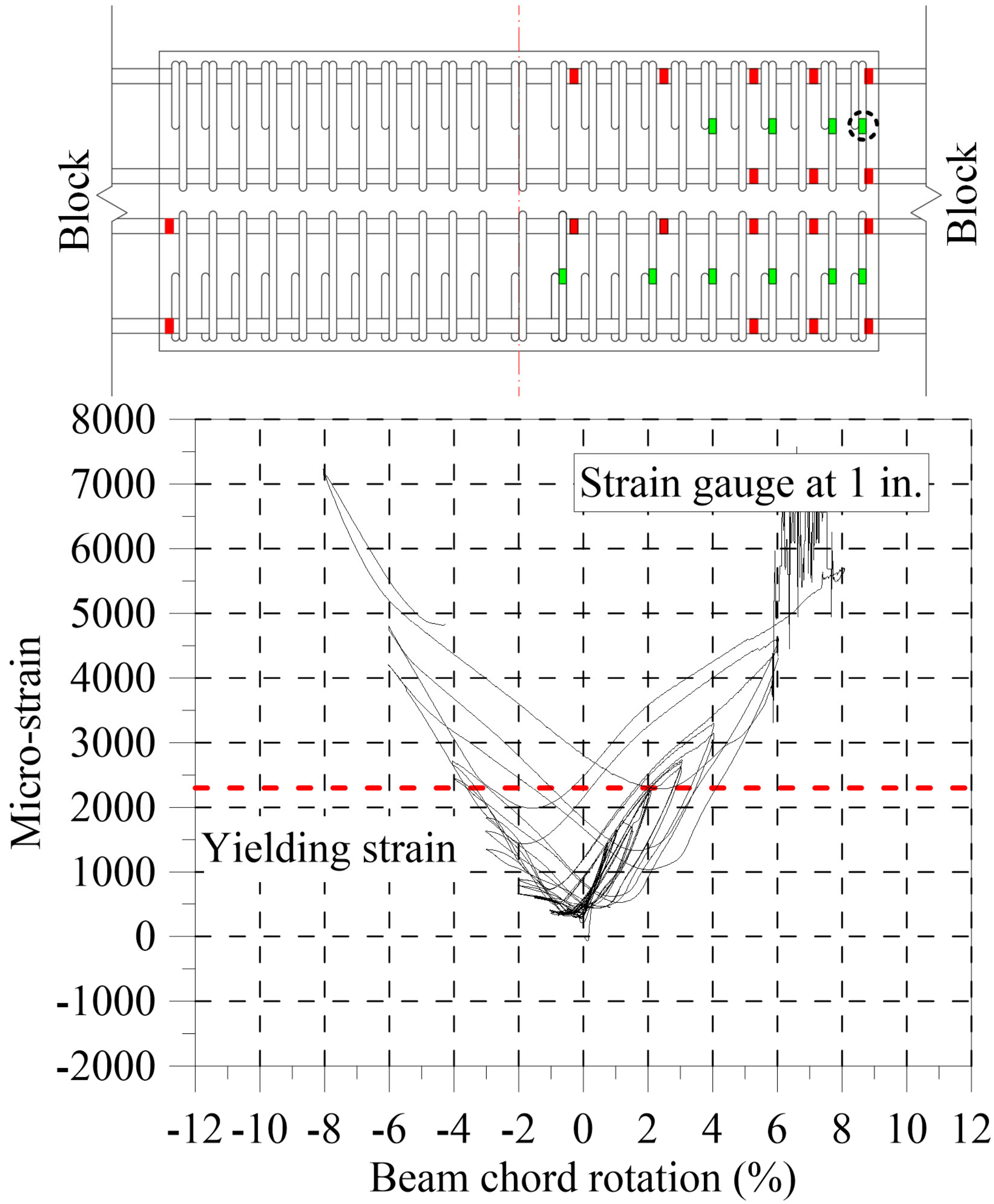

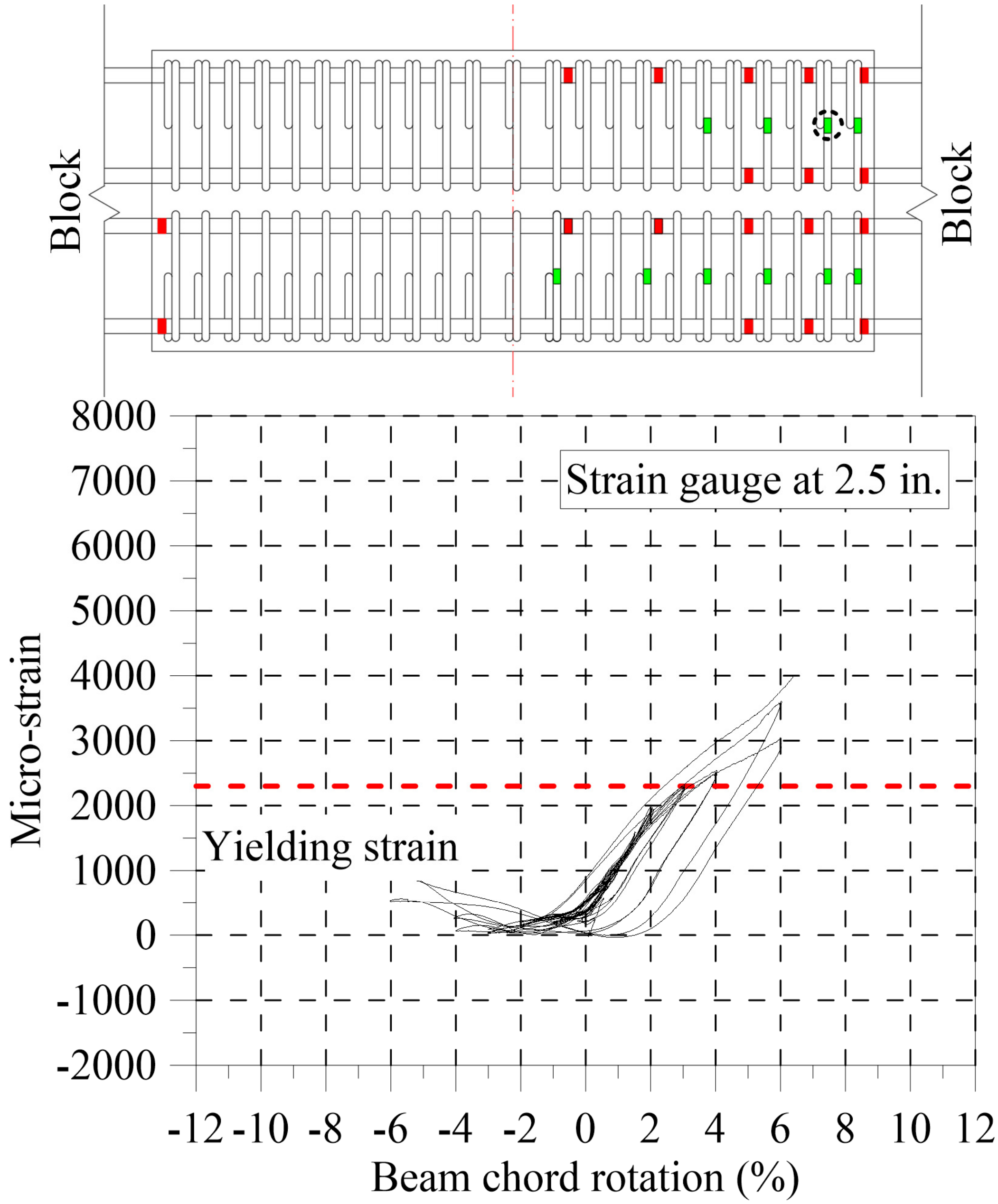
Block
Block
Strain gauge at 2.5 in.
Yielding strain
Micro-strain
Beam chord rotation (%)
8000
7000
6000
5000
4000
3000
2000
1000
0
-1000
-2000
-12
-10
-8
-6
-4
-2
0
2
4
6
8
10
12

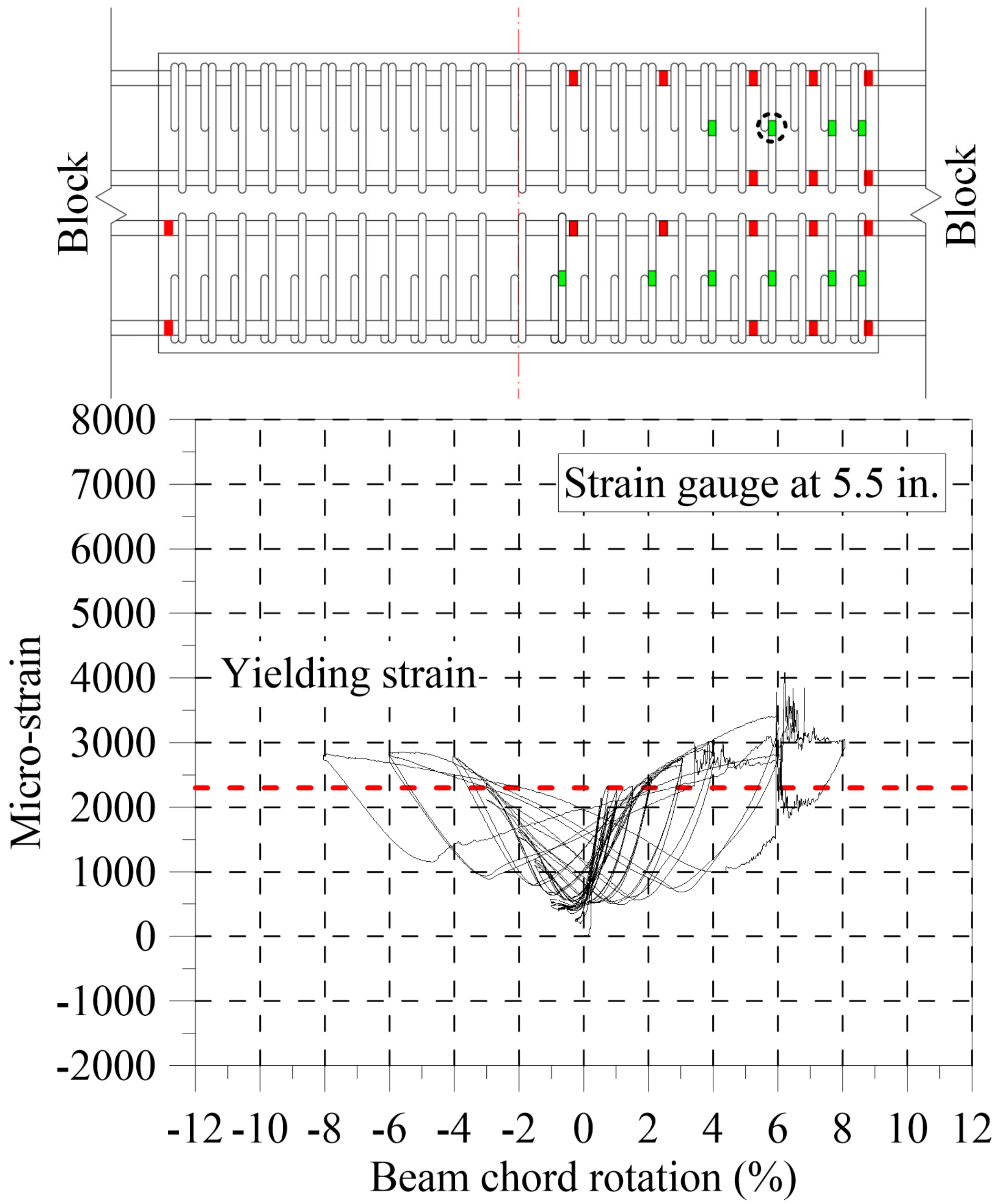
Block
Block
Strain gauge at 5.5 in.
Yielding strain
Micro-strain
Beam chord rotation (%)

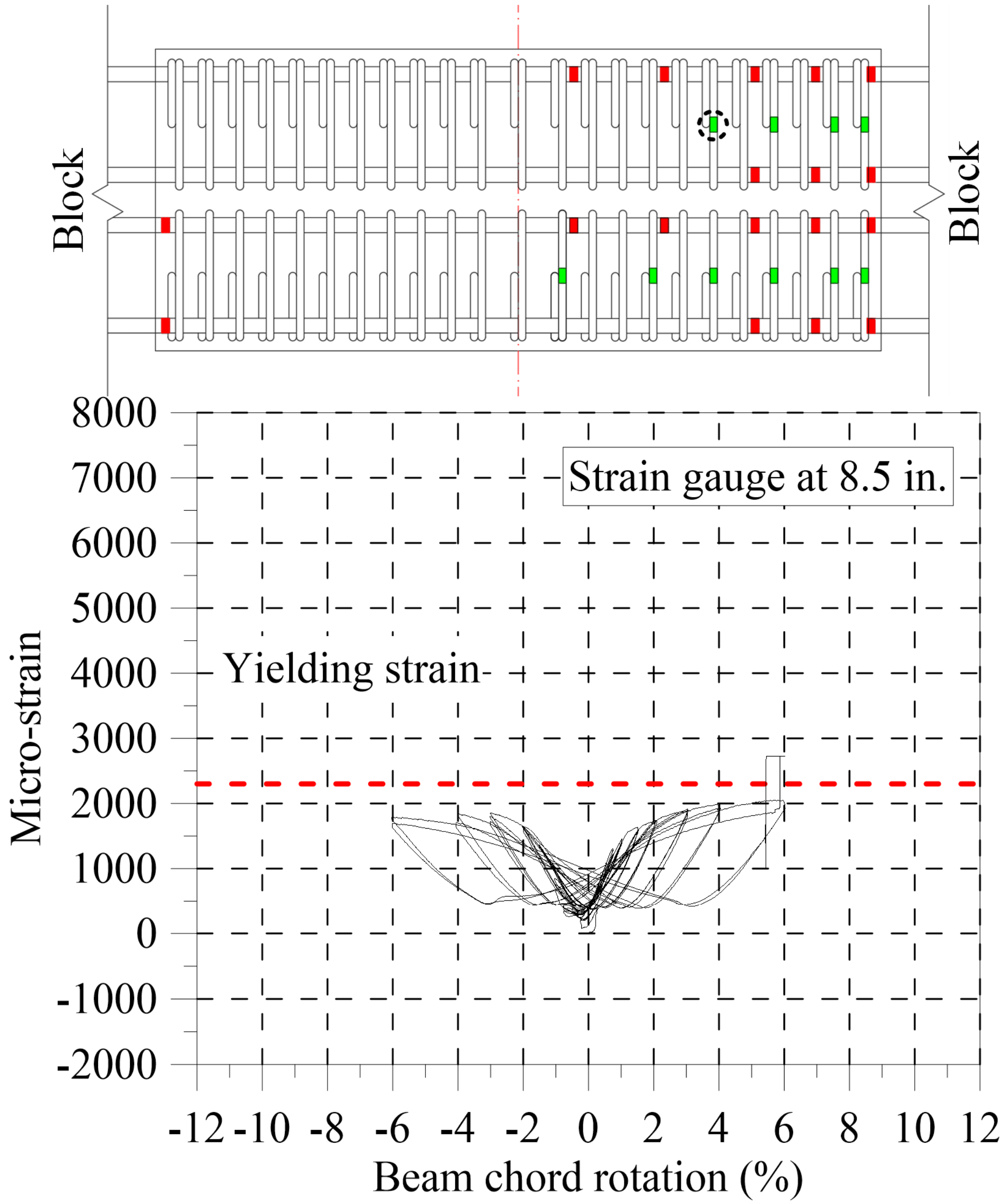
Block
Block
Strain gauge at 8.5 in.
Yielding strain
Micro-strain
Beam chord rotation (%)
8000
7000
6000
5000
4000
3000
2000
1000
0
-1000
-2000
-12
-10
-8
-6
-4
-2
0
2
4
6
8
10
12

C.2.1.3 Developed longitudinal reinforcement

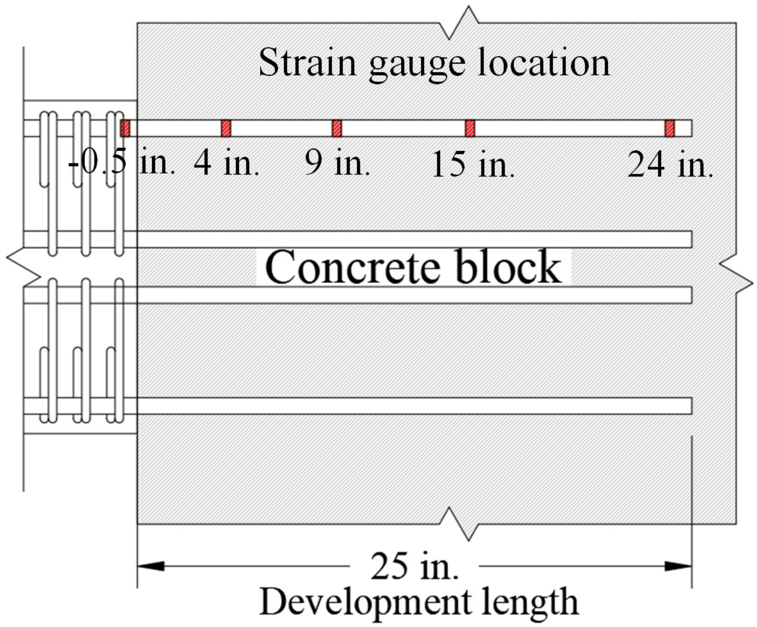

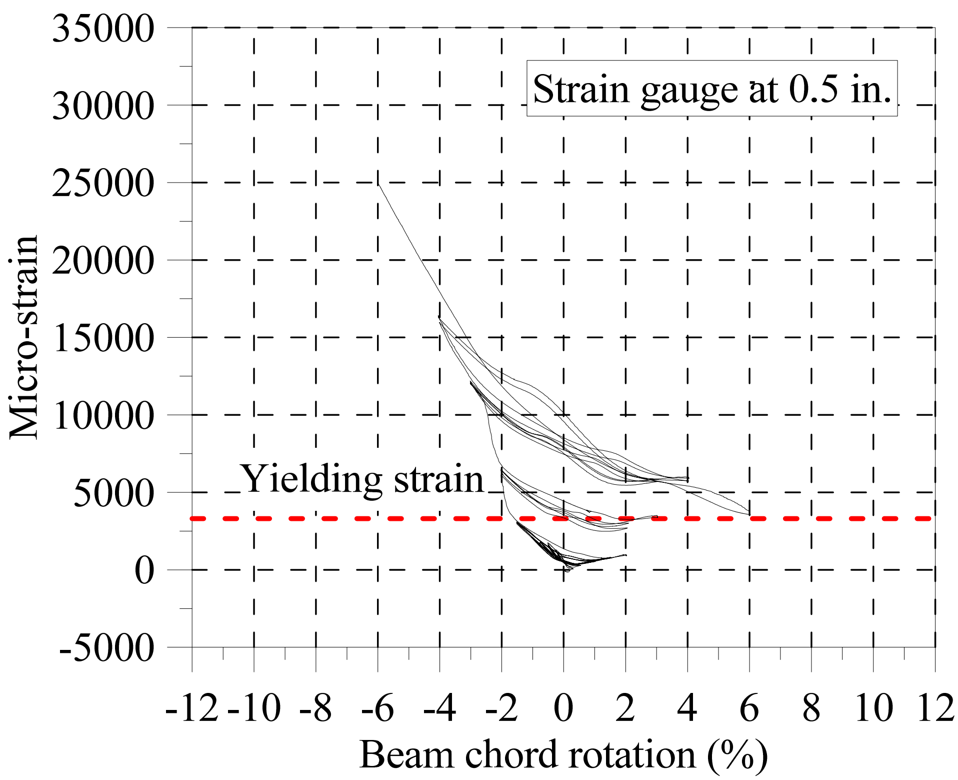

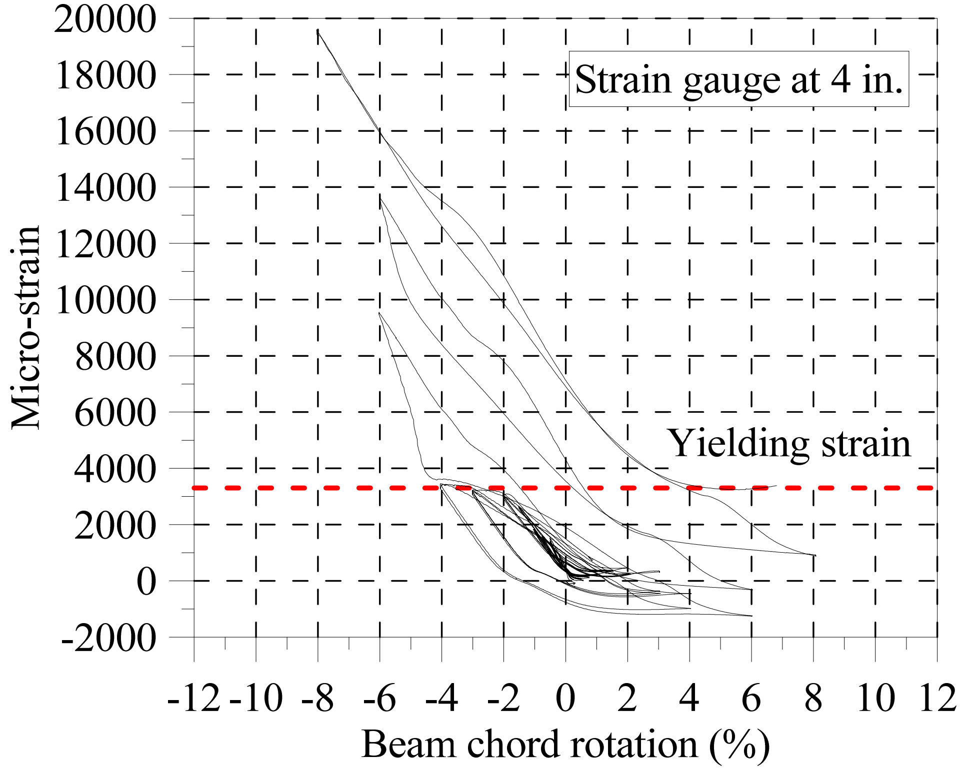
Strain gauge at 4 in.
Yielding strain
Micro-strain
20000
18000
16000
14000
12000
10000
8000
6000
4000
2000
0
-2000
-12 -10 -8 -6 -4 -2 0 2 4 6 8 10 12
Beam chord rotation (%)

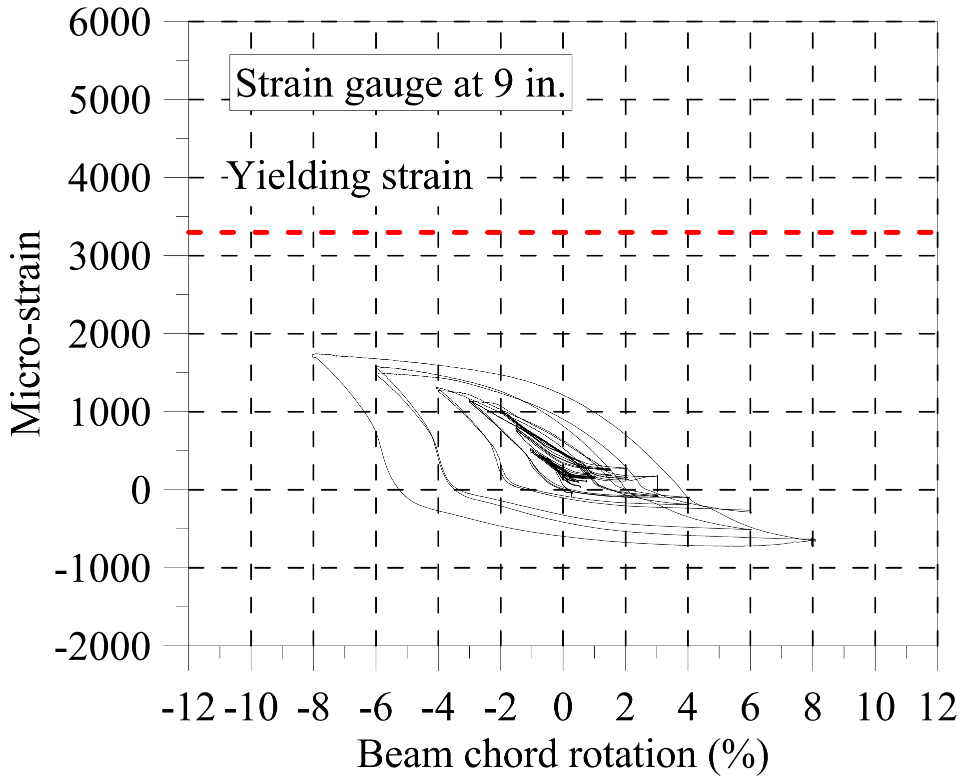
Strain gauge at 9 in.
Yielding strain
Micro-strain
6000
5000
4000
3000
2000
1000
0
-1000
-2000
-12 -10 -8 -6 -4 -2 0 2 4 6 8 10 12
Beam chord rotation (%)

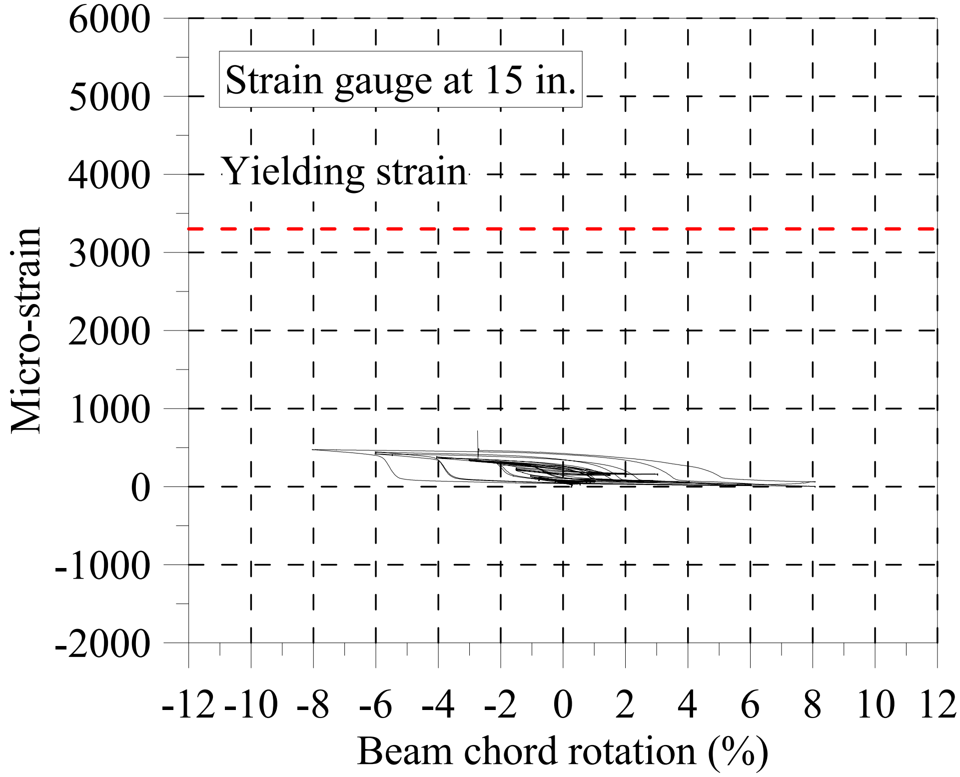
Strain gauge at 15 in.
Yielding strain
Micro-strain
6000
5000
4000
3000
2000
1000
0
-1000
-2000
-12 -10 -8 -6 -4 -2 0 2 4 6 8 10 12
Beam chord rotation (%)

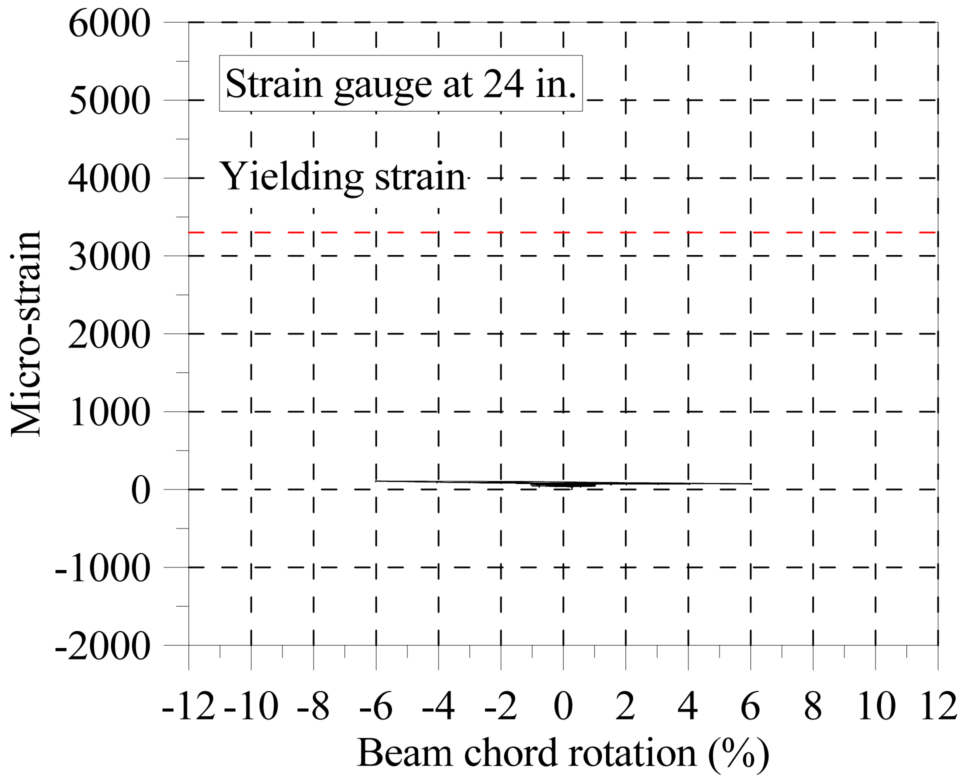
Strain gauge at 24 in.
Yielding strain
Micro-strain
6000
5000
4000
3000
2000
1000
0
-1000
-2000
-12 -10 -8 -6 -4 -2 0 2 4 6 8 10 12
Beam chord rotation (%)

C.2.2 Lower steel cage

C.2.2.1 Longitudinal reinforcement

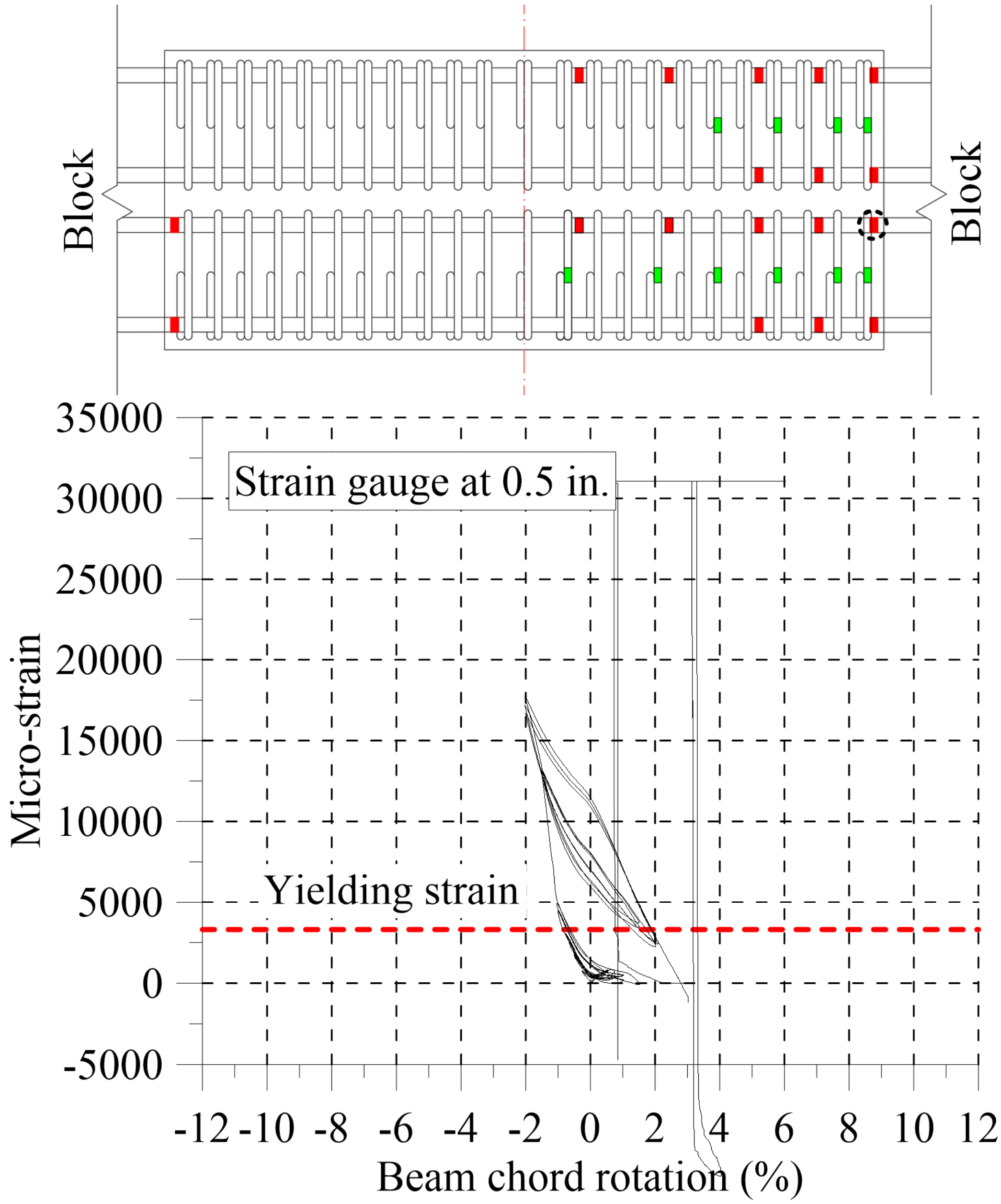

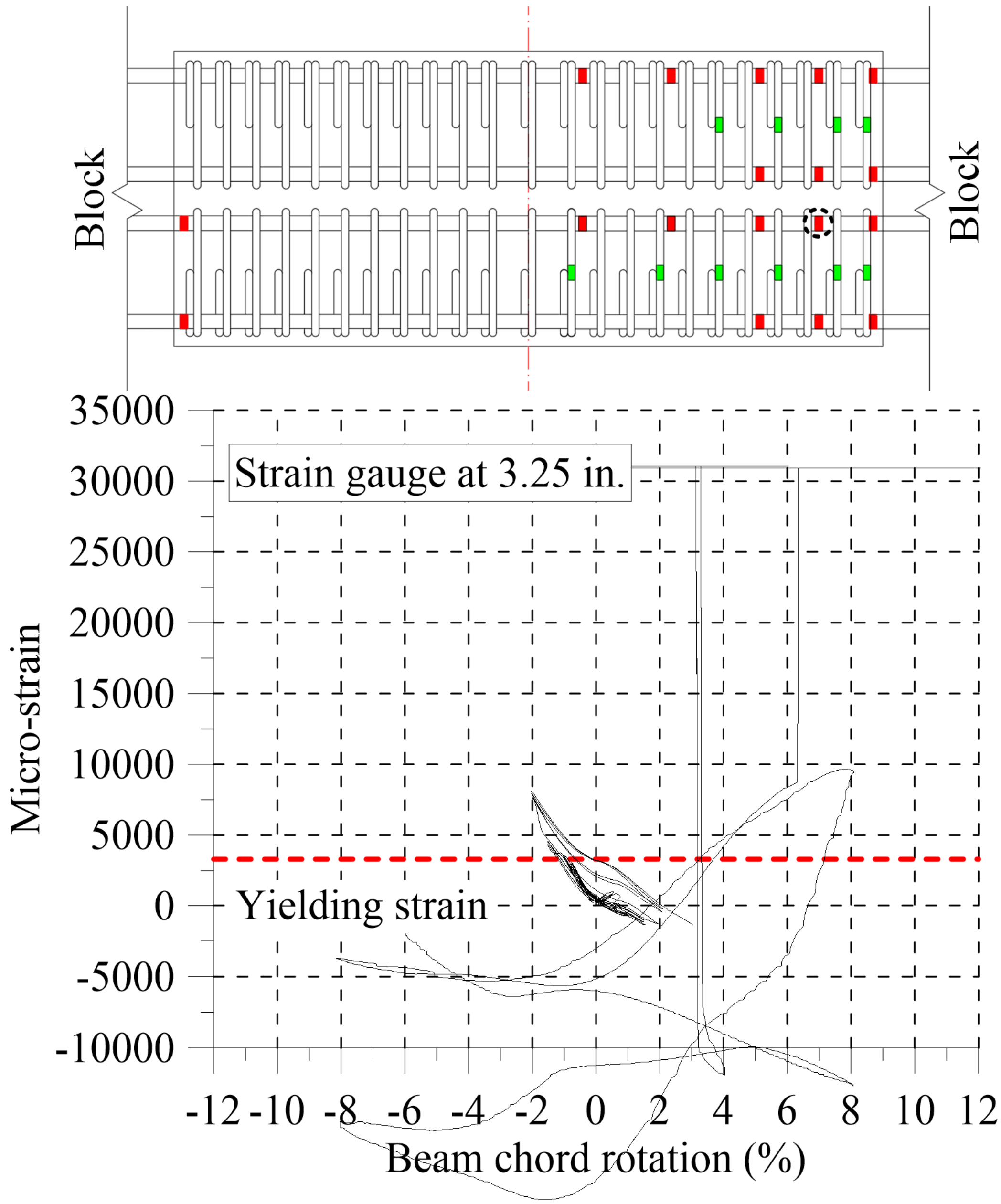
Block
Block
Strain gauge at 3.25 in.
Yielding strain
Micro-strain
Beam chord rotation (%)
35000
30000
25000
20000
15000
10000
5000
0
-5000
-10000
-12
-10
-8
-6
-4
-2
0
2
4
6
8
10
12

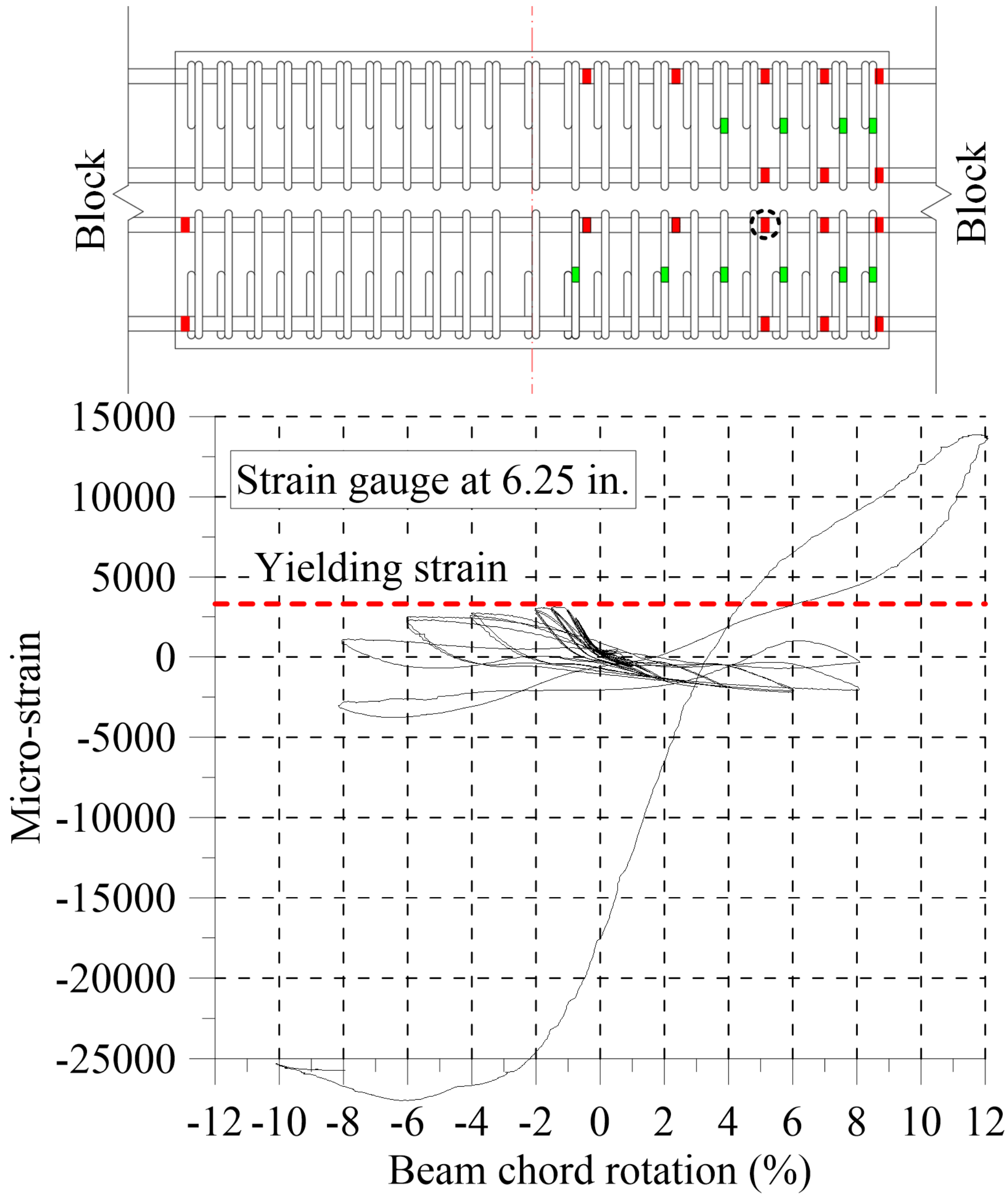

Block
Block
Strain gauge at 6.25 in.
Yielding strain
Micro-strain
15000
10000
5000
0
-5000
-10000
-15000
-20000
-25000
-12
-10
-8
-6
-4
-2
0
2
4
6
8
10
12
Beam chord rotation (%)

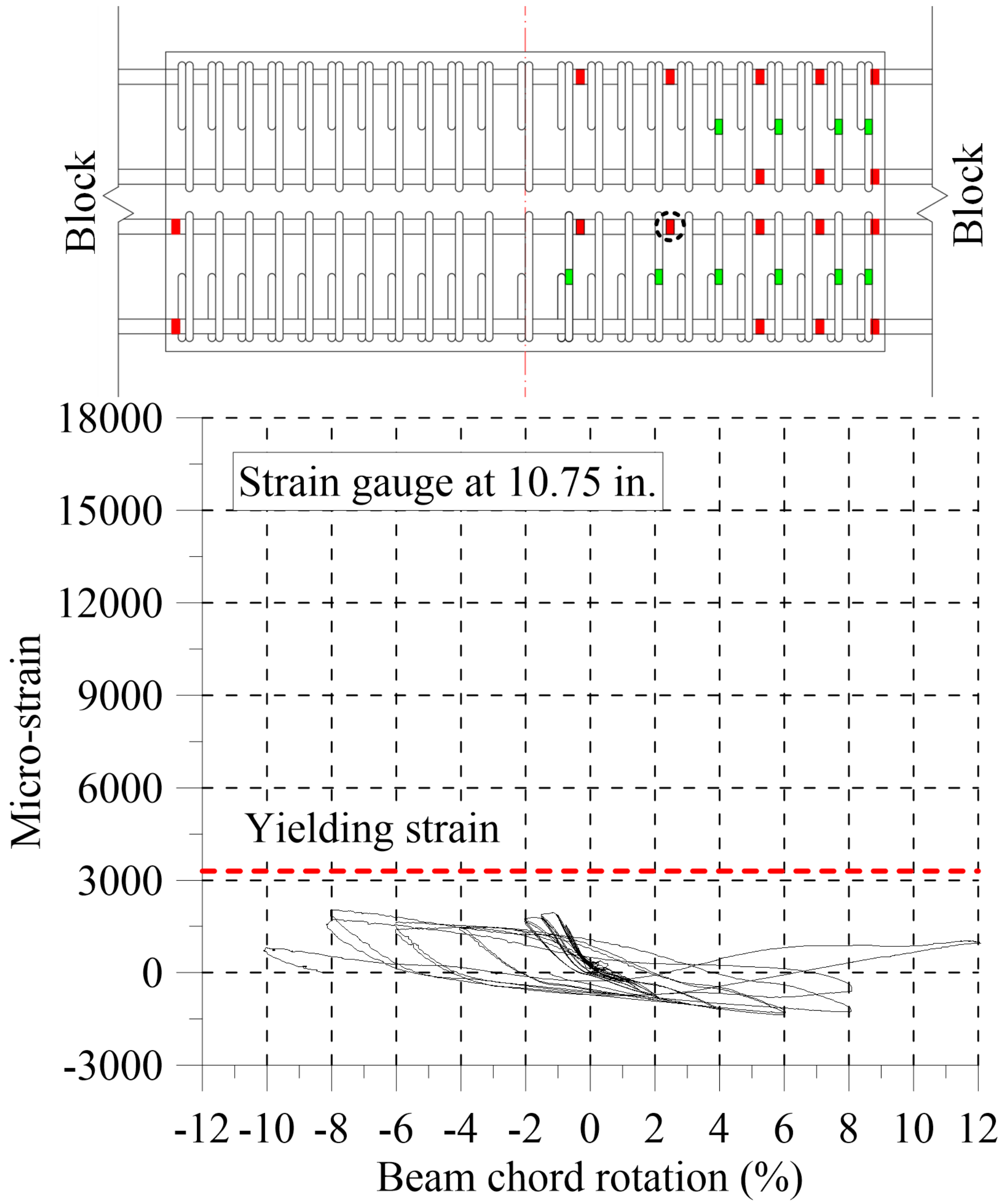
Block
Block
Strain gauge at 10.75 in.
Yielding strain
Micro-strain
18000
15000
12000
9000
6000
3000
0
-3000
-12
-10
-8
-6
-4
-2
0
2
4
6
8
10
12
Beam chord rotation (%)

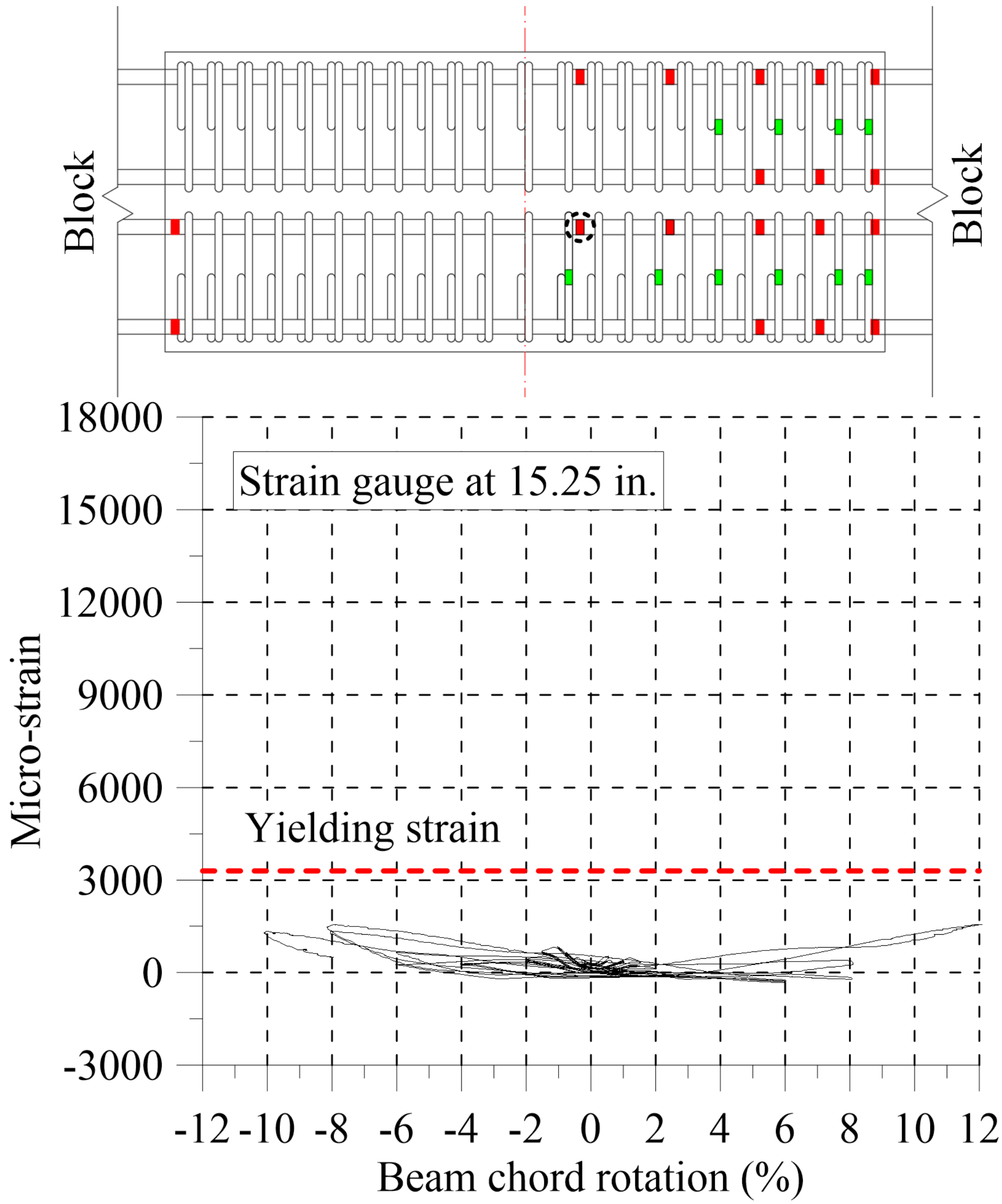
Block
Block
18000
15000
12000
9000
6000
3000
0
-3000
Micro-strain
Strain gauge at 15.25 in.
Yielding strain
-12 -10 -8 -6 -4 -2 0 2 4 6 8 10 12
Beam chord rotation (%)

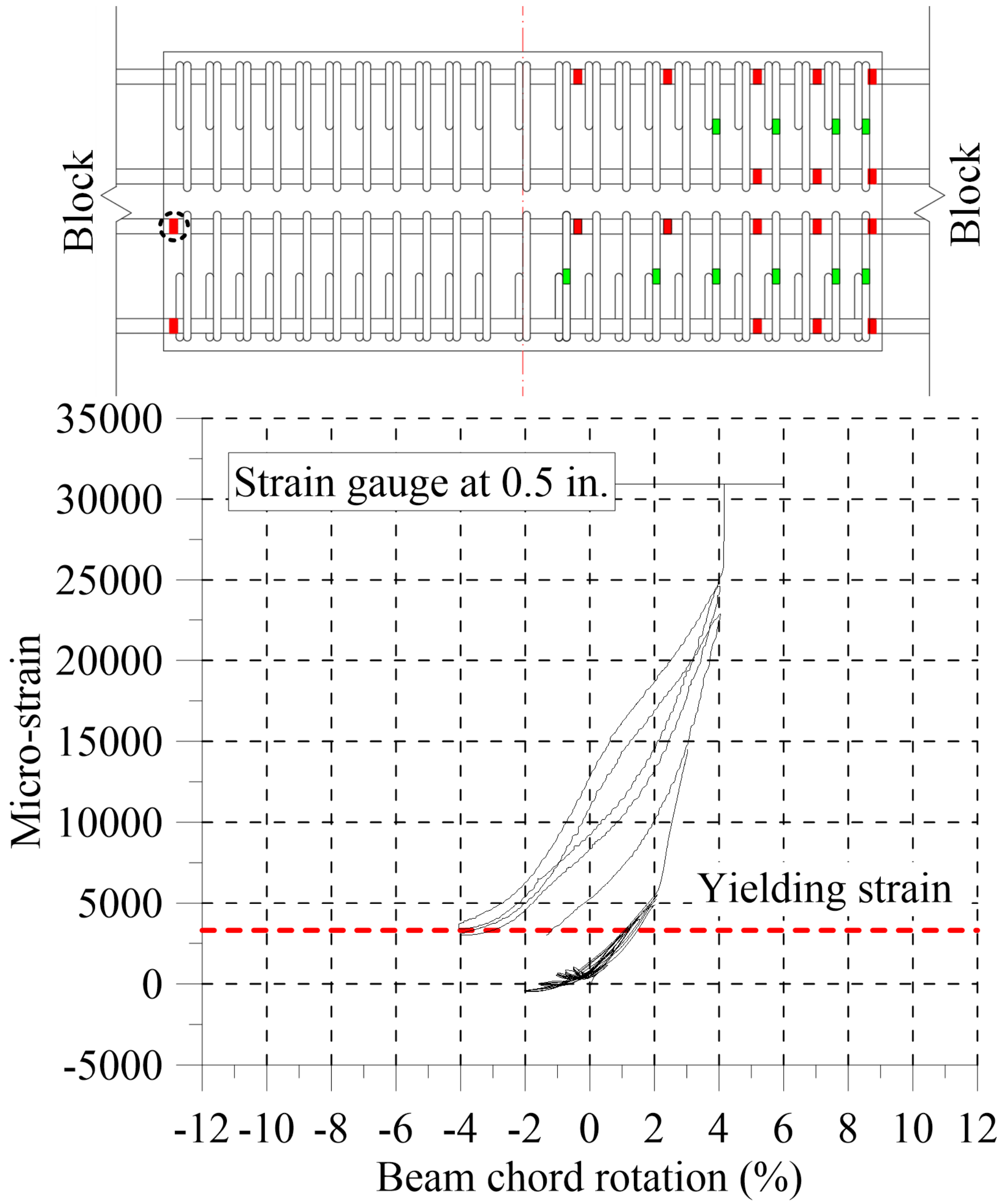

Block
Block
Strain gauge at 0.5 in.
Yielding strain
Micro-strain
Beam chord rotation (%)
35000
30000
25000
20000
15000
10000
5000
0
-5000
-12 -10 -8 -6 -4 -2 0 2 4 6 8 10 12

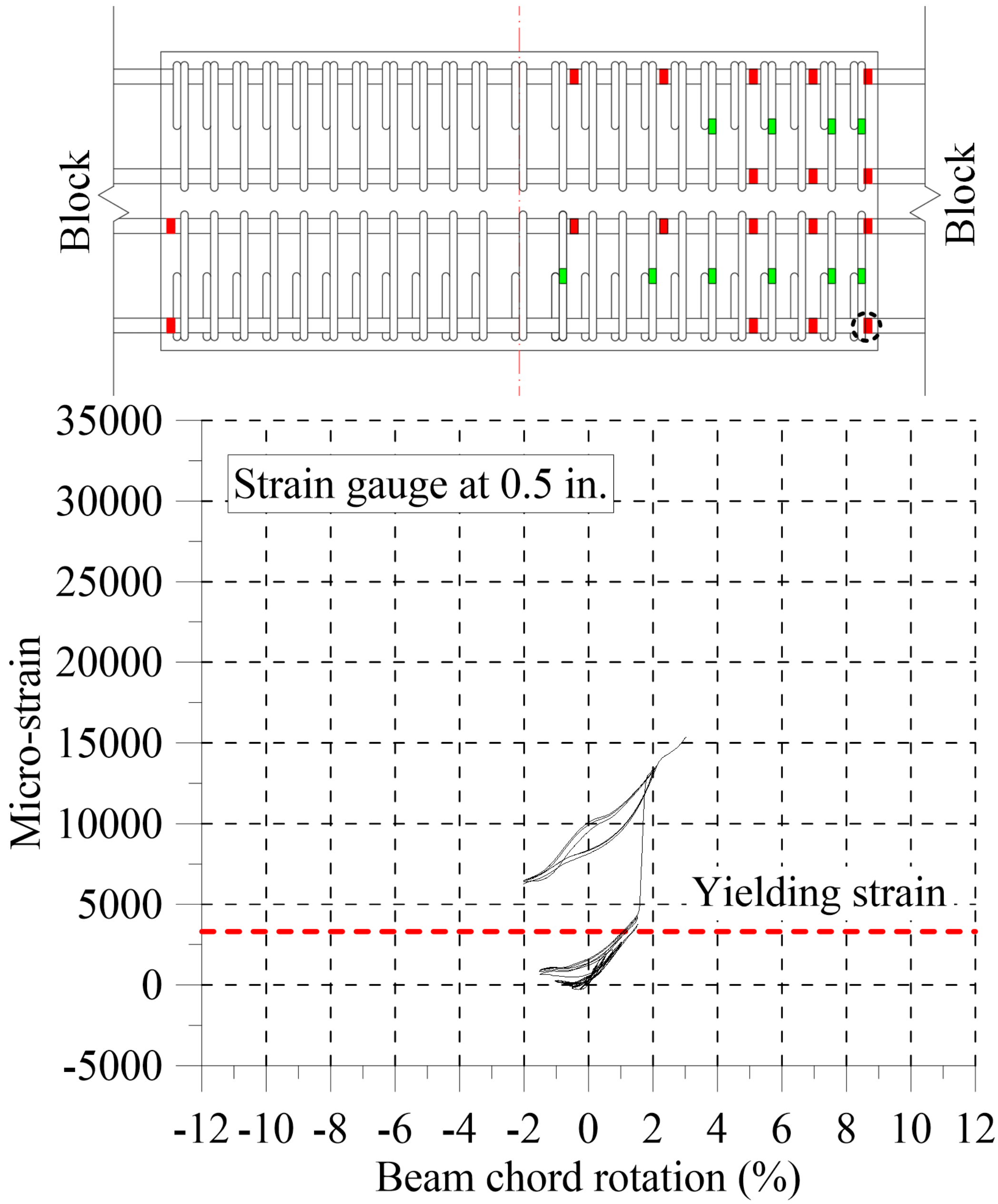
Block
Block
Strain gauge at 0.5 in.
Yielding strain
Micro-strain
Beam chord rotation (%)
35000
30000
25000
20000
15000
10000
5000
0
-5000
-12
-10
-8
-6
-4
-2
0
2
4
6
8
10
12

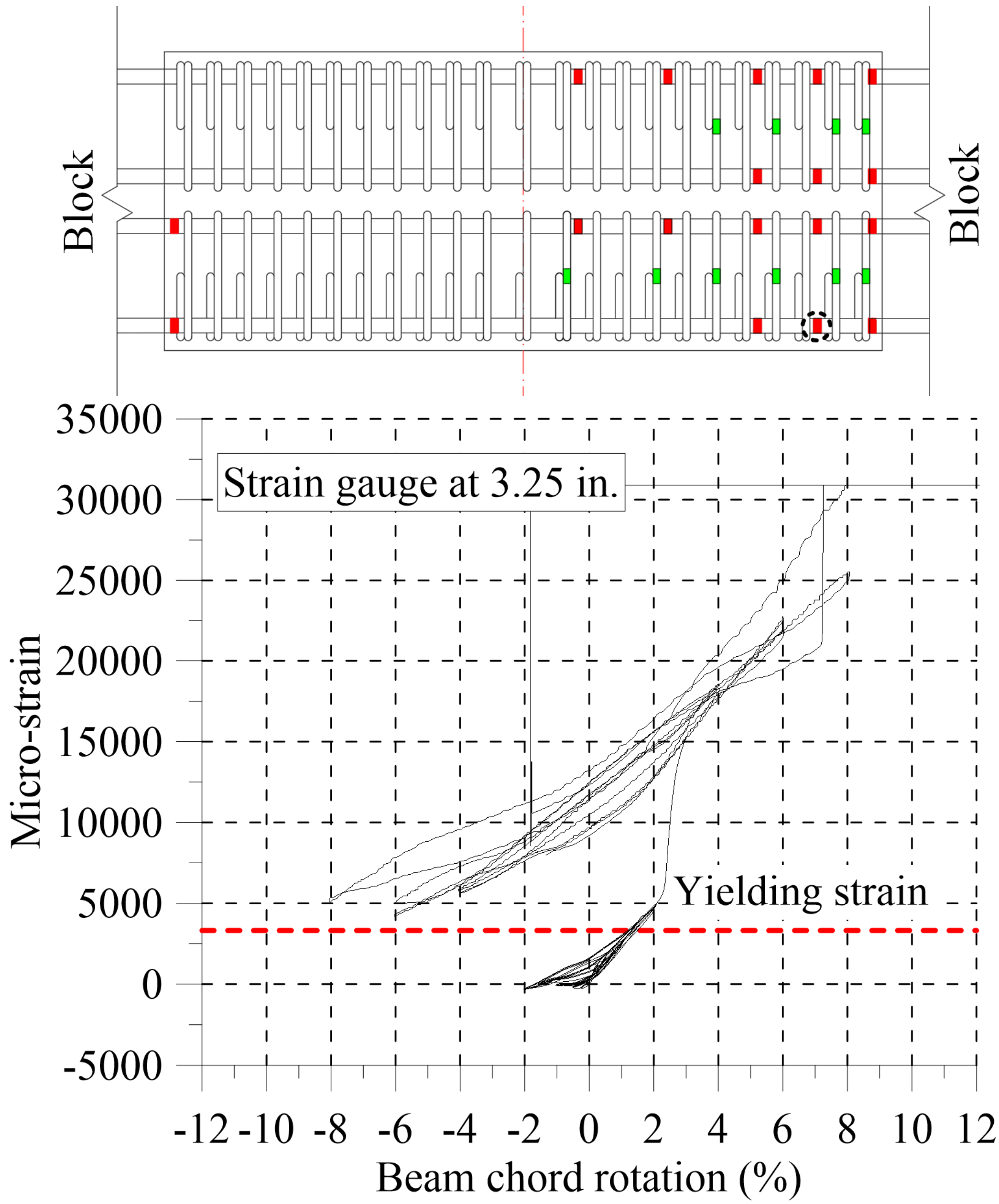
Block
Block
Strain gauge at 3.25 in.
Yielding strain
Micro-strain
35000
30000
25000
20000
15000
10000
5000
0
-5000
-12 -10 -8 -6 -4 -2 0 2 4 6 8 10 12
Beam chord rotation (%)

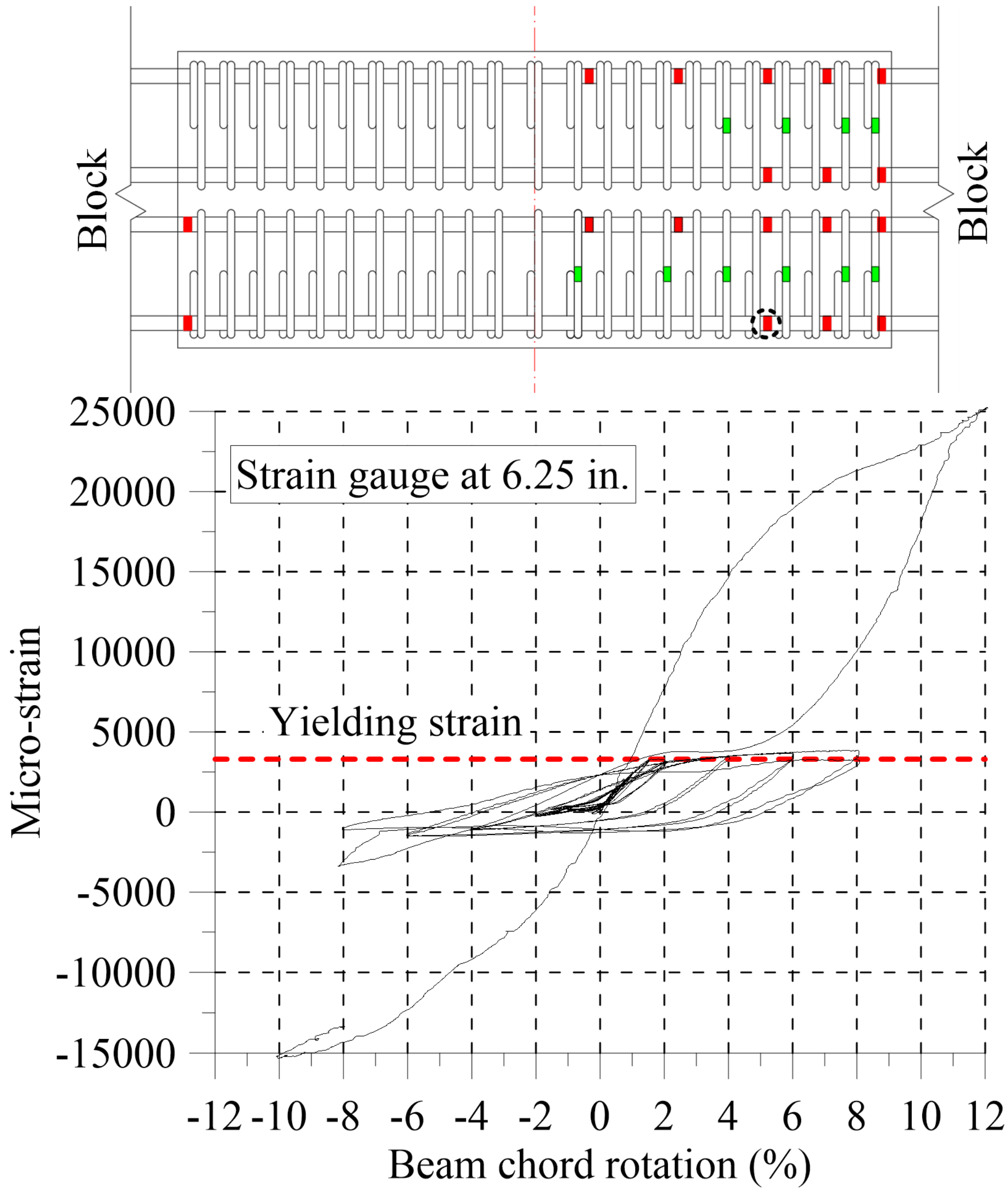
Block
Block
Strain gauge at 6.25 in.
Yielding strain
25000
20000
15000
10000
5000
0
-5000
-10000
-15000
Micro-strain
-12
-10
-8
-6
-4
-2
0
2
4
6
8
10
12
Beam chord rotation (%)

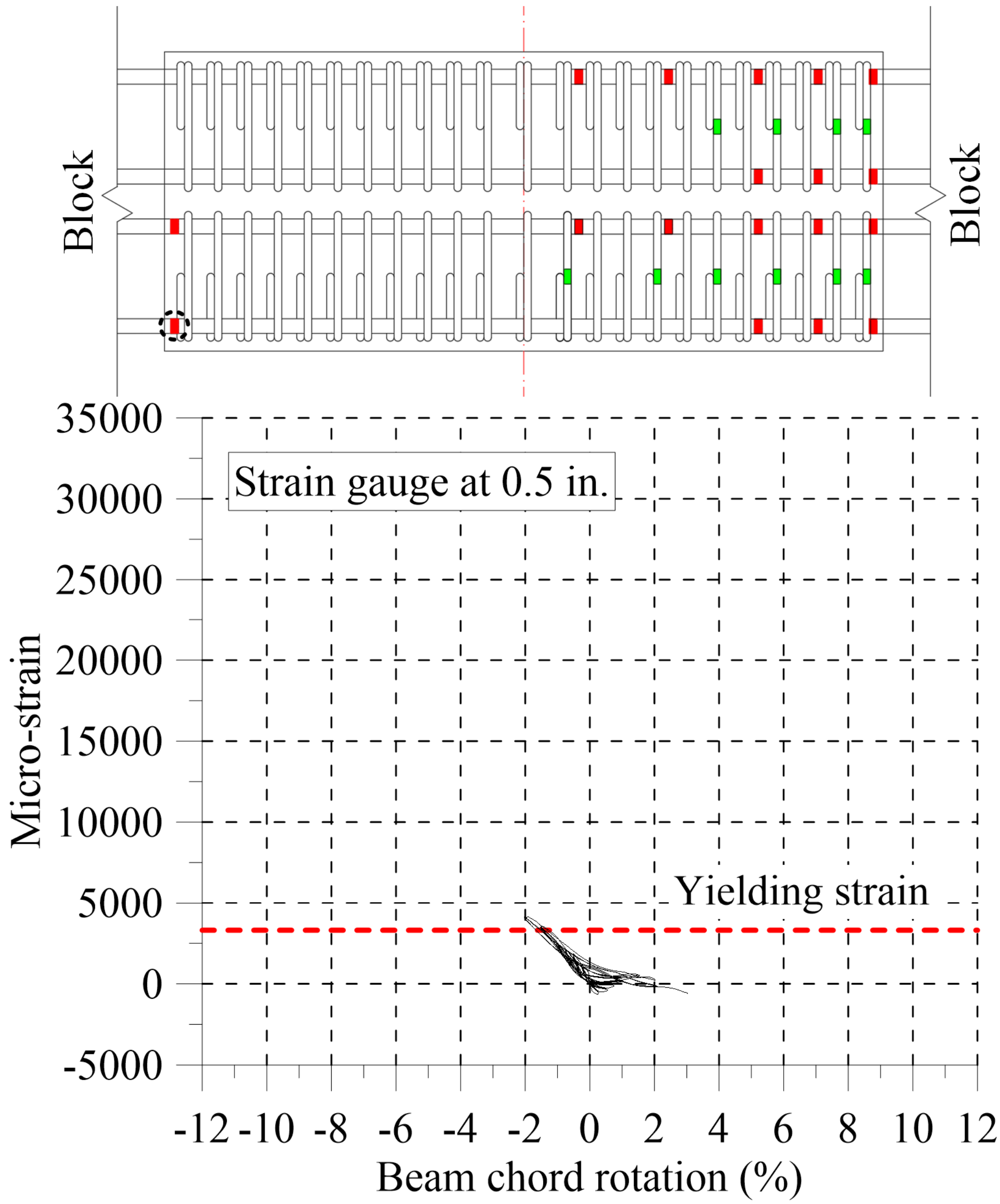
Block
Block
Strain gauge at 0.5 in.
Yielding strain
Micro-strain
35000
30000
25000
20000
15000
10000
5000
0
-5000
-12 -10 -8 -6 -4 -2 0 2 4 6 8 10 12
Beam chord rotation (%)

C.2.2.2 Transverse reinforcement

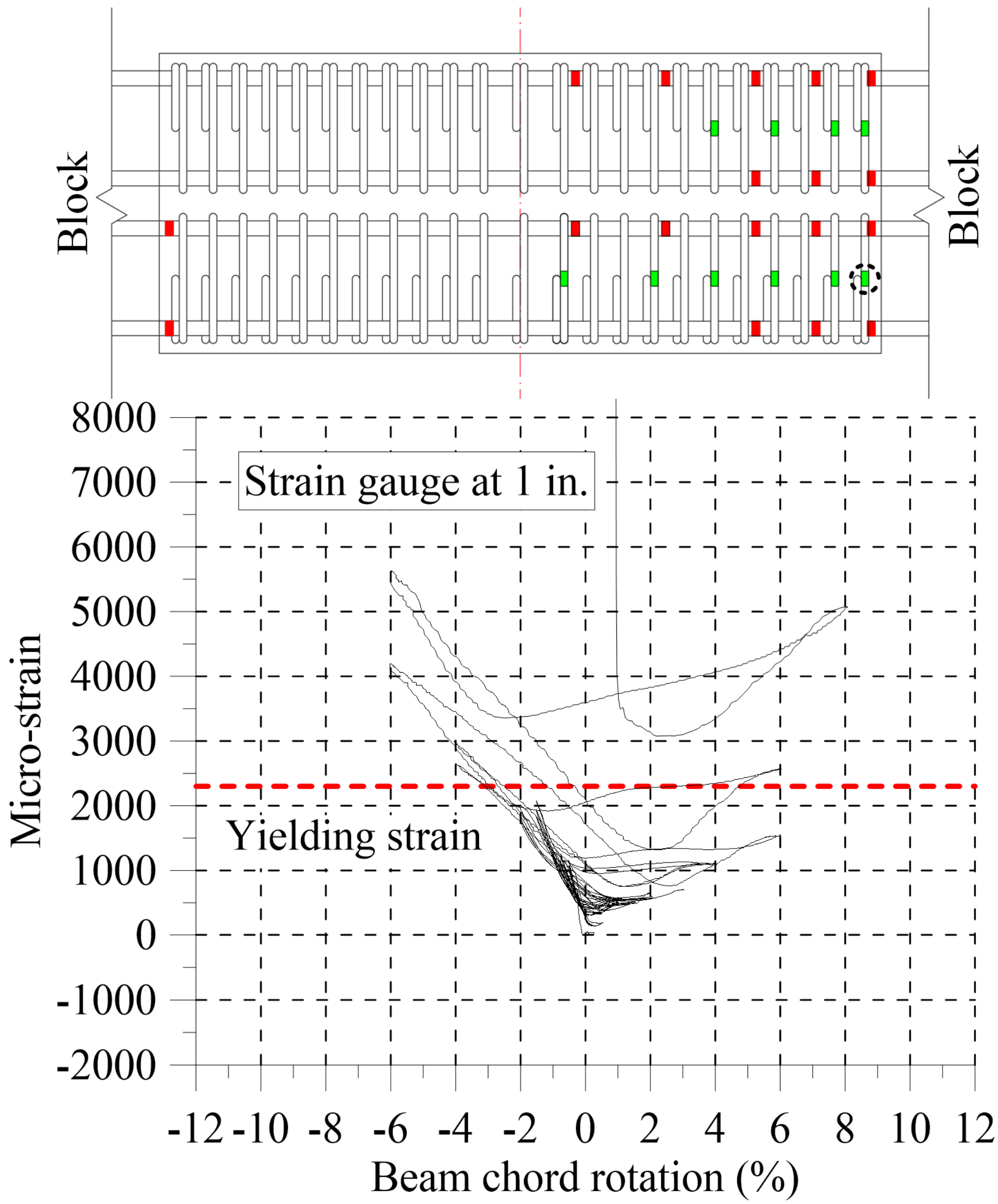

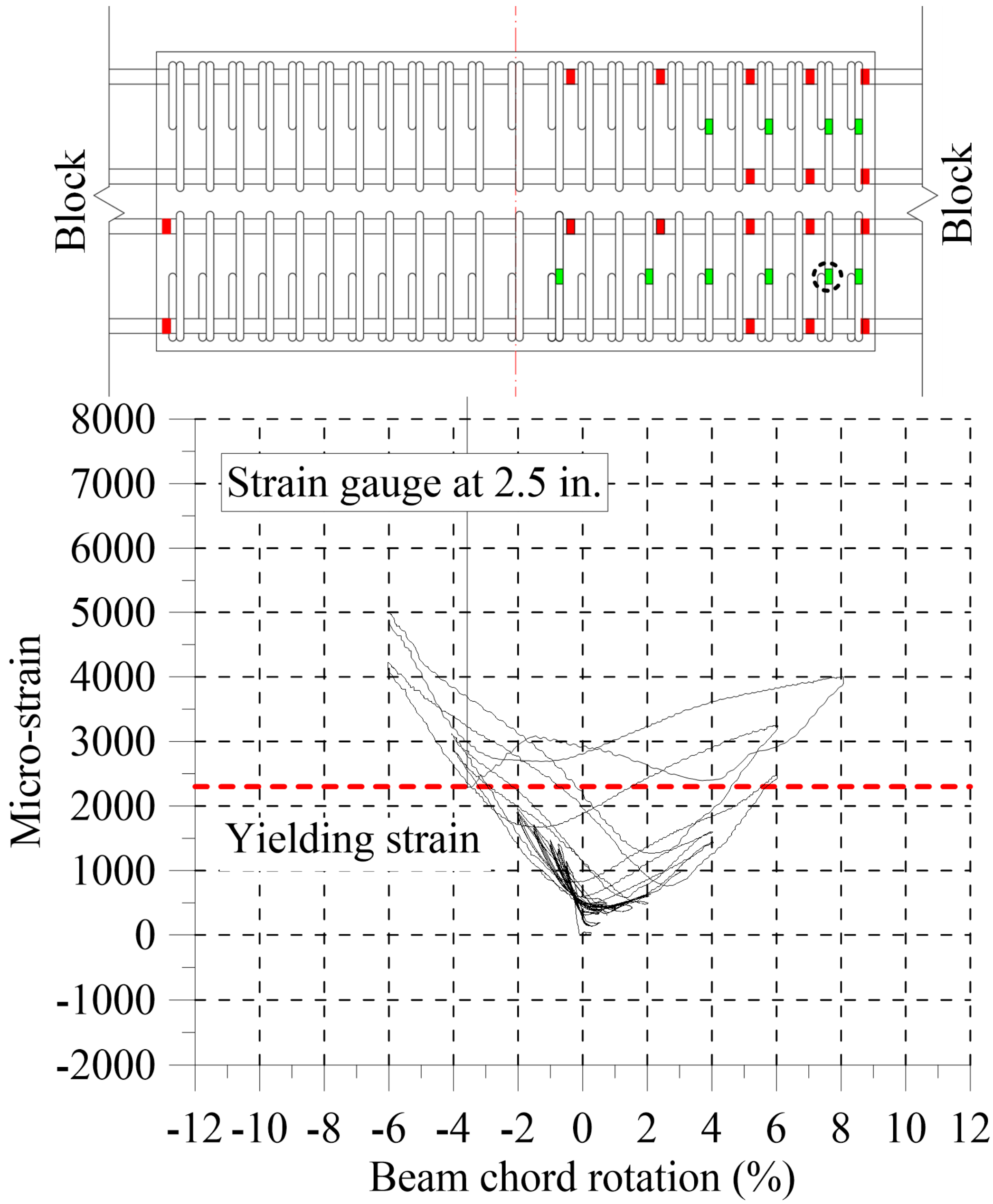

Block
Block
Strain gauge at 2.5 in.
Yielding strain
Micro-strain
Beam chord rotation (%)
8000
7000
6000
5000
4000
3000
2000
1000
0
-1000
-2000
-12
-10
-8
-6
-4
-2
0
2
4
6
8
10
12

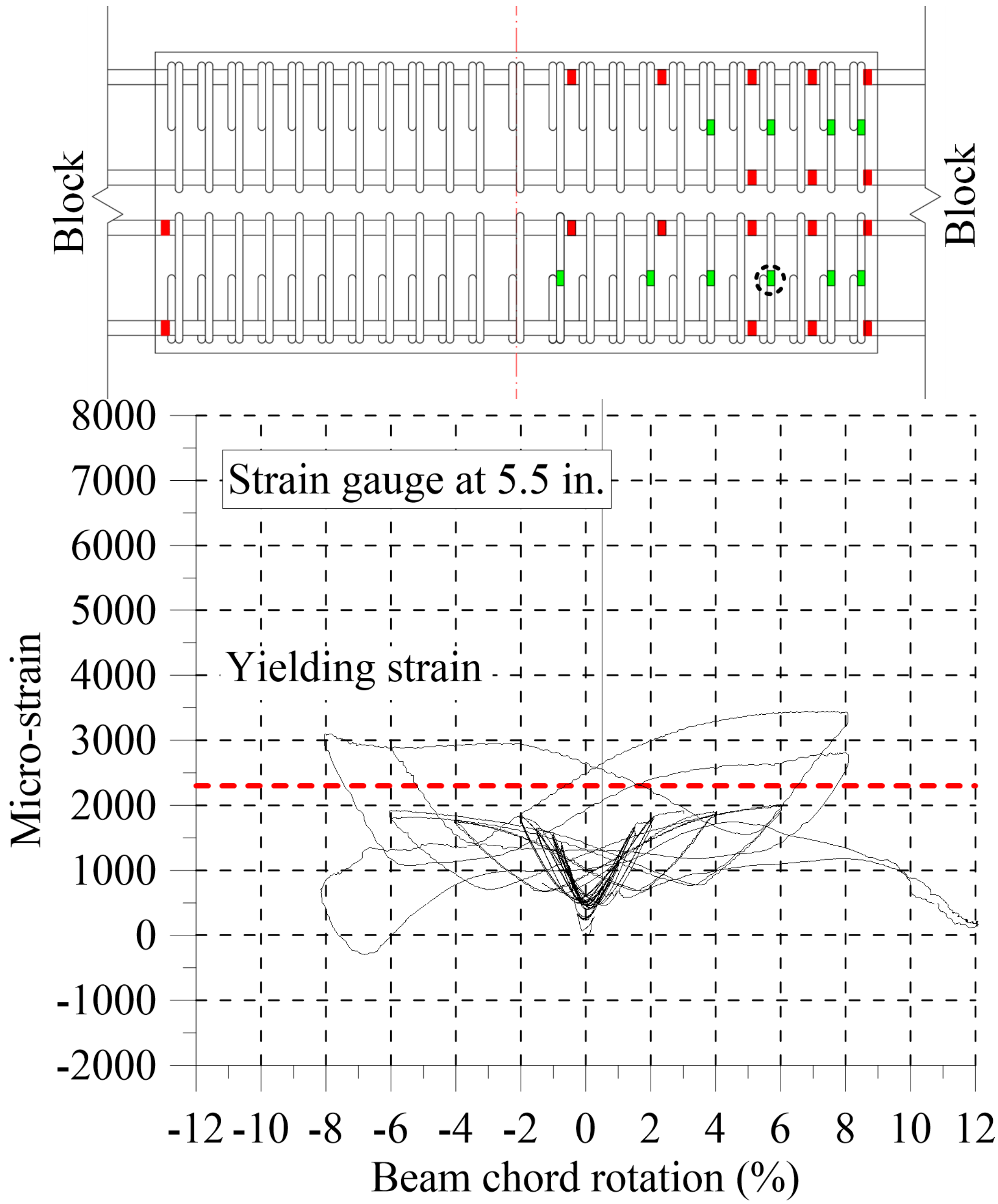

Block
Block
Strain gauge at 5.5 in.
Yielding strain
Micro-strain
8000
7000
6000
5000
4000
3000
2000
1000
0
-1000
-2000
-12 -10 -8 -6 -4 -2 0 2 4 6 8 10 12
Beam chord rotation (%)

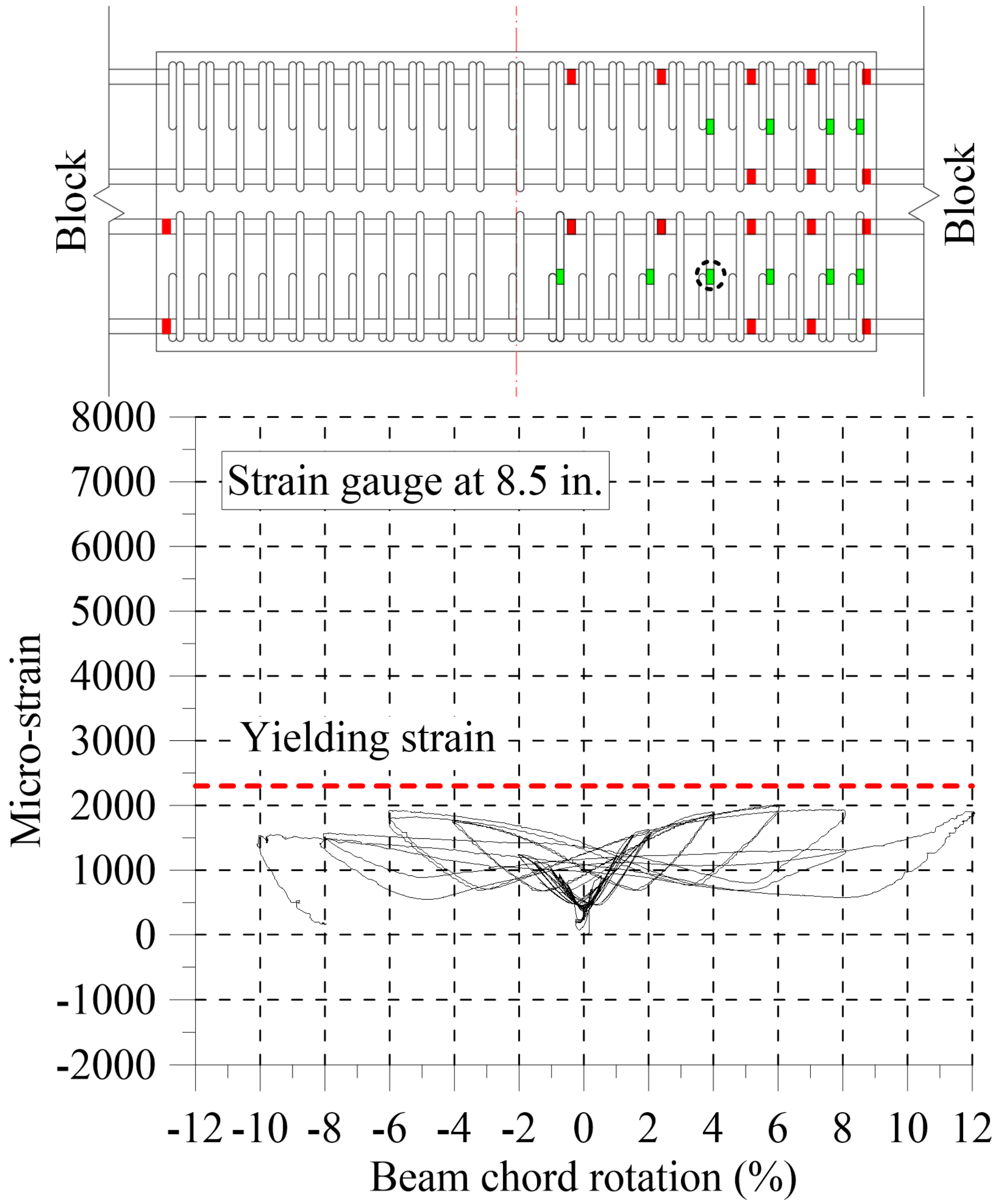

Block
Block
Strain gauge at 8.5 in.
Yielding strain
Micro-strain
8000
7000
6000
5000
4000
3000
2000
1000
0
-1000
-2000
-12
-10
-8
-6
-4
-2
0
2
4
6
8
10
12
Beam chord rotation (%)

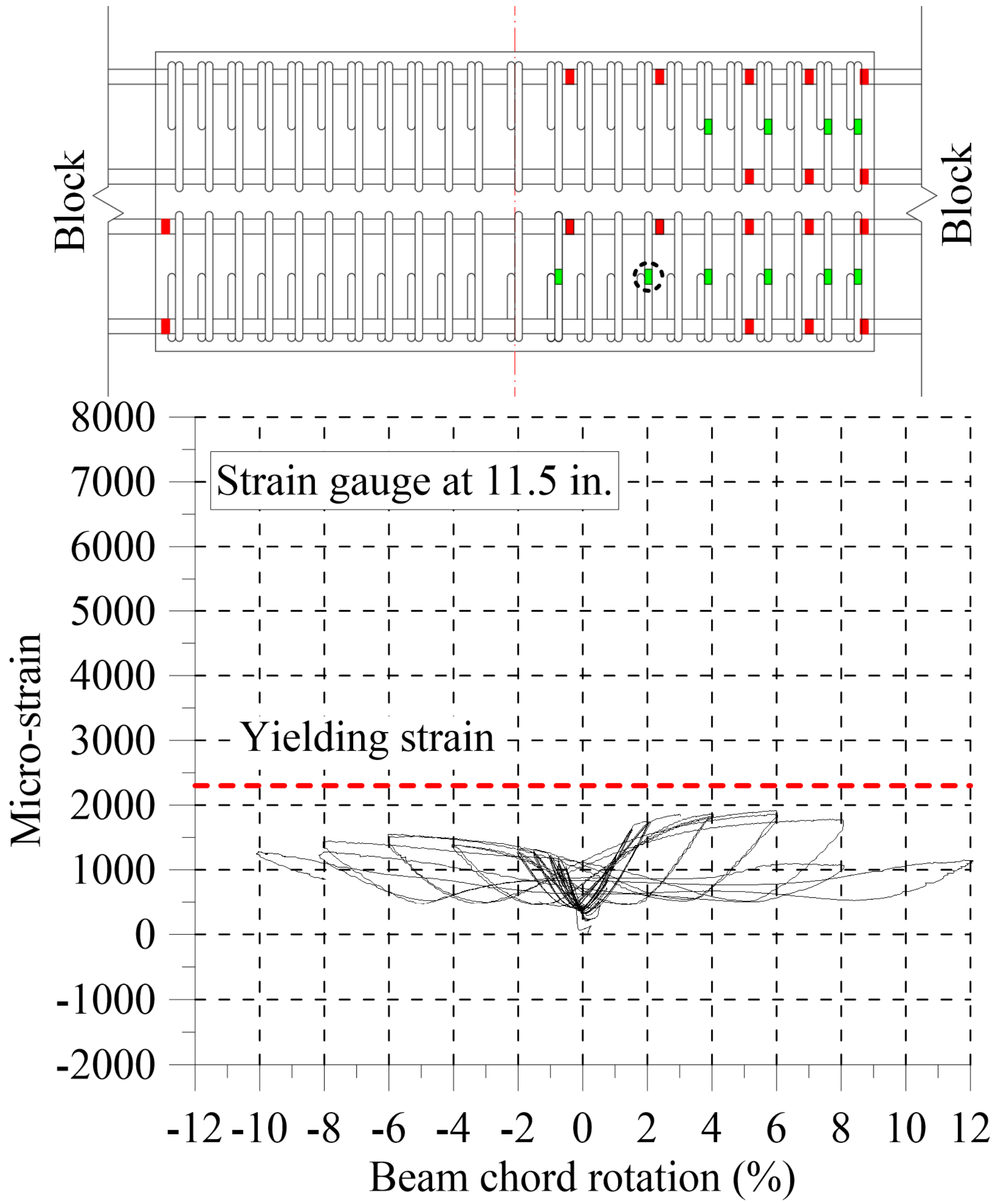

Block
Block
Strain gauge at 11.5 in.
Yielding strain
Micro-strain
8000
7000
6000
5000
4000
3000
2000
1000
0
-1000
-2000
-12
-10
-8
-6
-4
-2
0
2
4
6
8
10
12
Beam chord rotation (%)

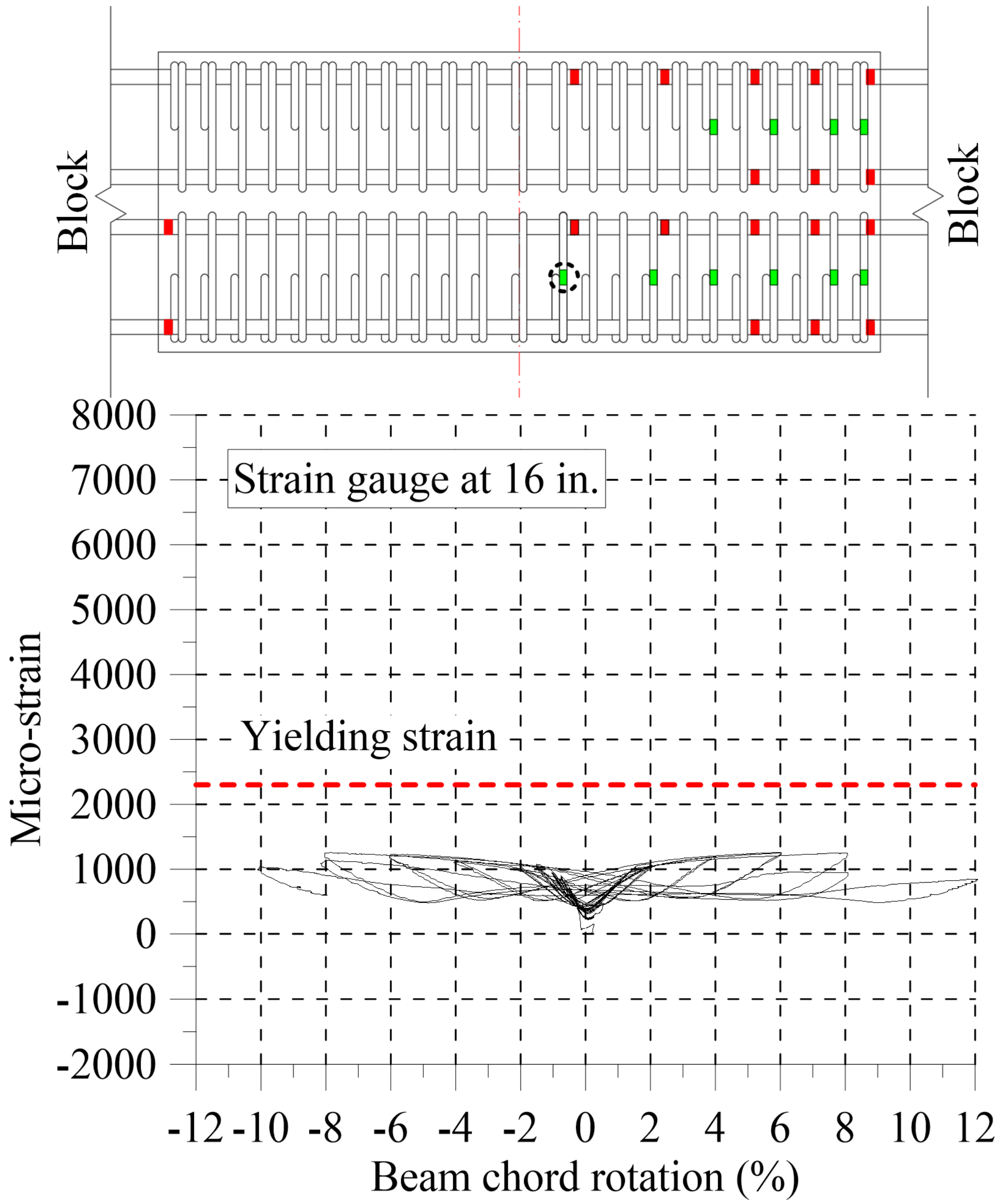

Block
Block
Strain gauge at 16 in.
Yielding strain
Micro-strain
8000
7000
6000
5000
4000
3000
2000
1000
0
-1000
-2000
-12 -10 -8 -6 -4 -2 0 2 4 6 8 10 12
Beam chord rotation (%)

C.2.3 Slab longitudinal reinforcement

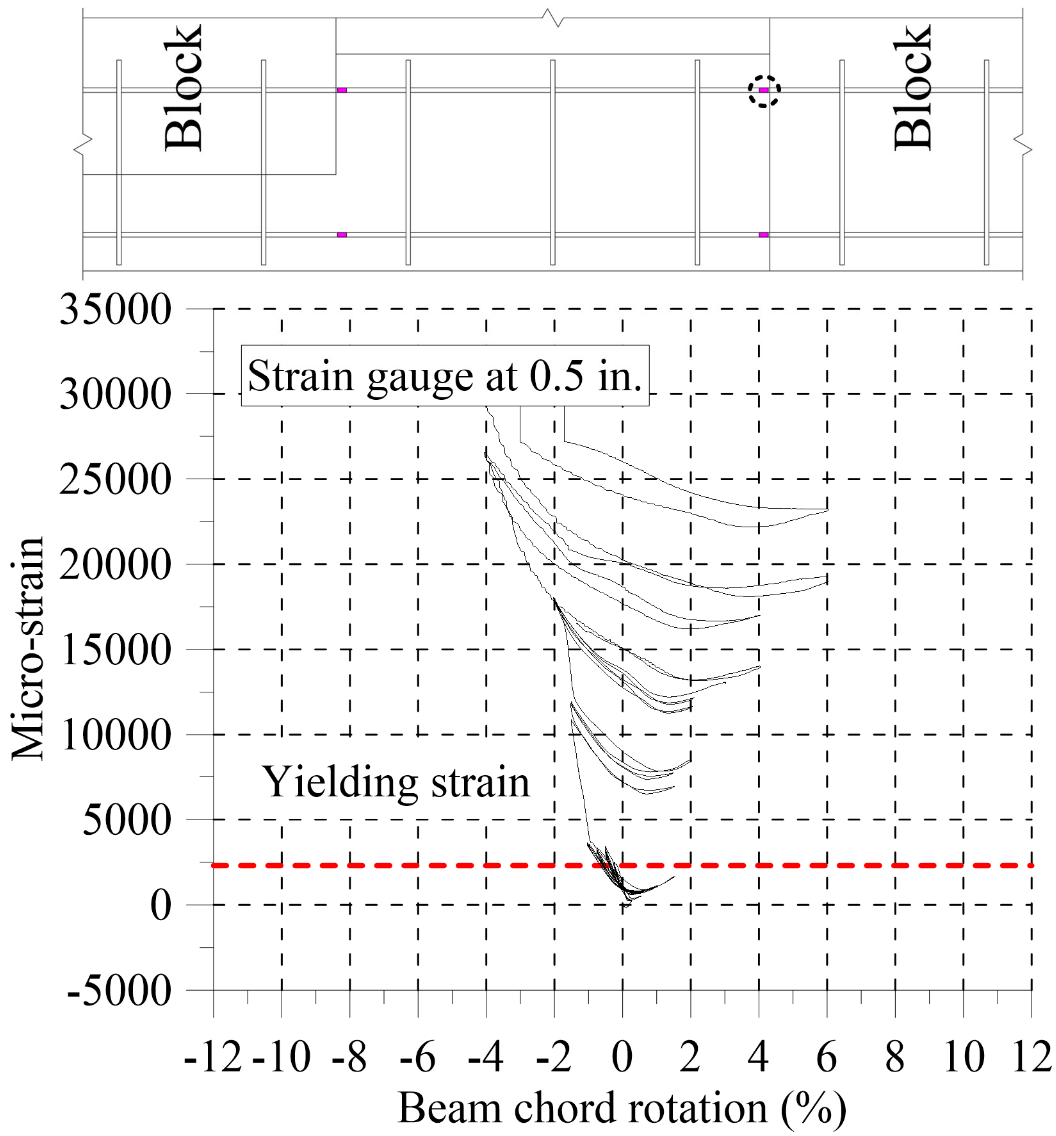

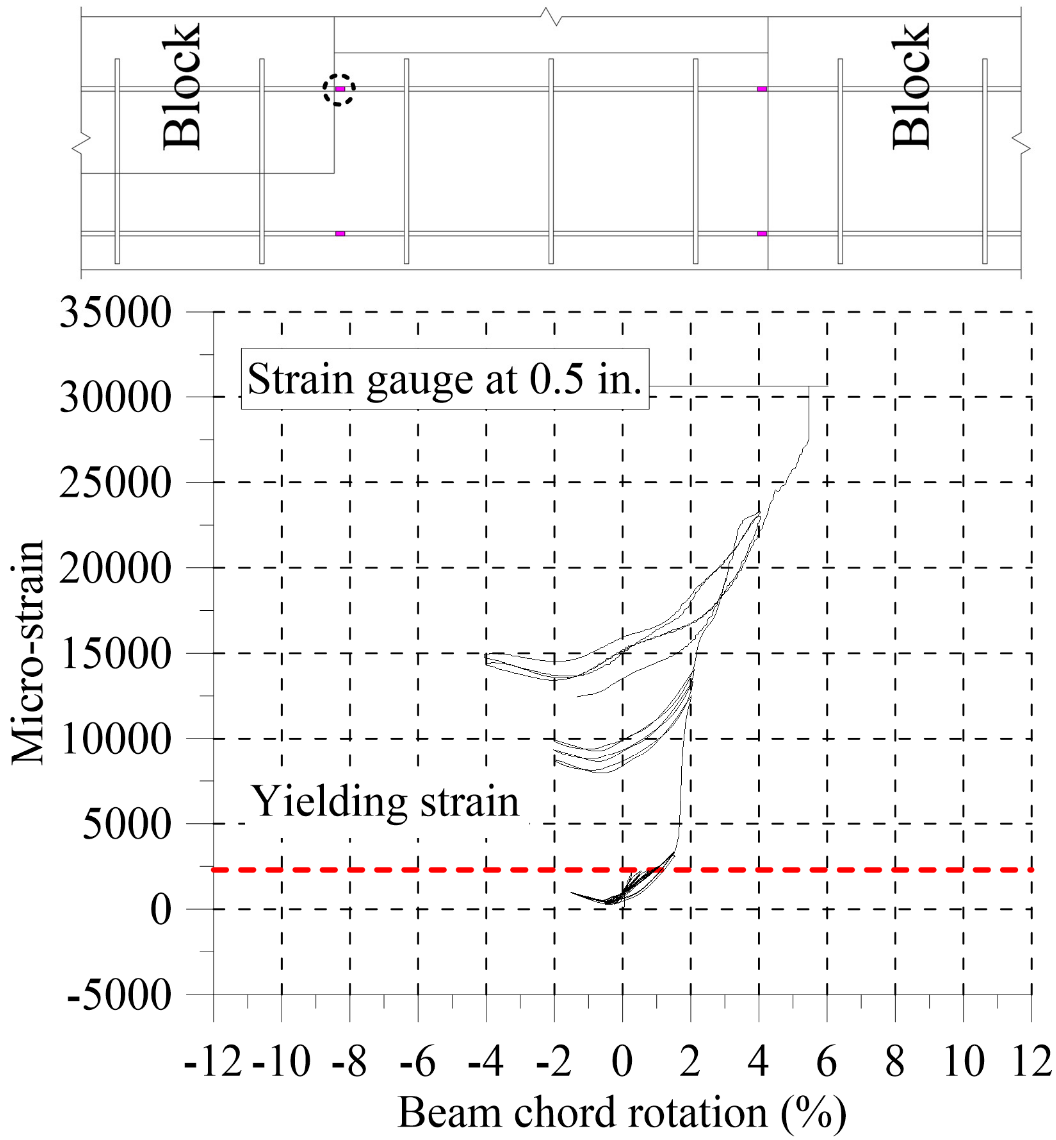

Block
Block
Strain gauge at 0.5 in.
Yielding strain
35000
30000
25000
20000
15000
10000
5000
0
-5000
Micro-strain
-12 -10 -8 -6 -4 -2 0 2 4 6 8 10 12
Beam chord rotation (%)

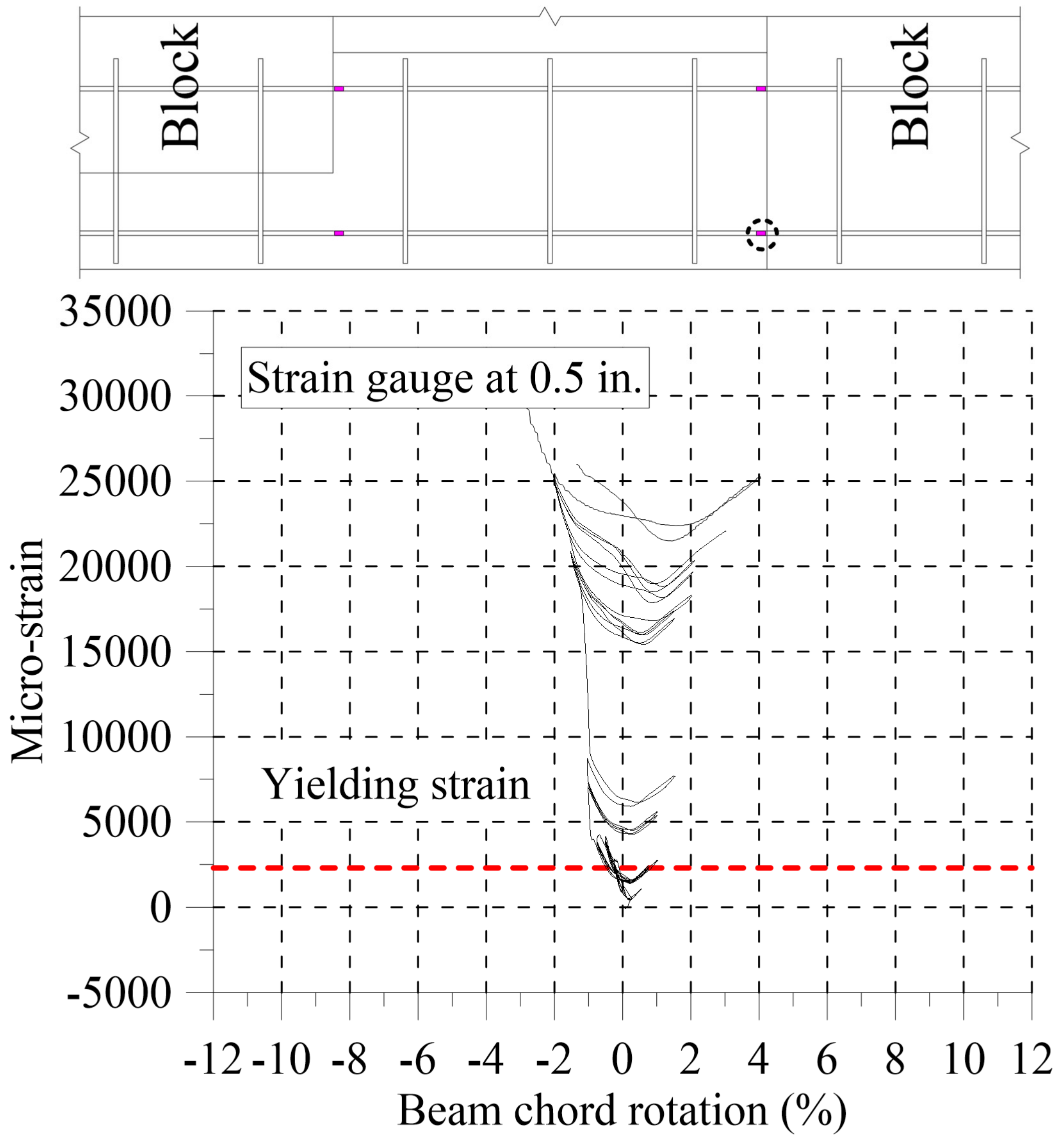

Block
Block
35000
30000
25000
20000
15000
10000
5000
0
-5000
Micro-strain
Strain gauge at 0.5 in.
Yielding strain
-12
-10
-8
-6
-4
-2
0
2
4
6
8
10
12
Beam chord rotation (%)

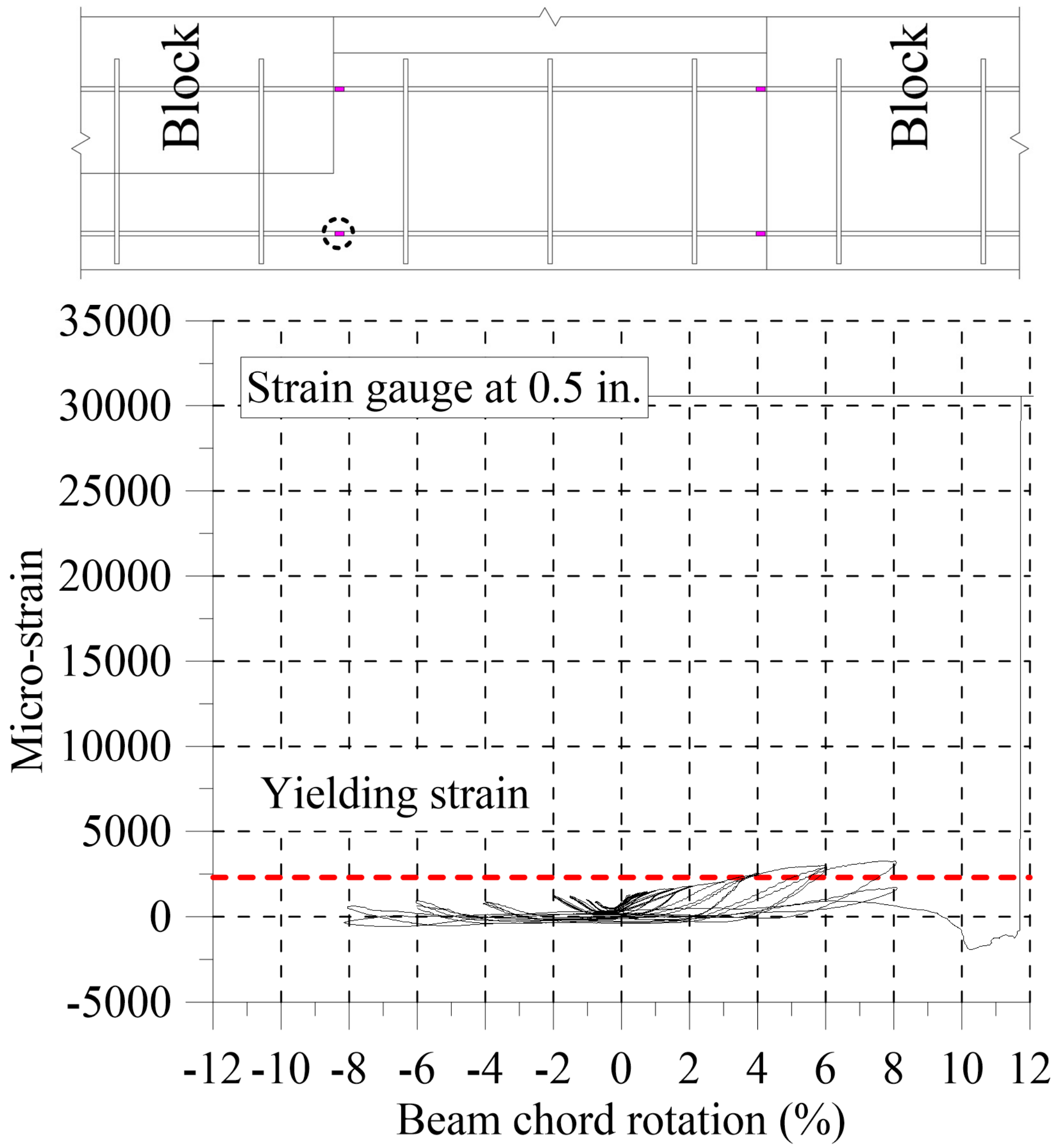
Block
Block
Strain gauge at 0.5 in.
Yielding strain
Micro-strain
Beam chord rotation (%)
35000
30000
25000
20000
15000
10000
5000
0
-5000
-12 -10 -8 -6 -4 -2 0 2 4 6 8 10 12

C.2.4 Steel links

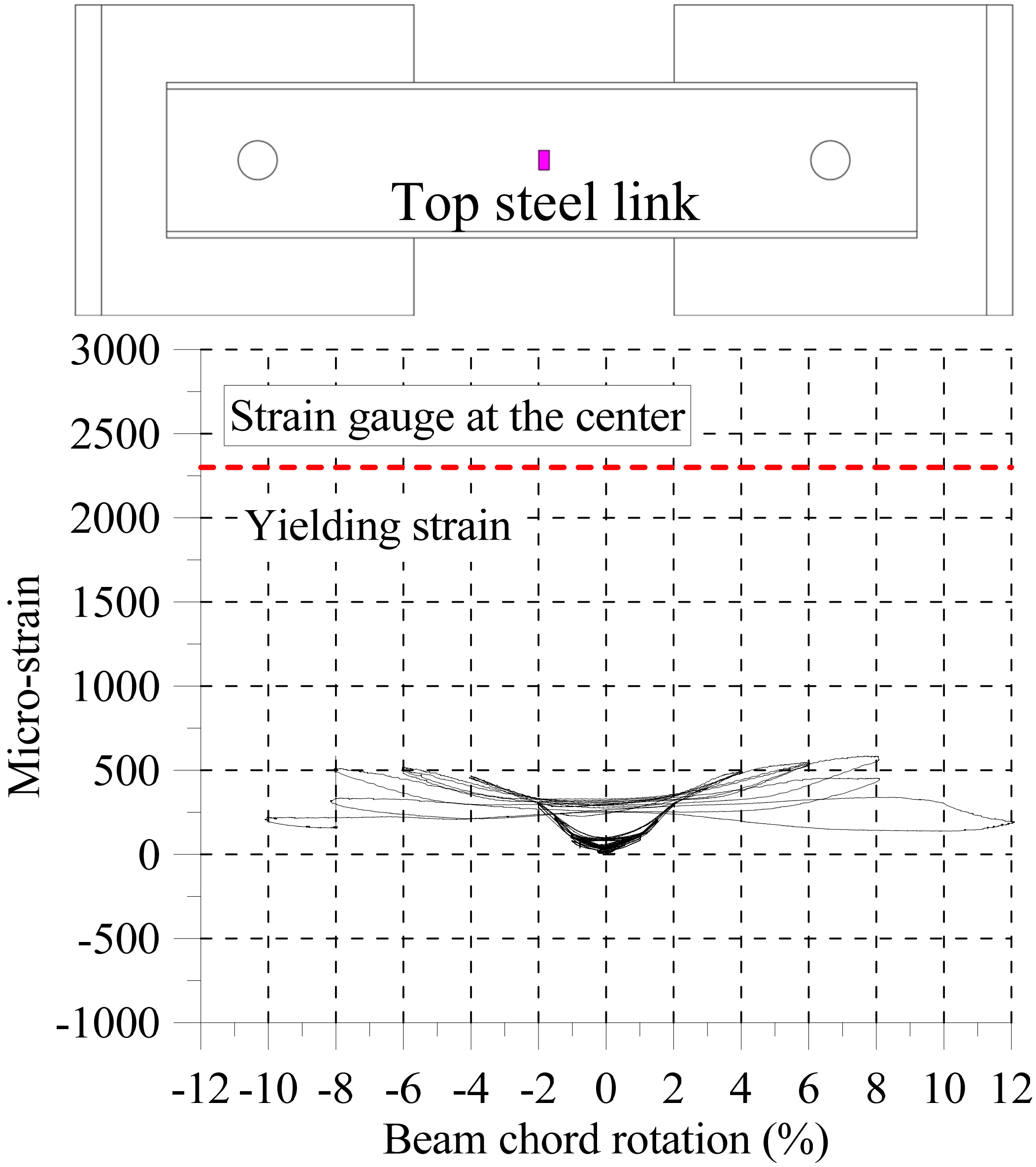

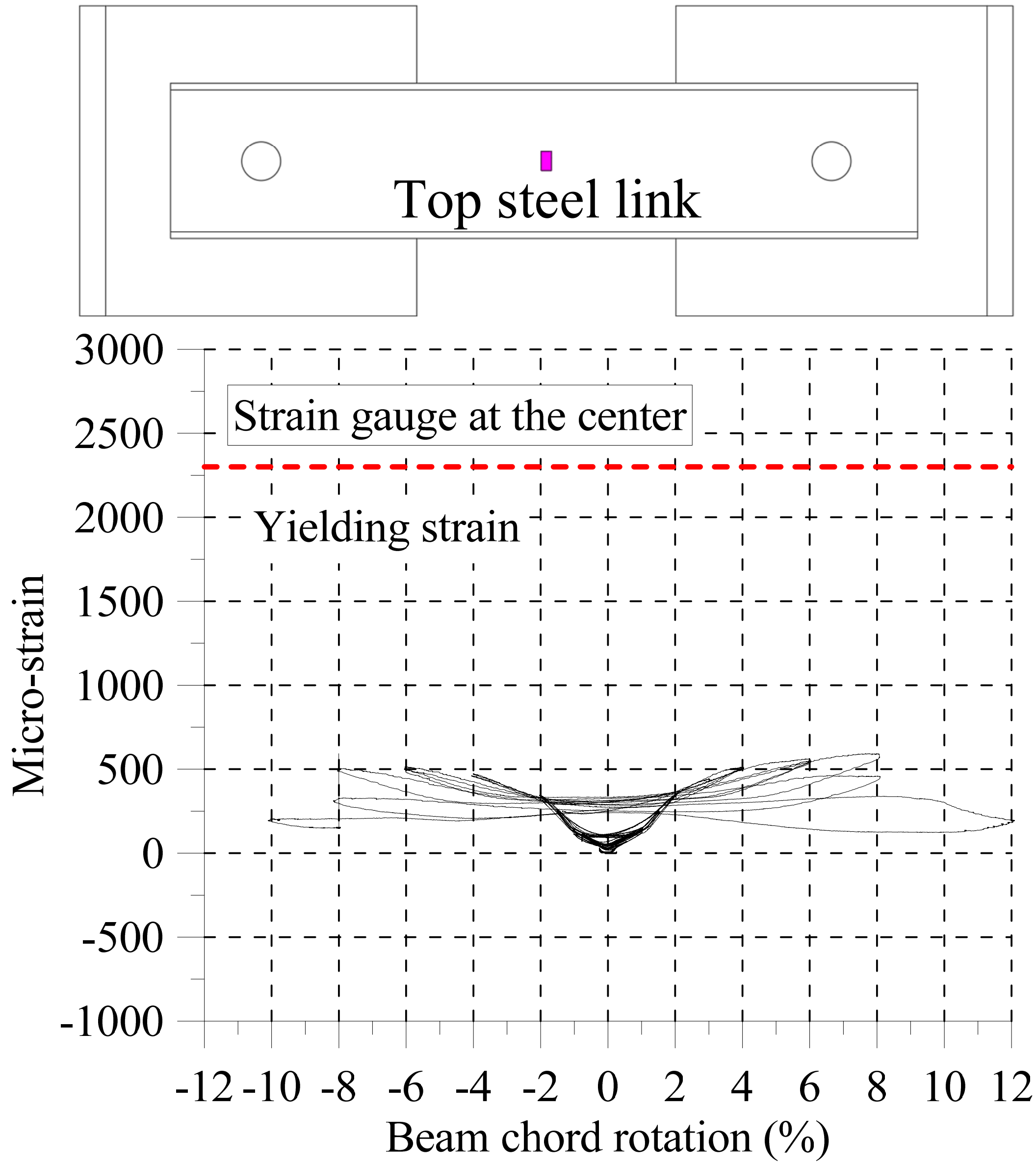

Top steel link
Strain gauge at the center
Yielding strain
Micro-strain
3000
2500
2000
1500
1000
500
0
-500
-1000
-12 -10 -8 -6 -4 -2 0 2 4 6 8 10 12
Beam chord rotation (%)

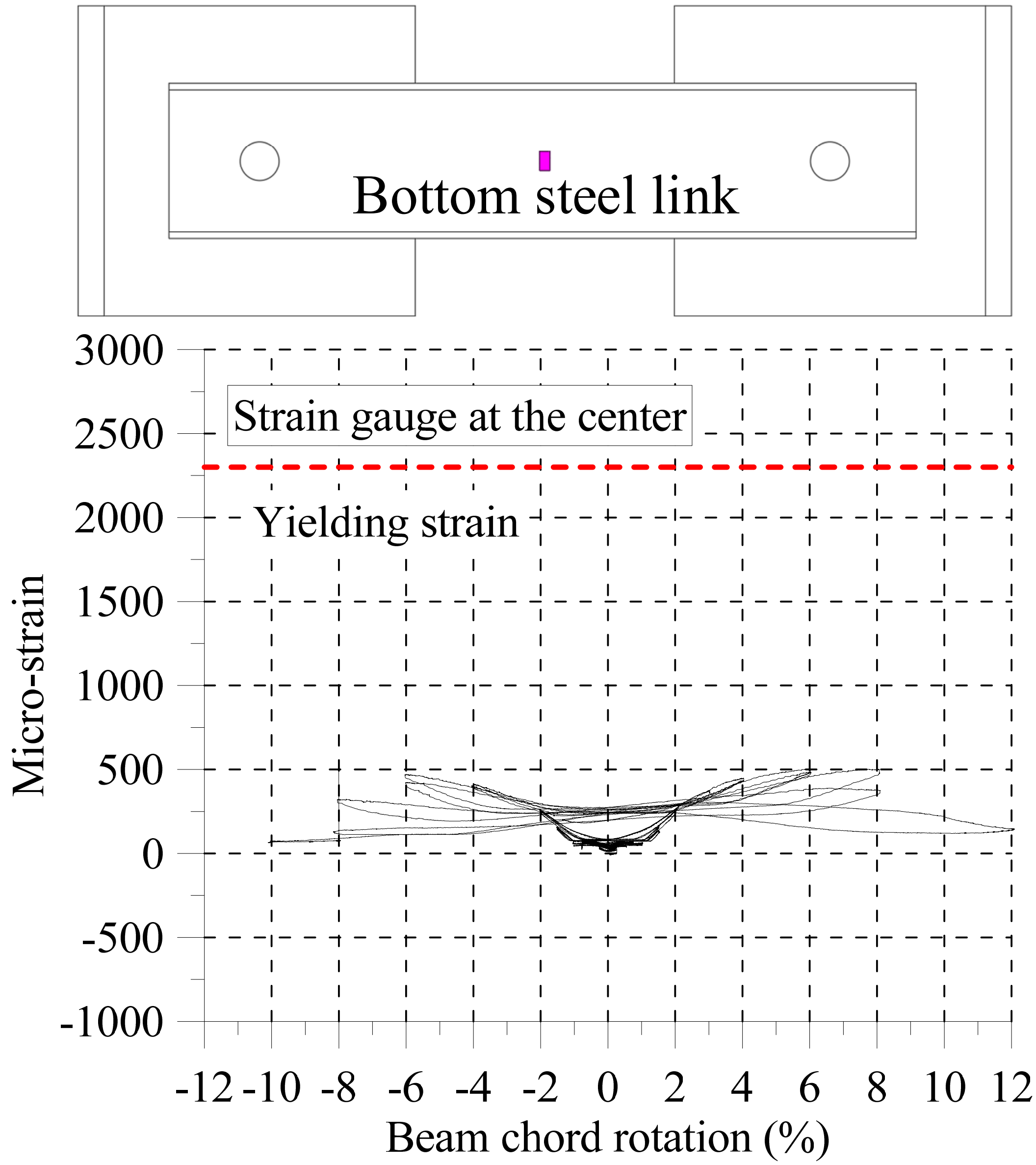
Bottom steel link
Strain gauge at the center
Yielding strain
Micro-strain
3000
2500
2000
1500
1000
500
0
-500
-1000
-12
-10
-8
-6
-4
-2
0
2
4
6
8
10
12
Beam chord rotation (%)

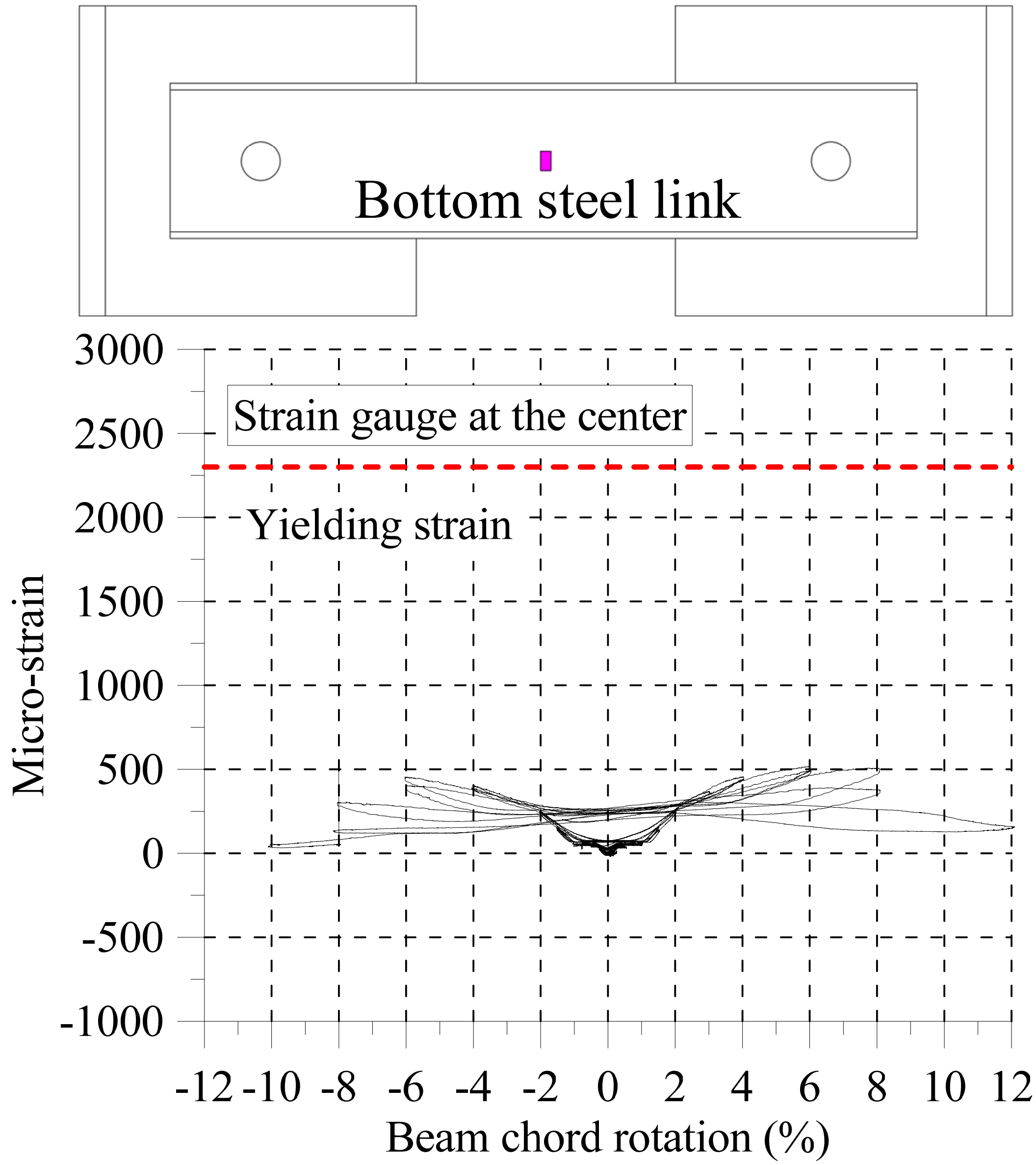

Bottom steel link
Strain gauge at the center
Yielding strain
Micro-strain
3000
2500
2000
1500
1000
500
0
-500
-1000
-12
-10
-8
-6
-4
-2
0
2
4
6
8
10
12
Beam chord rotation (%)

C.3 Full-scale 2.4 aspect ratio DBCB with the slab (FS-R2.4-S-3)

Measured strain versus chord rotation for each strain gauge attached to the reinforcing bars is plotted. The location of each strain gauge was indicated with a black dashed line circle on the plot.

C.3.1 Upper steel cage

C.3.1.1 Longitudinal reinforcement

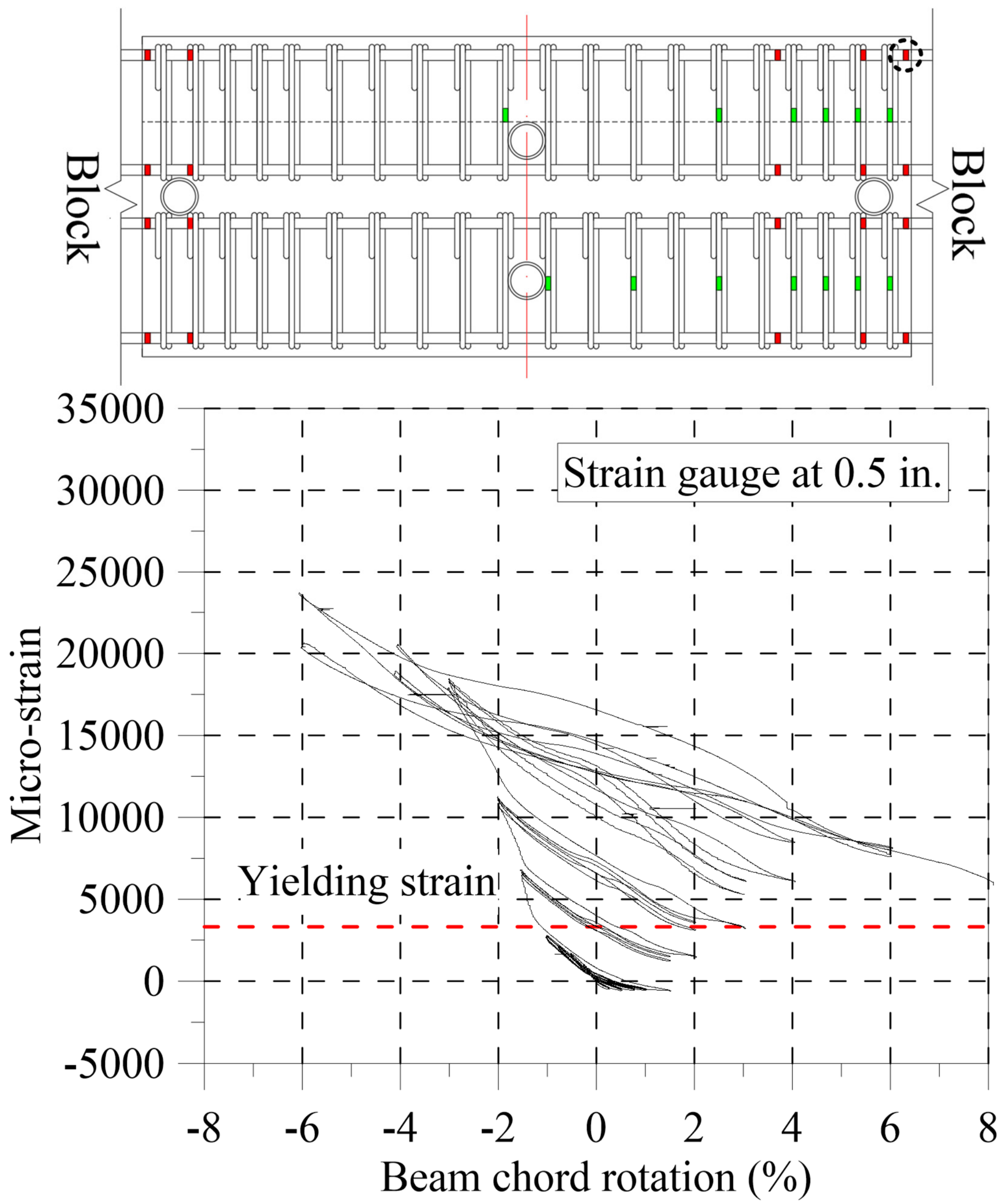

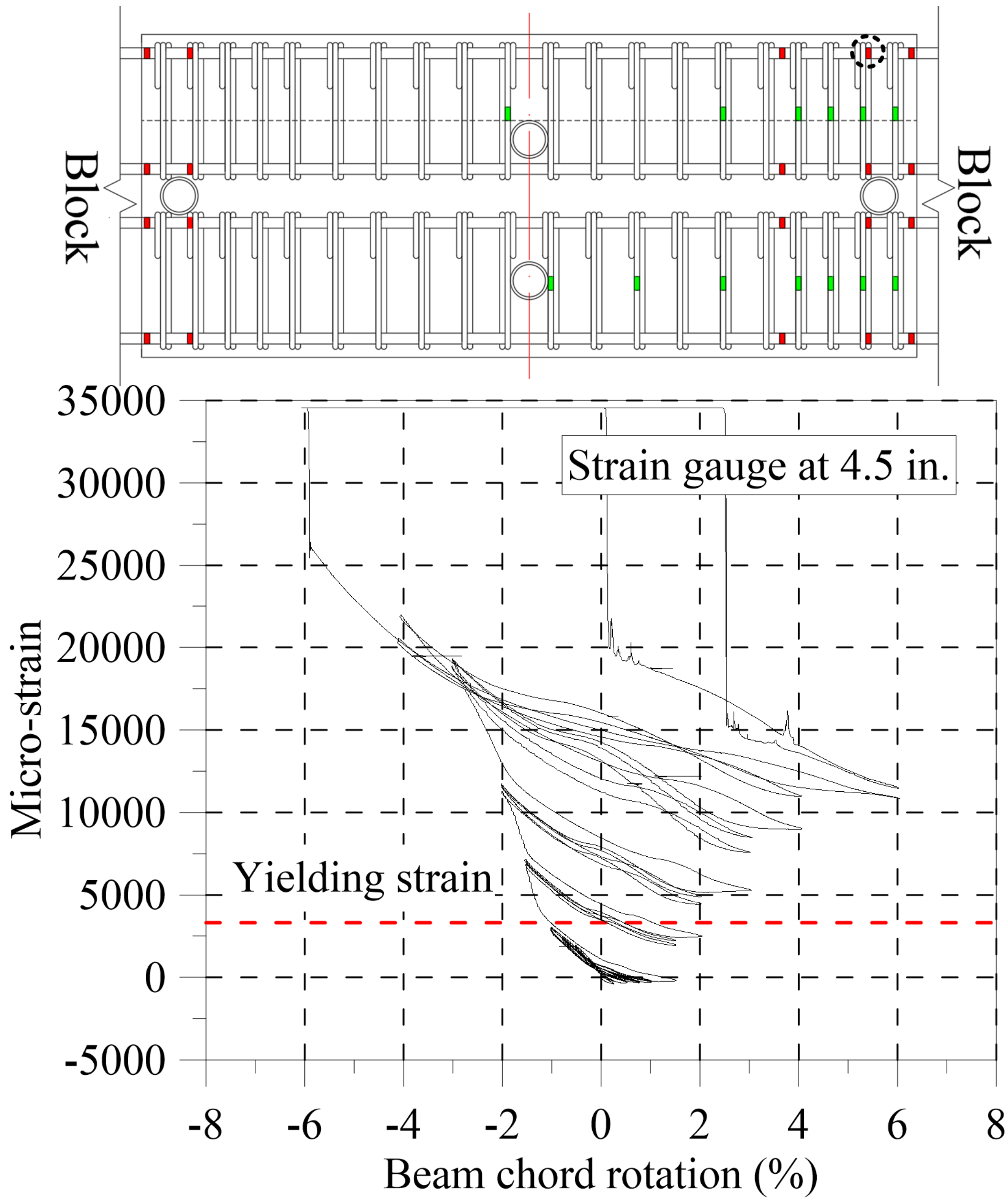

Block
Block
Strain gauge at 4.5 in.
Yielding strain
Micro-strain
35000
30000
25000
20000
15000
10000
5000
0
-5000
-8
-6
-4
-2
0
2
4
6
8
Beam chord rotation (%)

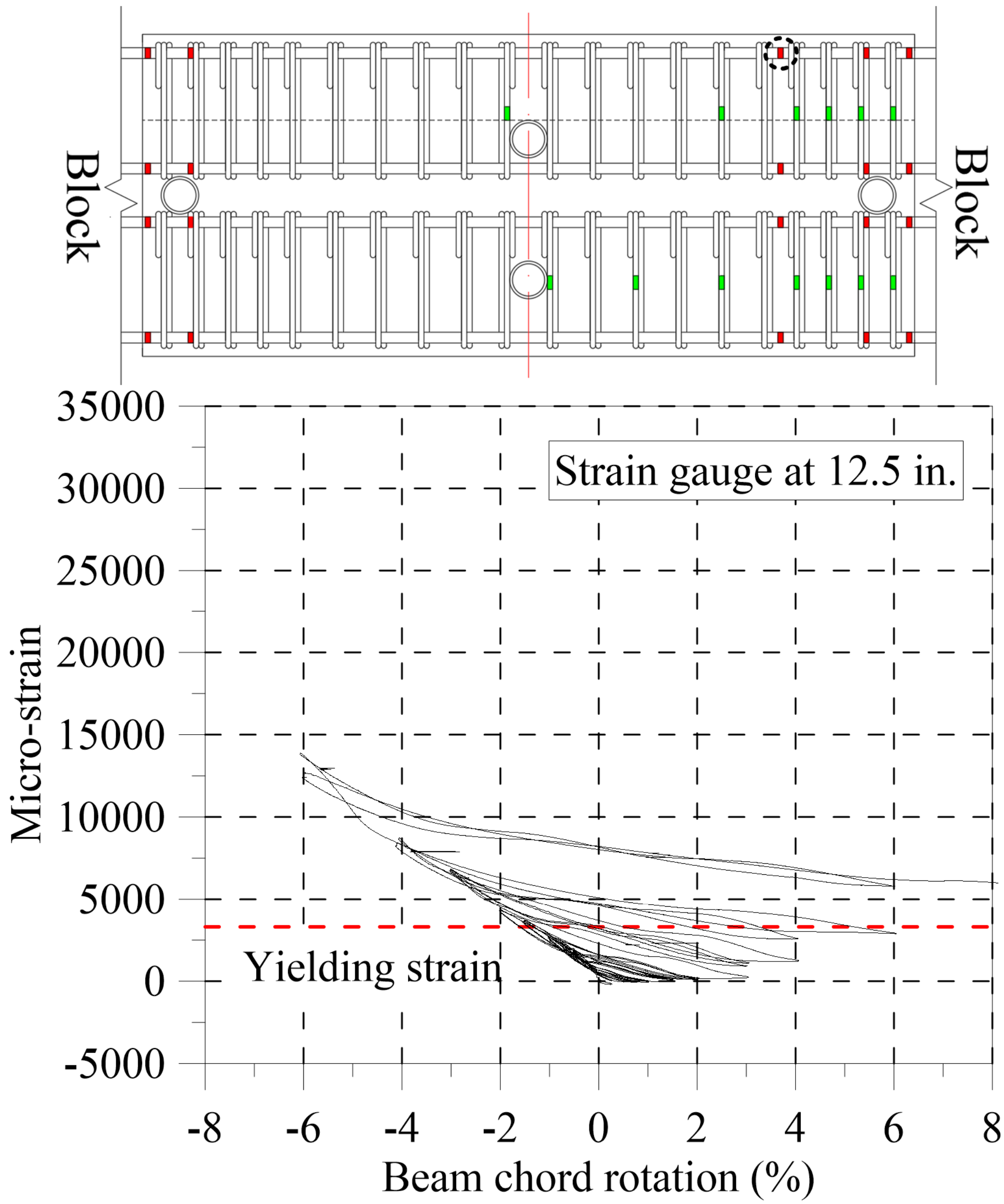

Block
Block
Strain gauge at 12.5 in.
Yielding strain
Micro-strain
35000
30000
25000
20000
15000
10000
5000
0
-5000
-8
-6
-4
-2
0
2
4
6
8
Beam chord rotation (%)

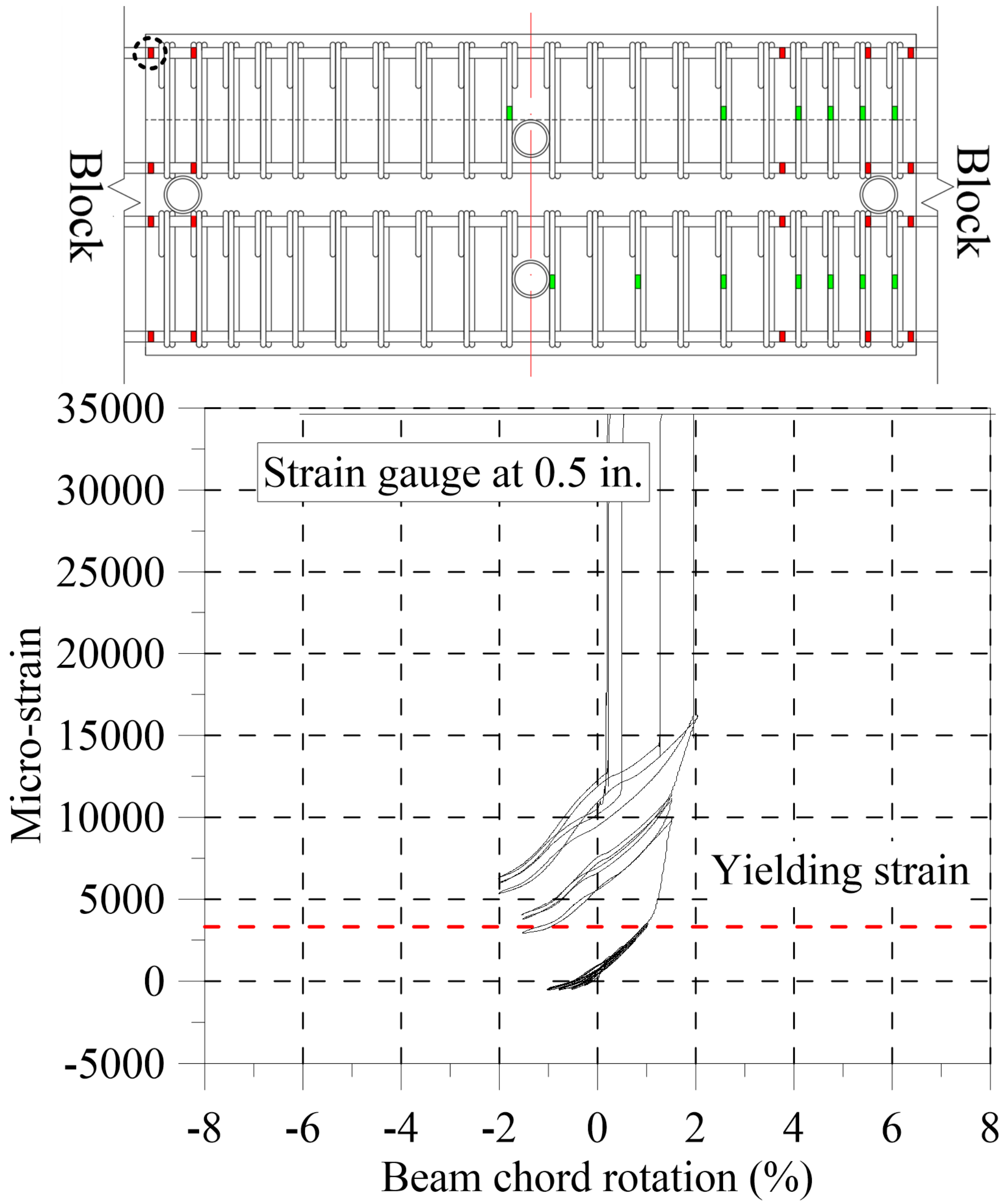
Block
Block
Strain gauge at 0.5 in.
Yielding strain
35000
30000
25000
20000
15000
10000
5000
0
-5000
Micro-strain
-8
-6
-4
-2
0
2
4
6
8
Beam chord rotation (%)

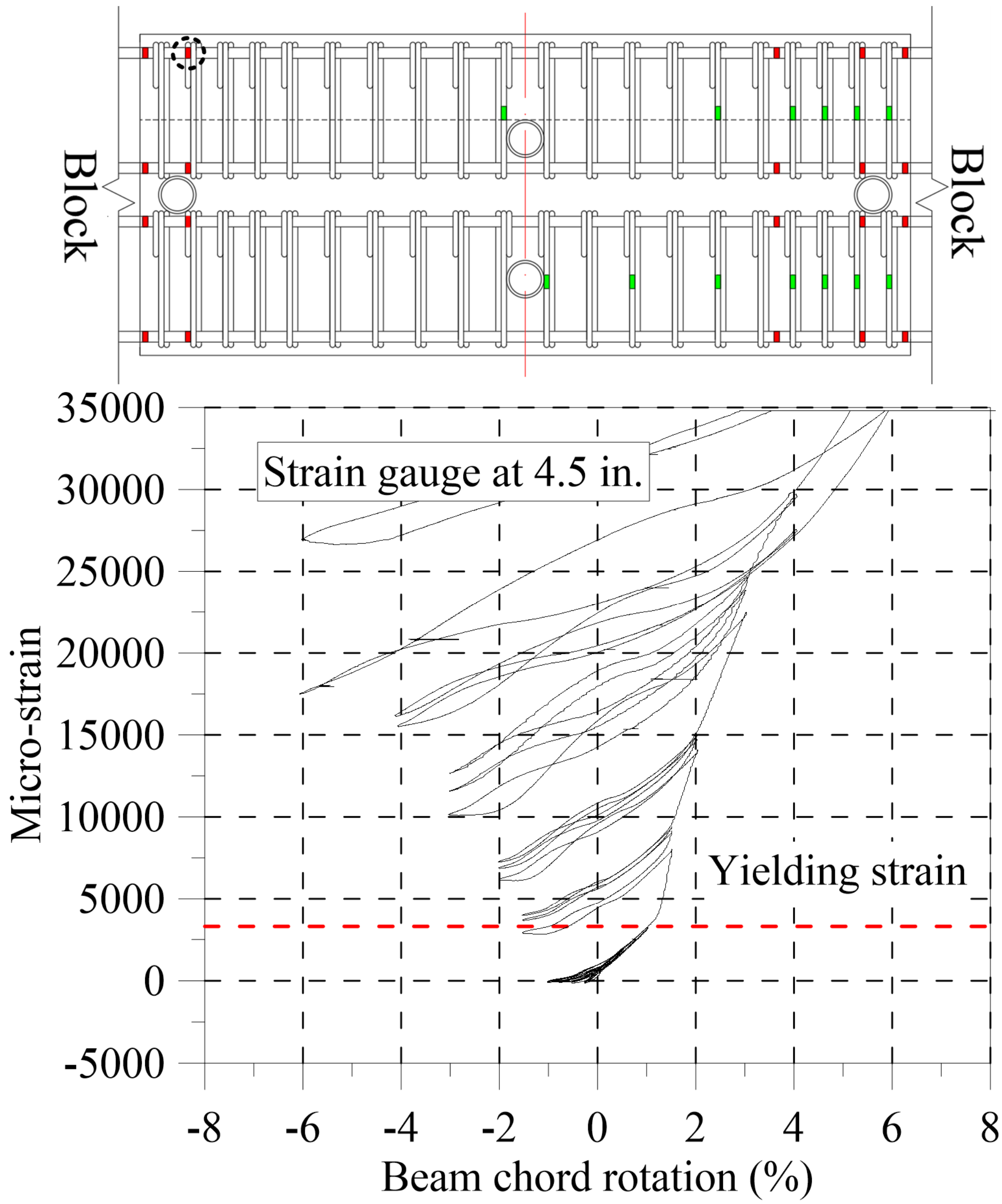
Block
Block
35000
30000
25000
20000
15000
10000
5000
0
-5000
Micro-strain
Strain gauge at 4.5 in.
Yielding strain
-8
-6
-4
-2
0
2
4
6
8
Beam chord rotation (%)

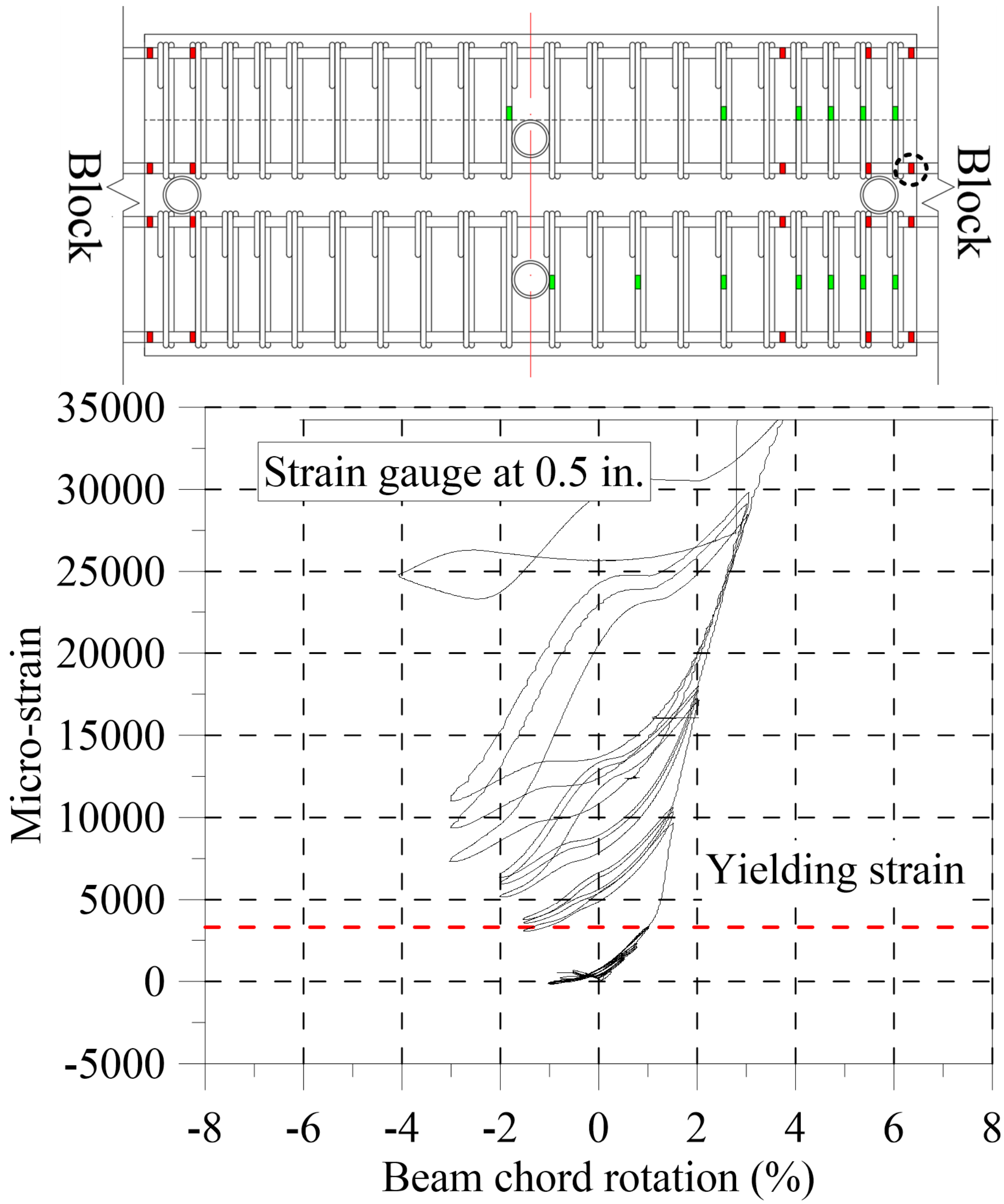

Block
Block
Strain gauge at 0.5 in.
Yielding strain
Micro-strain
Beam chord rotation (%)
35000
30000
25000
20000
15000
10000
5000
0
-5000
-8
-6
-4
-2
0
2
4
6
8

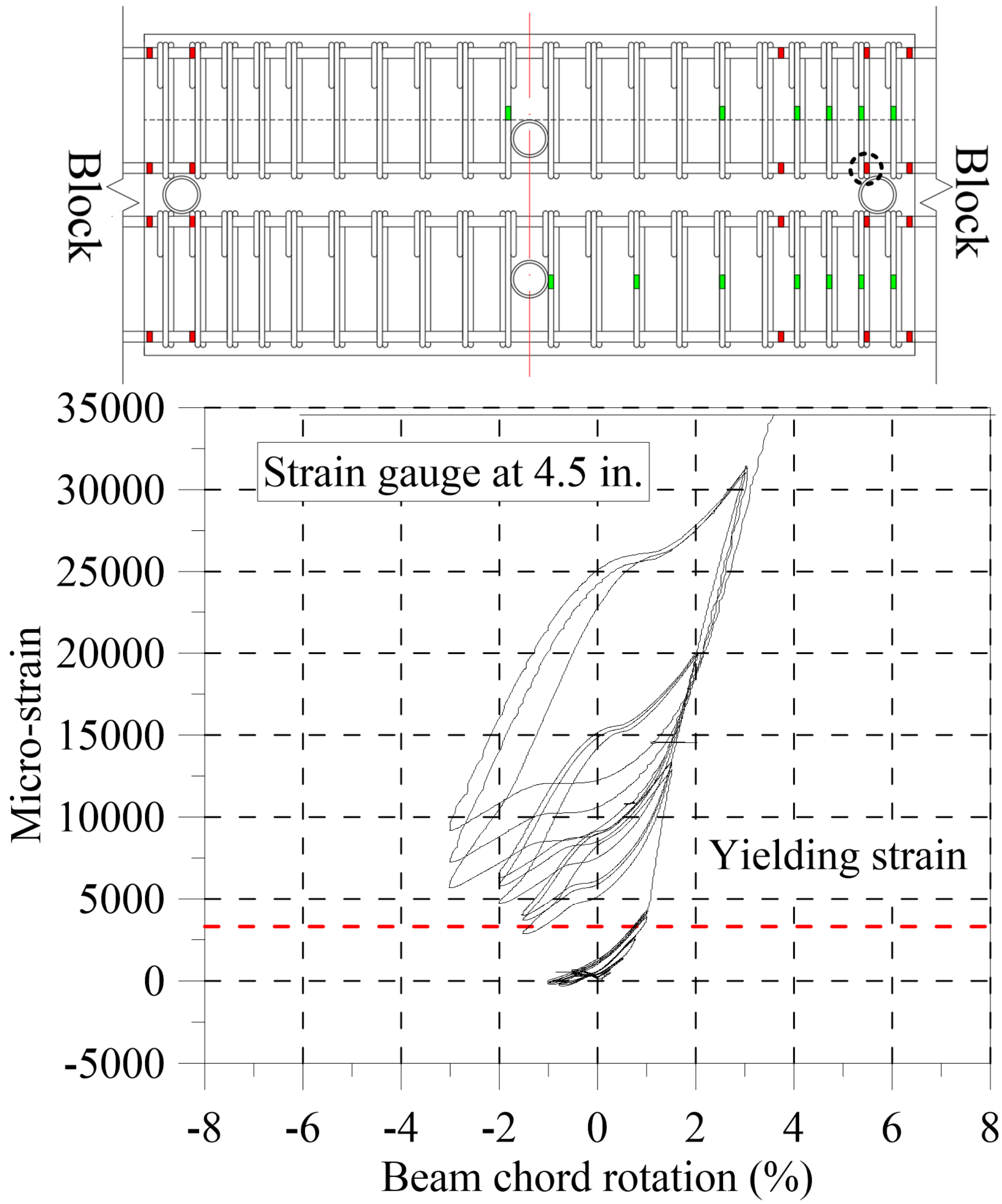

Block
Block
Strain gauge at 4.5 in.
Yielding strain
Micro-strain
Beam chord rotation (%)
35000
30000
25000
20000
15000
10000
5000
0
-5000
-8
-6
-4
-2
0
2
4
6
8

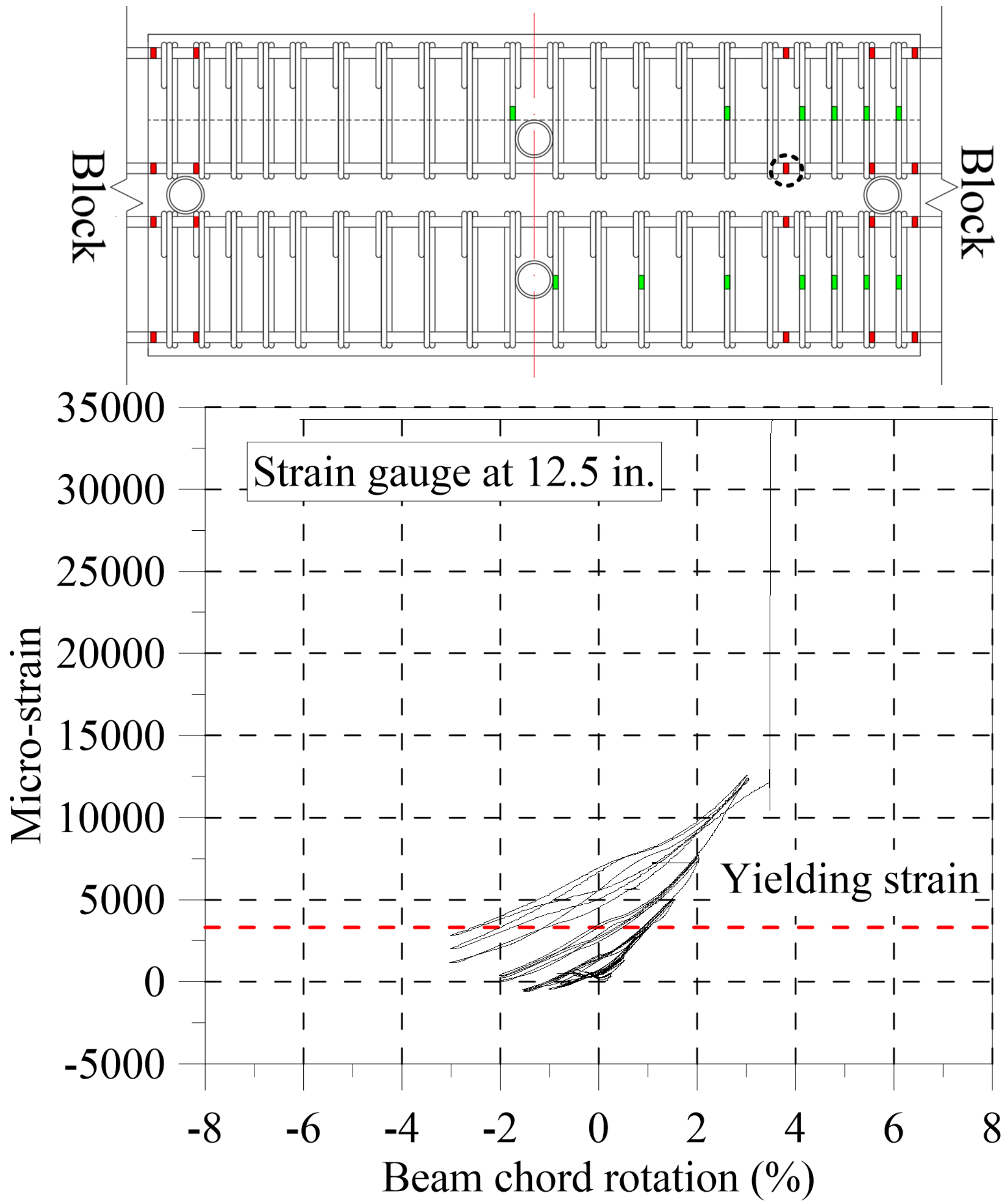
Block
Block
Strain gauge at 12.5 in.
Yielding strain
Micro-strain
Beam chord rotation (%)
35000
30000
25000
20000
15000
10000
5000
0
-5000
-8
-6
-4
-2
0
2
4
6
8

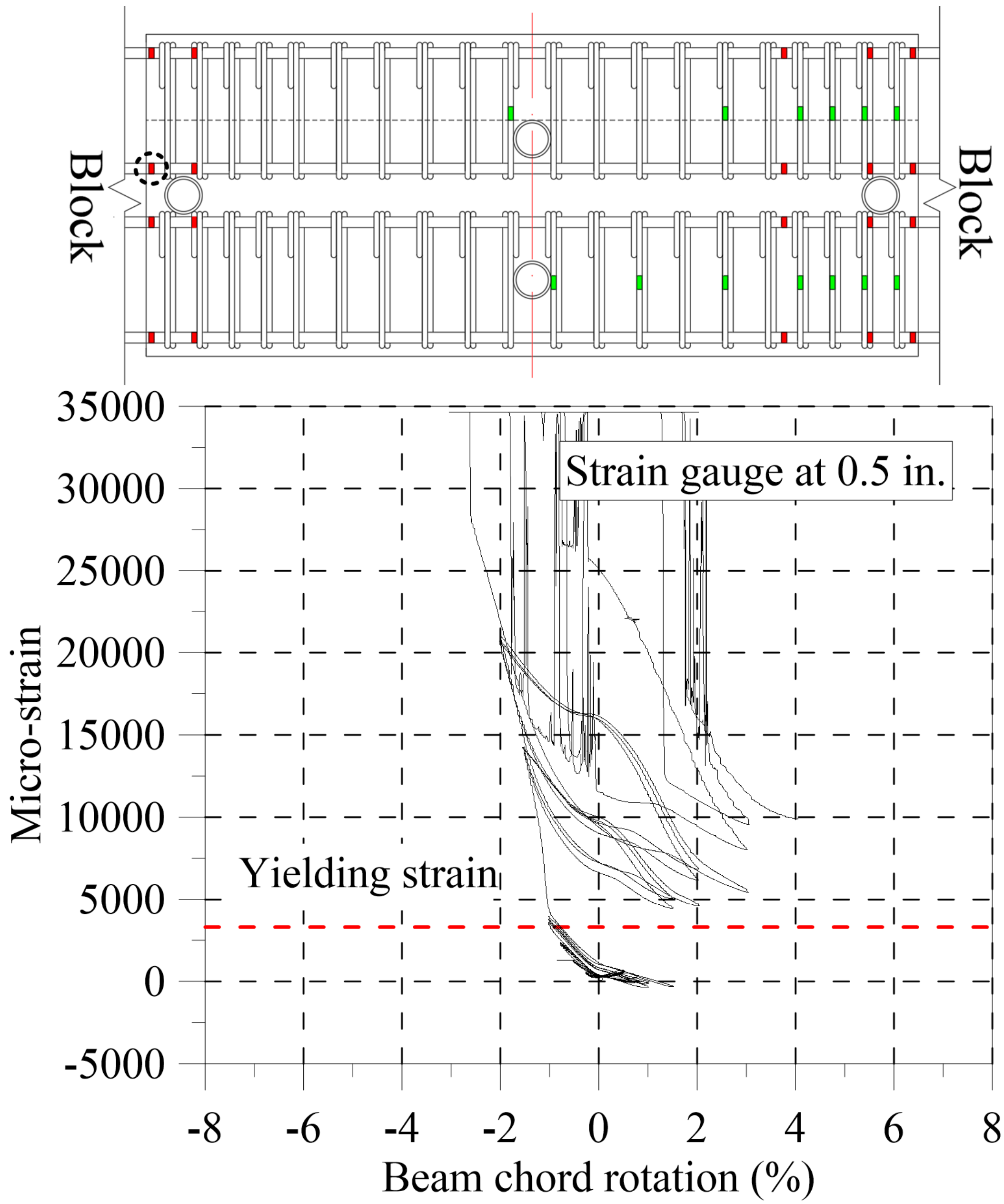
Block
Block
35000
30000
25000
20000
15000
10000
5000
0
-5000
Micro-strain
Strain gauge at 0.5 in.
Yielding strain
-8
-6
-4
-2
0
2
4
6
8
Beam chord rotation (%)

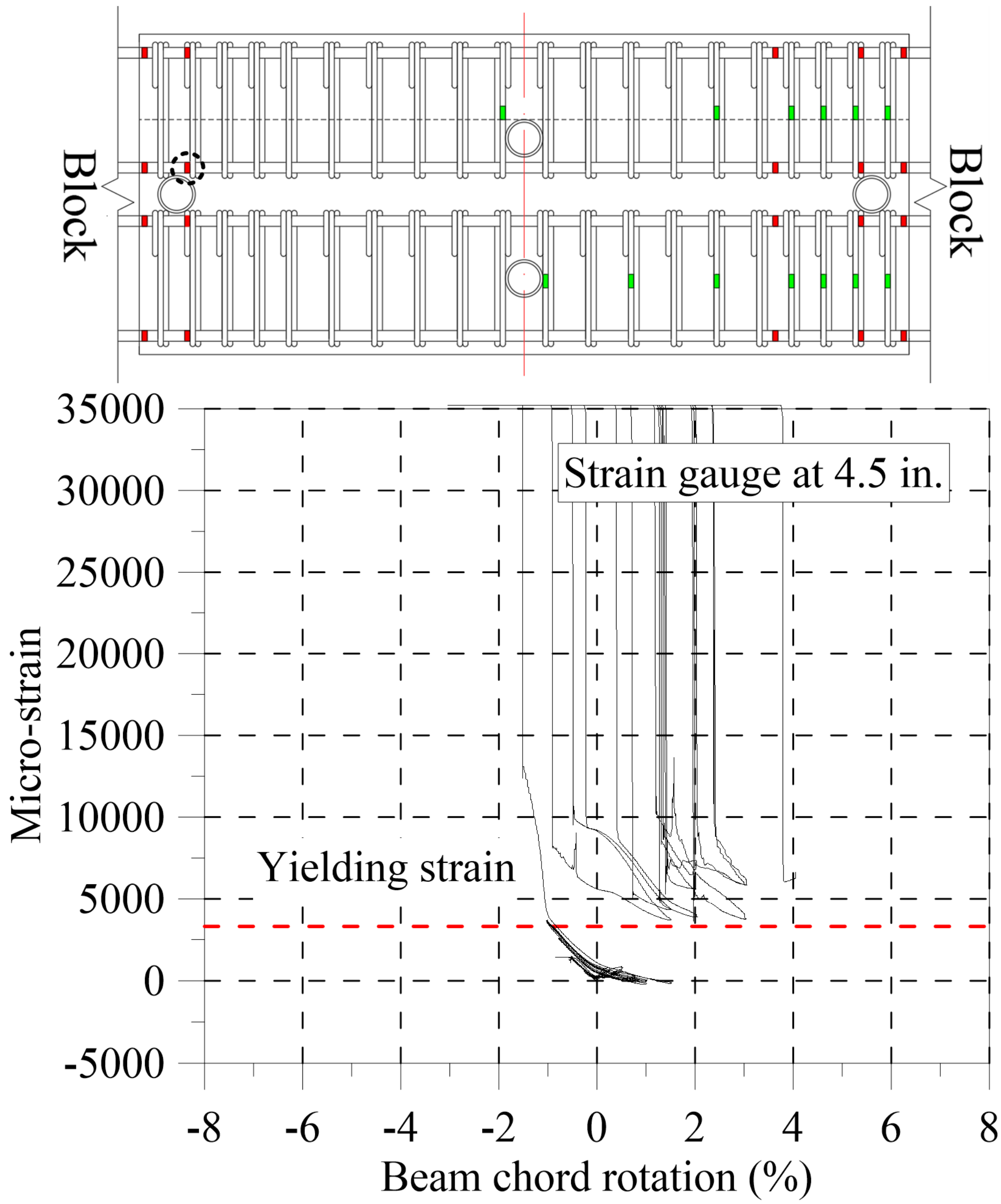

Block
Block
Strain gauge at 4.5 in.
Yielding strain
Micro-strain
35000
30000
25000
20000
15000
10000
5000
0
-5000
-8
-6
-4
-2
0
2
4
6
8
Beam chord rotation (%)

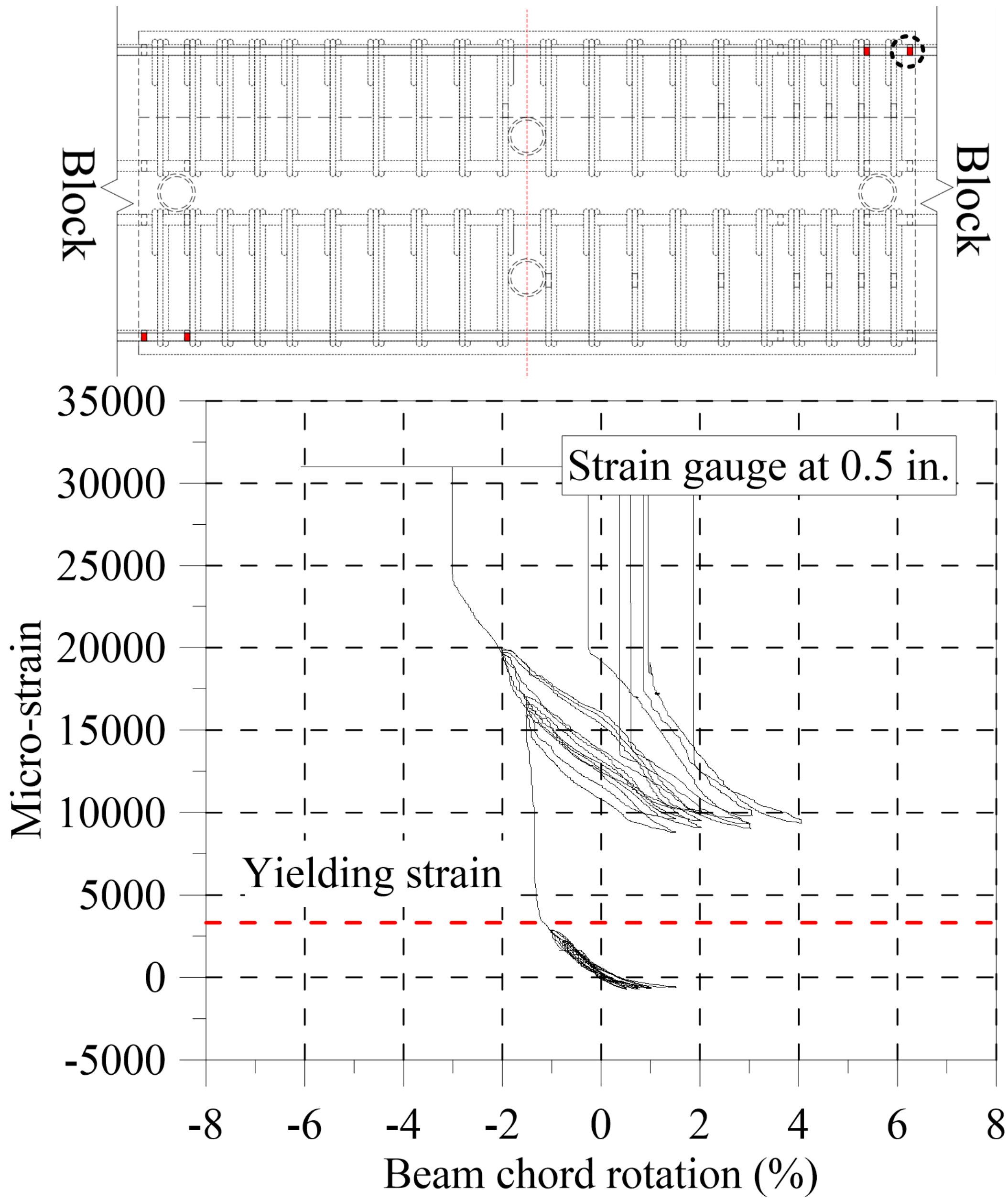
Block
Block
Strain gauge at 0.5 in.
Yielding strain
35000
30000
25000
20000
15000
10000
5000
0
-5000
Micro-strain
-8
-6
-4
-2
0
2
4
6
8
Beam chord rotation (%)

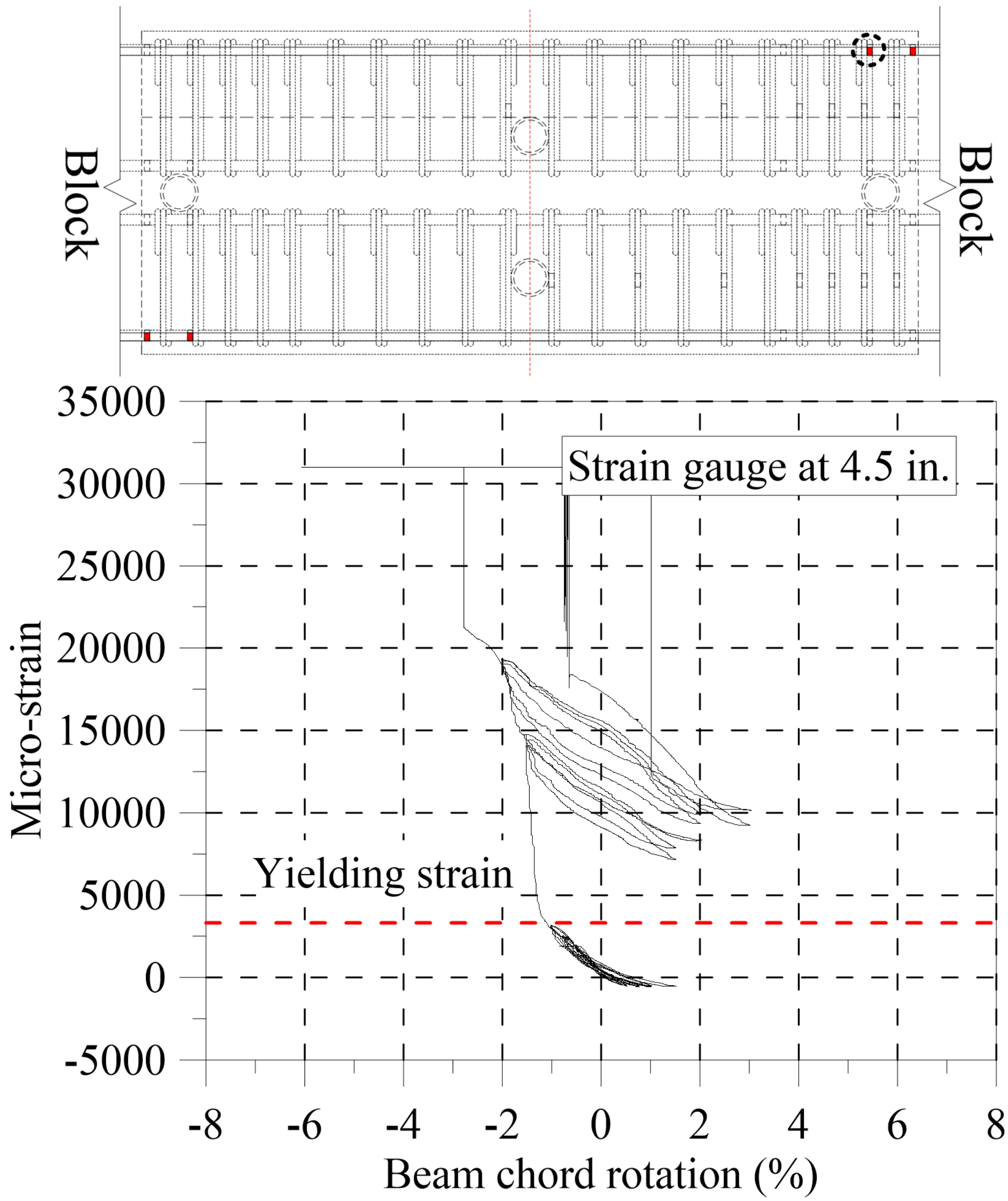
Block
Block
Strain gauge at 4.5 in.
Yielding strain
Micro-strain
Beam chord rotation (%)

C.3.1.2 Transverse reinforcement

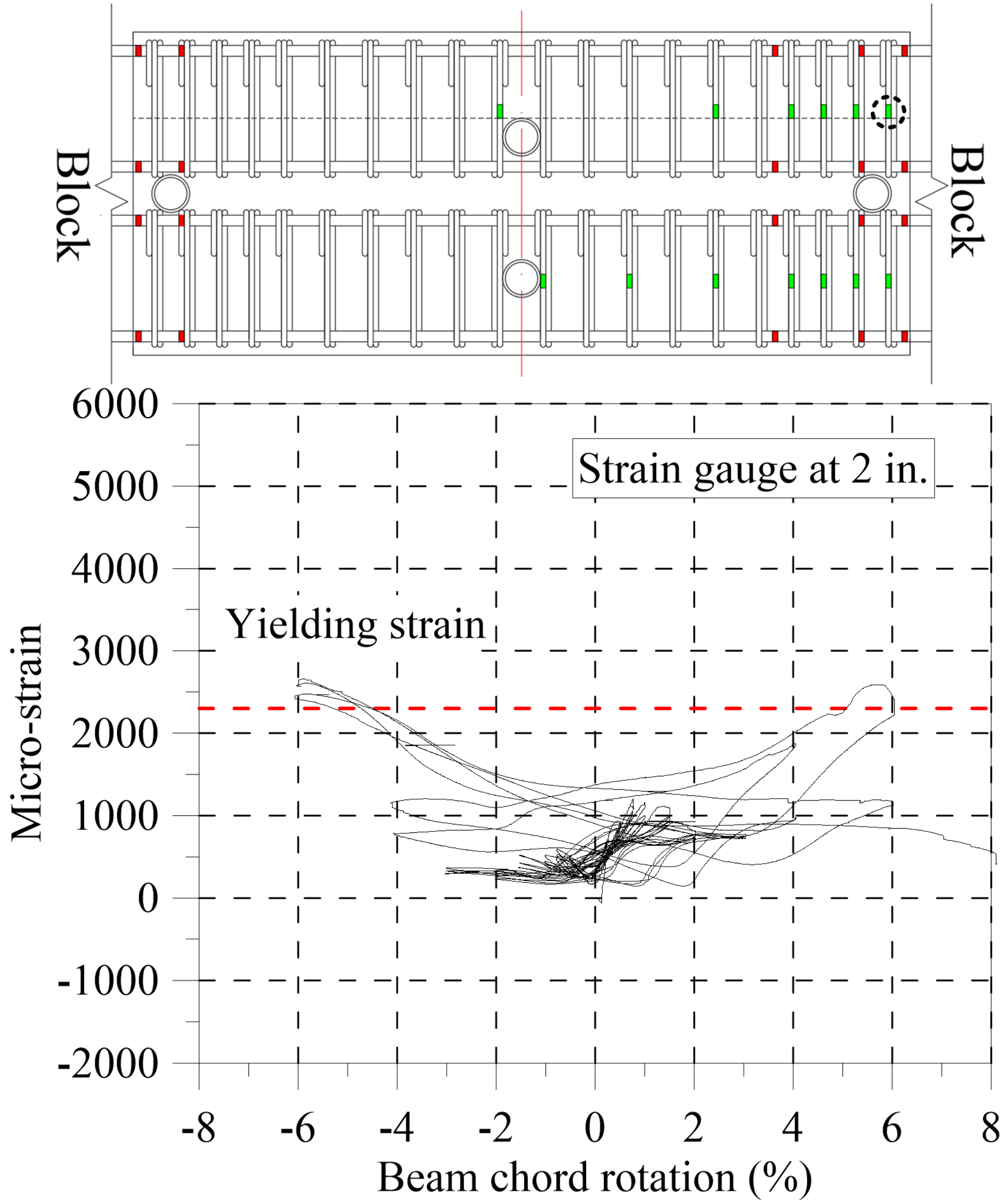

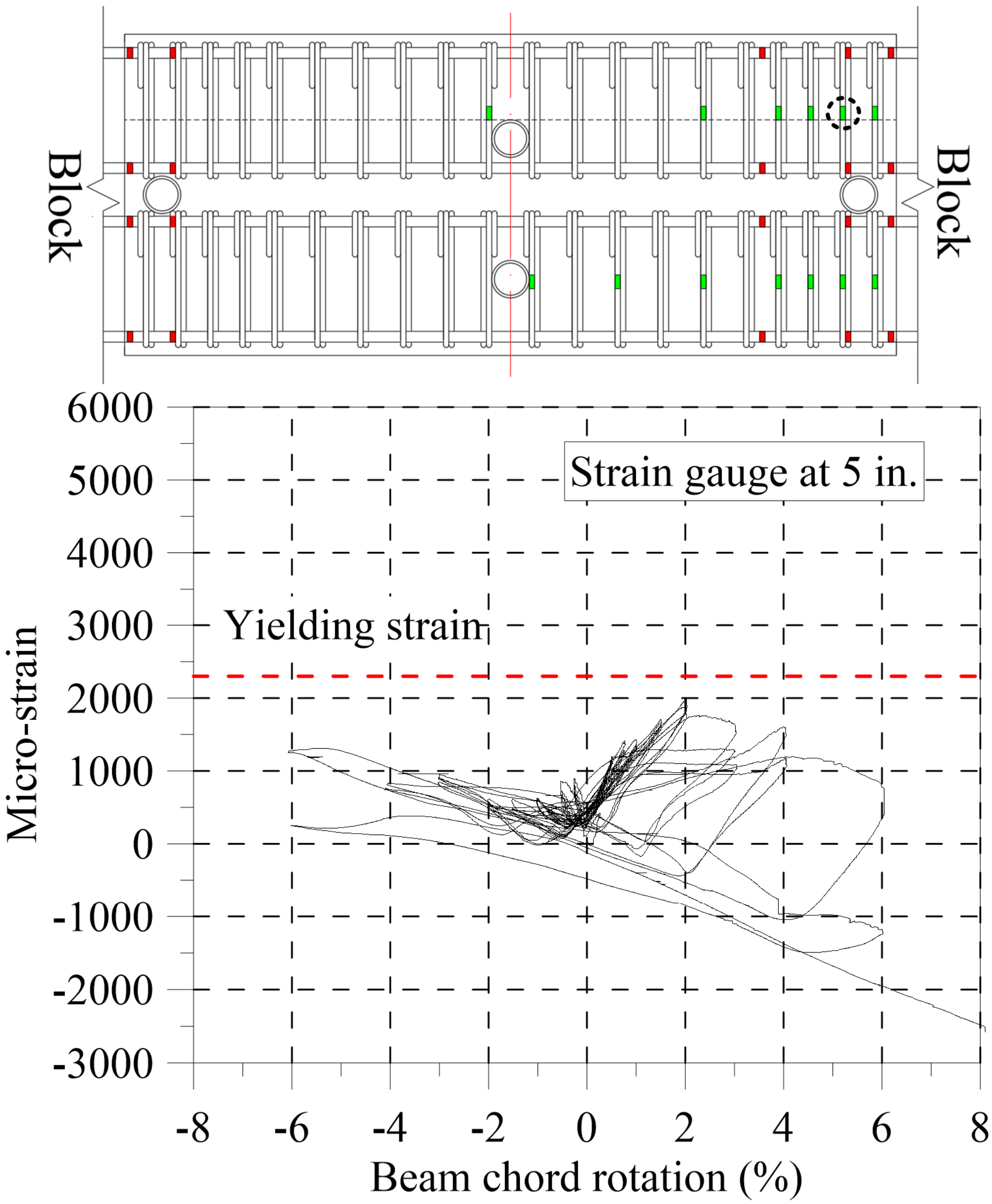

Block
Block
Strain gauge at 5 in.
Yielding strain
Micro-strain
Beam chord rotation (%)
6000
5000
4000
3000
2000
1000
0
-1000
-2000
-3000
-8
-6
-4
-2
0
2
4
6
8

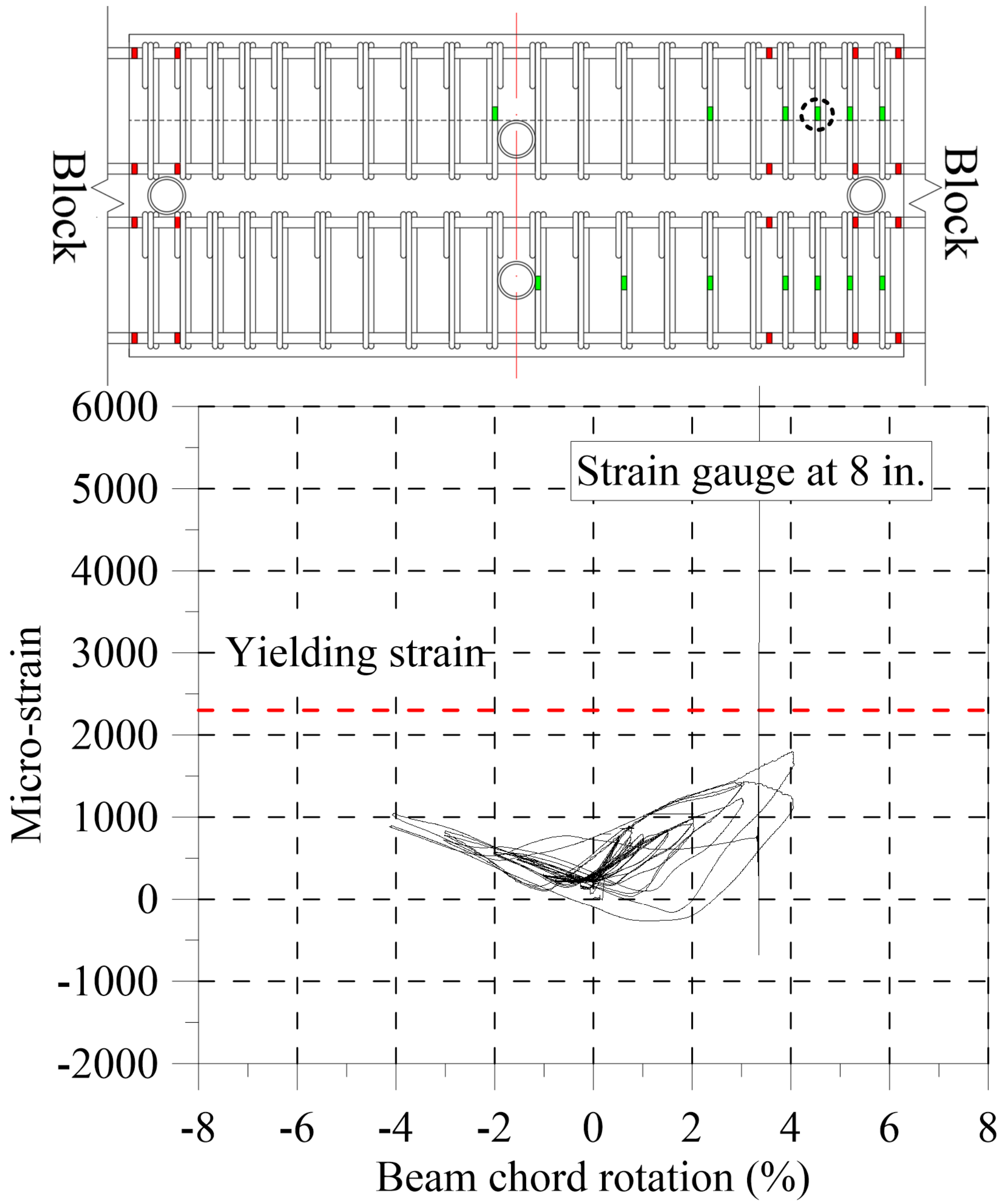
Block
Block
Strain gauge at 8 in.
Yielding strain
Micro-strain
Beam chord rotation (%)
6000
5000
4000
3000
2000
1000
0
-1000
-2000
-8
-6
-4
-2
0
2
4
6
8

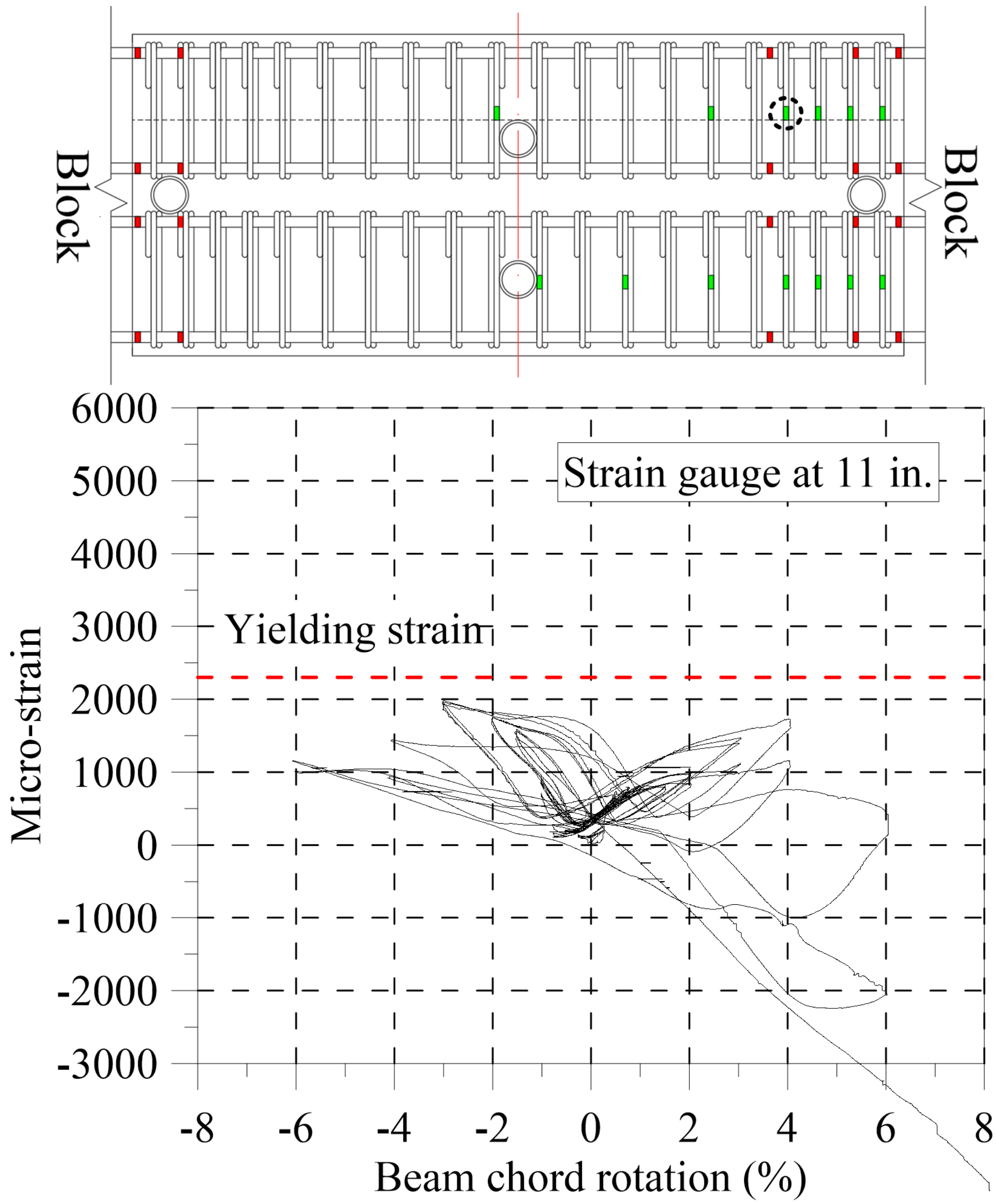

Block
Block
Strain gauge at 11 in.
Yielding strain
Micro-strain
Beam chord rotation (%)
6000
5000
4000
3000
2000
1000
0
-1000
-2000
-3000
-8
-6
-4
-2
0
2
4
6
8

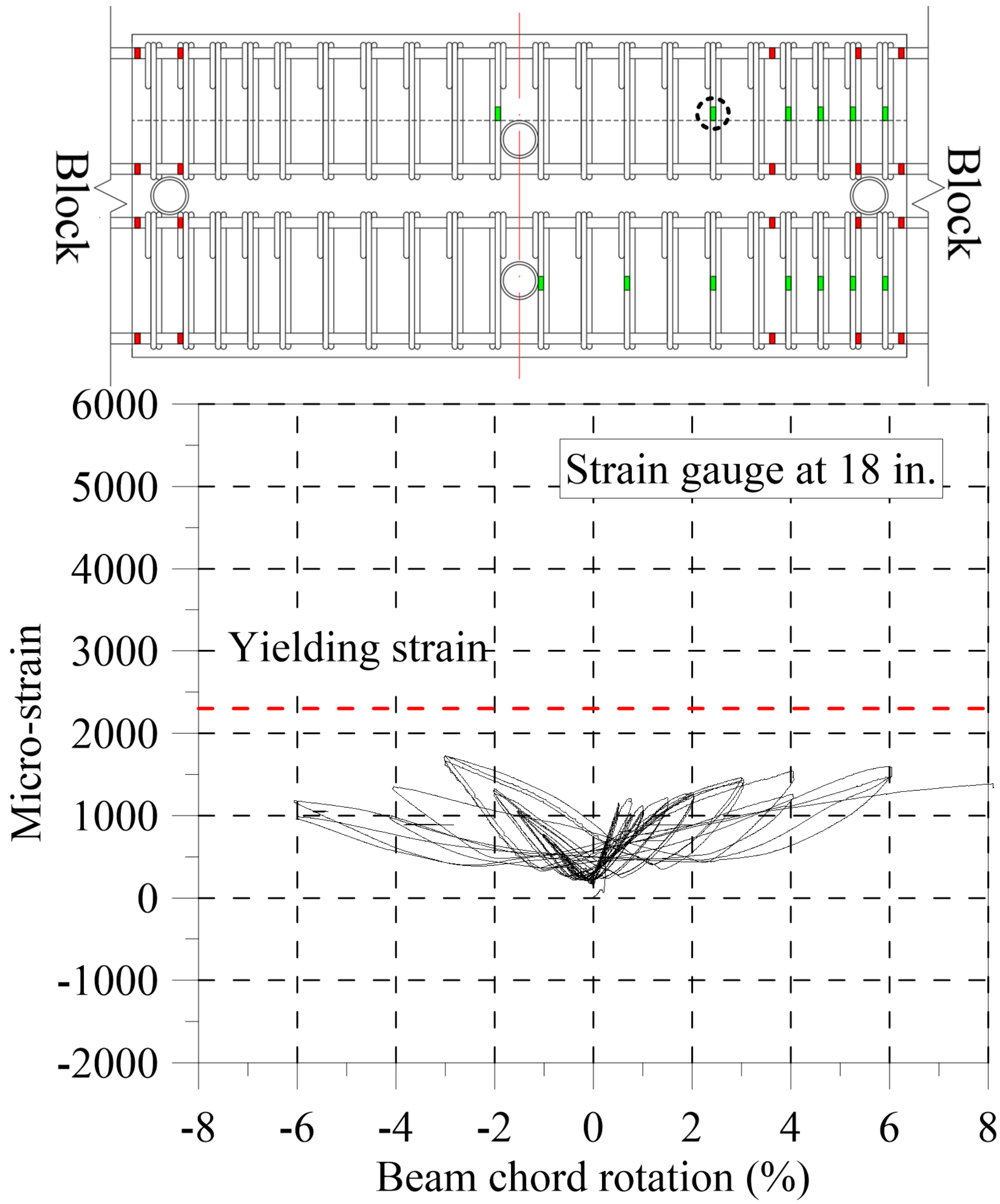
Block
Block
Strain gauge at 18 in.
Yielding strain
Micro-strain
6000
5000
4000
3000
2000
1000
0
-1000
-2000
-8
-6
-4
-2
0
2
4
6
8
Beam chord rotation (%)

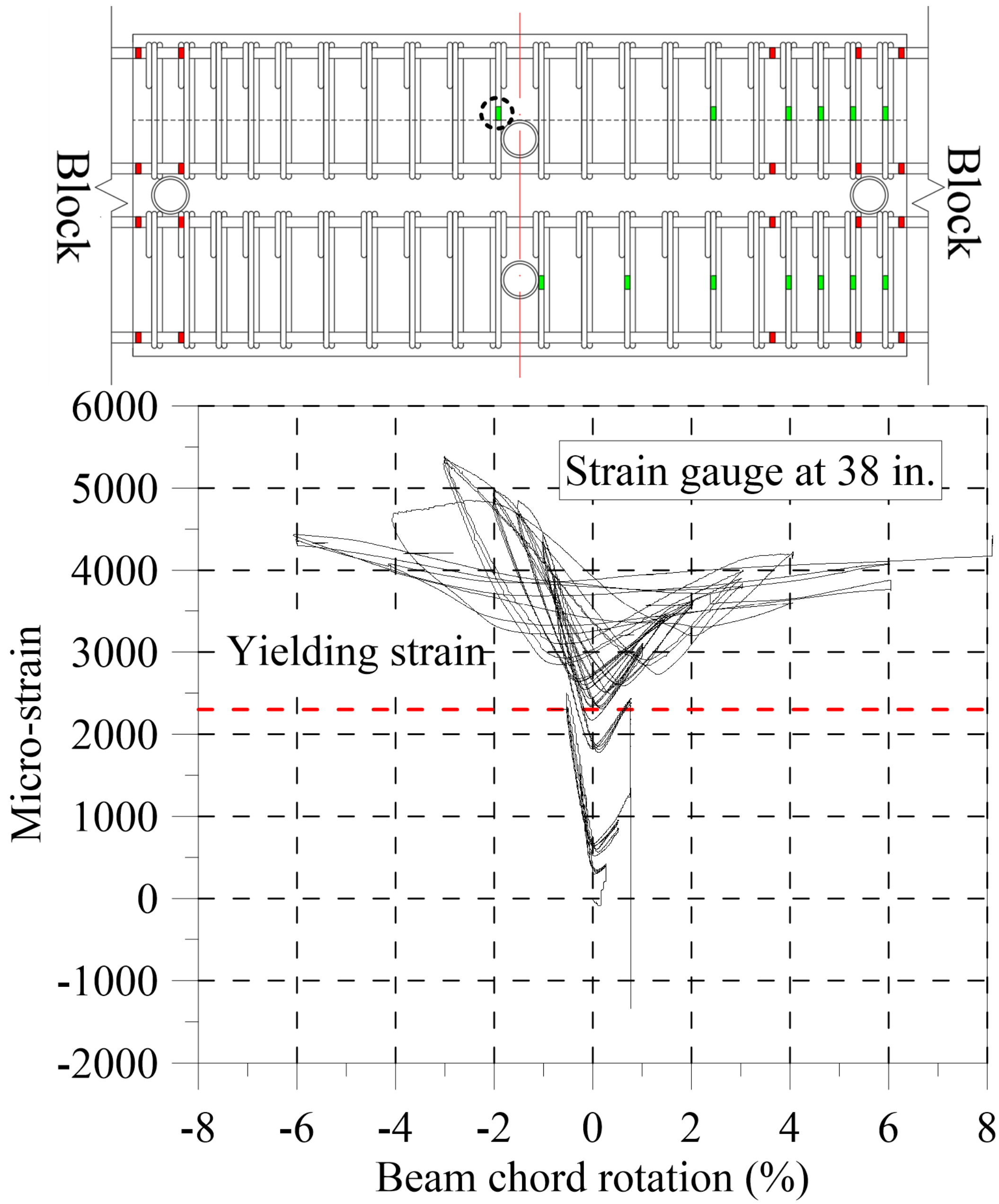
Block
Block
Strain gauge at 38 in.
Yielding strain
Micro-strain
Beam chord rotation (%)
6000
5000
4000
3000
2000
1000
0
-1000
-2000
-8
-6
-4
-2
0
2
4
6
8

C.3.1.3 Developed longitudinal reinforcement

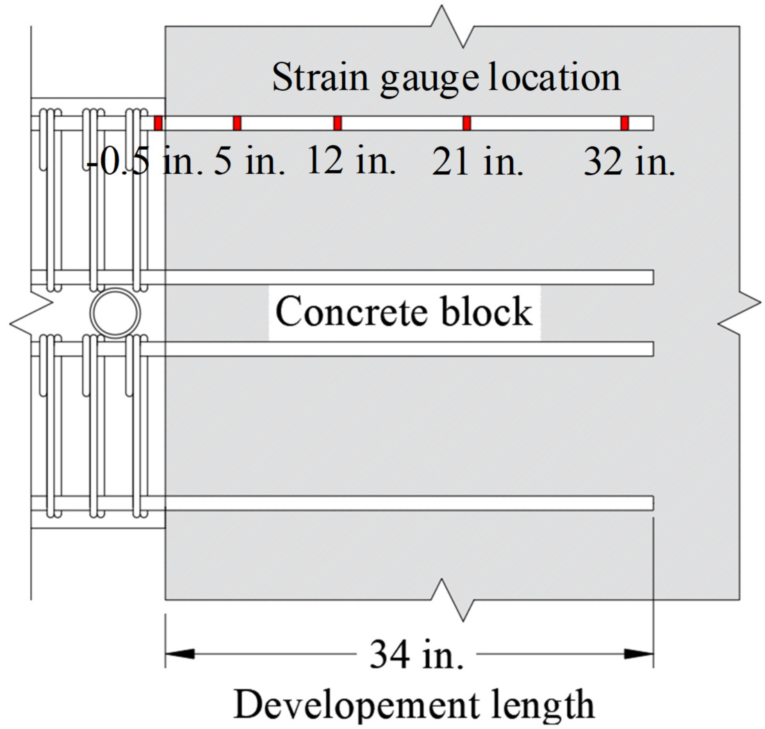

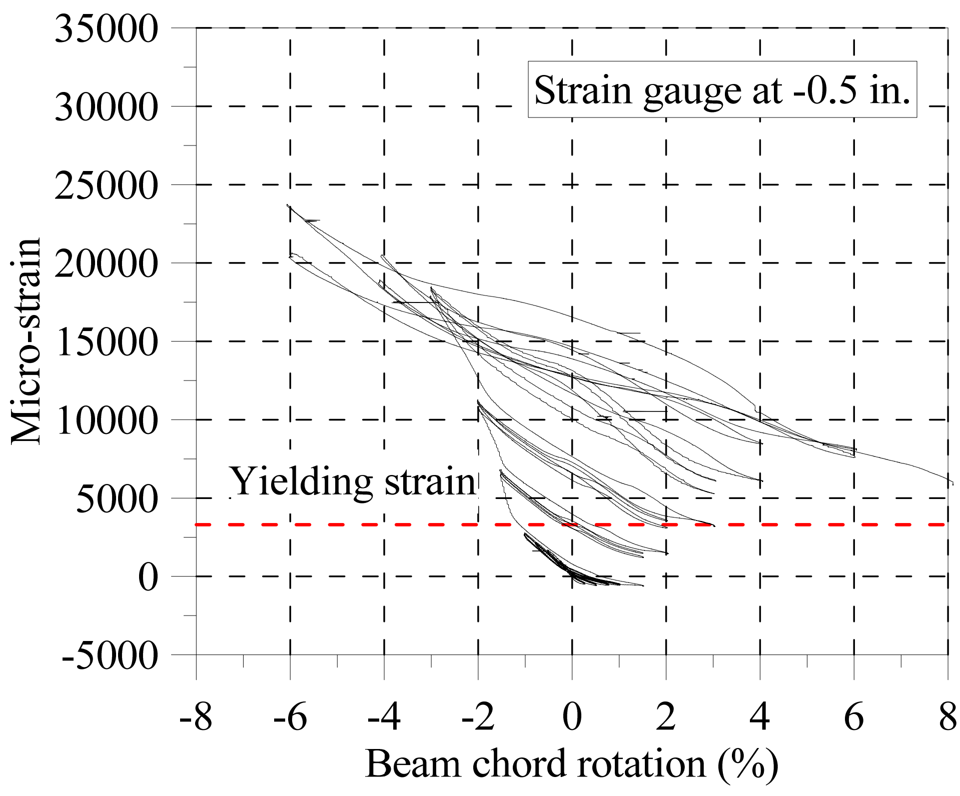

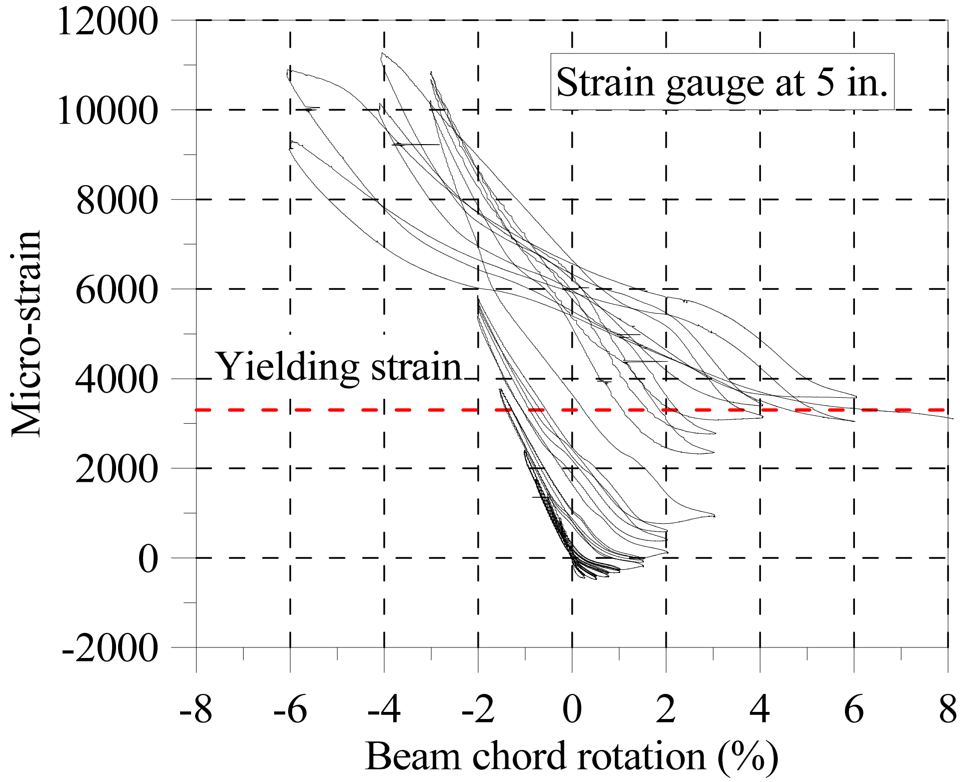
Strain gauge at 5 in.
Yielding strain
Micro-strain
Beam chord rotation (%)
12000
10000
8000
6000
4000
2000
0
-2000
-8
-6
-4
-2
0
2
4
6
8

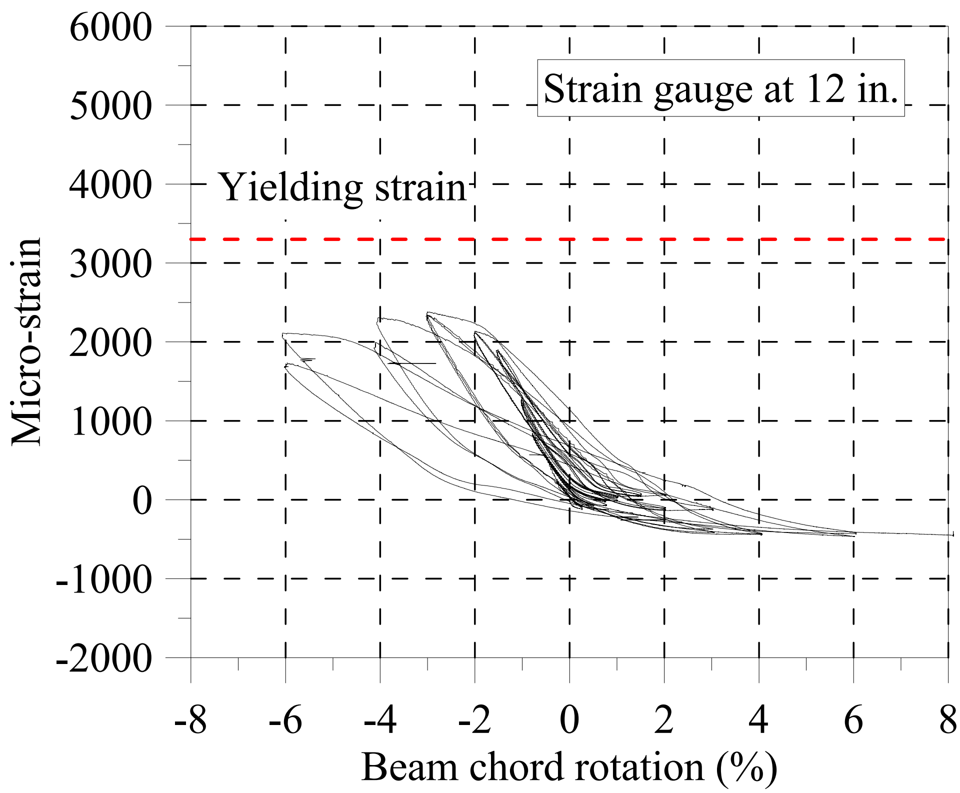
Strain gauge at 12 in.
Yielding strain
Micro-strain
Beam chord rotation (%)
6000
5000
4000
3000
2000
1000
0
-1000
-2000
-8
-6
-4
-2
0
2
4
6
8

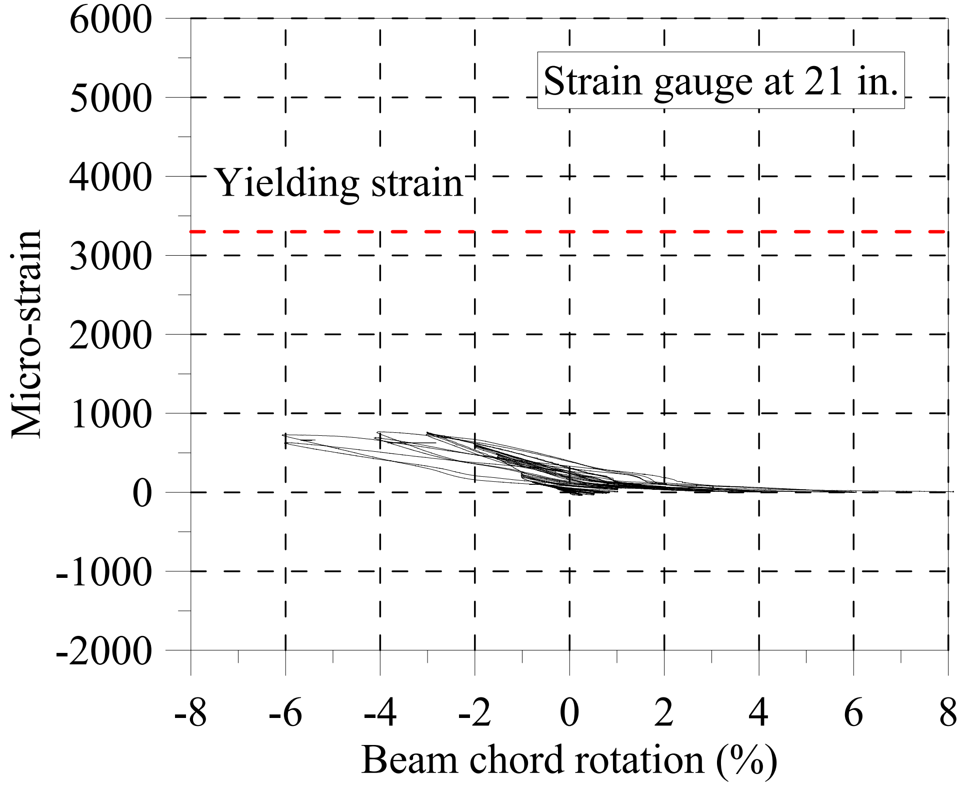
Strain gauge at 21 in.
Yielding strain
Micro-strain
6000
5000
4000
3000
2000
1000
0
-1000
-2000
-8
-6
-4
-2
0
2
4
6
8
Beam chord rotation (%)

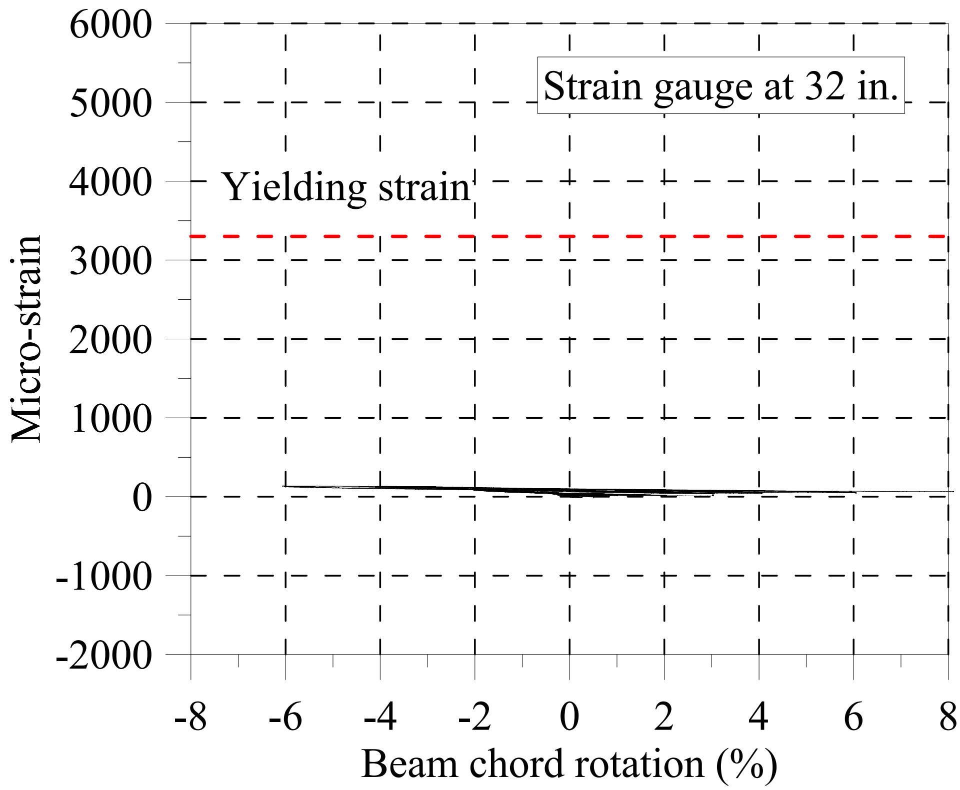
Strain gauge at 32 in.
Yielding strain
Micro-strain
6000
5000
4000
3000
2000
1000
0
-1000
-2000
-8
-6
-4
-2
0
2
4
6
8
Beam chord rotation (%)

C.3.2 Lower steel cage

C.3.2.1 Longitudinal reinforcement

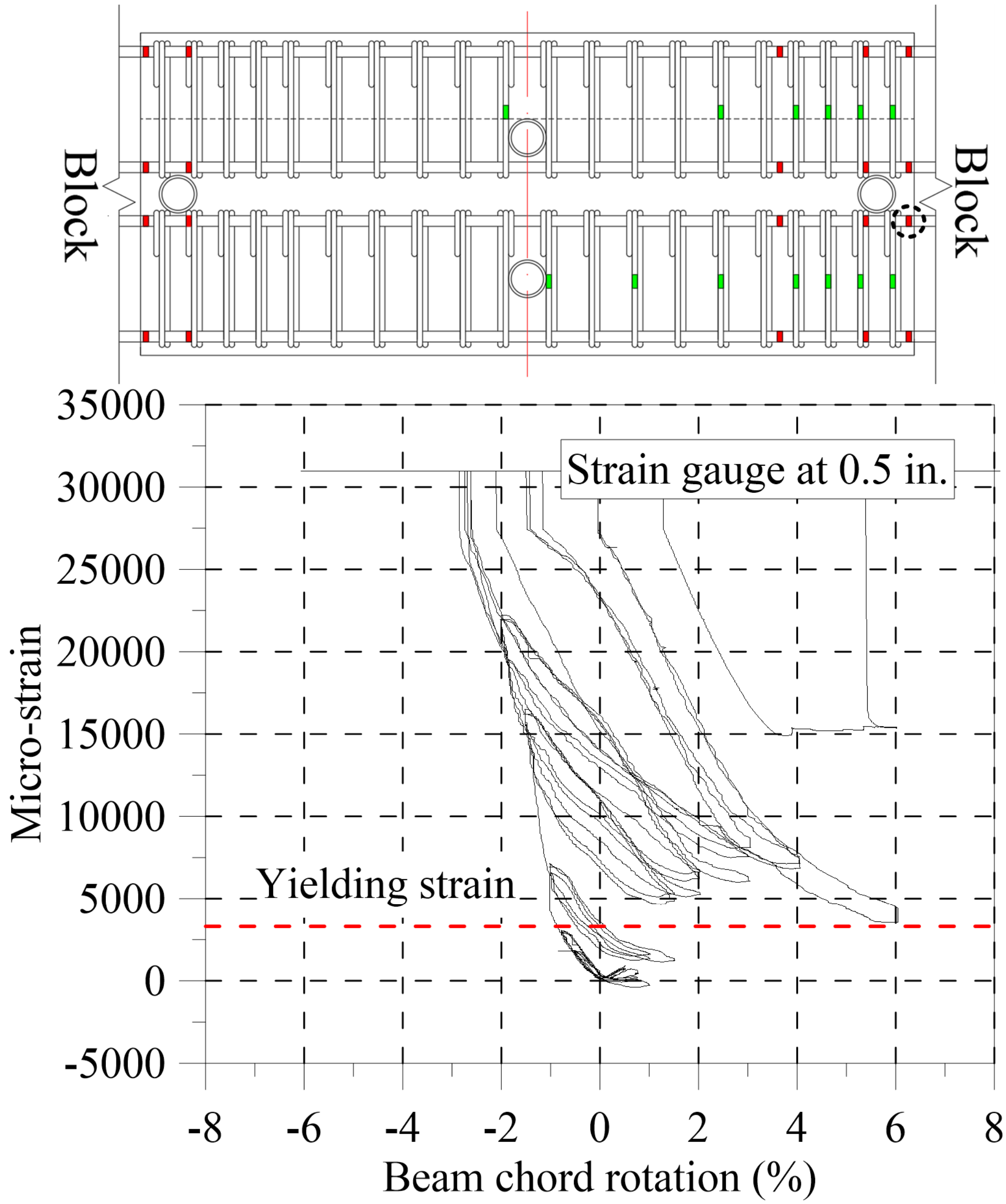

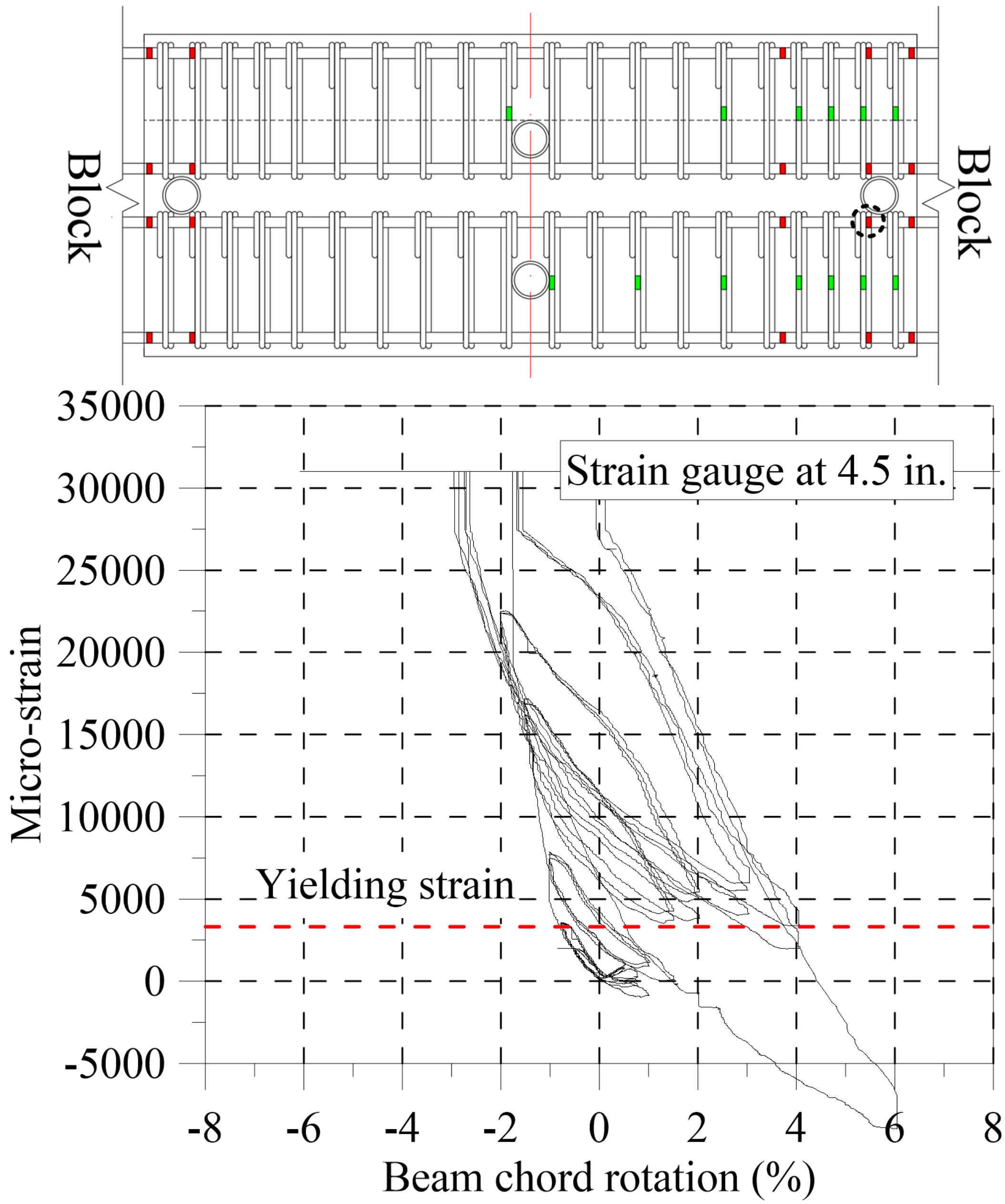

Block
Block
35000
30000
25000
20000
15000
10000
5000
0
-5000
Micro-strain
Strain gauge at 4.5 in.
Yielding strain
-8
-6
-4
-2
0
2
4
6
8
Beam chord rotation (%)

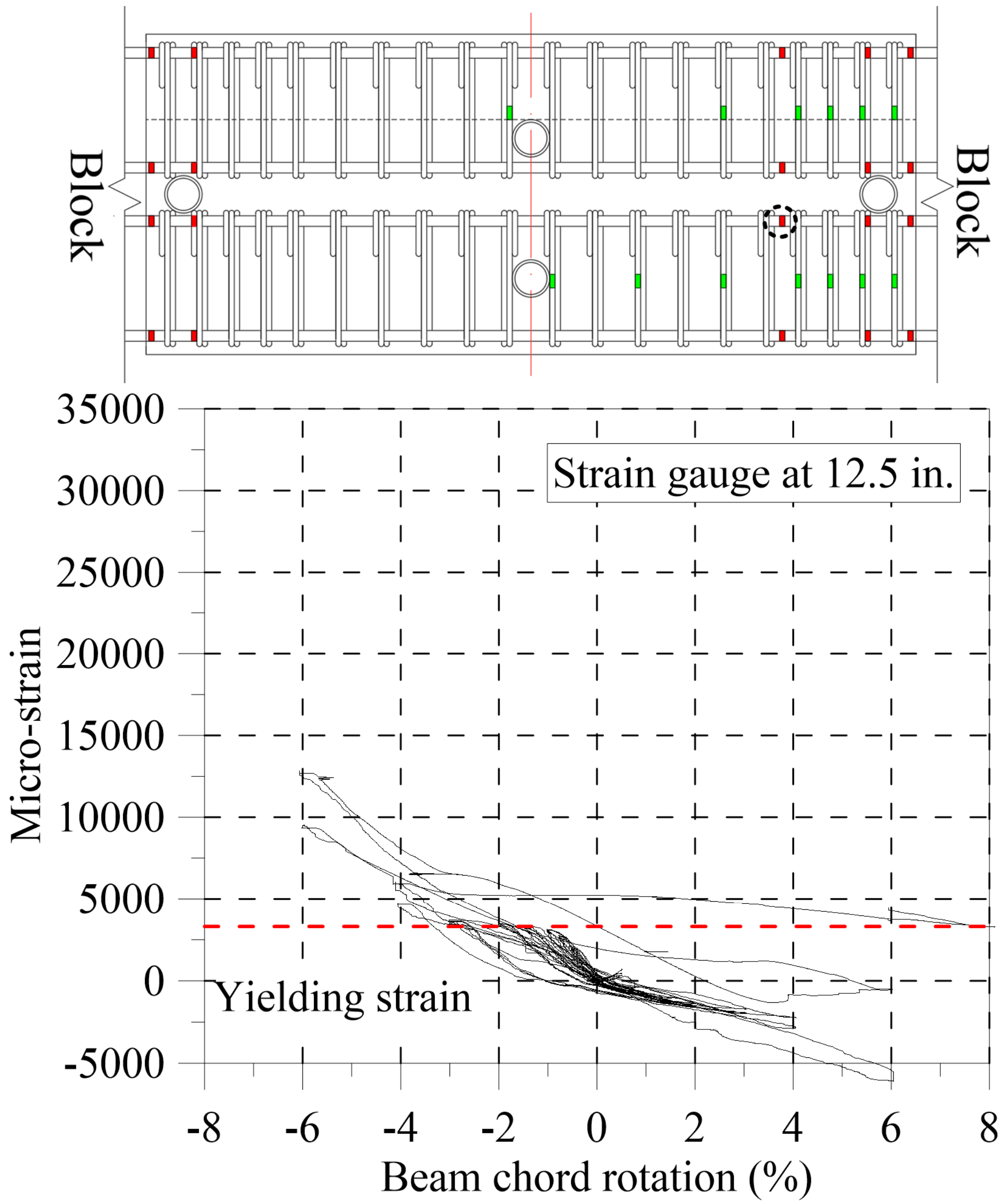

Block
Block
35000
30000
25000
20000
15000
10000
5000
0
-5000
Strain gauge at 12.5 in.
Yielding strain
Micro-strain
-8
-6
-4
-2
0
2
4
6
8
Beam chord rotation (%)

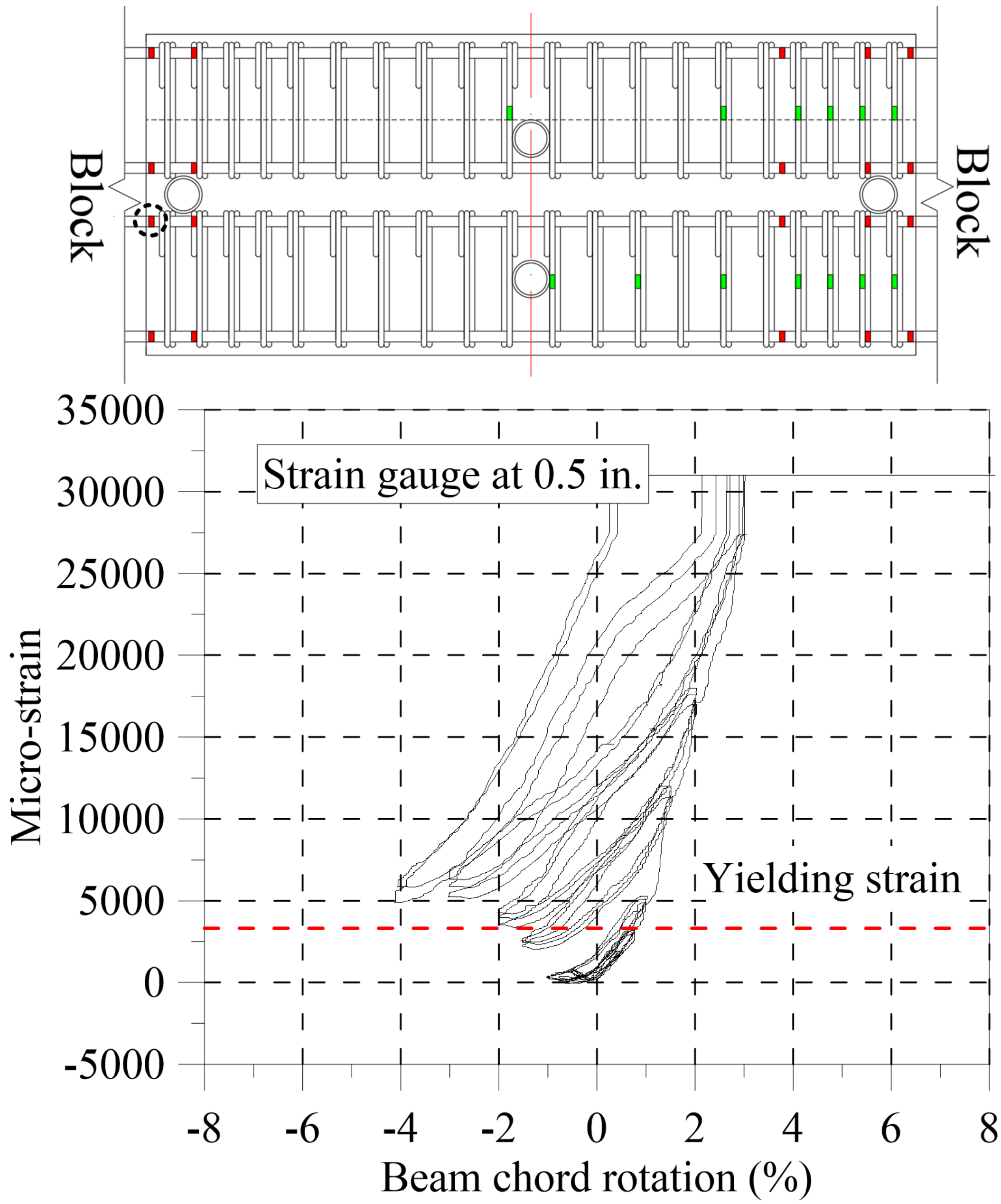
Block
Block
Strain gauge at 0.5 in.
Yielding strain
Micro-strain
Beam chord rotation (%)
35000
30000
25000
20000
15000
10000
5000
0
-5000
-8
-6
-4
-2
0
2
4
6
8

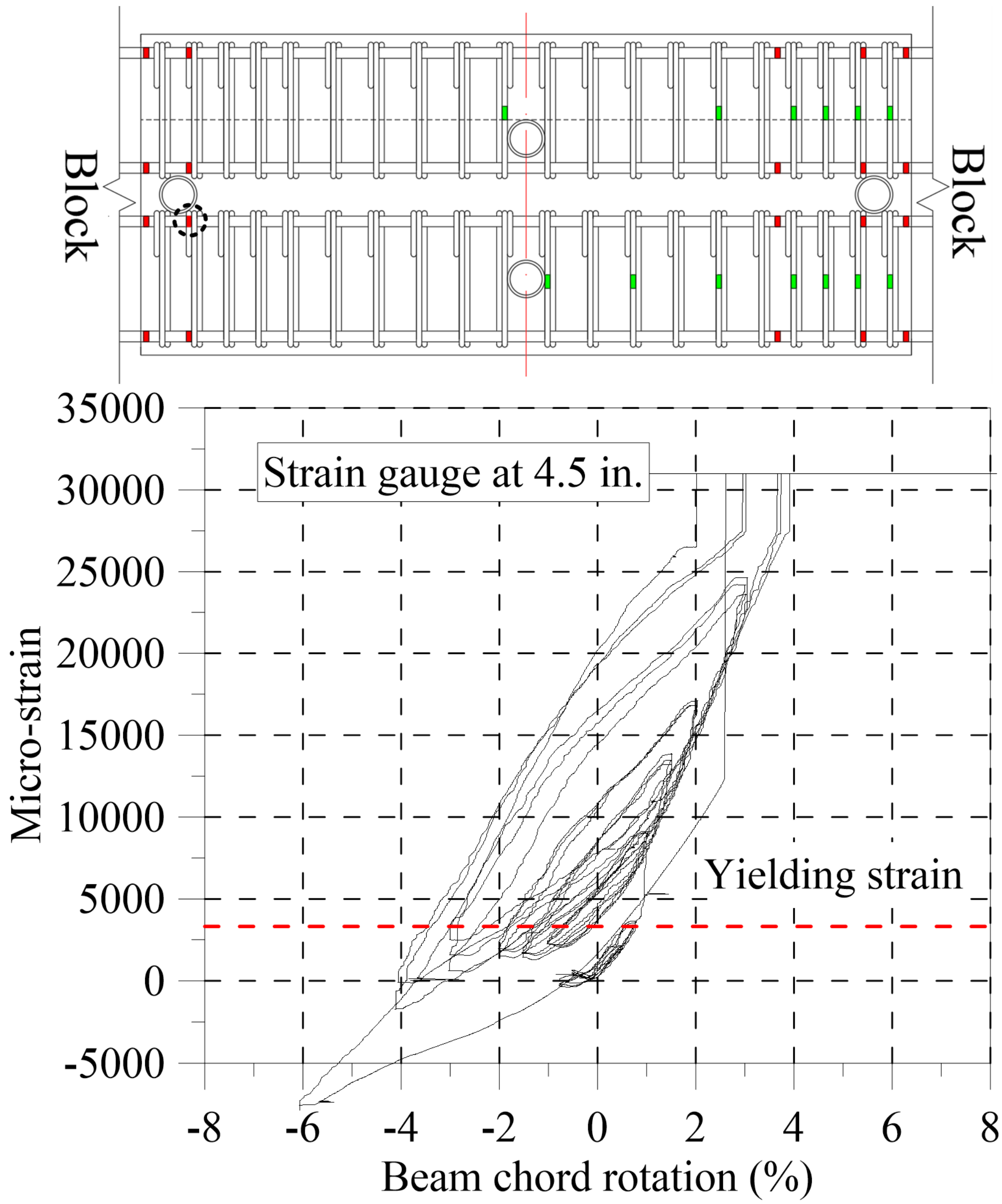
Block
Block
Strain gauge at 4.5 in.
Yielding strain
Micro-strain
Beam chord rotation (%)
35000
30000
25000
20000
15000
10000
5000
0
-5000
-8
-6
-4
-2
0
2
4
6
8

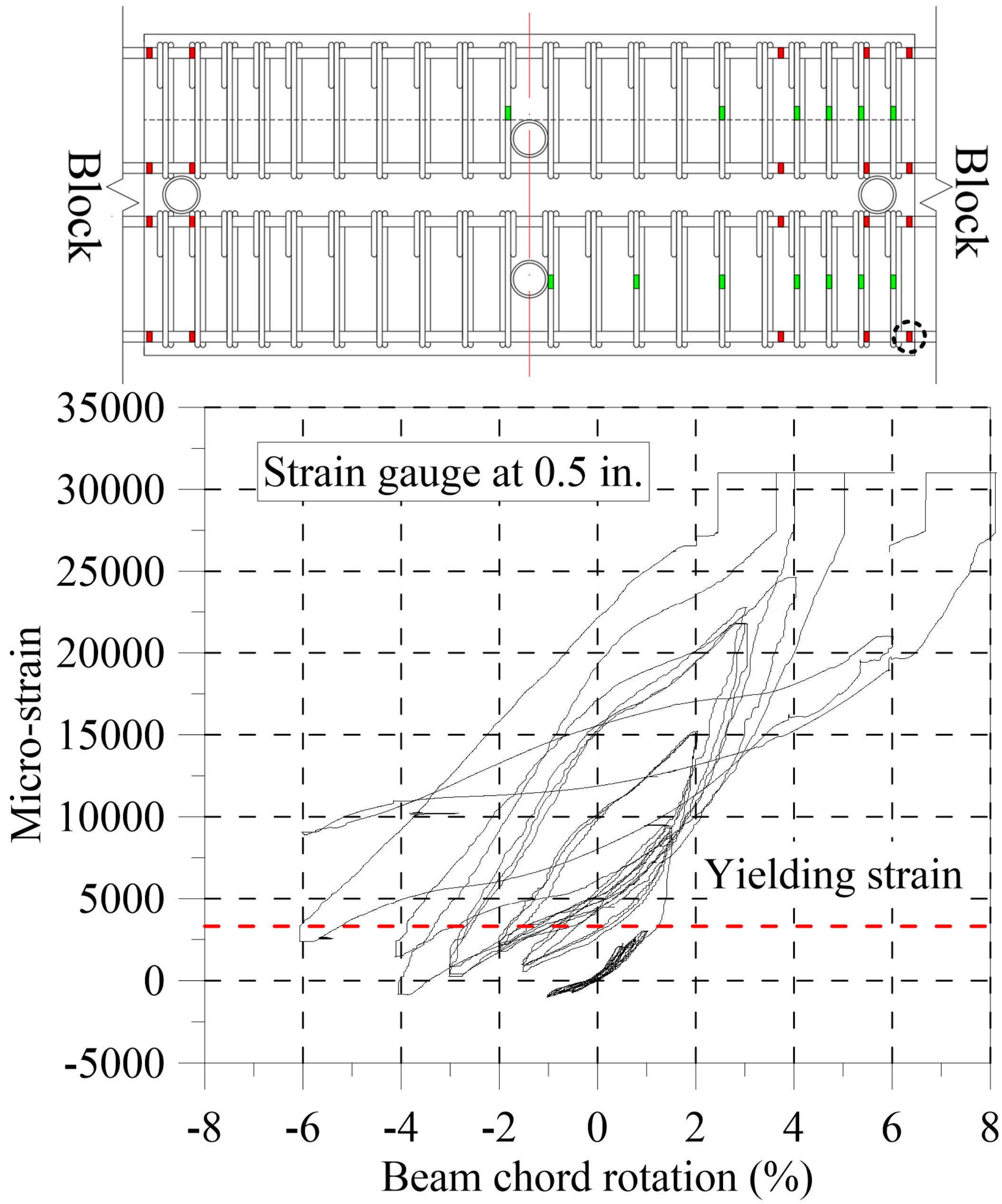
Block
Block
Strain gauge at 0.5 in.
Yielding strain
35000
30000
25000
20000
15000
10000
5000
0
-5000
Micro-strain
-8
-6
-4
-2
0
2
4
6
8
Beam chord rotation (%)

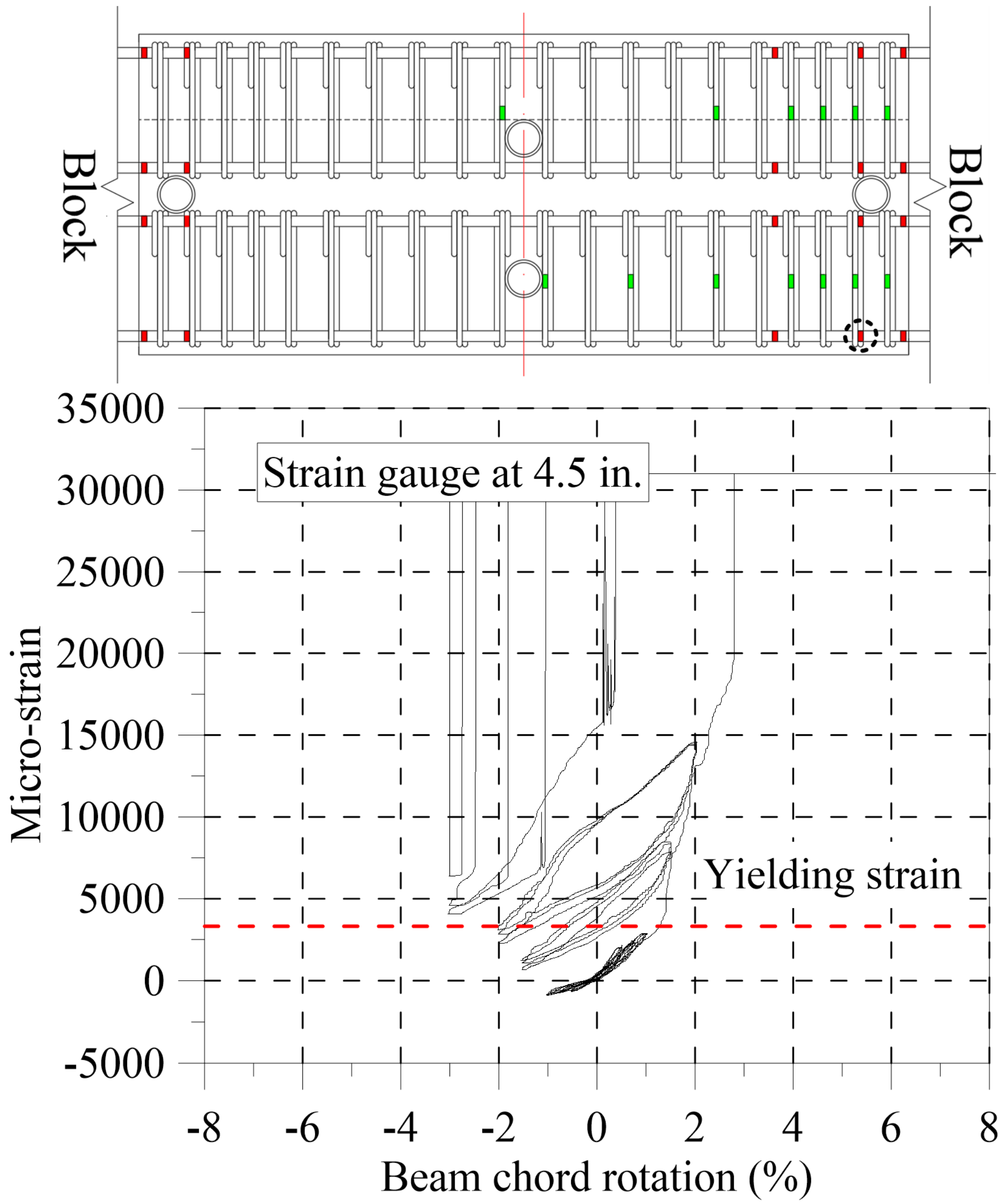
Block
Block
Strain gauge at 4.5 in.
Yielding strain
Micro-strain
Beam chord rotation (%)
35000
30000
25000
20000
15000
10000
5000
0
-5000
-8
-6
-4
-2
0
2
4
6
8

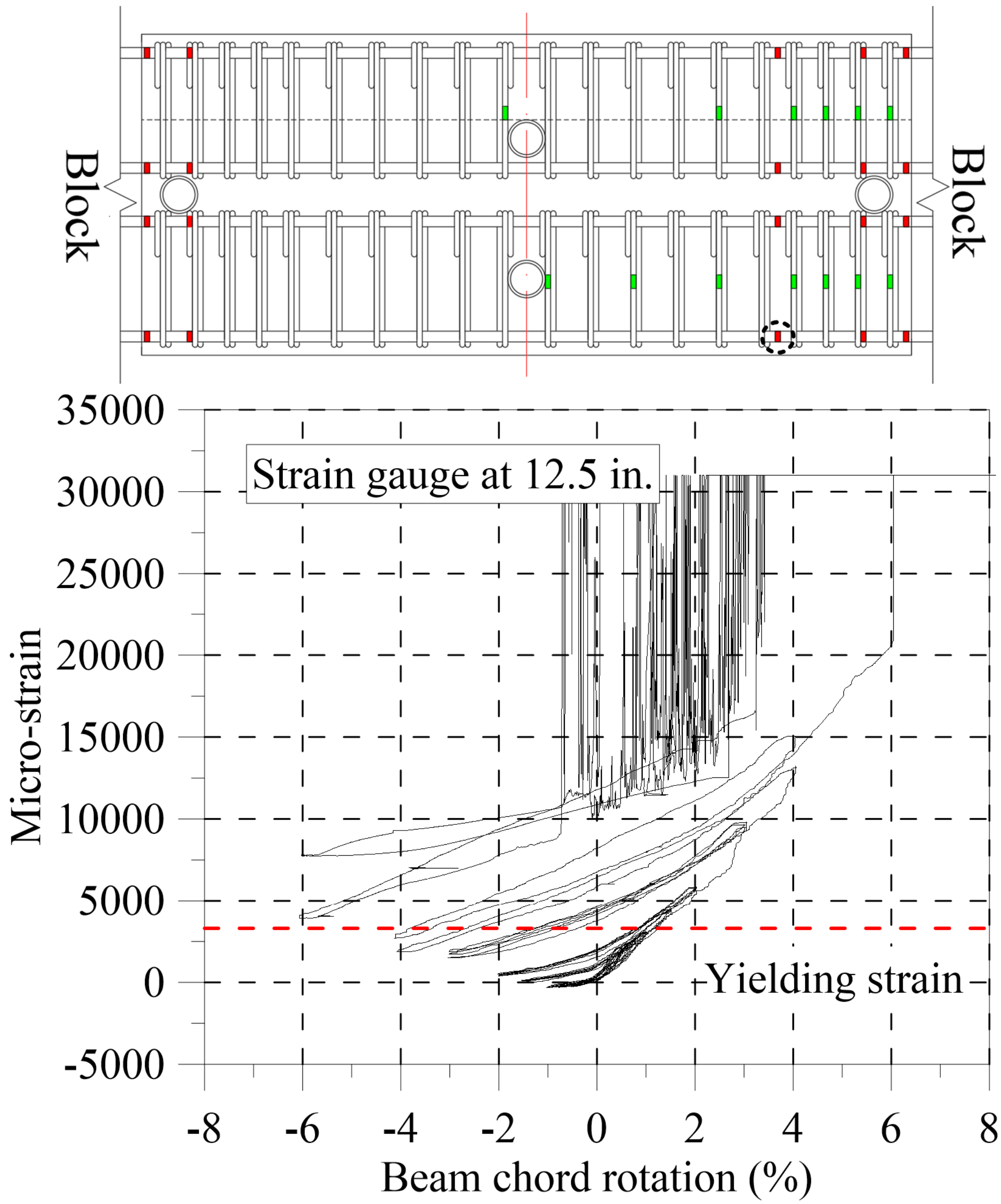

Block
Block
35000
30000
25000
20000
15000
10000
5000
0
-5000
Strain gauge at 12.5 in.
Yielding strain
Micro-strain
-8
-6
-4
-2
0
2
4
6
8
Beam chord rotation (%)

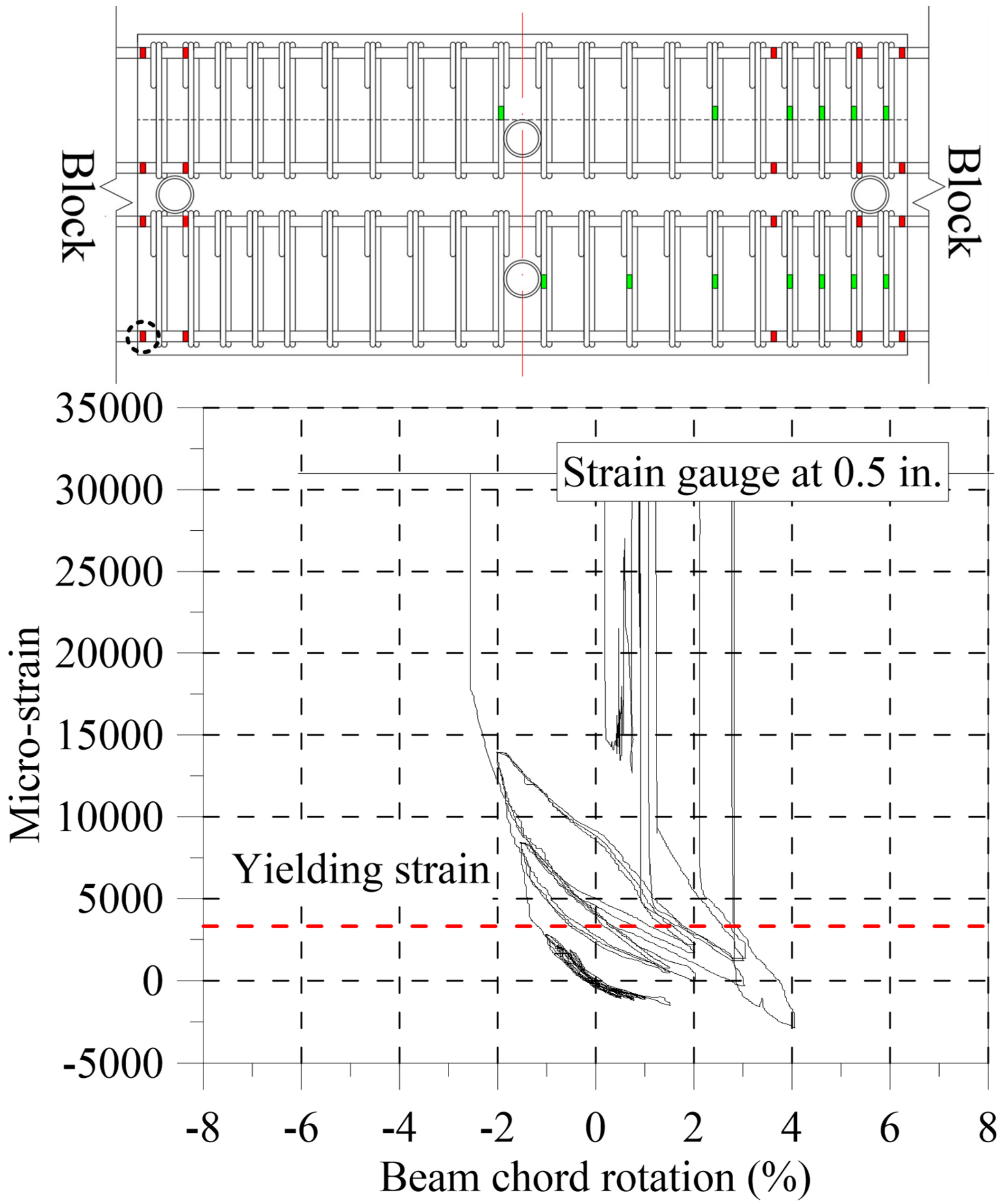
Block
Block
Strain gauge at 0.5 in.
Yielding strain
Micro-strain
35000
30000
25000
20000
15000
10000
5000
0
-5000
-8
-6
-4
-2
0
2
4
6
8
Beam chord rotation (%)

5

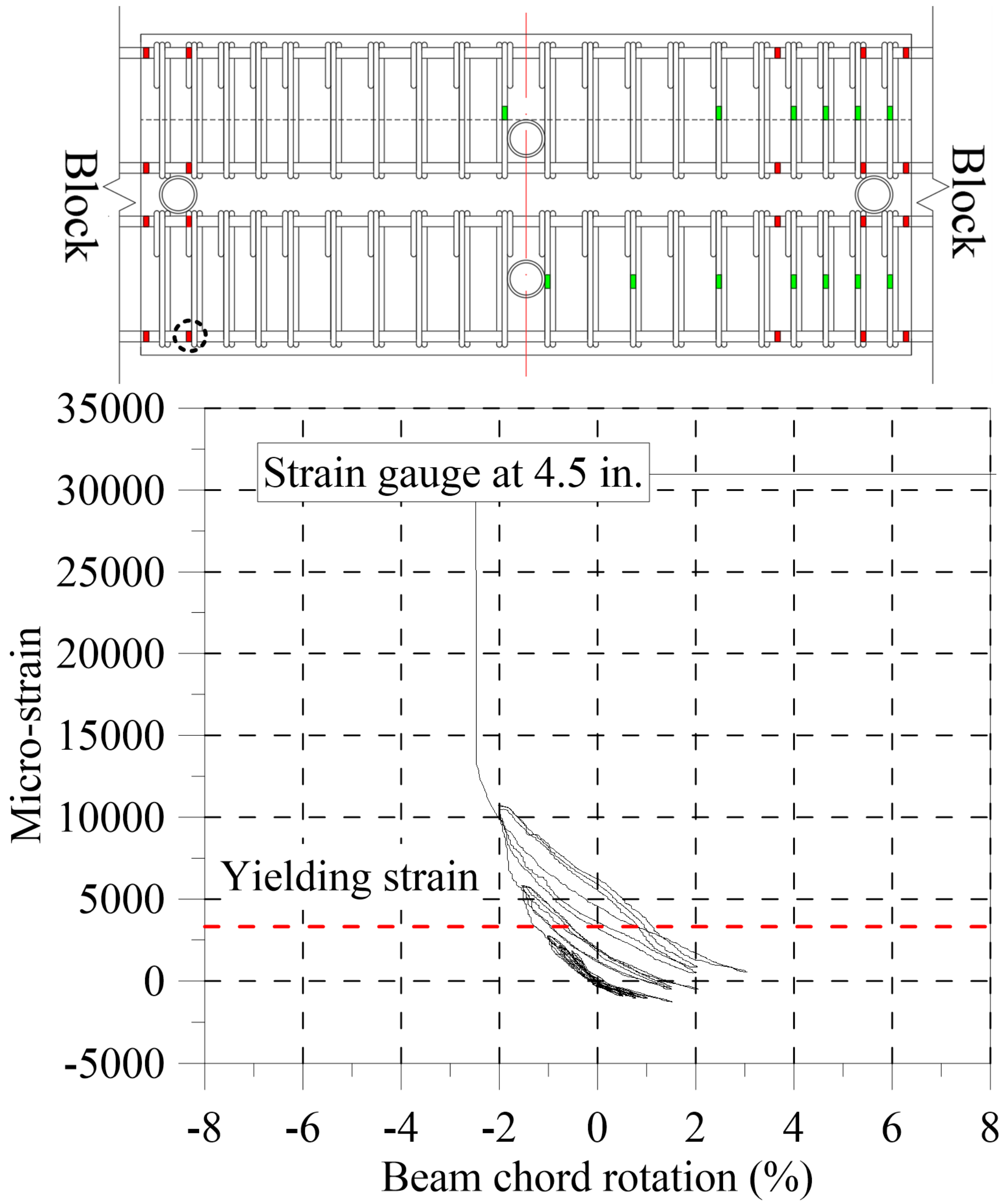
Block
Block
35000
30000
25000
20000
15000
10000
5000
0
-5000
Micro-strain
Strain gauge at 4.5 in.
Yielding strain
-8
-6
-4
-2
0
2
4
6
8
Beam chord rotation (%)

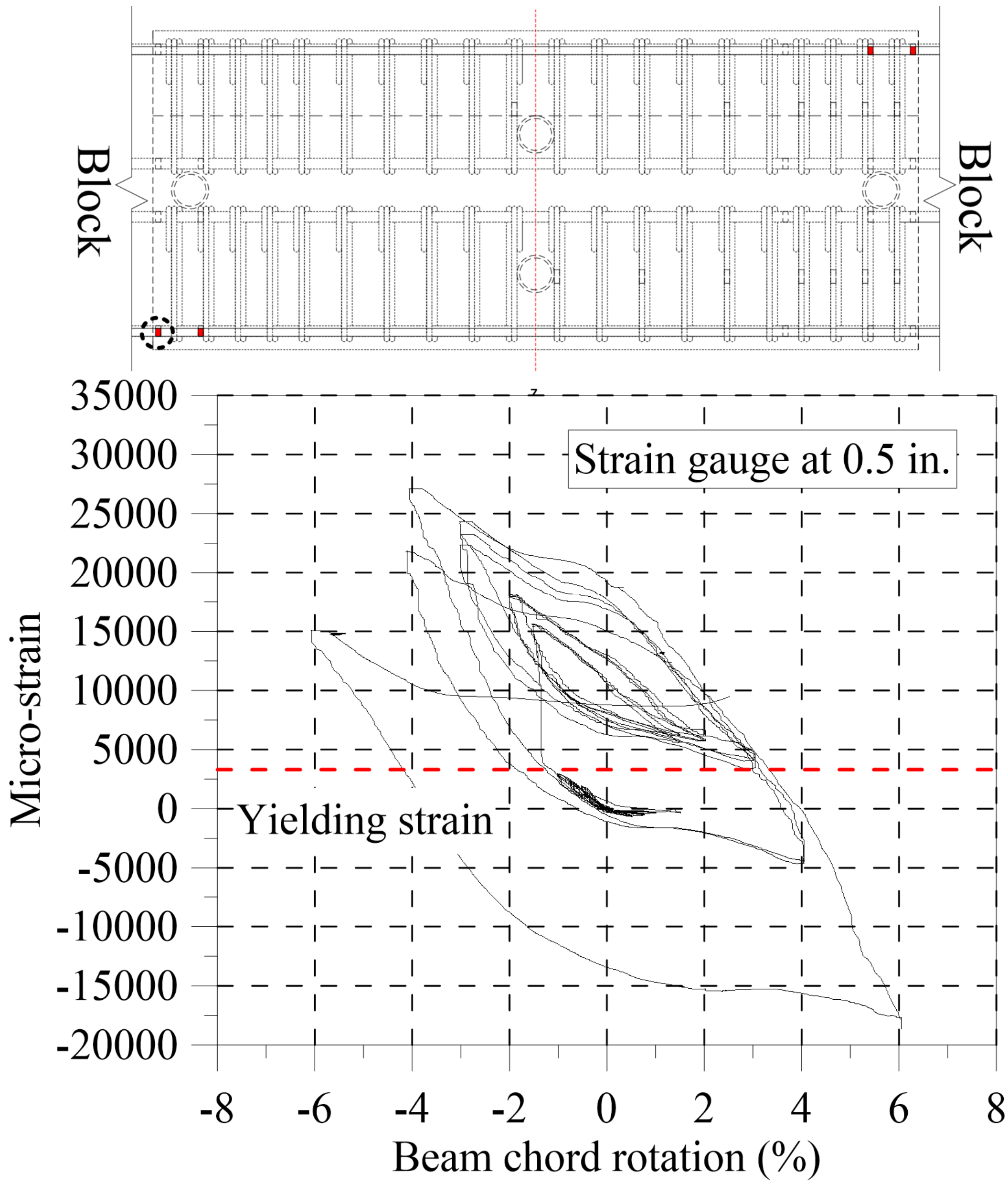

Block
Block
Strain gauge at 0.5 in.
Yielding strain
Micro-strain
Beam chord rotation (%)
35000
30000
25000
20000
15000
10000
5000
0
-5000
-10000
-15000
-20000
-8
-6
-4
-2
0
2
4
6
8

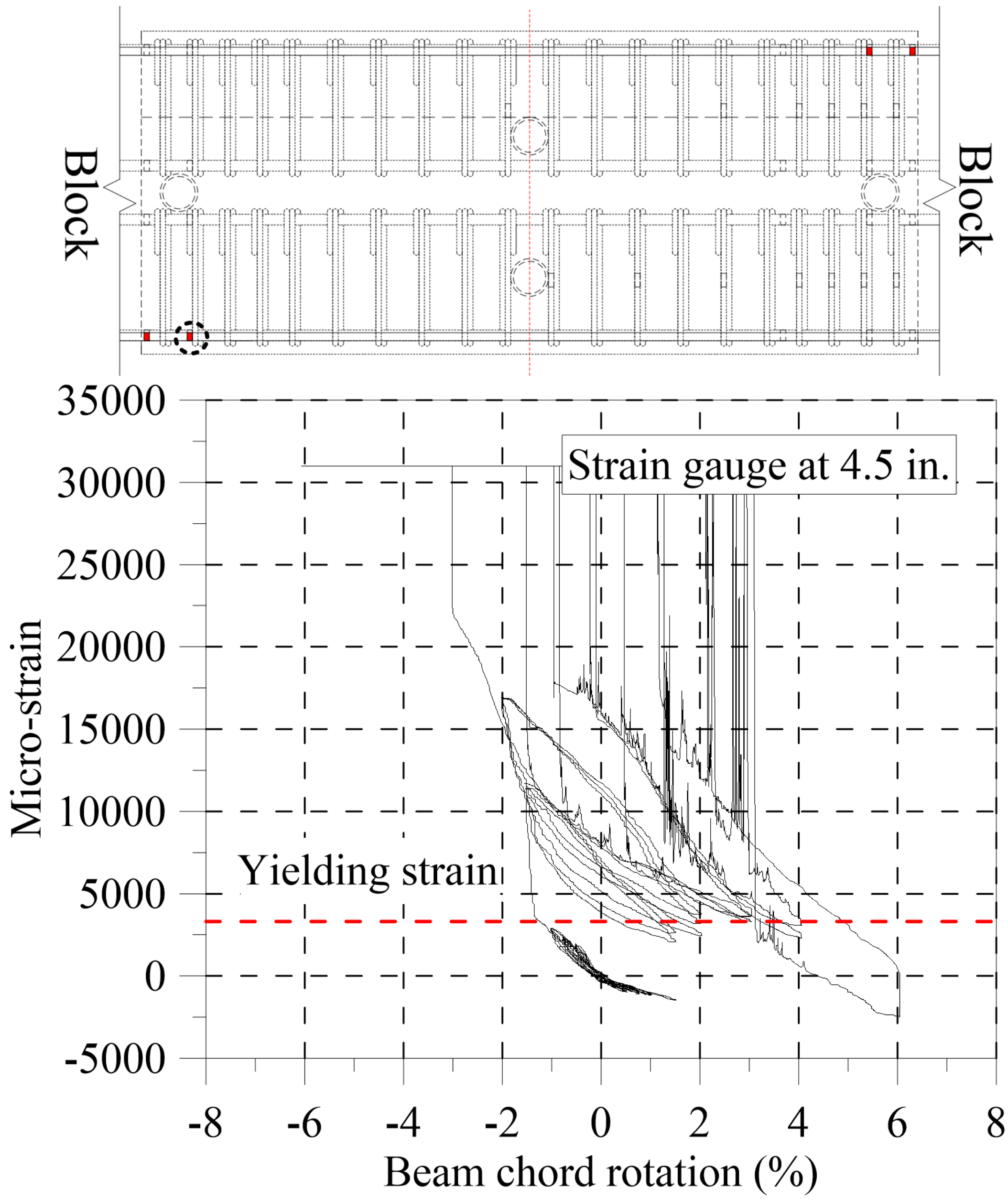
Block
Block
Strain gauge at 4.5 in.
Yielding strain
Micro-strain
Beam chord rotation (%)
35000
30000
25000
20000
15000
10000
5000
0
-5000
-8
-6
-4
-2
0
2
4
6
8

C.3.2.2 Transverse reinforcement

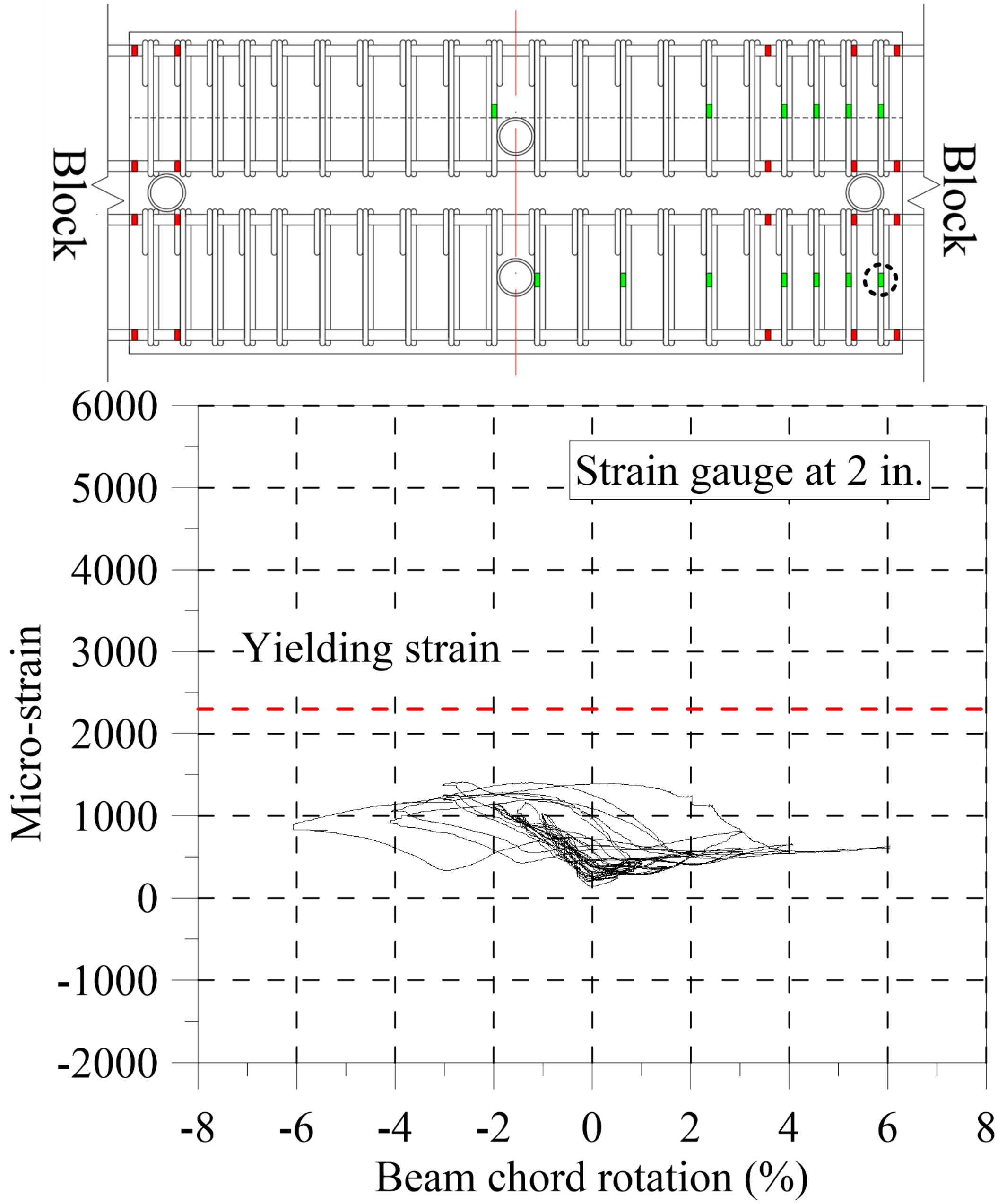

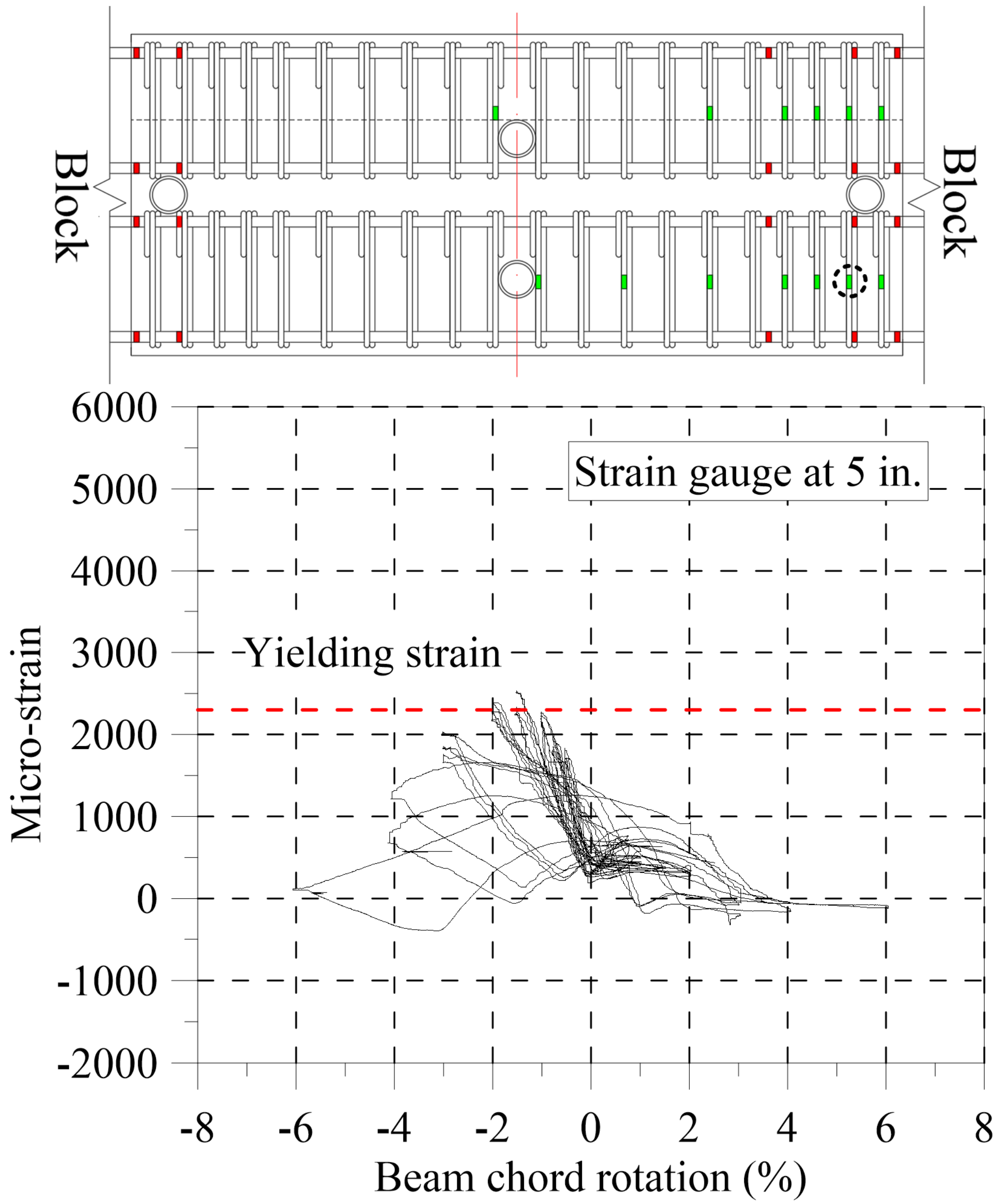

Block
Block
Strain gauge at 5 in.
Yielding strain
Micro-strain
Beam chord rotation (%)
6000
5000
4000
3000
2000
1000
0
-1000
-2000
-8
-6
-4
-2
0
2
4
6
8

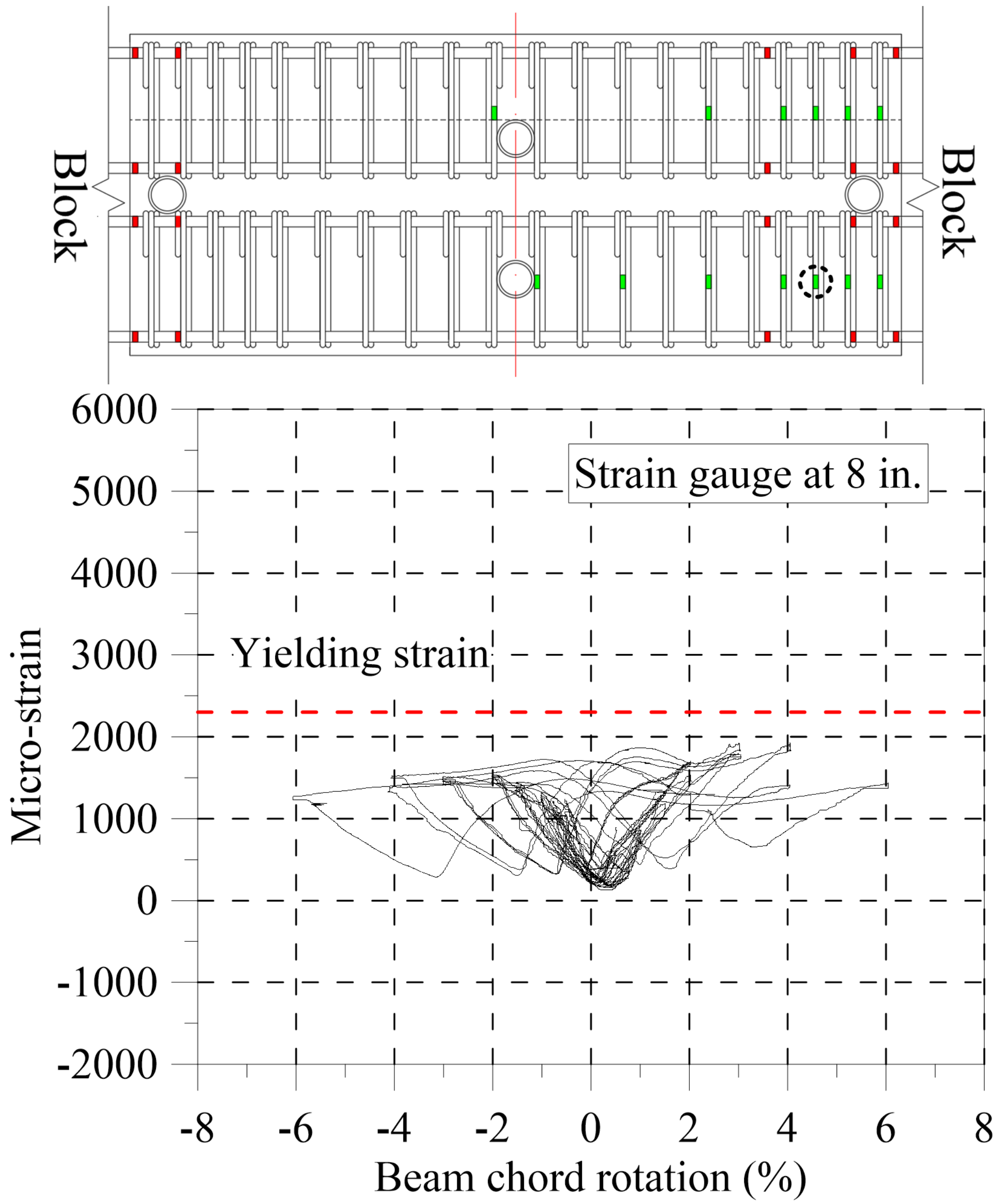
Block
Block
6000
5000
4000
3000
2000
1000
0
-1000
-2000
Strain gauge at 8 in.
Yielding strain
Micro-strain
-8
-6
-4
-2
0
2
4
6
8
Beam chord rotation (%)

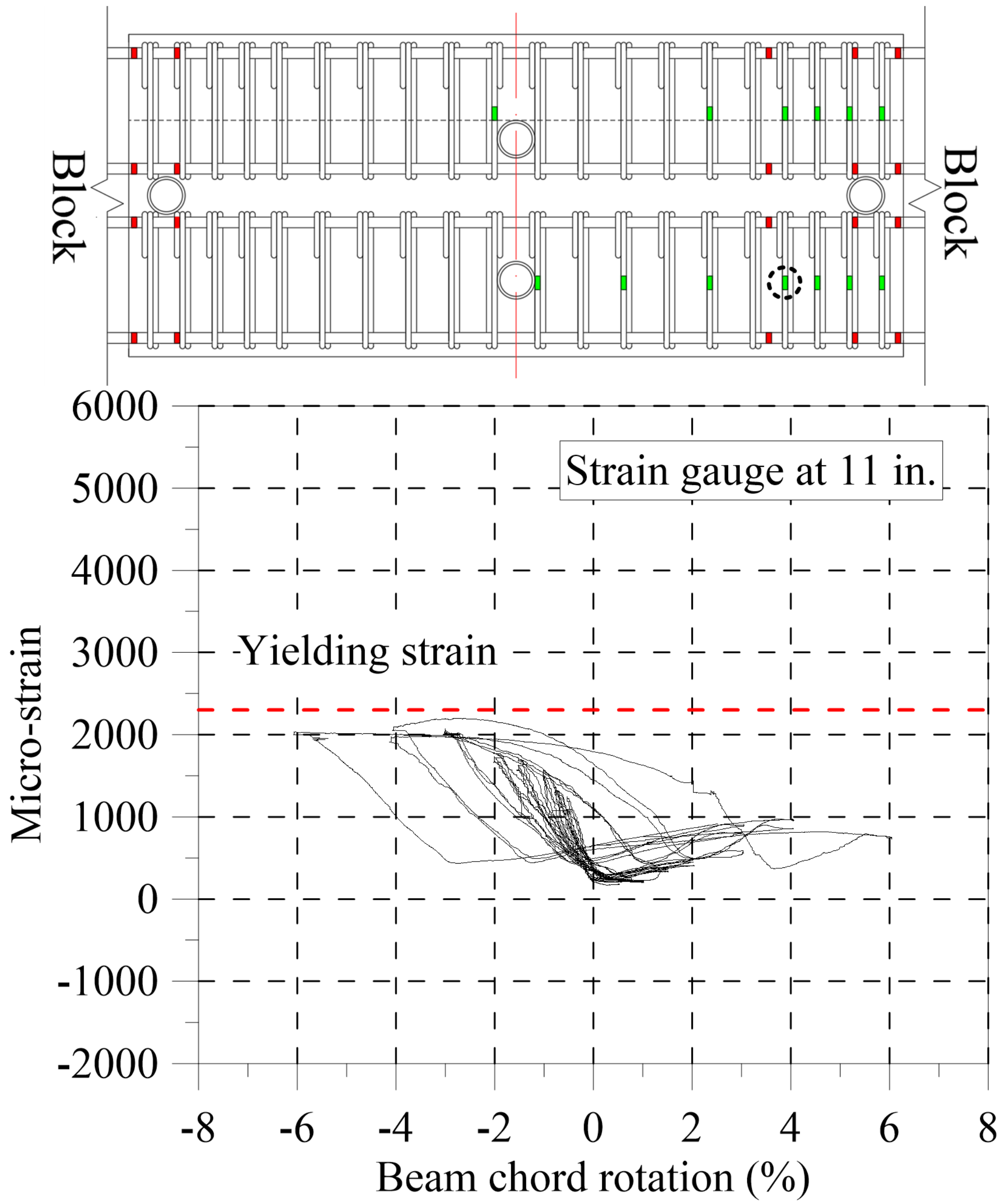

Block
Block
Strain gauge at 11 in.
Yielding strain
Micro-strain
Beam chord rotation (%)

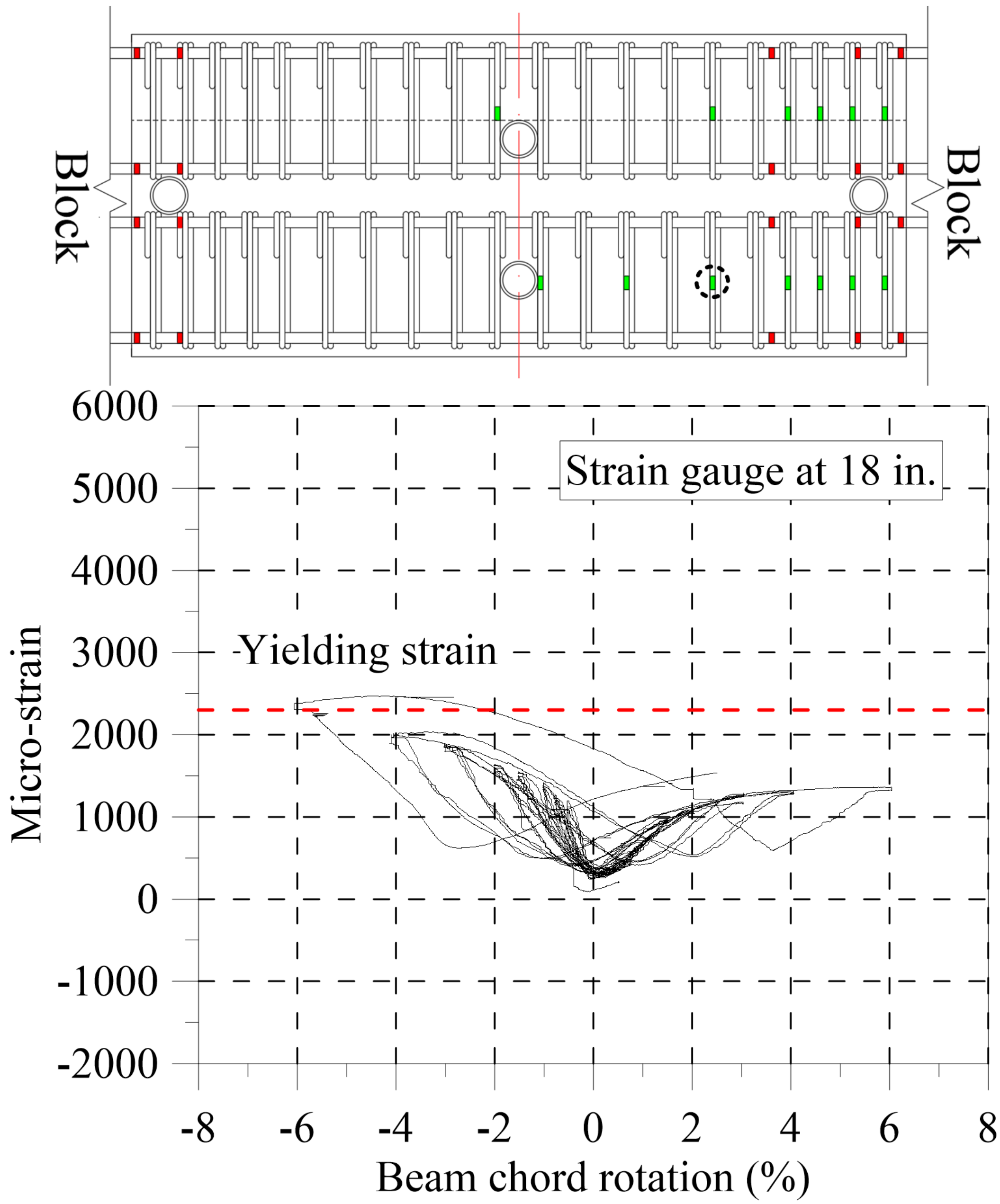

Block
Block
Strain gauge at 18 in.
Yielding strain
Micro-strain
Beam chord rotation (%)
6000
5000
4000
3000
2000
1000
0
-1000
-2000
-8
-6
-4
-2
0
2
4
6
8

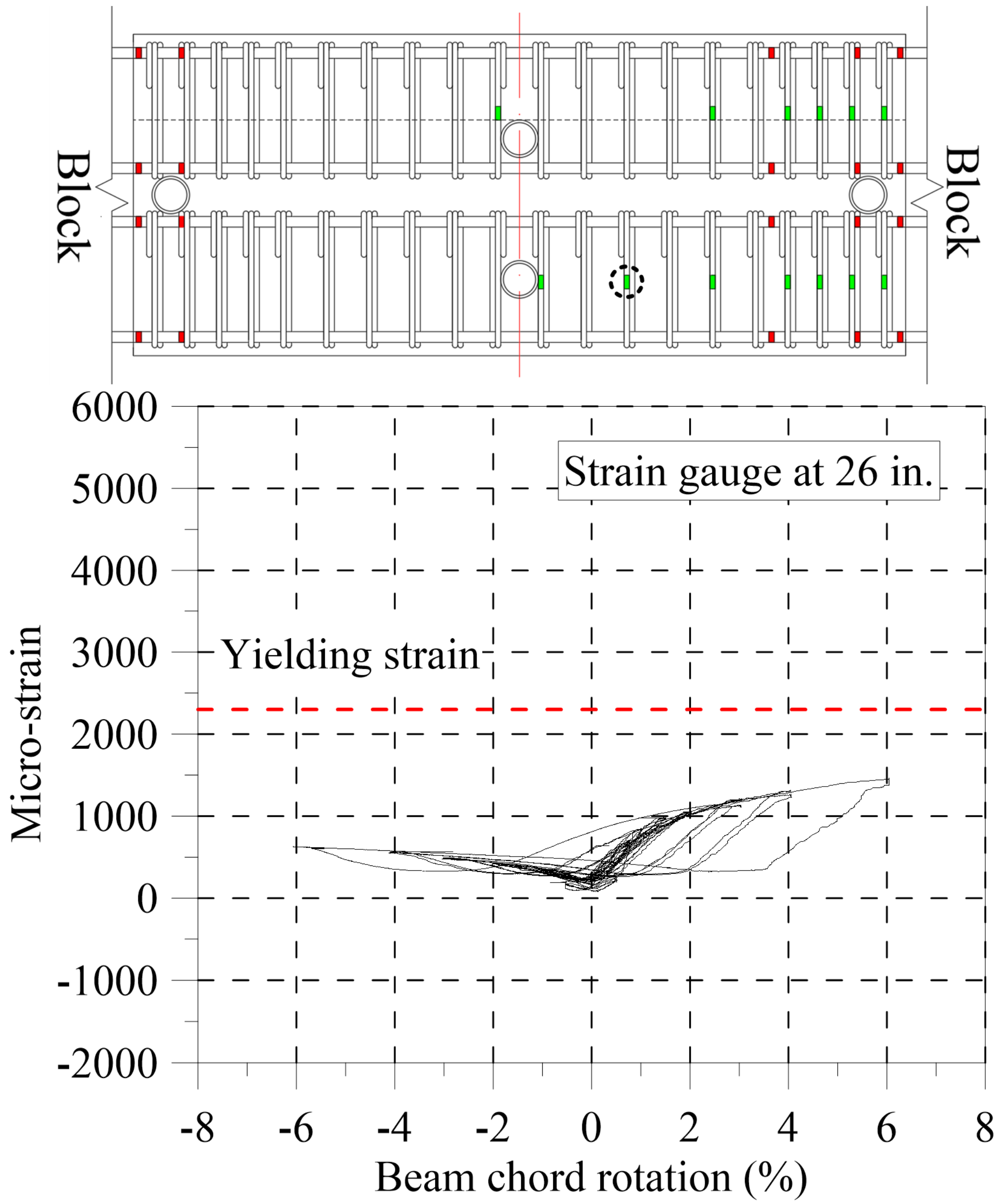
Block
Block
Strain gauge at 26 in.
Yielding strain
Micro-strain
Beam chord rotation (%)
6000
5000
4000
3000
2000
1000
0
-1000
-2000
-8
-6
-4
-2
0
2
4
6
8

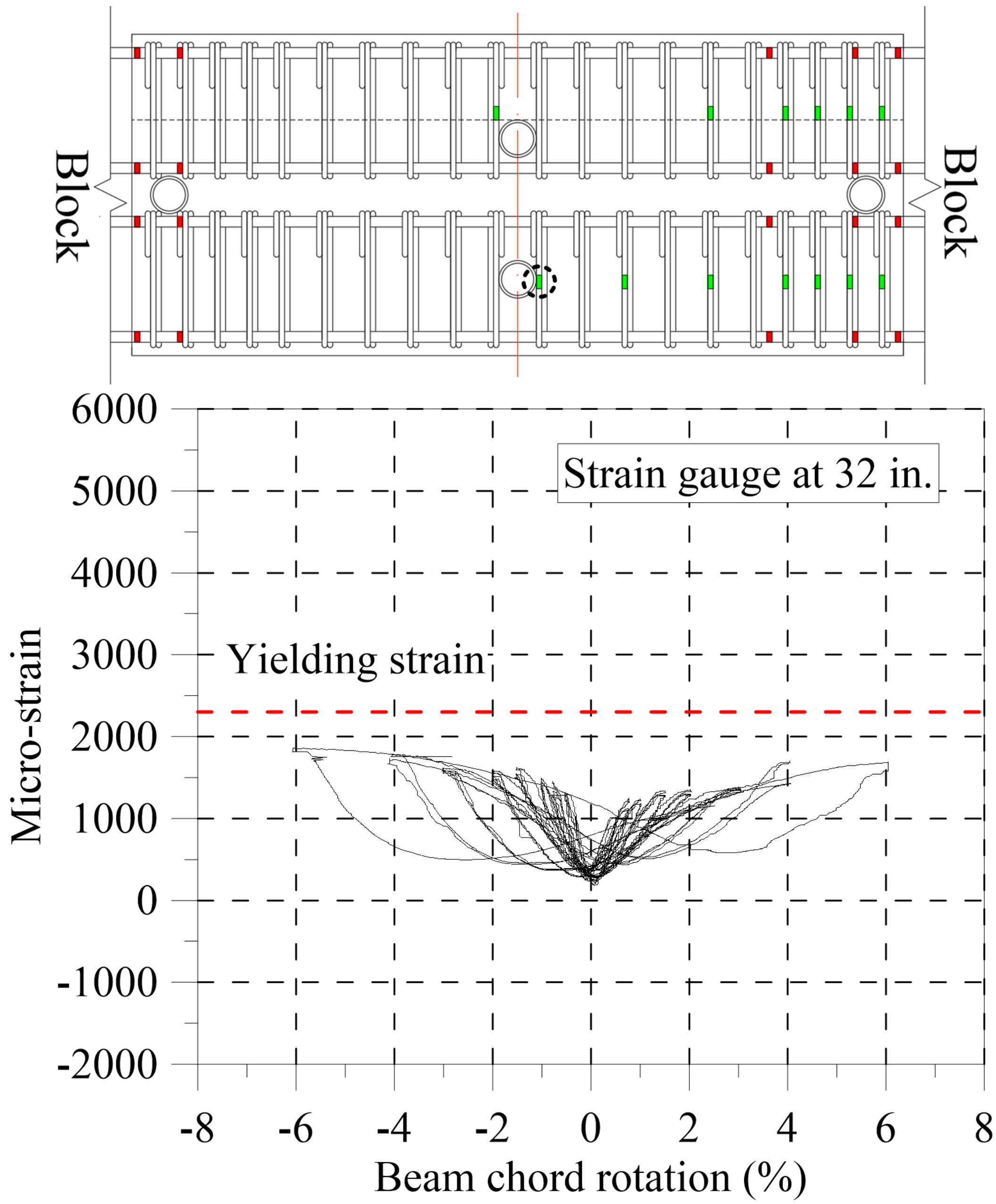

Block
Block
Strain gauge at 32 in.
Yielding strain
Micro-strain
Beam chord rotation (%)
6000
5000
4000
3000
2000
1000
0
-1000
-2000
-8
-6
-4
-2
0
2
4
6
8

C.3.3 Slab longitudinal reinforcement

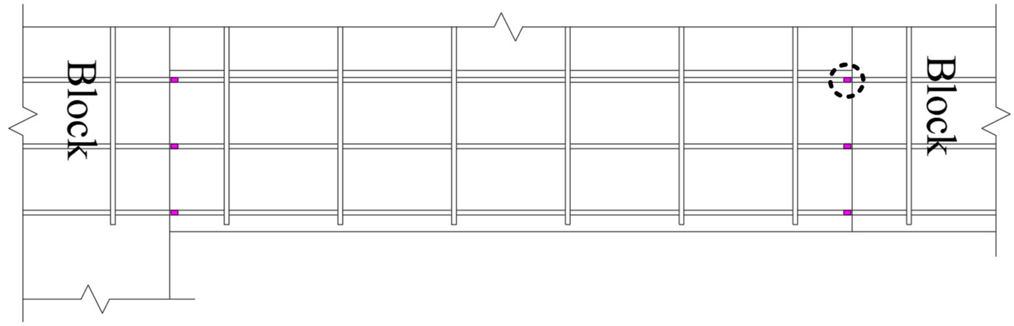

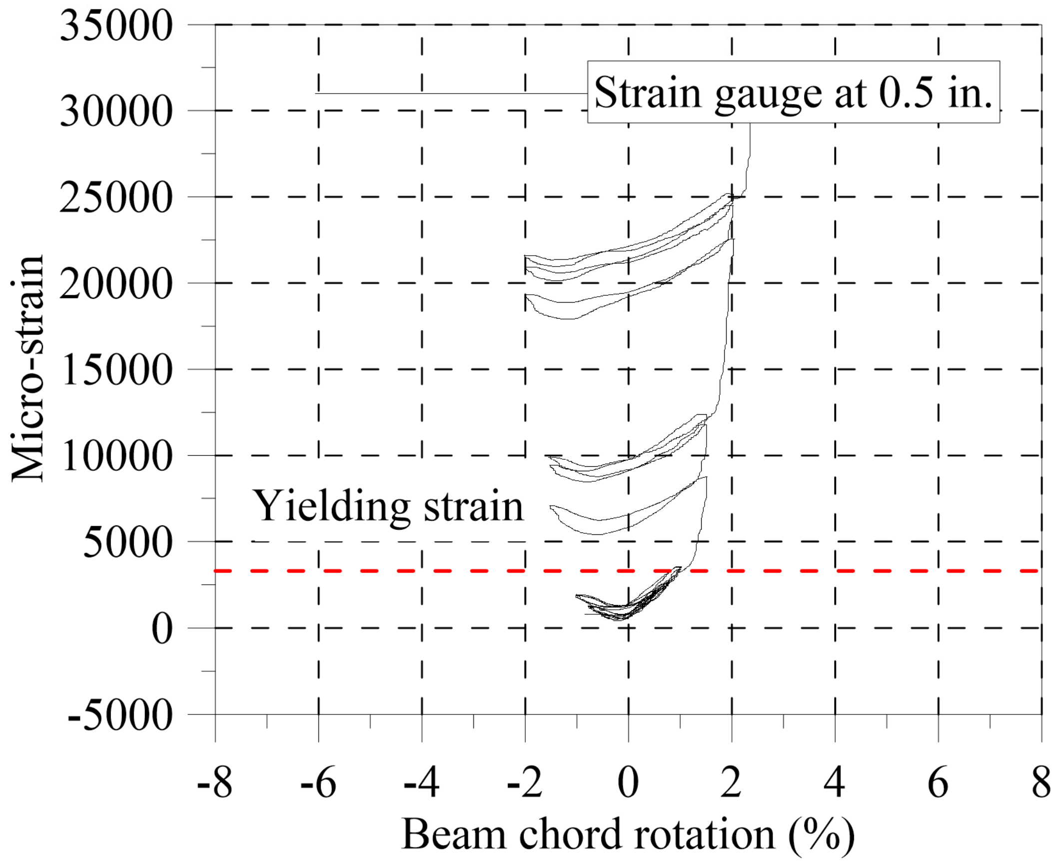

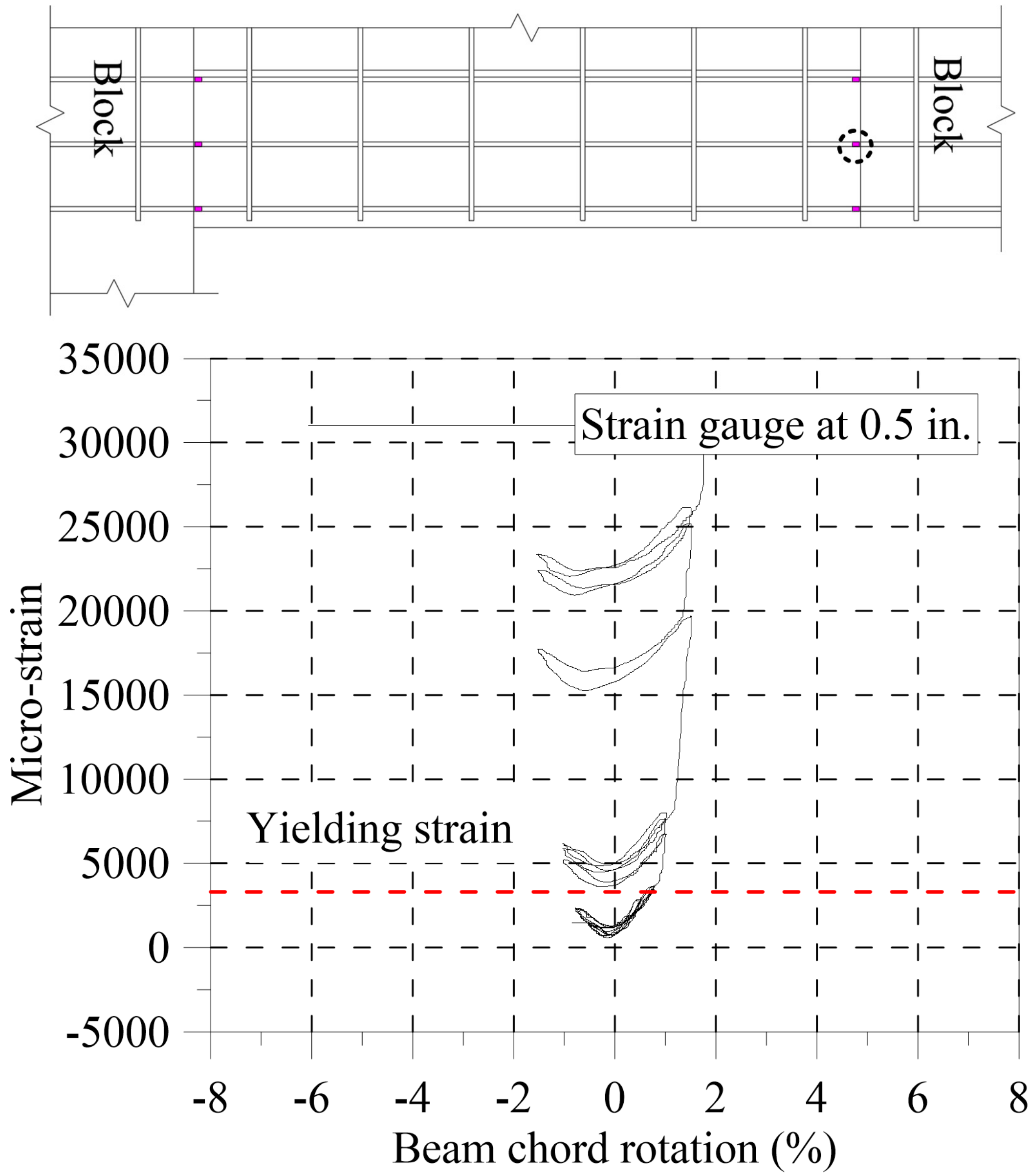
Block
Block
Strain gauge at 0.5 in.
Yielding strain
35000
30000
25000
20000
15000
10000
5000
0
-5000
Micro-strain
-8
-6
-4
-2
0
2
4
6
8
Beam chord rotation (%)

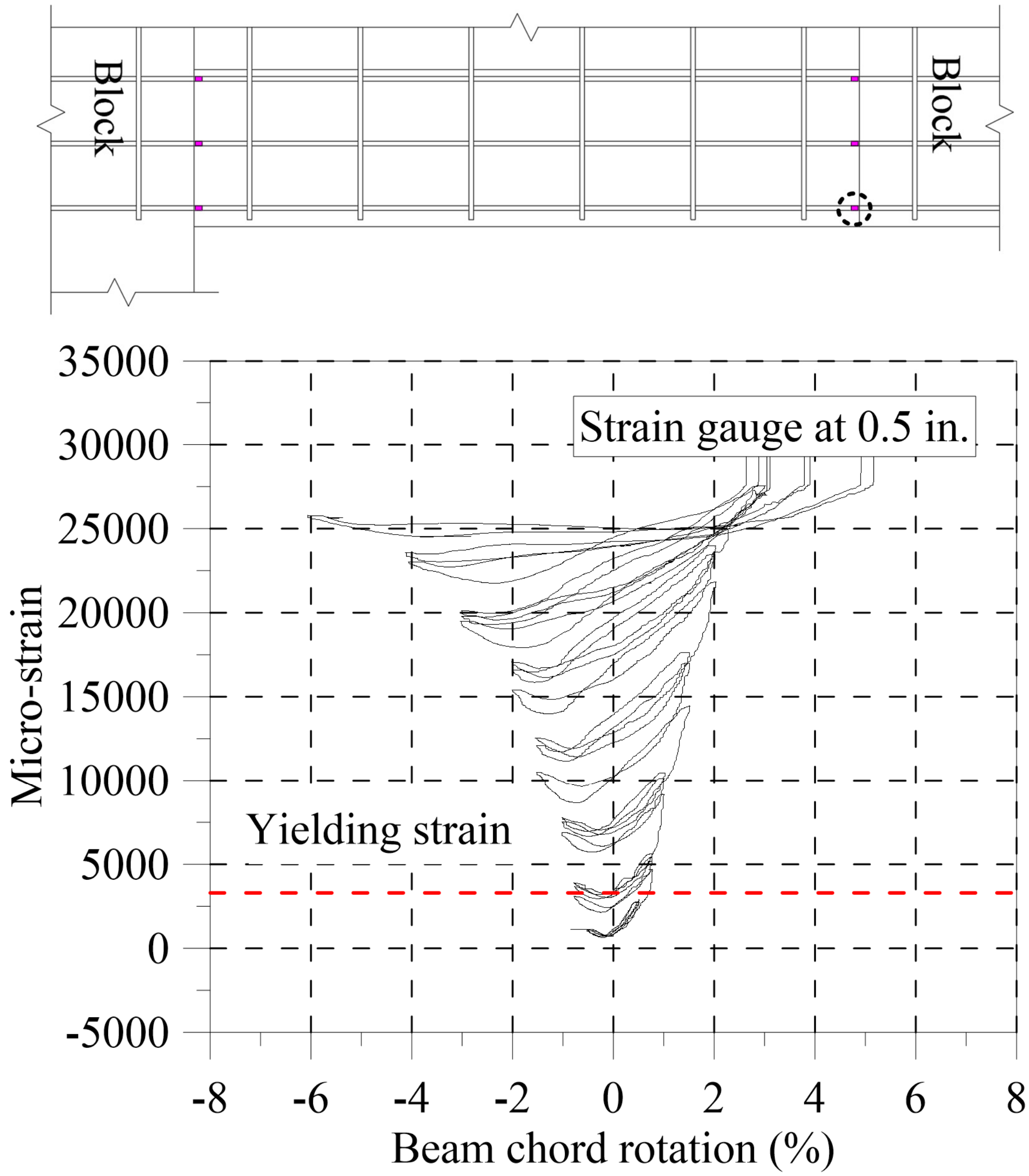
Block
Block
Strain gauge at 0.5 in.
Yielding strain
Micro-strain
35000
30000
25000
20000
15000
10000
5000
0
-5000
-8
-6
-4
-2
0
2
4
6
8
Beam chord rotation (%)

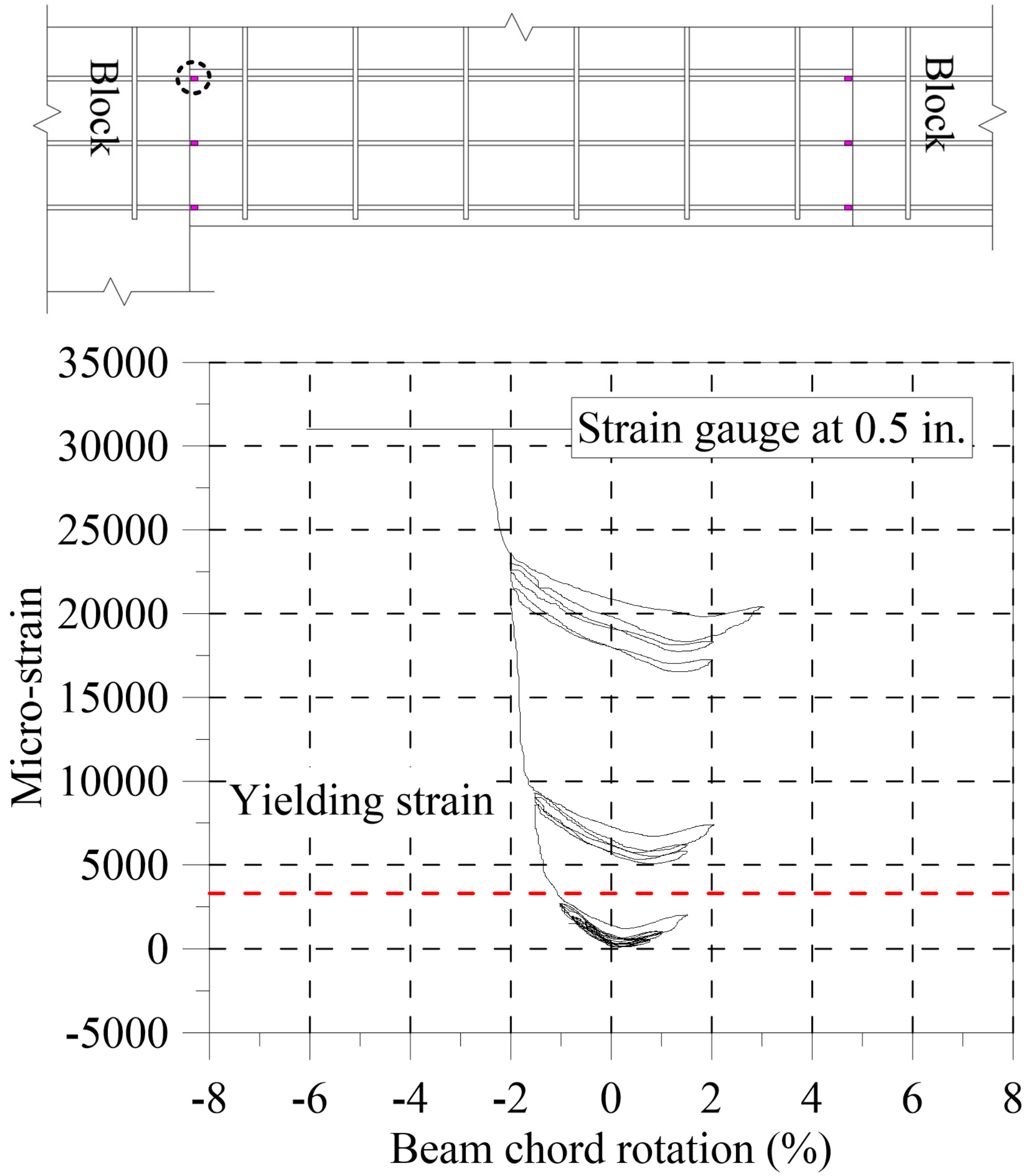
Block
Block
35000
30000
25000
20000
15000
10000
5000
0
-5000
Micro-strain
Strain gauge at 0.5 in.
Yielding strain
-8
-6
-4
-2
0
2
4
6
8
Beam chord rotation (%)

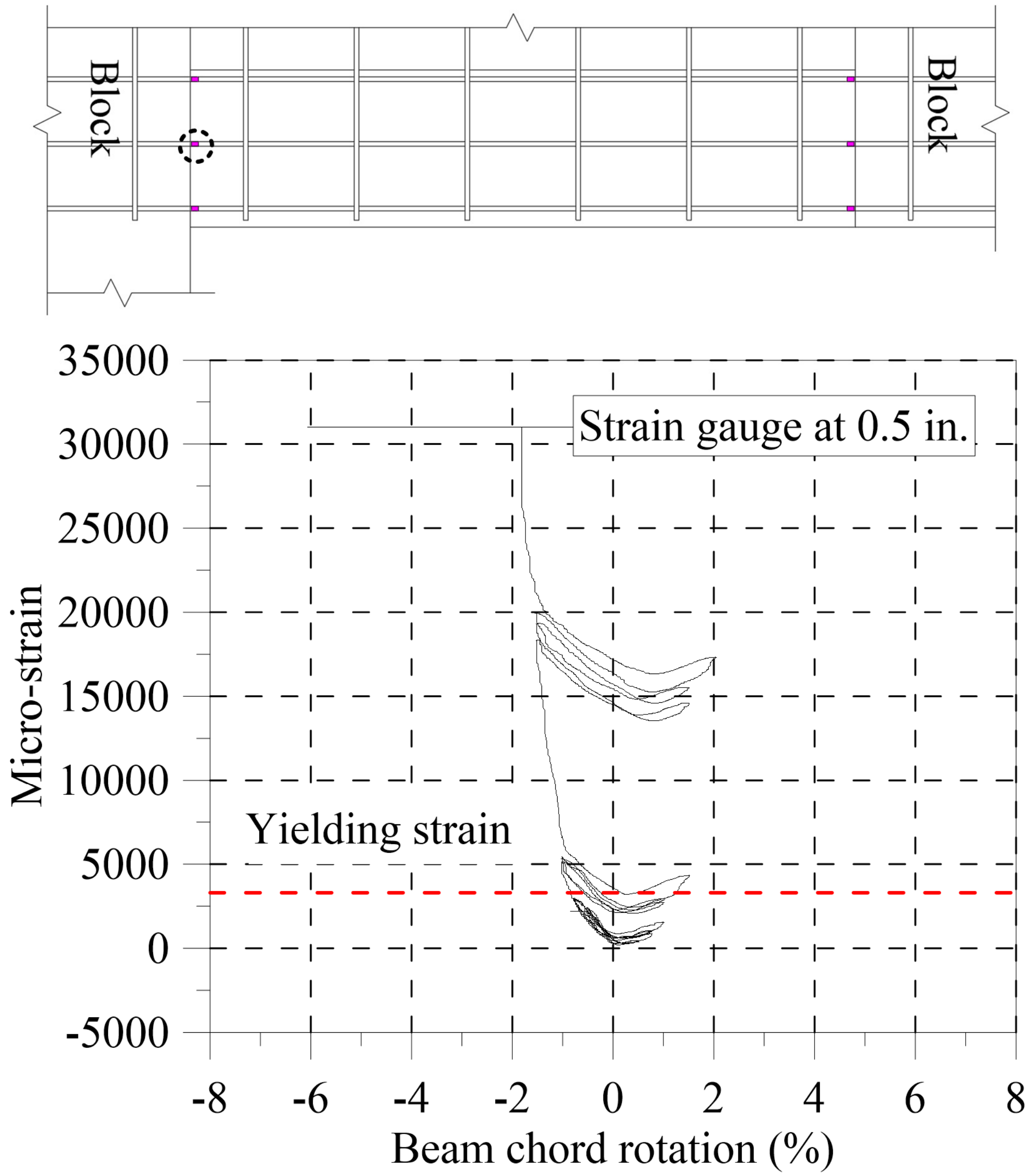
Block
Block
Strain gauge at 0.5 in.
Yielding strain
35000
30000
25000
20000
15000
10000
5000
0
-5000
Micro-strain
-8
-6
-4
-2
0
2
4
6
8
Beam chord rotation (%)

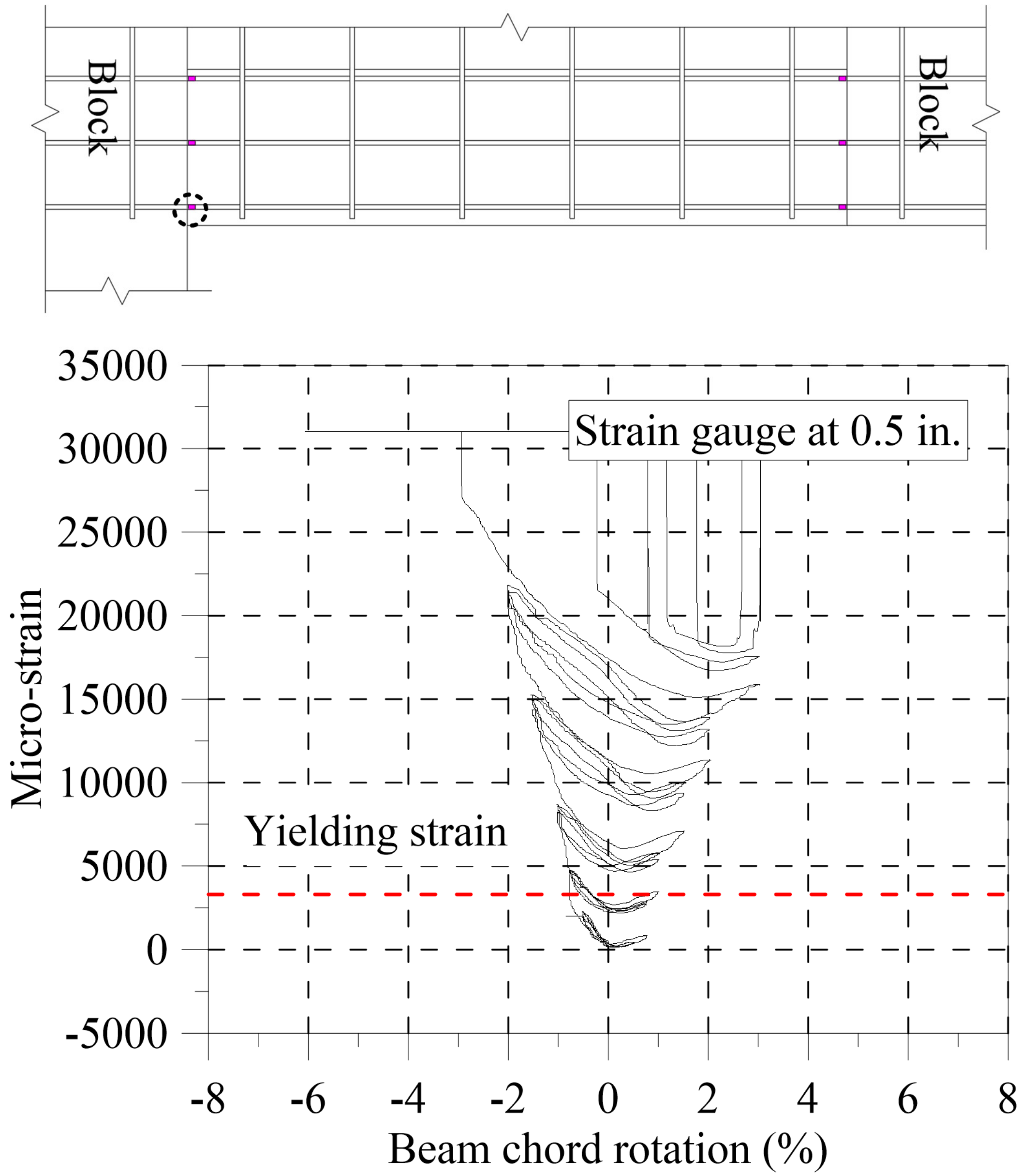
Block
Block
Strain gauge at 0.5 in.
Yielding strain
Micro-strain
Beam chord rotation (%)
35000
30000
25000
20000
15000
10000
5000
0
-5000
-8
-6
-4
-2
0
2
4
6
8

C.3.4 Steel links

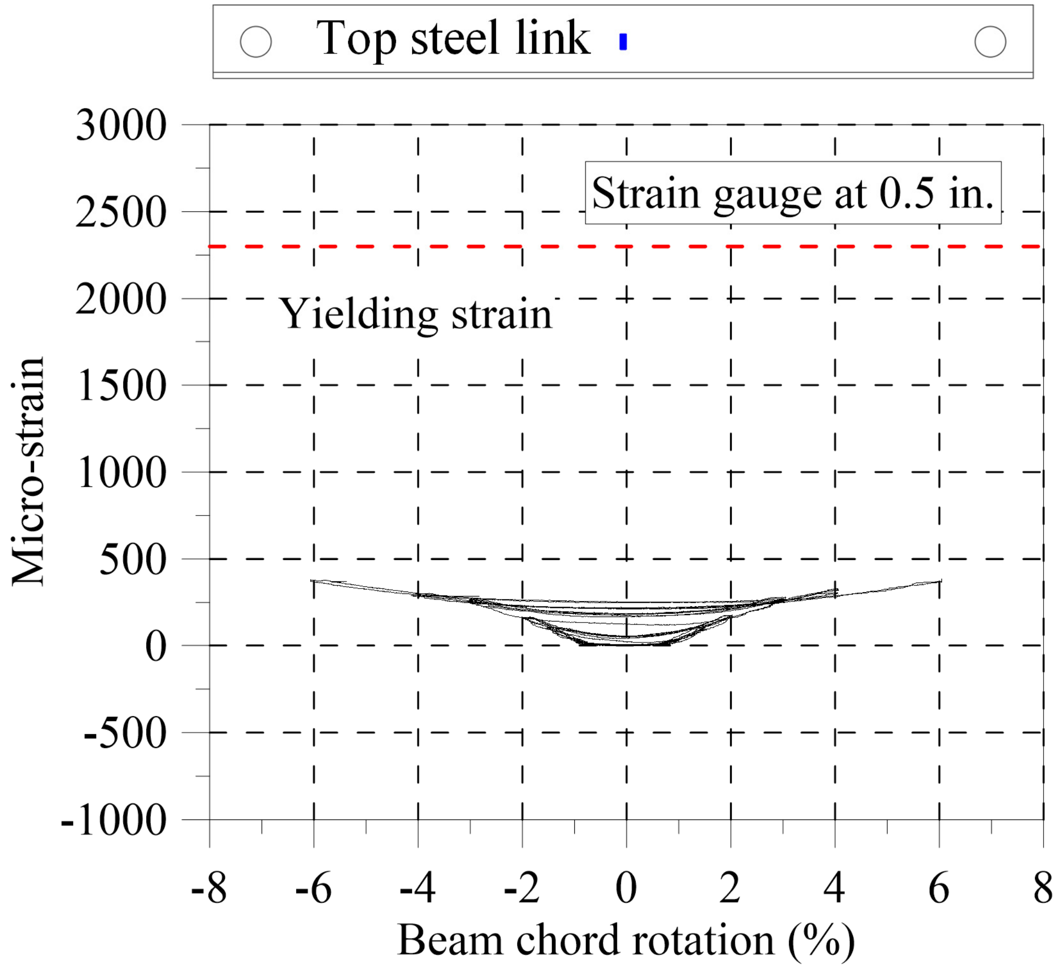

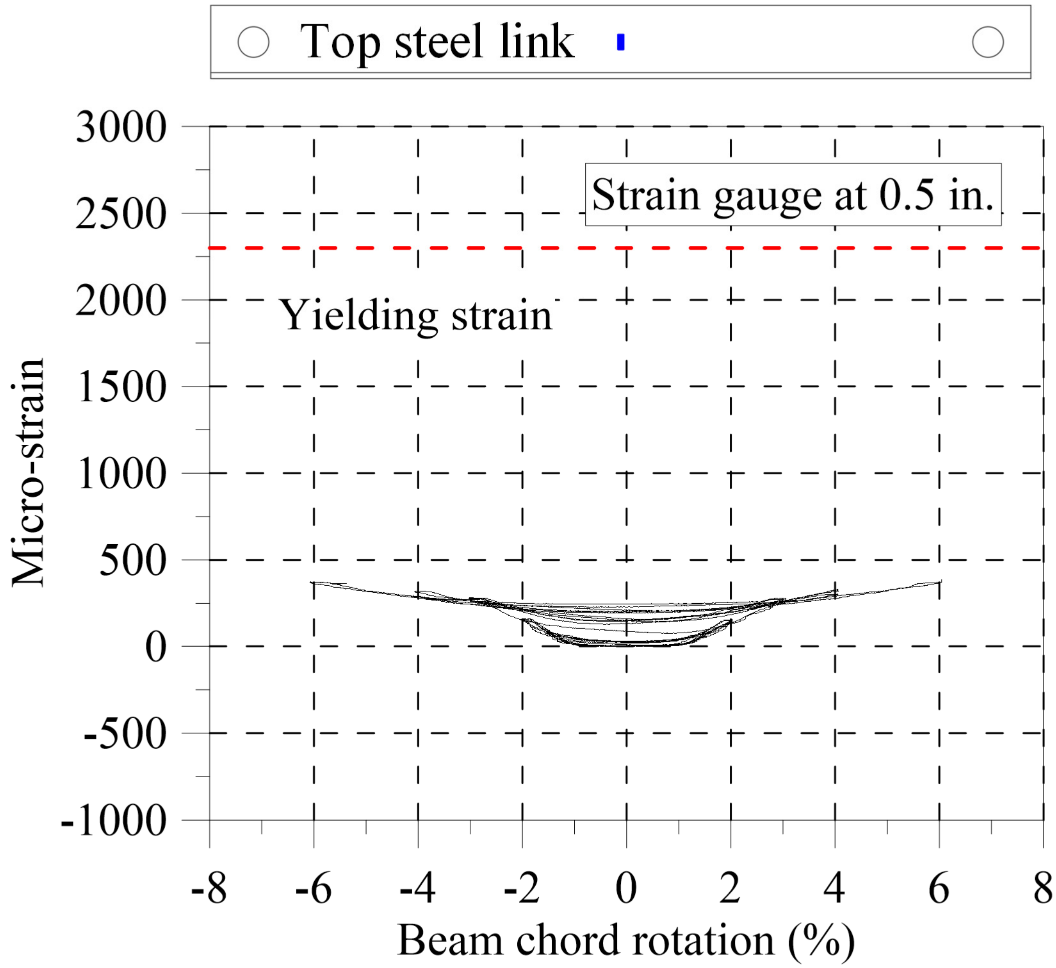

Top steel link
Strain gauge at 0.5 in.
Yielding strain
Micro-strain
3000
2500
2000
1500
1000
500
0
-500
-1000
-8
-6
-4
-2
0
2
4
6
8
Beam chord rotation (%)

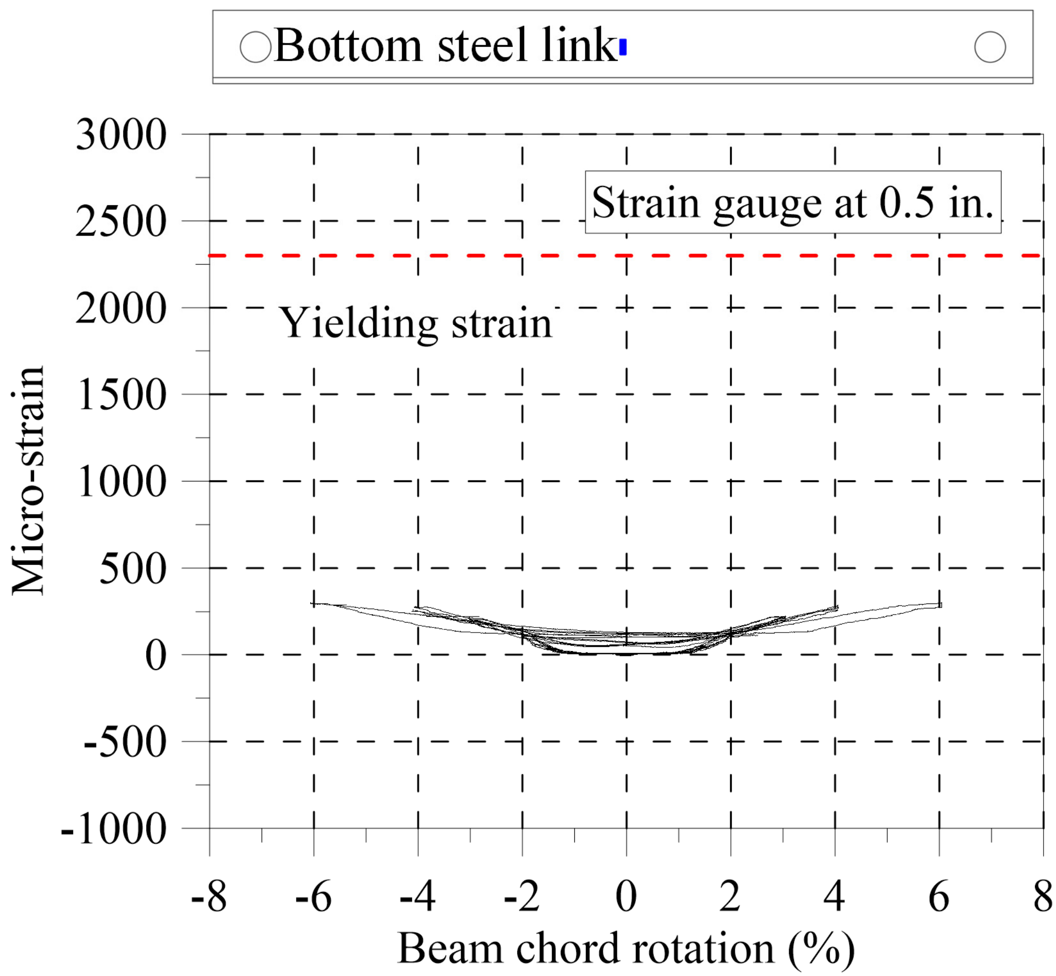
Bottom steel link
Strain gauge at 0.5 in.
Yielding strain
Micro-strain
3000
2500
2000
1500
1000
500
0
-500
-1000
-8
-6
-4
-2
0
2
4
6
8
Beam chord rotation (%)

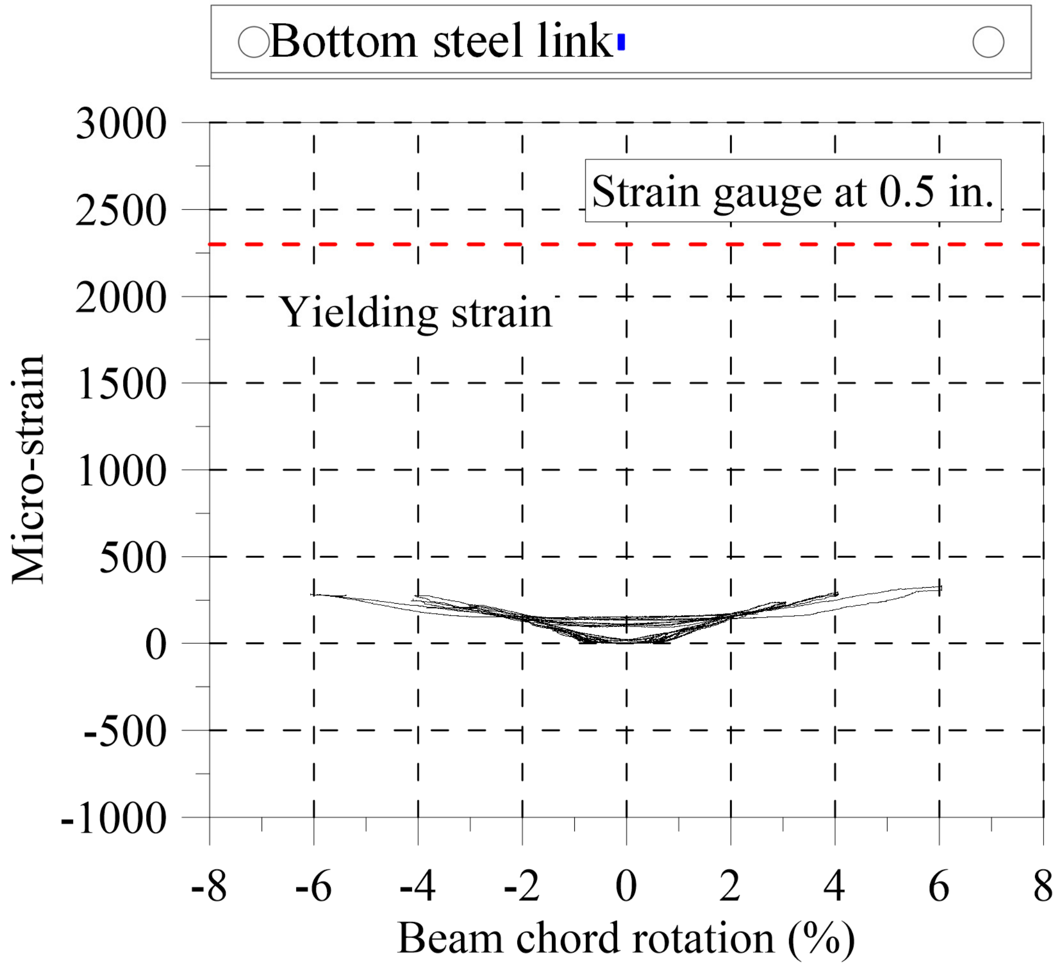

Bottom steel link
Strain gauge at 0.5 in.
Yielding strain
Micro-strain
3000
2500
2000
1500
1000
500
0
-500
-1000
-8
-6
-4
-2
0
2
4
6
8
Beam chord rotation (%)

APPENDIX D: EXAMPLE DESIGN

Uisng the revised flowchart for DBCB design, an example of a double-beam coupling beam was designed and compared to an example of a diagonally reinforced concrete coupling beam (CRSI, 2020) with an equivalent nominal shear capacity.

Dimensions of DBCB

The dimensions of a 2.3 aspect ratio DBCB are depicted in Fig. D.1. This DBCB has a height (h) of 42 in., a width (b_w) of 24 in., and a length (l_n) of 96 in., resulting in an aspect ratio (l_n/h) of 2.3.

Fig. D.1 Dimension of full-scale DBCB with 2.3 aspect ratio

Required shear strength (V_u)

A total required shear strength of V_u = 342.3 kips (CRSI, 2020) was used to design the 2.3 aspect ratio full-scale DBCB. The design interface shear strength of UCS was assumed as 0.3 ksi.

Nominal moment (M_n) for each beam

The required nominal moments (M_n) for each individual beam in DBCB is calculated by using the equation defined in the design flowchart shown in Fig. 6.1, with v_{UCS} assumed to be 0.3 ksi. The strength reduction factor, ϕ is 0.85.

$$M_n = \frac{l_n}{4}\left(\frac{V_u}{\phi} - \frac{v_{UCS} b_w h}{2}\right) = \frac{96}{4}\left(\frac{342.3}{0.85} - \frac{0.3 \times 24 \times 42}{2}\right) = 6{,}036 \text{ kip-in.}$$

Thickness of UCS, *w*

As illustrated in Fig. D.2, the thickness of the UCS, w, located between the top and bottom beams is 4 in. To accommodate utilities, PVC pipes with a nominal diameter of 3 in. can be inserted within the UCS and between the hoops. In order to minimize any adverse impact on the ductility of the DBCB, the PVC pipe is placed at the beam-to-wall interface, specifically at the very end of the UCS. Additionally, two PVC pipes with a nominal diameter of 4 in. are positioned at the mid-span and mid-height of both the top and bottom beams, as illustrated in Fig. D.4.

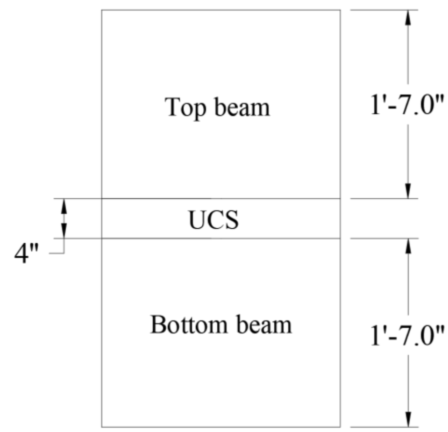

Fig. D.2 Thickness of UCS

Flexure strength design

Each individual beam of the DBCB was designed to ensure that its moment capacity is greater than or equal to the required nominal moment (M_n), which was calculated using a concrete crushing strain (ε_{cu}) of 0.004. The design process was conducted using spColumn software (spColumn, 2019). Fig. D.3 shows the location and sizes of longitudinal reinforcement for the 2.3 aspect ratio full-scale DBCB. Gr. 80 rebar ($f_y = 80$ ksi) was used for all longitudinal reinforcement.

Nominal design shear strength (V_n)

The nominal design shear strength of the specimen, V_n, is estimated based on the actual nominal moment strength, $(M_n)_{actual}$, = 6,107 kip-in., which is obtained from spColumn software, based on the actual longitudinal reinforcement used. Additionally, the interface shear strength of the UCS is taken into account.

For the entire DBCB (two beams):

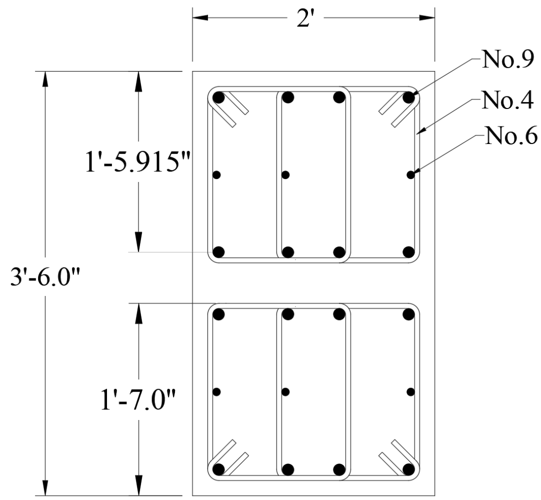

Fig. D.3 Longitudinal reinforcement details of the coupling beam specimen

$$V_{n\_total} = 2\left(\frac{v_{UCS} b_w h}{4} + \frac{2(M_n)_{actual}}{l_n}\right) = 2\left(\frac{0.3 \times 24 \times 42}{4} + \frac{2 \times 6{,}107}{96}\right) = 406 \text{ kips} = 5.2\sqrt{f_c'} A_{cw}$$

$$\phi V_{n\_total} = 0.85 \times 406 = 345.1 > V_u = 342.3 \text{ kips (O.K.)}$$

The maximum allowable shear strength by ACI 18.10.4.4 is $10\sqrt{f_c'} A_{cw}$ = 780.8 kips, where $f_c' = 6$ ksi, A_{cw} (= $b_w \times h$) is the area of DBCB. Note that when computing the nominal shear strength of the DBCB, the cross-sectional area considered is the gross area of the beam section, which is consistent with that of the DCBs.

Development length, l_d

The development length of longitudinal rebars is taken as 60% of length required by ACI 18.8.5.3 (ACI, 2019):

For the No. 8 rebar:

$$l_d = 0.6(3.25) f_y d_b / \left(65\lambda\sqrt{f_c'}\right) = 0.6(3.25)(80{,}000)(1.0) / \left[(65)(1)\sqrt{6{,}000}\right] = 35 \text{ in.}$$

For the No. 6 rebar:

$$l_d = 0.6(3.25) f_y d_b / \left(65\lambda\sqrt{f_c'}\right) = 0.6(3.25)(80{,}000)(0.75) / \left[(65)(1)\sqrt{6{,}000}\right] = 23 \text{ in.}$$

Transverse reinforcement design within the flexural yielding region

(a) Shear reinforcement requirement

The flexural yielding zone is defined as a length equal to the depth of each upper or lower beam, which is equivalent to half the overall depth of the entire DBCB (h/2). Based on the probable moment strength (M_{pr}) = 7,523 kip-in. obtained from spColumn software (StructurePoint, 2019) and the rebar tensile strength equivalent to 1.25 f_y (= 1.25×80 = 100 ksi), the probable design shear force (V_e) is calculated to determine the shear force (V_s) carried by the shear reinforcement of each beam.

$$V_e = \frac{2M_{pr}}{l_n} = \frac{2 \times 7{,}523}{96} = 157 \text{ kips}$$

The shear force (V_s) carried by shear reinforcement of each beam is calculated using the equation defined below, where strength reduction factor (ϕ) is 0.75. In accordance with ACI 18.6.5.2 (ACI, 2019), considering V_e > (V_u/2)/2 = 342.3/4 = 85.6 kips and neglecting the compressive force in the coupling beam, the contribution of concrete to the shear strength was ignored, namely, V_c = 0.

$$V_s = \frac{V_e}{\phi} - V_c = \frac{157}{0.75} - 0 = 209 \text{ kips}$$

This shear force corresponds to a shear force of $6.29\sqrt{f_c'}b_w d$ (in psi unit) or $0.52\sqrt{f_c'}b_w d$ (in MPa unit). Note that ACI 22.5.1.2 imposes an upper bound limit of $8\sqrt{f_c'}b_w d$ (in psi unit) or $0.67\sqrt{f_c'}b_w d$ (in MPa unit) for the shear force that can be carried by shear reinforcement in a beam. However, this limit was not applied in the DBCB specimen under consideration. This is because no severe diagonal concrete crushing was observed in the DBCB specimens even when the calculated V_s is much greater than $8\sqrt{f_c'}b_w d$.

The maximum leg spacing (s_{max}) across beam width of the shear reinforcement was determined according to ACI 9.7.6.2.2. For $V_s > 4\sqrt{f_c'}b_w d$ (= 209 kips > 133 kips):

s is lesser of $d/2$ and 12 in., or $s_{max\_w} = d/2 = 17.936/2 = 8.97$ in.

Note that according to ACI 9.7.6.2.2, the maximum spacing between the legs of shear reinforcement along the beam should be the lesser of $d/4$ and 12 in. if $V_s > 4\sqrt{f_c'}b_w d$. However, this requirement was not applied in this case, as the confinement requirement imposed a stricter spacing requirement.

Based on the beam width of 24 in. and the clear cover of 1.5 in, the spacing (20.5 in.) between legs (across width of the beam) is greater than 8.97 in. Therefore, two additional crossties are required across the width of the beam to satisfy $s_{max\_w} = 8.97$ in. These additional crossties also increase the shear strength. No. 4 rebar with Gr. 80 was used for the hoop and crosstie. Therefore,

$$s = \frac{A_v f_{yt} d}{V_s} = \frac{4 \times 0.2 \times 80 \times 17.936}{209} = 5.49 \text{ in.}$$

where A_v represents the total area of shear reinforcement within the spacing (s), while f_{yt} denotes the specified yield stress of the transverse reinforcement. Additionally, the value of d = 17.936 in. corresponds to the distance from the extreme compression fiber to the centroid of the longitudinal tension reinforcement in each of the upper or lower beams.

(b) Confinement requirement

The spacing of transverse reinforcement along the beam length should also meet the confinement requirement according to ACI 318 18.6.4.4 (ACI, 2019). Note that the requirement in ACI 18.6.4.4 is only applied over a length equal to half of overall DBCB depth ($h/2$) from both beam ends and a greater spacing is used $h/2$ (Fig. 6/2).

Within $h/2$ from both ends

s is lesser of $d/4$, 6 in., and $5 \times d_b$ for Grade 80 rebars.

Therefore, $s = d/4 = 17.936 / 4 = 4.48$ in. (governs)

Between $h/2$ and h from both ends

s is lesser of $d/3$, 6 in., and $5 \times d_b$ for Grade 80 rebars.

Therefore, $s = 5 \times d_b = 5 \times 1.128 = 5.64$ in. (governs)

where d_b is nominal diameter of the longitudinal rebars.

It should be noted that the final transverse spacing (s) is determined based on the more restrictive requirement between the confinement requirement and shear strength requirement (= 5.49 in.). Therefore, the spacing of the transverse reinforcement is determined by the confinement requirement of 4.48 in. within $h/2$ from both ends and the shear reinforcement requirement of 5.49 in. between $h/2$ and h from both ends. As a result, a spacing of 4 in. is used within $h/2$ from both ends to meet the confinement requirement. For ease of detailing, spacings of both 4.5 in. and 5 in. are employed between $h/2$ and h from both ends to satisfy the confinement requirement.

Transverse reinforcement design beyond *h*-distance

For the remaining middle length of the beam (= 12 in.), the design of transverse reinforcement is based on the shear strength requirement, 5.49 in. Therefore, a spacing of 5 in. is used for the remaining midspan.

Fig. D.4 (a) shows the reinforcement details of the 2.3 aspect ratio DBCB and Fig. D.4 (b) illustrates the cross-section details of the coupling beam. The first transverse reinforcement is located at 2 in. from the beam-to-wall interface according to ACI 18.6.4.4.

Minimum span-to-effective depth ratio of each individual beam

A minimum span-to-effective depth ratio of each individual beam should be checked to ensure that the UCS is large enough to allow the DBCB to separate (Choi and Chao, 2020):

$$\frac{l_n}{0.5(h-w)} \geq 5$$

$$\frac{l_n}{0.5(h-w)} = \frac{96}{0.5(42-4)} = 5.05 \geq 5 \quad \text{(O.K.)}$$

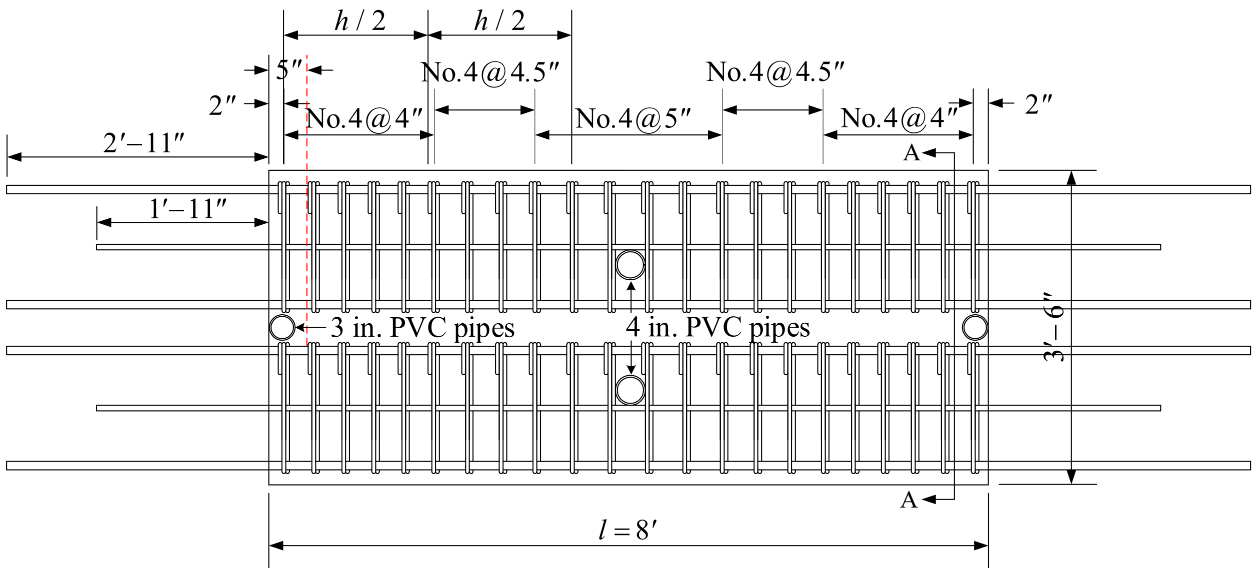

(a)

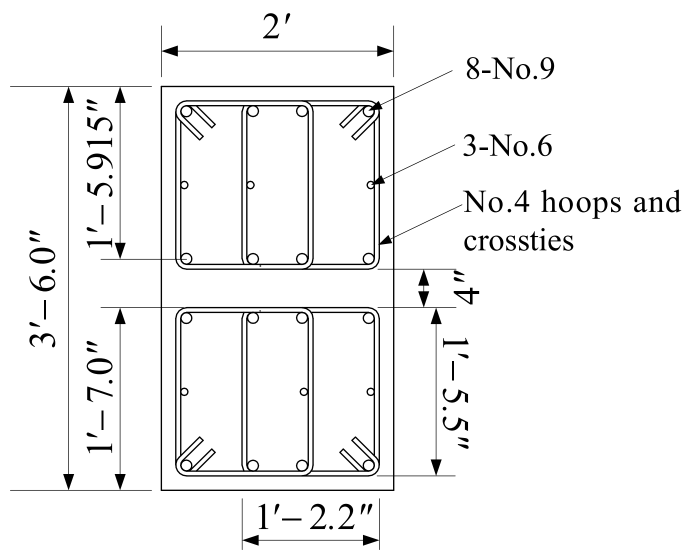

(b)

Fig. D.4 Reinforcement details of DBCB with 2.3 aspect ratio: (a) Longitudinal section (b) A-A cross-section

Design comparison between DBCB and DCB using two ACI detailing options

Fig. D.5 illustrates an example of a diagonally reinforced coupling beam (DCB) utilizing two ACI detailing options described in the "Design Guide on the ACI 318 Building Code Requirement for Structural Concrete" (CRSI, 2020). This DCB example has been designed with the same design shear force as the previously mentioned DBCB. As shown in Fig. D.5, two bundles of diagonal reinforcement comprising sixteen Grade 80 No. 10 bars are used within the DCB. In contrast, Fig. D.4 shows the design of the DBCB, where the primary longitudinal reinforcement consists of sixteen Grade 80 No. 9 bars and six Grade 80 No. 6 bars. Notably, the development length of the DBCB is 40% shorter than that of the DCB. Table D.1 provides a summary of the total weight of reinforcing bars utilized in the example designs of the DCBs and the DBCB. For the same required shear strength (V_u), the total weight of reinforcement in the DCBs is approximately 46% higher compared to that of the DBCB, as indicated in Table D.1.

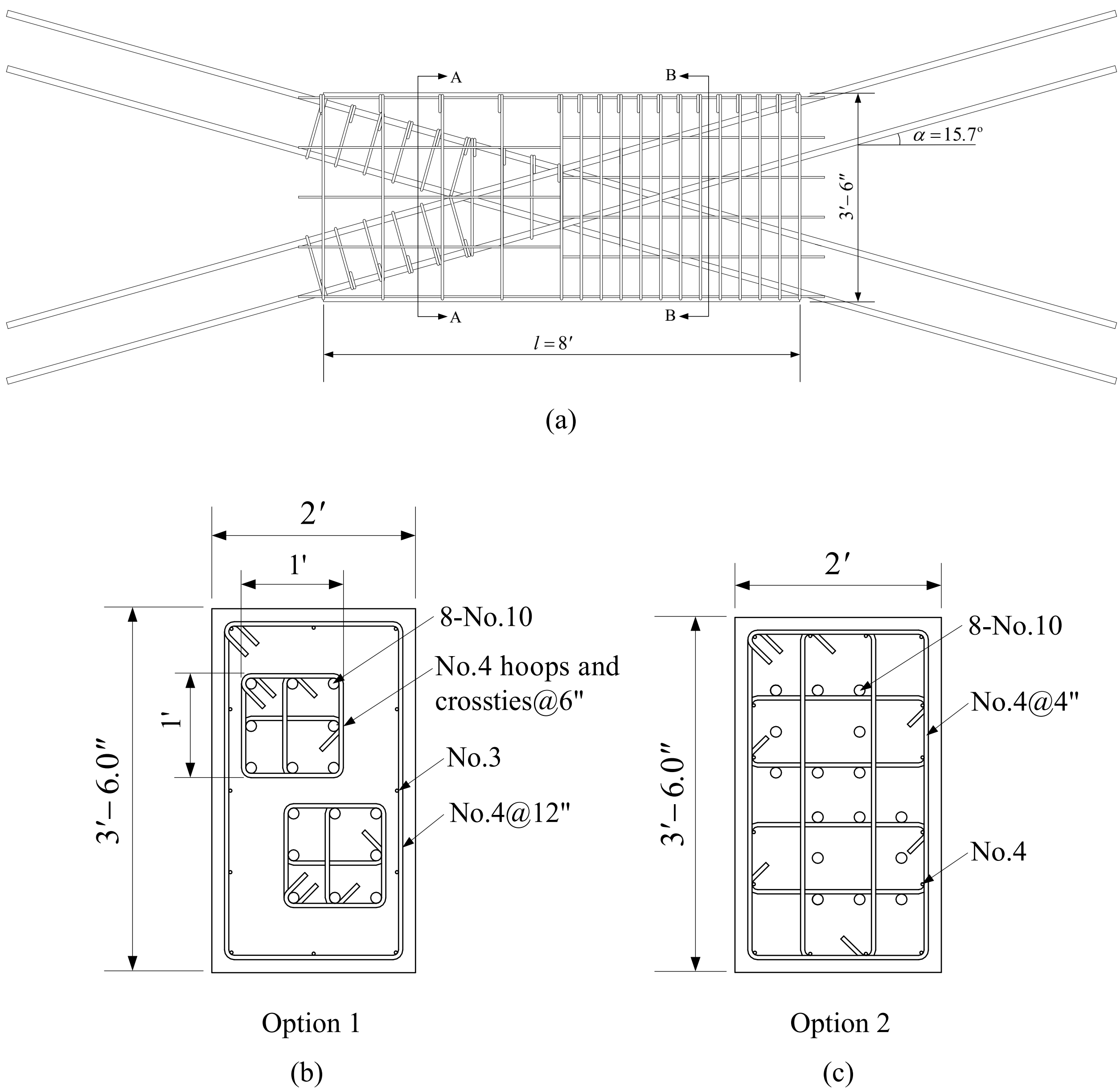

Fig. D.5 Reinforcement details of 2.3 aspect ratio DCB: (a) Longitudinal section (b) A-A cross-section (c) B-B cross-section

Table D.1 Design information and total weight of reinforcing bars

	Span-depth (aspect) ratio	V_u (kips)	$\phi\ V_n$ (kips)	Normalized nominal shear strength (psi) $\frac{V_n}{\sqrt{f_c'} A_{cw}}$	Total weight (lb)
DCB (option 1)	2.3	342.3	375.4	5.7	1,743
DCB (option 2)	2.3	342.3	375.4	5.7	1,810
DBCB	2.3	342.3	345.1	5.2	1,214